INVESTIGATIONS OF HEAT TRANSFER IN METAL-FOAM TUBES

A thesis submitted for the degree of

Doctor of Philosophy

by

Wei Lu

School of Engineering and Design

Brunel University

October 2008

Abstract

Nowadays metallic foams attract increasing attention in making compact heat exchangers due to its advanced thermal properties. In this project, the performance of forced convection and flow boiling heat transfer in metal-foam tubes has been investigated experimentally and theoretically. Compared to those of plain tubes, the research results reveal that the use of metal foam can significantly enhance heat transfer capabilities due to its strong fluid mixing capability and the high surface-area density.

In present study, the heat transfer performance and flow resistance of R134a vapour flow in metal-foam tubes have been measured. The results show that both the microstructure of metal foams and tube/foam attaching methods (contact thermal resistance) can significantly affect the heat transfer performance. Compared to plain tubes, the use of metal foams could improve the heat transfer by 5-15 times. To examine the effect of different tube/foam combining methods on heat transfer, a group of metal-foam tubes with different attaching methods have been tested experimentally.

Since no experimental result for two-phase heat transfer in metal foams can be found in the open literature despite their potential wide range applications, the boiling flow and heat transfer in horizontal metal-foam tubes are experimentally investigated. The results show that the two-phase flow resistance and heat transfer both increase as the pore size tends to be smaller for a given porosity. The boiling heat transfer will be enhanced by increasing the vapour quality for high mass flow rates, but it is not always true for low mass flow rates. This different heat transfer behaviour can be attributed to different flow patterns occurring inside the metal-foam tubes. The two-phase flow pattern can be indirectly inferred from the cross-sectional wall surface temperature fluctuations and the temperature difference between the wall surface and refrigerant fluid.

In addition to the experimental research, analytical and numerical investigations have been conducted to predict the heat transfer performance of forced convection and flow boiling heat transfer in these tubes. The effect of contact thermal resistance between the tube wall and metal foam structures was considered in the model. The results show that the overall thermal resistance of a metal-foam tube is a combination of the resistance of the metal-foam structure and the resistance between solid phase and fluid phase. The increase of relative density and the decrease of pore size of metal foams can reduce these resistances respectively. The thesis also reports the investigations of the effects of these parameters on enhancing the overall heat transfer performance. This was carried out through a detailed parametric analysis. The results show that the thermal performance of a metal-foam heat exchanger can be superior to that of conventional finned tube heat exchangers.

Statement of Copyright

Declaration

The work described in this thesis has not been previously submitted for a degree in this or any other university, and unless otherwise referenced it is the author's own work.

Publications for This PhD Research

- W. Lu, C.Y. Zhao and S.A. Tassou, Thermal analysis on metal-foam heat exchangers. Part I: Metal-foam pipes, *International Journal of Heat and Mass Transfer,* Volume 49, Issues 15-16, July 2006, Pages 2751-2761.

- C.Y. Zhao, W. Lu and S.A. Tassou, Thermal analysis on metal-foam heat exchangers. Part II: Tube heat exchangers, *International Journal of Heat and Mass Transfer,* Volume 49, Issues 15-16, July 2006, Pages 2762-2770.

- W. Lu, C.Y. Zhao, Z.Y. Xu and S.A. Tassou, The R134a Vapour Flow Heat Transfer In Horizontal Metal-Foam Tubes, *10th UK Heat Transfer Conference*, Edinburgh, 2007.

- C.Y. Zhao, W. Lu and S.A. Tassou, Experimental Investigations on Boiling Heat Transfer In Horizontal Metal-Foam Tubes, *10th UK Heat Transfer Conference*, Edinburgh, 2007.

- W. Lu and C.Y. Zhao, Numerical Modelling of Flow Boiling Heat Transfer In Horizontal Metal-Foam Tubes, *4th International Conference on Diffusion in Solids and Liquids, 2008.*

Acknowledgements

I would like to thank my supervisors, Dr. Changying Zhao and Prof. Savvas Tassou, for their invaluable assistance, advice, support, and inspiration during this programme of research.

I would like to thank UK Engineering and Physical Sciences Research Council (EPSRC grant number: GR/T24364/01) to provide fund for the project, Brunel University (Brief Award, WAE-DPA301) for supporting me, and I also wish to thank the assistance of Mr. Ian Stirling, Porvair Plc., for providing the test samples.

I would also like to thank the staff in Brunel University for their valuable and kind help. To name a few: Dr Zeyuan Xu, Dr Richad Watkins.

On a more personal note, special thank is also given to my husband, Qin Deng, for his unrelenting support.

Contents

List of Figures

List of Tables

Nomenclature

ã	Surface area density, m^{-1}
A_c	Cross-section area of test tube, m^2
A_i	Inner surface area of the test tube, m^2
C_D	Thermal dispersion coefficient
c_p	Heat capacity of fluid, J/kg K
d	Tube diameter, m
Da	Darcy number, K/R^2
d_f	Diameter of the fibre of metal foams, m
d_p	Pore size, m
f	Friction factor, $f = \frac{\Delta P d}{L \cdot \frac{1}{2} \rho u^2}$
F_I	Inertial variable
Fr	Froude number, $Fr = G^2 / (\rho_l^2 g D)$
g	Acceleration of gravity, 9.8 m/ s^2
G	Mass flux, Kg/ m^2 s
h	Heat transfer coefficient, $W/m^2 K$
h_{be}	Effective boiling heat transfer coefficient, $W/m^2 K$
h_c	Convective Heat transfer coefficient, $W/m^2 K$
h_{nb}	Heat transfer coefficient for nucleate boiling, $W/m^2 K$
h_i	Heat transfer coefficient for inner pipe, $W/m^2 K$
h_o	Heat transfer coefficient for annular channel, $W/m^2 K$
h_{sf}	Interfacial heat-transfer coefficient, $W/m^2 K$
J	Efficient index, J=Nu/f
k	Thermal conductivity, W/m K
k_d	Thermal dispersion conductivity, W/m K
k_e	Effective thermal conductivity, W/m K
k_f	Thermal conductivity of fluid, W/m K
k_{fe}	Effective thermal conductivity of fluid, W/m K

k_s	Thermal conductivity of solid, W/m K
k_{se}	Effective thermal conductivity of solid, W/m K
K	Permeability, m^2
L	Length, m
$\dot{m}$	Mass flow rate, Kg/s
M	Molecular weight
Nu	Nusselt Number, $Nu=2hR/k_f$
Nu_{sf}	Local Nusselt Number, $Nu_{sf}=h_{sf}d_p/k_f$
p	Pressure, Pa
P_{crit}	Critical pressure, Pa
ΔP	Pressure difference (Pa)
Pr	Prandtl number, $Pr=c_p\mu_f/k$
q	Heat flux, W/m
q_w	Heat flux, W/m^2
Q	Power, W
r	Radius, m
R	Inner radius of inner pipe, m
R_1	Outer radius of inner pipe, m
R_2	Inner radius of outer pipe, m
Re	Reynolds number, $Re=2uR/\upsilon$
Re_l	Local Reynolds number, $Re_l=ud_l/\upsilon$
T	Temperature, K
ΔT	Temperature difference, K
T_{in}	Inlet fluid temperature, K
U	Velocity along z direction, V_z, m/s
u_m	Mean fluid velocity along z direction, m/s
U	Dimensionless velocity along z direction, u/u_m
U_i	Overall heat-transfer coefficient based on the inside area of the tube, $W/m^2 K$
$\vec{V}$	Velocity vector
x	Vapour quality
x_{IA}	Vapour quality to separate the intermittent flow and annular flow

We	Weber number, We= $G^2 D/(\rho_l \sigma_l)$

Greek symbols

δ	Thickness, m
ε	Porosity
ε_V	vapour void fraction
θ	Dimensionless temperature, $\theta = \dfrac{T - T_w}{q_w R / k_{se}}$
θ_{dry}	Dry angle, radian
θ_{strat}	Dry angle in stratified flow, radian
σ	Surface tension, N/m
ρ	Density, Kg/m^3
μ	Viscosity of fluid, Pa·s
υ	Kinematic viscosity (m^2/s)
ω	Radian coordinate
ψ	Dimensionless radial coordinate, ψ = r/R

Subscripts

f	Fluid
l	Liquid
s	Solid
v	Vapour
W	Wall

Others

Σ	Sum
$< >$	Volume averaged value
∇	Total differential
∂	Partial differential

Chapter 1 Introduction

Recently, the use of high porosity metal foams has spread to a wide range of applications, such as aircraft wing structures in the aerospace industry, catalytic surfaces for chemical reactions, core structures for high strength panels, and containment matrices and burn rate enhancers for solid propellants (Stone et al., 1998, Bhattacharya et al., 2002). As a new kind of material, metal foams with their novel properties are attracting increasing attention. The advantages of metal foams lie on their low-density, large surface area in a limited volume and high-strength structure. Due to the high surface-area density and strong mixing capability for the fluid, open-cell metal foams are now regarded as one of the most promising materials for the manufacturing of efficient compact heat exchangers.

In this section, the researches on structure of metal foams and metal-foam tubes, the principle of two-phase flow and heat transfer and the background of modelling work are introduced to present a clear picture for the research.

1.1 Metal foams

Recent developments in processing technology have led to a range of novel lightweight materials for structural, thermal, acoustic and other engineering applications. A family of such materials, which is very promising for thermal management applications where a large amount of heat needs to be transported over a small volume, is high porosity open-cell metal foams. The structure of these foams is shown in Fig.1.1. The microstructure of typical metal foam consists of ligaments forming a network of inter-connected dodecahedral-like cells.

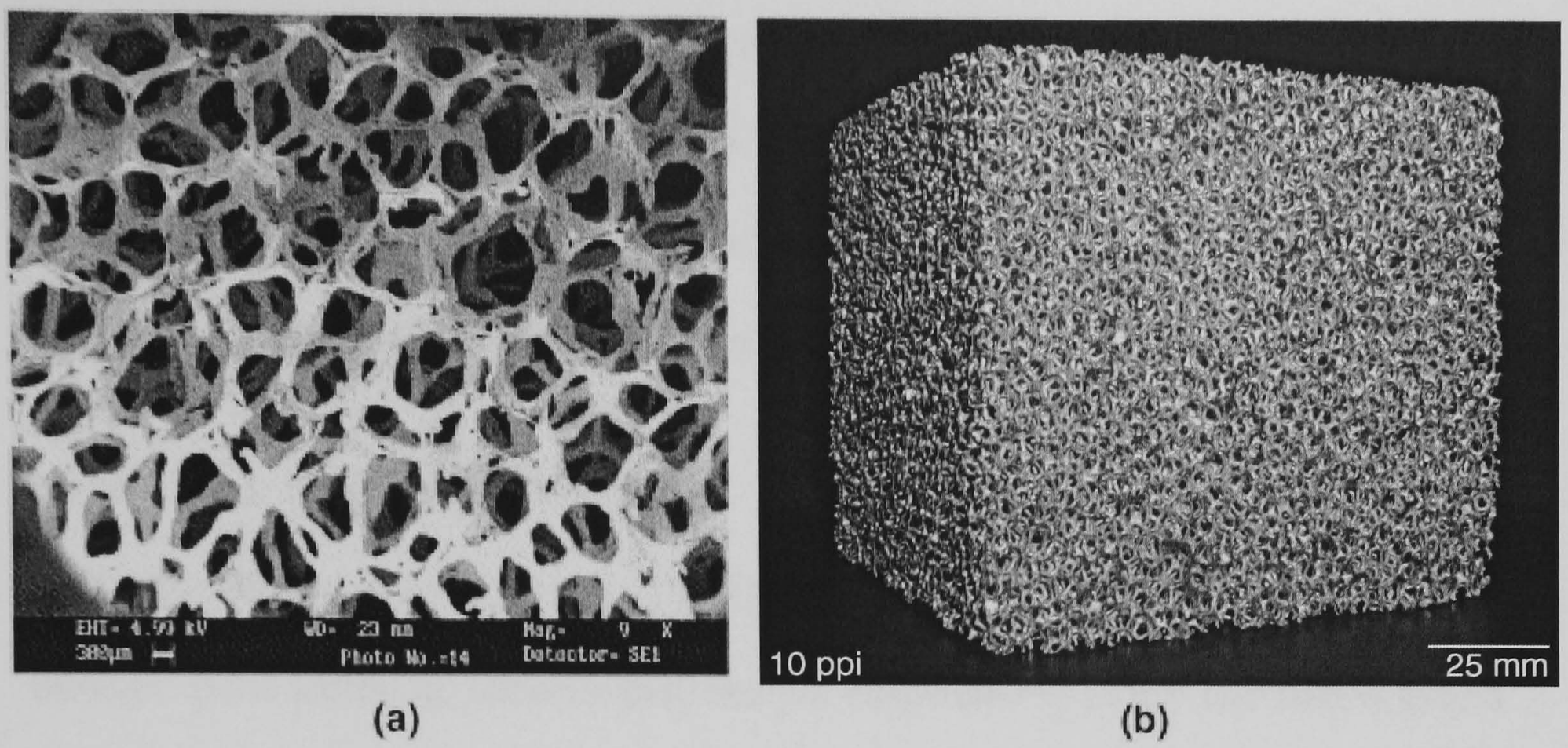

(a) (b)

Fig. 1.1 Metal foams: (a) cellular morphology of typical Porvair metal foam (Zhao, 2001), (b) A piece of metal foam sample.

The cells are randomly oriented, and mostly homogeneous in size and shape. To specify the characters of foam material, two independent foam variables, pore size and relative density, are generally used. The pore size (pore density) is the determinant parameter for foam characteristics. The cells of metal foam are generally 12 to 14 sided polyhedra whose pentagonal or hexagonal faces are formed by five or six ligaments (ERG, c2000). The open window in each of these faces defines the pore diameter and is expressed in terms of pores per linear inch (PPI). The range of standard pore density is 5-60 PPI. Higher pore density means larger surface area in unit volume. Metal foams provide a high surface area to volume ratio (500 ~ 10000 m^2/m^3) as well as an enhanced flow mixing due to their tortuosity of the fluid passages. The other foam variable, relative density, defines the volume of foam material relative to the volume of material in a solid block of the base material. When we account void volume, porosity (1- relative density) is used to specify the metal foams. As porosity is decreased, the ligaments become larger in diameter and stronger and then the strength of the foam structure is increased. Porosity is the

primary determinant of foam stiffness, strength, electrical conductivity and thermal conductivity. It can vary from 85% to 97%. Metal foams have attractive stiffness/strength properties. Furthermore, metallic foams can be processed in large quantities at low cost via the metal sintering route.

Metal foams have been manufactured for many years using a variety of novel techniques. Metal sintering is one of them to create open cell foams. In foam creation through metal sintering, metallic particles are suspended in slurry and coated over a polymeric foam substrate. The foam skeleton vaporizes during heat treatment and the metallic particles sinter together to create the product. Compared to other techniques, such as molten metal infiltration, chemical vapour decomposition, metal sintering method is thought to be the most cost-effective method and the most amenable to mass production. (Zhao et al., 2001)

The development of the metal sintering method for foam manufacture has led to decreasing manufacturing costs and an increasing interest in the study of the thermal and transport phenomena in high porosity open-cell metal foams. Calmidi and Mahajan (1999) measured the effective thermal conductivity of aluminum ERG foams by using both air and water as the fluid phase. The measurement was conducted at low temperatures, so the thermal radiation effect is neglected. An analytical model was also derived by Calmidi and Mahajan (1999) based on the two-dimensional hexagonal structure of the metal foam. As an extension of the Calmidi and Mahajan's work, Boomsma and Poulikakos (2001 a) proposed an effective thermal conductivity model based on a three-dimensional idealized cellular structure of a metal foam, and a good agreement with the test data (Calmidi and Mahajan, 1999) has been achieved. Zhao et al. (2004 c) measured the thermal conductivities of

steel alloy (FeCrAlY) foams under a range of temperatures 50-500 °C. The study showed that the thermal radiation plays a significant role on effective thermal conductivity at high temperatures. Also to examine the thermal radiation mechanism in metal foams, Zhao et al. (2004 b) conducted the spectral transmittance and reflectance measurements, from which the spectral extinction coefficient was deduced. An analytical model was also built based on the Rosseland diffusion equation and the metal foam microstructures in that paper (Zhao et al., 2004 b).

1.2 Complex assembly: tubes filled with metal foams

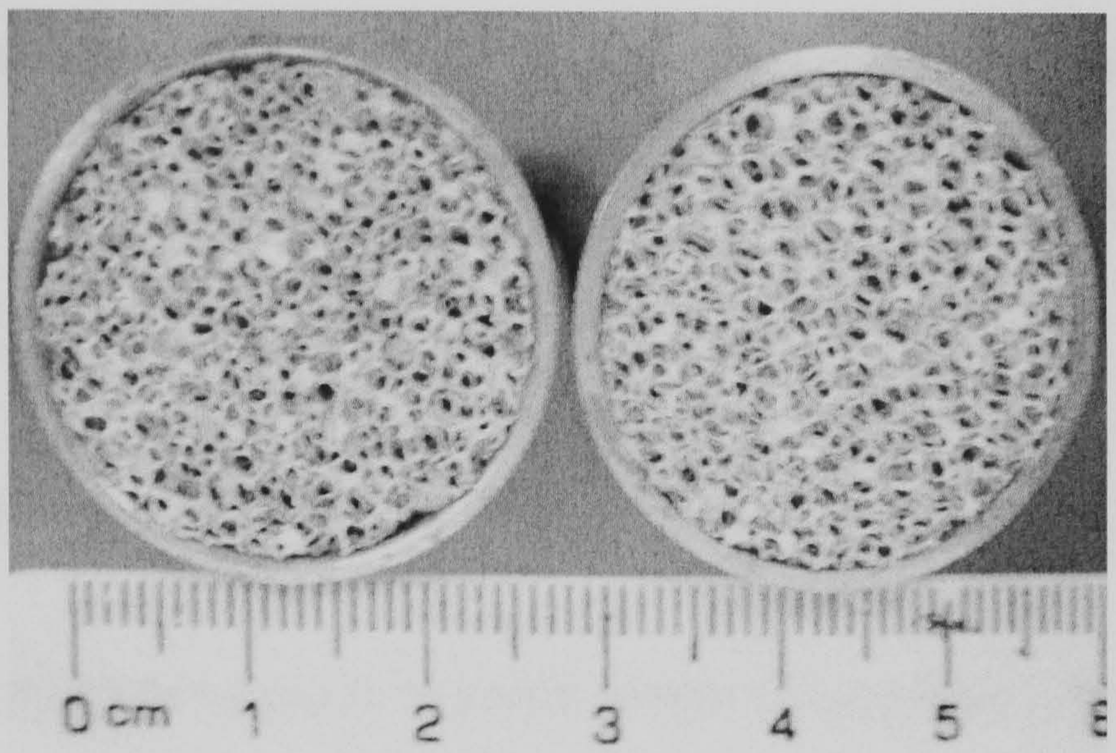

Fig.1.2 Metal-foam filled tubes

To effectively use metal-foam materials in heat exchange devices, it is necessary to combine the material with tubes or sheets for flow separation and heat transfer. Development efforts have been made at Porvair Advance Materials to successfully combine a variety of metal-foam materials with solid structures. Fig.1.2 shows an example of metal-foam tubes manufactured through a proper co-sintering technique. Metallic particles are used as welding materials and put between metal foams and tubes. Then these tubes are placed into furnace and the metallic particles will be sintered to connect the tubes and metal foams together. However, the conventional combination methods, (e.g. brazing, soldering, welding and crimping) can not solve the problem of gaps created between metal foams and the tube because the shrinkage occurs in the foam whereas little or no shrinkage occurs in the metal tube. These

gaps will reduce the heat transfer efficiency. Porvair Advance Materials has successfully combined a variety of metal foam materials with solid structure, which overcome the problem resulting from shrinkage. (Haack, et al., 2004) In order to make a metal-foam tube, a metal tube are powdered with metal composition, while the same or different powdered composition are used to coat a polymeric foam which is placed in contact with the powdered tube to form a composite. The composite is placed into furnace and sintered. The polymeric foam is volatilized and the metal foam which has good bond with the powdered tube wall is formed by the heat treatment. The problem of gaps can be eliminated by allowing the tube to shrink along with the metal foam for the co-formed metal-foam tube.

1.3 Mechanism of enhancing heat transfer with metal foams

The Fig. 1.3 shows the heat transfer taking place in metal foams (Zhao, 2003). For single phase flow (forced convection) in metal-foam tubes, their heat transfer performance is expected to be enhanced enormously due to the novel properties of open-cell metal foams, which have high surface-area density and strong mixing capability for the fluid.

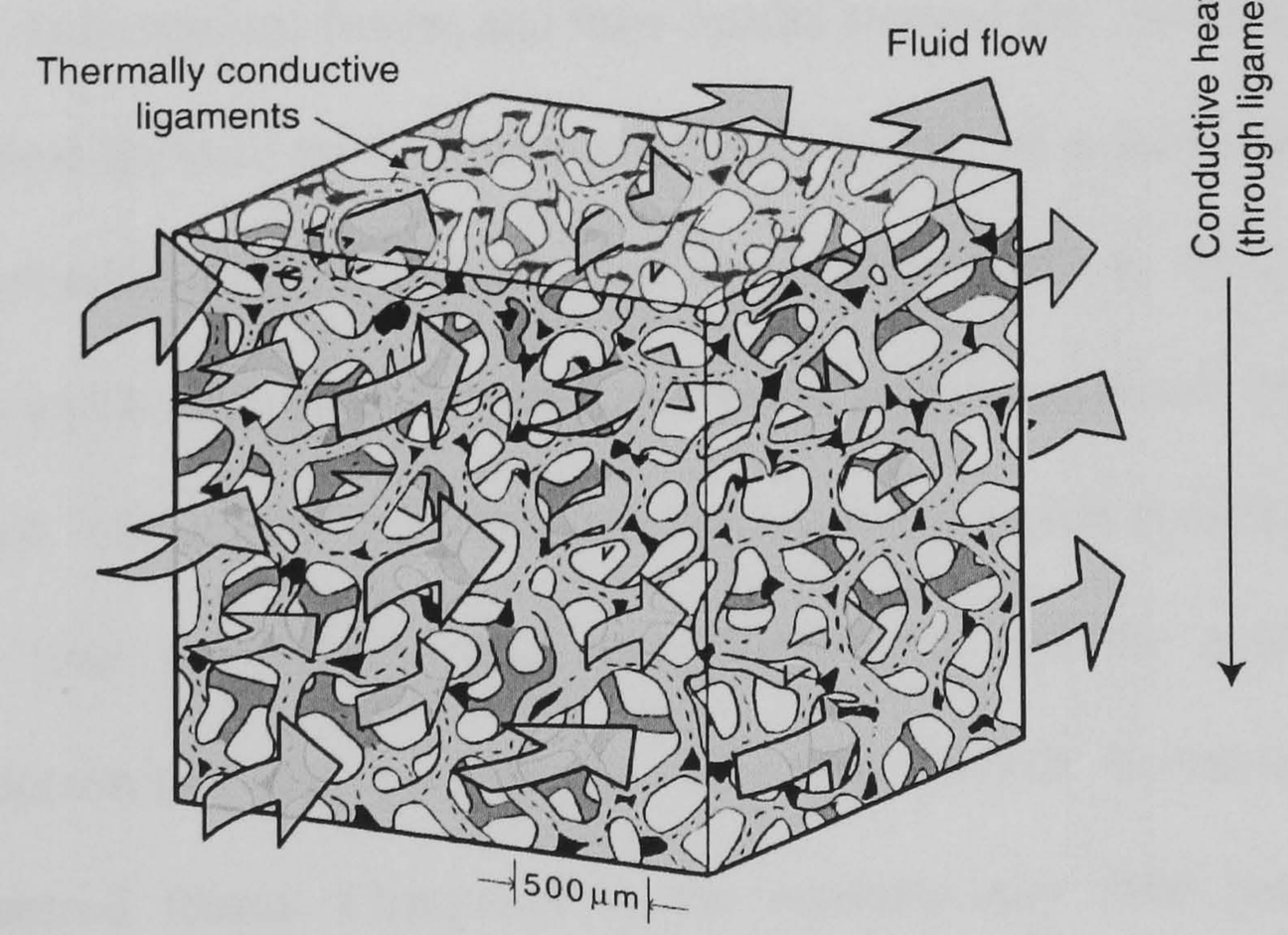

Fig.1.3 A diagram of forced convection in metal foams

For forced convections in metal foams, Hunt and Tien (1988) studied the effects of thermal dispersion on forced convection in metal foams with water as the fluid phase. Lee et al. (1993) investigated the application of metal foams as high-performance air-cooled heat sinks in electronics packaging. In their experimental study, they demonstrated that aluminium foams could dissipate heat fluxes up to 100 W/cm^2. Using the fin approach, Lu et al. (1998) have developed an analytical model to predict the metal foam-assisted heat transfer, where foam is modelled as inter-connected cylinders. Bastarows et al. (1998) studied the single-sided heating of a foam-filled channel for electronics cooling applications. The test results showed that brazed foam materials are much more effective at heat removal than epoxy-bonded samples, and the heat exchange performance is three times more efficient compared to a conventional fin-pin array. Calmidi and Mahajan (2000) conducted an experimental and numerical investigation on the forced convection in ERG aluminium foams with air as the fluid phase. Kim et al. (2000, 2001) experimentally studied the heat transport in aluminium foams, and their results showed that the foam material offers a better heat transfer performance compared to that of a louvered array, but at a greater pressure drop. Boomsma and Poulikakos (2001 b, 2002) studied the pressure drop and heat transfer for the compressed aluminium foams by using water as the coolant. The results indicated that the pre-compression porosity has little effect on the final permeability and foam coefficient, and the post-compression porosity determines the permeability and the overall hydraulic behaviour of the compressed foams. Compared to the commercially used heat exchangers, the metal foam heat exchangers demonstrated a favourable thermal resistance reduction, and hence a better heat transfer performance. The convective heat transfer and friction drag in a duct inserted with aluminium foams have been

experimentally studied by Hwang et al. (2002). Their results suggested that both the friction factor and the volumetric heat transfer coefficient have increased with decreasing foam porosity at a fixed Reynolds number. Bhattacharya et al. (2002) investigated the permeability and inertial coefficient of aluminium foam samples of different porosities and pore sizes. Based on comprehensive analytical and experimental investigations, they determined the thermo-physical properties of high porosity metal foams, such as effective thermal conductivity (k_e), permeability (K) etc. In their model, a parameter of tortuosity was introduced, and the predictions give very good agreements with the experimental data. Zhao et al. (2004 a) performed an experimental and numerical study on the forced convection in FeCrAlY and copper foams filled plate channels, in this study the effect of metal-foam microstructures (foam porosity and cell size) on heat transfer was examined. The natural convections in metal foams have been investigated by Zhao et al. (2005) and Phanikumar and Mahajan (2002). Both results showed that the natural convection takes place in a global domain rather than in a single cell, and thereby leading to high heat transfer capability.

For flow boiling in metal-foam tubes, the metal foam provides more active cavities for nucleate boiling to enhance boiling heat transfer. The large surface area density of metal foams enhances both boiling heat transfer and forced convection heat transfer. The metal foams make the liquid phase distribution flatter, which increases the wet area for wavy flow and reduces the possibility of partial dry-out for annular flow, i.e. the partial dry-out will appear in higher vapour quality.

Although, as indicated above, some investigations of heat transport in open-cell metal foams have been carried out, the work was mainly concentrated on metal-foam

plate channels. No research has been presented, as yet, in the open literature on metal-foam tubes and associated heat exchangers which have great potentials in industry. Furthermore, no research has been performed for heat transfer of two-phase flow in metal foams, even the mechanism of two-phase flow and heat transfer in plain tubes is not much clear (Huo, 2004). In order to take advantage of metal foams and make it widely used for civil needs, e.g. increasing the efficiency of heat transfer in refrigeration system and processing system, the heat transfer performance of flow boiling heat transfer in metal-foam tubes must be studied. The application of metal-foam in refrigeration system and mechanism of boiling heat transfer will be introduced in the following section.

1.4 The application of metal-foam tubes in refrigeration system

Refrigeration and air-conditioning systems are used to transfer energy from a lower temperature to a higher temperature and are widely used for air conditioning and process cooling. An ideal refrigeration cycle is shown in Fig.1.4 (a) (Moran and Shapiro, 2000). The compressor pumps refrigerant vapour from a relative low suction pressure to a higher pressure with temperature increase. Then the vapour with high pressure and high temperature passes though the condenser and is cooled until it becomes saturated liquid. The high pressure, saturated liquid is throttled down to a lower pressure when it passes through an expansion valve. This drop in pressure is accompanied by a drop in temperature so that the refrigerant enters the evaporator, which is placed in the heat source area, as low pressure low temperature mixture of liquid and vapour. Finally, the refrigerant passes through the evaporator where it draws heat from the heat source area, changes state to a vapour and enters the compressor for the repetition of the cycle.

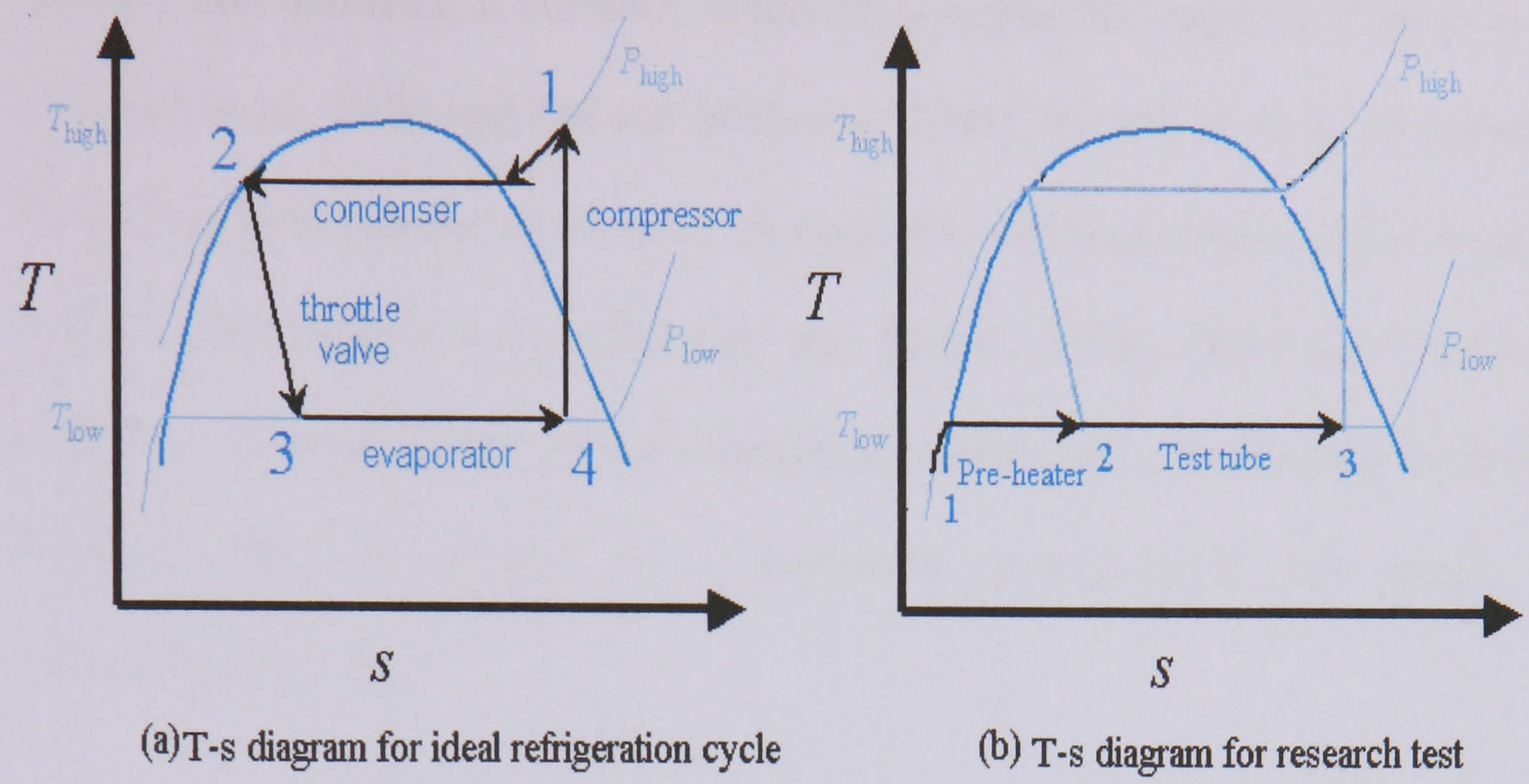

(a)T-s diagram for ideal refrigeration cycle (b) T-s diagram for research test

Fig. 1.4 T-s diagram for (a) refrigeration cycle and (b) research process in this project

Because the large thermal energy is required to change a liquid to a vapour, the refrigeration system can remove significant amount of heat out of heat source area. And the isothermal nature of the vaporization allows extraction of heat without raising the temperature of the working fluid to the temperature of whatever is being cooled. This is a benefit because the closer the working fluid temperature approaches that of the surroundings, the lower the rate of heat transfer. The isothermal process allows the fastest rate of heat transfer.

In UK, 17% of total electricity consumption is on cooling. As discussed above, the heat exchange takes place in the evaporator and condenser of refrigeration and air-conditioning systems. The efficiency of refrigeration systems can be improved by increasing the effectiveness of the evaporator and condenser. The performance of evaporator coils can be improved through heat transfer enhancement on the air side and refrigerant side. In an attempt to improve the refrigerant side heat transfer coefficient, research on evaporation/boiling heat transfer in small inner diameter tubes (<3 mm), which have larger surface-to-volume ratio than conventional tubes

above 5 mm diameter, is currently receiving considerable attention (Yen et al., 2003, Feldman et al., 2000 and Qu and Mudawar, 2003). Results to date have shown that the boiling heat transfer coefficient for small micro-finned tubes can be twice that of smooth conventional tubes (Browne and Bansal, 1999). This can lead to more compacted heat exchangers but at considerable additional complexities in design (for example flow distribution in a multi-tube arrangement) and much higher manufacturing costs.

Compared to micro tubes, metal-foam tubes of much larger diameter can offer larger surface area densities and can provide more boiling/condensation sites to increase two-phase heat transfer coefficients, so they could be used in the design of highly compact and inexpensive heat exchangers. The development of two-phase metal foam heat exchangers, however, requires an understanding of the underlying evaporation/boiling and condensation heat transfer mechanisms in metal foams. This study will focus on evaporation/boiling heat transfer in metal-foam heat exchangers (Process 2-3 in Fig.1.4 (b)). The condensation in a meat-foam tube or outside a tube attached with metal foams can be studied in future work.

1.5 Boiling heat transfer mechanism

In previous work, Zhao (2004a, b) and Lu et al. (2006) conducted fundamental investigations with numerical and analytical studies on single-phase thermal transport in metal foams. For forced convection with air as the coolant, the heat transfer performance of metal foams was found to be much better than current commonly used louvered fins. Although single-phase forced convection in metal foams has been studied to some extent, to the knowledge of the applicant, no work

has been done on two-phase flow (a boiling flow composed of a mixture of liquid and vapour) and heat transfer. Therefore, in order to analyze the mechanism of flow boiling heat transfer in metal-foam tubes, the mechanism of pooling boiling, flow boiling and the factors effected on enhanced boiling heat transfer have been reviewed.

a) Mechanism of pool boiling heat transfer (e.g. nucleate boiling heat transfer)

The pooling boiling includes nucleate boiling, transition boiling and film boiling. For the condition of this research (low heat flux and high heat transfer coefficient), the nucleate boiling is the main issue to investigate.

From the heat transfer point of view, the nucleate boiling heat transfer is controlled by the following three heat transfer mechanisms (Shi et al., 1995):

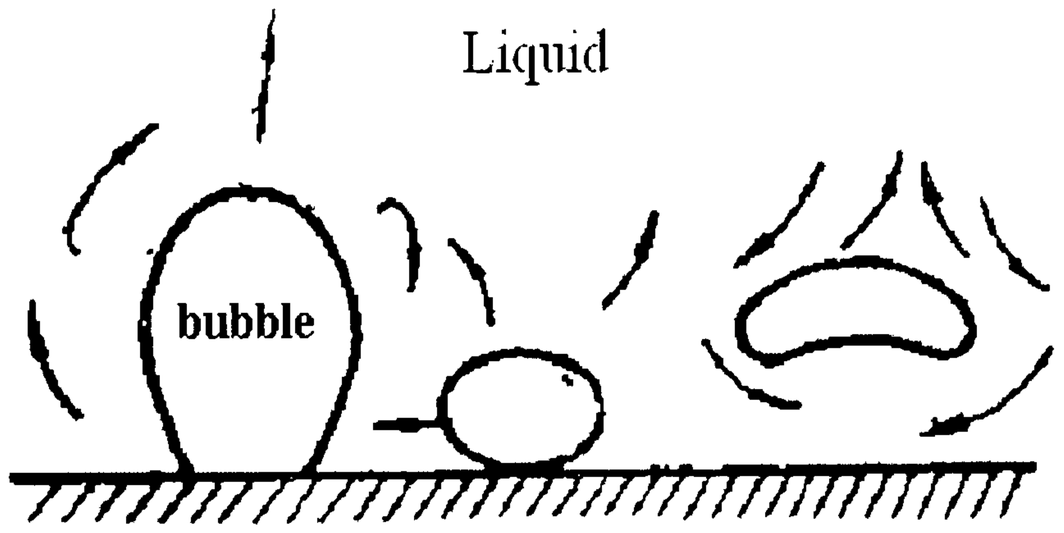

Fig.1.5 Bubble agitation mechanism

- Bubble agitation mechanism (Thome, 2004): the motions of bubbles enhance the convection heat transfer between the heated wall and liquid, shown as Fig.1.5. Forming, growing and departing bubbles induce intense convection in the liquid adjacent to the heated wall, which make the heat transfer performance of pool boiling much higher than that of natural convection.
- Vapour-liquid exchange mechanism (Forster and Grelf, 1950): As shown in Fig.1.6, the growing bubbles push the superheated liquid layer on the heated wall away from the heated surface, and after they departed from the surface, the cold

liquid in bulk area replaces the space occupied by the bubbles and then will be heated into superheated liquid and wait for the forming of next generation of bubbles. Sensible heat is transported away by the cyclic exchange of hot liquid – vapour – cold liquid. The density of active boiling sites, the frequency of depart bubbles and their influence area play important roles in this mechanism because it works only when the bubbles depart from the heated surface. When the heat flux increases to some extent and the bubbles generate continually, the cold liquid has less chance to reach the heated surface, the boiling heat transfer performance weakens. These help us to understand the phenomenon of departure from nucleate boiling (DNB).

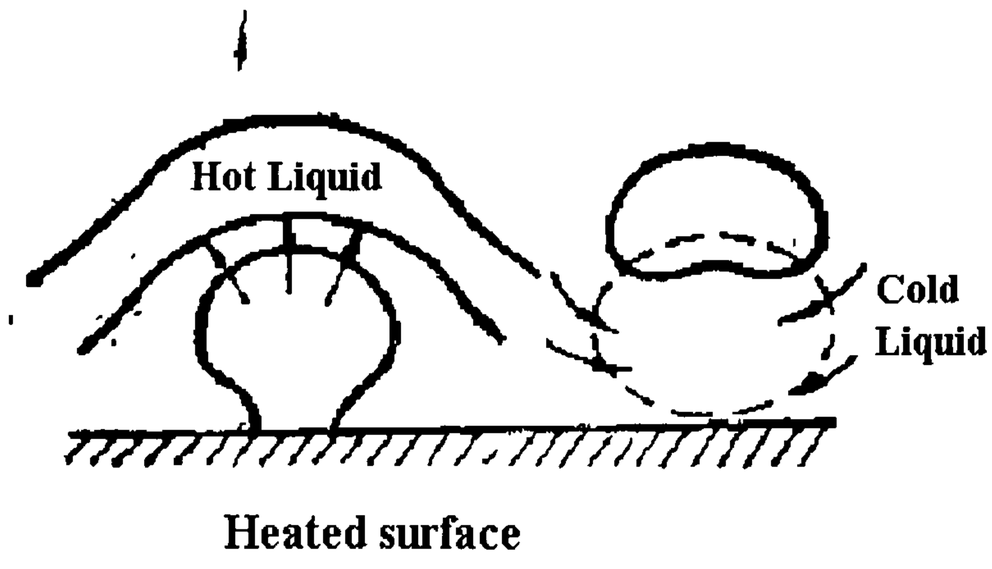

Fig.1.6 Vapour-liquid exchange mechanism

- Evaporation mechanism: Snyder (1956) indicated that there is a thin layer of liquid trapped between a rapidly growing bubble and the surface, as shown in Fig.1.7. In the process of bubble growing, micro-evaporation occurs in the thin liquid layer and large quantity of energy has been absorbed as latent heat by the bubble. Since the bubbles raise much faster than liquid natural convection currents and contain a large amount of energy, this is a very efficient heat transfer mechanism. More and Mesler (1961) used

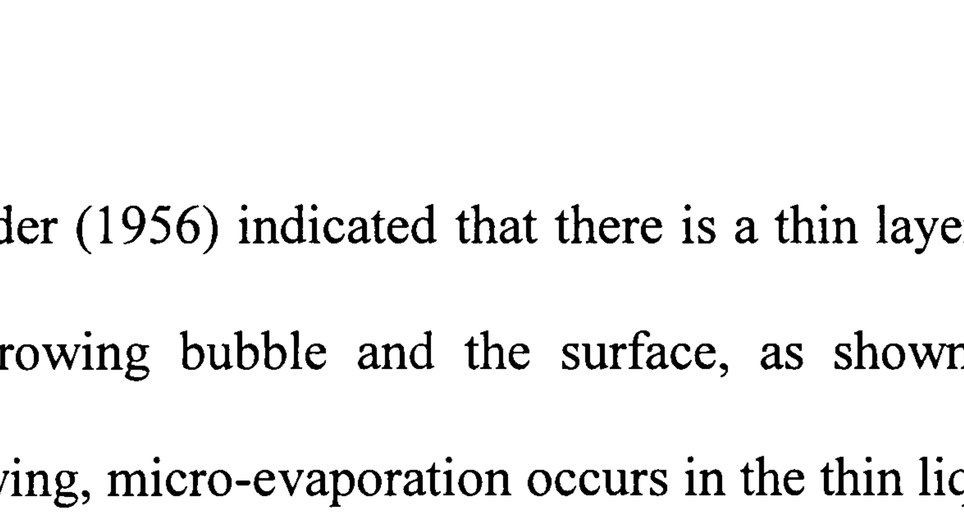

Fig.1.7 Evaporation mechanism

micro-thermocouple to measure the local temperature of the heated surface beneath a growing bubble in pool nucleate boiling. They found that the wall temperature decreased suddenly with rapidly growing bubble (10°C with in 2ms), which can only be caused by evaporation, and then increased while the liquid layer dries out. Tests done by Hospell and Mesler (1964) and Sharp (1964) also proved the existence of a thin liquid layer and the thickness of the thin liquid layer they measured is between 0.5~2.5μm.

The above three mechanisms are not mutually exclusive, and each is competing for the same heat. According to this analysis, the generation of bubbles plays the main role in nucleate boiling heat transfer. Therefore, the number of active cavities where bubbles can form and depart is the most important issue for pool boiling. The main factors which have significant effects on the number of active sites are analyzed as following. The Fig.1.8 represents the size of active cavities in heterogeneous boiling, in which the liquid temperature in boundary layer has been regard as linear distribution and c_1 and c_2 are coefficients depended on angle θ. From this figure, it can be seen that the size of active sites which can generate bubbles continuously in pool boiling depends on the wall temperature (or heat flux). Because the bubble can only become larger when it can absorb heat from outside, i.e., the temperature of superheated liquid T_L is higher than the temperature at top of bubble T_b. Therefore, the bubbles size y_b is between y_{min} and y_{max} and their cavities are active in case 2, but there is no active site in case 1. From this figure, it is clear that higher wall temperature leads to wider size range of active sites. So when the heat flux increases, the number of cavities which can form bubbles increases, then, leads to enhancement of pool boiling heat transfer performance. That means the pool boiling heat transfer

coefficient is a function of heat flux, as the heat flux is increased, more and more nucleation sites become activated. In a word, the main factors which have significant effects on the number of active sites are surface conditions, fluid properties and heat flux.

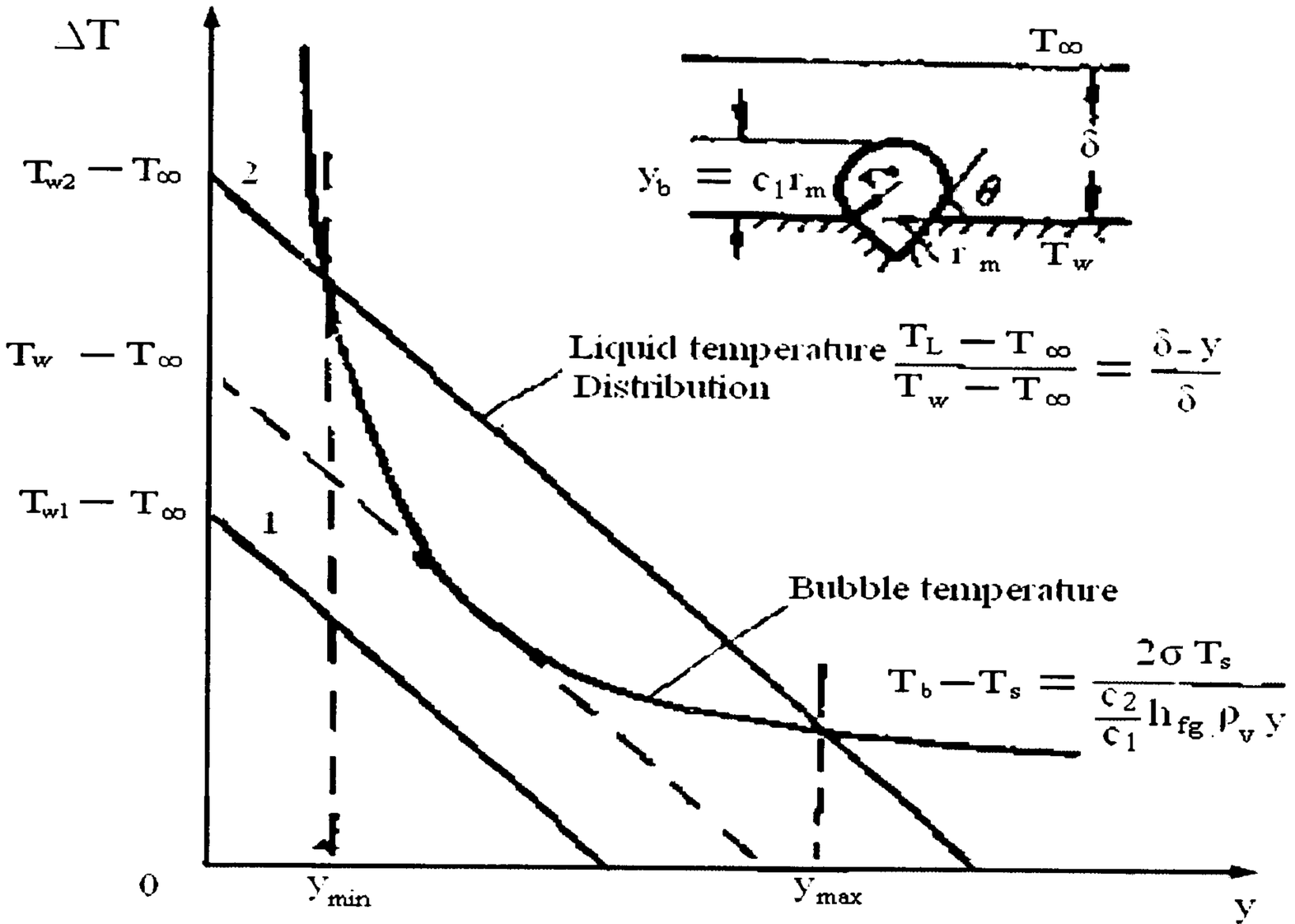

Fig. 1.8 Effect of wall temperature on size of active sites in pooling boiling (Hsu and Graham, 1976)

Considering the effect of pressure on heat transfer coefficient, the nucleate boiling heat transfer coefficient increases with the increase of pressure because the properties of fluid changed with the pressure and the variation of pressure also influences the mechanism of growth and departure of the bubbles. In addition, the factors which influence the evaporation, such as molecular weight, the temperature difference

between heated wall and saturated bulk liquid, will influence the pooling heat transfer too.

b) Flow patterns for flow boiling

Two-phase flow is more complex because it is a mixer of two phases, the gas and liquid. For two-phase flows, where the heating surface is the channel wall confining the flow, it is widely accepted that the boiling heat transfer is governed by two mechanisms: nucleate boiling and forced convection boiling (Qu and Mudawar, 2003). In the nucleate boiling dominant region, liquid near the heated channel wall is superheated to a sufficient degree to sustain the nucleation and growth of vapour bubbles. The nucleate boiling heat transfer coefficient is dependent on heat flux, but generally is far less sensitive to mass velocity and vapour quality. In forced convection boiling, however, there is a suppression of bubble nucleation along the heated wall, so the heat is transferred mainly by single-phase convection through the thin annular liquid film. The convective boiling heat transfer coefficient is dependent on mass velocity and vapour quality, but is fairly independent of heat flux. Nucleate boiling in plain tubes is normally associated with the bubbly and slug flow patterns, and forced convection boiling is more related to the annular flow pattern.

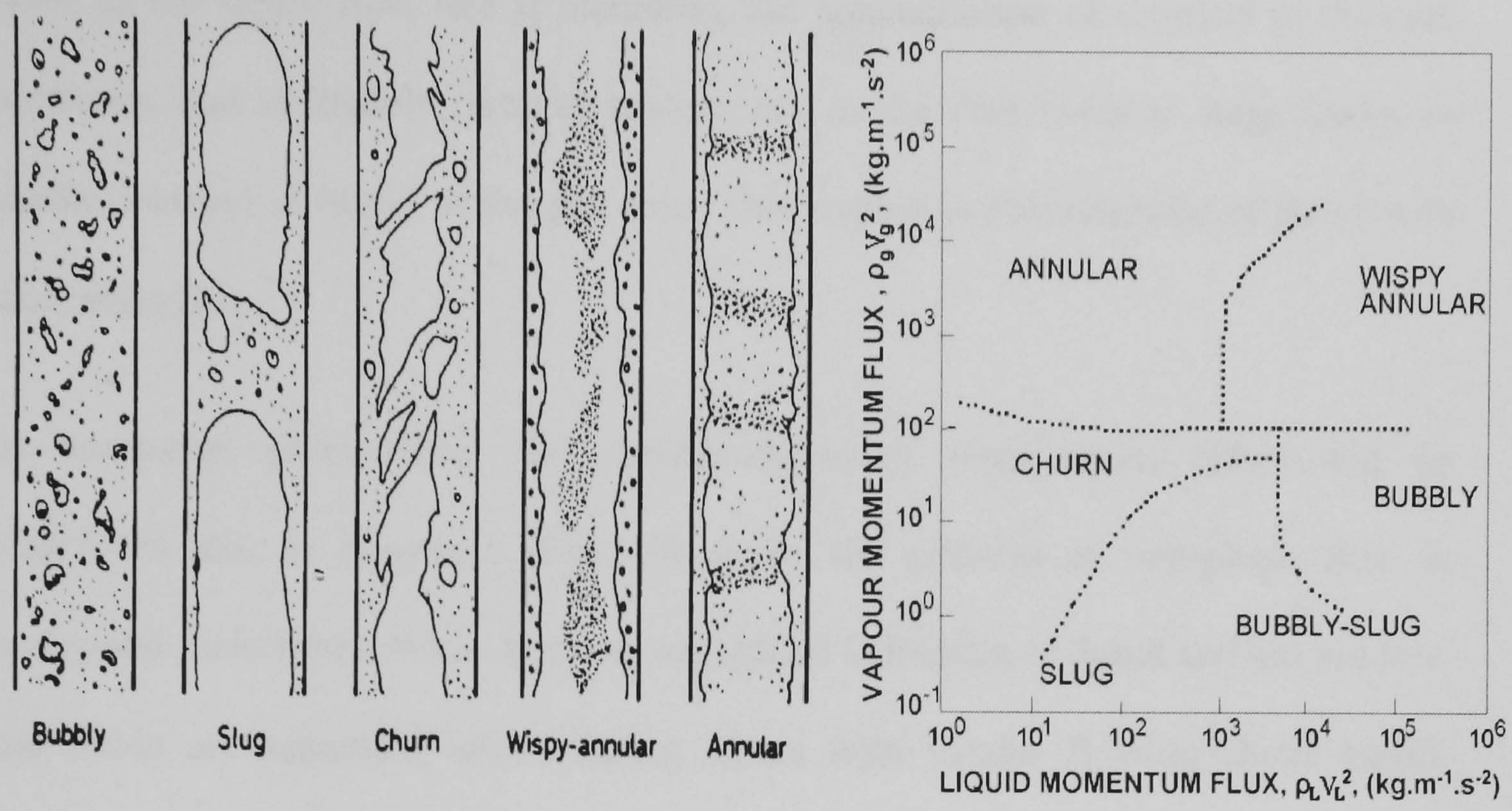

Fig. 1.9 Flow patterns and regime map (Hewitt and Roberts, 1969) of vertical upwards two-phase flow

Fig.1.9 shows the flow patterns and flow pattern map in vertical upwards boiling flow. The V_L and V_G represent superficial velocities of liquid and gas, respectively. ($V_L = Q_L/A$ and $V_G = Q_G/A$, where Q_L and Q_G are volumetric flow rate of liquid and gas and A is cross-sectional area of the tube). When the vapour momentum flux ($\rho_G V_G^2$) is lower than 100 kg/(m·s^2) and the liquid momentum flux ($\rho_L V_L^2$) is high, we have bubble flow. The size and velocity of bubble depend on the balance of dynamic, buoyancy and surface tension forces. When void fraction increases, the superficial velocities of liquid (V_L) decreases, then, large bubbles appear and some of them occupy the whole cross section as plug or slug flow. Churn flow is chaotic and unstable with the increase of void fraction (increase of superficial velocity of vapour (V_G) and decrease of superficial velocity of liquid (V_L)). When vapour momentum flux is larger than 100 kg/(m·s^2), flow becomes gradually steady giving a liquid film on the wall and a continuous vapour core to form annular flow. In wispy-annular

flow, as the liquid flow rate is increased, the concentration of droplets in the core increases, and ultimately, droplet coalescence in the core leads to large lumps or streaks (wisps) of liquid in the gas core. This regime is characteristic of flows with high mass flux.

In horizontal plain tubes, the non-homogeneous stratification effect will be significant due to buoyancy. Fig.1.10 shows the patterns of two-phase flow in horizontal plain tubes. When both the superficial velocities of liquid and gas are low, the fluids are separated into different layers with vapour flowing above liquid. Stratified flow is more likely to occur at low flow rates and in tubes with large diameters. When vapour flow rate increases, the interface between the fluids becomes mixed and irregular, the flow pattern transits to wavy stratified flow. With the increase of the superficial velocity of liquid, the slug flow, plug flow and bubble flow in a horizontal tube like the relevant flow patterns in vertical upwards flow, but the plugs, slugs and bubbles tend to occupy the upper part of tube due to buoyancy. Annular flow happens while the vapour flow rate is high enough to push the liquid layer up to the top of the tube wall. The bubble flow in a horizontal tube only happens when the liquid superficial velocity is higher than 3 m/s.

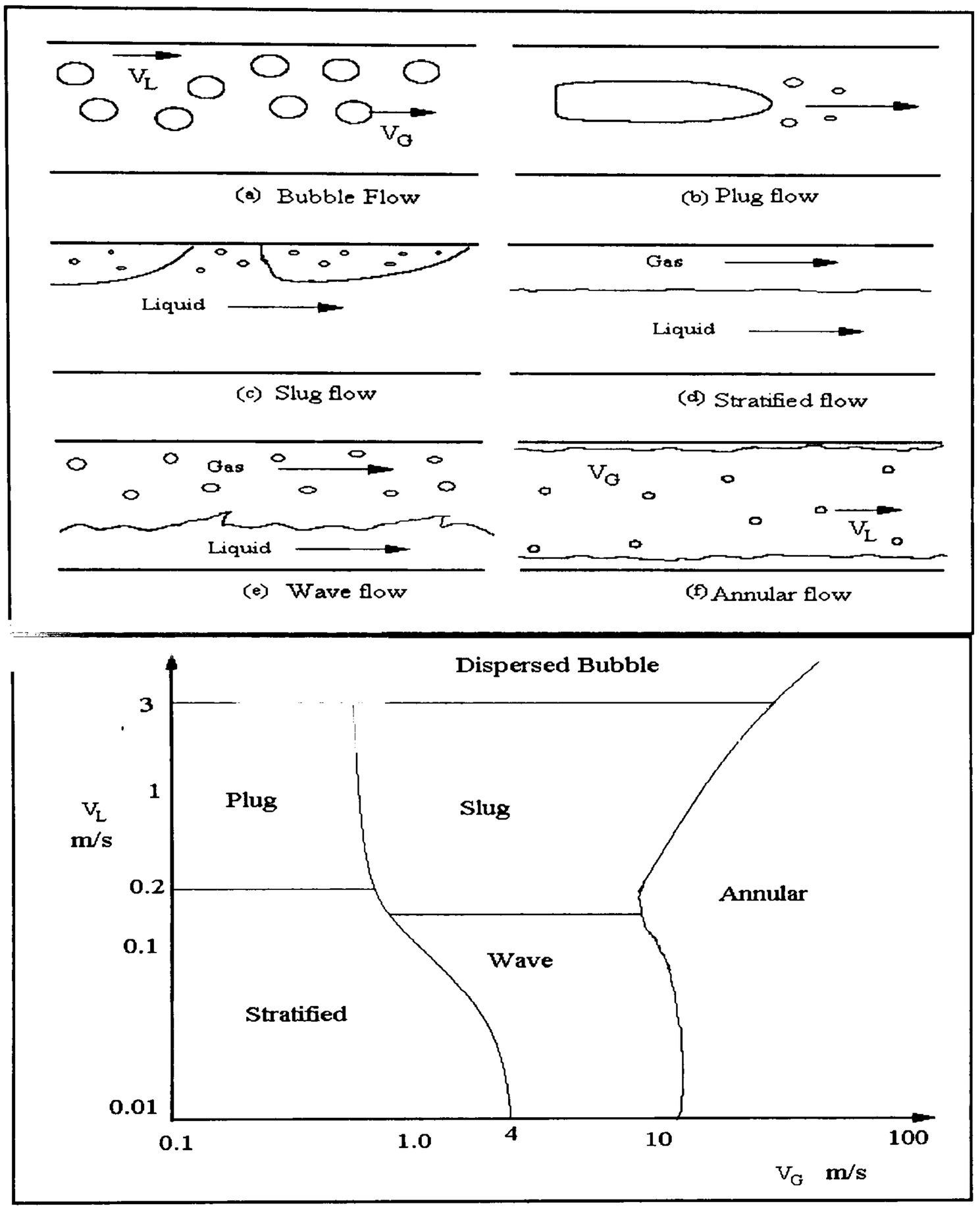

Fig. 1.10 Flow patterns and regime map (Mandhane, 1974): horizontal two-phase flow (Chisholm,1983 and Christy, 2003)

In flow boiling (diabatic flow with heat addition), the void fraction of an element of fluid increases as it proceeds along the channel; the flow patterns, therefore, can be expected to differ from those of an adiabatic or isothermal flow. The flow patterns of flow boiling in a horizontal tube heated by a uniform low heat flux are shown in Fig.1.11 (Collier and Thome, 1996).

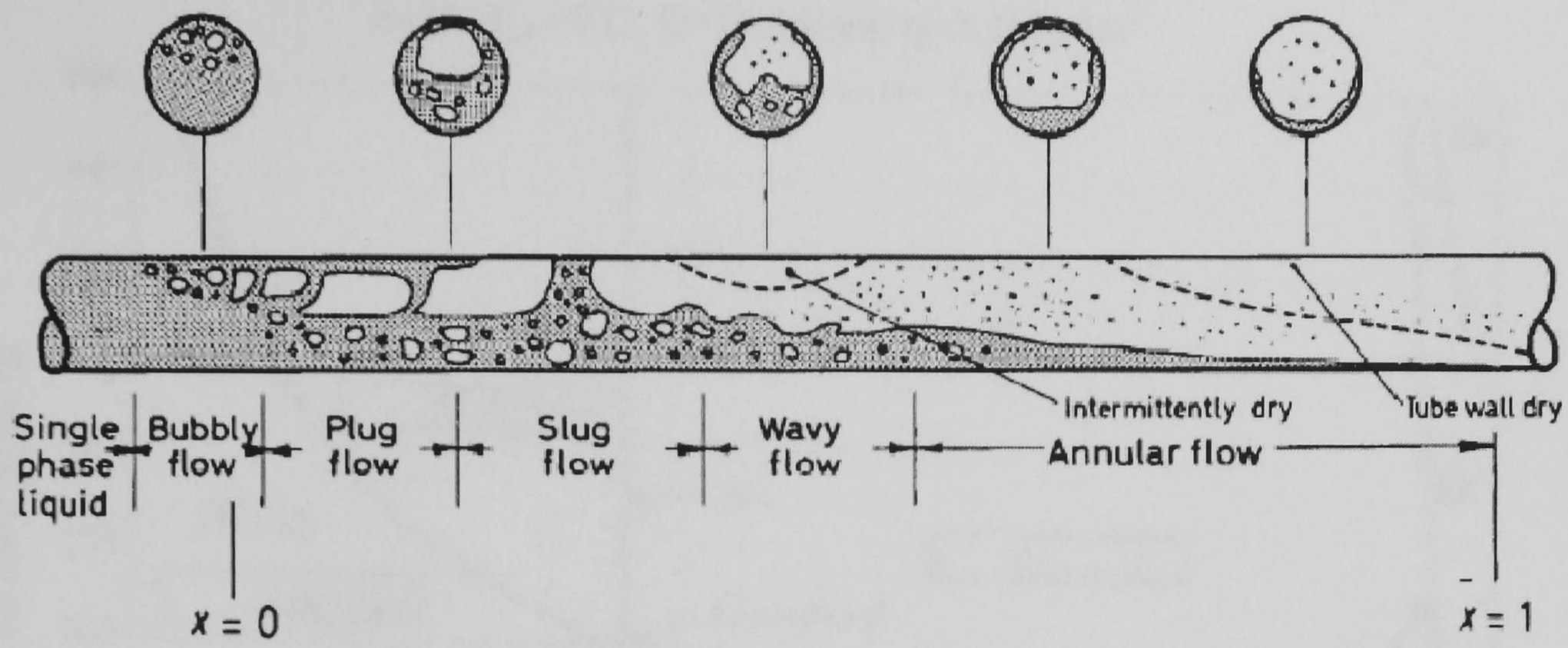

Fig. 1.11 Flow boiling in a horizontal heated tube

In this figure, the liquid just below saturated temperature enters the heated tube from left with low velocity (less than 1m/s). The fluid absorbs heat from the tube wall and evaporates, so the void fraction of fluid increases steadily along the flow direction. While the bulk liquid is subcooled (flow region on the left of vapour quality equates zero (x=0)), a superheated liquid layer exists next to the wall. Bubbles nucleate and grow adjacent to the super heated liquid layer, but they are in process of collapse by recondensation no matter they are still attached to the wall or carried along with the stream. With the increase of void fraction, the flow pattern changes from bubbly flow to plug flow, slug flow, wavy flow or annular flow. In wavy flow region, the fluid is unstable and upper part of tube wall contact with vapour directly. When dry-out happens (in wavy flow or partially annular flow), the temperature of tube wall increases significantly, which makes the metal tube weak and fatigue. When the vapour quality increases to over 90%, the liquid film attached to the tube wall disappeared, the bulk fluid is vapour with small droplets, and then the flow pattern turns to mist flow, which is also shown in the Fig. 1.12, the flow pattern map proposed by Wojtan et al. (2005 a) for a horizontal heated tube.

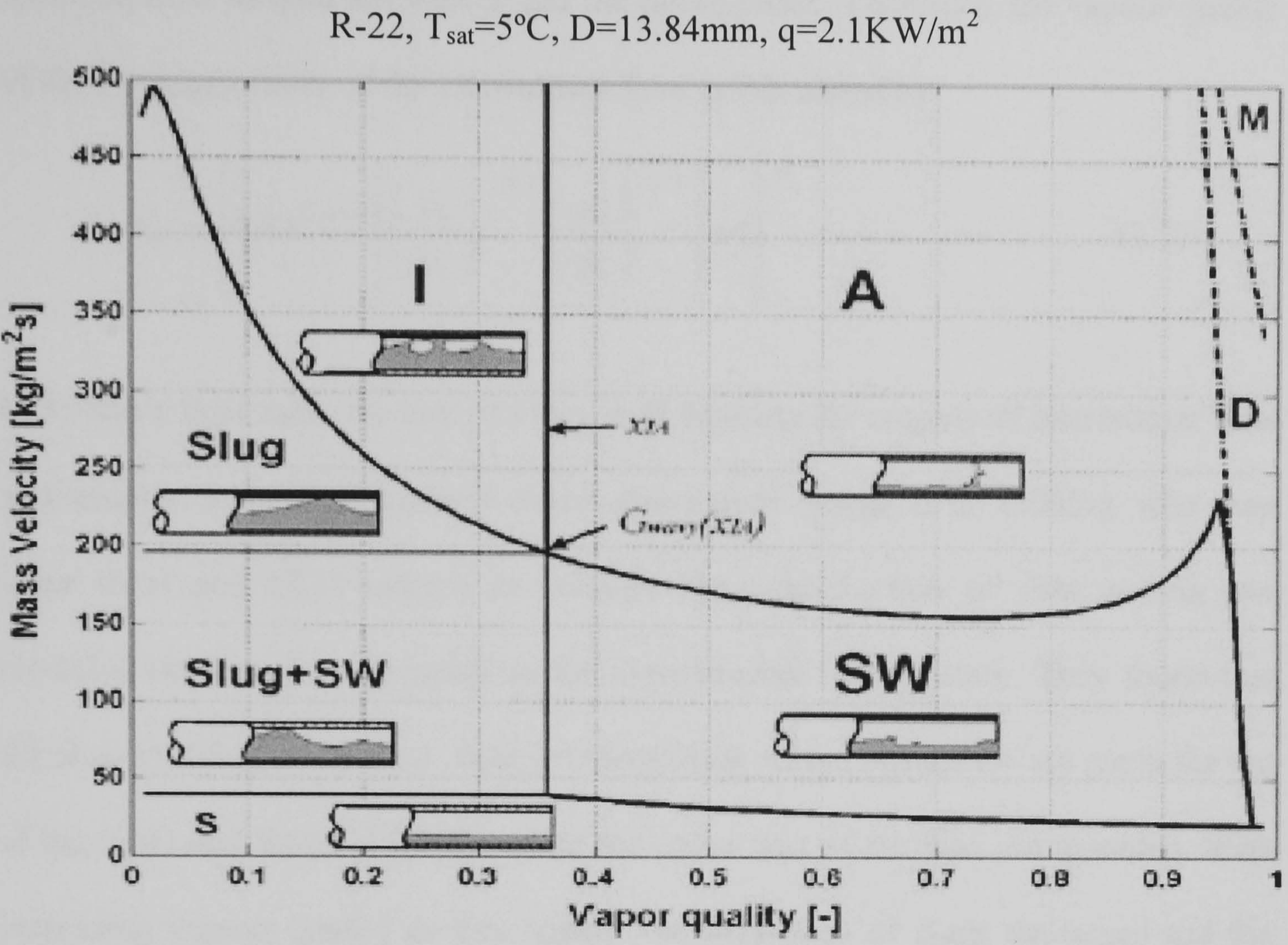

Fig. 1.12 Two-phase flow pattern map of a horizontal heated tube (Wojtan et al., 2005a)

This flow pattern map is based on the optical test and Thome-Ei Hajal version (Ei Hajal et al., 2003) of Kattan-Thome-Favrat flow pattern map. (Kattan et al., 1998 a) It shows clearly that when the mass flow rate is high, the flow pattern transits from slug flow to intermitted flow, annular flow and mist flow with the increase of vapour quality. When the mass flow rate is just below 200kg/m^{2}s in this case, the flow pattern turns from slug-wavy flow to stratified wavy flow and annular flow, as shown in Fig. 1.12. When mass flow rate is low, the liquid phase can not rewet the top of the tube, then, only the wavy flow or stratified flow can appear. In a plain tube, Kattan et al. (1998a) proposed that the boundary curve of the intermittent flow (plug flow, slug flow) is defined by a fixed Martinelli parameter X_{tt}=0.34 for

turbulent flow of both the vapour and the liquid phase. Therefore, the vapour quality of the boundary curve of the intermittent flow is calculated by

$$x_{IA} = \left\{ 0.34^{1/0.875} \left[\left(\frac{\rho_v}{\rho_l} \right)^{-1/1.75} \left(\frac{\mu_l}{\mu_v} \right)^{-1/7} \right] + 1 \right\}^{-1} \tag{1.1}$$

In Kattan's flow map, the line of $x=x_{IA}$ is to separate the regions of intermittent flow and annular flow. With the new observations from Wojan et al. (2005a), who used layer sheet and CCD camera to measure the void fraction of flow boiling and modified the former map based on the experimental investigation. They found that for slug-stratified wavy flow, both low amplitude waves (which do not reach the top of the tube) and liquid slugs that wash the upper part of the tube are recorded. With increasing vapour quality in this region, the frequency of slugs decreases and the small amplitude waves become dominate (as it was illustrated above). The slugs disappear completely approximately at a vapour quality of x_{IA}. And the stratified flow was not detected at any of the mass velocities tested. In their new version of the map, which is represented in Fig. 1.12, the line of $x= x_{IA}$ separates the regions for intermittent flow (plug, slug, slug/wavy flow) from those of the annular and stratified-wavy flow.

However, the boiling heat transfer characteristics in metal-foam tubes may be different. The metal foam structures not only provide more boiling sites to promote nucleate boiling heat transfer, but also constrain bubble growth and even break up the bubbles when the flow is obstructed by the foam ligaments with different orientation angles. This tends to homogenize the flow field and enhance heat transfer. Some distinctive and interesting boiling transport phenomena would be

expected, which could lead to different boiling heat transfer characteristics than those of plain channel flows.

The evaporation/boiling mechanism in metal foams is very complicated due to the inherent complexity of evaporation in the porous microstructure of the foam. The two-phase flow and heat transfer at the micro pore level can be considered as heat transfer either in numerous micro-tortuous channels or across an inter-connected cylindrical matrix. The heat transfer coefficient in such arrangement is expected to be much higher than the heat transfer coefficient in micro-tubes, if one considers the improvement that has been achieved in single-phase heat transfer. In addition to the higher heat transfer coefficients, high porosity metal foams (usually over 85%) in large inner-diameter tubes can reduce the required velocity to meet a given heat transfer duty reducing pressure drop and alleviating the effect of foam structure on flow resistance. For the condition of two-phase flow getting through a metal-foam tube, which contains three phases (gas, liquid and immovable metal-foam ligament), it is more complicated and similar to the situation of two-phase flow cross tube bundle.

1.6 Theoretical study for metal-foam tubes

The above sections introduced the material and principles of heat transfer in two-phase flow. This section will analyze the methods from the mathematic modelling point of view. The methodology of modelling work is to define the problem that needs to be analyzed first. Then, the proper differential equations for the analyzed region, for example, continuous equation, momentum equation, energy equation, etc, and relative boundary conditions can be decided according to the problem. To solve

the problem, some reasonable assumptions may be introduced to simplify the equations. Both analytical method and numerical method can be used to solve the group of equations with boundary conditions. In analytical method, the solutions for the form of each equation should be deduced and the studied, and variables can be represented as functions of other independent parameters. Therefore, the equations for complex problem are hard to solve by analytical method, because the forms of solutions for complex equations or equations in complex region are difficult to get. There are only a few situations which can be studied by analytical method. On the other hand, the numerical method can be worked out for almost any practical problem with availability of computers which have high calculation speed and large memory space (Patankar, 1980). To solve a practical problem, the discretization equations are derived by numerical method from differential equations for the studied domain with grid. Then the distributions of studied variables can be represented by values for finite grids. The discretization equations will be calculated until their convergence can be proved.

The widely used methods for deriving the discretization equations are finite volume method (FVM), finite element method (FEM), finite difference method (FDM) and finite analytic method (FAM), etc (Tao, 2001). The FVM divides the studied domain into finite control volumes, each of them is represented by one point. The discretization equations can be derived by integrating conservation equations (e.g momentum equation, energy equation) in every control volume. So the discretization equations keep the conversion character and have meaning in physics. This method is the most popular method for numerical modelling and it is employed in this research.

The FEM is good at studying irregular domain but it uses huge computation time. The FDM and FAM are also used by some researchers for their particular work.

Generally speaking, the numerical method is more time consuming for the iterative calculation and carrying out the final results. However, it is used widely to solve the problem with complex geometry shape or complex equations. Some commercial software had been developed and could be used for numerical method, like Fluent, Star CD, etc.

As far as this research is concerned, the single phase flow in a metal-foam filed tubes can be modelled by both analytical method, which needs more proper assumptions, and numerical method. However, for flow boiling heat transfer, which is much more complex, only the numerical method is suitable. Moreover, although there are some commercial software can be chosen, for the complex problem like flow boiling in a metal-foam tube, it is hard to find a proper commercial software to model the problem. Therefore, the modelling for two-phase flow dropped in programming CFD code with introducing empirical correlations and flow patterns from experimental results.

Due to the complicated boiling mechanism in metal-foam tubes, the process of modelling work has been divided into three stages. Firstly, the analytical method is used to predict the single-phase flow and the heat transfer in metal-foam tubes, and then numerical method will be used for single-phase flow. Finally, the numerical method will be used to model the two-phase flow and heat transfer in these tubes. The following section introduces the differential equations which are used in modelling work.

a) Momentum equations

In principle, high porosity metal foams with open cells can be treated as a porous medium (Zhao et al., 2004 a). Darcy (Bejan, 1995) first summarised the correlation for the flow in porous media based on experimental observations. He discovered that the area-averaged fluid velocity through a column of porous material is proportional to the pressure gradient established along the column. Subsequent experiments proved that the area-averaged velocity is, in addition, inversely proportional to the viscosity (μ) of the fluid seeping through the porous material. For a one-dimensional forced flow, Darcy's law can be represented as equation 1.2. However, it neglects the viscous force acting along the impermeable surface (solid boundary). For this reason, when the Reynolds number based on the pore diameter for the channel/pipe flows exceeds 1-10, significant deviations from test results were found by Fand et al. (1986). To solve this problem, the Brinkman-extended Darcy model (Vafai and Tien, 1981) was proposed to consider the effect of the impermeable boundary, and has since been extensively used for non-Darcy flows. Zhao and Lu (2001) and Kim et al. (2000) both used the Brinkman-extended Darcy model for the analysis of channel heat sinks. Nazar et al. (2003) applied the model for the theoretical study of the mixed convective boundary layer flow past a horizontal circular cylinder embedded in a porous medium. In the present study, the Brinkman extended Darcy model (Equation 1.3) is employed as the momentum equation to analyze the velocity distribution in metal-foam tubes in analytical modelling. However, when the velocity increases to high level, the form-drag factor can not be neglected. Forchheimer extended Darcy Model (equation 1.4) considering both viscous force and inertia

force are adopted for numerical modelling which make the modelling can be used in wider range.

Equations for momentum conservation

- Darcy Law

$$u=\frac{K}{\mu}\langle-\frac{dP}{dx}\rangle, \tag{1.2}$$

where K is an empirical constant called permeability.

- Brinkman-Darcy Model

$$\frac{1}{\varepsilon}\langle(\vec{V}\cdot\nabla)\rho_f\vec{V}\rangle=-\nabla\langle p\rangle_f+\frac{\mu_f}{\varepsilon}\nabla^2\langle\vec{V}\rangle-\frac{\mu_f}{K}\langle\vec{V}\rangle \tag{1.3}$$

$\langle\ \rangle$ means a volume averaged value.

- Forchheimer -Darcy Model

$$\frac{1}{\varepsilon}\langle(\vec{V}\cdot\nabla)\rho_f\vec{V}\rangle=-\nabla\langle p\rangle_f+\frac{\mu_f}{\varepsilon}\nabla^2\langle\vec{V}\rangle-\frac{\mu_f}{K}\langle\vec{V}\rangle-\rho_f F_I\left|\langle\vec{V}\rangle\cdot\langle\vec{V}\rangle\right|J_1 \tag{1.4}$$

Where F_I is Forchheimer coefficient

b) Energy equations for solid foam structure and fluid

For modelling the heat transfer in a porous medium, the one-equation equilibrium model or the two-equation non-equilibrium model are commonly used (Bejan, 1995). The one-equation equilibrium model assumes that there is no temperature difference between the local fluid and solid phase while the two-equation non-equilibrium model treats the fluid and solid separately, considering the local temperature difference between them. The two-equation non-equilibrium model is more difficult to apply because it requires information on the interfacial heat-transfer coefficient, which is usually determined through experimental investigations. Due to this

difficulty, some investigators have used the one-equation model for the analysis of convection heat transfer in a general porous medium (Nazar et al., 2003). However, the one equation model is only valid when the local temperature difference between fluid and solid is negligibly small. This will not be the case in heat exchanger applications where the difference in the thermal conductivities of the fluid and solid is significant (Calmidi and Mahajan, 2000 and Zhao et al. 2001). For this reason the two-equation non-equilibrium heat transfer model will be used in this research to study the heat transfer performance of metal-foam tubes.

Energy balance equations for solid and fluid phases

$$0 = \nabla \cdot \{k_{se} \nabla \langle T_s \rangle\} - h_{sf} \tilde{a}(\langle T_s \rangle - \langle T_f \rangle) \tag{1.5}$$

$$\langle \rho \rangle_f C_f \langle \vec{V} \rangle \nabla T_f = \nabla \cdot \{(k_{fe} + k_d) \cdot \nabla \langle T_f \rangle\} + h_{sf} \tilde{a}(\langle T_s \rangle - \langle T_f \rangle) \tag{1.6}$$

The equations above are essential for heat transfer in porous media. The parameters used in these equations can be specified for different problems. To predict the heat transfer performance in single-phase or two-phase flow in metal-foam tubes, the correlations which were derived particularly for metal-foam structure have been employed calculate the parameters in these equations. The details will be discussed in the following chapters of modelling work.

1.7 Aims and objectives

The main aim of the project is to experimentally and theoretically investigate the heat transfer performance of metal-foam tubes in forced flow and flow boiling conditions with applications to refrigeration and heat pump systems. The factors determining the

pressure drop and boiling heat transfer in metal foams are identified and their effects are quantitatively examined.

To perform the experimental test, a facility to investigate the heat transfer and two-phase flow in metal foam tubes is established.

To study the effect of metal-foam microstructure on heat transfer enhancement and assess the test rigs, the forced convection heat transfer of R134a vapour flow in different metal-foam tubes is investigated.

It is known that the perfect contact between the metal foam and tube wall is crucial to reduce the contact resistance and improve heat transfer efficiency. Therefore, another objective is to examine the effect of contact quality on heat transfer performance. The metal-foam tubes using the best binding method are chosen for the following tests.

To study the effect of metal-foam microstructure on boiling heat transfer and two-phase flow, copper-foam tubes with different cell sizes and different relative densities are employed. In all measurements for flow boiling heat transfer, the operating pressure, heat flux and mass flux are varied to examine their effects on overall heat transfer performance.

Also, in an attempt to examine the enhancement effect induced by metal foams, single-phase flow and two-phase flow heat transfer measurements in plain tubes with the same size under the same conditions are carried out.

Finally, theoretical modeling methods (analytical method and numerical method) are used to indentify the key factors and predict their effects on the heat transport

performance for single-phase flow and two-phase flow in metal-foam tubes and relative heat exchangers.

1.8 The outline of this thesis

The chapter **One** introduces the background of this research. What is metal foam and metal-foam tubes and why these tubes can enhance heat transfer performance have been defined and analyzed. To apply these tubes for refrigeration system, the mechanism of boiling heat transfer (pool boiling and flow boiling in normal tubes) has been reviewed. Moreover, the forms of Navier-Stokes equations employed as momentum conservation and energy balance equations for theoretical studies of heat transfer in metal-foam tubes have been proposed.

The chapter **Two** describes the design of test facilities and test procedures in details. In this chapter, the range of test parameters have been defined, the details of construction of test section and test rigs and how the test rigs were controlled and operated have been presented. There are also descriptions of data acquisition system and sensors calibration. Finally, the procedures for test preparation and experimental tests have been set.

The chapter **Three** presents an experimental study of R134a vapour flow heat transfer and pressure loss in metal-foam pipes. The heat transfer performance for different metal-foam micro-structures (different pore size, relative density and materials) has been investigated. To examine the effect of different tube/foam combination on heat transfer, a group of metal-foam tubes with different attaching methods, provided by Porvair Advance Materials, were experimentally tested. The heat transfer performance of a plain tube was also tested in the same conditions to

compare against the performance of metal-foam tubes.

The chapter **Four** presents the theoretical study of single phase flow in metal-foam tubes. An analytical method is used to study the forced convection heat transfer performance in these tubes. The key parameters have been located and the effect of each parameter has been analyzed.

However, the analytical method neglects the axially heat conduction and kinetic resistance to simplify the equations. In order to consider their effects, a numerical method with new momentum model is employed to predict the pressure loss and heat transfer of forced convection in metal-foam tubes. Considering the contact thermal resistance between tube wall and metal foams, the predictions have good agreement with experimental results on overall heat transfer performance. The comparison between predictions of numerical and analytical methods and experimental data illustrates that only the numerical predictions have good agreements with test data on pressure drop at high Reynolds number. But for heat transfer performance, both methods have similar predictions in normal situations.

Therefore, the analytical method, which needs less computer time, is used to study heat transfer performance of metal-foam heat exchangers. Compared to the results with finned heat exchanger, the predictions suggest that the metal-foam heat exchanger has a lot of potentials for making compact heat exchangers.

The chapter **Five** experimentally investigates the flow boiling heat transfer in metal-foam tubes. The wall temperature distributions and fluctuations have been analyzed to reveal the flow patterns inside the tubes due to a lack of directly visualized view.

The effects of heat flux, mass flow rate, operating pressure and foam microstructures on boiling heat transfer and pressure drop have been analyzed.

The chapter **Six** uses numerical method to predict the heat transfer performance of two-phase flow in horizontal metal-foam tubes based on the flow pattern map summarised from experimental results. The effects of metal-foam microstructure and other parameters on overall heat transfer performance of flow boiling in metal-foam tubes have been analyzed. Compared to the experimental results, the predictions show reasonable agreements and reveal that the increase of pore density may enhance nucleate boiling heat transfer significantly by increasing the number of active cavities.

Finally, the chapter **Seven** concludes this research and gives some suggestions for future work.

Chapter 2 Test Facility Establishment

To perform the experimental tests, a test rig must be established. Fig. 2.1 shows the test rigs built up for the experimental investigation. In this study, the heat transfer performance of single-phase and two-phase flow in horizontal copper alloy foams filled copper tubes has been investigated. Initially superheated vapour of R134a is used as the working fluid to test forced convection heat transfer in metal-foam tubes and assess the test rig. Subsequently, the investigations on flow boiling heat transfer in these tubes have been carried out. To enable copper foam tubes can be used widely in heat transfer applications, the effects of heat flux, mass flux and operating pressure on boiling heat transfer and pressure drop have been tested.

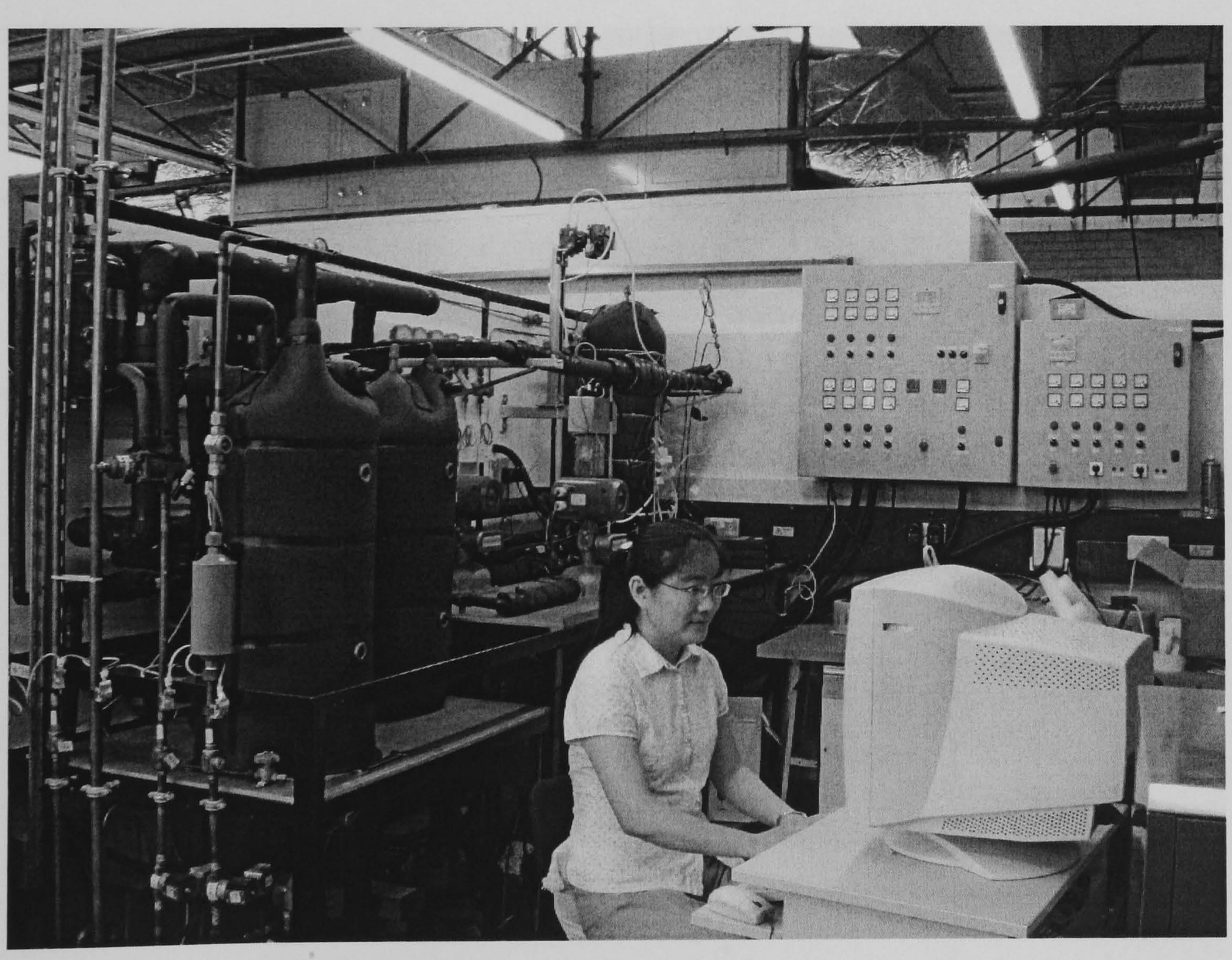

Fig. 2.1 Photograph of test rig

2.1 Measurable parameters

The parameters which need to be measured can be divided into two groups according to their importance for the research. The key parameters, which will be collected and used for analysis afterwards, must be measured with carefully calibrated instruments to ensure the accurateness of experimental results. The other parameters are measured to monitor the state of the system.

The key parameters for this research are: mass flow rate, pressures and temperatures at the inlet of the test section and before pre-heater, the temperature at the outlet, pressure difference between inlet and outlet of test section, the temperature distribution of outer wall of test tubes, the power inputs in test section and pre-heater, and geometry of test tubes (e.g. inner diameter, length, outer diameter, metal foam cell size, porosity). The ranges of experimental parameters are listed in table 2.1, where the left column shows the range for design and the right column indicates the range of experimental test.

Table 2.1 Design and test ranges of each parameter

Parameters	Design Range	Test Range
Test tube inner diameter (mm)	20	26
Length of test tube (mm)	1000	150
Metal foam cell size (pores per inch, PPI)	10, 20, 30	20, 40
Porosity (%)	95, 90, 85	95, 90, 85
Pressure range (bar)	2~20	2~6
Corresponding evaporation Temperature (°C)	-10~67.5	0~21

Vapour quality	0~0.9	0~0.9
Heat flux (KW/m^2)	0~150	0~20
Mass flux (Kg/m^2s)	20~300	20~160
Mass flow rate (kg/hr)	20~300	20~300
Superficial liquid velocity (m/s)	0.01~0.1	0.01~0.1
Superficial vapour velocity (m/s)	1~15	1~5

The other parameters include pressures and temperatures in the test rigs except test section and pre-heater, such as in R404a tank, R134a tank, inlet and outlet of compressor, accumulator tank.

2.2 The experimental apparatus

In order to describe clearly, the whole system needs to be divided into several subsystems. They are test section, test loop, cooling system, control system and data acquisition system.

2.2.1 Test Section

All the test tubes are copper tubes at 150 mm length, 26 mm inner diameter and the wall thickness of them is 1.3mm. The detail properties of metal foams filled in each test tube are in shown table. 2.2, where PPI represents pores per inch. All the parameters listed in the table are provided by producer instead of being measured individually. The plain tube is a copper tube same size as other metal-foam tubes.

Table 2.2 Properties of test tubes

Tube Number	Pore size	Relative density	Material
Group 1 (6 tubes, 1-1~1-6)	20PPI	5%	14%Ag86%Cu
2	20PPI	5%	8%Ag92%Cu
3	40PPI	10%	8%Ag92%Cu
4	20PPI	10%	8%Ag92%Cu
5	20PPI	15%	14%Ag86%Cu
6	20PPI	15%	100%Cu
7 (plain tube)	X	X	X

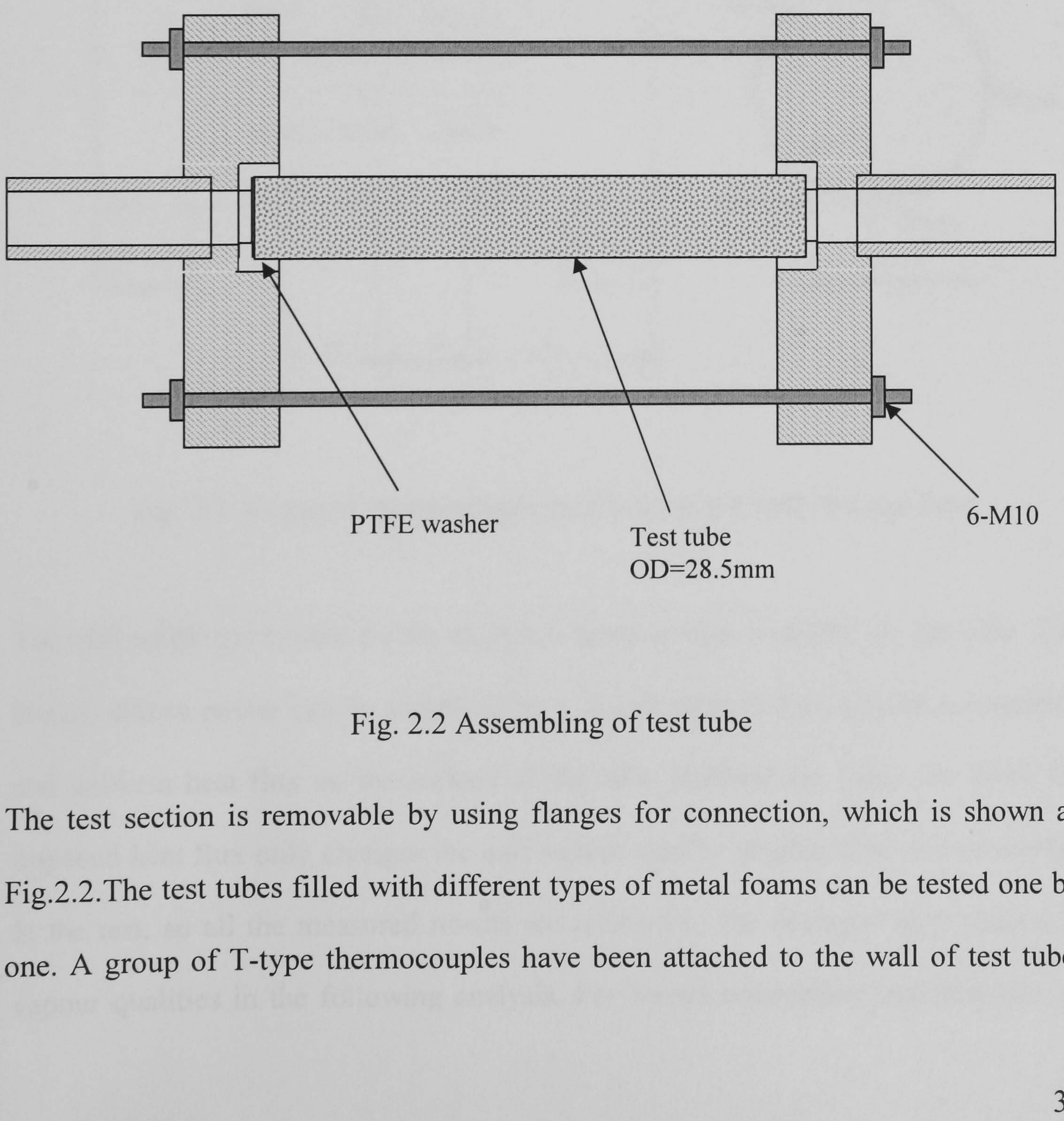

Fig. 2.2 Assembling of test tube

The test section is removable by using flanges for connection, which is shown as Fig.2.2.The test tubes filled with different types of metal foams can be tested one by one. A group of T-type thermocouples have been attached to the wall of test tube,

shown in Fig.2.3. The thin foil T-type (copper-constantan) thermocouples are attached on 3 outer wall-surface locations along the flow direction to monitor the temperature variation along the tubes. At each location, 3 thermocouples are placed on the circumference of the tube at 90° from each other (top, bottom and middle) and 1 thermocouple is attached to upper-side of the test tube. The inner wall temperatures along the circumference and length of the tube which are used to obtain the heat transfer coefficients will be calculated from the measured outer wall temperature, thermal resistance of the tube and heat flux.

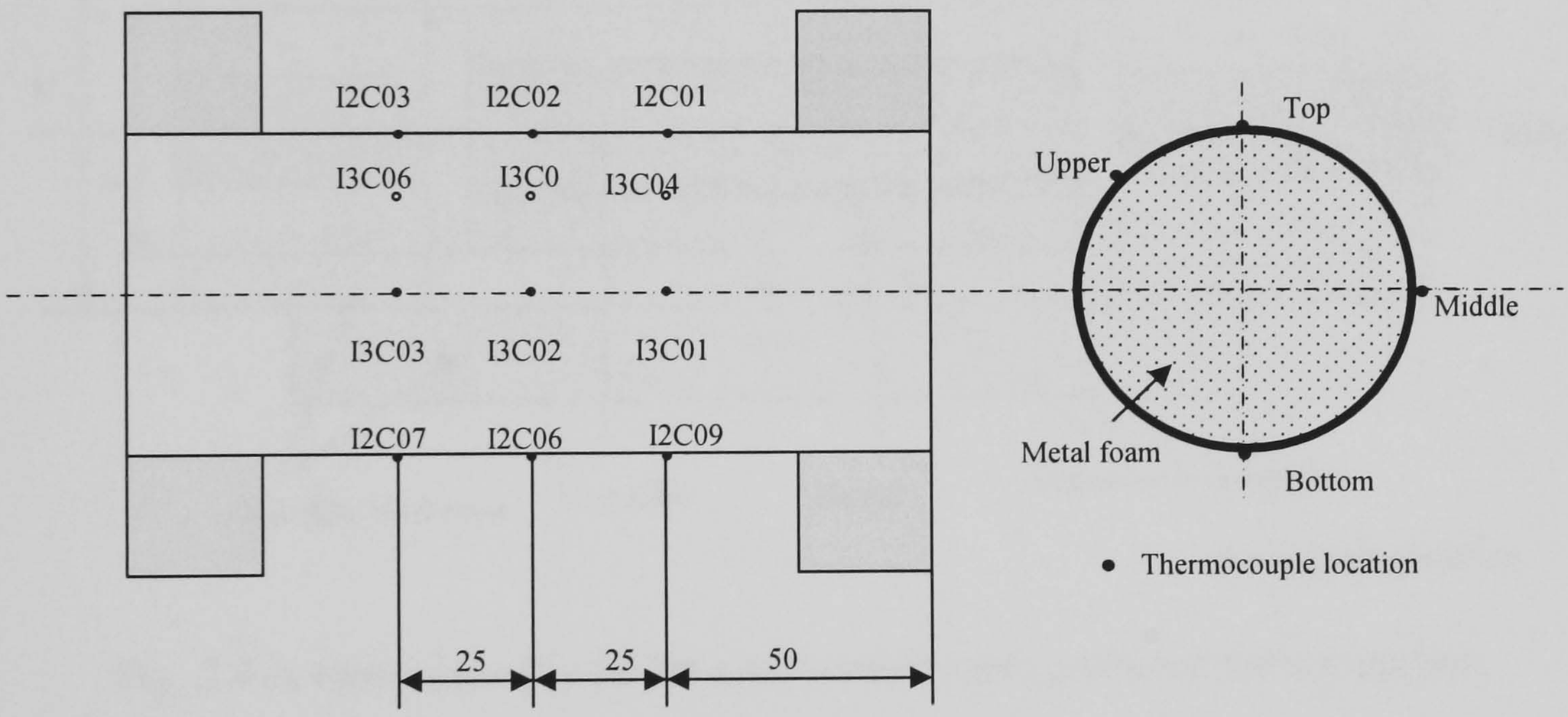

Fig. 2.3 A case of thermocouple positions on the wall of a test tube

The test tubes are heated by an electrical heating tape wrapped on the tube. The heater, whose power can be measured by a digital multi-meter, applies controllable and uniform heat flux on the surface of the tube. Because the tubes are short, the imposed heat flux only changes the exit vapour quality slightly from the inlet point in the test, so all the measured results are referred to the averaged inlet and outlet vapour qualities in the following analysis. For forced convection heat transfer, the

mean temperature of inlet and outlet fluid temperatures is used for analysing overall heat transfer performance. The test section is insulated with Superwool (a kind of mineral wool) mat and Armaflex pipe insulation to minimize heat loss. The test section is schematically shown in Fig. 2.4. Some thermocouples are used for monitoring. The temperature recorded at points a and b can be used to calculate the heat loss from insulation.

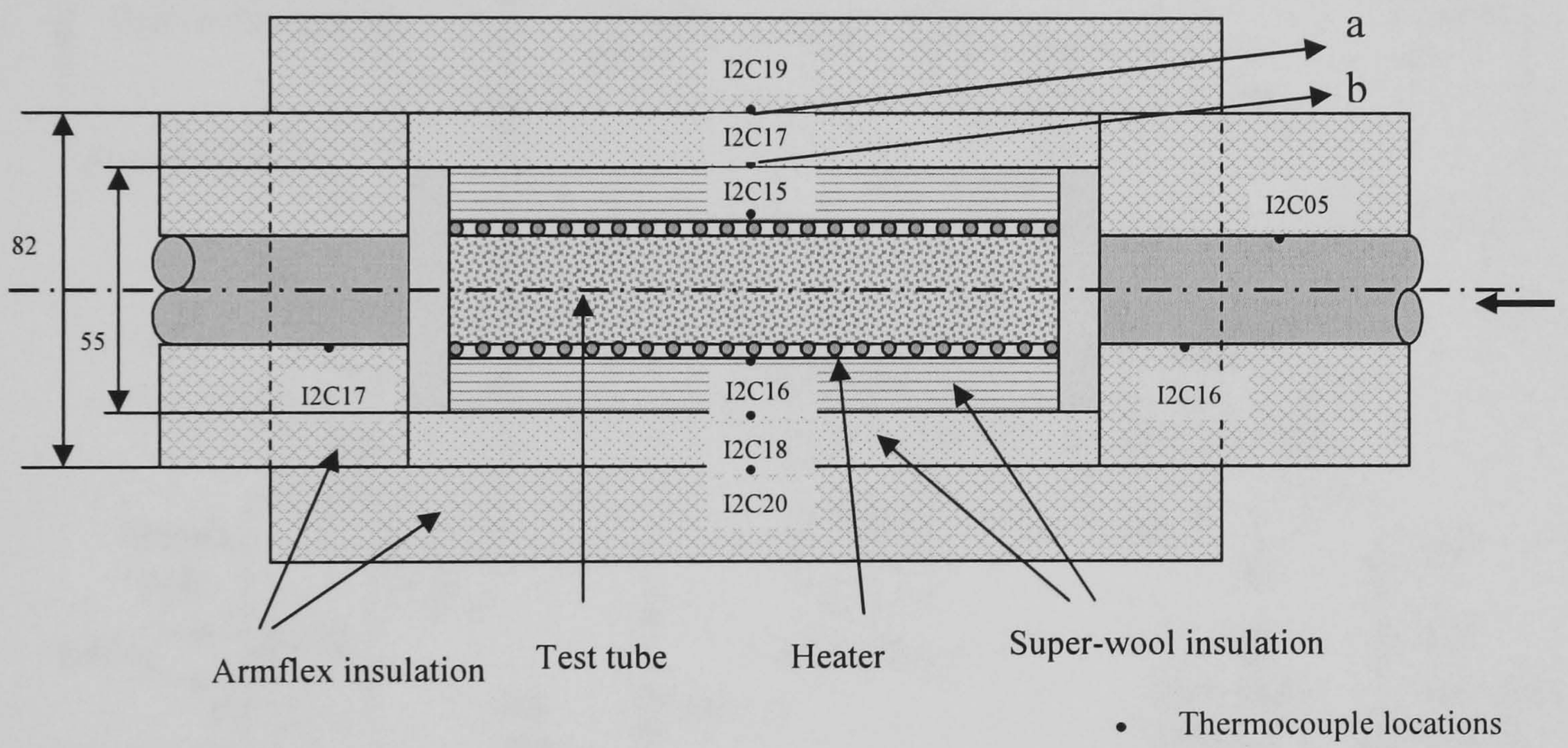

Fig. 2.4 A case of the Insulation and thermocouple positions for test section

2.2.2 Test Loop

Fig. 2.5 shows a schematic diagram of the experimental apparatus of the test loop. It consists of a gear pump for working fluid (R134a) circulation, two Coriolis mass flow meters, pre-heaters (8 electrical heaters, 1KW each), a test section (described in above section), three heat exchangers cooled by refrigeration system (one for sub-cooling the R134a and the other two for condensing it), an electrically heated reservoir which is cooled by refrigeration system and an electric power supply system in the test section. The reservoir is a steel tank and is filled by two-phase

saturated R134a, the vapour state occupies the upper part, while the liquid state occupies the lower part. The required system pressure can be maintained by an automatically controlled heater in the tank which can heat the liquid R134a and

Fig. 2.5 Schematic drawing of the test loop

generate more vapour in the reservoir and rise the pressure when the system pressure is below the required test value. When the pressure is above the required value, the

heater will be switched off and the cooling coil makes the vapour condensed into liquid state and then reduces the system pressure. Because the R134a is thin fluid, the conventional seal cannot prevent leakage. Therefore, a magnetically coupled gear pump (Tuthill TXS5.3PPPN3WN0000) is used to circulate the liquid fluid without any lubrication oil on the fluid side. An ABB inverter is used to modify the speed of the pump rotor and adjust the mass flow rate. A filter is applied to remove the solid particles. Before the fluid enters into the mass flow meters, it will first be sub-cooled in heat exchanger I in case of possible evaporation in pipes. Two Coriolis mass flow meters have been used to measure the refrigerant mass flow rate, one for low flow rate (20 ~ 100 kg/hr) and the other for high flow rate (100 ~ 350 kg/hr). Then the pressures and temperatures will be measured before the pre-heaters and at the inlet and outlet of the test section. A group of well-insulated pre-heaters can heat the liquid R134a to evaporate it to provide a superheated vapour flow through the test section. In addition, the power of pre-heaters can be adjusted to control the inlet temperature of vapour R134a to the test section. For two-phase flow, the adjustable pre-heaters can heat the R134a to saturated state and evaporate some of it to provide a two-phase flow through the test section. The inlet vapour quality can be controlled at the required value by adjust the power of pre-heaters. The enthalpy of the sub-cooled R134a before the pre-heaters can be determined from its pressure and temperature, thus the vapour quality and enthalpy at the inlet of test section can be determined by an energy balance on the pre-heater section. The temperature and pressure of the two-phase R134a at the inlet and outlet of the test section have been measured. The exit quality can be calculated from an energy balance between the imposed heat flux and enthalpy change of the fluid across the test section. The pressure drop in the test section is measured by a differential pressure transducer.

Sight glasses have been put before and after the test section to monitor the flow state in the test section. Test tube with flanges is changeable to investigate the effect of metal-foam microstructure on heat transfer and pressure loss. After the R134a passes through the test section, it can be separated into liquid state and vapour state by flowing though a gas-liquid separator. The liquid part directly returns to the tank while the vapour part is condensed back to the liquid state in the heat exchanger II and III. The two heat exchangers are in parallel, one for low load (2KW for vapour flow) and the other for middle load (4KW). Both of them can be isolated respectively according to the load of system or be used to cover the full load (6KW). Then the condensed fluid returns to the tank and is stored there. The whole test rigs including cooling system (if necessary) have been insulated by using pipe insulation materials. All measurements have been performed under steady state conditions and it usually takes 30- 120minutes to reach steady state after any change of parameters.

2.2.3 Cooling system

The cooling system (as shown in Fig.2.6) is used to carry the heat away from the R134a test loop through a cooling coil and three heat exchangers. It uses R404a as refrigerant since its saturated temperature at low pressure is much lower than others (-20°C to -40°C). The system contains two cycles, one cycle is for providing cooling fluid (R404a) to heat exchangers in test loop and taking the heat away, the other is a standard refrigeration system which releases the heat to environment. The system facilities include a R404a tank, a R404a pump, three heat exchangers (also shown in test loop), a cooling coil, a compressor, an oil separator, a R404a condenser, a R404a receiver, a filter dryer, an oil tank, thermostatic liquid level control equipment and a hot gas bypass regulator. The system can regulate its cooling capacity automatically

to adapt the heating load from the R134a experimental system. It is also protected by a high-low pressure switch and a power supply with overload protection device. When the system is started up, the compressor sucks R404a vapour from the R404a tank to turn the tank into an evaporator. The hot compressed R404a vapour comes out from the compressor and then goes into the oil separator, in which most oil is separated from R404a vapour and sent back to the compressor.

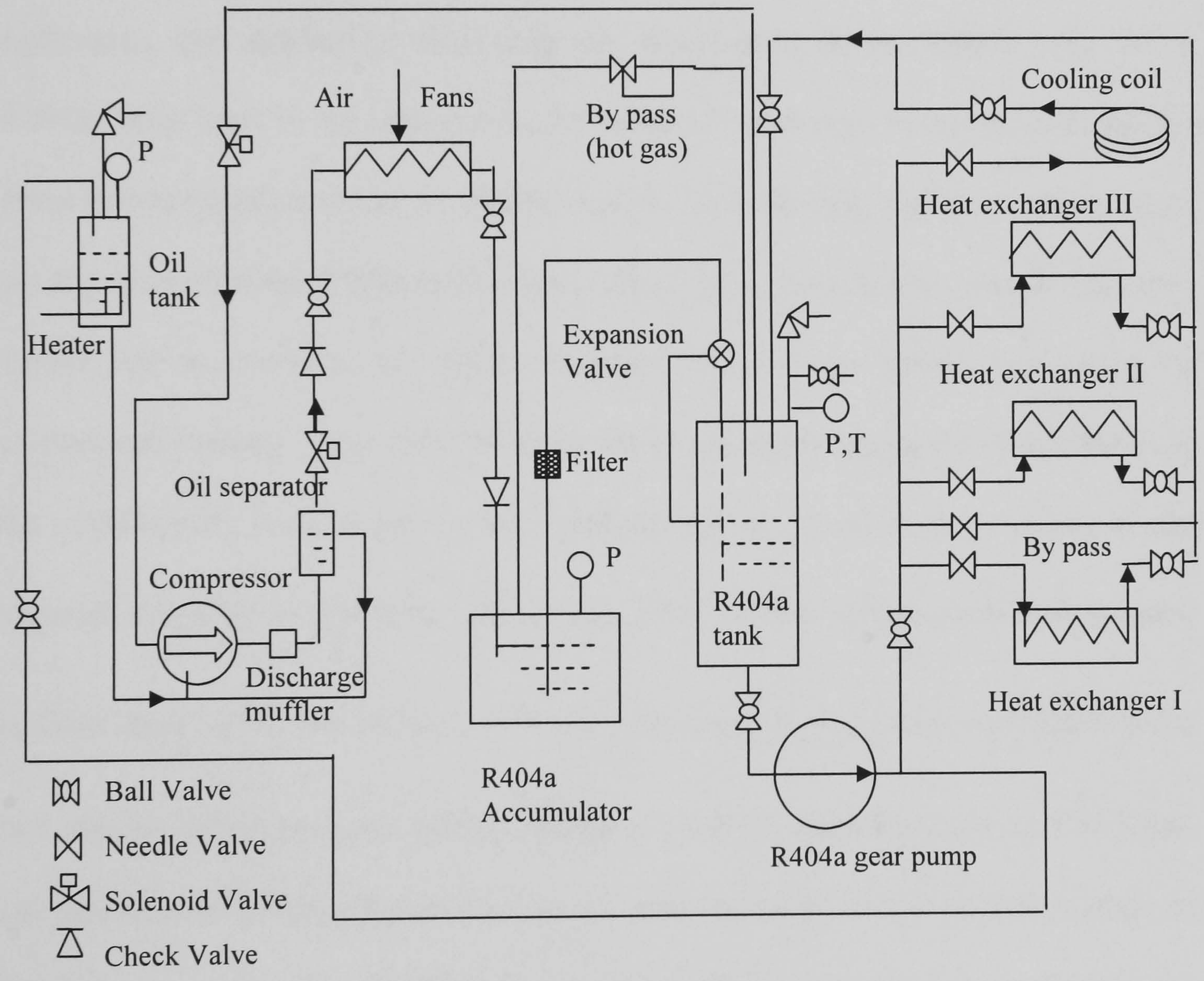

Fig. 2.6 Schematic drawing of Refrigeration Subsystem

After the oil separator, R404a vapour with high pressure and high temperature goes to the R404a condenser with fans linked with the compressor, i.e. they can run automatically when the compressor is running, but each fan can be switched off

manually to adjust the cooling capability to suit for the load and weather. In the condenser, the hot vapour is cooled down to liquid and sent to the R404a receiver, then goes into the R404a tank through a filter dryer, a sight glass, a solenoid valve and a thermostatic liquid level control equipment. The small amount of vapour left on the top part of receiver goes back to the R404a tank via a hot gas bypass line. The thermostatic liquid level control equipment has two functions, one is working as an expanding valve which can decrease R404a temperature down to -40 ℃ after the equipment, and another is controlling the liquid level in the R404a tank. When R404a liquid level in the tank is low, the solenoid valve will be opened and then let more R404a liquid stored in the R404a receiver into the tank. On the contrary, when the liquid level in the R404a tank is high enough, the valve will be closed. The extra R404a can be stored in the R404a receiver. The hot gas bypass line keeps the compressor running all the time when the load is changed during the experiments. In the experiments, the hot gas bypass regulator can be preset to the pressure of the required saturated temperature, for example, -20℃. When the temperature in the tank is lower than -20℃, the pressure difference between the evaporation pressure in the tank and the preset pressure is high enough to push the regulator open and let hotter gas into the tank to keep the pressure in the tank and then prevent the temperature in the tank from going down further. The regulator closes when the temperature in the tank is higher than the set value. The cold liquid in the R404a tank is pumped to the three heat exchangers and cooling coil, which can be opted out individually, by a circulating pump to cool the R134a in test loop. The flow rates, i.e. the cooling capacities, are controlled by the needle valves located before three heat exchangers and cooling coil. The pump is selected for the maximum load, so a needle valve is

installed in the bypass line to let the extra R404a goes back to the tank. The oil from R404a compressor will deposit in the R404a tank gradually due to the efficiency of the oil separator is impossible to be 100% and the return vapour only can carry very limited oil back to the compressor. Therefore, one oil return system is designed and built for separating oil from R404a and re-injecting to the compressor. So the oil/R404a mixture can be pumped from R404a tank to an oil tank by the R404a pump. The mixture is heated here by an inside cartridge heater. The evaporated R404a flows out and the retained oil flows back to the compressor oil pool by gravity and pressure difference.

2.2.4 System Control

To maintain the system in demanded steady state, which is ideal for test, PID (Proportional-Integral-Differential) controllers and other devices are used.

- **Pressure control**

As described in test loop, a heater and the cooling coil in R134a tank are used to control the system pressure. To maintain the system pressure in steady state, the pressure between pre-heaters is chosen as controlled parameter. The signal from absolute pressure transducer will be sent to PID controller which compares it with the set value (required pressure) and then output signals to control the heater in R134a tank. For example, when the system pressure is below the required test value, the heater in R134a tank can be automatically switched on and heat the saturated liquid in the tank to generate more vapour and then enhance the system pressure to the required system pressure. Otherwise, the heater can be switched off automatically and the cooling coil makes the vapour condensed into liquid

state and then reduces the system pressure to match the required pressure. Then the system pressure can be maintained by the heater in R134a tank controlled by PID controller and the cooling coil in the tank. Furthermore, the system pressure also depends on the heat balance of the whole system. The PID controller will stand by when the system reaches steady state.

- **Temperature control**

For two-phase flow, because the fluid entering the test section is in two-phase state, the temperature at the inlet of test section is kept the same as saturated temperature and depends on the pressure there. Therefore, it can not be used to monitor the state of fluid. The temperature measured in the middle of pre-heaters is used as controlled parameter to maintain the temperature of fluid into the test section since the fluid there is sub-cooled and independent from pressure and the power of pre-heaters after that point is set to be a constant. The signals from the thermo-couple measuring the inlet temperature of pre-heater will be sent to PID controller, which records and compares it with the set value (required temperature) and then output signals to control the first one of pre-hearers. The temperature at the point will be maintained on required temperature and so to the temperature before the test section. The heater mainly compensates the variation happened in heat exchanger I. However, because this research is interested in steady state, the PID controller is not in use to avoid disturbance. The temperature control only depends on the heat balance between cooling system and power input of pre-heaters in steady state.

- **Mass flow rate control**

The magnetic gear pump with an inverter, which can change the frequency of input alternating current for the pump and make the pump operate in variable speed, can accelerate the work fluid (R134a) in different mass flow rates. To make the mass flow rate reach the required values, two needle valves, which can be adjusted finely, are installed after mass flow meters. When the pump is switched on, adjust the speed of the pump to provide enough power to pump the fluid just above the required flow rate, turn on the heater and condenser and let the system run steadily at set pressure and temperature. Slightly adjust the needle valve to let the mass flow rate near to the required values until it reaches the require value at set pressure and temperature.

- **System heat balance control**

In order to enable the system reach steady state for experimental test, the capacity of refrigeration system should match the amount of heat generated by all the heaters in test loop and gained from equipments and environment. If the capacity of the refrigeration system is less than the load of the test loop, the heat generated by heaters and gained from environment can not been taken away, then the system will become hotter and can not reach steady state. On the other hand, the system will become cooler until the compressor has been stopped when the capacity of refrigeration system is larger than the load of the test loop. Therefore, the heat balance of the system should be controlled. Firstly, a compressor that can provide enough cooling for the system. The capacity of the refrigeration system depends on the evaporation temperature and environmental temperature. When the system load is low, the R404a in cooling system will become cooler and then the cooling capacity of refrigeration system will reduces and vice versa. Secondly, the fans

used for condenser can be switched off individually, so the capacity of cooling system can be reduced by switching off a fan at low load. Thirdly, for each heat exchanger, there is a needle valve to adjust the flow rate of refrigerant to match the need of test loop. Furthermore, a hot gas bypass regulator has been used to modulate the capacity of the refrigeration system. For example, while compressor is oversized, the suction pressure and temperature will become low. When the pressure of R404a tank is lower than the set point (which can be adjusted) of hot gas bypass regulator, the regulator will open and divert high-pressure refrigerant vapour from the top of accumulate tank to R404a tank to maintain a nearly constant pressure at R404a tank. The refrigerant temperature in R404a tank will be kept at fixed temperature. The hot gas bypass regulator can stabilize the system balance point by keeping the compressor more fully loaded.

2.2.5 Data acquisition system

A computer controlled 60-channel data acquisition system with LabVIEW data logging software is used to record and display experimental data, like pressures, mass flow rates, surface temperatures, etc.

- Data acquisition network

The data gained by measurement instruments need to be transferred into digital forms for computer analyzing. The data logger with plug-in data acquisition boards can gain the signals of current inputs and voltage inputs and output voltage signals. The data acquisition network used in this project is shown in Fig.2.7. It is comprised by a computer and three Solartron IMPs (isolated measurement pods) connected by S-net cable and PCI card. The address of each IMP card can be set and they are

recognized by the computer. Each IMP has 20 channels to connect with sensors and can measure current and voltage signals in different ranges, including micro-voltage signals from thermocouples. When the data acquisition system is running, the computer will scan each channel of the IMPs one by one to collect the value for monitored parameters. The IMP1 is used to monitor key parameters including mass flow rate (2 channels), pressures and temperatures at the inlet of the test section and before pre-heater, the temperature at the test section outlet, pressure difference between inlet and outlet of test section. The 12 thermocouples which have been attached to the wall of a test tube to measure the temperature distribution of outer wall of the test tube are wired to IMP2 and IMP3. Additional thermocouples are connected to spare channels in these pods for the purpose of measuring the wall temperatures of pre-heater, room temperature, and temperatures at different positions of insulation for test section.

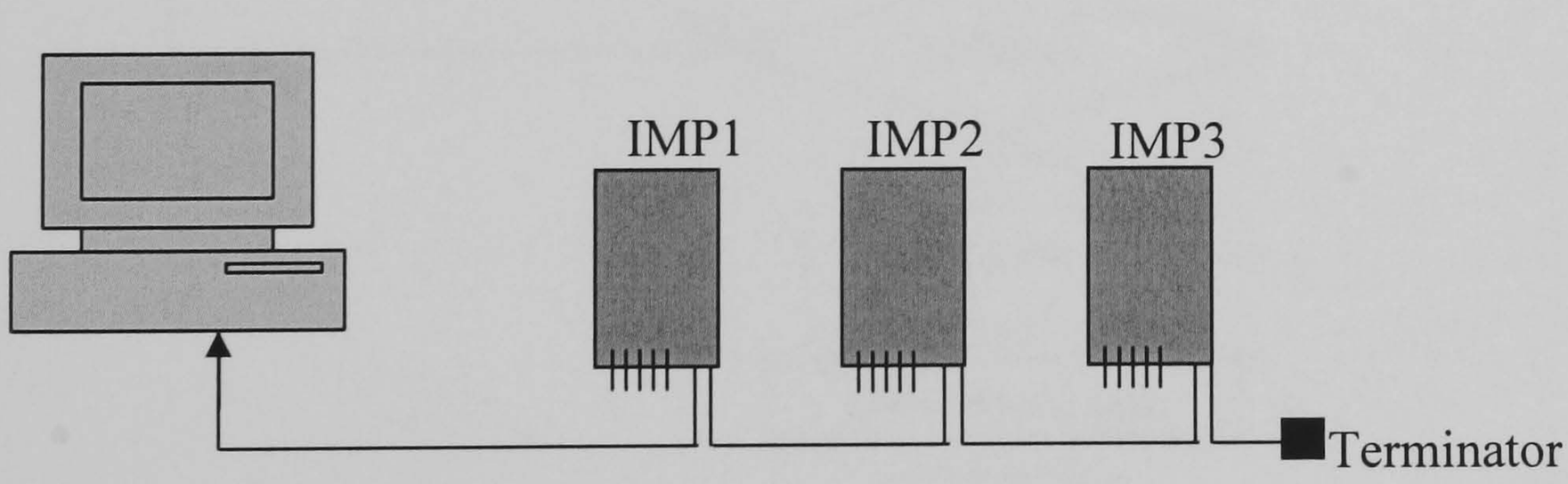

Fig. 2.7 Data acquisition network

- Data acquisition software

Data acquisition software is used to scan the channels of IMPs, display the value of each monitored parameter, save the data for processing. The wildly used software (LabVIEW) and LabVIEW-IMP driver have been installed in a computer with

Windows operating system. There are some LabVIEW modules provided by IMP vendor which can be used to setup and control IMPs.

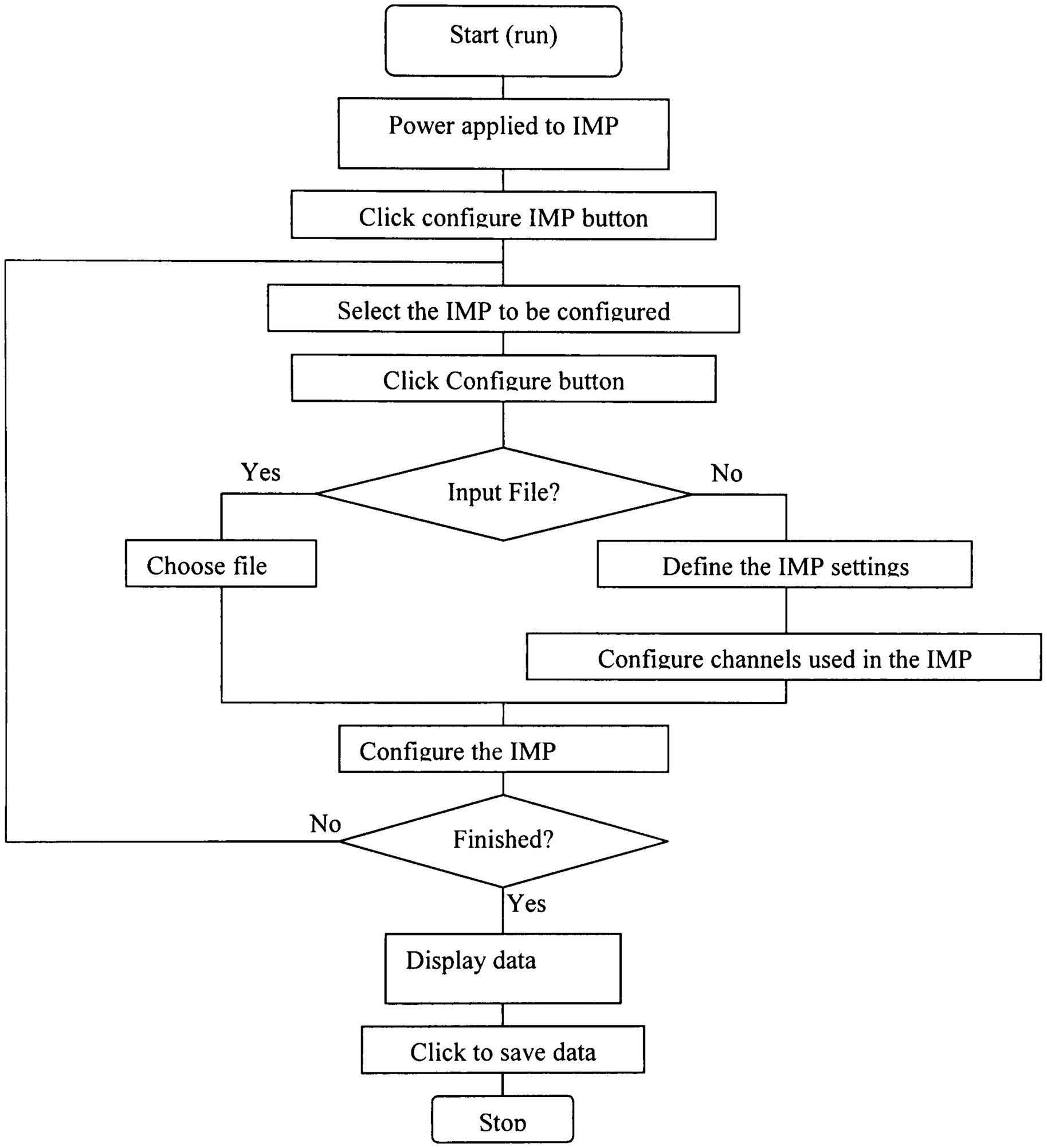

Fig. 2.8 Flow chart of setup and operation of data acquisition system

The flow chart in Fig. 2.8 (modified from user guide for IMP3595 75A LabVIEW/BridgeVIEW – Drivers for IMPs) shows how to setup the data acquisition system. With the sensors connected to the IMPs, the communication between computer and IMPs has been established as the first step, the computer gets the

address of each IMP and provides power to them through the PCI cards and S-net line. Secondly, each IMP has been configured by configuring every channel of the IMP individually or loading saved file. When all the IMPs have been configured, the network is ready to scan the channels and store the data obtained from each sensor. By using LabVIEW software, the properties of signal measured by each channel can be pre-defined, the raw data need to be converted into meaningful information by signal processing and mathematics processing, such as curve fitting, statistics and visualization.

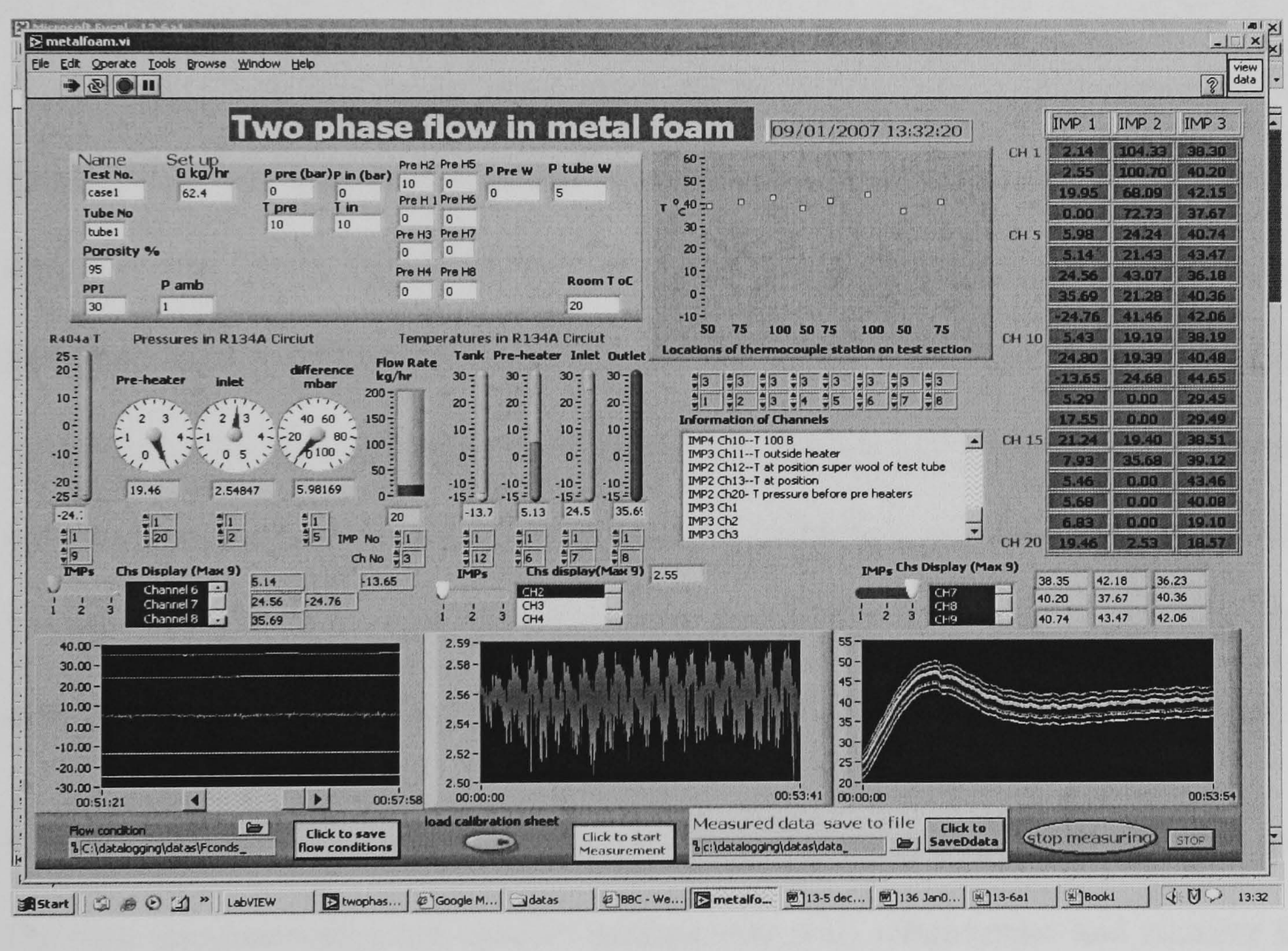

Fig. 2.9 Data display and record window for two-phase flow test

The Fig. 2.9 is a snapshot of the display window (designed by Dr Z.Y. Xu) which can display scanned data and monitor their trends and save them. The data can be used for further analysis and mathematics processing.

2.3 Instruments calibration

All the instruments (including pressure transducers, differential pressure transducer, mass flow meters and thermocouples) used to measure data for this project have been calibrated under the condition of wiring with data acquisition system and proper power sources (shown in Appendix C). Therefore, the influence of data logger doesn't need to be measured separately.

Pressure transducers: After the pressure transducers had been wired to data acquisition and right power source, they were installed on pressure calibration device (Dead weight pressure gauge tester produced by Bryans Aeroequipment UTD) one by one. The calibration of absolute pressure transducers (Omega PX01C0-500GI) indicates that the accuracy of them is $\leq\pm0.05\%$, that is $\leq\pm1250$Pa. Due to the limitation of the calibration device (It can not calibrate pressure under 10psi), the calibration done by Calibration & Measurement Service Ltd for differential pressure transducer (Omega PX771A-100DI) has been employed as well as the calibration done in lab. The two sets of calibrations are perfect match to each other. The accuracy for the differential pressure transducer is $\leq\pm0.1\%$, which equals ±170Pa.

Thermocouples: There are two kinds of T type thermocouples used in this project. The thin thermocouples are used to measure the wall temperature and monitor the heaters. The armoured thermocouples have been put into the centre of tubes to measure the fluid temperatures. In the test run, all the thermocouples were calibrated by using ice point and accurate mercury-in-glass thermometer. For each thermocouple, 20 values have been recorded and the mean of them is used to

compare with the reference temperature (0.02 °C). The results are shown in the following table.

Table 2.3 Calibration data for thermocouples based on ice-water reference

$T_{measure}$ - $T_{reference}$	Mean (°C)	Max (°C)	Min (°C)	Standard deviation
Thin thermocouples	-0.050	-0.023	-0.101	0.025
Armoured thermocouples	0.053	0.096	0.022	0.030

The measurements in table 2.3 indicate that there are ≤±0.1 °C differences between measured temperature and reference temperature. The $T_{reference}$-$T_{measure}$ is used to correct the zero point and the function for T type thermocouple embedded in IMP system is used for each thermocouple. After the test run, all the thermocouples have been calibrated by Omega thermocouple calibration system which contains a precise thermometer (F250 MkII Precision Thermometer, accuracy of ±0.01 °C), a heater, a cooler and a stainless steel pool in which the mixture of 40% antifreeze and 60% water is used as circling liquid. The thermocouples have been calibrated at four points (40.012 °C, 24.712 °C, 0.010 °C and -9.948 °C) which covers the whole test range. For each thermocouple, 20 values have been recorded for each temperature point and the mean of them is calculated to compare with the relative reference temperature. For each thermocouple at every temperature point, the error is less than ±0.1°C, as shown in Table 2.4. The calibration data were used to revise the function for each thermocouple.

Table 2.4 Calibration data for thermocouples from thermocouple calibration system

$T_{measure} - T_{reference}$	Mean (°C)	Max (°C)	Min (°C)	Standard deviation
Thin thermocouples	-0.019	0.030	-0.081	0.025
Armoured thermocouples	0.058	0.096	0.022	0.027

Mass flow meter: The mass flow meters used for this test are KROHNE OPTIMASS MFS 7150 S04 and S03. They are Coriolis mass flow meter instead of volumetric flow meter. These meters were calibrated with water by the producer. After they arrived to the laboratory, they have been calibrated with water because the density of measure liquid should have no influence on Coriolis flow meter. The calibrations using fluid of R134a have also been performed to exam the former calibrations after the meters have been fitted into the test rigs. The results proved that the error is within ±1%. However, the calibrations by producer for these meters are more professional and accurate, so they have been adopted for this research. The limits of error of mass flow rate including that of data acquisition system is within ±0.12%. Therefore, the accuracy is ±0.12 Kg/hr for small mass flow meter S03 and ±0.42 Kg/hr for large mass flow meter S04.

2.4 Test procedures

After the establishment of test rigs, the prepare work and test were performed.

The procedures before test:

a. Leakage test: Inject nitrogen gas into system to 1.5 fold of design pressure. Switch off particular valves to separate the rigs into several independent

parts, each of them has a pressure gauge. Hold several days and compare system pressure measured before and after to inspect leakage. If the system pressure reduced, use detective spray on test rig to find the leak point, then repair it after release of pressure and do the test again until there is no leakage.

b. Vacuumed test loop: use vacuum pump to absorb gas from the test loop and refrigeration loop to make sure there is no air or water steam in the system.

c. Injecting fluid: Inject liquid phase R404a into vacuumed refrigeration loop to 3bar, start the compressor and then continue to inject to required level. Inject 5 L ester oil for compressor. Inject liquid phase R134a into vacuumed test loop to 3bar. Start the pump and continue to inject refrigerant to required level.

The procedures during the test:

a. Change test tube: the test tubes are changeable with using flange to connect it with other pipe. The leakage test must be performed and the system must be vacuumed before test.

b. Test run: perform single-phase tests in a metal-foam tube with various heat/mass fluxes to check all the facilities and measure the heat loss to environment. It can be used for correction of two-phase flow.

c. Measure heat transfer and pressure resistance for forced flow and two-phase flows in plain tubes with various heat/mass flux for comparison.

d. Measure pressure drop and heat transfer in single-phase flows in each metal-foam test tube with various mass fluxes.

e. Measure two-phase flows in metal-foam tubes with various heat/mass fluxes for a given metal-foam cell size and porosity (cell size 20 ppi, porosity 90%).

f. Measure two-phase flows in metal-foam tubes at chosen heat/mass fluxes for different metal-foam cell sizes (40ppi, porosity 90%).

g. Measure two-phase flows in metal-foam tubes at chosen heat/mass fluxes for different metal-foam porosities (porosity 85%, cell size 20 ppi).

h. Measure two-phase flows in metal-foam tubes at chosen heat/mass fluxes for different metal-foam materials (100%Cu or 14%Ag86%Cu, porosity 85% and cell size 20 ppi).

Chapter 3 Experimental Investigation on Forced Convection

Although some investigations on heat transport in open-cell metal foams have been carried out, the previous work mainly concentrated on metal-foam plate channels, and no research work has been reported yet in the open literatures on experimental study for force convection in metal-foam tubes, which has more potential applications in industry. Also the heat transfer for R134a vapour flow in metal foams has not been investigated, which is very important for designing the metal foam two-phase heat exchangers used in refrigeration systems. It is known that the perfect contact between the metal foam and tube wall is crucial to reduce the contact resistance and improve the heat transfer. In this chapter, another important objective is to examine the effect of different tube/foam combining methods on heat transfer.

In this chapter, an experimental study of forced R134a superheated vapour flow heat transfer performance and flow resistance in metal-foam tubes will be presented. The effect of metal foam microstructures (pore size, relative density) on heat transfer performance will be investigated. To examine the effect of different tube/foam combining methods on heat transfer, a group of metal-foam tubes with different attaching methods will be tested.

3.1 Test conditions

To investigate the single-phase forced flow in horizantal metal-foam tubes, superheated vapour R134a is use as fluid to investigate the heat transfer and pressure loss for different metal-foam tubes. The test rigs described in Charpter Two are used for this test. It can also be regarded as pilot test for the test facality. The well-insulated pre-heaters are used to vaporize the liquid R134a after the mass flow

meters and heat it to superheated vapour. The operating pressure is maintained at 3.5 bar and the average vapour temperature is about 30 °C by adjusting the PID controller and the Pre-heaters. The power input is 60 W for all metal-foam tubes and 20 W for the plain tube. The tested copper tubes are 150 mm long and the inner diameter is 26 mm. In this investigation, 11 metal-foam tubes and 1 plain tube are tested, the details of each tube can be found in Table 2.2.

3.2 Data reduction

In this part, the non-dimensional Reynolds number and Nusselt number are defined as formula (3.1) and (3.2):

$$\mathrm{Re} = \frac{\rho u d}{\mu} = \frac{\dot{m} d}{A_c \mu} , \qquad (3.1)$$

where u is velocity of fluid, $\dot{m}$ is mass flow rate (Kg/s), d and A_c are inner diameter and cross-section area of test tube. ρ, μ are density and viscosity of fluid, respectively.

$$Nu = \frac{hd}{k} = \frac{q_w d}{\Delta T k} , \qquad (3.2)$$

where the h represents heat transfer coefficient and k is thermal conductivity of fluid. ΔT is temperature difference between the averaged inner wall surface temperature and the fluid average temperature. The q_w is input heat flux (W/m^2), which can be calculated by

$$q_w = \frac{Q}{A_i} = \frac{Q_{heaterinput} - Q_{loss}}{A_i} , \qquad (3.3)$$

where A_i is inner surface area of the test tube, $\pi d L_{heat}$, $Q_{heaterinput}$ is the power of the heater in test section. Q_{loss} is the heat lost from the insulation which can be calculated

by heat conduction through the insulation, the points a and b represent thermocouple locations in different insulation layers, as shown in Fig. 2.4. The k is thermal conductivity of insulation.

$$Q_{loss} = -\frac{kL(T_a - T_b)}{\ln(d_a / d_b)} \tag{3.4}$$

Alternatively, the heat loss can be calculated as the difference between heat input and the heat absorbed by the liquid.

$$Q_{loss} = Q_{heaterinput} - Q_{absorption} \ , \tag{3.5}$$

where $Q_{absorption} = \dot{m}\ c_p\ (T_{out}-T_{in})$, in which $\dot{m}$ and c_p are mass flow rate (kg/s) and specific heat capacity (J/kg K), and T_{in} and T_{out} are temperature at input and output of test section. From the experimental results, the value of equation 3.4 were matching the value of equation 3.5, so the equation 3.4 can also be used to calculate the heat loss for two phase flow in the following chapter.

The uncertainties in the present experimental results were estimated by the single-sample experiment analysis described by Kline and McClintock (1953). The uncertainties for the heat transfer coefficient, Reynolds number and Nusselt number were mainly attributed to the variation of power input, temperature, and the thermophysical properties of fluid. For example, the uncertainty of the Nusselt number can be expressed by

$$\frac{\delta Nu}{Nu} = \sqrt{(\frac{\delta q_w}{q_w})^2 + (\frac{\delta d}{d})^2 + (\frac{\delta \Delta T}{\Delta T})^2 + (\frac{\delta k}{k})^2} \tag{3.6}$$

The uncertainty of power input was estimated as less than 5%, which includes the published accuracies (0.5%) of the Programmable Power Meter (Hameg HM8115-2)

and the estimated error brought by axial heat conduction. The geometric uncertainty of the test tubes was very low and estimated as one percent. The error in the estimation of ΔT (temperature difference between the averaged inner wall surface temperature and the fluid average temperature) was 0.5 °C, that includes the error of thermocouples (0.1 °C) calibrated with data acquisition system and the estimated error brought by the contact thermal resistance of thermocouple attachment. Therefore, the uncertainty in temperature difference was less than 7% based on a representative value of ΔT was 8 °C. The thermophysical properties (e.g. thermal conductivity (k)) was retrieved from database of National Institute of Standards and Technology (NIST) by using measured temperature and pressure, the error of thermal conductivity was estimated to be less than one percent. Therefore, the uncertainty in Nusselt number was less than 9%. The accuracy of pressure drop measurement was $\leq \pm 170$Pa, considered the assembling error, then the uncertainty of pressure drop was less than 5% based on a representative value of $\Delta P/L$ was 30 KPa/m.

3.3 Experimental results and discussions

3.3.1 Heat transfer performance

- ***Effect of tube/foam binding methods on heat transfer***

It is realized that the contact quality between the tube surface and the metal foam structures will have a direct effect on the thermal contact resistance, and thereby affecting the heat transfer. To examine the effect of different tube/foam combining methods on heat transfer, a group of metal-foam tubes with different attaching

methods have been experimentally tested for R134a superheated vapour flow heat transfer, as shown in Fig. 3.1.

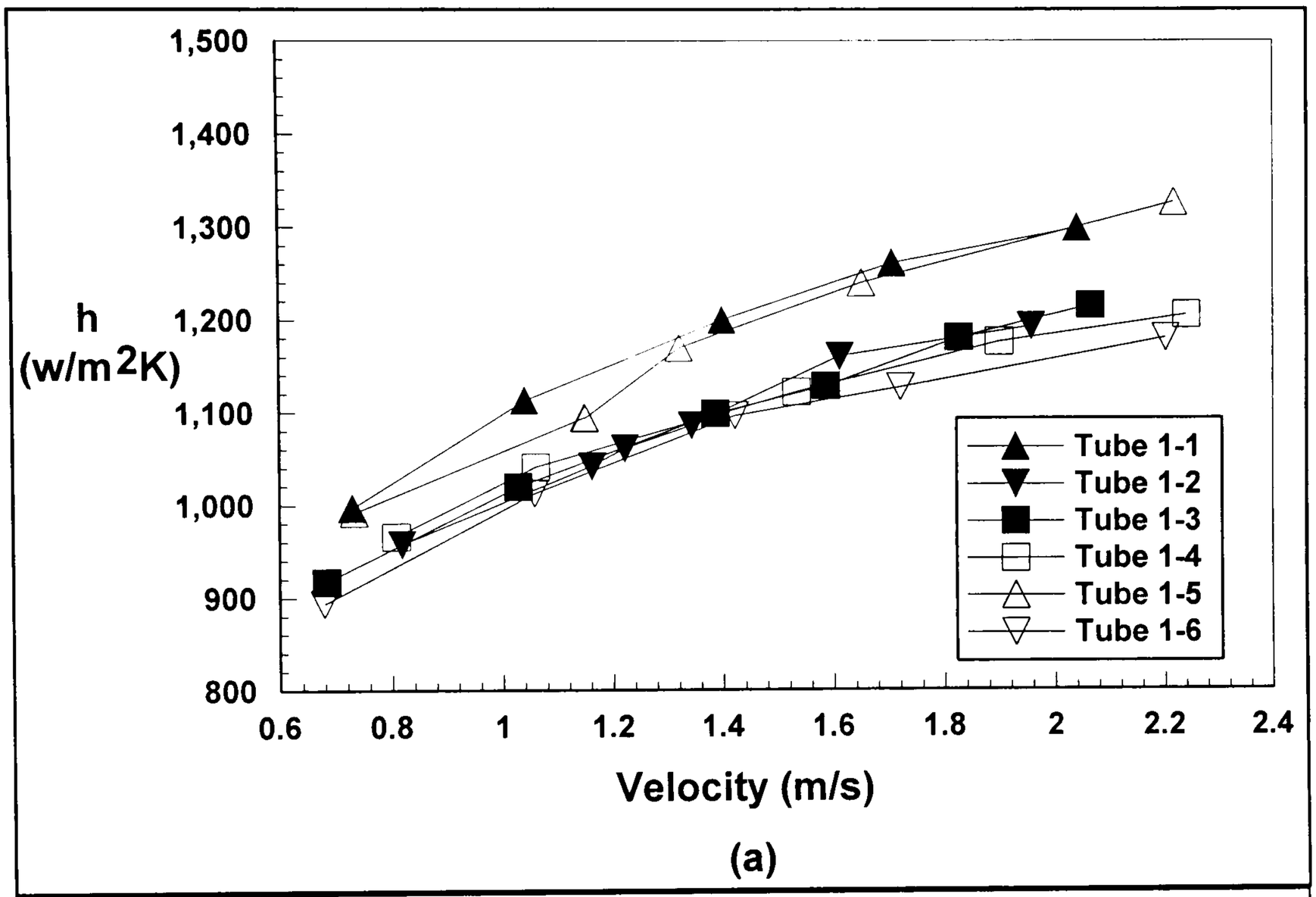

Fig. 3.1 Effect of tube/foam binding methods on heat transfer, (a) heat transfer coefficient and (b) Nusselt number

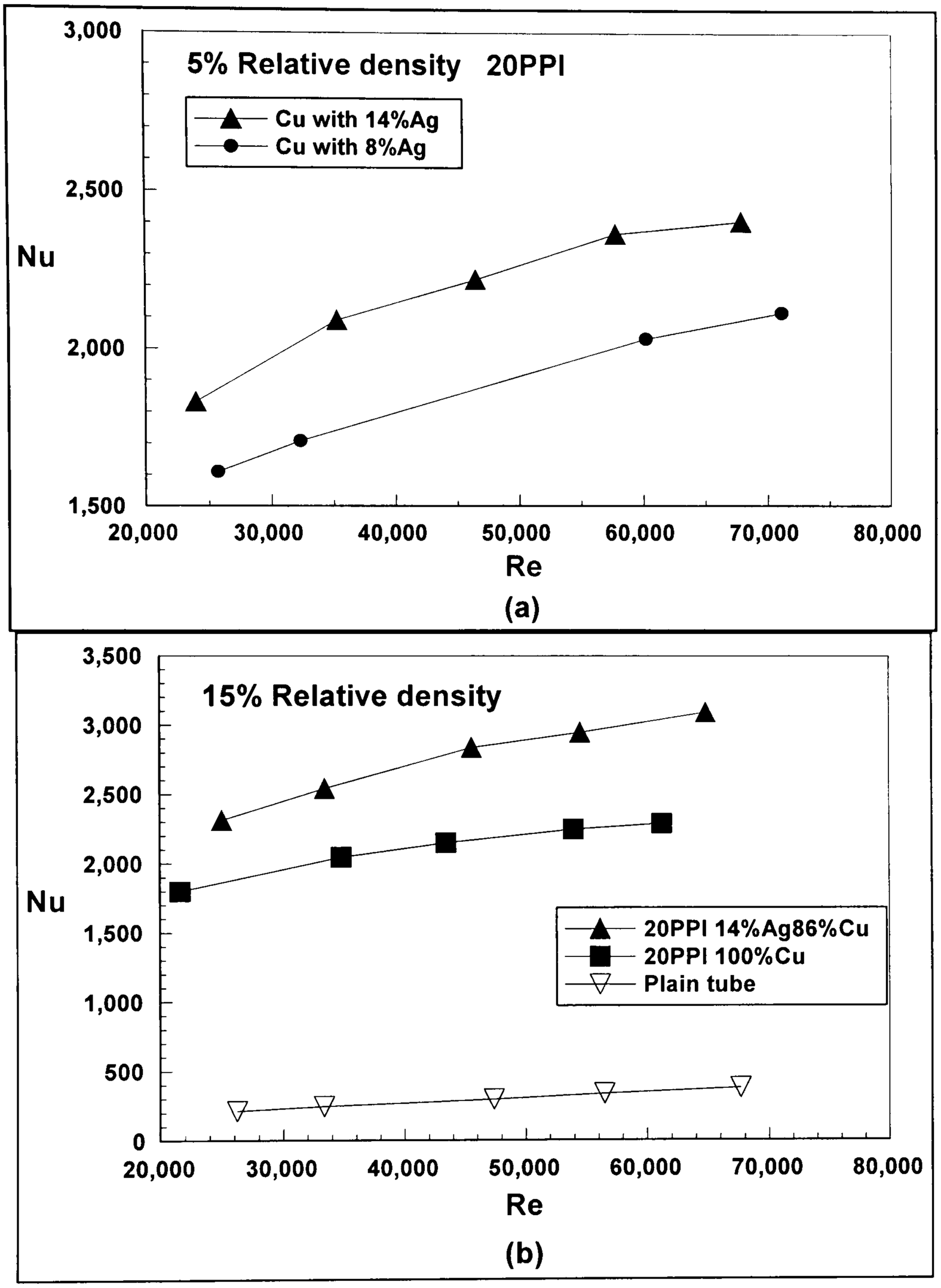

Fig. 3.2 Effect of metal-foam material on heat transfer performance, (a) 5% relative density and (b) 15% relative density

Fig. 3.1 (a) presents the heat transfer coefficient (h) as a function of vapour velocity. For the group of tubes labelled 1-X (20 ppi (pores per inch), 5% relative density), the tube 1-1 and tube 1-5 give the best heat transfer performance due to the different attaching methods, though the microstructure of the whole group tubes (1-X) is same (20 ppi and 5% relative density). This implies that the combining methods used in

tubes 1-1 and 1-5 are superior to other methods as far as heat transfer is concerned. Therefore, the tubes combined by method of tube 1-1 have been chosen for tests of the following research.

Fig. 3.2 shows the effect of different metal-foam materials on heat transfer. The results for metal foams with 5% relative density and 20 PPI are presented in Fig. 3.2 (a), while the results for 15% relative density and 20 PPI are given in Fig. 3.2 (b). The results show that more silver in metal foams results in better heat transfer performance. The significant improvement caused by silver addition reveals that different metal foam composition has a direct effect on its overall thermal conductivity, and perhaps more importantly, it directly affects the attachment quality with the tubes.

- ***Effect of metal-foam microstructures***

The effect of metal-foam microstructures (e.g. cell size ppi and relative density) on heat transfer was examined, as shown in Fig. 3.3, for 134a vapour flow. Here relative density represents the ratio of metal foam density and pure material density. Fig. 3.3 (a) and (b) present the effect of relative density on heat transfer of metal-foam (8%Ag92%Cu) filled tubes for a given pore size 20 ppi. The result shows that the heat transfer can be dramatically enhanced by improving the relative density (decreasing the porosity), as expected. In this figure the experimental results for empty tubes are also included, and the results reveal that the heat transfer is enhanced by an order of magnitude due to the metal foam effect. Compared to that of the plain tube, the use of metal foams could improve the heat transfer by 5-10 times due to the enhanced surface area density and flow mixing.

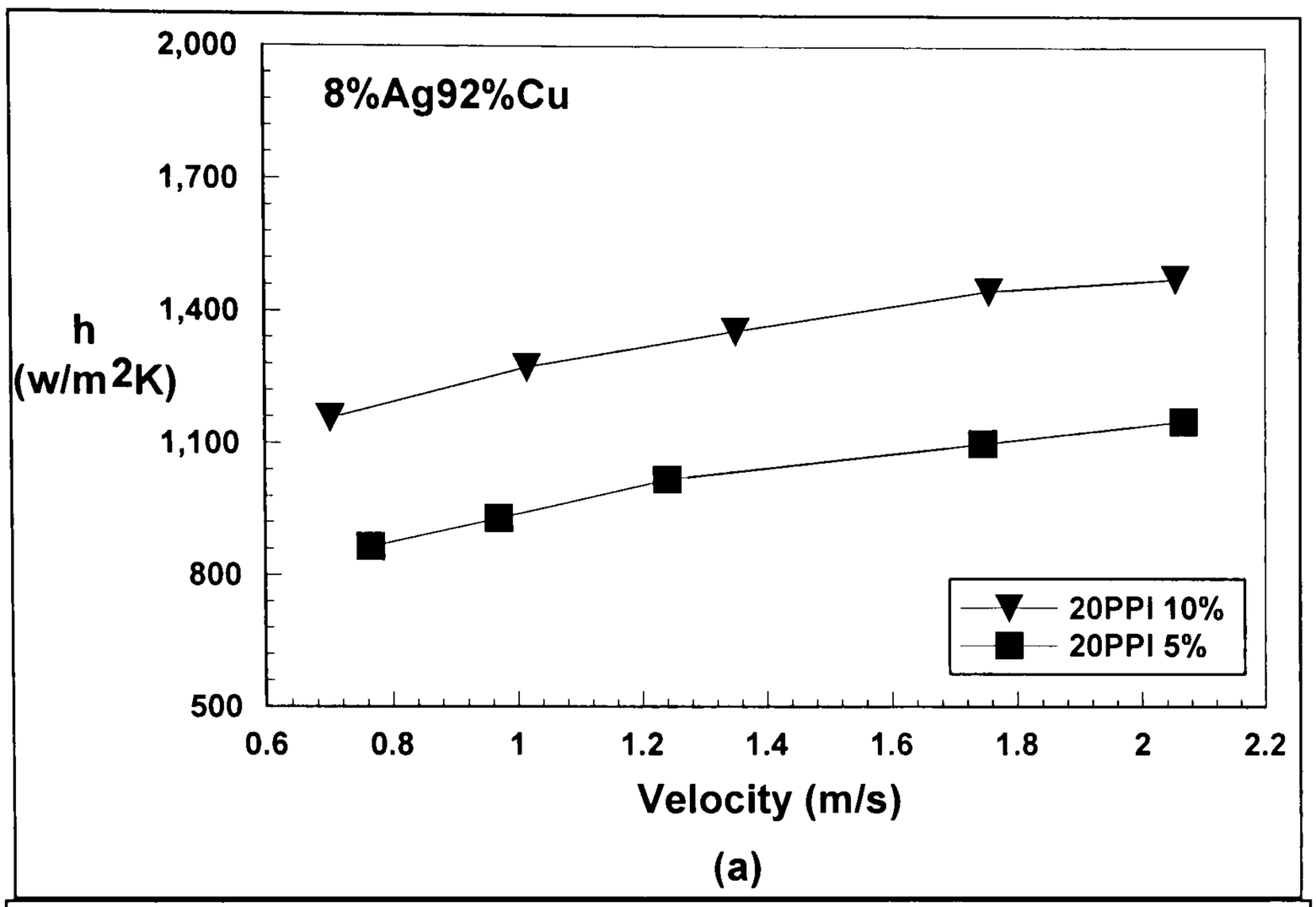

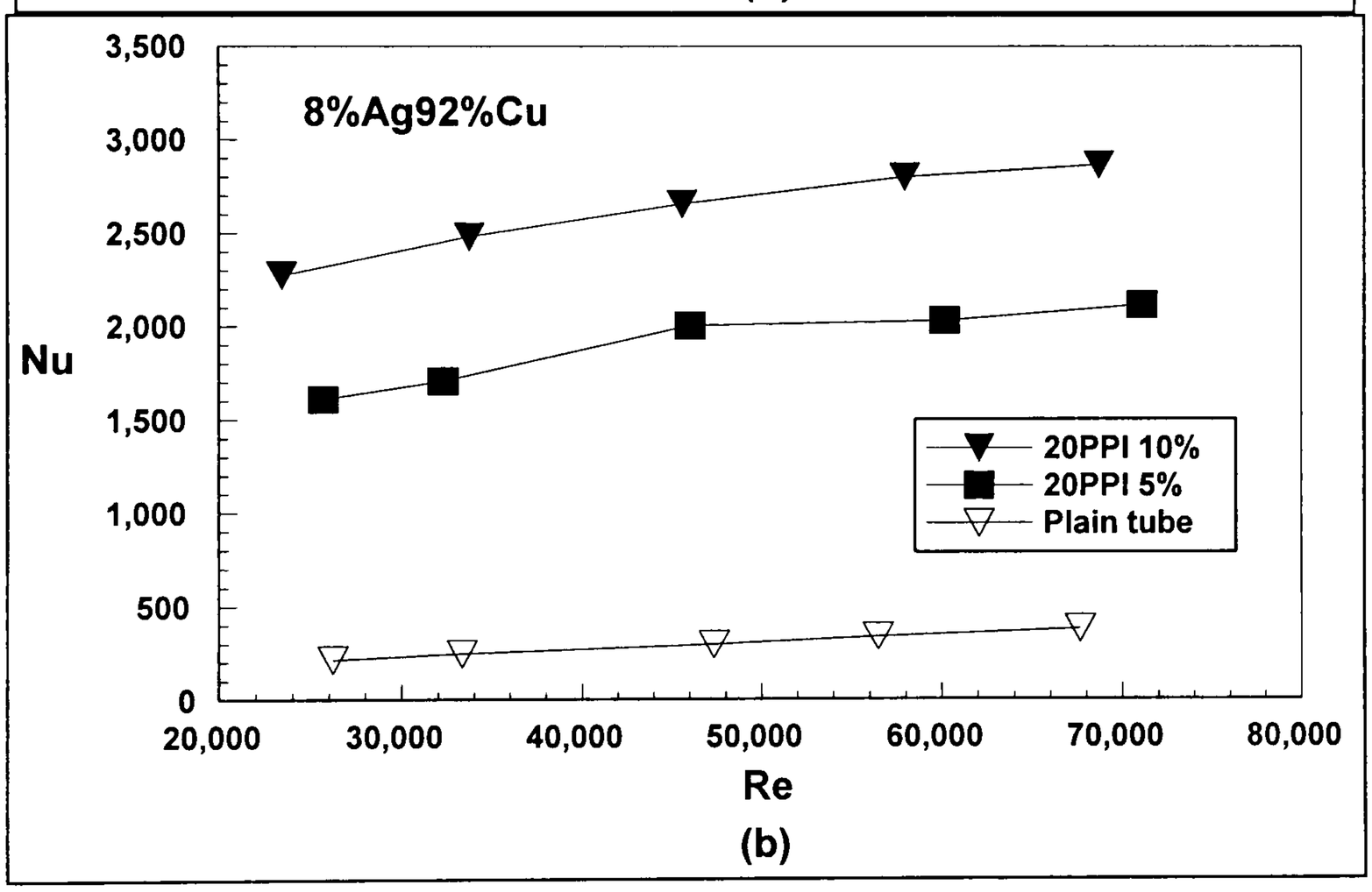

Fig. 3.3 The effect of relative density on (a) heat transfer coefficient and (b) Nusselt number

Fig. 3.4 presents the effect of metal-foam pore size on overall heat transfer performance. The results show that the heat transfer (heat transfer coefficient and Nessult number) increases significantly with the increase of pore density (decrease of pore size from 20 PPI to 40 PPI), owing to more heat transfer area and flow mixing. Also the heat transfer coefficient increases with the velocity, as expected. Compared

to the heat transfer of plain tubes, again the use of metal foams can enhance the heat transfer by 8-15 times.

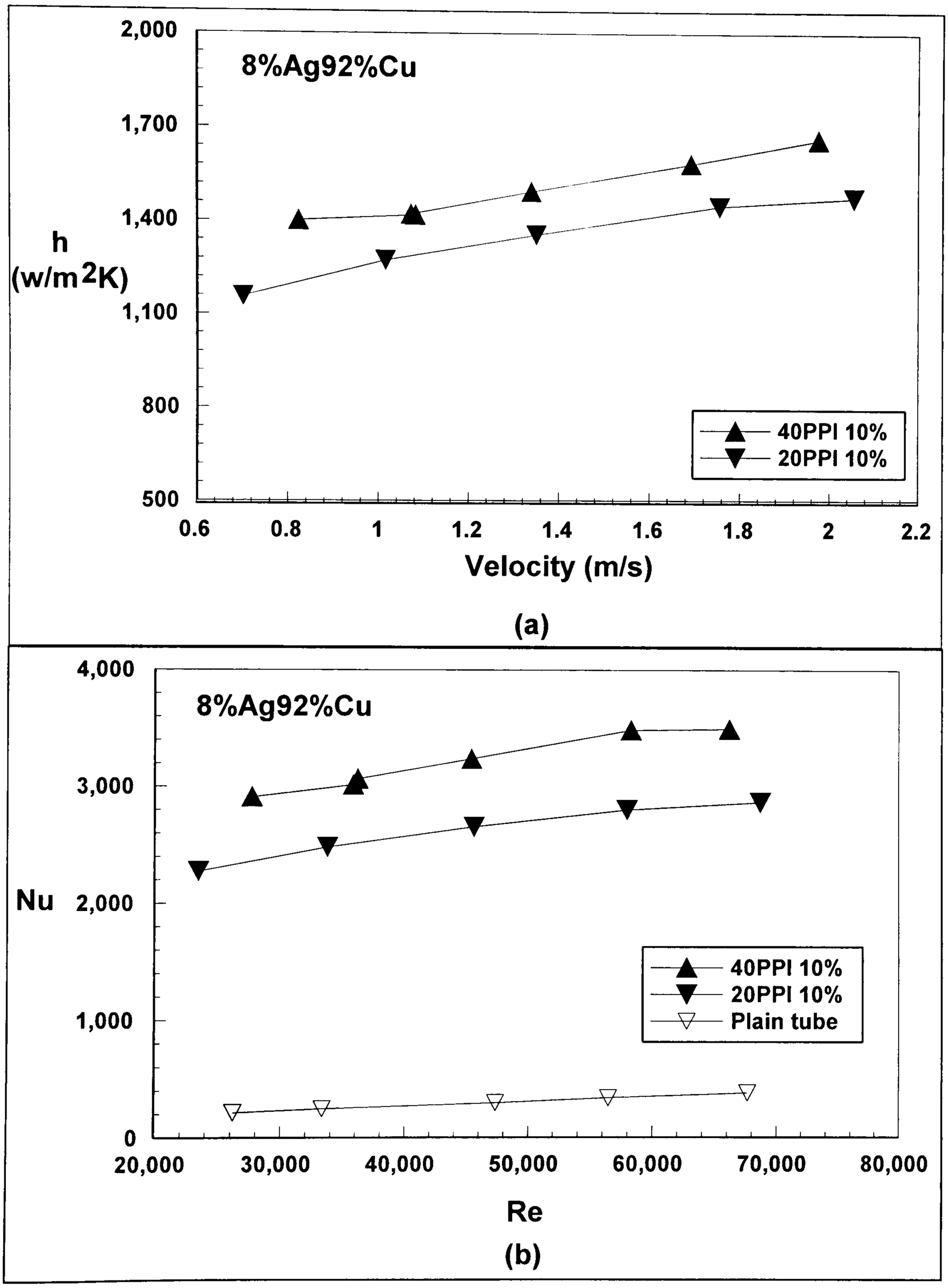

Fig. 3.4 The effect of pore size on (a) heat transfer coefficient and (b) Nusselt number

3.3.2 Pressure drop

Along with the heat transfer performance, the pressure drop caused by test tubes is also a very important factor. The measured results of pressure drop per unit length for different metal-foam tubes have been presented in Fig. 3.5 for different cell size effect and different porosity effect. It indicates that the pressure drop increases signifacantly with increasing relative density or pore density (PPI).

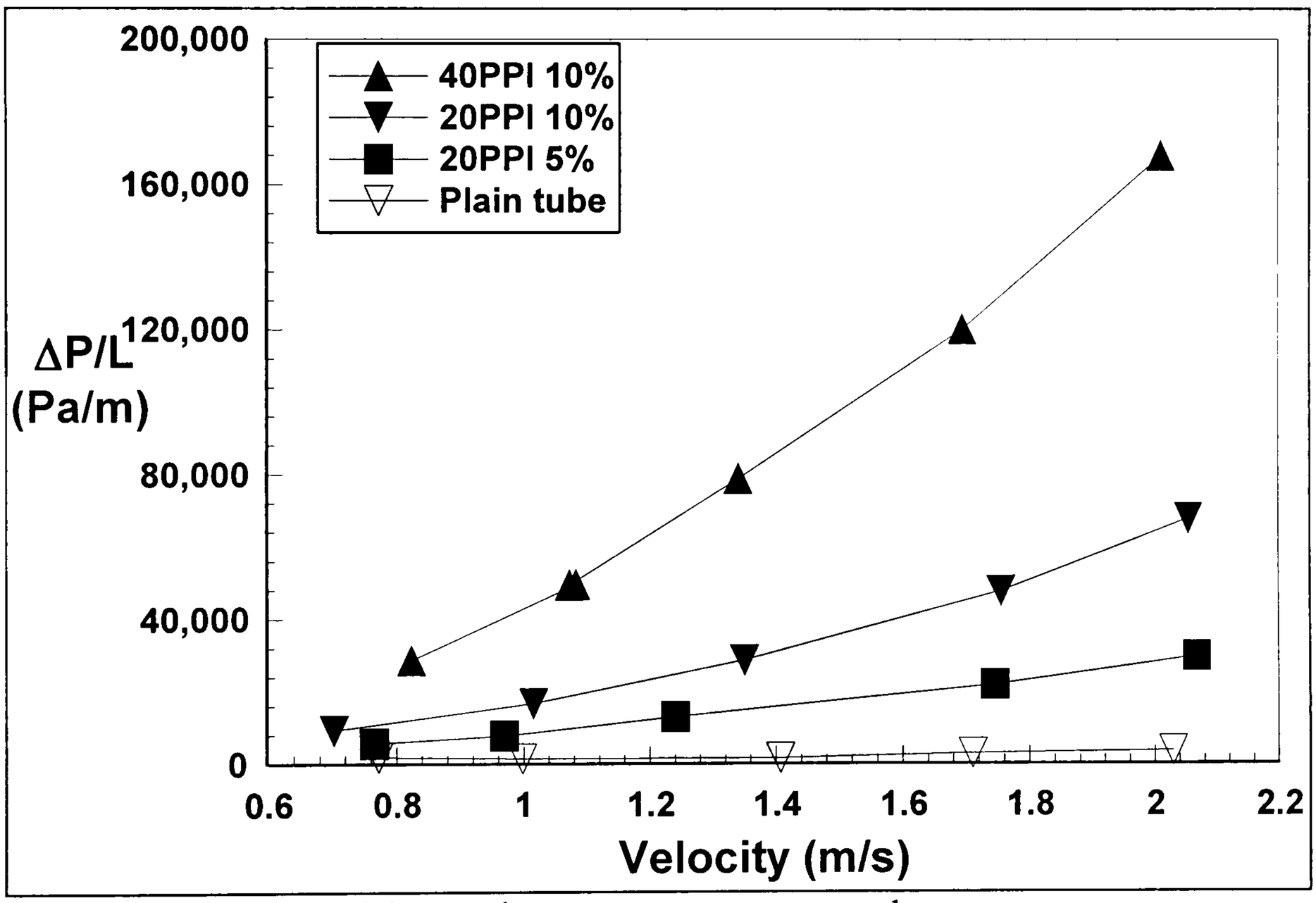

Fig. 3.5 Effect of metal foam microstructure on pressure loss

From the pressure drop measurements, the friction factor for each sample, defined as

$$f = \frac{\Delta P d}{L \cdot \frac{1}{2} \rho u^2}, \tag{3.7}$$

can be calculated. The results are ploted in Fig. 3.6. The results show that the friction factor increases with the increase of relative density or pore density (PPI), similar to

the pressure drop. Moreover, the friction factor for each tube essentially approaches to a constant, as expected for turbulent flow at high Reynolds numbers.

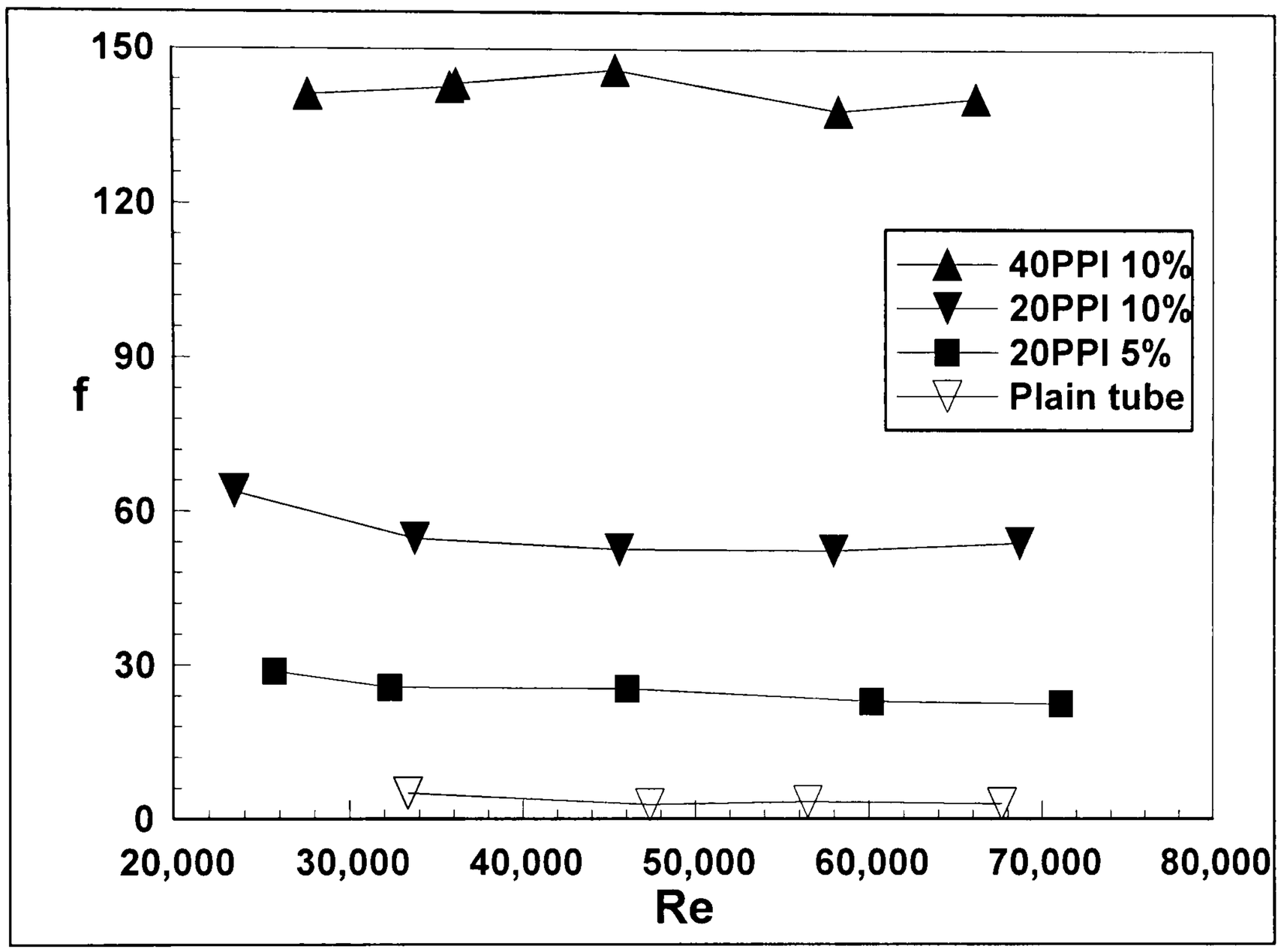

Fig. 3.6 Friction factors for different metal-foam microstructure

Therefore, it is clear that the increase of pore density and/or relative density causes more pressure loss but it can enhance the overall heat transfer performance in return. To give an overall assessment, the nondimesional efficiency index,

$$J = \frac{Nu}{f}, \tag{3.8}$$

which represents the ratio between heat transfer and flow resistance, has been adopted. It can been seen from Fig. 3.7 that the nondimesional efficiency index, which can be plotted as a function of the Renoynolds number, decreases with the increase of relative density or decrease of pore size (PPI), which comfirm that the

pressure drop increases at a faster pace than heat transfer does. Therefore, when the metal foams with high pore density and relative density are used for compact heat exchanger, more pressure loss accours as expences to get the same amount of heat transfered. However, the nondimesional efficiency index for these tube trends to close each other with the reduce of Reynolds number, which means the metal-foam tube may have nearly the same efficiency as plain tube in lower Reynolds number, i.e. the metal-foam tube is good at the enhance heat transfer in worse condition. In additon, although it costs more pump power, the use of metal foam can make more compact heat exchangers which can save more geometic space and materials.

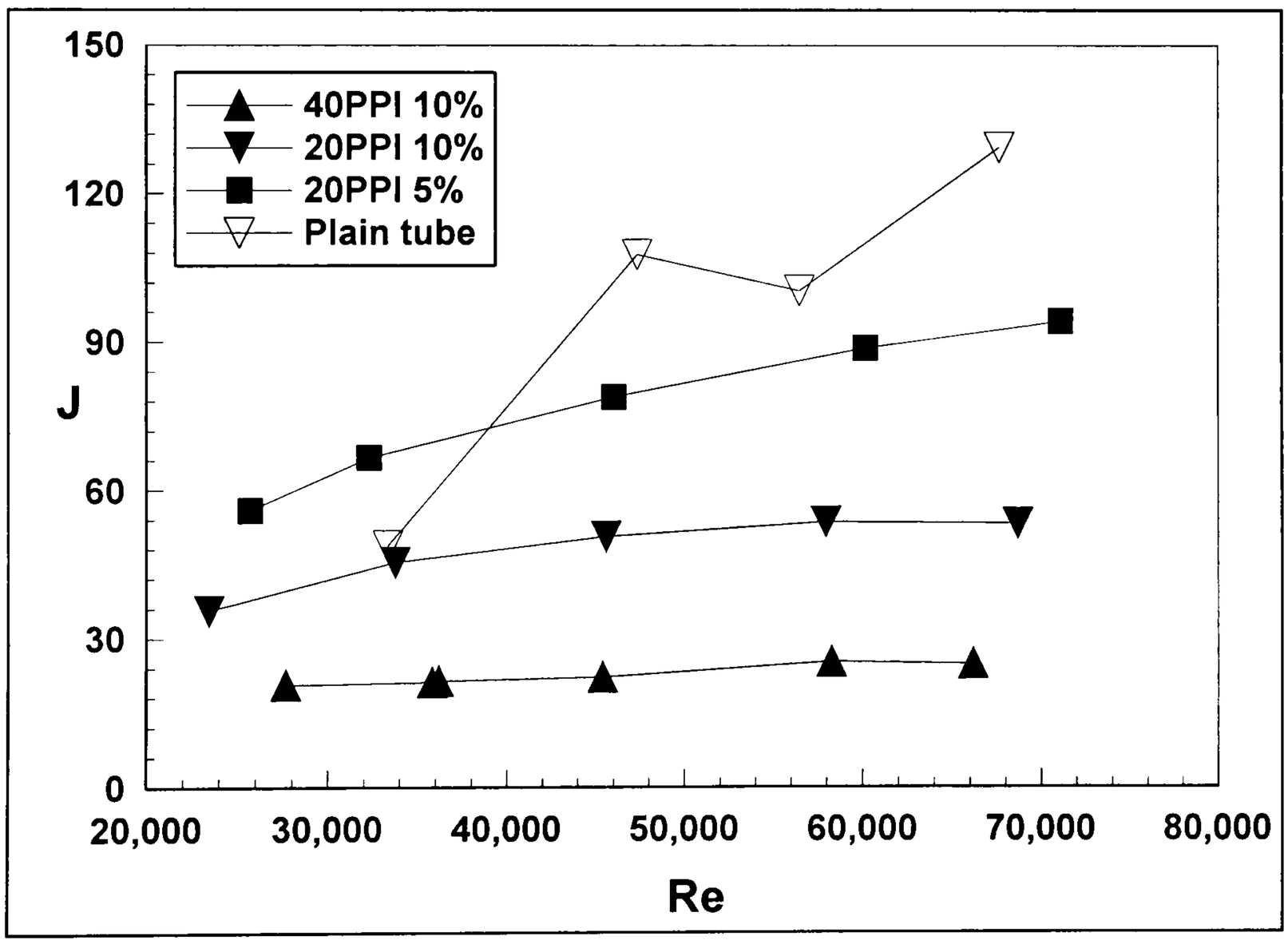

Fig. 3.7 Efficient index for different metal-foam microstructure

3.4 Conclusions

In this chapter, the experimental results have been presented for forced R134a vapour flow heat transfer in metal-foam tubes. The results show that the use of metal foams

brings enormous improvement for heat transfer especially when the heat transfer capability of the fluid itself is low as vapour R134a. The heat transfer in metal-foam tubes is enhanced by decreasing the cell size and/or increasing the relative density at the expense of higher flow resistance. Also the results revealed that the attachment quality between the tube and foam has a significant influence on overall heat transfer performance of metal-foam tube.

Chapter 4 Theoretical Modelling for Forced Convection

The detailed modelling of two-phase heat transfer in metal foams is extremely difficult and challenging because it involves the phase change and interfacial heat transfer among liquid film, vapour and solid metal-foam ligaments. Due to the complexities of modelling for two-phase heat transfer in metal foams, the modelling work of heat transfer performance in metal-foam tubes begins with analytical study for single-phase flow in metal-foam tubes, which has more potential applications in industry. Then, the numerical method using Forchheimer-Darcy Model for momentum equation is employed to determine the effect of inertia force on overall heat transfer performance of forced convection in metal-foam tubes. Finally, the numerical method has also been used to model the two-phase flow and heat transfer in these tubes. In this chapter, the analytical and numerical modelling work for single-phase flow in metal-foam tubes is represented.

This research aims to study the forced flow and heat transfer performance in metal-foam tubes and tube heat exchangers. Firstly, the details of analytical method and numerical method used to solve equations of momentum and energy in metal-foam tubes are provided. Then, the velocity distributions, temperature distributions, overall Nusselt numbers and pressure drop are presented to study the effects of different parameters on heat transfer and fluid flow in metal-foam tube, which can be regard as inner tube of tube heat exchanger. Furthermore, results predicted by these methods for inner tube are compared with experimental data to examine the predictions. Finally, the analytical method is used for analysing the heat transfer performance of metal-foam heat exchangers.

4.1.1 Analytical modelling for forced convection inside a tube

Although the heat transport in open-cell metal foam attracted much attention recently, the research which has been done is very limited due to the complicated heat transfer mechanism in metal foams filled channels. Our review also suggests that there is no thermal transport study in high porosity metal foams that is based on analytical solutions, which are helpful in identifying and studying the effects of variables of engineering importance and extending to more practical research (e.g. optimization of metal-foam heat exchangers) without tedious numerical computations. Furthermore, all the investigations were based on plate channels or cubic form, there is no research based on cylinder channels shape while the metal-foam tubes is more promising and can be widely applied for practical applications, along with the mature technique for embedding metal foams into tubes. Finally, most of research focused on specific kind of metal foams, such as aluminium foams or copper foams, with air as fluid, but this work studies the performance of the metal foam in general, regardless of particular materials.

4.1.1 Problem description

The problem under consideration in this section is forced convective flow through metal-foam tube as shown in Fig.4.1. The direction of fluid flow is parallel to z (axis of tube). The diameter of the tube is 2R, and the length of the tube is L. The wall of the tube is uniformly heated and the fluid (such as water or air) is assumed to flow through the open-cell metal-foam area, removing heat from the wall of the tube without phase change.

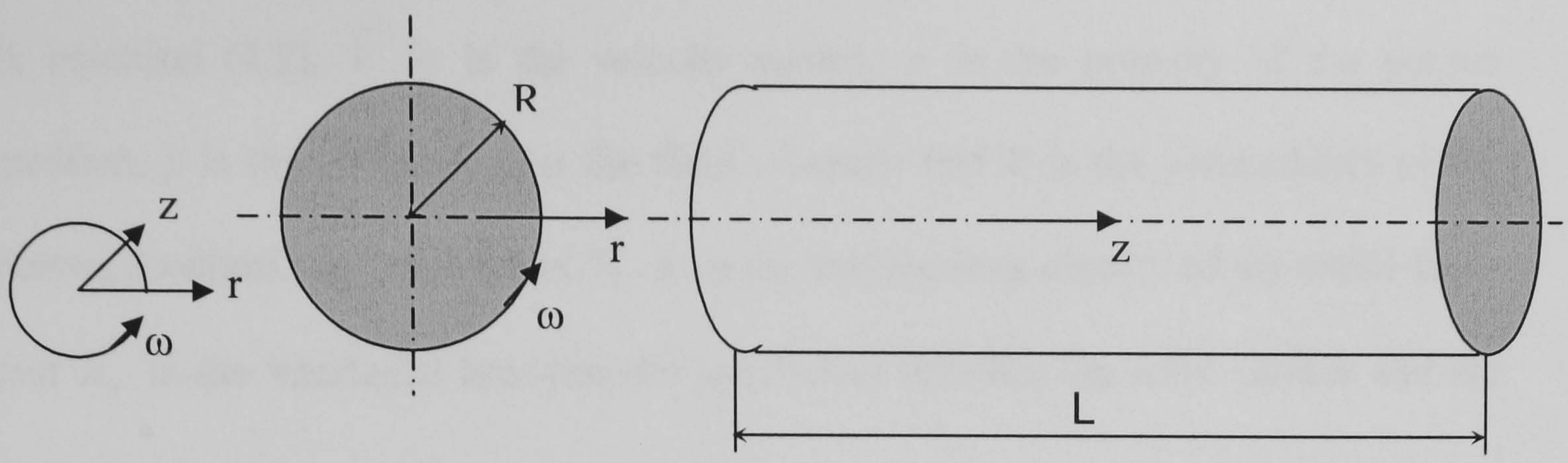

Fig. 4.1 Metal-foam tube: geometry and definition

4.1.2 Mathematical formulations and their analytical solutions

Mathematical formulations

As mentioned earlier, the momentum equation employed is based on the Brinkman extended Darcy model (Vafai and Tien, 1981) and the energy equations for both fluid and solid used, are based on the two-equation non-equilibrium heat transfer model proposed by Calmidi and Mahajan (1999). These are detailed below:

- Mass conservation equation

$$\nabla(\rho\vec{V}) = 0 \tag{4.1}$$

- Momentum equation (Brinkman-Darcy Model)

$$\frac{1}{\varepsilon}\langle(\vec{V}\cdot\nabla)\rho_f\vec{V}\rangle = -\nabla\langle p\rangle_f + \frac{\mu_f}{\varepsilon}\nabla^2\langle\vec{V}\rangle - \frac{\mu_f}{K}\langle\vec{V}\rangle \tag{4.2}$$

$\langle\ \rangle$ means a volume averaged value.

- Energy balance equations for the solid and fluid,

$$0 = \nabla\cdot\{k_{se}\nabla\langle T_s\rangle\} - h_{sf}\tilde{a}(\langle T_s\rangle - \langle T_f\rangle) \tag{4.3}$$

$$\langle\rho\rangle_f C_f\langle\vec{V}\rangle\nabla T_f = \nabla\cdot\{(k_{fe}+k_d)\cdot\nabla\langle T_f\rangle\} + h_{sf}\tilde{a}(\langle T_s\rangle - \langle T_f\rangle) \tag{4.4}$$

In equation (4.2), $\vec{V}$ is is the velocity vector, ε is the porosity of the porous medium, p is the pressure, μ_f is the fluid viscosity and K is the permeability of the porous medium. In equation (4.3), ã is the surface area density of the metal foam and h_{sf} is the interfacial heat-transfer coefficient between the solid surface and the fluid. C_f and ρ_f are the heat capacity and density of fluid respectively, whereas k_{se} and k_{fe} are the effective thermal conductivities of solid and fluid.

In the analysis it is assumed that the flow is both hydraulically and thermally fully developed. All thermo-physical properties of the solid and fluid, e.g., thermal conductivity, density, specific heat and viscosity, are assumed to be temperature independent. Natural convection and radiation are negligible. The porous medium is assumed homogeneous and isentropic, and thus the problem can be considered axially symmetrical. In addition, Calmidi and Mahajan (2000) and Phanikumar and Mahajan (2002) concluded from their studies that the enhancing effect of thermal dispersion (k_d) is extremely low due to the relatively high conductivity of the solid matrix. Therefore, The term k_d is dropped to simplify the analysis. Based on these assumptions, equations (4.1 ~ 4.4) can be simplified as follows:

$$0 = -\frac{dp}{dz} + \frac{\mu_f}{\varepsilon}\left(\frac{\partial^2 u}{\partial r^2} + \frac{1}{r}\frac{\partial u}{\partial r}\right) - \frac{\mu_f}{K}u \tag{4.5}$$

$$0 = k_{se}\left(\frac{\partial^2 T_s}{\partial r^2} + \frac{1}{r}\frac{\partial T_s}{\partial r}\right\} - h_{sf}a(T_s - T_f) \tag{4.6}$$

$$\varepsilon\rho_f C_f u\frac{dT_f}{dz} = k_{fe}\cdot\left(\frac{\partial^2 T_f}{\partial r^2} + \frac{1}{r}\frac{\partial T_f}{\partial r}\right) + h_{sf}a(T_s - T_f) \tag{4.7}$$

Where brackets 〈 〉 are dropped for simplicity, and u is the velocity along the z direction, V_z.

Boundary conditions

For the metal-foam tubes directly heated from outside surface with constant heat flux, the applied heat is transferred to the solid and fluid phases by conduction and convection. As discussed by Zhao et al. (2004a) and Lee and Vafai (1999), because the thermal conductivity of the thin metal wall of tube is significantly higher than that of the fluid, the temperature at the interface between metal foams and the substrate can be considered to be uniform regardless of whether it is in contact with the solid or fluid. Consequently, the boundary conditions of metal-foam tube can be specified as follows:

When r=R, u=0, $T_s = T_f = T_w$, (4.8)

When r=0, $\frac{\partial u}{\partial r} = \frac{\partial T_f}{\partial r} = \frac{\partial T_s}{\partial r} = 0$ (4.9)

Where T_w implies the temperature at the interface. This temperature is not known a *priori* and must be obtained as part of the solution.

Parameters in equations

To proceed further, there are parameters in the above equations that need to be established. They are permeability (K), effective thermal conductivities of the solid and fluid phases (k_{se} and k_{fe}), surface area density (ã) and the interfacial heat-transfer coefficient (h_{sf}).

- Permeability (K)

The permeability (K) of metal foams, which is the key parameter for solving the momentum equation, has been investigated by several researchers. Zhao et al.

(2004a) suggested a specific formulation for K, which is proposed by Calmidi based on experimental data.

$$\frac{K}{d_P^2} = 0.00073(1-\varepsilon)^{-0.224}(d_f / d_p)^{-1.11} \tag{4.10}$$

where d_P is the pore size (d_p=0.0254/ppi meter, ppi: pores per inch), d_f is the fibre diameter of metal foams ($\frac{d_f}{d_P} = 1.18\sqrt{\frac{(1-\varepsilon)}{3\pi}}(\frac{1}{1-e^{-((1-\varepsilon)/0.04)}})$).

- Effective thermal conductivities of the solid and fluid (k_{se} and k_{fe})

To determine the effective thermal conductivity of open-cell metal foams, k_e, the following correlation, which is based on the three-dimensional cellular morphology, was proposed by K. Boomsma and D. Poulikakos. (2001)

$$k_e = \frac{\sqrt{2}}{2(R_A + R_B + R_C + R_D)}, \tag{4.11}$$

Where

$$R_A = \frac{4d}{(2e^2 + \pi d(1-e))k_s + (4 - 2e^2 - \pi d(1-e))k_f}$$

$$R_B = \frac{(e-2d)^2}{(e-2d)e^2 k_s + (2e - 4d - (e-2d)e^2)k_f}$$

$$R_C = \frac{(\sqrt{2}-2e)^2}{2\pi d^2(1-2e\sqrt{2})k_s + 2(\sqrt{2} - 2e - \pi d^2(1-2e\sqrt{2}))k_f}$$

$$R_D = \frac{2e}{e^2 k_s + (4-e^2)k_f}$$

$$d = \sqrt{\frac{\sqrt{2}(2 - (5/8)e^3\sqrt{2} - 2\varepsilon)}{\pi(3 - 4e\sqrt{2} - e)}}, \quad e=0.339$$

After the overall effective thermal conductivity is obtained, the effective solid conductivity, k_{se}, can be established by setting k_f =0. Similarly, the effective fluid conductivity, k_{fe} , can be determined by setting k_s=0.

- Surface area density (ã)

The solid-fluid interfacial surface area density for an array of parallel cylinders intersecting in three mutually perpendicular directions, whose cylinder diameter is d and interval is a, is $\frac{3\pi d}{a^2}$. However, the topology of metal foams is different from the cross-cylinder. Furthermore, the cross section of the fibre is not circular when the porosity of metal foams is higher than 0.85. Shape factors must be introduced when the formula of cross-cylinder is used to simplified the structure of metal foams, which are $a=0.59d_P$, and $d=(1-e^{-((1-\varepsilon)/0.04)})\cdot d_f$. Then the surface area density of metal foams becomes (Zhao et al., 2001):

$$\tilde{a}=\frac{3\pi d_f(1-e^{-((1-\varepsilon)/0.04)})}{(0.59d_P)^2} \tag{4.12}$$

- The interfacial heat-transfer coefficient (h_{sf})

The interfacial heat-transfer coefficient for packed beds is usually calculated using a correlation proposed by Wakao et al. (1979). However, no such general correlation exists for metal foams. So the following correlation developed by Zhukauskas (1987), which is valid for staggered cylinders, is used to estimate h_{sf}:

$$Nu_{sf}=\frac{h_{sf}d}{k_f}=\begin{cases}0.76\,\mathrm{Re}_l^{0.4}\,\mathrm{Pr}^{0.37}, & (10^0\le \mathrm{Re}_d\le 4\cdot 10^1)\\ 0.52\,\mathrm{Re}_l^{0.5}\,\mathrm{Pr}^{0.37}, & (4\cdot 10^1\le \mathrm{Re}_d\le 10^3)\\ 0.26\,\mathrm{Re}_l^{0.6}\,\mathrm{Pr}^{0.37}, & (10^3\le \mathrm{Re}_d\le 2\cdot 10^5)\end{cases} \tag{4.13}$$

where Re_l is the local Reynolds number, $Re_l = ud_l/\nu$. For metal foams, as discussed above, the cross-section of the fibres is not circular and to account for this the shape factor, $d_l = (1 - e^{-((1-\varepsilon)/0.04)}) \cdot d_f$, is introduced as well.

4.1.3 Normalisation of equations

Equations and boundary conditions can be non-dimensionalised by introducing the following dimensionless variables:

$$Da = K/R^2,\ \psi = r/R,\ P = \frac{K}{\mu_f u_m}\frac{dp}{dz},\ \theta_s = \frac{T_s - T_w}{q_w R/k_{se}},\ \theta_f = \frac{T_f - T_w}{q_w R/k_{se}},$$

$$D = h_{sf}\,\tilde{a}\,R^2/k_{se},\ C = \frac{k_{fe}}{k_{se}},\ U = \frac{u}{u_m}, \tag{4.14}$$

where q_w is the heat flux over the surface of the tube and u and u_m are the local velocity and mean velocity along the axial direction, respectively.

Due to the assumption of fully developed flow subjected to a constant heat flux, the equations $\frac{\partial p}{\partial z} = const$ and $\frac{\partial T_w}{\partial z} = \frac{\partial T_f}{\partial z} = \frac{\partial T_s}{\partial z} = const$ hold. And all the heat applied to the tube wall has been taken away by the fluid, $q_w = \varepsilon \rho_f C_f u_m \frac{\pi R^2}{2\pi R}\frac{\partial T_f}{\partial z}$. Then, the dimensionless equations and boundary conditions can be expressed as follows.

- The dimensionless momentum equation:

$$U = -P + \frac{Da}{\varepsilon}\left(\frac{\partial^2 U}{\partial \psi^2} + \frac{1}{\psi}\frac{\partial U}{\partial \psi}\right) \tag{4.15}$$

- The dimensionless energy balance equations for the solid and fluid:

$$0 = \frac{\partial^2 \theta_s}{\partial \psi^2} + \frac{1}{\psi}\frac{\partial \theta_s}{\partial \psi} - D(\theta_s - \theta_f) \tag{4.16}$$

$$2U = C \cdot (\frac{\partial^2 \theta_f}{\partial \psi^2} + \frac{1}{\psi}\frac{\partial \theta_f}{\partial \psi}) + D(\theta_s - \theta_f) \tag{4.17}$$

- The dimensionless boundary conditions are:

$$U = \theta_s = \theta_f = 0 \text{ at } \psi = 1, \tag{4.18}$$

$$\frac{dU}{d\psi} = \frac{\partial \theta_s}{\partial \psi} = \frac{\partial \theta_f}{\partial \psi} = 0 \text{ at } \psi = 0, \tag{4.19}$$

4.1.4 Analytical solutions of the equations

The above equations can be treated as equations of the form $\frac{\partial^2 Y}{\partial z} + \frac{1}{z}\frac{\partial Y}{\partial z} - Y = 0$ and

$\frac{\partial^2 Y}{\partial z} + \frac{1}{z}\frac{\partial Y}{\partial z} = C$. The latter is easy to solve. The standard solutions of the former, $J_0(z)$ and $Y_0(z)$ are given in the Appendix A. Based on these, equations (4.15~4.17) can be analytically solved under boundary conditions (4.18) and (4.19).

Dimensionless velocity distribution

The velocity distribution can be obtained by solving the momentum equation (4.15), as

$$U = P\frac{J_0(\sqrt{\frac{\varepsilon}{Da}}\psi)}{J_0(\sqrt{\frac{\varepsilon}{Da}})} - P \tag{4.20}$$

From the continuum equation the following relationship is valid $\frac{1}{A}\int_A U dA = 1$,

namely, $\frac{1}{\pi}\int_0^{2\pi}\int_0^1 P(J_0(\sqrt{\frac{\varepsilon}{Da}}\psi)/J_0(\sqrt{\frac{\varepsilon}{Da}}))\psi d\psi d\theta = 1$.

Hence,

$$P=\frac{J_0(\sqrt{\frac{\varepsilon}{Da}})}{2\sqrt{\frac{Da}{\varepsilon}}J_1(\sqrt{\frac{\varepsilon}{Da}})-J_0(\sqrt{\frac{\varepsilon}{Da}})} \tag{4.21}$$

From equation (4.14), a formulation for the pressure drop can be deduced as:

$$\frac{dp}{dz}=\frac{\mu_f u_m}{K}P, \tag{4.22}$$

Integrating both sides, equation (4.22) becomes:

$$\Delta p=\int_0^L \frac{\mu_f u_m}{K}Pdz=\frac{\mu_f u_m}{K}PL \tag{4.23}$$

Finally, the friction factor is given by:

$$f=\frac{\Delta\langle p\rangle 2R}{L\rho_f u_m^2/2}=\frac{4\mu_f}{K\rho_f u_m}P\cdot R=\frac{8P}{Da\cdot \mathrm{Re}} \tag{4.24}$$

Dimensionless temperature distributions

After the velocity distribution is determined, the temperature profile can be obtained from the solution of equations (4.16) and (4.17).

$$\theta_s=2P(-\frac{1}{4}\psi^2+\frac{\frac{Da}{\varepsilon}}{J_0(\sqrt{\frac{\varepsilon}{Da}})}J_0(\sqrt{\frac{\varepsilon}{Da}}\psi)+\frac{1}{4}-\frac{Da}{\varepsilon})-C\theta_f \tag{4.25}$$

$$\theta_f=\frac{2P}{C+1}(-\frac{1}{4}\psi^2+\frac{\frac{Da}{\varepsilon}}{J_0(\sqrt{\frac{\varepsilon}{Da}})}J_0(\sqrt{\frac{\varepsilon}{Da}}\psi)+\frac{1}{4}-\frac{Da}{\varepsilon}-B\cdot\frac{1}{J_0(\sqrt{\frac{(C+1)D}{C}})}$$
$$\cdot J_0(\sqrt{\frac{(C+1)D}{C}}\psi)+A\cdot\frac{1}{J_0(\sqrt{\frac{\varepsilon}{Da}})}J_0(\sqrt{\frac{\varepsilon}{Da}}\psi)+\frac{1}{(C+1)\cdot D}) \tag{4.26}$$

Where A= $\frac{1}{(C\cdot\frac{\varepsilon}{Da}-(C+1)\cdot D)}$ and B= $\frac{C\cdot\frac{\varepsilon}{Da}}{(C+1)\cdot D\cdot(C\cdot\frac{\varepsilon}{Da}-(C+1)\cdot D)}$, therefore,

B-A= $\frac{1}{(C+1)\cdot D}$.

Heat transfer performance

From the analytical solutions for velocity and temperature distributions, the overall Nusselt number of a metal-foam tube can be determined as:

$$Nu=\frac{\bar{h}}{k_f}2R=\frac{2Rq_w}{k_f(T_w-T_{f,b})}=-\frac{2k_{se}}{k_f\theta_{f,b}}=-\frac{2}{(k_f/k_{fe})\cdot C\theta_{f,b}} \tag{4.27}$$

Where $\bar{h}$ is the overall heat-transfer coefficient between the surface and the fluid based on the bulk-mean temperature and $\theta_{f,b}$ is the dimensionless bulk-mean fluid temperature averaged along the cross section of the channel, given by

$$\theta_{f,b}=\frac{T_{f,b}-T_w}{q_wR/k_{se}}=\frac{\int_0^{2\pi}\int_0^1 U\theta_f\psi d\psi d\vartheta}{\int_0^{2\pi}\int_0^1 U\psi d\psi d\vartheta}=2\int_0^1 U\theta_f\psi d\psi$$

$$=\frac{4P^2}{C+1}\left((A+\frac{Da}{\varepsilon})\int_0^1\left(\frac{J_0(\sqrt{\frac{\varepsilon}{Da}}\psi)}{J_0(\sqrt{\frac{\varepsilon}{Da}})}\right)^2\psi d\psi-B\int_0^1\frac{J_0(\sqrt{\frac{(C+1)D}{C}}\psi)}{J_0(\sqrt{\frac{(C+1)D}{C}})}\frac{J_0(\sqrt{\frac{\varepsilon}{Da}}\psi)}{J_0(\sqrt{\frac{\varepsilon}{Da}})}\psi d\psi\right.$$

$$\left.-\frac{1}{4}\int_0^1\frac{J_0(\sqrt{\frac{\varepsilon}{Da}}\psi)}{J_0(\sqrt{\frac{\varepsilon}{Da}})}\psi^3 d\psi-(2A+2\frac{Da}{\varepsilon}-B-\frac{1}{4})\frac{J_1(\sqrt{\frac{\varepsilon}{Da}})}{J_0(\sqrt{\frac{\varepsilon}{Da}})}\sqrt{\frac{Da}{\varepsilon}}\right)$$

$$+B\frac{J_1(\sqrt{\frac{(C+1)D}{C}})}{J_0(\sqrt{\frac{(C+1)D}{C}})}\sqrt{\frac{C}{(C+1)D}}+\frac{1}{2}(A+\frac{Da}{\varepsilon}-B-\frac{1}{8})) \qquad (4.28)$$

Analysis of the solutions

From the above analytical solutions, it can be seen that the non-dimensional velocity (U) is a function of $\sqrt{\frac{\varepsilon}{Da}}$. Similarly, the non-dimensional temperatures (θ_s and θ_f) and the overall Nusselt number of metal-foam tubes are the functions of $\sqrt{\frac{\varepsilon}{Da}}$, $\sqrt{\frac{(C+1)D}{C}}$, and C. From the above equations (4.10-4.14), the following results can be deduced, as:

$\sqrt{\frac{\varepsilon}{Da}} = f_1(\varepsilon)\ \frac{R}{d_p}$, $\sqrt{\frac{(C+1)D}{C}} = f_2(\varepsilon)((C+1)\,Re_d^{\,n}Pr^{0.37})^{1/2}\frac{R}{d_p}$, and $C=\frac{k_{fe}}{k_{se}} = f_c(\varepsilon)\ \frac{k_f}{k_s}$,

where $Re_d=\frac{Re\cdot d}{2R} = 0.5\,Re\frac{d_p}{R}\frac{d_f}{d_p}(1-e^{-((1-\varepsilon)/0.04)}))=0.5\,Re\frac{d_p}{R}$ $f_d(\varepsilon)$, $f_1(\varepsilon)$, $f_2(\varepsilon)$, $f_d(\varepsilon)$, and $f_c(\varepsilon)$ are all functions of porosity (ε). Therefore, the heat transfer performance depends on four independent parameters, R/d_p (geometry parameter), ε (porosity of metal foam), Re (Reynolds number, $2uR/\upsilon$) and k_f/k_s (fluid-solid thermal conductivity ratio).

4.1.5 Results and discussions

Velocity distributions

From the analytical solutions, it is shown that the non-dimensional velocity distribution (u/u_m), varies with R/d_p (geometry parameter) and ε (porosity of metal

foams). Fig.4.2 shows the velocity distribution in metal-foam tubes of different geometries and pore sizes. It can be seen that the metal foam can homogenize the flow compared to hollow channel flows, and the boundary layer becomes thinner with the increase of the ratio of tube diameter to pore size (R/d_p,). Compared with R/d_p, it is clear in Fig.4.3 that the variation of porosity (ε) has less influence on velocity distributions in tubes filled with high porosity metal foams, though the decrease of porosity can also make the velocity distribution become flatter.

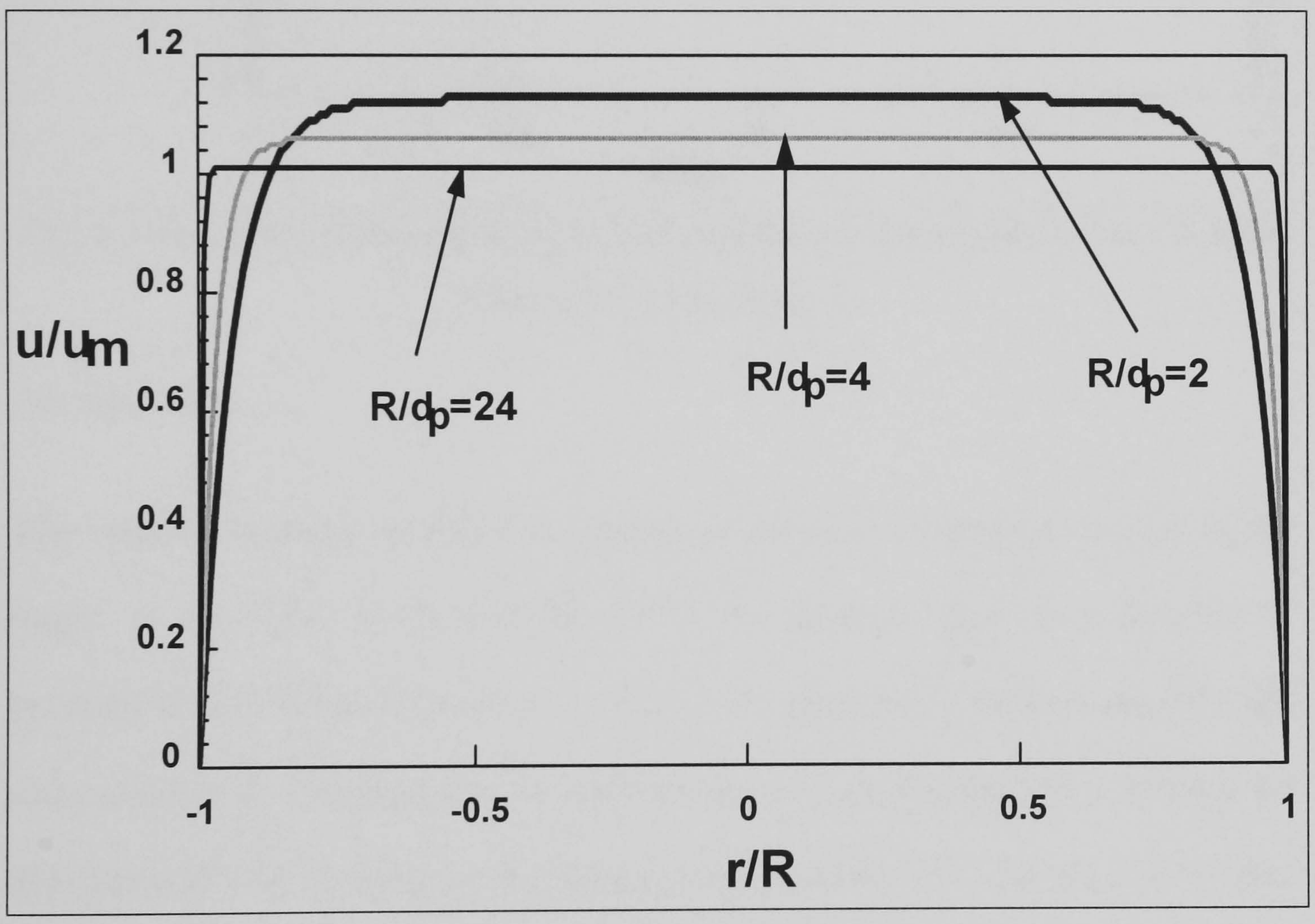

Fig. 4.2 The effect of R/d_p on dimensionless velocity distributions (ε=0.9)

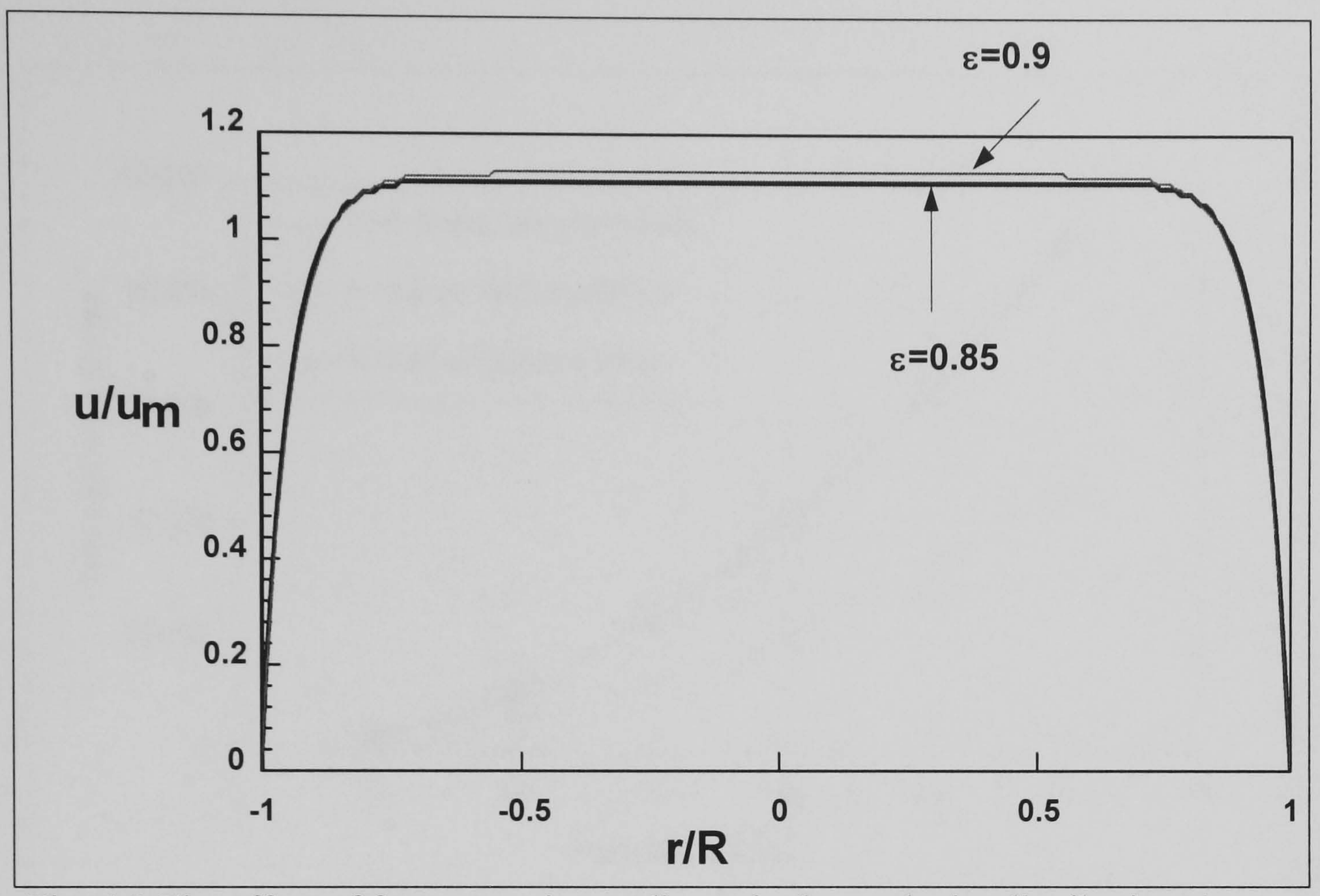

Fig. 4.3 The effect of foam porosity on dimensionless velocity distributions in meta-foam filled tubes (R/d_p=2)

Pressure drop

This section considers the effect of different parameters on pressure drop along the length of the tube. From formula (4.23), the pressure drop is a function of permeability (K) of the metal foam which in turn depends on the pore density (ppi) and porosity (ε). Consequently, the pressure drop of single-phase flow through the tube increases exponentially with increase of pore density (i.e. the decrease of pore size), as shown in Fig. 4.4. It is noted that the pressure drop of air through two tubes of different diameters but the same pore density is almost identical indicating that the pressure drop is mainly caused by the solid structure of the metal foam rather than the tube wall. Fig.4.5 shows the variation of pressure drop with the porosity at selected pore densities. As expected, the pressure drop increases with the decrease of porosity and increase in the pore density.

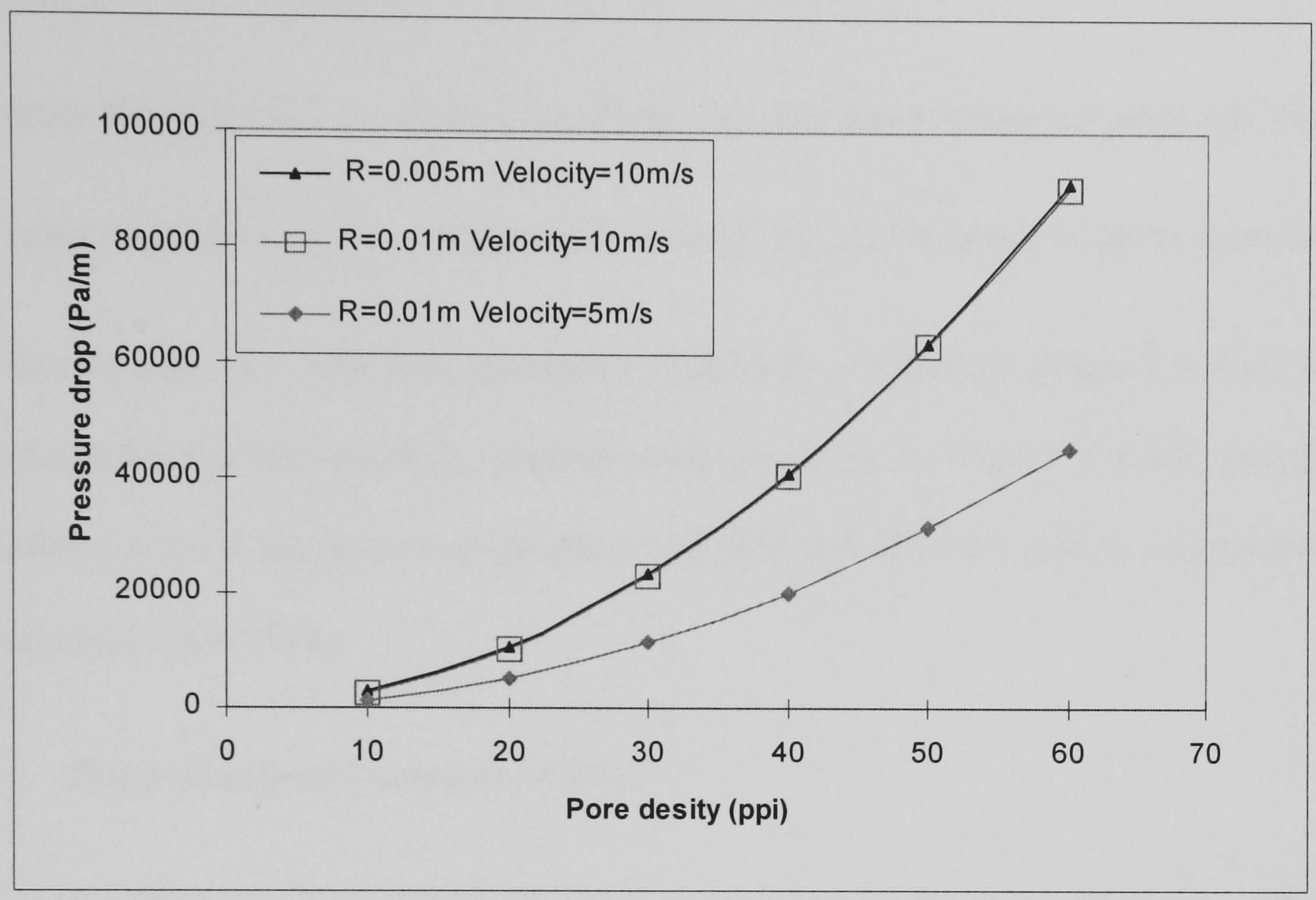

Fig. 4.4 Pressure drop per unit length along metal-foam tubes (porosity=0.9)

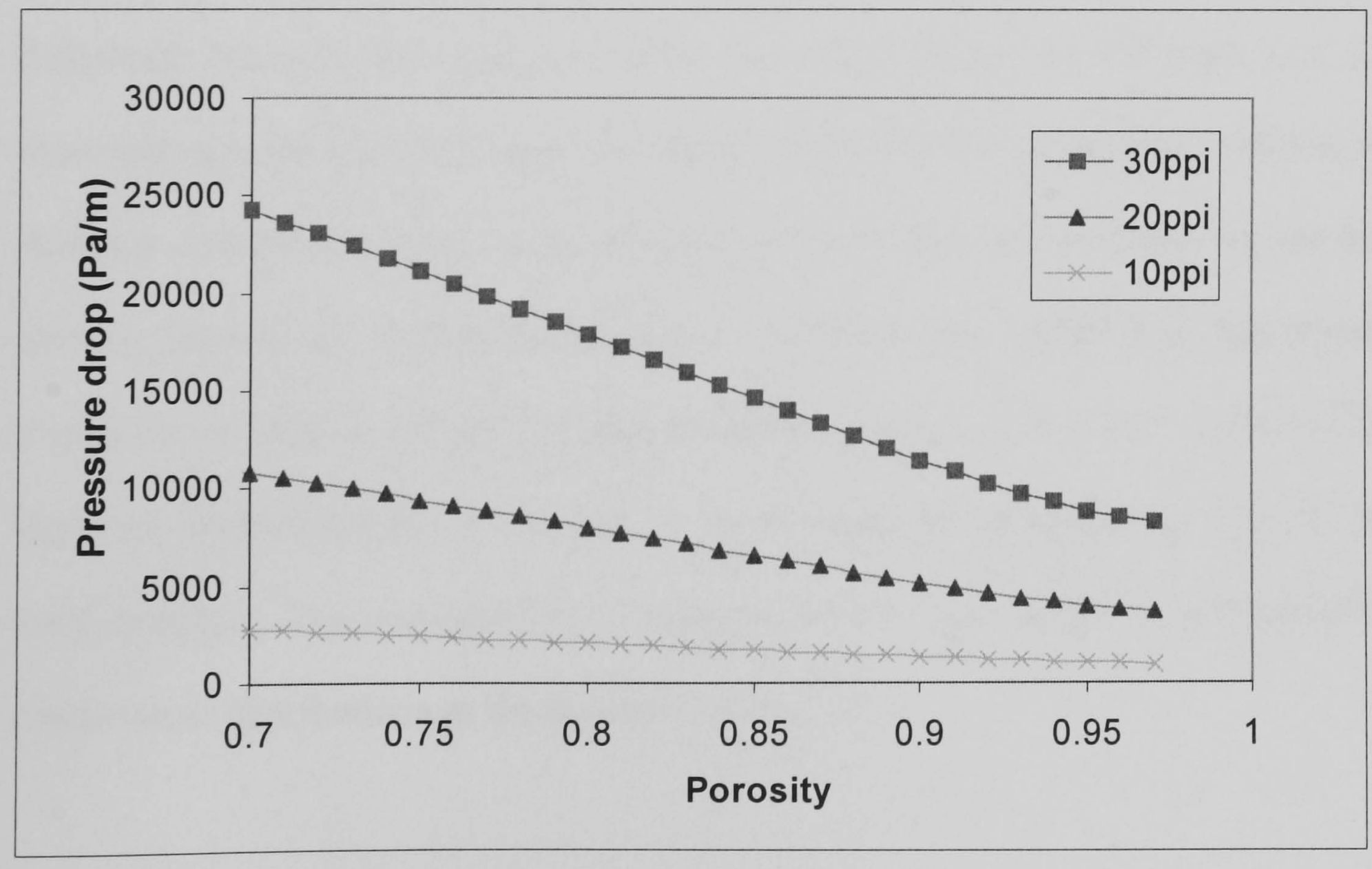

Fig. 4.5 Variation of pressure drop with porosity (R = 0.01m, Velocity = 5m/s)

Temperature distributions

From the analytical solutions, it is shown that the non-dimensional solid and fluid temperature ($\theta=\frac{T-T_w}{q_w R/k_s}$, which use k_s instead of k_{se} for θ_s and θ_f in above formulas) distributions vary with R/d_p (geometry parameter), ε (porosity of metal foams), Re (Reynolds number) and k_f/k_s (thermal conductivity ratio). Fig.4.6~Fig.4.9 show the effects of these parameters on dimensionless solid and fluid temperature distributions in metal-foam tubes.

- Effect of geometry parameter (R/d_p)

Fig.4.6 shows both the solid and fluid temperature distributions at selected radius-pore size ratio. The pore density has a lower effect on the solid temperature distribution compared to the fluid temperature distribution. The temperature difference between the solid and fluid decreases sharply as the pore size (d_p) decreases (i.e. pore density (ppi) increases). With all other parameters constant, the decrease of pore size leads to an increase in the wetted area available for the heat transfer between the solid and fluid phases. This leads to a higher local heat-transfer coefficient as well as a higher interfacial surface density (shown in formula (4.12)). Both are responsible for the reduction of the temperature difference between the solid and fluid. The increase of tube diameter has the same effects on dimensionless temperature distributions as the decrease of pore size.

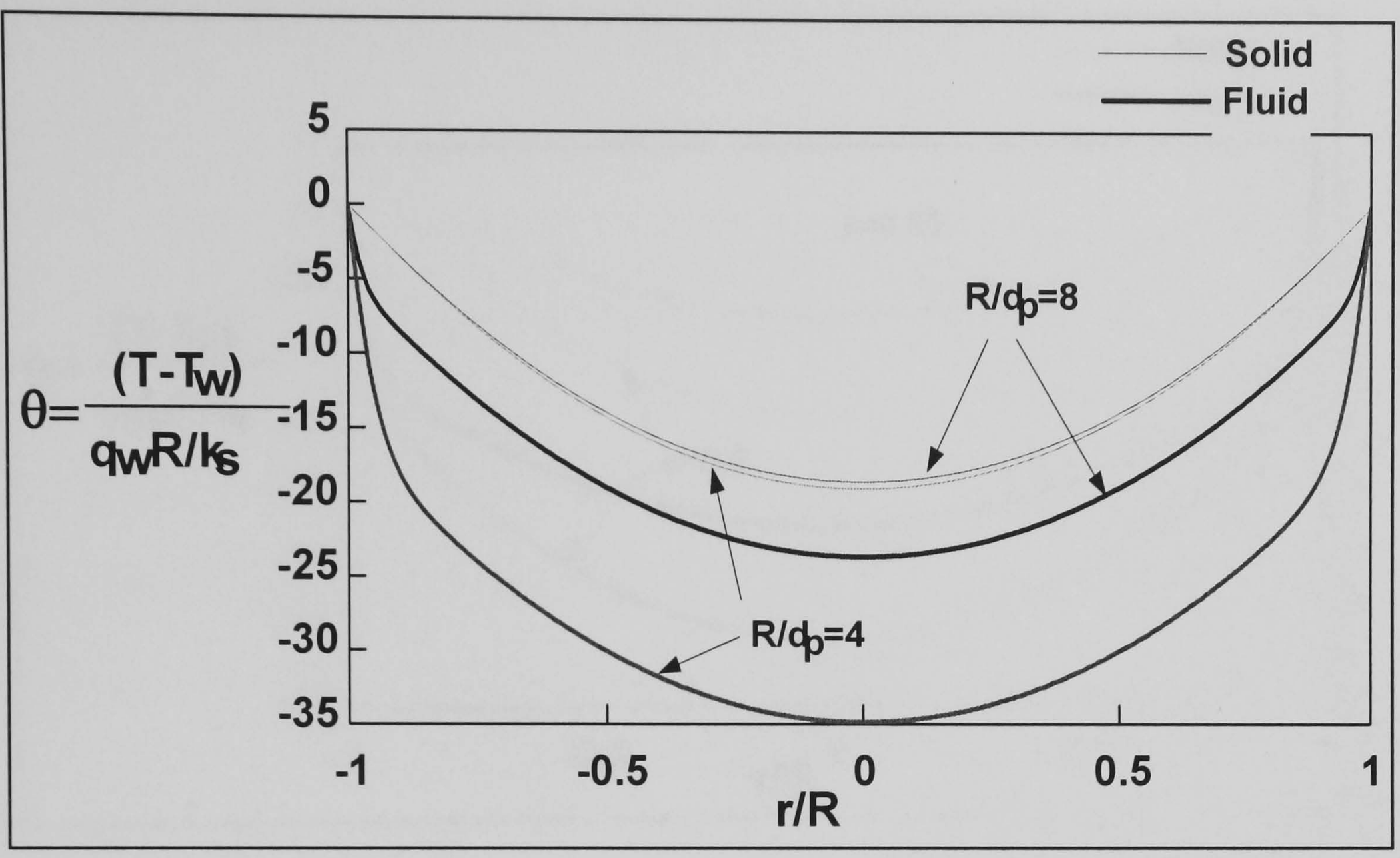

Fig. 4.6 Effect of R/d_p on temperature distributions in tubes filled with metal foams, with Re=2000, porosity=0.9, k_f/k_s=0.0001

- Effect of porosity of metal foams (ε)

Fig.4.7 reveals that the variation of the porosity of metal foams has a significant effect on both solid and fluid temperature distributions. As shown in this figure, the solid and fluid temperatures decrease much more quickly from the heated surface to the centre as the porosity of the metal foam increases from 85% to 90%, while the temperature difference between the solid and fluid reduces slightly, because the decrease of porosity of metal foams enhances the heat conduction through the fibres of metal foams.

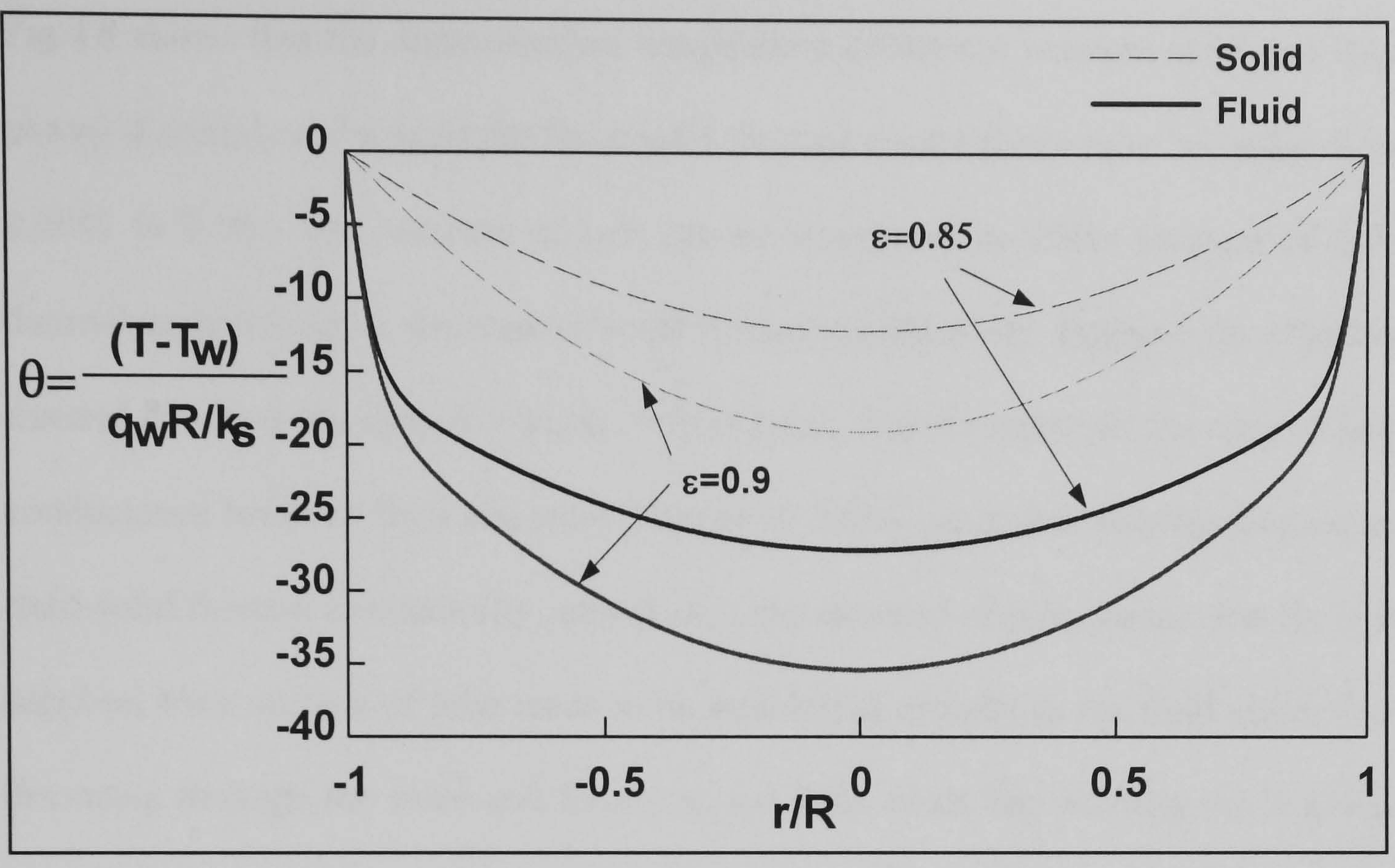

Fig. 4.7 Effect of porosity (ε) on temperature distribution in metal-foam (R/d_p =4) filled tubes.

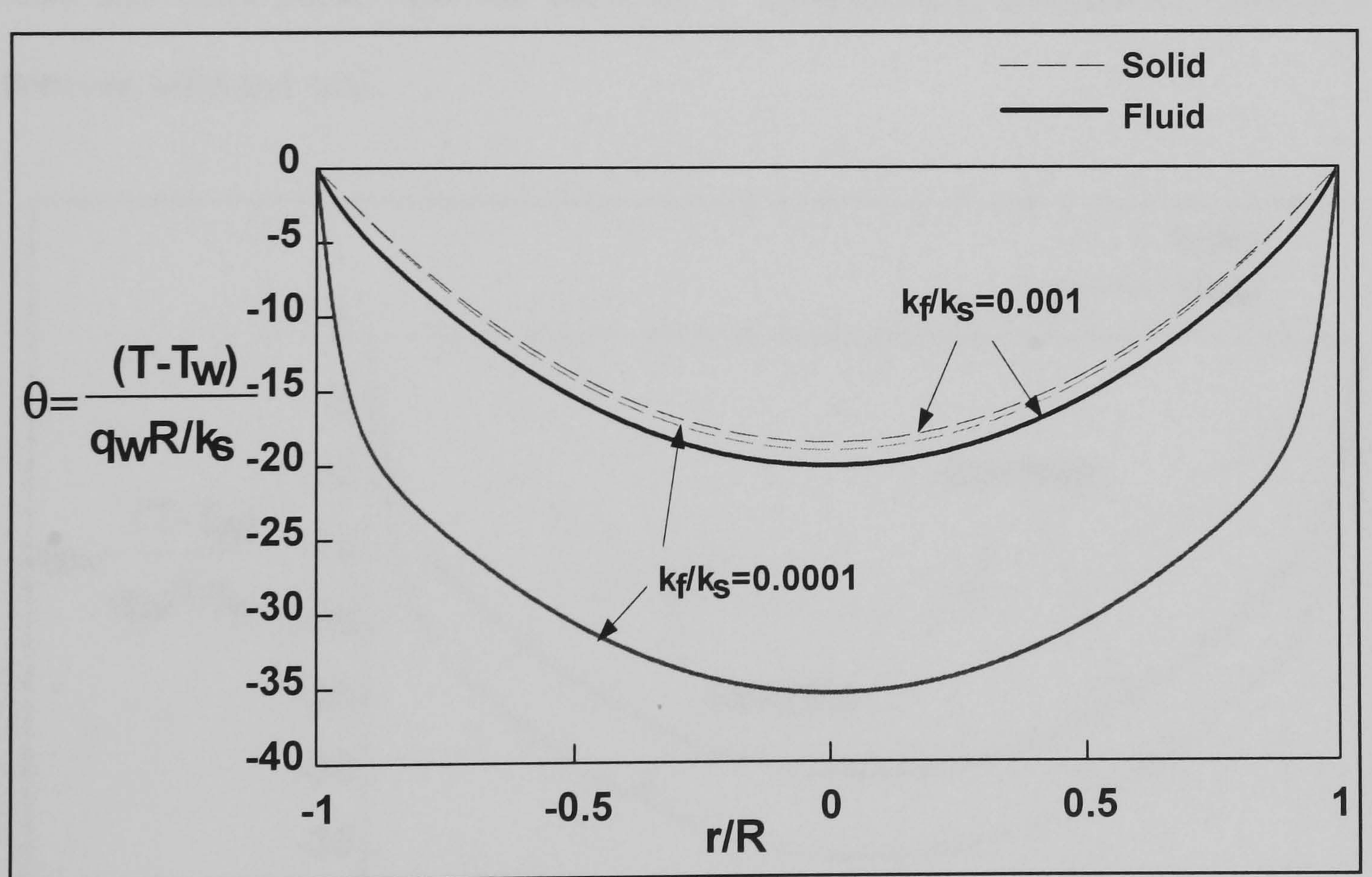

Fig. 4.8 Effect of k_f/k_s on temperature distributions in tubes filled with metal foams (R/d_p =4, porosity=0.9).

- Effect of fluid-solid thermal conductivity ratio (k_f/k_s)

Fig.4.8 shows that the dimensionless temperature difference between solid and fluid phases distinctly reduces as the fluid-solid thermal conductivity ratio increases from 0.0001 to 0.001. The increase of k_f/k_s can be interpreted as either increase of fluid thermal conductivity or decrease of solid thermal conductivity. Because the effective thermal conductivity ratio ($C = k_{fe}/k_{se} = f_c(\varepsilon)\, k_f/k_s$), which represents the ratio of heat conductance between fluid and solid (Kim et al, 2000), increases with the increase of fluid-solid thermal conductivity ratio (k_f/k_s), the increase of k_f/k_s means that the heat supplied from surface of tube tends to be transferred directly to the fluid rather than detouring through the solid and finally to the fluid while the porosity (ε) is given. This implies the decrease in the amount of heat transfer between the phases, which in turns results in the decrease of the dimensionless temperature difference between the fluid and solid phases and the decrease of dimensionless temperature difference between solid and wall.

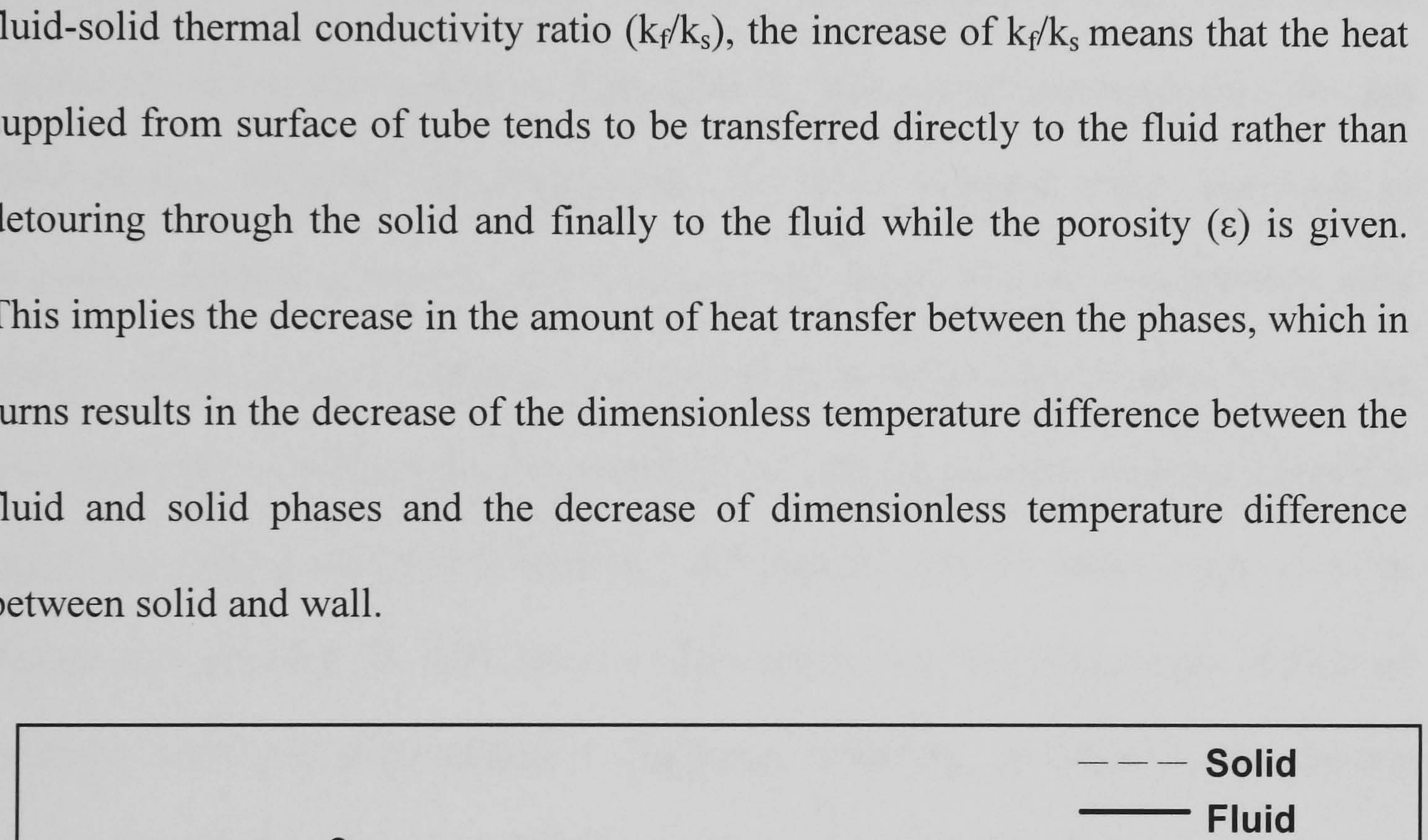

Fig. 4.9 Effect of Re on temperature distributions in tubes filled with metal foams (R/d_p =4, porosity=0.9, k_f/k_s=0.0001)

- Effect of dynamic parameter (Re)

In this section, the effect of on heat transfer and temperature distributions is considered. The Reynolds number is defined as Re= u2R/ν. Fig.4.9 represents the solid and fluid temperature distributions as different Reynolds numbers (Re) applied. The increase of Reynolds number leads to the increase of local heat transfer coefficient and in turn results in enhancing the heat transfer between the solid and fluid phases. Therefore, the temperature difference between phases decreases as Reynolds number increases. But owing to the small thermal conductivity ratio (k_f/k_s=0.0001), the solid temperature distributions is nearly kept the same form. From the temperature distributions, the results reveal that the porosity of metal foams has significant effects on solid temperature distributions and the pore density of metal foams and velocity of fluid have certain effects on the temperature difference between solid and fluid phases in particular situations. In addition, the thermal physical properties of solid and fluid bring their relevant influences.

Overall heat transfer in metal-foam tubes

To examine the heat transfer rate between the heated wall and the fluid, the overall Nusselt number, defined as $Nu = \frac{\bar{h}}{k_f} 2R$, was used (equation (4.27)). From the analytical solutions, it is shown that the Nusselt number depends on four parameters: ε (porosity), R/d_p (geometry parameter), k_f/k_s (fluid-solid thermal conductivity ratio) and Re (Reynolds number). Fig.4.10-Fig.4.16 present the effects of these parameters on the overall heat transfer coefficient (Nusselt number) for metal- foam filled tubes.

- Effect of thermal conductivity ratio (k_f/k_s)

Fig.4.10 and Fig.4.11 shows that the Nu increasing dramatically with the decrease of fluid-solid thermal conductivity ratio (k_f/k_s). It is obvious that the higher thermal conductivity the metal used for the foams has, the more enhancement the metal foams can bring to overall heat transfer. When the solid thermal conductivity is close to that of the fluid ($k_f/k_s>0.1$), as shown in Fig.4.10, the use of metal foams has little effect on overall heat transfer. When $k_f/k_s<0.1$, the overall heat transfer (Nusselt number) rises significantly with the increase of the solid thermal conductivity k_s, (see Fig.4.15) and decrease of k_f/k_s down to a value of 0.00001. At relatively high values of k_f/k_s above 0.001, the geometry parameter R/d_p (depends on pore density) has very little effect on the Nusselt number which implies that the main thermal resistance is that of heat conduction through the solid fibres. At values of k_f/k_s below 0.001, the Nusselt number increases with decrease pore size (d_p), indicating that the thermal resistance between metal foams and fluid begins to become significant.

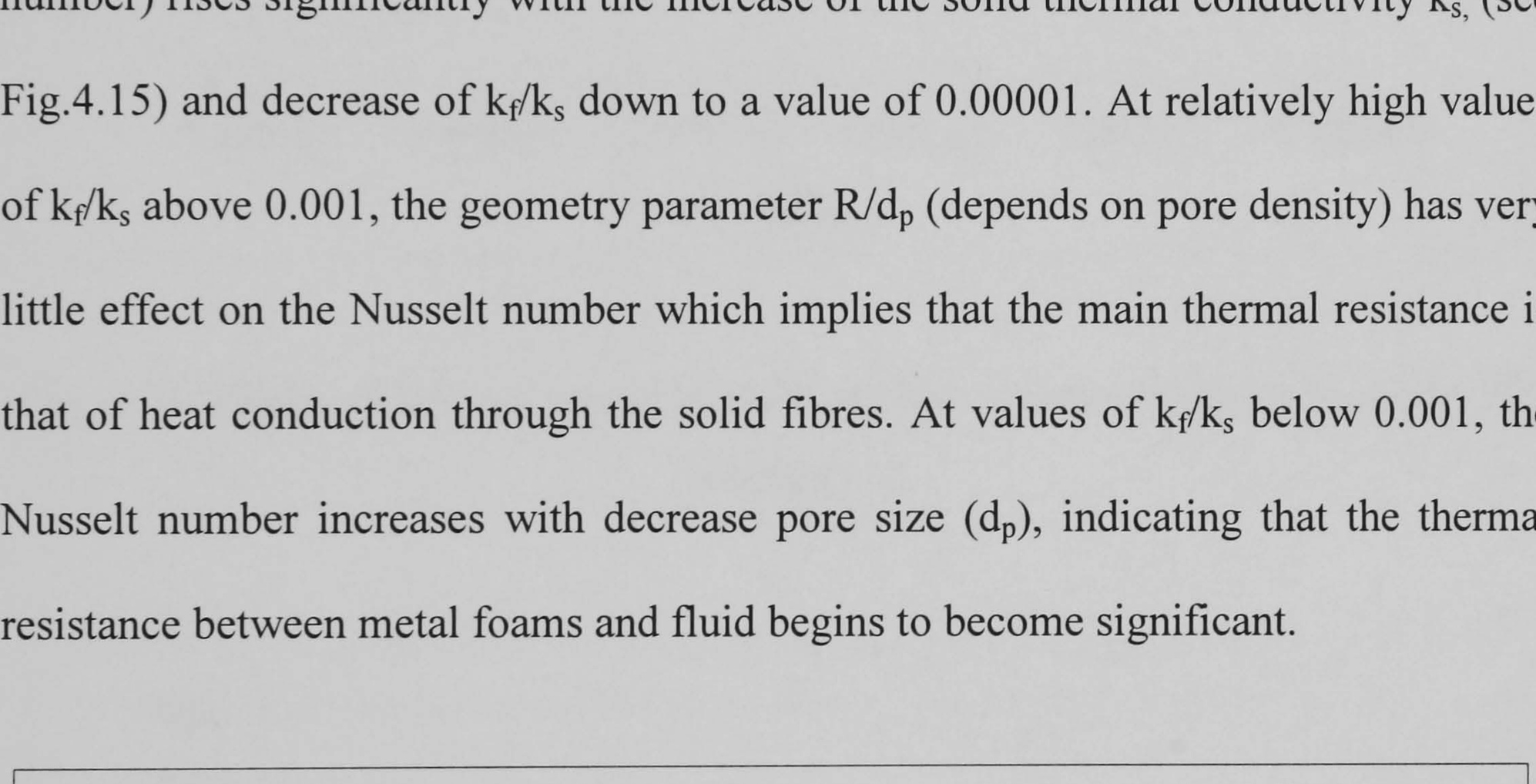

Fig. 4.10 Effects of k_f/k_s on overall Nusselt number in metal-foam tubes, as Re=2000 and porosity=0.9.

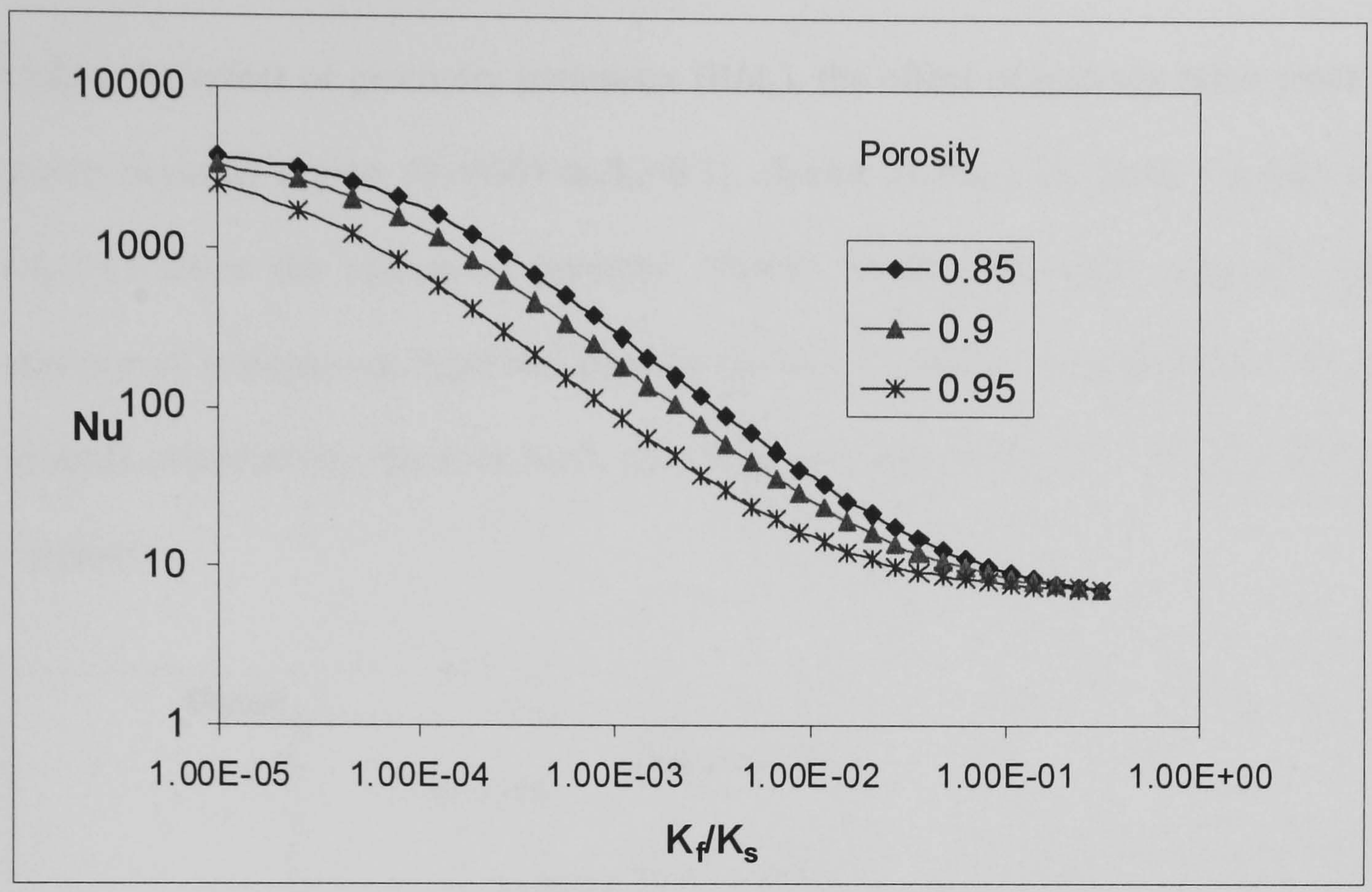

Fig. 4.11 Effects of k_f/k_s on overall Nusselt number in metal-foam tubes, as Re=2000 and R/d_p=8.

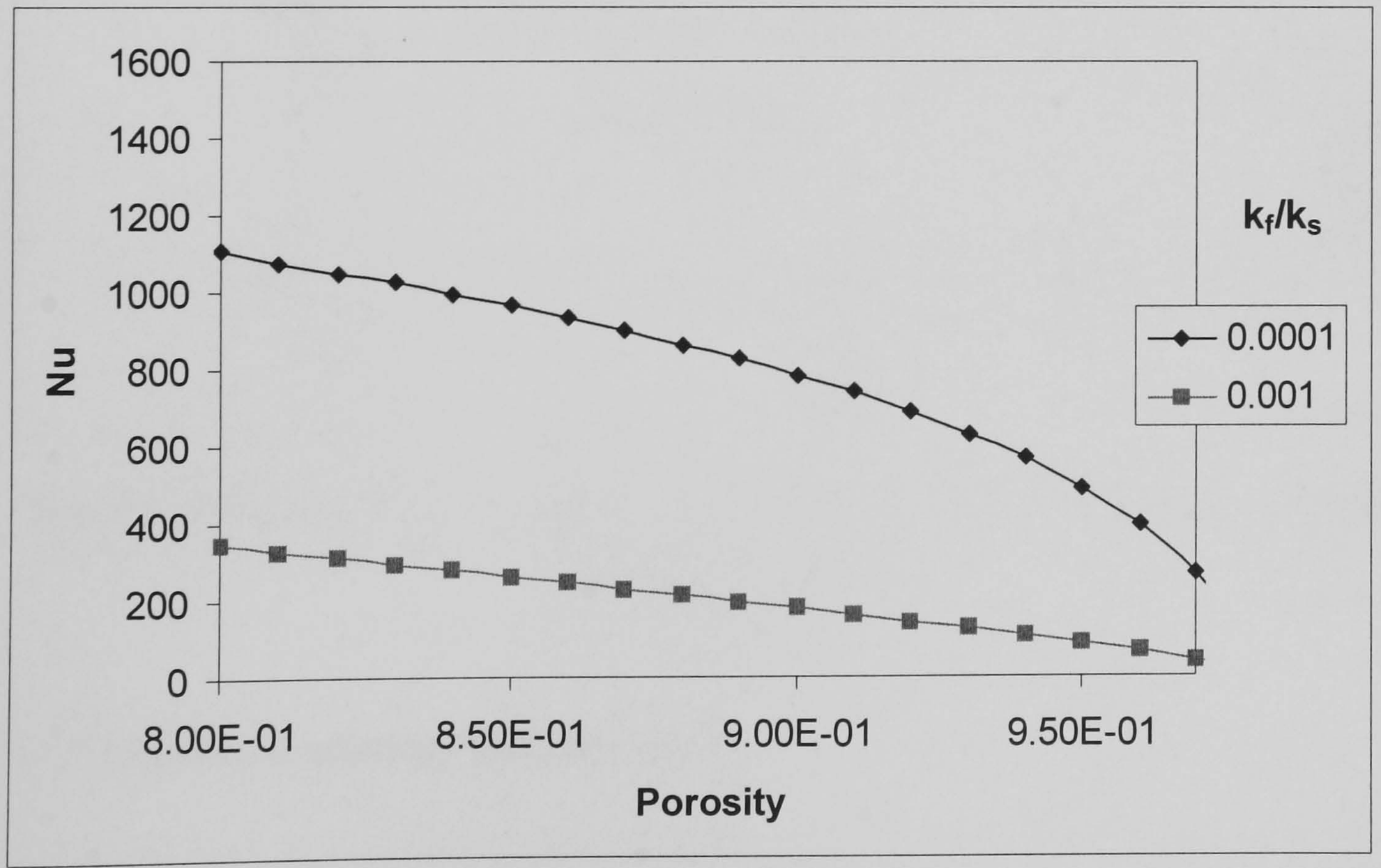

Fig. 4.12 Effects of porosity (ε) on overall Nusselt number in metal-foam tubes, as Re=2000 and R/d_p=4.

- Effect of porosity (ε)

Unlike the effect of geometry parameter (R/d_p), the effect of porosity takes place in whole research region ($0.00001<k_f/k_s<0.1$), shown as Fig.4.11. Both Fig.4.11 and Fig.4.12 show the effects of porosity: Nusselt number increases gradually with decrease of porosity, as expected, because the fibre diameter and associated effective thermal conductivity increase with decreasing porosity when pore density (ppi) is constant.

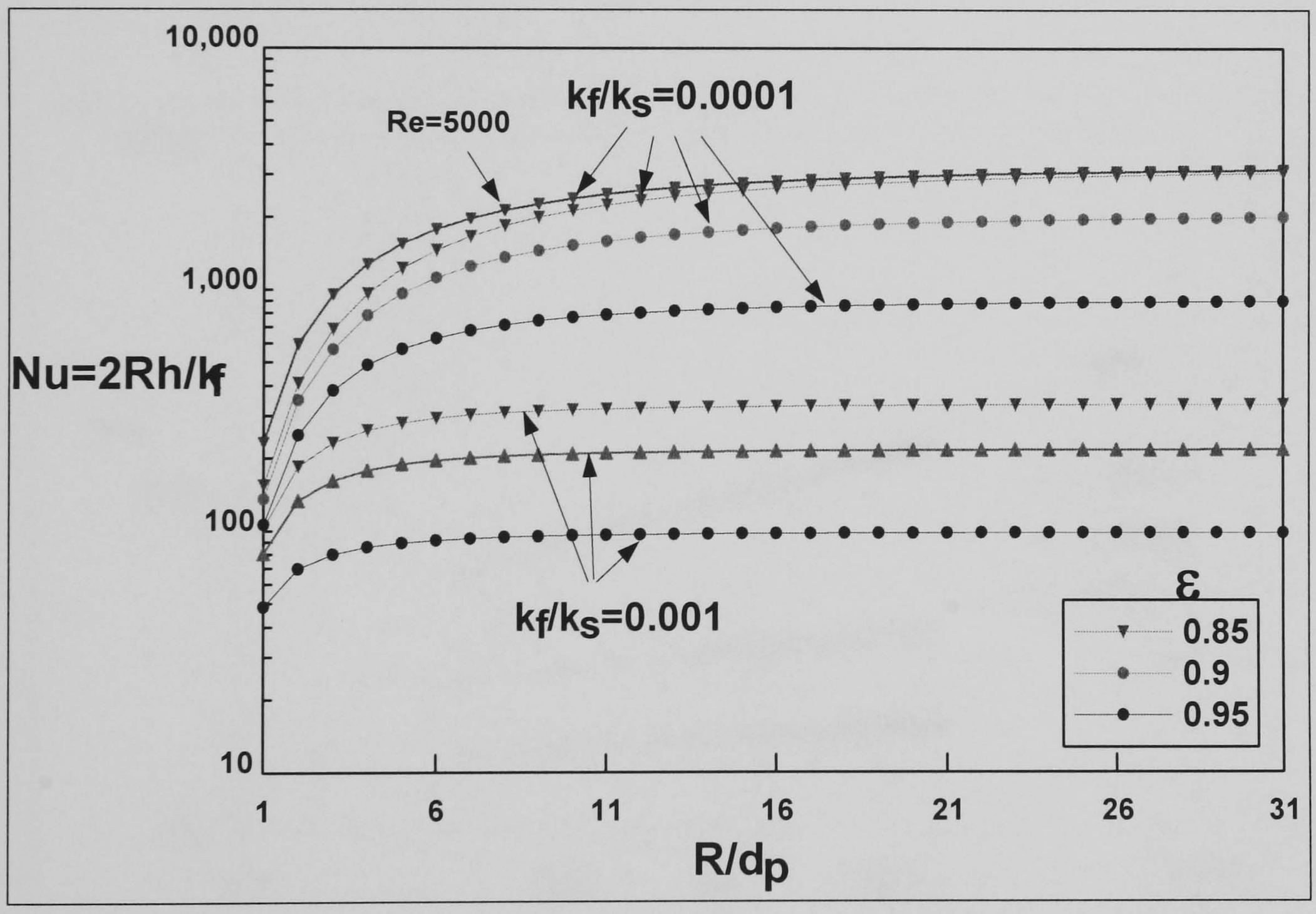

Fig. 4.13 Effects of R/d_p on overall Nusselt number in metal-foam tubes of different situations (Re=2000).

- The effect of geometry parameter (R/d_p)

Fig.4.13 shows the effects of geometry parameter (R/d_p) on overall heat transfer (Nusselt number) at selected fluid-solid thermal conductivity ratio, porosity and

Reynolds number. The overall heat transfer (Nu) is improved quickly with increase of R/d_p when the R/d_p is small, but the Nusselt number tends to reach a plateau when the R/d_p becomes larger, especially at low fluid-solid thermal conductivity ratio or high porosity or Reynolds number. In the main time, decrease of d_p (i.e. increase of pore density) causes more pressure drop. Therefore, R/d_p needn't be too large, for example, from Fig.4.13, it can be found that there is very little enhancement on heat transfer at R/d_p >10 when fluid-solid thermal conductivity ratio (k_f/k_s) is 0.001 or R/d_p >25 when k_f/k_s is 0.0001 in these cases.

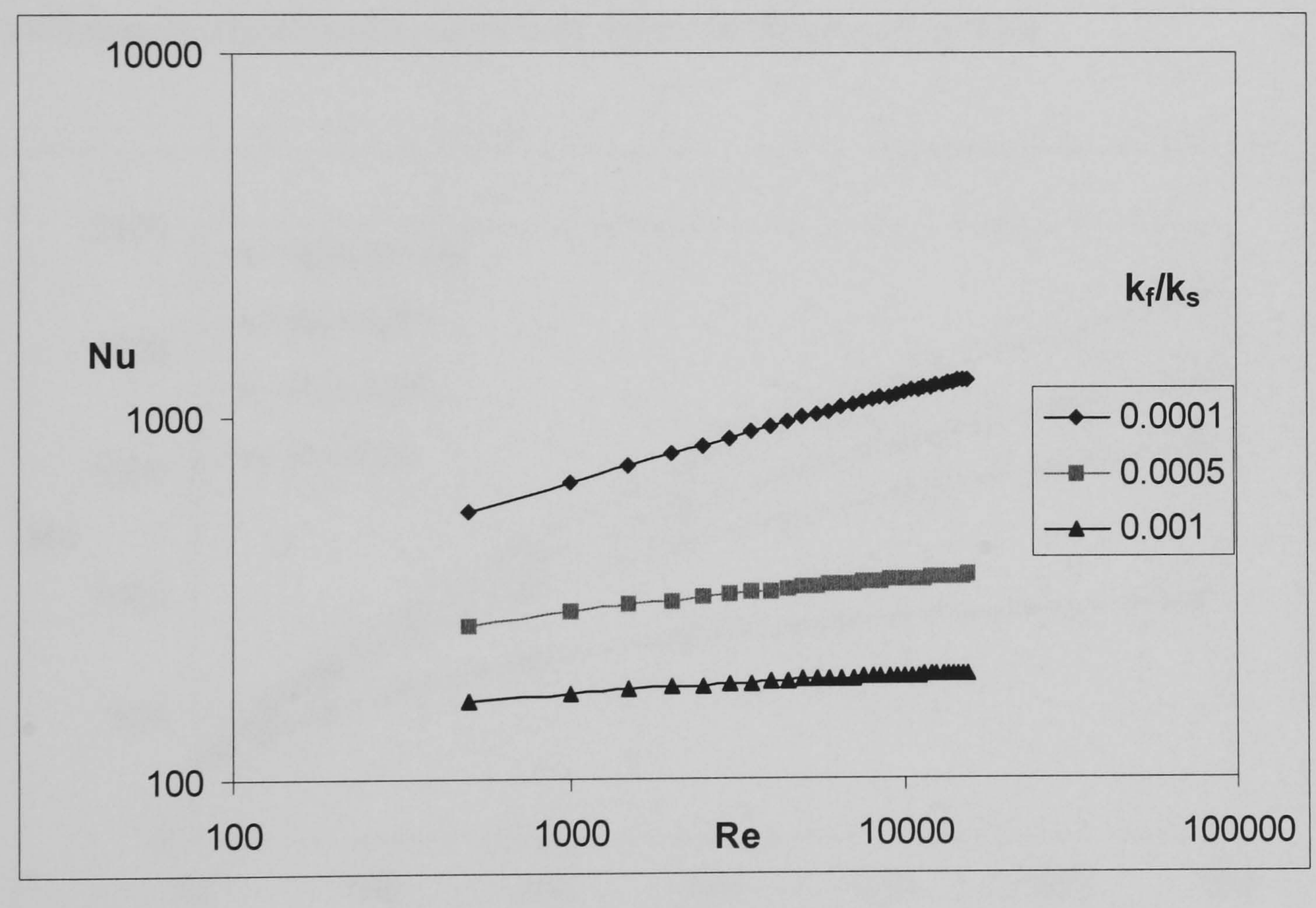

Fig. 4.14 Effects of Reynolds number (Re) on overall Nusselt number in metal-foam tubes, as porosity=0.9 and R/d_p=4.

- Effect of Reynolds number

It is obvious that overall heat transfer (Nusselt number) rises with increase of fluid velocity (Reynolds number). The Fig.4.14 shows the relationship between them. When the Reynolds number becomes higher, the Nusselt number increases as well. But the overall Nusselt number increases very slowly when fluid-solid thermal conductivity ratio (k_f/k_s) or R/d_p (shown in Fig.4.15 and Fig. 4.16) is high. Therefore, it is clear that the Reynolds number has much less effects than parameters of metal foams on improving overall heat transfer. Therefore, the high heat transfer performance can be reached with low fluid velocity in metal foam filled tubes. Compared to plain (hollow) tubes, the use of metal foams can enhance heat transfer performance significantly, up to forty times, as shown in Fig. 4.16.

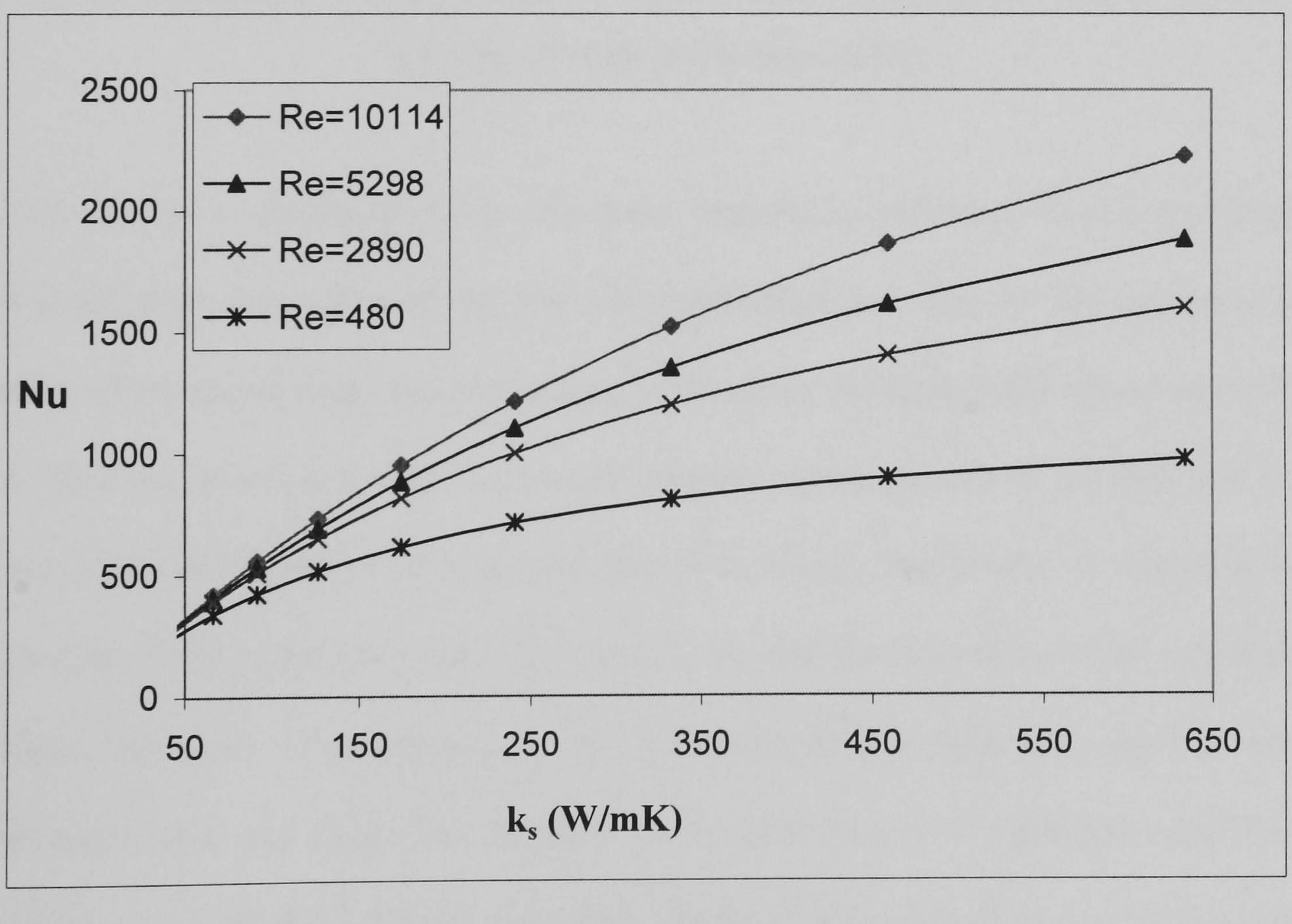

Fig. 4.15 Variation of Nusselt number with solid thermal conductivity (k_s) for air flowing through metal-foam tubes.

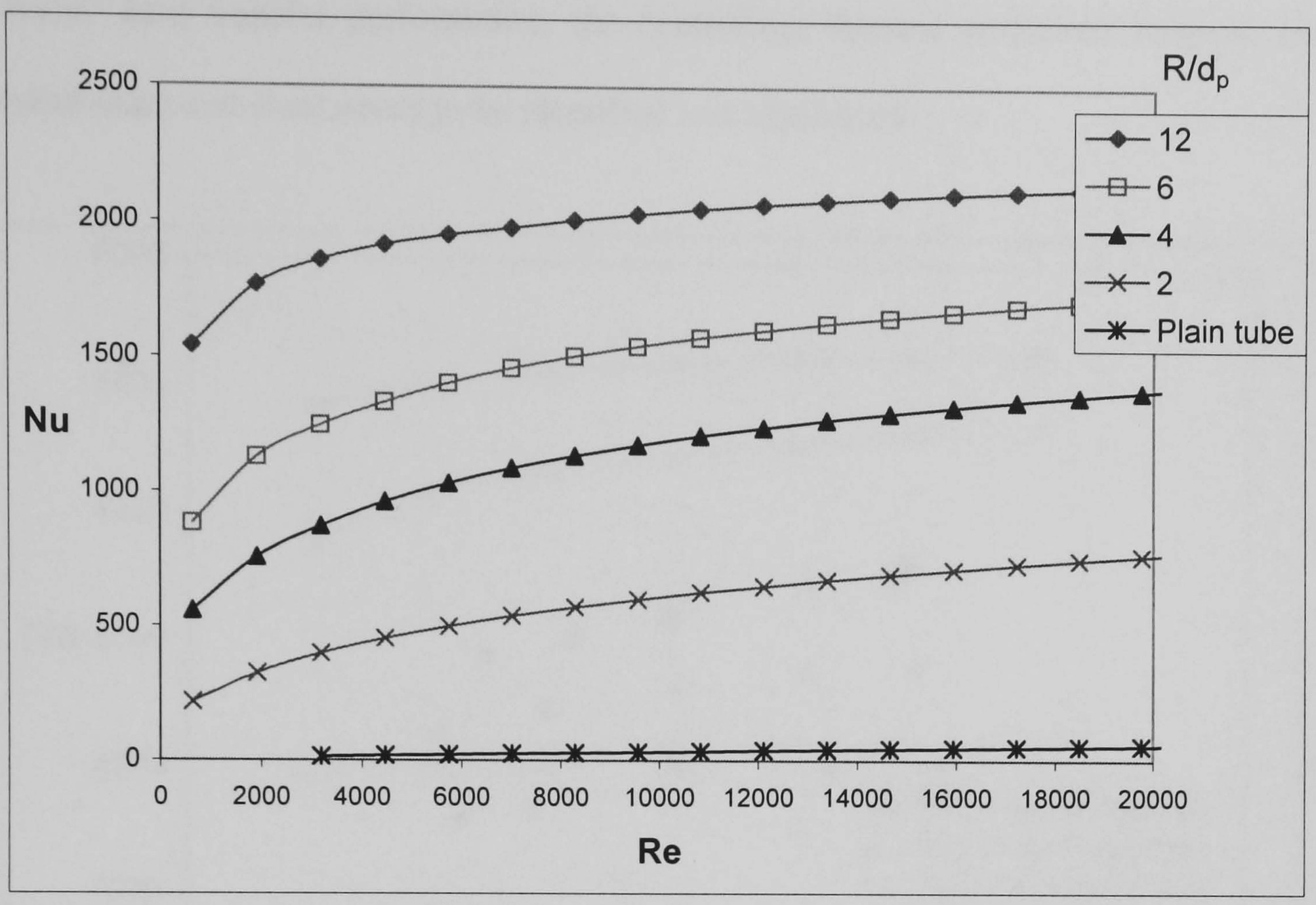

Fig. 4.16 Variation of Nusselt number with Reynolds number (porosity=0.9) for air flowing through metal-foam tubes.

From the above results, it can be concluded that the overall heat transfer coefficient in metal-foam tubes depends on both the conduction heat transfer through the solid fibres of the metal foam and convection heat transfer from the solid (fibres and wall) to the fluid. In other words, the overall thermal resistance can be divided into two parts, thermal resistance of solid and that of the fluid. The former is related to the porosity of the metal foam, the diameter of tube and the thermal conductivity of the foam. The latter is influenced by the properties of the fluid and interface area between solid and fluid. The increase of relative density (=1-porosity) and pore density ($1/d_p$) of metal foams can greatly increase the conduction area of the solid fibres and the convection heat-transfer area, thereby reducing thermal resistance and enhancing the overall heat transfer. Therefore, in order to effectively improve the

overall heat transfer performance, the controlling thermal resistance between the metal foam and fluid needs to be identified and minimised.

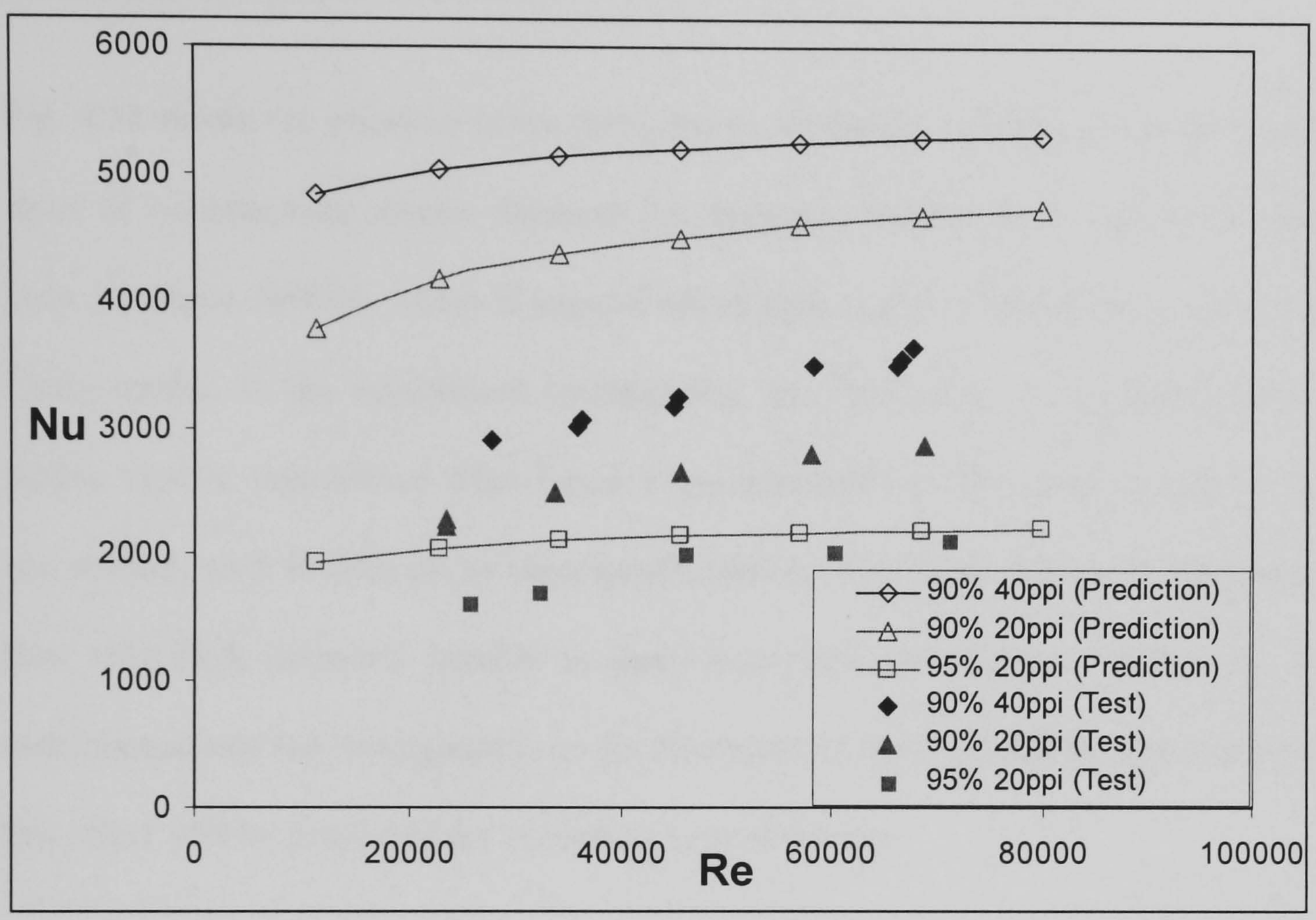

Fig. 4.17 Heat transfer performance for different samples: Analytical modelling versus experimental results.

4.1.6 Comparison between analytical solution and experimental data

For heat transfer in metal-foam tube, there is no experimental datum published from other researchers. Therefore, the experimental results obtained in this research were used to compare with the analytical solutions. Fig. 4.17 shows the comparison of between the heat transfer performance predicted by analytical modelling and that measured in experimental test. The results of analytical solutions show that the decrease of porosity from 95% to 90% or increase of pore density from 20 ppi to 40 ppi brings significant improvement to overall heat transfer performance (Nusselt number) while the same phenomena have been detected in experimental results.

However, the modelling predictions doesn't take the contact thermal resistance between tube and metal foams into account, which results in overestimating the heat transfer performance of these tubes.

Fig. 4.18 shows the pressure drops predicted by analytical modelling can not match those of experimental results. Because the Reynolds number for experimental data were all above 200000, which is beyond the modelling range of Brinkman extended Darcy model. In the experiment investigation, the fluid used in experimental test, R134a vapour, was heated from liquid to superheated vapour before it entered the test section, so it is difficult to keep steady state for low mass flow rate. For forced flow with high Reynolds number in metal-foam tube, the effect of form force of metal foams can not be neglected, so the Forchheimer-Darcy Model which considers this effect will be employed for modelling in next section.

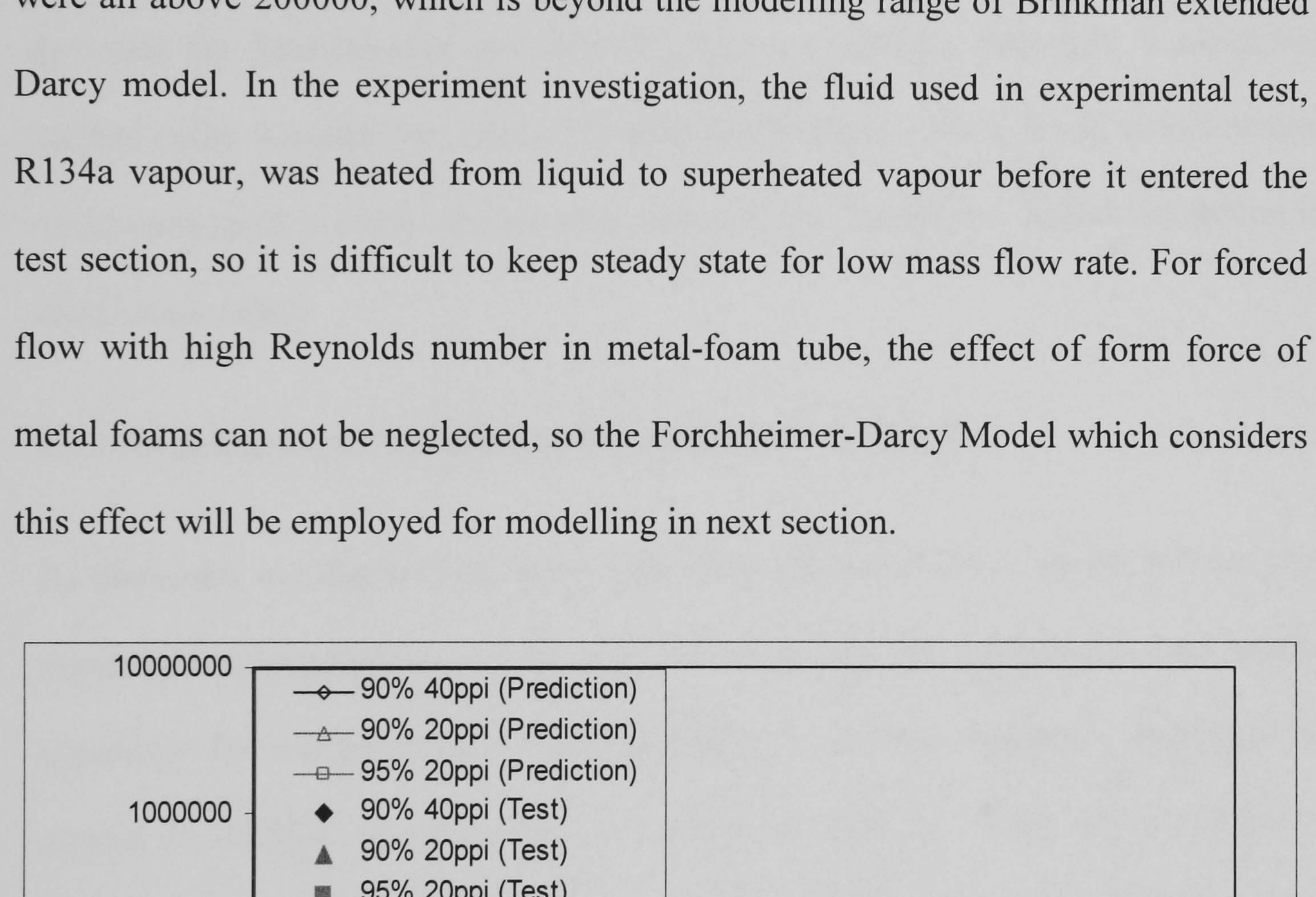

Fig. 4.18 Comparison of pressure drop between analytical solution and experimental results

4.2 Numerical modelling for forced convection

Although the analytical method is helpful in identifying and studying the effects of variables of engineering importance without tedious numerical computations, this method neglects the axially heat conduction and kinetic resistance to simplify the equations and make them can be solved analytically. Consequently, that brings deviation for heat transfer and pressure drop predictions. Therefore, a numerical method using Forchheimer-Darcy Model (considering the form force) as momentum equation is used to model the pressure loss and heat transfer of forced convection in metal-foam tubes.

4.2.1 Mathematical formulations for numerical modelling

As discussed in Chapter One, the Forchheimer extended Darcy model and the two-equation non-equilibrium model will be employed for momentum and energy equations for numerical modelling respectively. So, the equations employed for analytical method are also used in numerical method except the Forchheimer extended Darcy model is adopted for momentum equation, which is simplified by the analytical method to solve the equation.

- Momentum equation (Forchheimer -Darcy Model)

$$\frac{1}{\varepsilon}\langle(\vec{V}\cdot\nabla)\rho_f\vec{V}\rangle = -\nabla\langle p\rangle_f + \frac{\mu_f}{\varepsilon}\nabla^2\langle\vec{V}\rangle - \frac{\mu_f}{K}\langle\vec{V}\rangle - \rho_f F_I[\langle\vec{V}\rangle\cdot\langle\vec{V}\rangle]J_1 \quad (4.29)$$

$\langle\ \rangle$ means a volume averaged value.

In which, $\vec{V}$ is velocity vector, $J_1 = \vec{V} / \left|\vec{V}\right|$, ε is porosity of porous medium, p is the pressure, μ_f is the fluid viscosity and K is the permeability of the porous medium.

In analyzing the problem, the flow is assumed to be hydrodynamically fully developed. All thermo-physical properties of solid and fluid phase, e.g., thermal conductivity, density, specific heat and viscosity, are assumed to be temperature independent. Natural convection and radiation are negligible. The porous medium is homogeneous and isotropic, i.e., the velocity, the fluid and solid temperatures are independent of the radian coordinate. The problem can be considered as a two-dimensional problem. Then the above mentioned equations can be written in the following form, valid for axisymmetrical geometries:

$$0 = -\frac{dp}{dz} + \frac{\mu_f}{\varepsilon}\left(\frac{\partial^2 u}{\partial r} + \frac{1}{r}\frac{\partial u}{\partial r}\right) - \frac{\mu_f}{K}u - \rho_f F_I u^2 \tag{4.30}$$

$$0 = k_{se}\left(\frac{\partial^2 T_s}{\partial r^2} + \frac{1}{r}\frac{\partial T_s}{\partial r}\right) + k_{se}\left(\frac{\partial^2 T_s}{\partial z^2}\right) - h_{sf}a(T_s - T_f) \tag{4.31}$$

$$\varepsilon\rho_f C_f V_z \frac{dT_f}{dz} = (k_{fe} + k_d)\cdot\left(\frac{\partial^2 T_f}{\partial r^2} + \frac{1}{r}\frac{\partial T_f}{\partial r}\right) + (k_{fe} + k_d)\cdot\left(\frac{\partial^2 T_f}{\partial z^2}\right) + h_{sf}a(T_s - T_f) \tag{4.32}$$

4.2.2 Boundary conditions

For the metal-foam tubes directly heated from outside surface with constant heat flux, the applied heat is transferred to the solid and fluid phases by conduction and convection. As discussed in previous chapter, the temperature at the interface between metal foams and the substrate can be considered to be uniform regardless of whether it is in contact with the solid or fluid phase. In the centre of tube, the

gradients of the velocity, the solid and fluid temperatures along r direction equal zero. The gradients of solid temperature equal zero at inlet and outlet boundaries. The gradient of fluid temperature equals zero when z=L, while the fluid temperature equals inlet temperature of fluid when z=0. Consequently, the boundary conditions of metal-foam tube are specified as follows:

$$u=0,\ T_s = T_f,\ \text{and}\ q = q_W = k_{fe}\frac{\partial T_f}{\partial r}\Big|_{r=R} + k_{se}\frac{\partial T_s}{\partial r}\Big|_{r=R} \qquad \text{at r=R}$$

$$\frac{\partial V_z}{\partial r} = \frac{\partial T_f}{\partial r} = \frac{\partial T_s}{\partial r} = 0 \qquad \text{at r=0} \qquad (4.33)$$

$$T_f = T_{in}\ \text{and}\ \frac{\partial T_s}{\partial z} = 0 \qquad \text{at z=0}$$

$$\frac{\partial T_f}{\partial z} = 0\ \text{and}\ \frac{\partial T_s}{\partial z} = 0 \qquad \text{at z=L}$$

4.2.3 Initial conditions

In this research, the average temperature of fluid is controlled at 30 °C for experimental test. So the inlet temperature T_{in} was set to 25 °C and so to the initial condition of fluid. And the initial condition for temperature for solid phase was set as 30 °C.

$$u=u_{mean}\ \text{except}\ u|_{r=R}=0, \qquad (4.34)$$

$$T_s=30,\ T_f=25$$

4.2.4 Modelling on Porvair metal foams

Before proceeding further, the parameters in above equation must be solved. In previous section, some parameters have been established, but the Forchheimer

coefficient (F_I) has not been analyzed. Zhao et al. (2004c) have proposed a formulation in form of

$$F_I = C(1-\varepsilon)^n / d_p \tag{4.35}$$

to calculate the effect of form force based on the microstructure of metal foams, where C and n can be specified for particular cases. Based on experimental data of Zhao et al.(2004c), the constants *C* and *n* for FeCrAlY foams are *C* = 29.613 and *n* = 1.5226. For copper foams C=7.861, n=0.5134. Based on the experimental results of this research in chapter 3, C=12 and n=1 are adopted for solving momentum equation.

As for the effect of thermal dispersion (k_d), a widely adopted expression is (Calmidi and Mahajan, 2000):

$$k_d = C_D(\mathrm{Re}_k \, \mathrm{Pr}_e)\frac{u}{u_m}k_e \tag{4.36}$$

Where $\mathrm{Re}_k = \frac{u_m\sqrt{K}}{\upsilon}$, the Reynolds number based on permeability, $\mathrm{Pr}_e = \frac{\mu C_f}{k_e}$ is the Prandtl number based on effective conductivity, u_m is the average flow velocity entering the tube and C_D (=0.1) is the thermal dispersion coefficient.

Because mean temperature of the fluid in experimental work is 30 °C, so the thermo-physical properties of fluid at 30 °C are used as fluid properties in the modelling work. If not specified, the diameter and length of the modelling tube are 26 mm and 150mm.

4.2.5 Numerical Procedures

The combined continuity, momentum, and energy equations are solved numerically with the SIMPLE (Semi-Implicit Method for Pressure Linked Equations) algorithm (Patankar, 1980). The FVM (finite volume method) is used to derive the discretization equations. The control volume formulation utilized in this algorithm ensures the continuity of convective and diffusive fluxes, as well as overall momentum and energy conservation. The harmonic mean formulation adopted for the interface diffusion coefficients between two control volumes can handle abrupt changes in these coefficients. For all of the cases studied, it is found that a uniform grid of 150×140 used in the z and r directions can ensure the mesh independence of the solution. The governing equations were solved by using the alternate direction iteration numerical scheme. The iteration is terminated when changes in target variables u, T_s and T_f are less than 10^{-4} between successive iterations.

4.2.6 Results and discussions

4.2.6.1 Velocity distribution

The Fig. 4.19 and 4.20 show the predicted velocity distributions for the tube with 5% relative density and 20ppi foams. From these figures, it is clear that the velocity distribution is very flat and the boundary layer of a metal-foam tube is very thin because the metal foams make the flow more homogenous. The Fig. 4.19 shows the velocity distributions for the tube with different mass flow rate. The trends of both distributions are very similar.

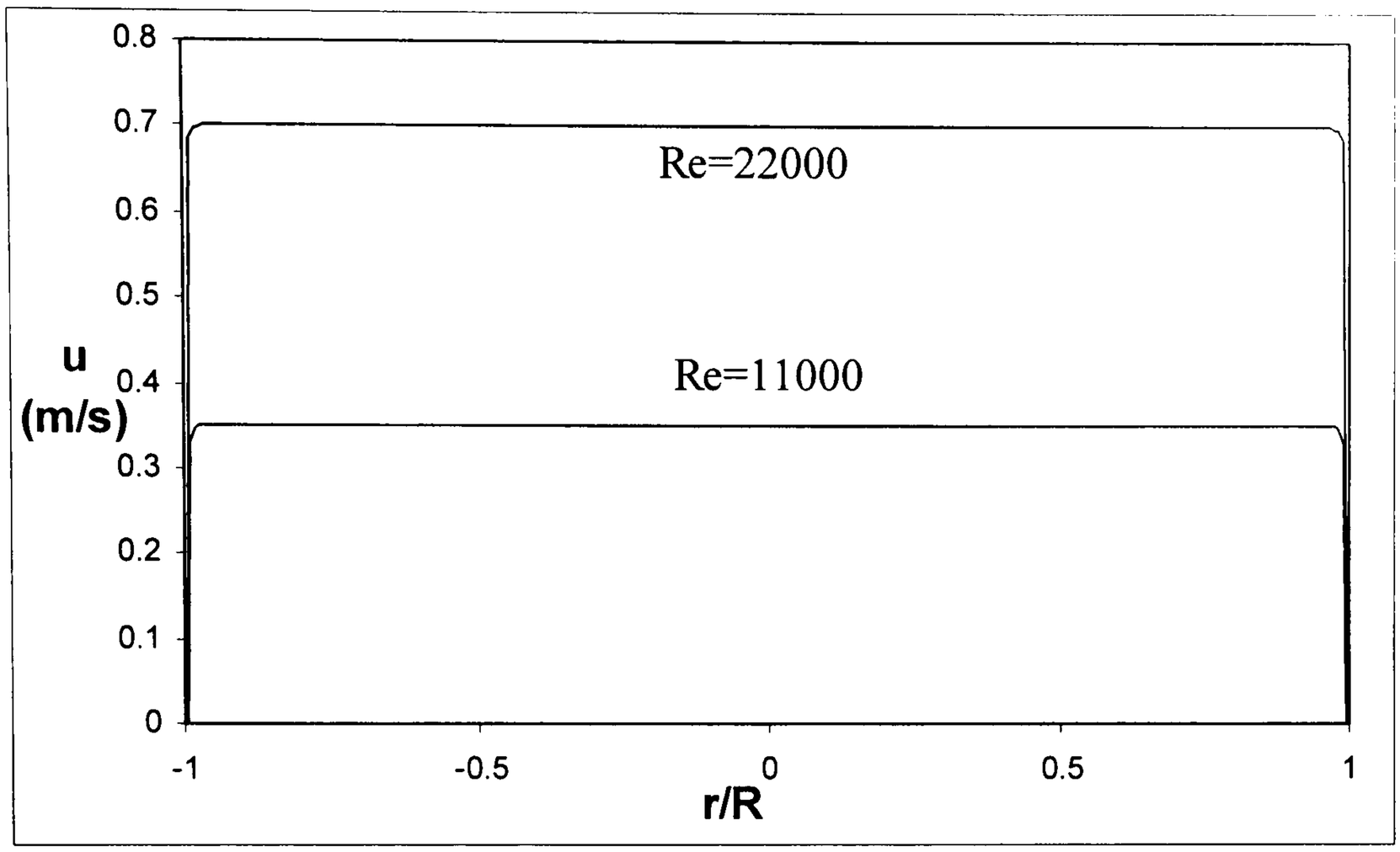

Fig. 4.19 The velocity distribution for tube with 5% relative density, 20ppi foams

As shown in Fig.4.20, compared with velocity distribution predicted by Brinkman extended Darcy model (analytical solution), the distribution calculated by Forchheimer extended Darcy model (numerical modelling) has thinner boundary layer because it introduces form force which unifies the velocity distribution. However, the main part (more than 90% in this case) of velocities for both model are near to mean velocity, and the heat transfer performance in metal-foam tube depends mostly on metal foams instead of boundary layer for plain tube, which means that the difference between two velocity distributions may have less effect on overall heat transfer performance.

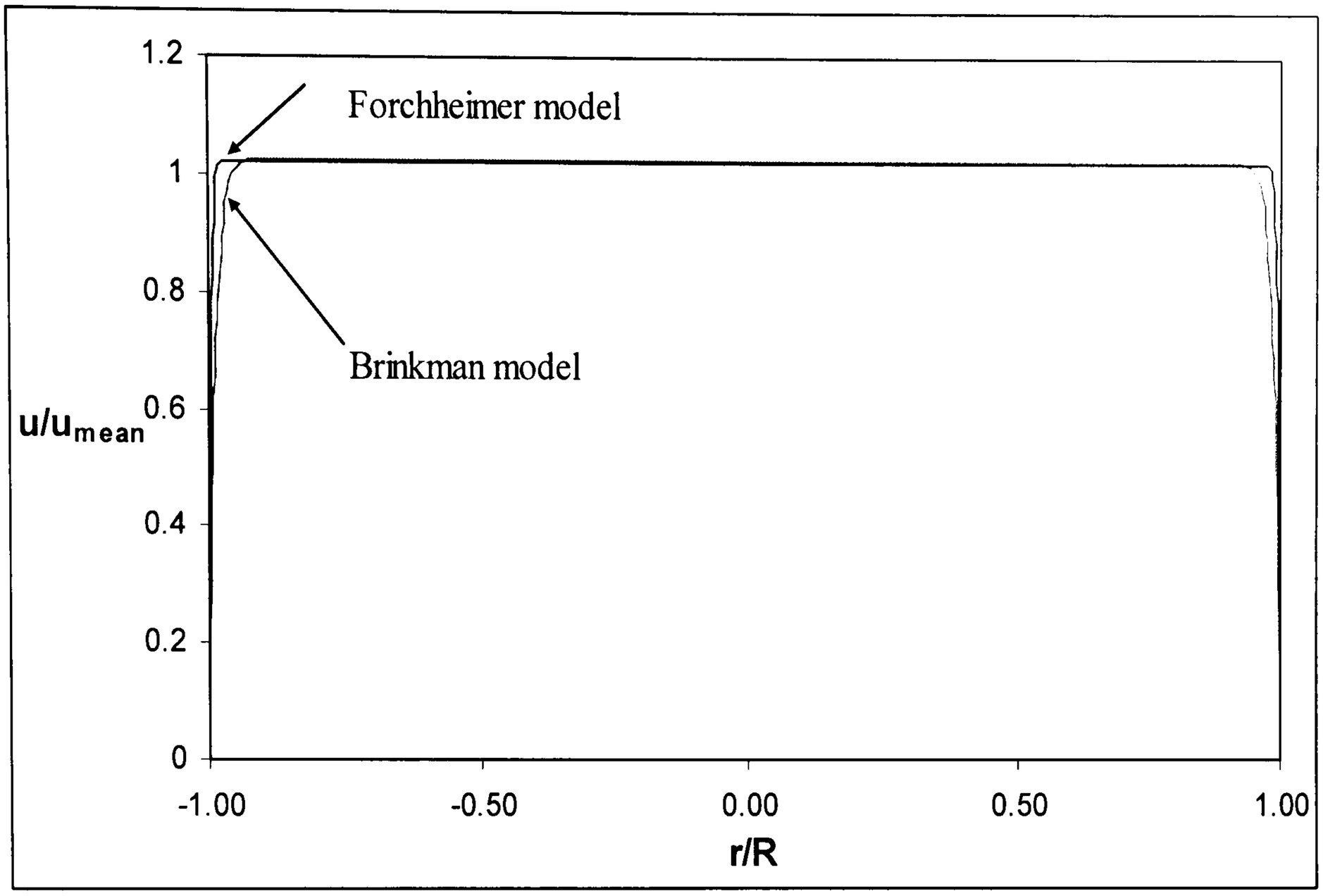

Fig. 4.20 The velocity distribution for tube with 5% relative density, 20ppi foams

4.2.6.2 Pressure drop

The pressure drops per unit length for tubes with different foam microstructure have been plotted in Fig. 4.21. The lines represent the modeling results and the points represent the data from experimental work. From these charts, it is clear that the pressure drop increases dramatically with the increase of relative density (from 5% to 10%) and pore density (from 20 ppi to 40 ppi). Fig. 4.21(a) shows the pressure loss increases dramatically with the increase of average velocity, especially when velocity is high. Because when velocity is very low (Darcy model), the viscous term (Darcy term) is dominated, and the pressure drop is linear with the increase of velocity. While the velocity increases, the form force (Forchheimer factor, which is proportional to square of velocity) becomes a more important issue for pressure loss.

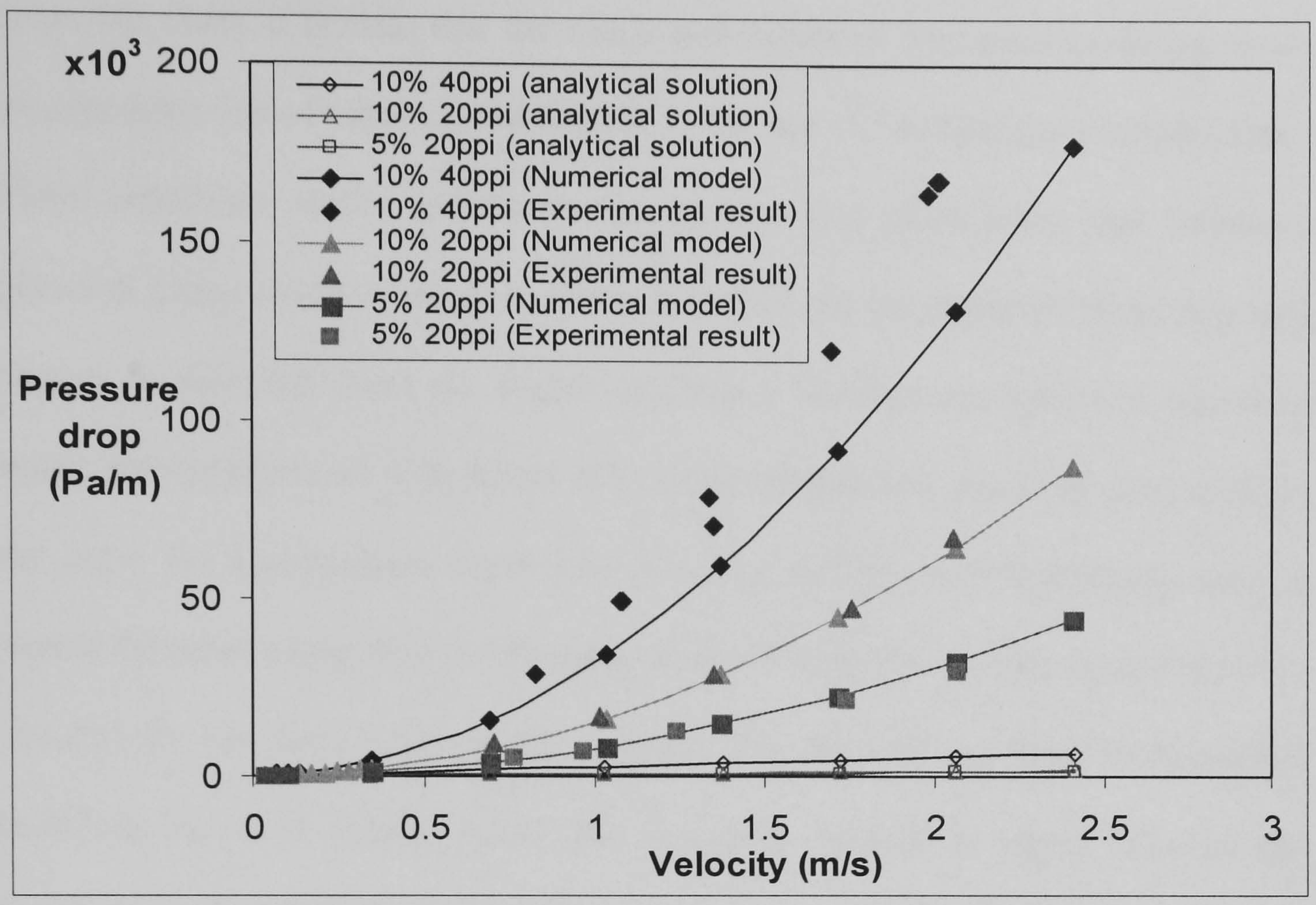

(a)

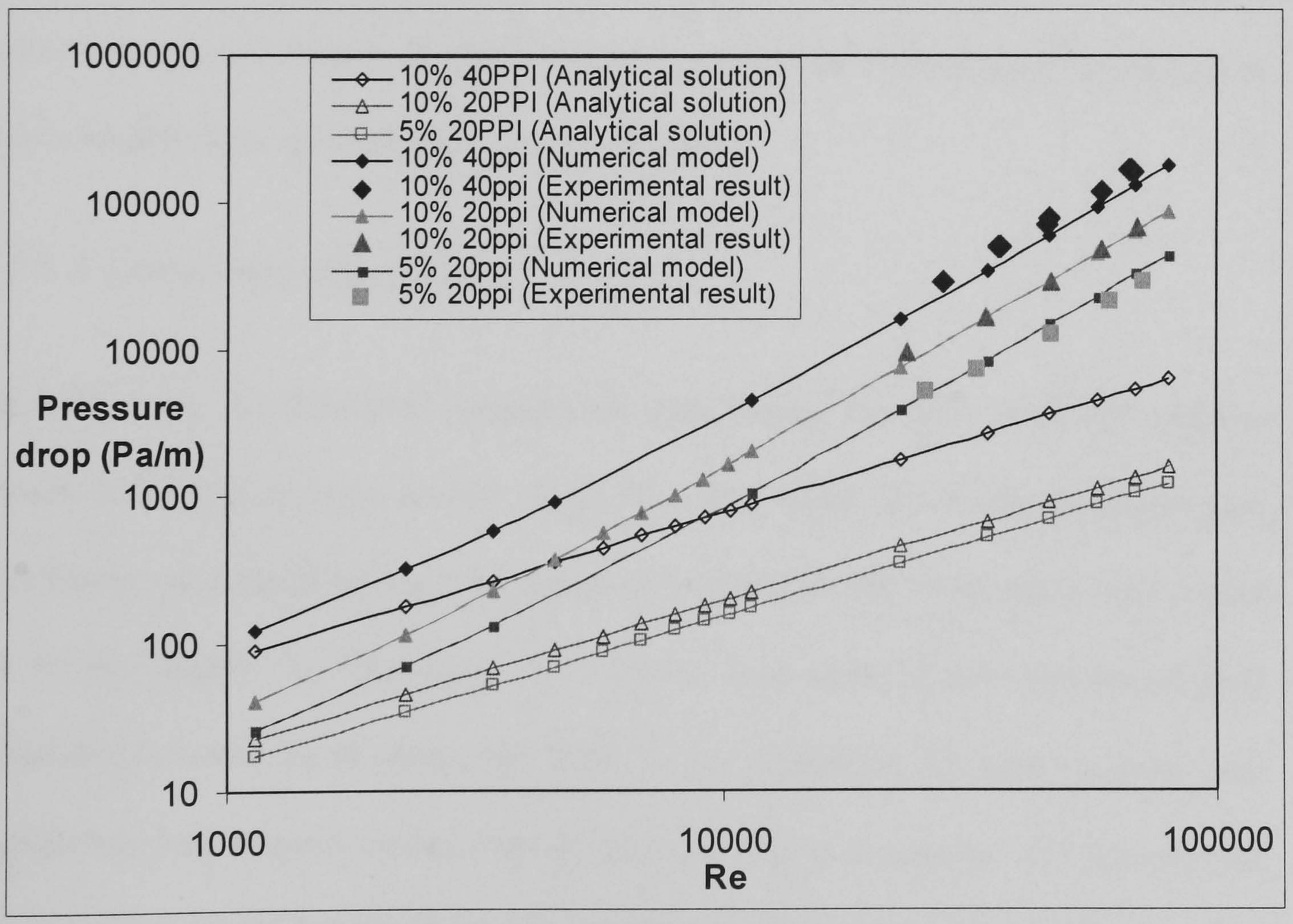

(b)

Fig. 4.21Comparison between prediction and test data on unit length pressure drops with different foam microstructure, varying with (a) velocity, (b) Reynolds number (in logarithmic scale)

From this chart, it is clear that the trends and values of numerical modeling results are marching that of experimental results. So the use of Forchheimer extended Darcy model reflect the reality and model the velocity field much better than Brinkman extended Darcy model because the form force can not be neglected when Reynolds number is high. But there are slightly difference between the results of numerical model and experimental data, where more experimental data should be used to adjust and prove the Forchheimer coefficient (F_1). Fig. 4.21(b) uses logarithmic scale to present the relationship between Pressure drop and Reynolds number (proportional to velocity) for the same tubes in Fig. 4.21(a). The slope of the lines for numerical modelling becomes sharper when the Reynolds number is higher because the Forchheimer factor is more dominant. Compared with the results of analytical solution which use Brinkman extended Darcy model, the predictions of Forchheimer-Darcy Model show good agreement with test data.

4.2.6. 3 Temperature distributions

Fig.4.22 show the predicted temperature distribution for tube with 10% relative density and 20ppi at cross-section of z/L=0.5. The upper line is for the temperature distribution of metal foams and the lower line represents the temperature distribution for R134a vapour. In this chart, it is shown that there is obvious temperature difference between solid phase and fluid phase. Therefore, the two-equation non-equilibrium heat transfer model must be used for energy equations. The temperature of solid phase (metal foams) decreases smoothly from the tube wall to the tube centre while the temperature of fluid phase drops sharply near the tube wall due the effect of boundary layer. Its trend is almost the same as that of solid phase because the fluid absorbs heat from solid phase in tube centre.

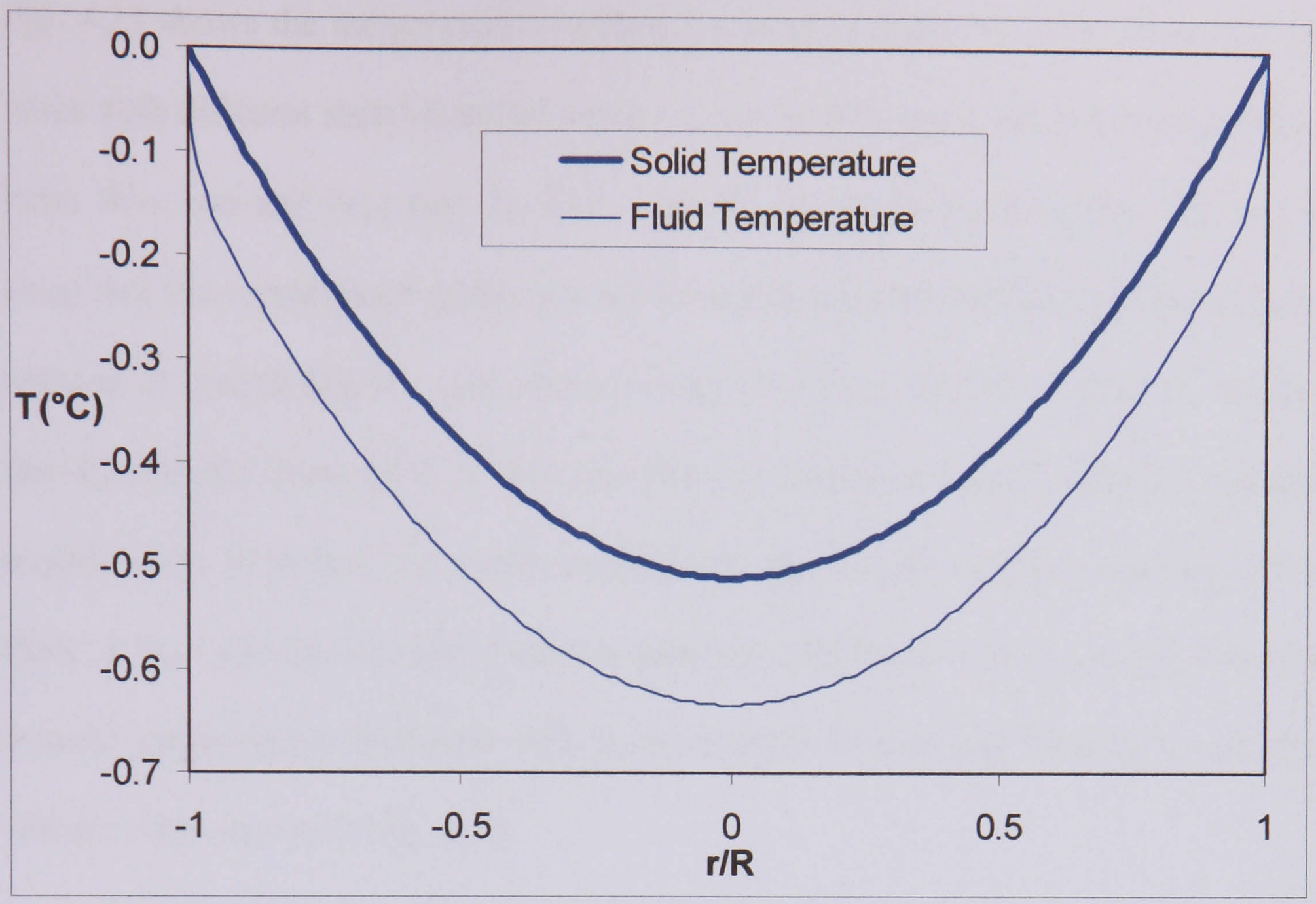

Fig. 4.22 Temperature distribution for tube with 10% relative density, 20ppi foams at z/L=0.5

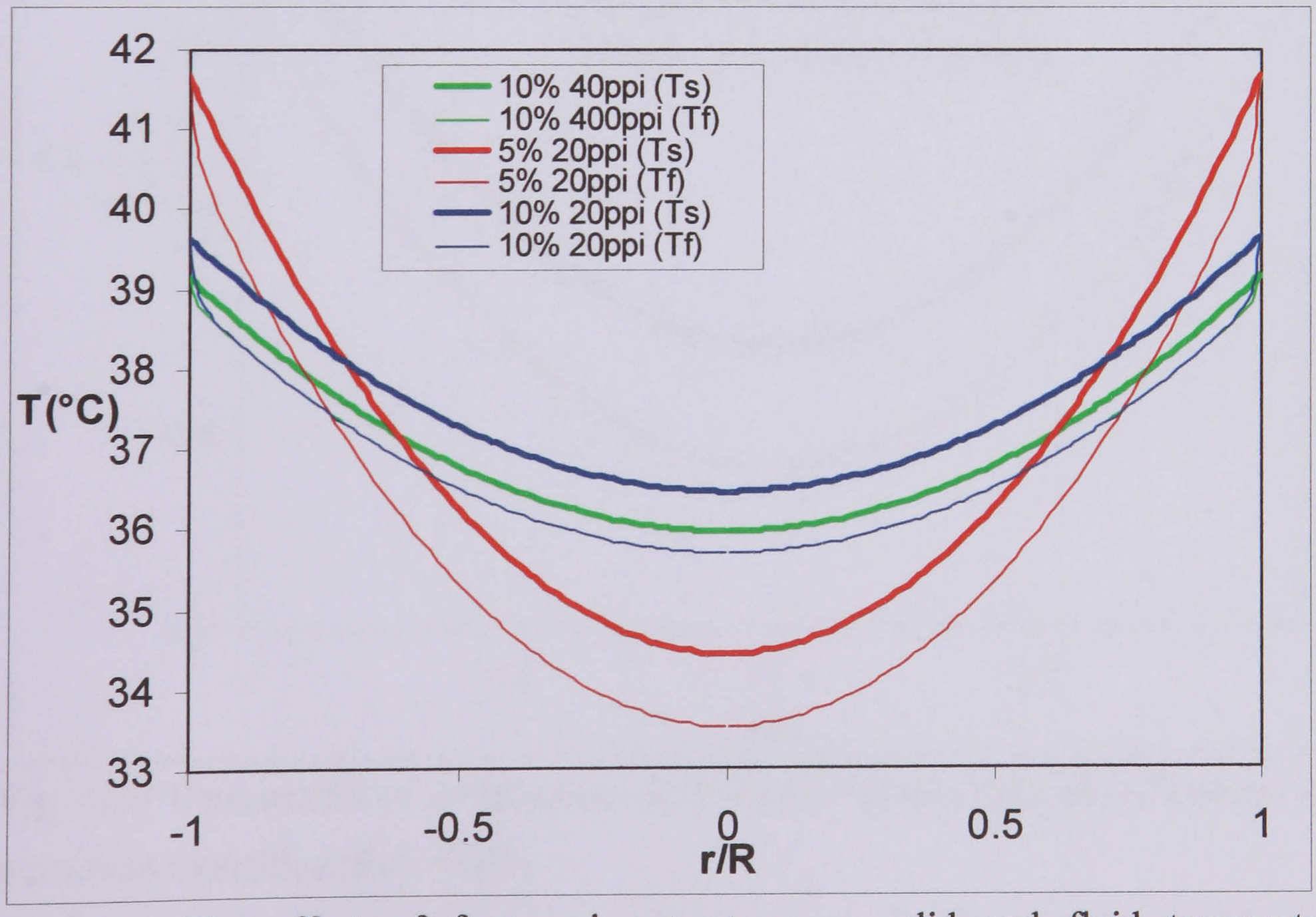

Fig. 4.23 The effect of foam microstructure on solid and fluid temperature distribution at z/L=0.5.

Fig. 4.23 shows the temperature distributions of solid phase and fluid phase for the tubes with different metal-foam microstructures. In this figure, the inlet temperature, mass flow rate and heat flux for each tube are the constants. From this chart, it is clear that the temperature difference between solid phase and fluid phase has been reduced by increasing the pore density from 20 PPI to 40 PPI. When the relative density reduced from 10% to 5%, the thermal resistance of solid phase increases significantly, therefore, the solid temperature distribution becomes sharper while there is less change in solid-fluid temperature difference. Consequently, the heat transfer performance decreases with lower relative density and lower pore density, which is also shown in Fig. 4.25.

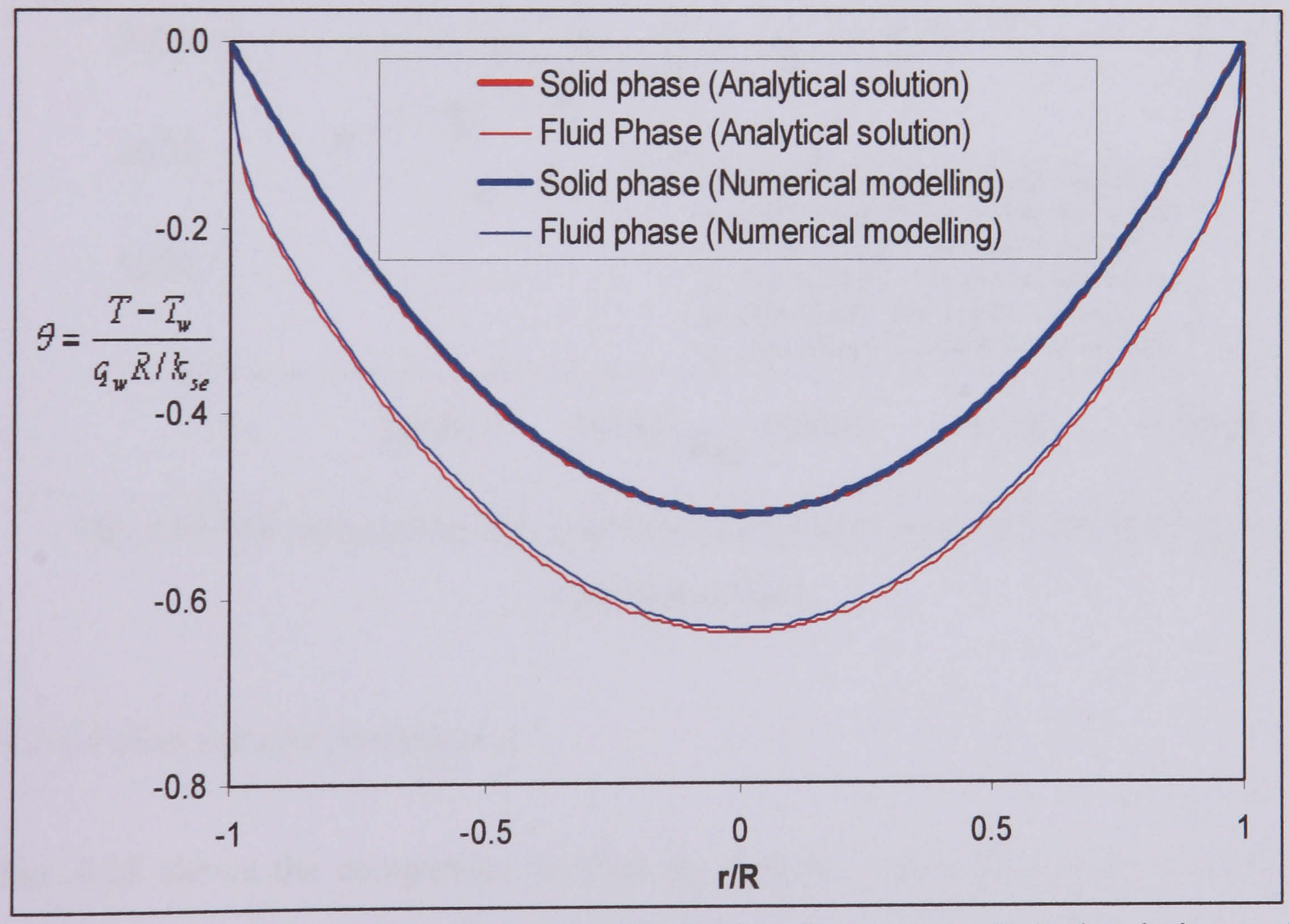

Fig. 4.24 Comparison of temperature distribution between analytical solution and numerical modelling (Re=11000)

Fig. 4.24 shows the comparison between analytical solution and numerical modelling for solid and fluid phase temperature fields. The non-dimensional temperature has

been used to compare these results. Although the two models with different momentum equations predict different pressure drop in these tube, it is clear that there is only slightly difference between the temperature distributions predicted by the two models, which results in slight difference between their predictions on heat transfer performance.

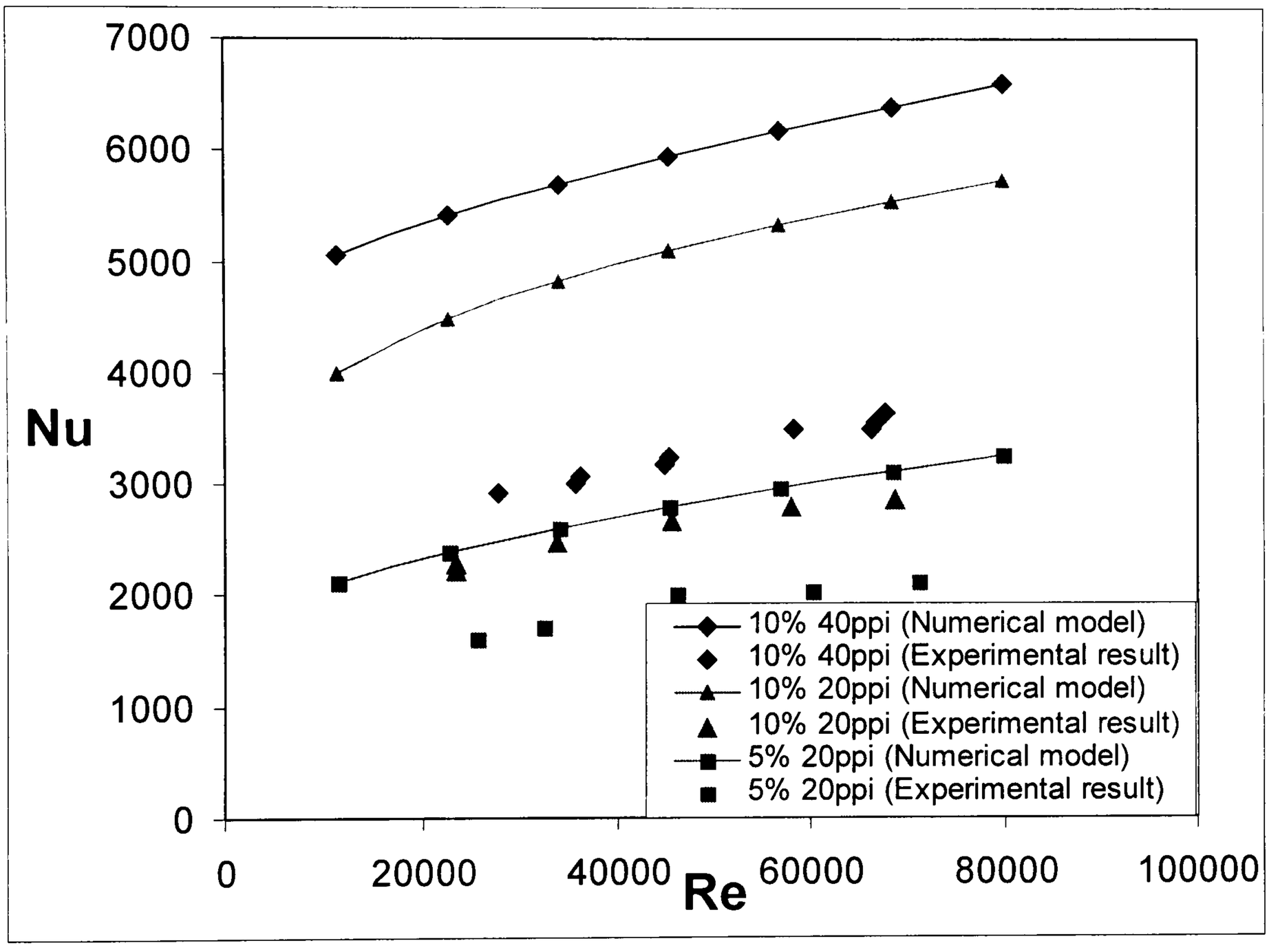

Fig. 4.25 The comparison of Nusselt number between numerical predictions and experimental data.

4.2.6.4 Heat transfer performance

Fig. 4.25 shows the comparison between numerical predictions and experimental results on heat transfer performance of three types of metal-foam tubes varying with Reynolds number. Both numerical predictions and experimental data indicate that the heat transfer performance (Nusselt number) can be enhanced by increasing pore

density or relative density of metal foams or increasing Reynolds number. With the increase of Reynolds number, the theoretical predictions for heat transfer shows the same trend as the test data, i.e. the Nusselt number increases with the increase of Reynolds number in the same trend. However, the values of predictions are higher than that of experimental results, because the numerical modelling doesn't consider the contact thermal resistance between the tube wall and metal foams. In reality, the attachment between tube wall and metal foams isn't perfect. Therefore, the effect of contact resistance, which makes the heat transfer performance worse, can not be neglected. In addition, the parameters of the test tubes are nominal values provided by the producer. There are deviations lying in real properties of test samples from the nominal values (Zhao, 2004a), which also brings difference between the modelling predictions and experimental results.

The Fig. 4.26 shows the difference of Nusselt number predicted by analytical solution and numerical modelling with different momentum equations. In general, the predictions of numerical modelling is higher than those of analytical method because the former considers the form force in momentum equation, which has thinner boundary layer attaching the tube wall in results of higher heat transfer performance, and the two-dimensional modelling considered the inlet effect which has higher local heat transfer coefficient than thermally fully developed flow for the latter. Although the numerical results are much higher than analytical results when the Reynolds number is high at 80000 due to the inlet effect taking place longer in the short tubes (150mm), the difference between Nusselt numbers predicted by two models is less than 10% when Reynolds number is less than 20000. When the tube is longer, where the inlet effect can be neglected, the difference between them becomes

smaller. Therefore, for modelling of heat exchanger in next section, the analytical method is employed to analyze the heat transfer performance of metal-foam heat exchanger due to its simplicity.

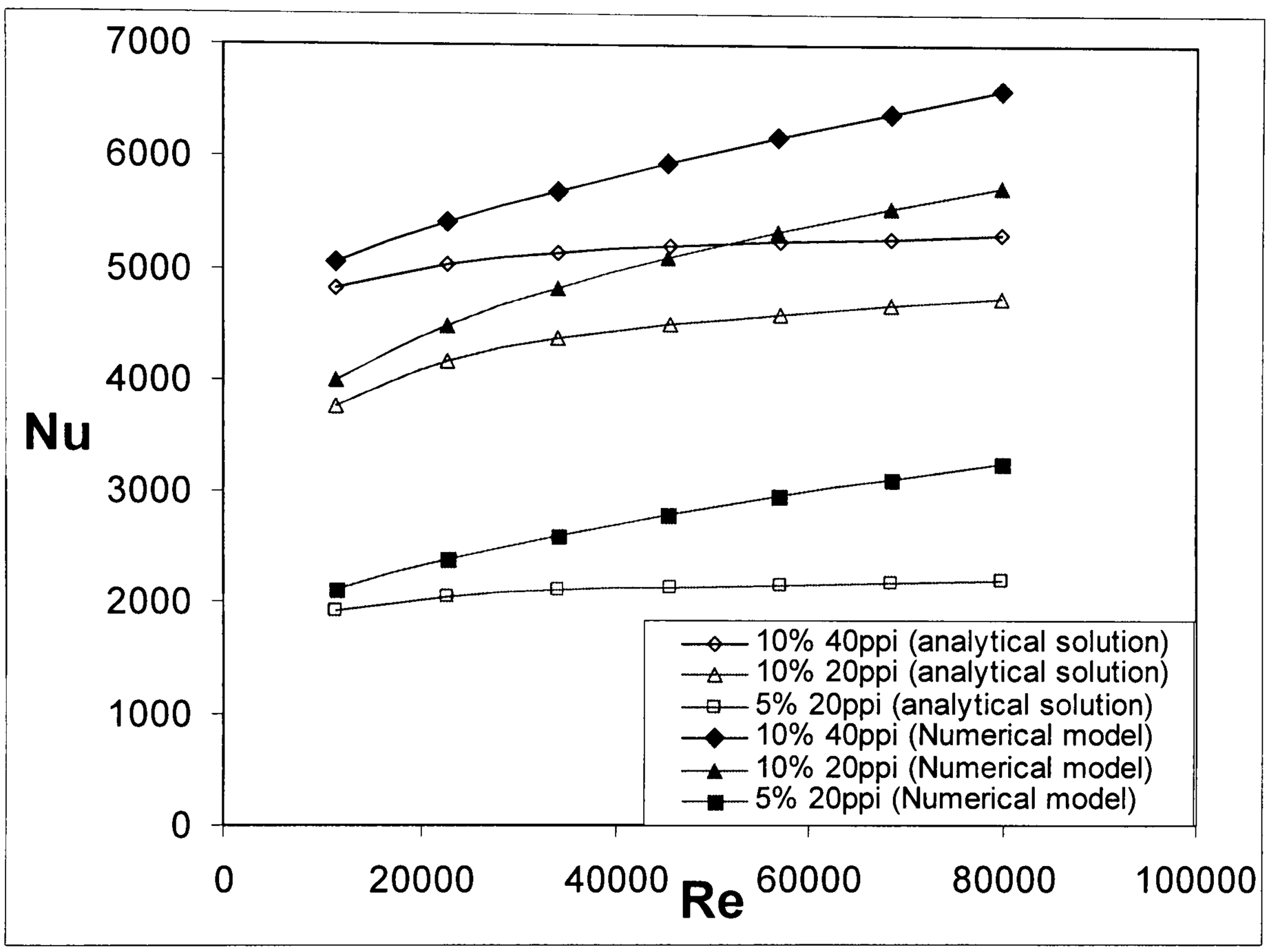

Fig. 4.26 Comparison of heat transfer performance between analytical solution and numerical modelling.

4.2.6.5 The effect of contact thermal resistance on overall heat transfer

To exam the effect of contact thermal resistance between tube wall and metal foams on overall heat transfer performance, it is assumed that the thermal conductivity of 0.09 mm layer of metal foams attached to tube wall has been reduced to 200 W/m·K instead of thermal conductivity of copper used for numerical modelling. Fig. 4.27 shows the comparison between predictions by numerical modelling with consideration of contact thermal resistance and experimental results. From this chart,

it is clear that the predictions considered the effect of contact thermal resistance have good agreement with the experimental data, which implies that the effect of contact resistance is the main source of deviation. Compare to numerical results for ideal conditions in Fig. 4.24 or 4.25, the predicted overall heat transfer performance in tube with decreased thermal conductivity in very thin boundary layer becomes significantly worse.

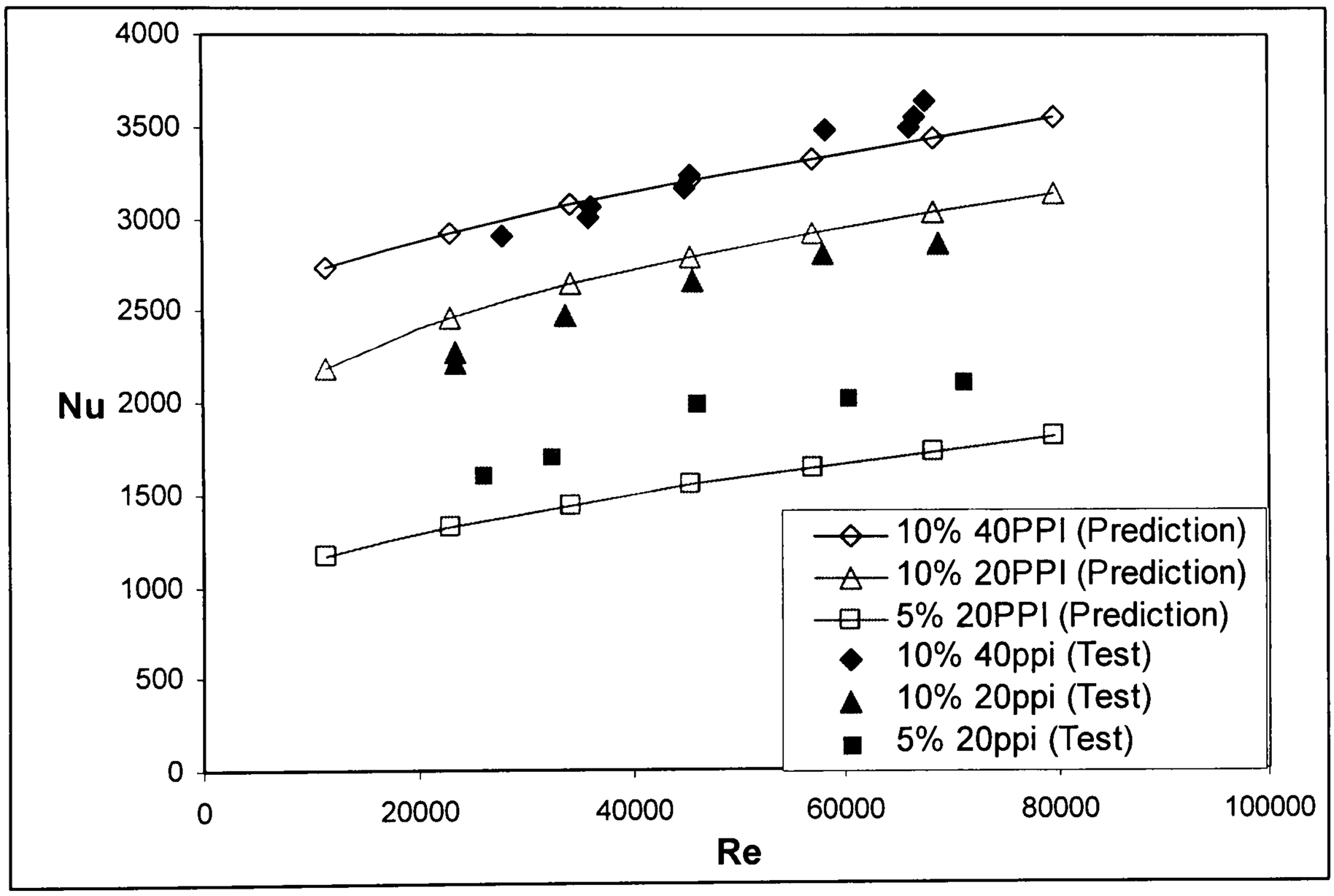

Fig. 4.27 Comparison between experimental data and numerical predictions considered contact thermal resistance.

4.3 Modelling for forced convection in metal-foam heat exchangers

Both analytical method and numerical method have been used for analyzing the forced convection heat transfer in metal-foam tube. The comparison between numerical method, analytical method and experimental results shows that only the numerical method has good predictions on pressure drop when Reynolds number is high. But for normal conditions, both theoretical methods have similar predictions of

heat transfer performance. Therefore, the analytical method, which needs less computer time, is employed to study the heat transfer performance of metal-foam heat exchangers in this section. The Brinkman-extended Darcy momentum model and two-equation heat transfer model for porous media are employed. The effects of different parameters (such as pore size, porosity, geometrical size, etc) on the heat transfer and fluid flow performance of metal-foam tube heat exchangers are discussed. Furthermore, the overall performances of metal-foam tube heat exchangers are compared with those of conventional finned tube heat exchangers.

4.3.1 Physical problem

The problem under consideration is the analysis of the thermal performance of a counter-flow tube-in-tube heat exchanger as shown in Fig.4.28. The heat exchanger comprises of two concentric tubes forming an inner section and an outer annular section, both filled with metal foams. Fluid flows axially through both sections in a counter-flow arrangement. The outer tube is assumed to be perfectly insulated so there is no heat transfer between the tube's outer surface area and the surroundings. The heat flux through the wall of the inner tube is assumed to be constant so the thermal boundary conditions of the inner surface of the outer section can be assumed to constant heat flux. The solution for the inner tube was presented in above section. The solution for the outer tube is presented in the following sections.

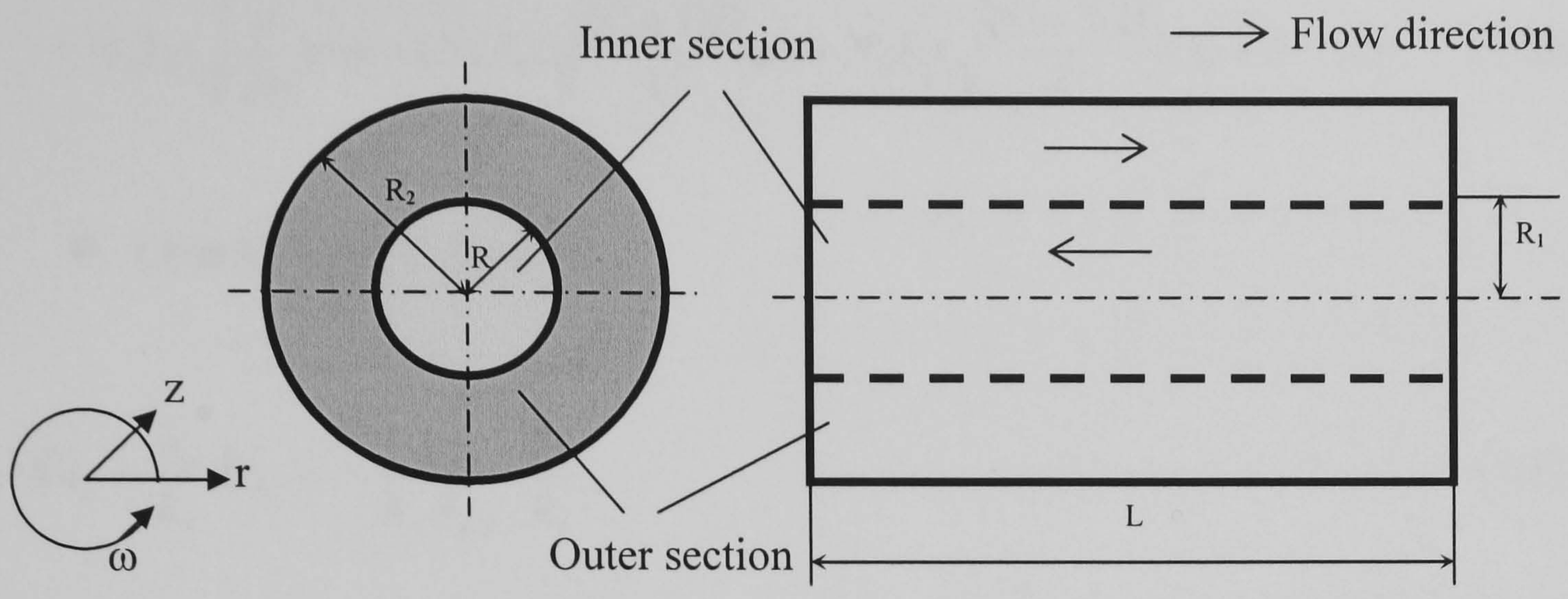

Fig. 4.28 Heat exchanger filled with metal foams: geometry and definition

4.3.2 Analytical solution for outer section

The same forms of momentum equations and energy balance equations were also used for analyzing the velocity distribution and heat transfer in outer section.

- The velocity solution

$$\mathrm{U}=\mathrm{P}\left(N_1 \cdot J_0\left(\sqrt{\frac{\varepsilon}{Da}}\psi\right)+N_2 \cdot Y_0\left(\sqrt{\frac{\varepsilon}{Da}}\psi\right)\right)\text{-P}, \tag{4.37}$$

- The temperature solutions for solid and fluid

$$\theta_s=\frac{2P}{\left(\frac{R_2}{R_1}\right)^2-1}\left(-\frac{1}{4}\psi^2+N_3\ln\psi+N_4+N_1\frac{Da}{\varepsilon}J_0\left(\sqrt{\frac{\varepsilon}{Da}}\psi\right)+N_2\frac{Da}{\varepsilon}Y_0\left(\sqrt{\frac{\varepsilon}{Da}}\psi\right)\right)\text{-}C\theta_f \tag{4.38}$$

$$\theta_f=\frac{2P}{C+1}\left(\frac{1}{\left(\frac{R_2}{R_1}\right)^2-1}\left(-\frac{1}{4}\psi^2+N_3\ln\psi+N_4+\left(A+\frac{Da}{\varepsilon}\right)\left(N_1J_0\left(\sqrt{\frac{\varepsilon}{Da}}\psi\right)\right.\right.\right.$$

$$+N_2 Y_0(\sqrt{\frac{\varepsilon}{Da}}\psi)) - (N_5 J_0(\sqrt{\frac{(C+1)D}{C}}\psi) + N_6 Y_0(\sqrt{\frac{(C+1)D}{C}}\psi)) + B - A)) \quad (4.39)$$

- Overall Nusselt number

$$\overline{Nu}_o = \frac{\bar{h}_o}{k_f} D_H = -\frac{k_{se}}{k_f \theta_{f,b}} \frac{D_H}{R_1}, \quad (4.40)$$

The parameters appeared in above formulas can also be found in Appendix B.

4.3.3 Analytical solution for heat exchangers

The overall heat transfer in a metal-foam tube-in-tube heat exchanger can be expressed as:

$$Q = U_i A_i (T_A - T_B) \quad (4.41)$$

Where $U_i = \dfrac{1}{\dfrac{1}{h_i} + \dfrac{R \cdot \ln(R_1 / R)}{k_s} + \dfrac{R}{R_1 h_o}}$, $A_i=2\pi RL$, T_A and T_B are the fluid temperatures, and h_i and h_o are the inside and outside convection heat-transfer coefficients for inner tube and outer section, respectively(Holman,1992).

4.3.4 Results and discussions

4.3.4.1 Dimensionless velocity and temperature distributions

Fig. 4.29 and Fig. 4.30 show the predicted dimensionless velocity and temperature distributions, respectively, in the inner and outer tubes of the metal-foam tube heat exchanger. The curves in the centre part of the diagrams represent the distributions

in the inner tube, and the curves at two ends represent the distributions in the outer tube. As can be seen from Fig. 4.29, the shape of the dimensionless velocity distribution in the outer tube is similar to that in the inner tube, with the velocity increasing from zero at the boundary (tube wall) to its maximum value in the centre of the passage.

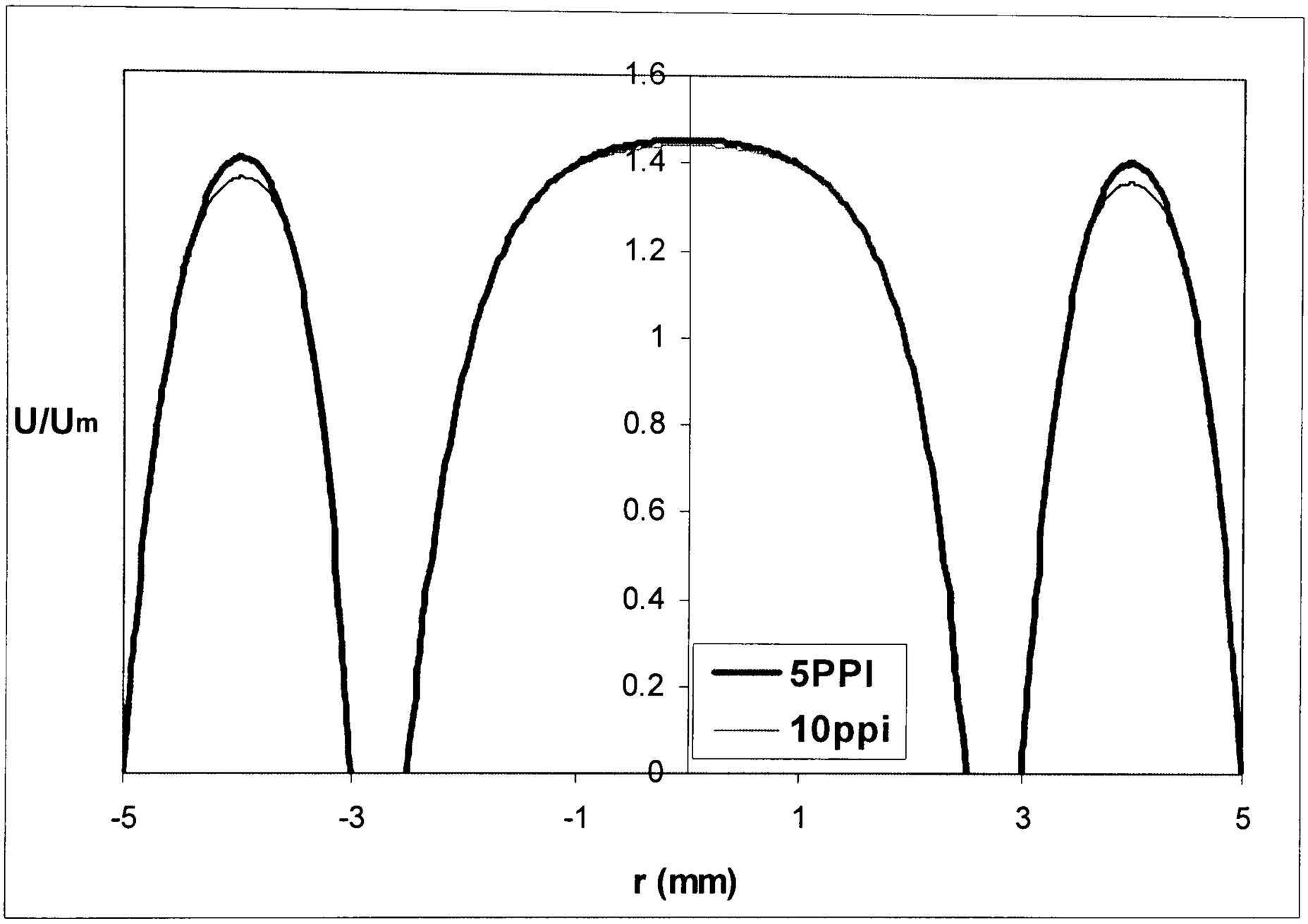

Fig. 4.29 Dimensionless velocity distributions in tube heat exchanger

In the equation of the dimensionless temperature, $\theta=\frac{T-T_w}{q_w R_1 / k_{se}}$, q_w is positive when the fluid absorbs heat from the wall and negative when the fluid transfers heat to the wall. As expected, Fig. 4.30 shows that the temperatures of the fluid and solid are the same on the boundary wall. In the inner tube, the fluid temperature reduces from maximum in the centre to minimum on the tube wall. The temperature variation in the foam, although of similar trend, is much more gradual than the temperature

variation in the fluid. Unlike the dimensionless temperature distribution in the inner tube, the dimensionless solid (foam) temperature in the outer tube decreases from the inner wall to reach minimum value on insulated wall. The dimensionless fluid temperature first decreases from the inner wall to a minimum at the centre of the passage and then increases slightly towards the outer wall. Fig. 4.29 also shows that increasing the pore density improves the velocity distribution and reduces the temperature difference between the solid and fluid (Fig. 4.30).

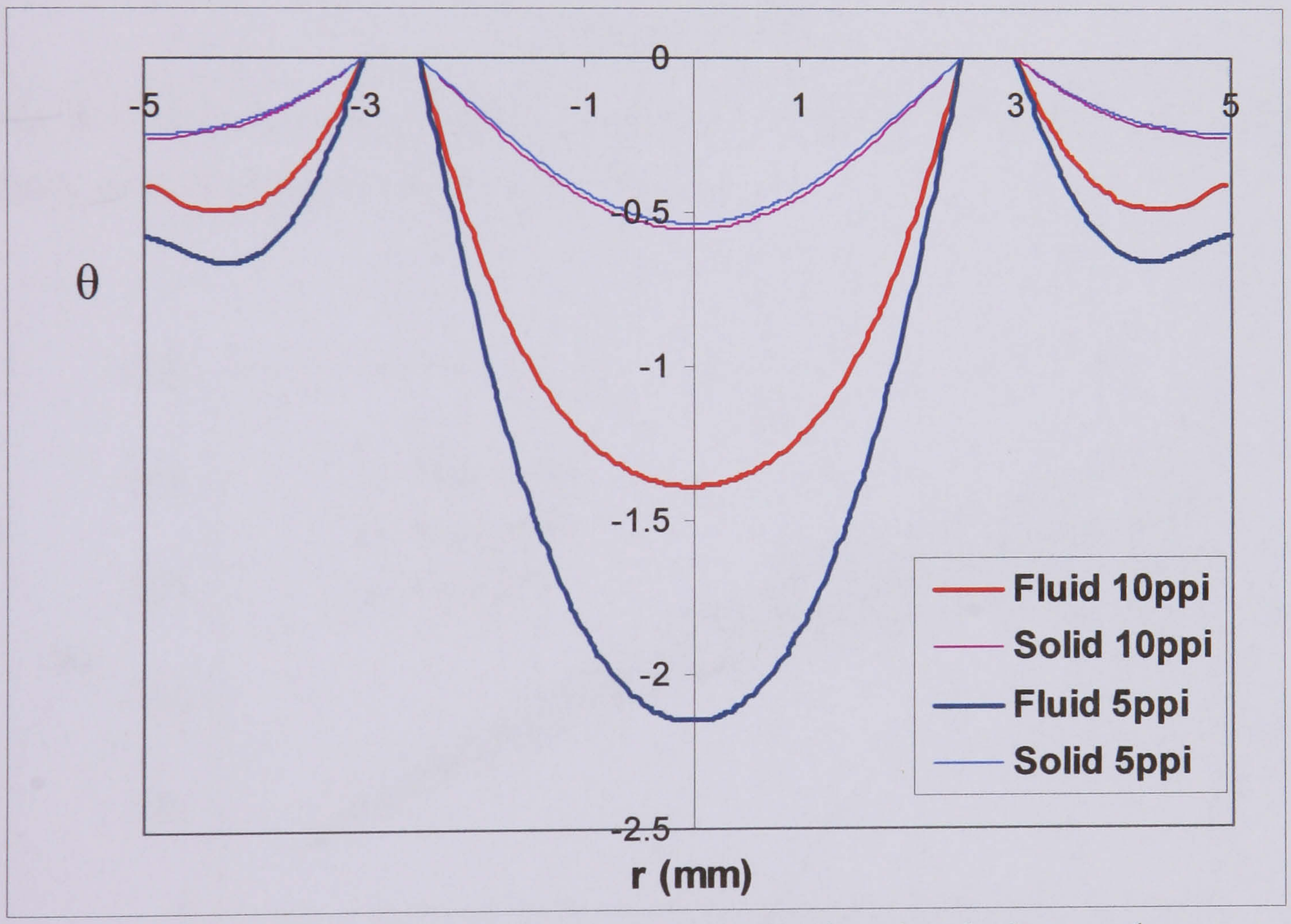

Fig. 4.30 Dimensionless temperature distributions in tube heat exchanger

4.3.4.2 Heat transfer performance in metal-foam compact heat exchanger

- Heat transfer in outer annular channel

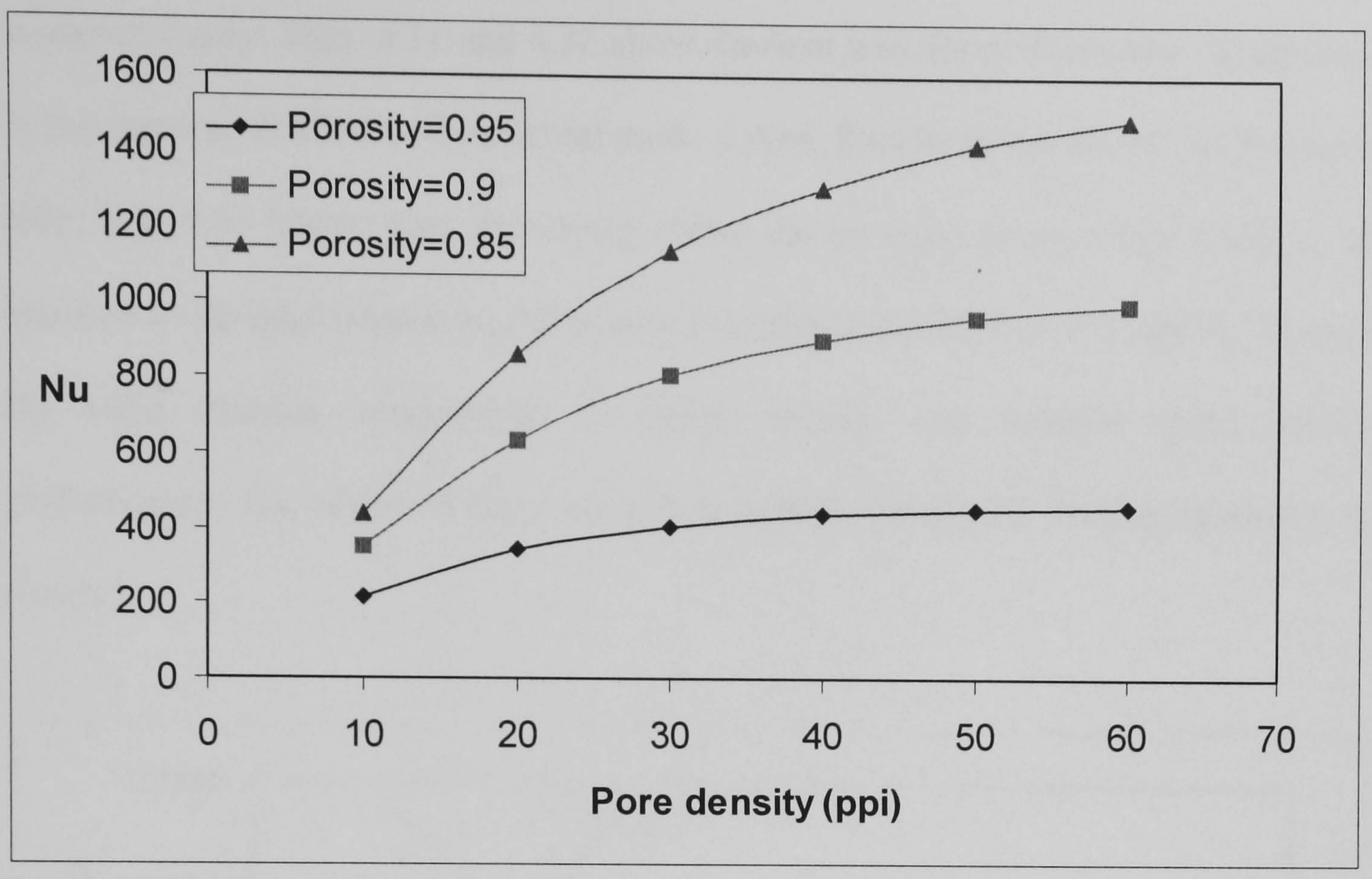

Fig. 4.31 Nu-Pore density diagram in outer section filled with selected porosity copper foam, air used as fluid, velocity of air is 5m/s.

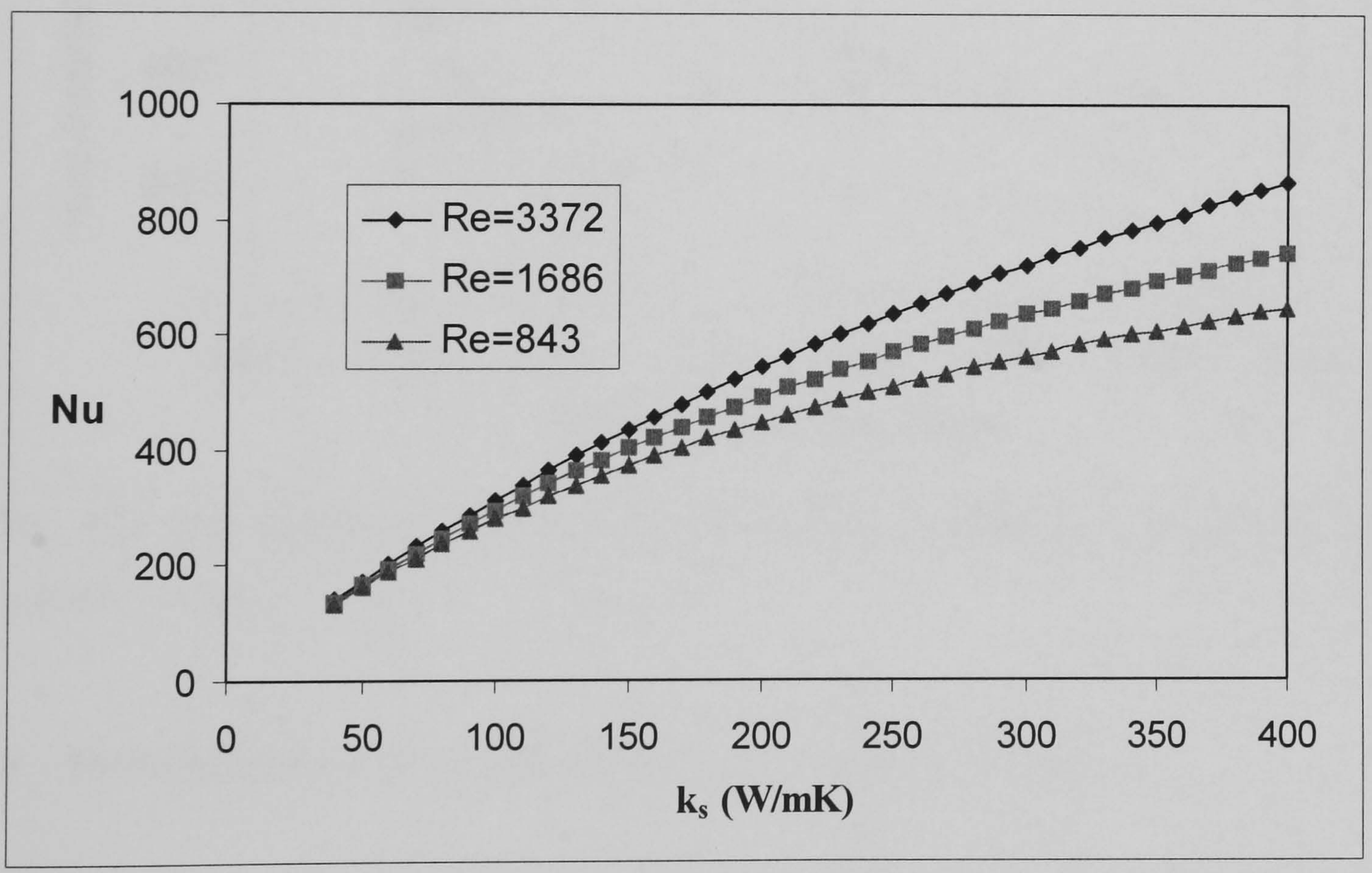

Fig. 4.32 Nu-k_s (solid thermal conductivity) diagram in outer section for different Reynolds numbers.

To apply this analytical solution to the metal-foam tube heat exchanger, the fluid flow and heat transfer through the metal-foam annular channel (outer tube) is

analyzed firstly. Figs. 4.31 and 4.32 show the heat transfer performance for air flow in the outer tube filled with different metal foams. Similar to the results for the inner tube, Fig. 4.31 shows that decreasing either the porosity or pore size leads to an increase in the heat transfer performance. It is also shown in Fig. 4.32 that increasing the solid thermal conductivity or fluid velocity can enhance heat transfer performance. The effect of fluid velocity is greater for higher thermal conductivity foams.

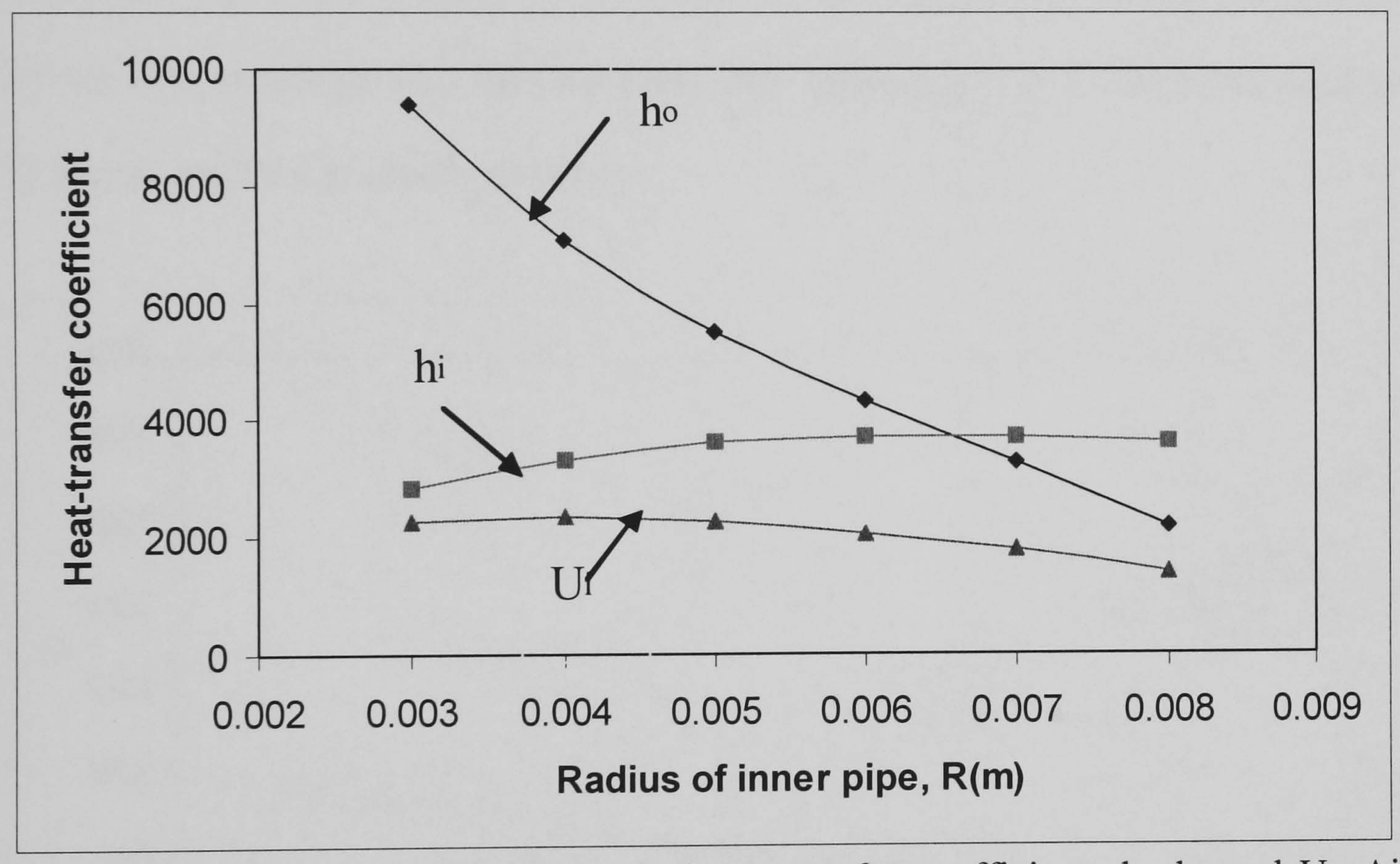

Fig. 4.33 The relationship between the heat transfer coefficients h_i, h_o and U_i, Air velocity=10m/s.

- **Overall heat transfer coefficient for metal-foam heat exchangers**

From the above formula (4.41), the overall heat transfer in the heat exchanger can be quantified as $Q = U_i A_i (T_A - T_B) = U_i A_i \Delta T$. It is known that the overall heat-transfer coefficient for heat exchanger (U_i) increases with increase of heat-transfer coefficients for inner section (h_i) and that for outer section (h_o). To analyze the effect

of the flow cross sectional area ratio ($\pi R^2/(\pi R_2^2-\pi R_1^2)$) on the overall heat transfer coefficient, the radius of the outer tube (R_2) was set at 10mm and the wall thickness of the inner tube (R_1-R) at 0.5mm. The flow cross-sectional area ratio would therefore vary only with the radius of the inner tube (R). The results are shown in Fig. 4.33. It can be seen that as the inner tube diameter increases, the cross-sectional area of the inner tube increases and the area of outer channel decreases. This causes an increase in the inside heat transfer coefficient (h_i) and a decrease in the outside heat-transfer coefficient (h_o). As a consequence, the overall heat-transfer coefficient for the heat exchanger (U_i) first increases with increasing h_i to a maximum value at R=4 mm, and then gradually decreases.

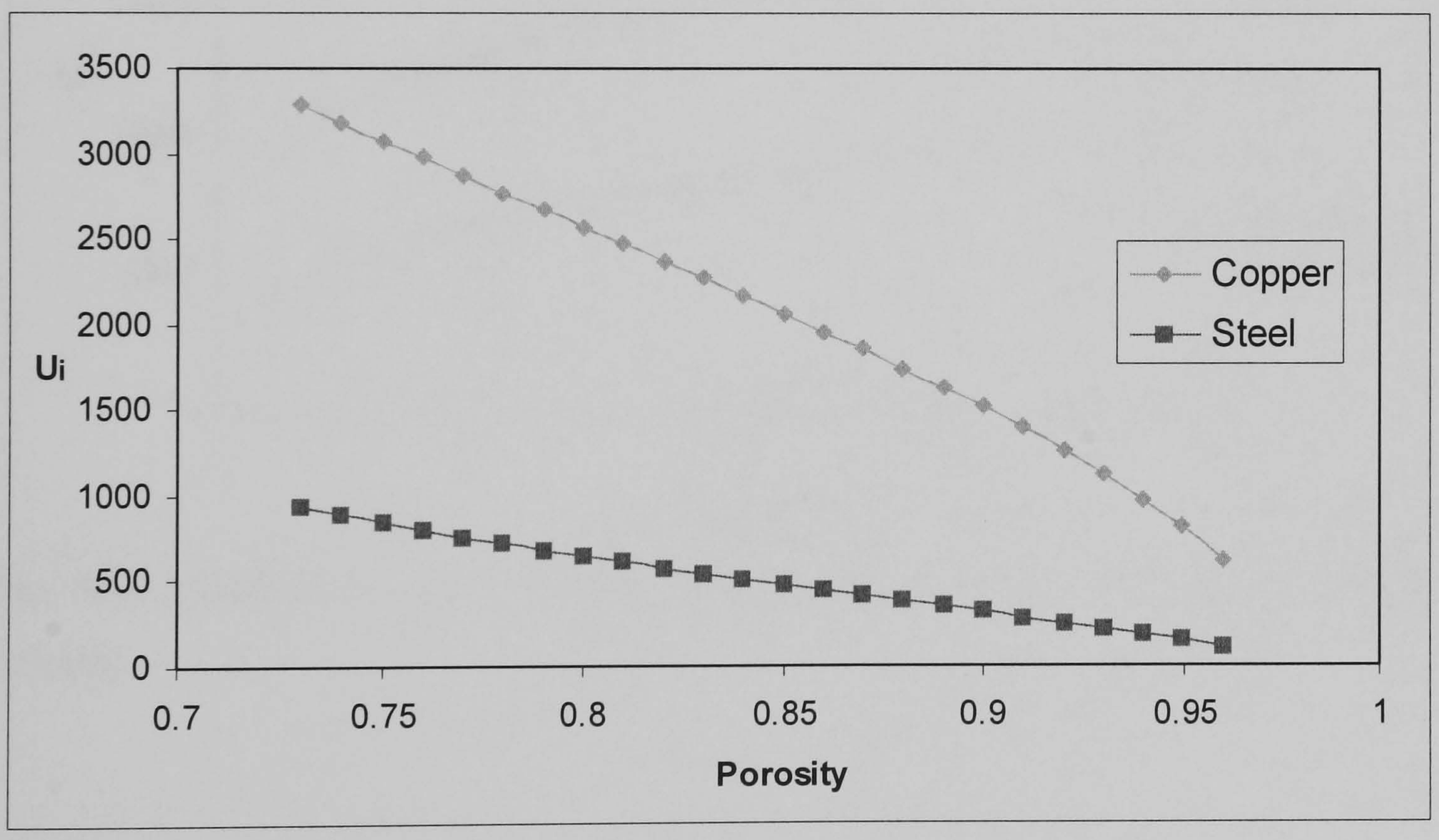

Fig. 4.34 Variation of overall heat-transfer coefficient of heat exchanger with metal foam porosity

Fig.4.34 shows the effect of porosity on the overall heat transfer coefficient of the heat exchanger for air velocity through the tubes of 10 m/s. It can be seen that as the porosity increases the overall heat transfer coefficient reduces. Fig. 4.34 also shows

that the overall heat transfer coefficient increases with increase of thermal conductivity, copper exhibits a higher overall heat transfer coefficient than steel, but this increase diminishes as porosity approaches unity. The effect of pore density and flow velocity on the performance of the heat exchanger is shown in Fig. 4.35. It can be seen that for a constant porosity of 0.9, increasing either the flow velocity or the pore density leads to an increase in the overall heat transfer coefficient.

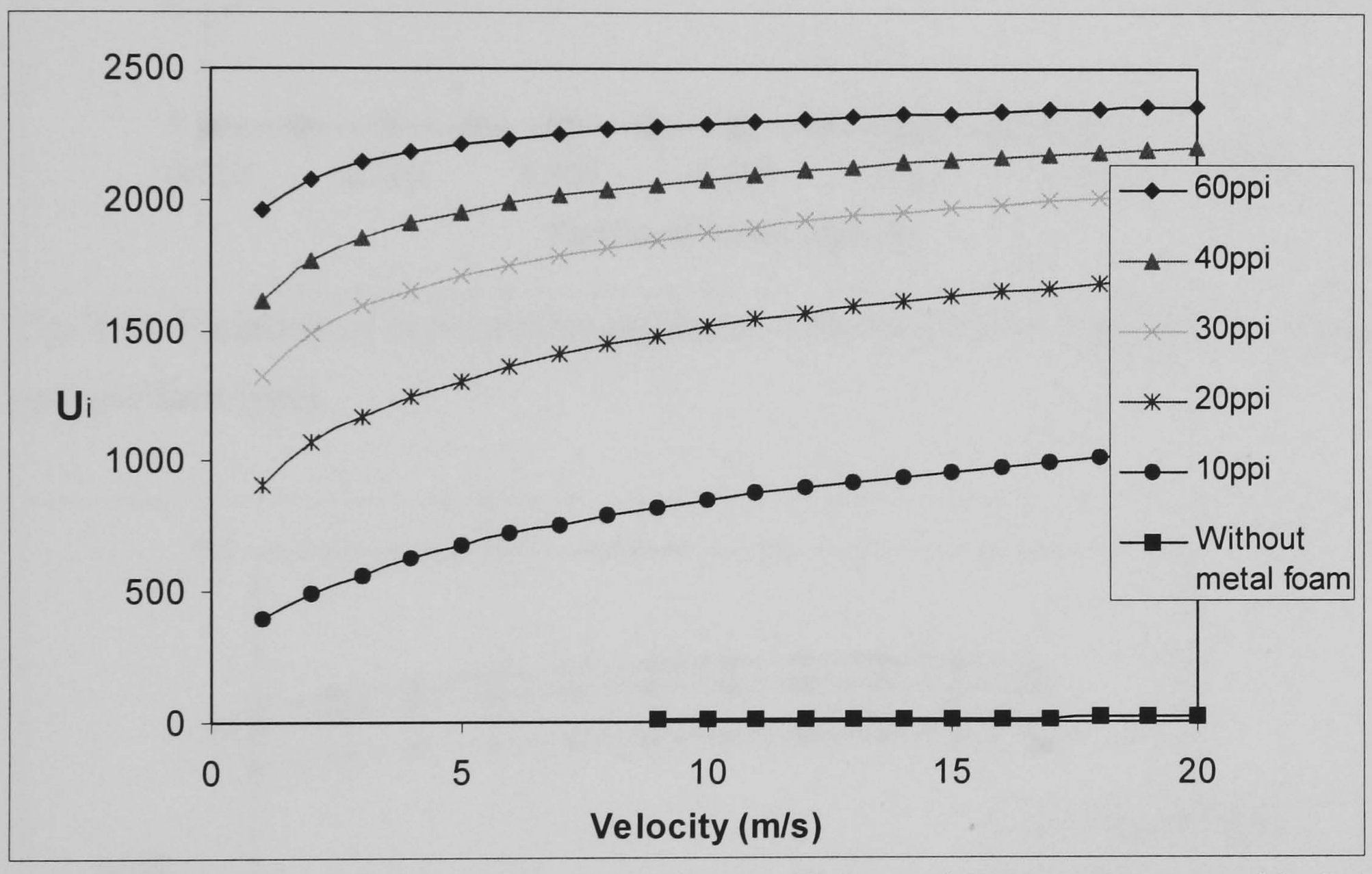

Fig. 4.35 Variation of overall heat-transfer coefficient of heat exchanger with fluid velocity.

- **Parametric analysis of heat exchanger**

From equation (4.41), the overall heat transfer in the heat exchanger can be quantified as $Q = U_i A_i (T_A - T_B) = U_i A_i \Delta T$. If q represents heat transfer per unit length i.e. $q=Q/L$, then $q= U_i 2R \Delta T$ and the heat-transfer capacity of the heat exchanger per unit length becomes $q/\Delta T = U_i 2R$.

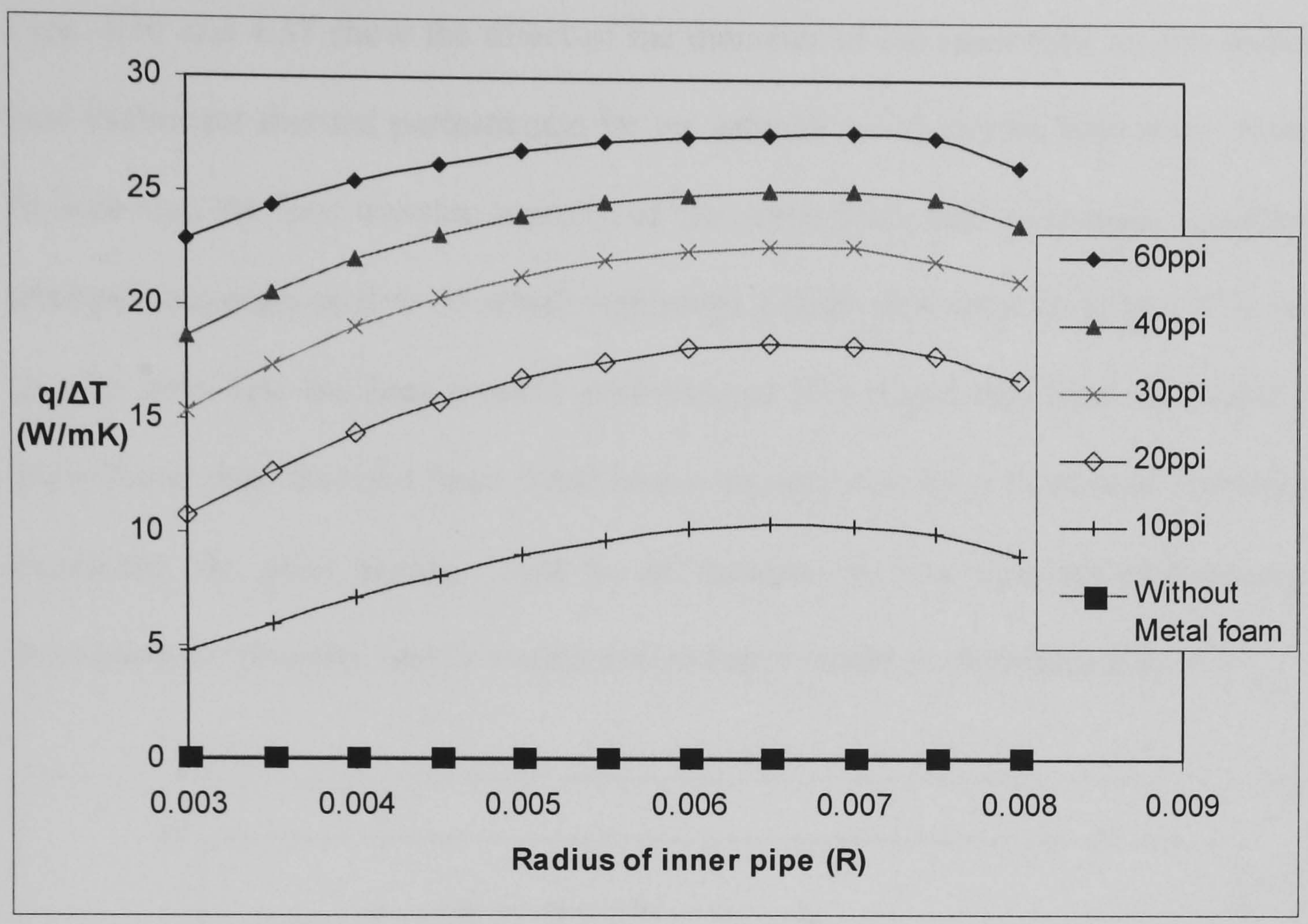

Fig. 4.36 Variation of heat-transfer capability with diameter of inner tube at selected pore per inch (ppi).

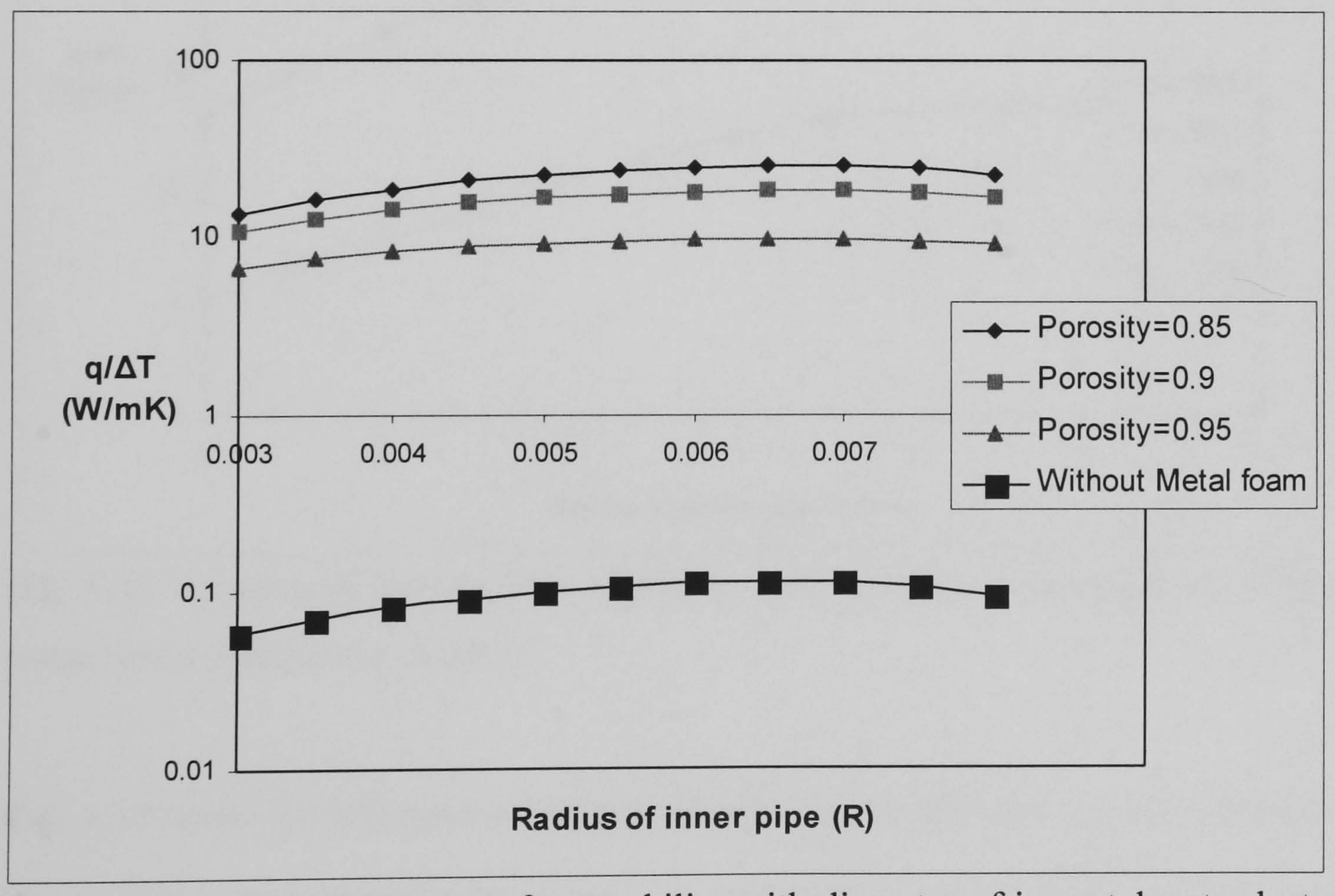

Fig. 4.37 Variation of heat-transfer capability with diameter of inner tube at selected porosities.

Figs. 4.36 and 4.37 show the effect of the diameter of the inner tube on the overall heat exchanger thermal performance for air velocity of 10 m/s on both sides. It can be seen that the heat-transfer capacity of the metal-foam heat exchanger examined reached maximum at R=0.65 which represents a foam area ratio close to 1.0. It can also be seen that the heat transfer performance of a plain tube heat exchanger is much lower than that of a foam filled heat exchanger and for a foam heat exchanger increasing the pore density leads to an increase in heat transfer performance. Increasing the porosity causes a reduction in heat transfer performance (Fig. 4.37).

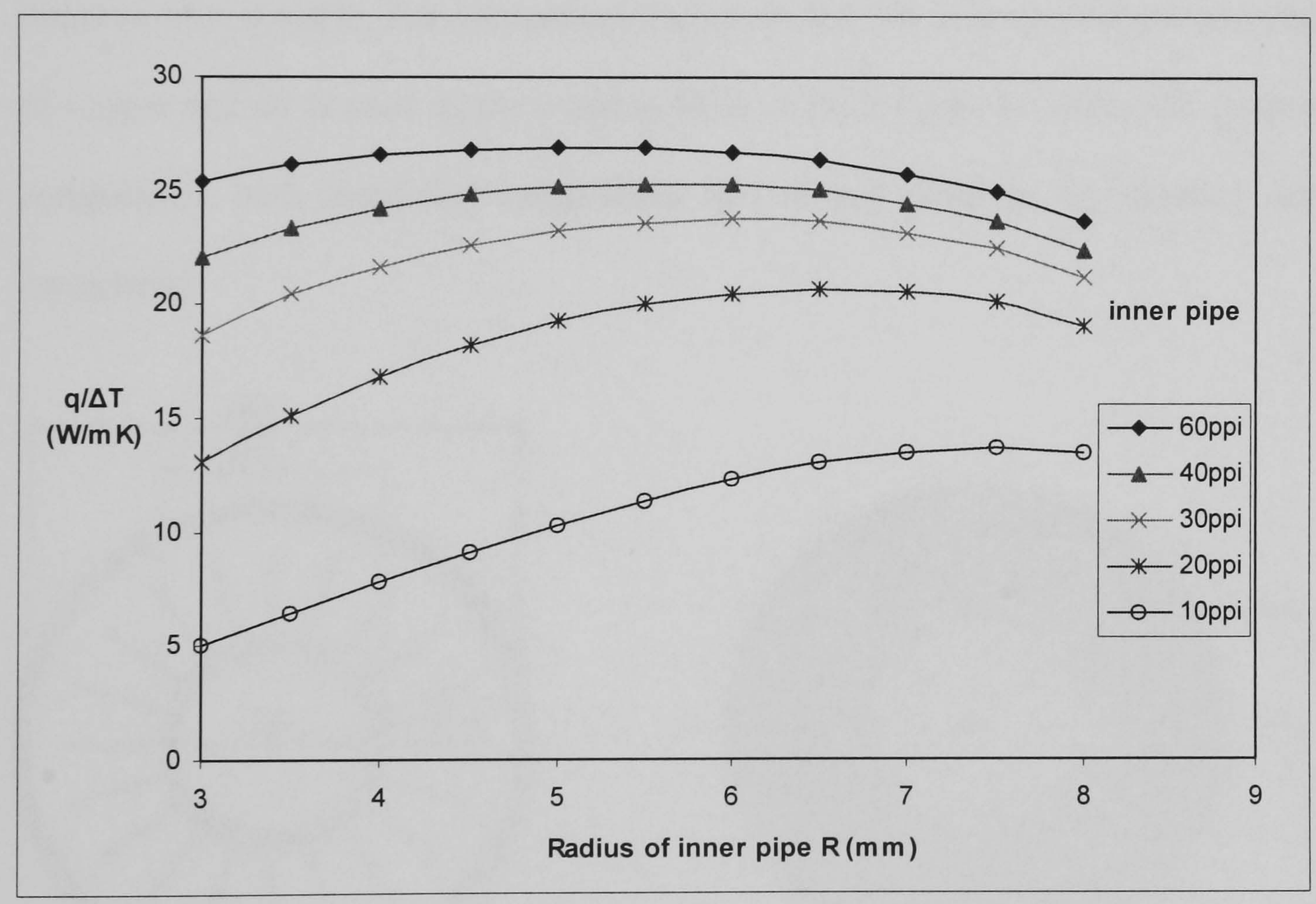

Fig. 4.38 Variation of heat-transfer capability with diameter of inner tube for 20ppi metal foams filled outer channel.

Fig. 4.38 shows the influence of the pore density on the optimal inner tube diameter for maximum heat transfer. It can be seen that, with the pore density of the outer tube constant at 20 ppi, increasing the inner tube pore density from 10 ppi to 60 ppi, reduces the optimum inner tube radius from R=7.5 mm to R=5 mm. It can therefore

be concluded that the optimum inner tube diameter or flow cross sectional area ratio varies with the relative pore densities of the metal foams filled on both sides of heat exchanger.

4.3.5 Comparison with conventional finned tube heat exchangers

Fig. 4.39 shows the configuration of a conventional finned tube heat exchanger (a) and a metal-foam tube-in-tube heat exchanger (b). For the conventional heat exchanger an inner grooved tube is assumed with fins on its external surface to improve heat transfer. For comparison purposes the two heat exchangers are made of copper and air is used as the working fluid on both sides. To widen the range of comparison, both spiral and longitudinal fins of and different fin densities were considered.

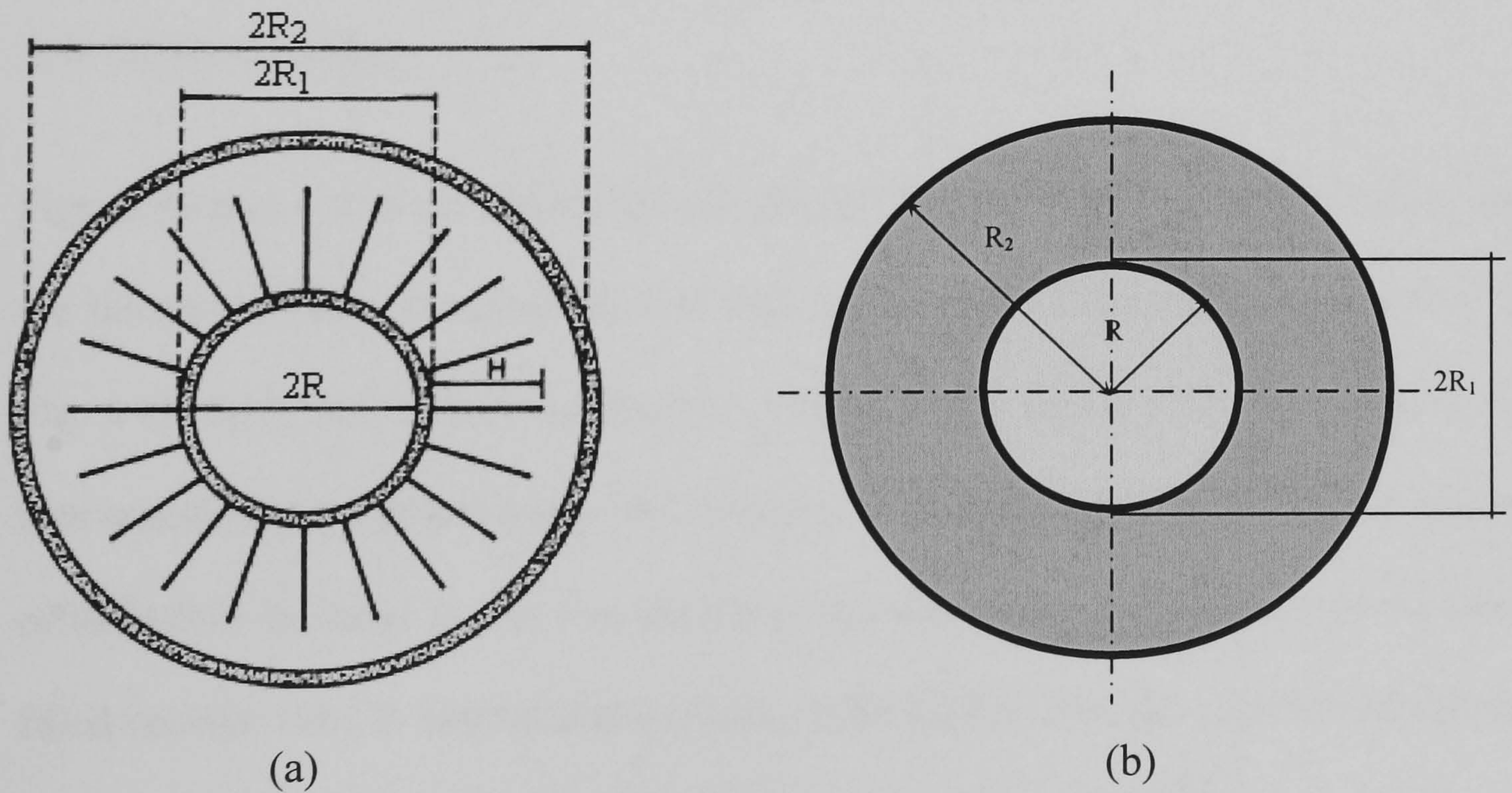

(a) (b)

Fig. 4.39 Geometry of conventional finned tube heat exchanger (R=6mm, R_1=6.5mm, R_2=10mm). (a) the heat exchanger with inner grooved tube (spiral grooves: s=0.1mm, H=1mm) and fins (longitudinal fins: 20fins, H=2.5mm, t=0.075mm), (b) metal foam filled heat exchanger.

To calculate the heat transfer rate of the conventional compact heat exchanger, the following empirical correlations were employed.

For smooth tubes (Holman, 1992):

$$h_i = \frac{k}{d_i} 0.023 \,\mathrm{Re}_d^{\,0.8} \,\mathrm{Pr}^{0.3} \tag{4.42}$$

For spiral groove tubes (Wang et al., 2005):

$$h_i = \frac{k}{d_i} 0.363 \,\mathrm{Re}_d^{\,0.6} \,\mathrm{Pr}^{0.3} (H/d_i)^{0.103} (S/d_i)^{-0.29} \tag{4.43}$$

The fin efficiency is determined from (Holman, 1992):

$$\eta = \frac{\tanh(mH)}{mH} = \frac{\tanh(\sqrt{2h_o/(kt)}H)}{\sqrt{2h_o/(kt)}} \tag{4.44}$$

Where H is the depth of the fins or grooves, S is the pitch of the spiral grooves and, t, is the fin thickness.

Figs. 4.40 and 4.41 show comparisons between the metal-foam annular channel and the finned channels. Longitudinal fins were assumed for Fig.4.40, and spiral fins for Fig. 4.41. Both charts show that the use of metal foams can significantly improve the heat transfer performance due to the enlarged surface area density and strong mixing of fluid flow in metal foams. For the same area density the performance of the foam filled annular tube is approximately three times higher than the performance of the longitudinally finned tube. Using spiral instead of longitudinal fins improves the performance of the conventional heat exchanger (Fig.4.41) but this is still much inferior to the performance of the metal-foam annular channel.

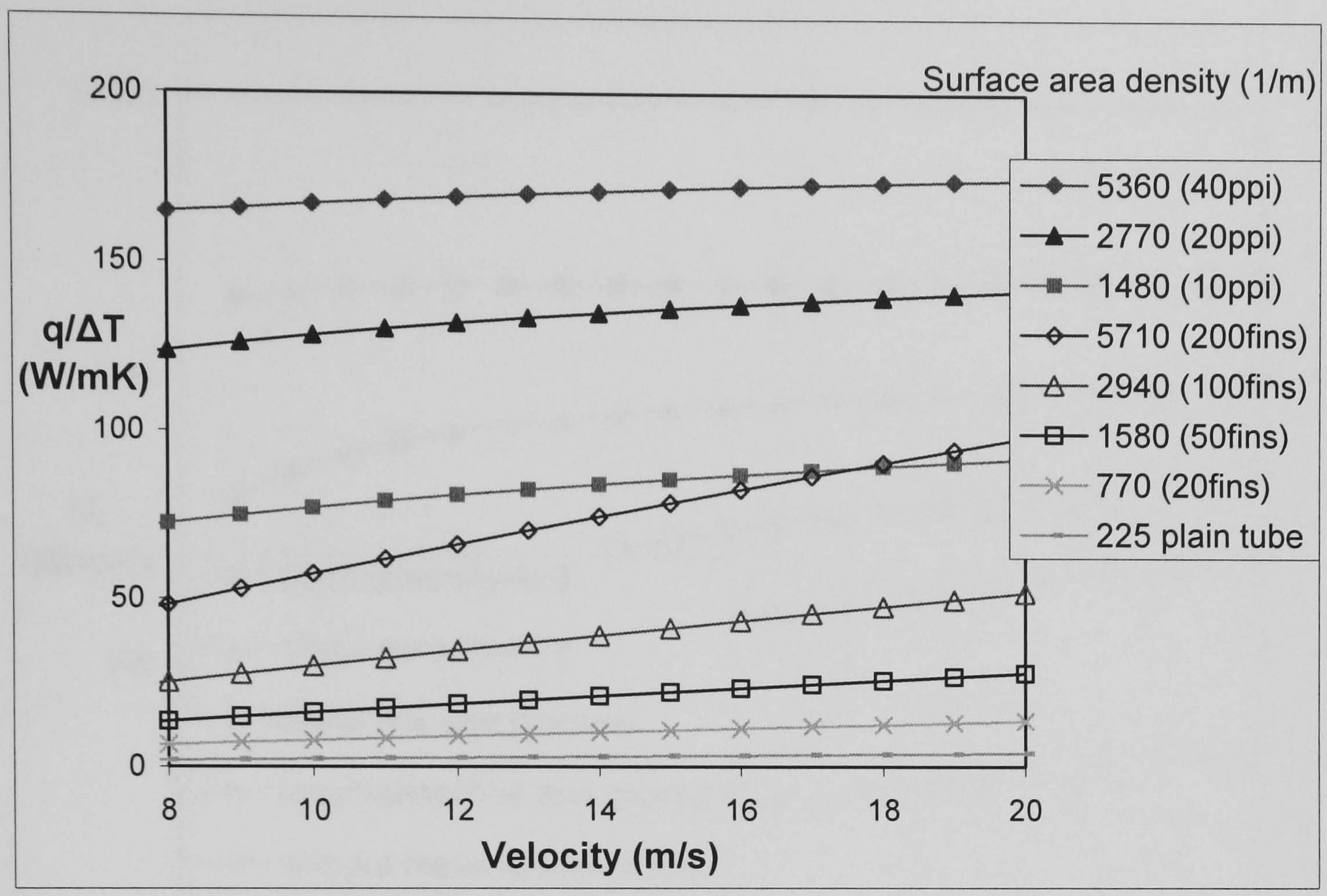

Fig. 4.40 The effect of velocity on heat transfer performance: metal foams (ε =0.9) versus longitudinal fins (fin depth=2.5mm).

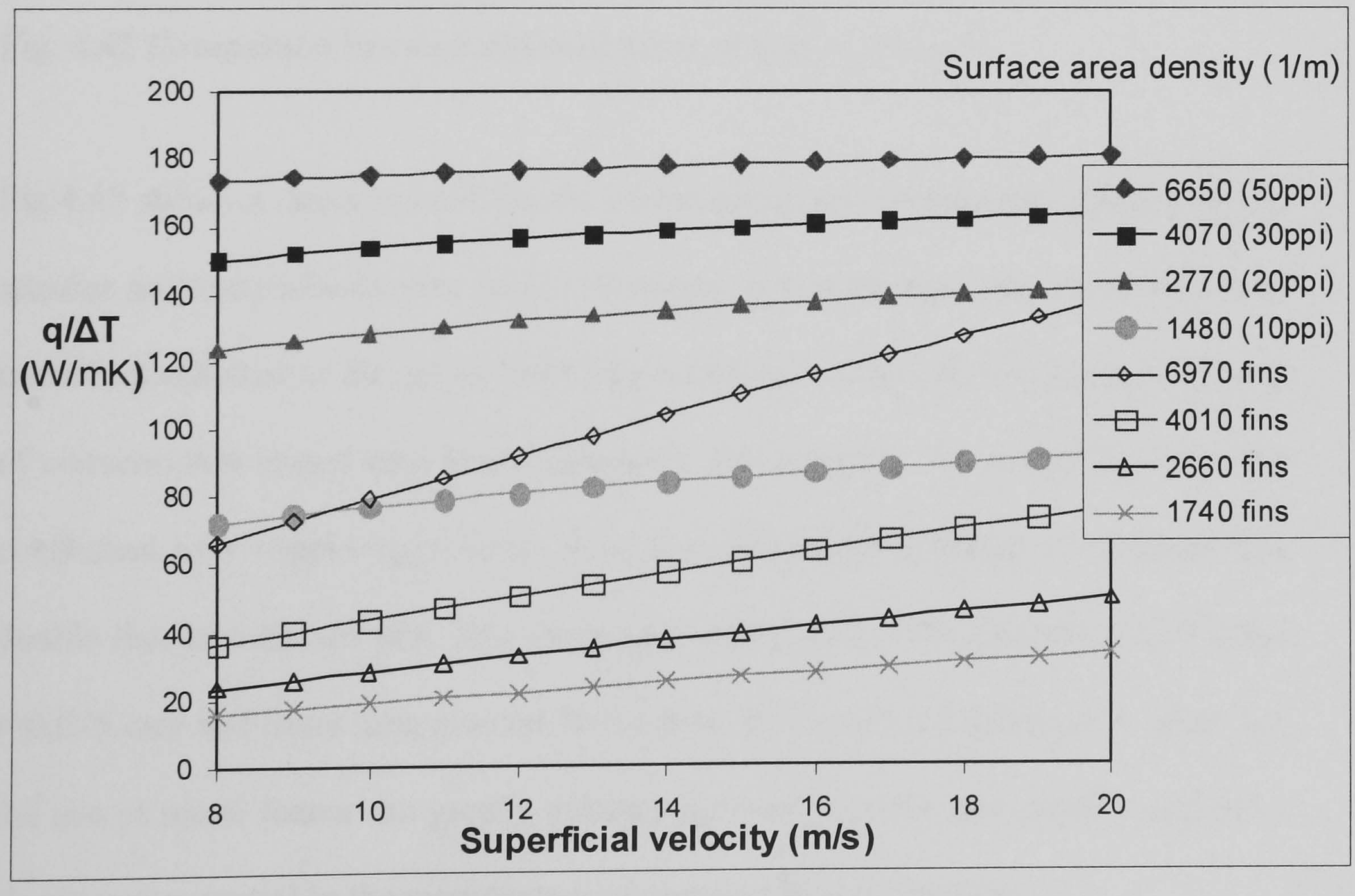

Fig. 4.41 The effect of velocity on heat transfer performance: metal foams (ε=0.9) versus spiral fins.

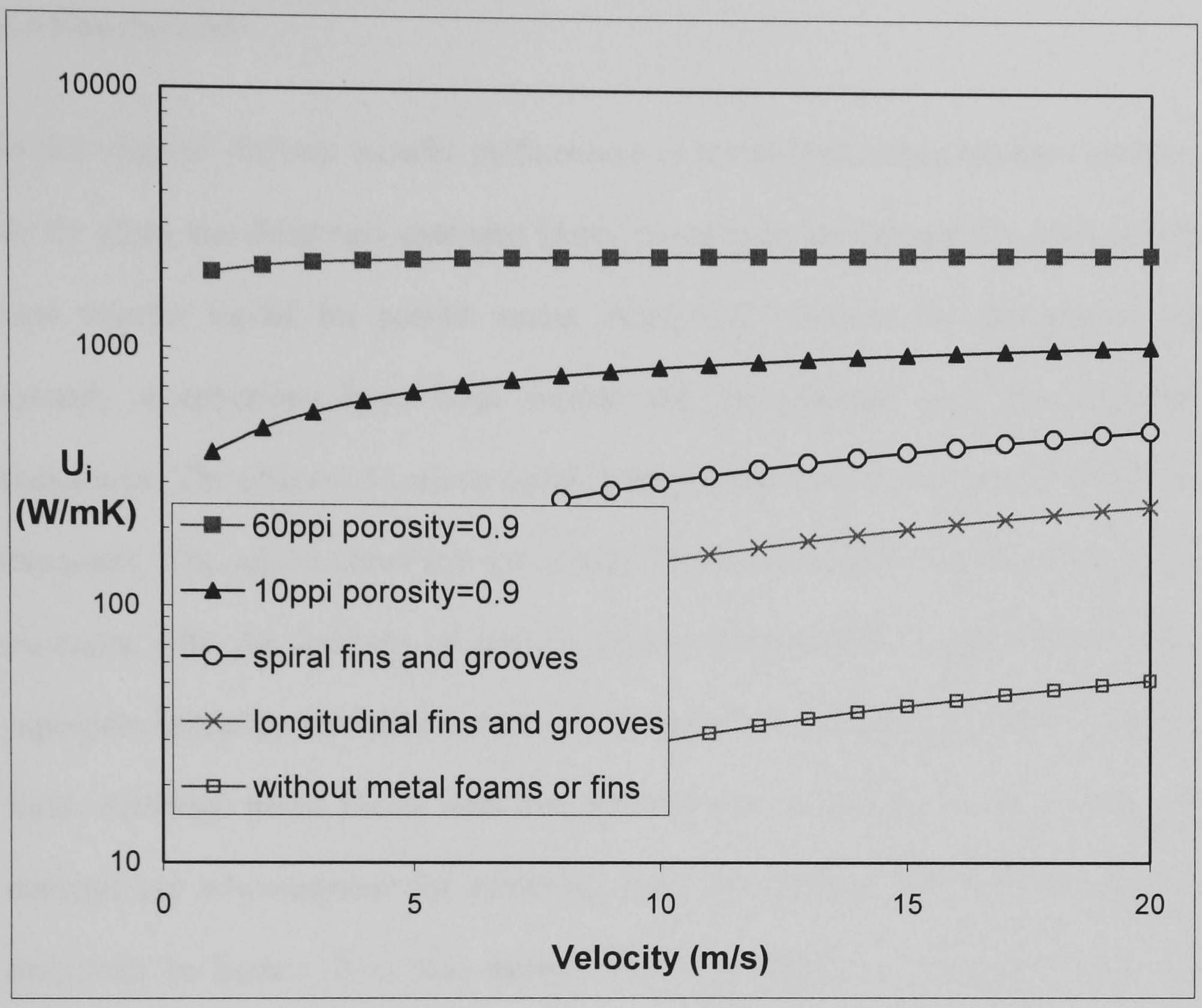

Fig. 4.42 Comparison between different kinds of heat exchangers

Fig.4.42 shows a comparison between conventional and metal-foam (both core and annular sections) tube-in-tube heat exchangers. It can be seen that the overall heat transfer coefficient of the metal-foam heat exchanger is significantly higher than that of conventional finned tube heat exchangers. For example, the overall heat transfer coefficient of a 10ppi copper-foam filled heat exchanger is shown to be more than double that of a finned tube heat exchanger (spiral fins 5000 fins/meter, H=1 mm, t=0.075 mm and inner tube grooves S=0.1 mm, H=1 mm). Therefore, it is clear that the use of metal foams can greatly enhance the heat transfer, and metal foams have significant potential in the manufacture of compact heat exchangers.

4.4 Conclusions

In this chapter, the heat transfer performance of metal-foam tubes has been analyzed firstly using the Brinkman-extended Darcy momentum model and the two-equation heat transfer model for porous media. Analytical solutions for temperature and velocity distributions have been carried out for constant heat flux boundary conditions. The effects of various metal foam parameters on heat transfer have been examined. The results show that the overall Nusselt number of the metal-foam tube increases with the increase of relative density (1-porosity) or pore density (ppi), especially when the thermal conductivity of the solid is much higher than that of the fluid. Although metal foams with low porosity and small pore size (i.e. high pore density) are advantageous for achieving high heat transfer performance, pressure drop will be higher. It is also shown when low thermal conductivity foams are employed (e.g. $k_f/k_s>0.001$) the effect of pore density is quite small and thus low pore density foams can be used which will also lead to lower pressure drop. Finally, compared to plain tubes, the use of metal foams can enhance heat transfer performance significantly.

Next, the numerical method, which use the Forchheimer-extended Darcy momentum model and the two-equation heat transfer model for porous media, has been employed to analyze the heat transfer performance of forced flow in metal-foam tubes. The velocity and temperature distributions have been plotted and compared with the results of analytical solutions using Brinkman-extended Darcy model. The comparison between the two methods shows only the predictions by numerical method have good agreement with test data on pressure drop, but the overall heat transfer performances predicted by both methods are similar when Reynolds number

is less than 20000 due to the similar velocity distribution they predicted. The results also reveal that the contact thermal resistance (attachment quality) between tube wall and metal foams has significant influence on overall heat transfer performance of metal-foam tube.

Finally, the heat transfer performance of metal-foam tube heat exchangers has also been analyzed. The analytical solutions for temperature and velocity distributions have been obtained for both the inner and outer channels of tube-in-tube heat exchangers. It is shown that the heat transfer capacity of the metal-foam tube heat exchanger increases with either the increase of pore density (ppi) or the decrease of porosity. The use of metal foams can significantly enhance the heat transfer performance of tube-in-tube heat exchangers compared to that of conventional finned tube heat exchangers due to the high surface area density and strong flow mixing. The study shows that the thermal performance of a metal-foam heat exchanger can be superior to that of conventional finned tube heat exchangers. The results also showed that the heat transfer performance of metal-foam tube-in-tube heat exchangers is a function of the ratio of the flow cross sectional area and relative pore densities of the metal foams filled on both sides of heat exchanger.

Chapter 5 Experimental Investigations on Boiling Heat Transfer

Refrigeration systems are widely used for refrigeration, air conditioning and heat pump units. There are enormous interests in improving the efficiency of refrigeration systems by making compact heat exchangers with enhanced tubes. Since metal foams have superior performance to conventional heat exchangers, they are potential materials to be used to improve the efficiency of refrigeration systems. But there is no experimental data available for two-phase flow in metal-foam tubes in the open literatures. In order to assess the overall performance of the metal-foam evaporators, the fundamental study of the two-phase flow and heat transfer in horizontal metal-foam tubes are carried out with using R134a as fluid.

The boiling mechanism in metal foams is very complicated due to the inherent complexities of flow boiling heat transfer in the porous microstructure of the foam. For channel flows, it is widely accepted that the flow boiling heat transfer is governed by two mechanisms: nucleate boiling and forced convection boiling (Qu and Mudawar, 2003). The nucleate boiling heat transfer coefficient is dependent upon heat flux, but generally is far less sensitive to mass velocity and vapour quality, while the convective boiling heat transfer coefficient is dependent on mass velocity and vapour quality, but is fairly independent of heat flux. Nucleate boiling in plain tubes is normally associated with the bubbly and slug flow patterns, and forced convection boiling is more related to the annular flow pattern. The metal foam structures not only provide more boiling sites to promote heat transfer, but can also constrain bubble growth and even break up the bubbles when the flow is obstructed by the foam ligaments with different orientation angles. This tends to homogenize

the flow field and enhance heat transfer. Some distinctive and interesting boiling transport phenomena would be expected, which could lead to different boiling heat transfer characteristics from those for plain channel flows.

In this chapter, the flow boiling in metal-foam tubes has been experimentally investigated. In order to assess the overall heat transfer performance of the metal-foam evaporators, the fundamental study of the two-phase flow and heat transfer in horizontal metal-foam tubes are carried out with R134a as fluid. The effects of heat flux, mass flow rate, operating pressure and foam microstructures on boiling heat transfer and pressure drop are presented in followings.

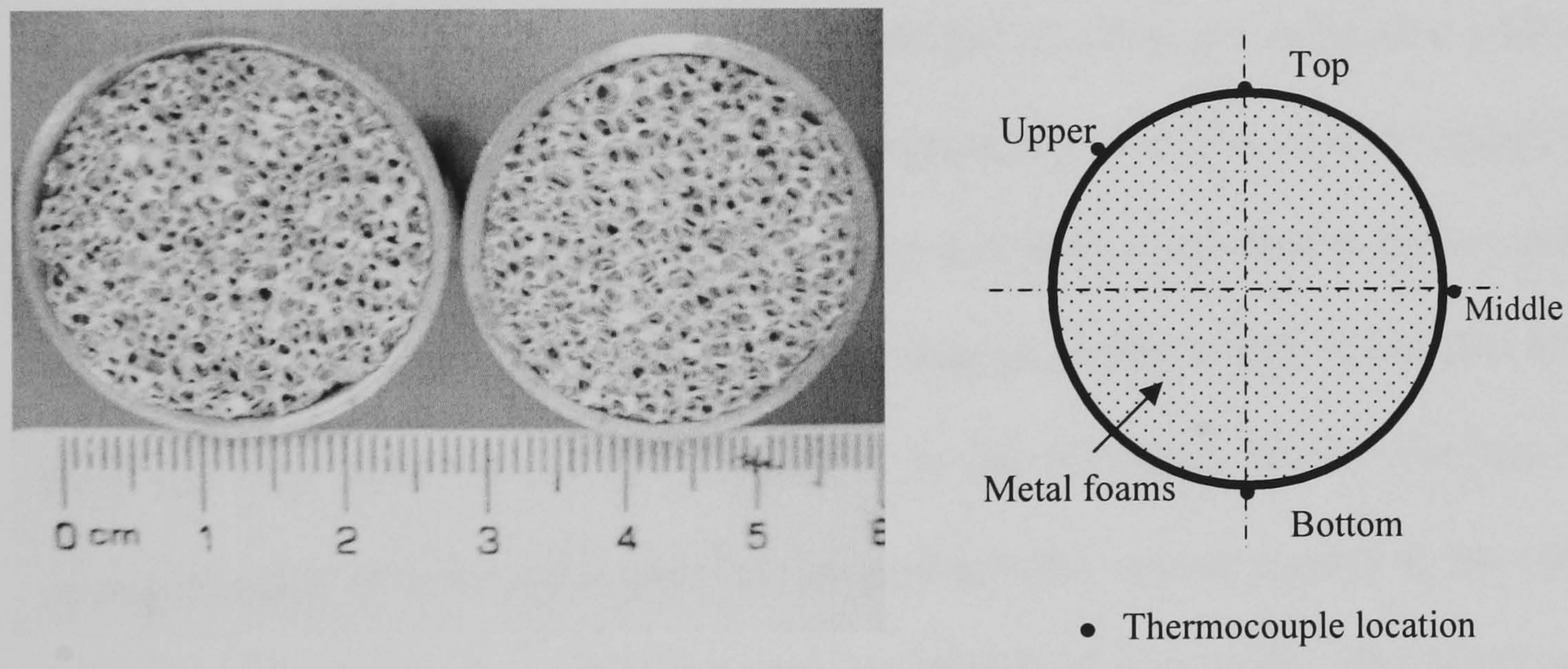

Fig. 5.1 Test section

5.1 Test conditions

In this research, the overall heat transfer coefficients and pressure drop of flow boiling inside horizontal metal-foam tubes (provided by Porvair and also used for vapour flow tests) were measured mainly at 3.5bar varying the mass flux within the range of 25-160 kg/m^{2}s when the system keeps steady state. The cross-section of test

tube with thermocouple locations is shown in Fig. 5.1, the details of thermocouples locations can also be found in Fig.2.3. As described in previous chapter, the tested copper foam filled tubes are 150 mm long with the inner diameter of 26 mm. The details of the test tubes, which also be used for forced convection, can be found in Table 2.2. These tubes have been instrumented with 12 thin foil T-type (copper-constantan) thermocouples (exposed measure junctions) which have been attached on three outer wall-surface locations along the flow direction to monitor the temperature variation along the tubes. At each location, 3 thermocouples are placed on the circumference of the tube at 90^{o} from each other and the other one is attached on the upper side of the tube. Due to the short tubes, the pressure drop have been considered as linear along the tube length, and so to the saturated temperature, i.e. the saturated temperatures at the cross-sections of thermocouple locations are calculated with the measured inlet and outlet temperature and the geometry sizes. For each test point, the pressure of averaged inlet and outlet pressures has been controlled at the set point. The imposed heat flux only changes the exit vapour quality a little (Less than 0.04) from the inlet point in the test, therefore, in the following results analysis, the averaged value of inlet and outlet vapour qualities (the vapour quality at the centre cross-section of the test tube) is used as identified parameter. The inner wall temperatures along the circumference and length of the tube which are used to obtain the heat transfer coefficients are calculated from the measured outer wall temperature and heat flux. The test tubes are heated by a flexible surface heater which applies controlled and uniform heat flux on the surface of the tube. The test section has been insulated with thermal insulation material to minimize heat loss.

The uncertainties in the present experimental results were estimated by the single-sample experiment analysis described by Kline and McClintock (1953). The uncertainty for the heat transfer coefficient was mainly attributed to the variation of power input and temperature difference. The uncertainty of the heat transfer coefficient can be expressed by

$$\frac{\delta h}{h} = \sqrt{(\frac{\delta q_w}{q_w})^2 + (\frac{\delta \Delta T}{\Delta T})^2} \tag{5.1}$$

The uncertainty of power input was estimated as less than 5%, which includes the published accuracies (0.5%) of the Programmable Power Meter (Hameg HM8115-2), the estimated error brought by axial heat conduction and the geometric uncertainty of the test tubes, which was very low and estimated as less than one percent. The error in the estimation of ΔT (temperature difference between the averaged inner wall surface temperature and the fluid average temperature) was 0.5 °C, that includes the error of thermocouples (0.1 °C) calibrated with data acquisition system and the estimated error brought by the contact thermal resistance of thermocouple attachment. Therefore, the uncertainty in temperature difference was 10% based on a representative value of ΔT was 5 °C. Therefore, the uncertainty in heat transfer coefficient was less than 12%. The accuracy of pressure drop measurement was ≤±170Pa, considered the assembling effect, then the uncertainty of pressure drop was less than 2% based on a representative value of ΔP/L was 0.1 MPa/m. The experimental results are discussed in the flow sections.

5.2 Pressure drop

In this study the pressure drop has been measured by pressure transducers. For the metal foam with the microstructure of 20 ppi (pore number per inch) and 90% porosity, Fig. 5.2 shows the variation of pressure drop per unit length as a function of vapour quality for a series of mass flow rates. It can be seen that the pressure drop dramatically increases as the vapour quality rises. This can be attributed to the higher vapour velocity due to the increased mass percentage of vapour (higher vapour quality). Also the pressure drop increases with the mass flow rates, as expected. For a given porosity (90%) and a mass flow rate (106 kg/m^2s), the effect of metal-foam cell size on pressure drop is presented in Fig. 5.3.

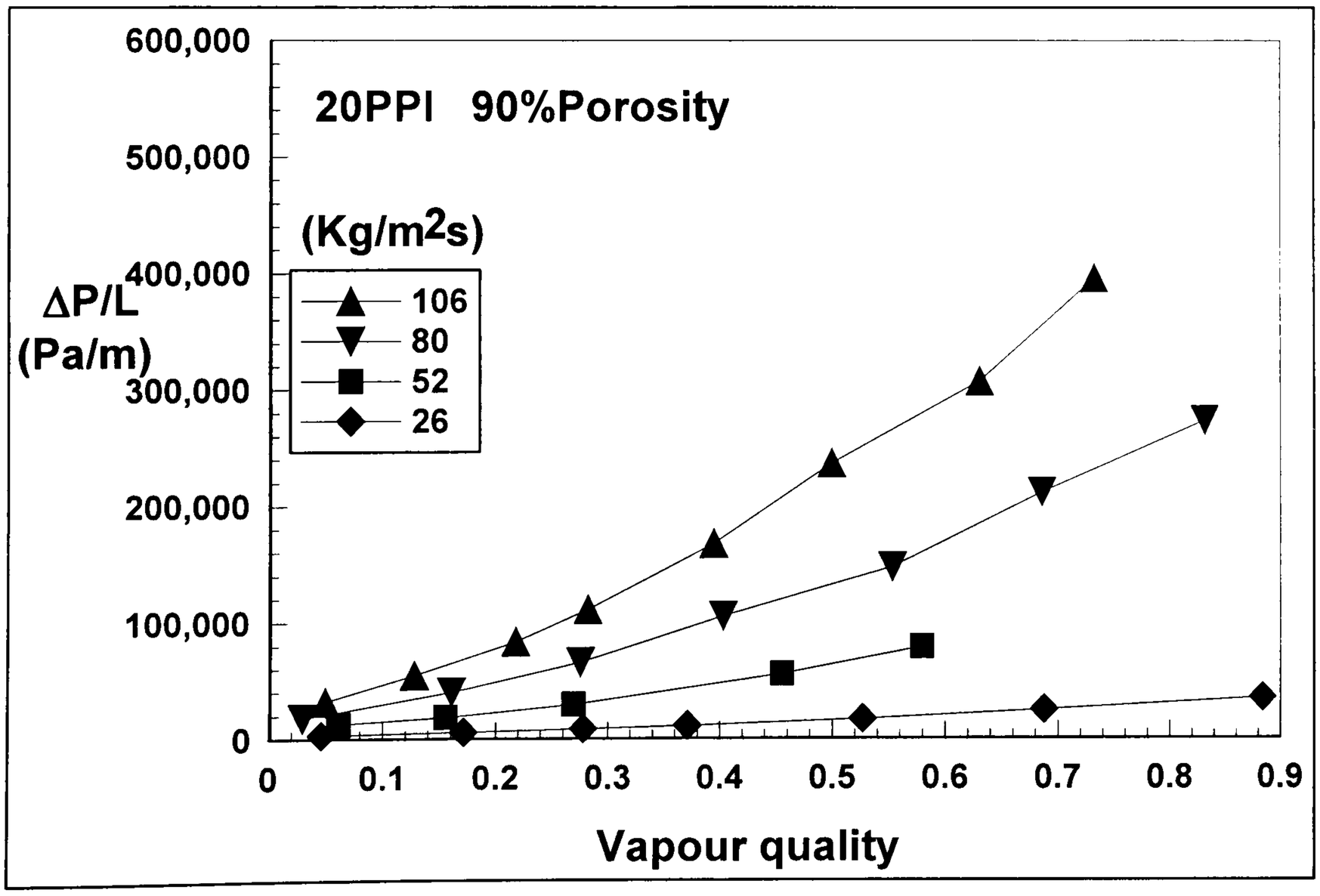

Fig. 5.2 Variation of pressure drop per unit length as a function of vapour quality

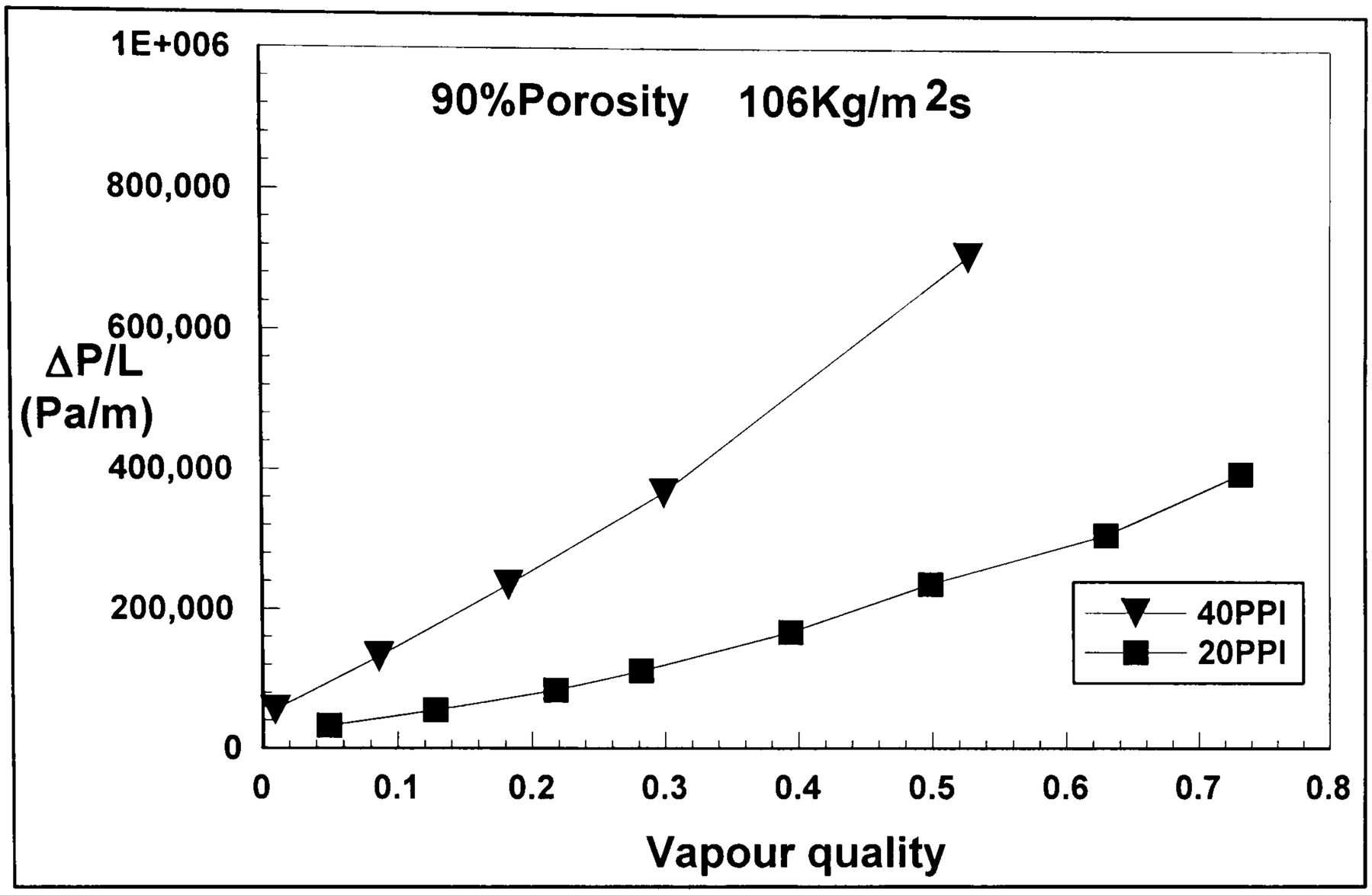

Fig. 5.3 Effect of metal-foam cell size on pressure drop

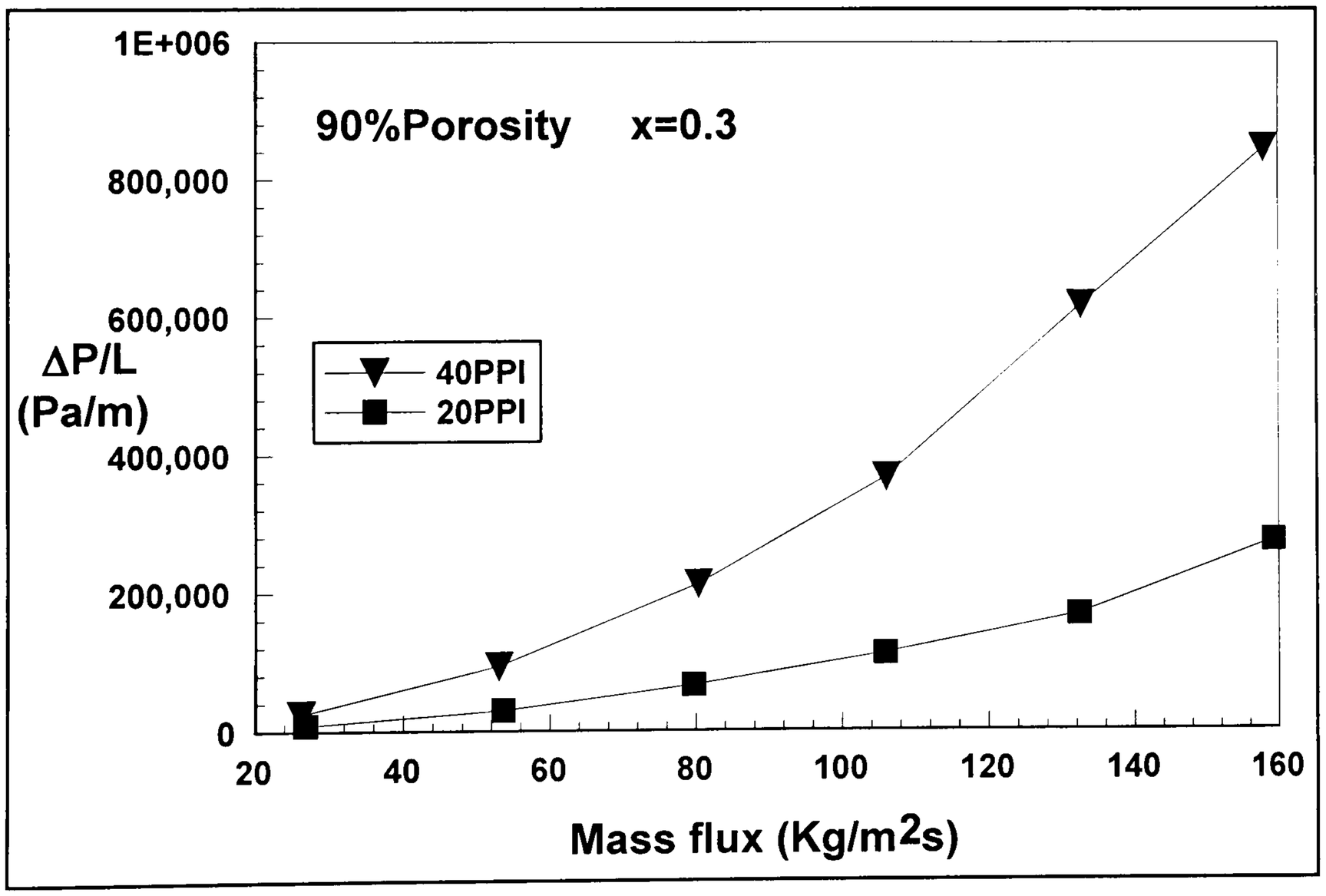

Fig. 5.4 Variation of pressure drop as a function of mass flow rate

As the cell size becomes smaller (40 ppi), the pressure drop significantly increases, and this implies that the two phase flow encounters much more flow resistance for

smaller cell size due to the presence of metal-foam structures. This result is similar to the situation for single phase flow (Calmidi el al., 2000 and Zhao et al., 2004 a). The flow resistance in the metal-foam channels mainly comprises three parts, channel surface drag resistance, Darcy viscous resistance and form resistance induced by metal-foam structures. The latter two resistances are caused by the presence of foam structures. For a given porosity (90%) and a given vapour quality (x = 0.3), the variation of pressure drop as a function of mass flow rate is shown in Fig. 5.4 for two different cell sizes. As expected, the pressure drop increases as the mass flow rate rises. Fig. 5.5 presents the effect of operating pressure on pressure drop. As the operating pressure rises, the vapour density is getting higher, and this leads to lower vapour velocity for a higher operating pressure, and thereby causing the less pressure drop.

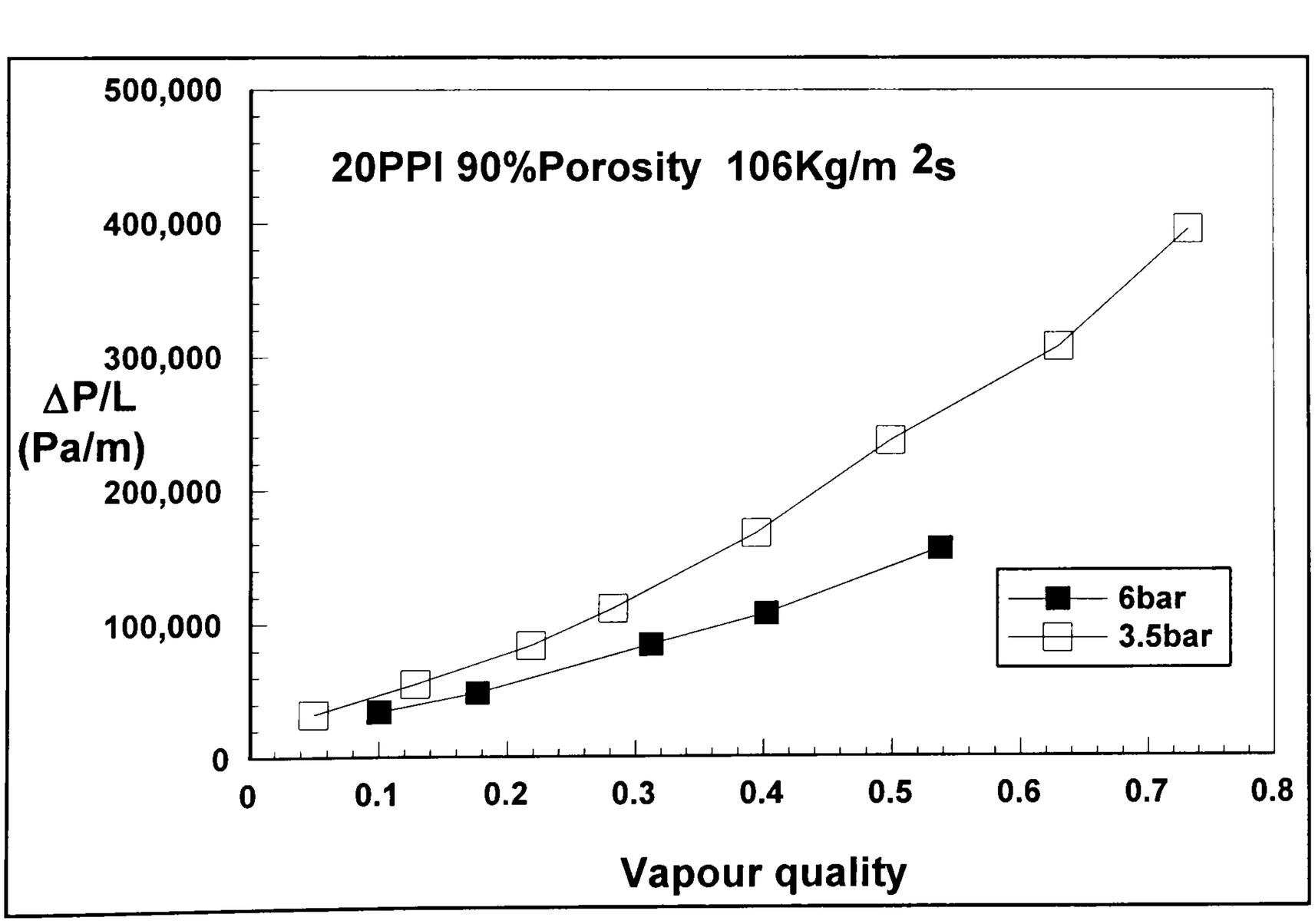

Fig. 5.5 Effect of operating pressure on pressure drop

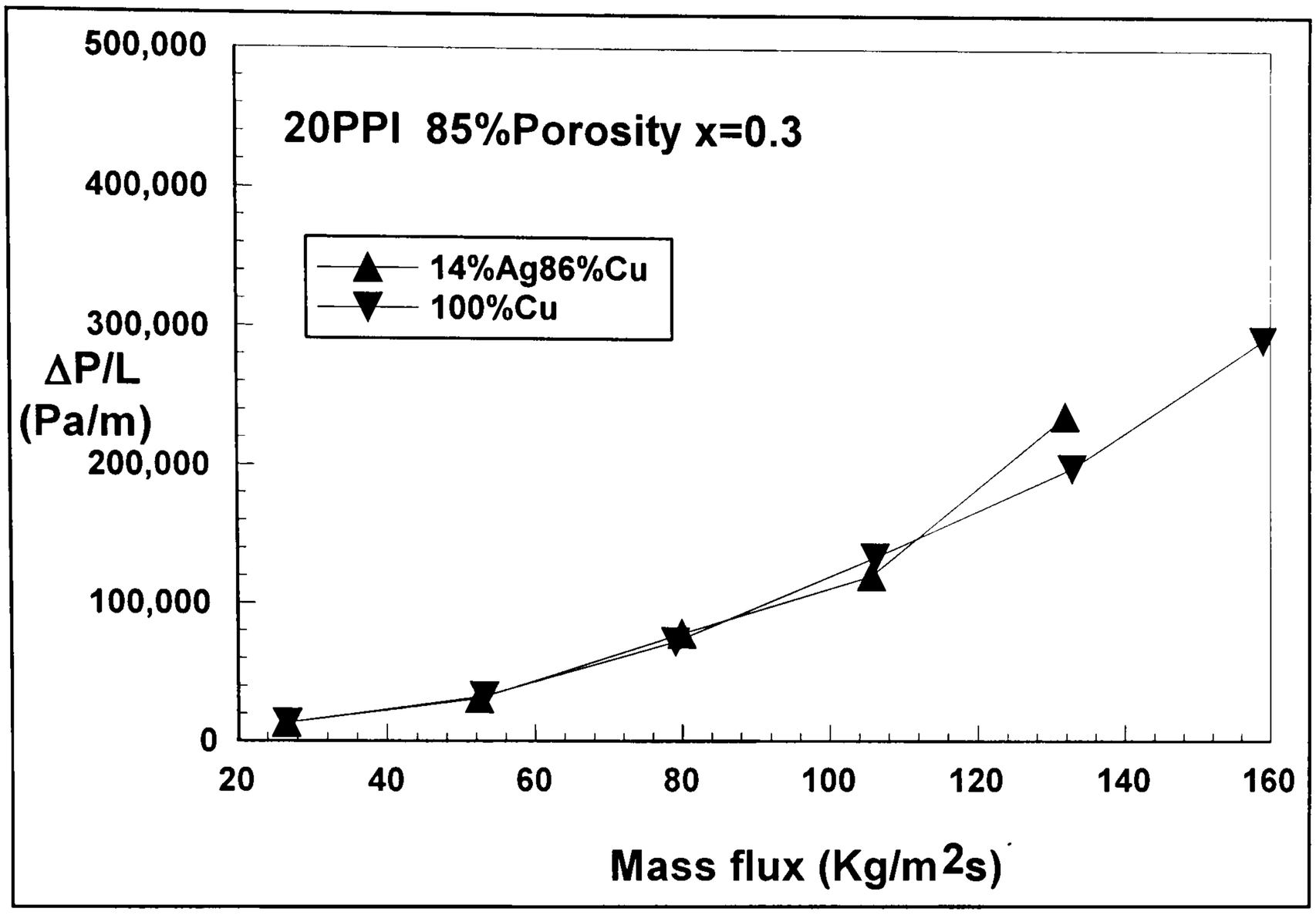

Fig. 5.6 Effect of metal foam materials on pressure drop

For Porvair metal foams used in this research, the addition of silver in foams doesn't introduce difference on pressure drop when porosity and pore size are the same, as shown in Fig. 5.6, which means that the silver addition doesn't have effect on metal-foam microstructures.

5.3 Temperature fluctuations and flow patterns in metal-foam tubes

As well known, the two phase flow exhibits different flow patterns, such as slug flow, wavy flow, annular flow, etc., under different conditions, e.g. in different mass flow rates, vapour quality, heat flux, etc. For the boiling heat transfer in plain tubes, the flow patterns can be directly visualized through optical techniques. However, for two-phase flow in metal-foam tubes studied in this research, the presence of metal foam structures blocks the direct view on the flow patterns inside. This problem can

be partially addressed by monitoring and analysing the wall temperature distributions.

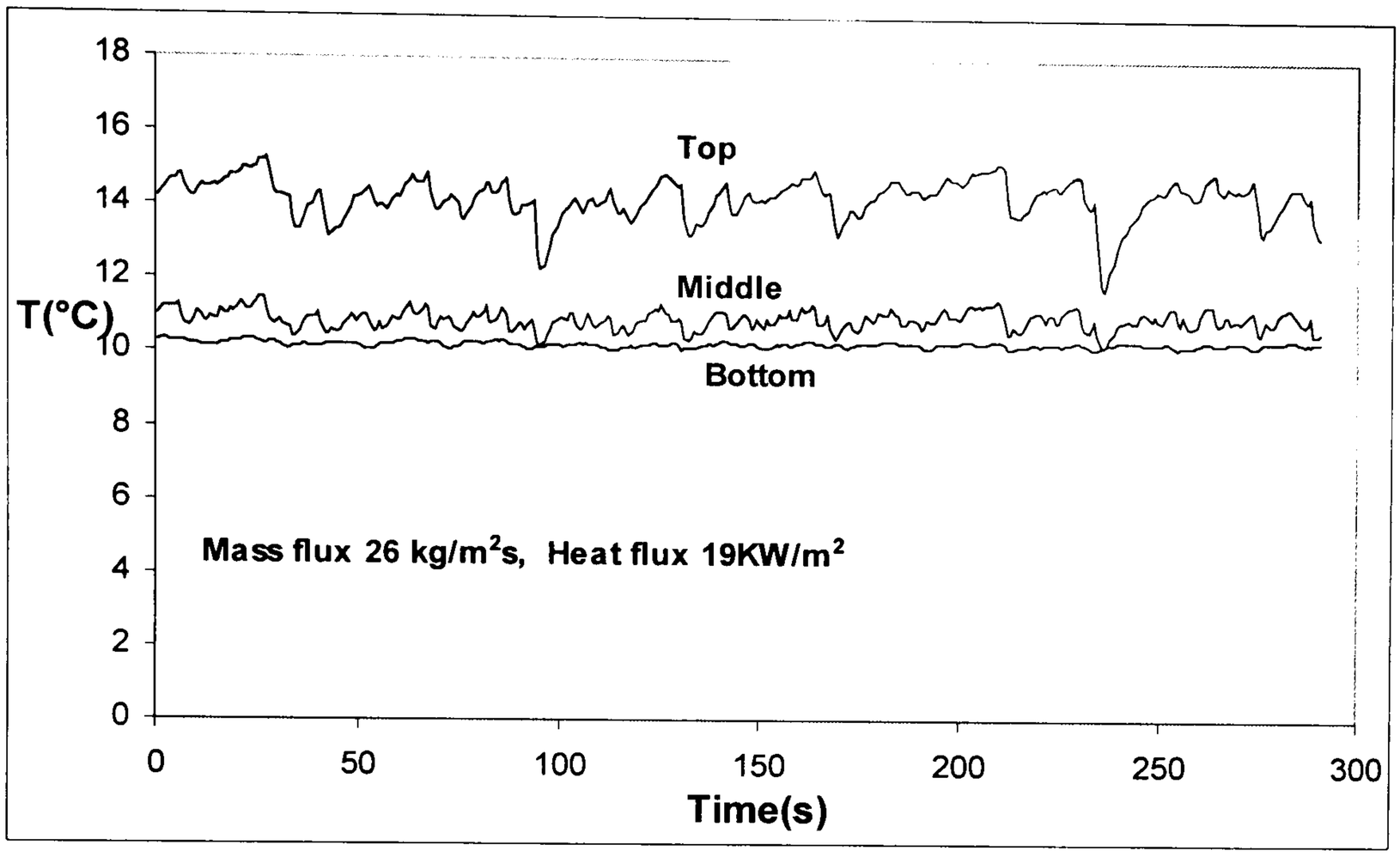

(a)

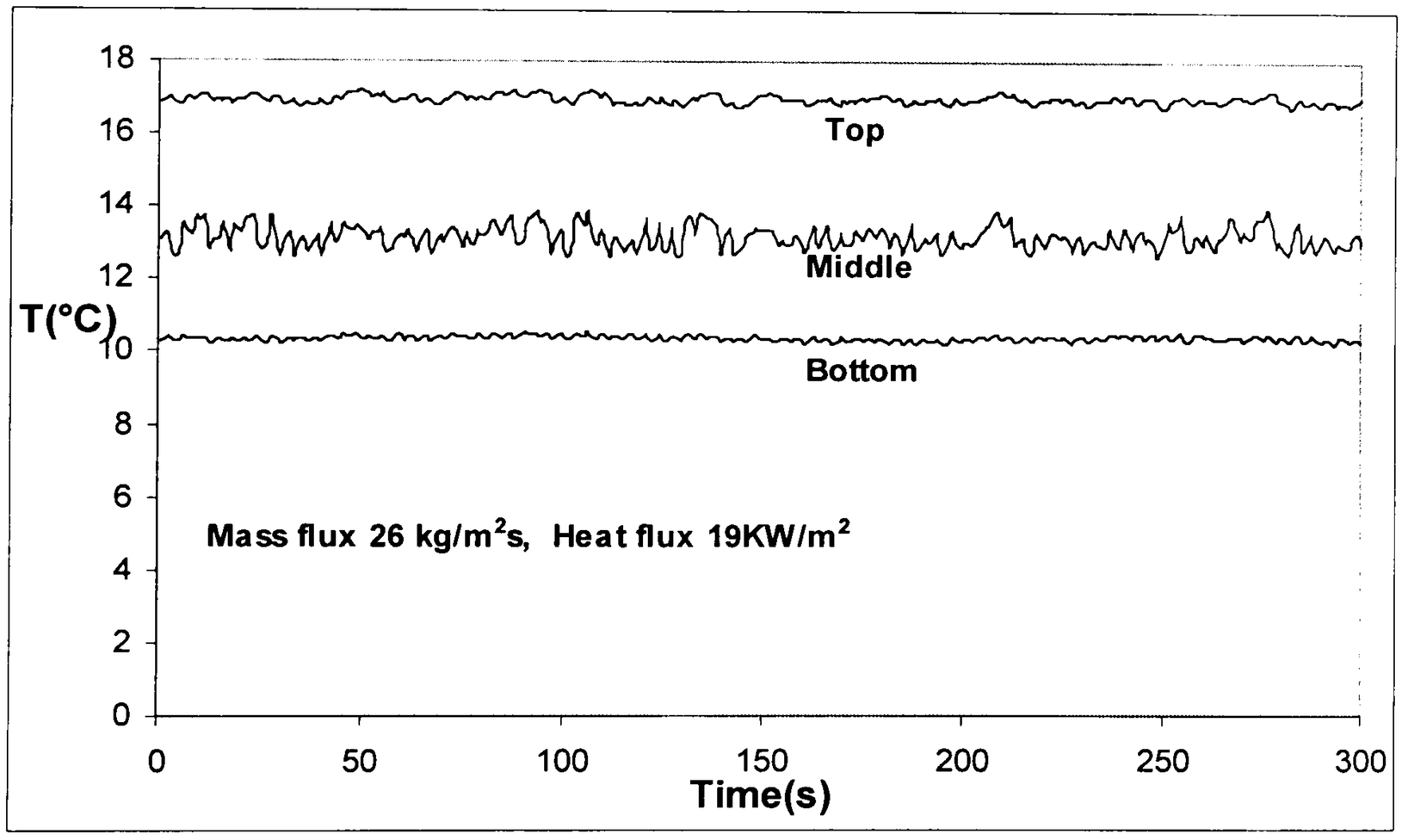

(b)

Fig. 5.7 Wall temperature's fluctuations for vapour quality at x = 0.18 (a) and x = 0.53 (b) for the low mass flow rate of 26 kg/m^{2}s

5.3.1 Wall temperature analysis

Fig. 5.7 and Fig. 5.8 present the wall temperature's fluctuations with time for different mass flow rates. In both figures and the below figures, the legend "Top,

middle and bottom" refers to the top, middle and bottom wall temperatures over the cross section, as shown in Fig. 5.1.

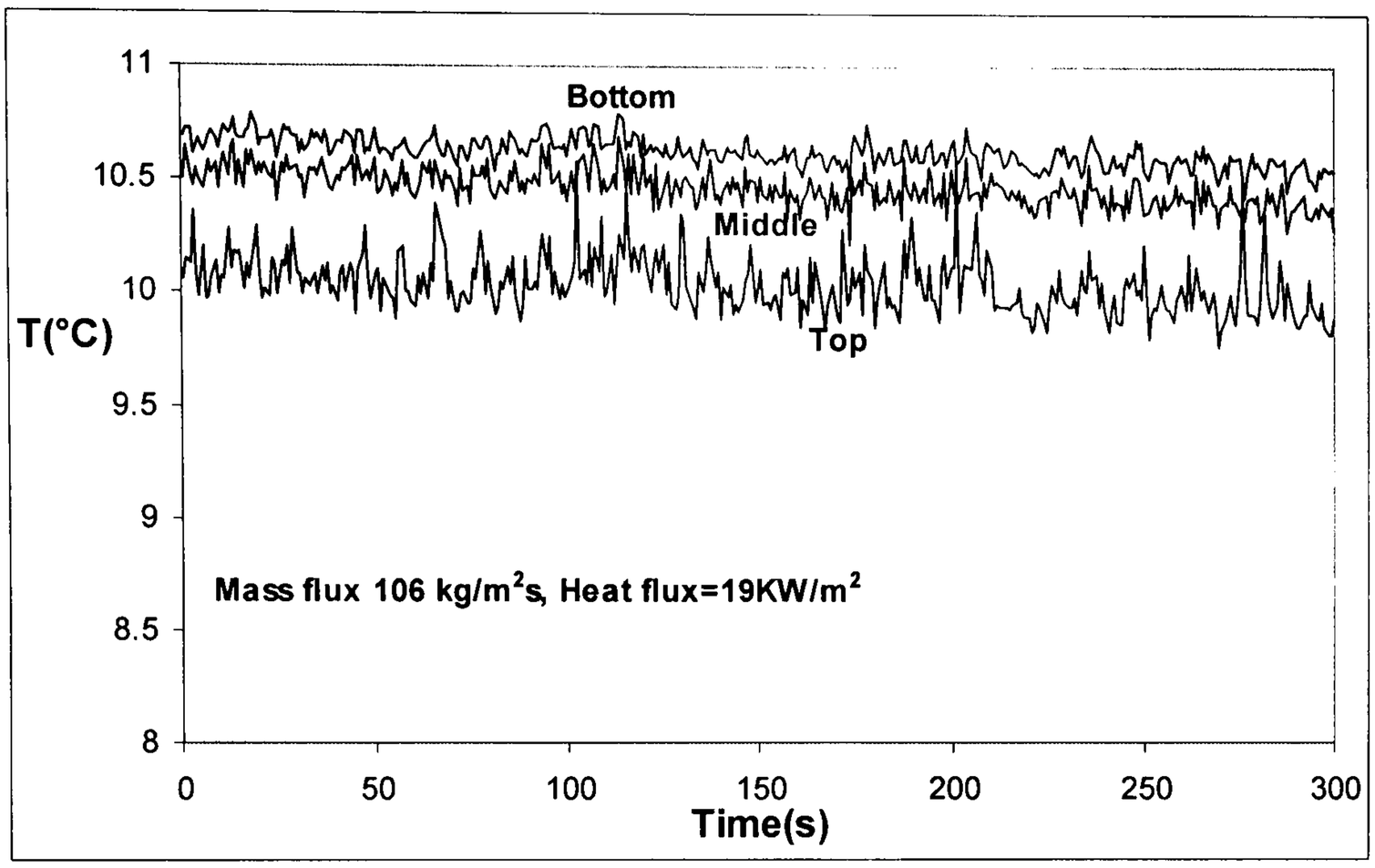

(a)

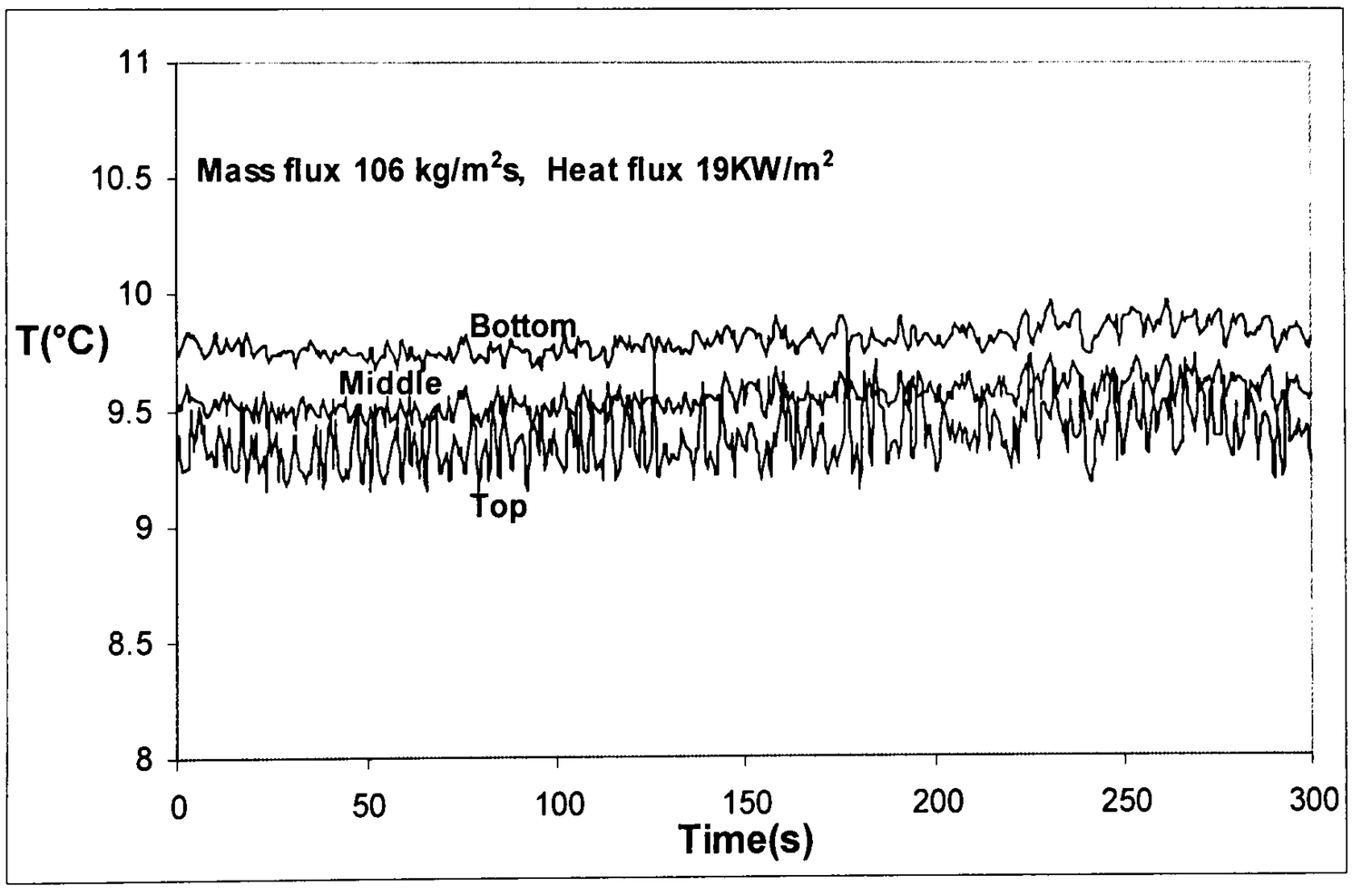

(b)

Fig. 5.8 Wall temperature's fluctuations for vapour quality at x = 0.22 (a) and x = 0.63 (b) for the high mass flow rate of 106 kg/m^{2}s

Figs. 5.7 (a) and (b) show the variation of wall temperature for vapour quality at x = 0.18 and x = 0.53, respectively, for the low mass flow rate of 26 kg/m^{2}s. Both figures reveal that the wall temperature at the bottom is pretty stable, while the temperatures

at the top and middle exhibit strong fluctuations, particularly for the case of vapour quality x = 0.18. This implies that the lower part of the tube is always filled with liquid refrigerant, but this may not be the case for upper part of the tube. The different wall temperature behaviour is determined by different two phase flow patterns. The flow pattern in Fig. 5.7 (a) can be judged as slug/wavy flow from the measured wall temperatures. The upper part of the tube is occupied by liquid or vapour intermittently, thereby causing strong temperature fluctuations. As the vapour quality increases to 0.53 from 0.18, the two-phase flow pattern gradually changes to stratified wavy flow where the upper part is occupied by vapour. Therefore the top wall temperature fluctuation diminishes, but the wall temperature at middle point shows more fluctuant. Fig. 5.8 (a) and (b) show the variation of wall temperature fluctuation for vapour quality at x = 0.22 and x = 0.63, respectively, for the high mass flow rate of 106 kg/m^{2}s. Both figures indicate that the temperature distributions are uniformly distributed, and the high velocity causes the wall temperatures to fluctuate slightly but with high frequency. This wall temperature distribution indicates that the flow pattern is more like annular flow, where the whole tube wall surface is wetted by liquid phase.

Fig. 5.9 (a) and (b) present the distribution of temperature difference between the wall surface and refrigerant for two different mass flow rates. The wall temperature exhibits large difference over the cross section for smaller mass flux, G = 26 kg/m^{2}s, particularly at high vapour quality regime, as shown in Fig. 5.9 (a). The flow pattern at this smaller mass flow rate is believed to be stratified wavy flow for the majority of the vapour flow regime. The upper part of the tube is occupied by vapour, whilst the lower part is liquid. This flow pattern determines the measured temperature

distribution over the cross section, namely, the temperature difference between tube wall and saturation temperature of upper part is higher than that of lower part of the cross section though the metal foam structure tends to homogenize the temperature distribution over the cross section.

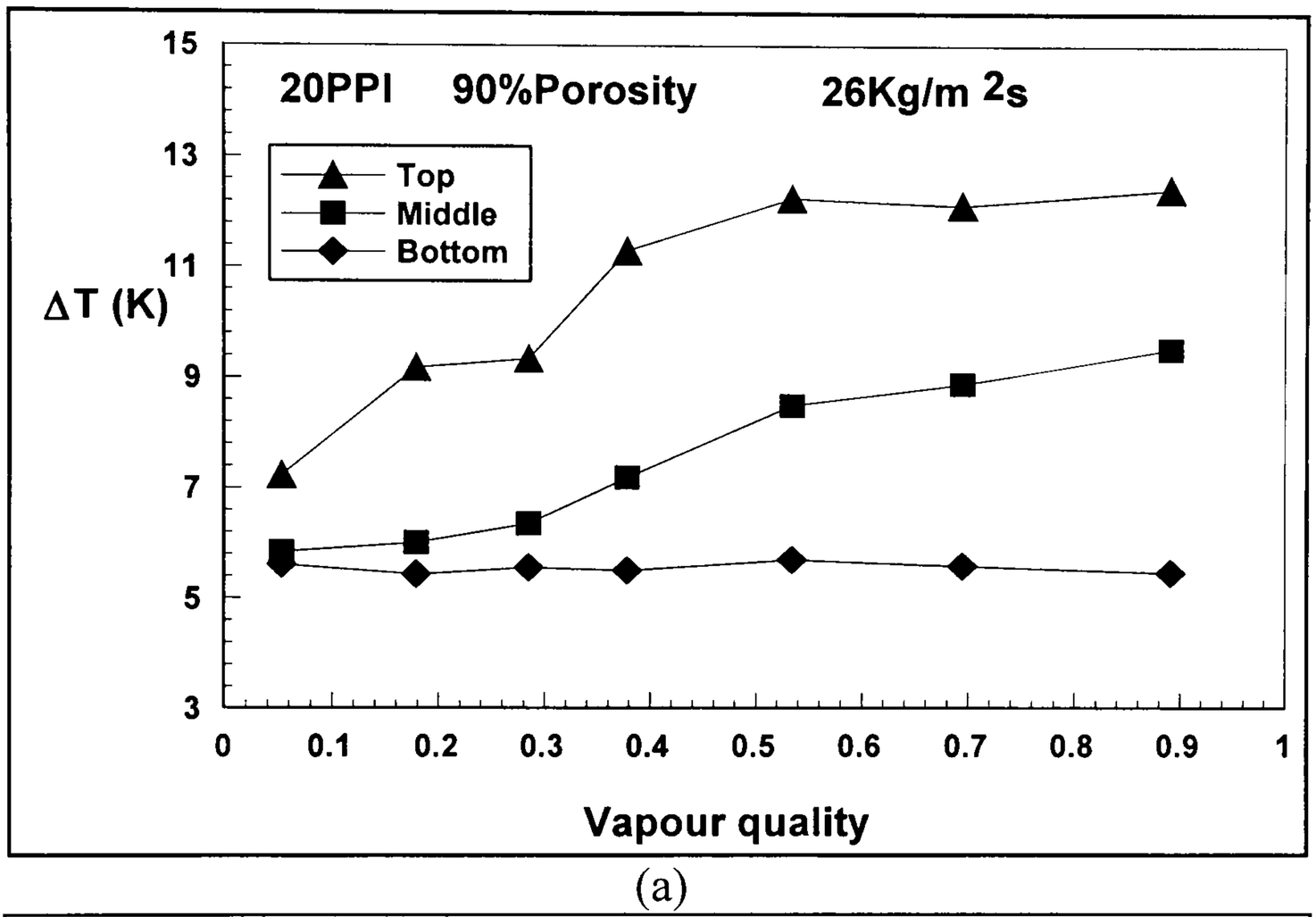

(a)

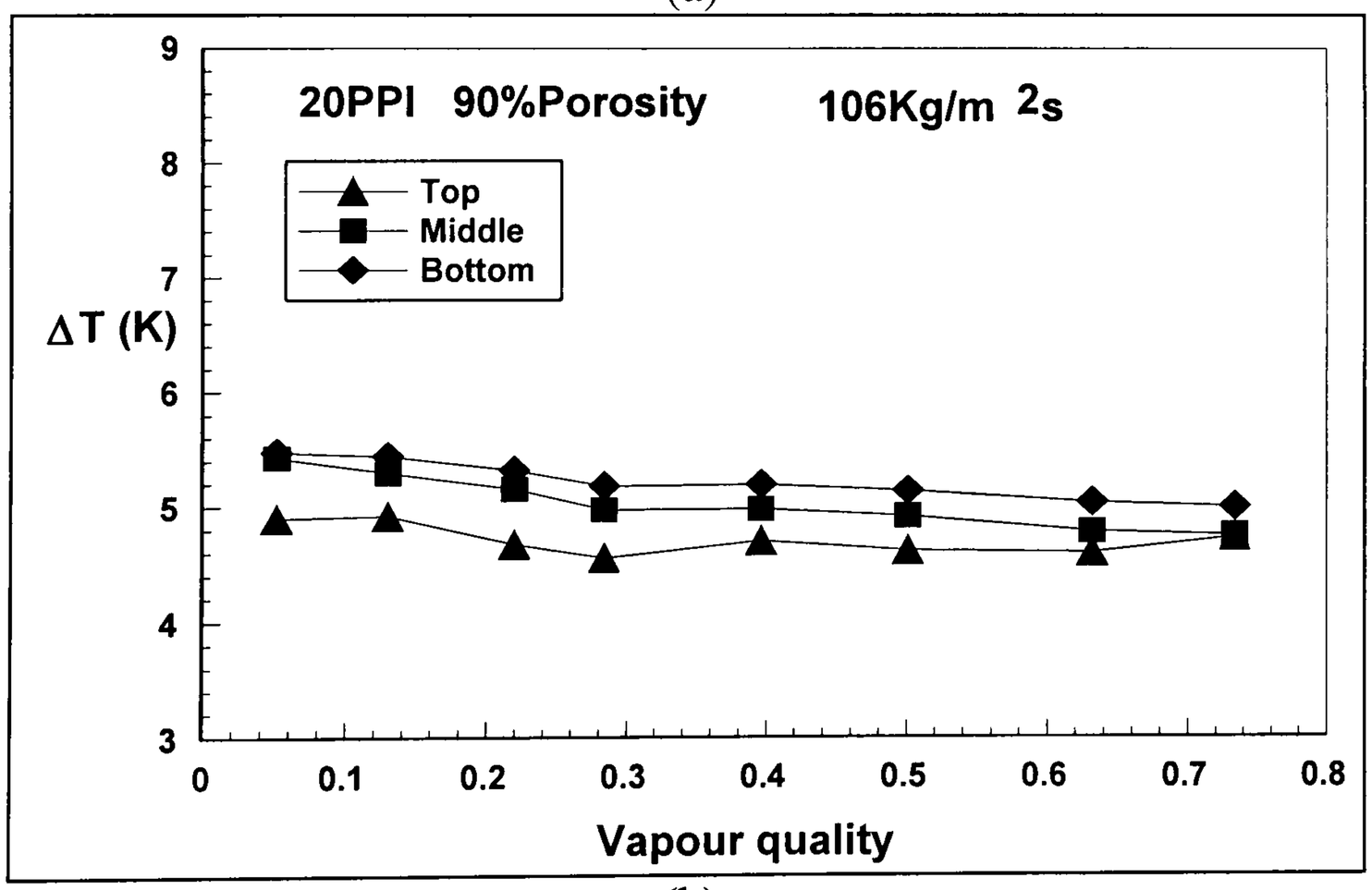

(b)

Fig. 5.9 Temperature difference between the wall surface and refrigerant for two different mass flow rates: (a) 26 kg/m^{2}s (b) 106 kg/m^{2}s

When the vapour quality is lower than 0.3, the void fraction is also relatively low, the fluctuation of wall temperate on the upper part of tube reveals the same characters of slug-wavy flow, which means the liquid can reach the upper part of tube wall intermittently, then the difference between temperature difference on the top and bottom are relatively small. With the increase of vapour quality, the vapour phase occupies more volume (almost entire volume) and more surface of tube wall, then the wet area of tube wall, which has high heat transfer coefficient thanks to boiling heat transfer, shrinks, then the heat transfer performance of upper part tube wall becomes worse and the temperature differences on the top and middle points increase.

For the larger mass flow rate of 106 kg/m^{2}s, the temperature difference over the cross section is dramatically reduced, as shown in Fig. 5.9(b). The flow pattern for this case should be more like annular flow, thus a thin liquid film adheres to the whole wall surface, and also under the help of metal foam structure the wall temperature exhibits pretty uniform distribution over the cross section. With the increase of vapour quality, the liquid film become thinner, which encourages the convection boiling heat transfer, therefore, the temperature differences at different locations drop slightly.

5.3.2 Flow pattern map for metal-foam tubes

From the above analysis, it is expected that the flow patterns in metal foam filled tube have some similar characters as those in plain tube, for example, they both show the characters of wavy flow and annular flow, although the criteria for them are somehow different. To have an overview of regime map for metal-foam tubes, the

details of more test data have been analyzed. Some of the data are presented in appendix D where more charts shows the wall temperature varying with time for different test samples in difference conditions (in term of mass flux, vapour quality, heat flux and pressure). In each chart, each line represents the wall temperature measured directly by the thermocouple attached to the test tube. The locations of thermocouples are shown in Fig. 5.1, which is at the top, 45 degree upper side, middle side and bottom of the tube. The distributions of time averaged temperature difference between the inner wall surface and fluid are also summarized in charts for each condition.

Firstly, to draw a flow pattern map for a metal-foam tube, for example, the tube with foams of 20PPI, 90% porosity and materials of 8%Ag92%Cu, the data for the tube (the charts in Appendix D1) have been analyzed. From these experimental results, it could be found that when the mass flux is as low as 26kg/m^{2}s, wall temperature distributions are very different for different vapour quality. When vapour quality is really low as x=0.05 or 0.07, the temperatures on the top and bottom surface are close to each other, but the figures reveal that the wall temperatures at the middle side and bottom are stable (although they change periodically with the control period of PID controller), while the wall temperatures at the top and upper side, which depart from that at bottom some times, exhibit strong fluctuations. This implies that the lower part of the tube is always filled with liquid refrigerant, but this may not be the case for upper part of the tube. The peak of fluctuations implies there is a big bubble or a group of bubbles attaching to the upper part of tube wall and making the wall temperature increasing. With the movements of the bubbles (i.e the gas phase is

replaced by liquid phase), the wall temperatures of upper part of tube drop close to the temperature of bottom. This strongly implies that it is slug flow.

While the vapour quality increases to 0.17 or 0.38, the wall temperatures at the bottom are still pretty stable. But values of the other wall temperatures increase with the higher vapour quality. Although they still have strong fluctuation, but they could not reach the same temperature as the bottom one and the fluctuation become weak with increase of vapour quality, especially for wall temperature on the top. This implies the slug flow is weakened with increase of vapour quality which brings more vapour occupying the upper tube and the liquid phase have less chance to wet the upper part of tube wall. This showed that the boiling flow is wavy flow with partial slug flow.

While the vapour quality increases to just over 0.49, the fluctuation of wall temperatures at top and upper points are weak, which means the slug/wavy flow has change to stratified wavy flow in this situation. The fluctuation and the value of middle side wall temperature implies the wet area of wavy flow only wet the bottom part of the tube and have little influence to middle point while the upper part of tube dries out.

With the increase of vapour quality, which means the wet area become less and less, the wall temperatures are stable. But compared with the stable low bottom wall temperature at x=0.90 with heat flux of 9 KW/m^2, the fluctuation in bottom wall temperature at x=0.89 with heat flux of 19 KW/m^2 shows the higher heat flux makes the dry-out at the bottom of tube happen in lower vapour quality.

When the mass flux increases, the fluid velocity is increased as well and then the liquid phase wets more tube wall. For example, when vapour quality is as low as 0.07, it is plug flow (the whole tube wall is wetted) when mass flux is 80 Kg/m^2s instead of slug flow (the top of the tube wall dries out periodically) when mass flux is 26 Kg/m^2s. When vapour quality increases to 0.16, the tube wall is partial wetted when mass flux is 52 Kg/m^2s but the liquid phase wets nearly the whole tube wall when mass flux increases to 80 Kg/m^2s. With the increase of vapour quality, the higher mass flux will also strengthen the stratified wavy flow. The wall temperature differences between top and bottom of test tube are reduced and the temperature at middle point departs from that at bottom at higher vapour quality, which means that the liquid phase wets more area of tube wall with increase of mass flux. While the mass flux is as high as 106Kg/m^2s, the wall temperature are close to each other, the plug flow transits to annular flow directly in which the liquid phase wets the whole tube wall at all time because the mass flow rate is high enough to strengthen the wavy flow to annular flow. However, when the vapour quality increases to 0.73, the temperature at the top point shows a little difference from the other temperatures. With reference of other charts, it indicates that the partial dry-out begins because the liquid layer of annular flow is too thin.

Based on the above analysis, the flow pattern map for the metal-foam tube is shown in Fig. 5.10. Using the same method, the test data for other tubes have been analyzed and the flow pattern map of all the test tubes can be concluded in Fig. 5.11. This chart shows the clear regimes for different flow patterns.

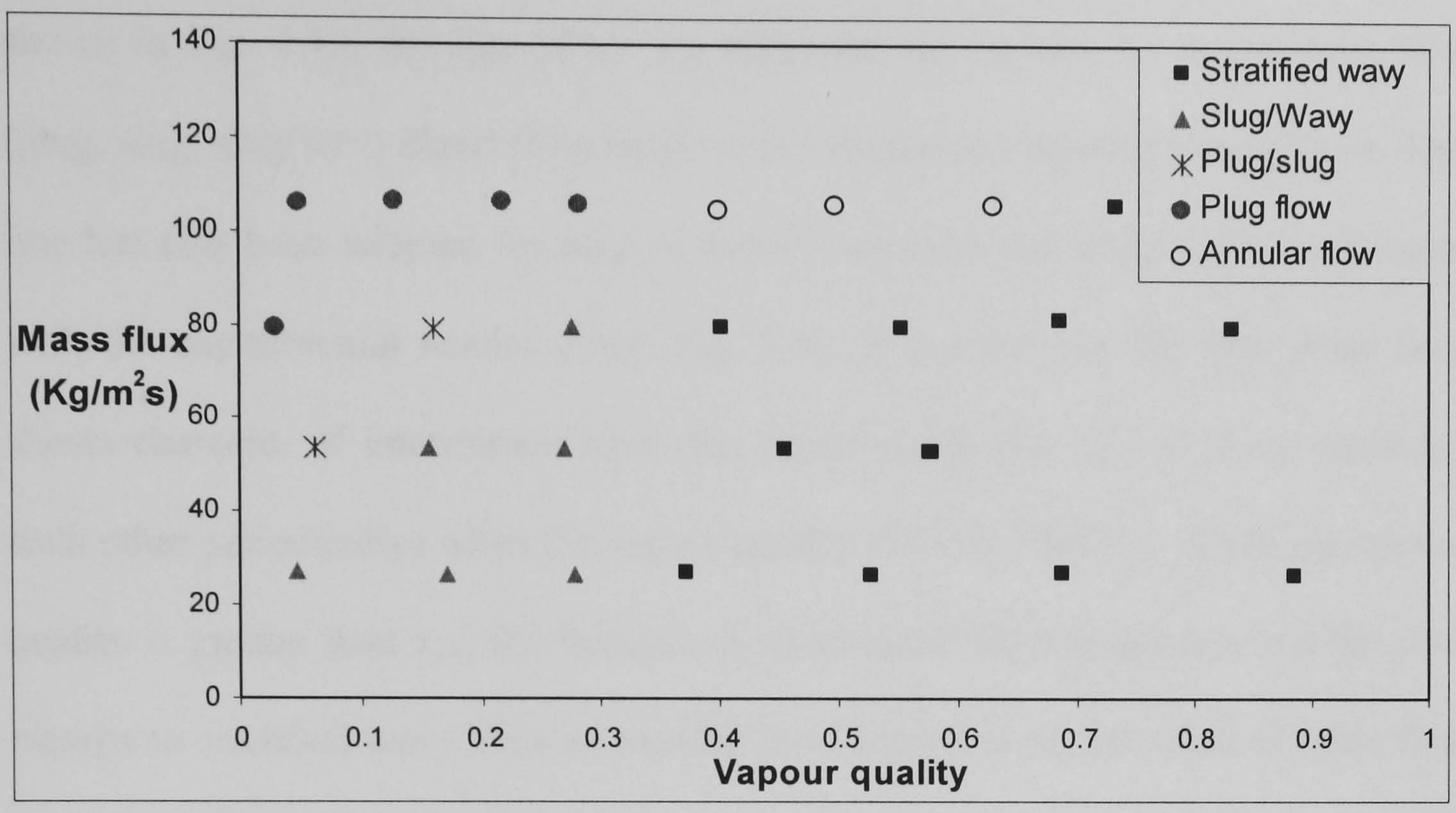

Fig. 5.10 The flow pattern map for R134a flow boiling in horizontal tube filled with 20 ppi, 90% porosity metal foams (3.5 bar, 19KW/m^2)

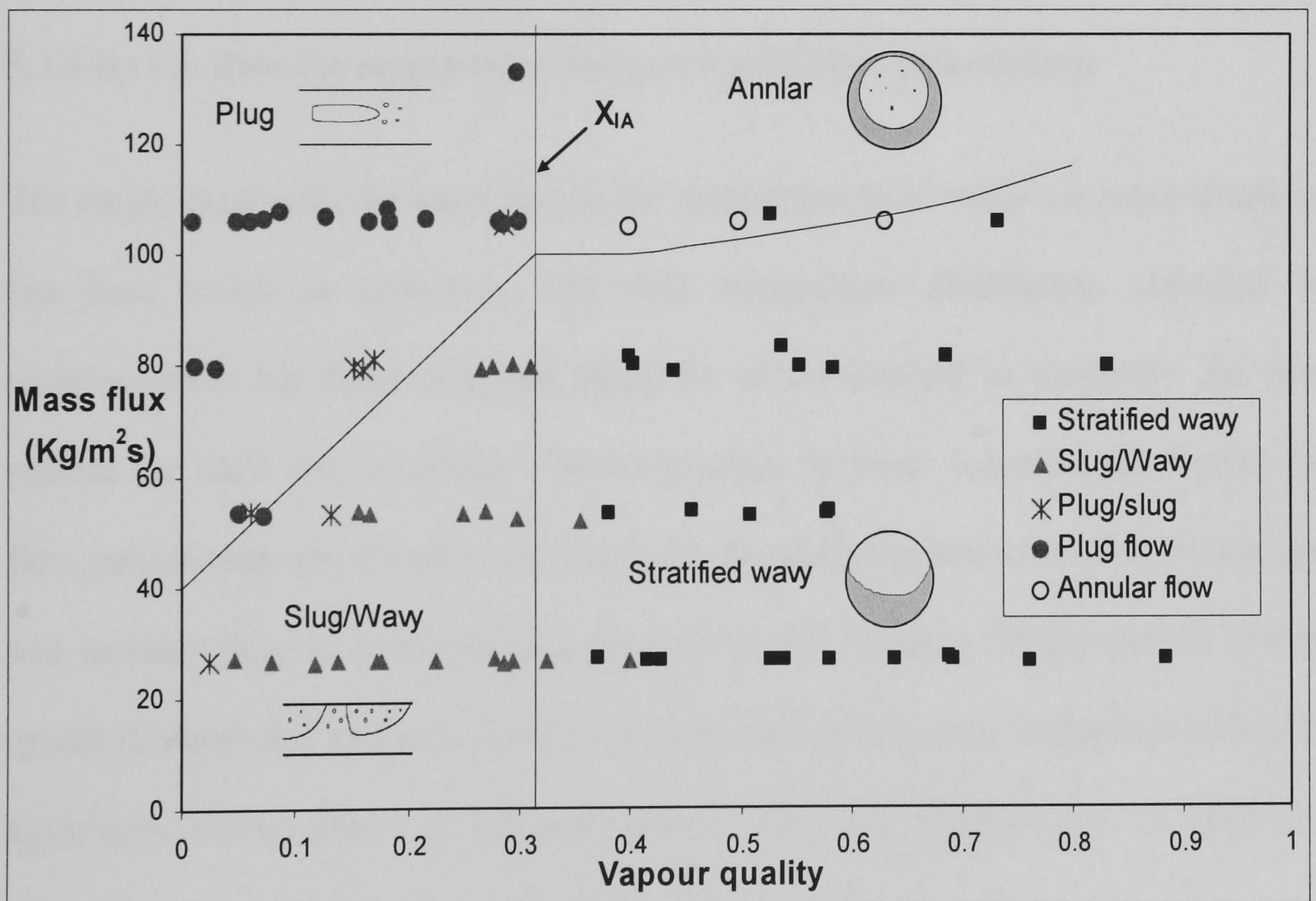

Fig. 5.11 The flow pattern map for metal-foam tubes.

In flow pattern map for plain tube, the transition from slug/wavy flows to fully stratified-wavy flows without any slugs appears approximately to occur at $x = x_{IA}$. As

shown in Fig. 1.12, the line of x= x_{IA} separates the regions for intermittent flow (plug, slug, slug/wavy flow) from those of the annular and stratified-wavy flow. This line has also been adopted for map of metal-foam tube and shows good agreement with the experimental results. From Fig. 5.11, it is clear that the two-phase flow shows character of intermittent flow (the liquid phase and vapour phase replacing each other periodically) when the vapour quality is lower than x_{IA}. When the vapour quality is greater than x_{IA}, the features of intermittent flow disappears and the flow transits to stratified wavy flow or annular flow depended on the value of mass flux. In addition, when vapour quality increases to some extent, the annular flow partially dries out and the flow pattern transits to stratified wavy flow.

5.3.3 R134a data for empty tube compared with flow pattern map

The empty tube with the same size as the metal-foam tube under the same situations has been tested as reference. The wall temperature distribution measured by thermocouples has been analyzed using the above method to determine the flow pattern for each test condition. The comparison between experimental results and flow pattern map are shown in the Fig. 5.12, in which the line to separate wavy flow and annular flow is calculated by formula of the Kattan (1998a) revised Steiner model (Steiner and Taborek, 1992,) for horizontal empty tube. Instead of adding 50 kg/m^2s by Kattan based on his experimental data, this formula use -30 kg/m^2s to adjust the inlet effect of the short test tube. The form for G_{wavy} is

$$G_{wavy} = \{\frac{16A_{vd}^3 gd\rho_l\rho_v}{x^2\pi^2(1-(2h_{ld}-1)^2)^{0.5}}[\frac{\pi^2}{25h_{ld}^2}(1-x)^{-F_1(q)}(\frac{We}{Fr})_l^{-F_2(q)}+1]\}^{0.5}-30, \quad (5.2)$$

where $F_1(q) = 646(q/q_{crit})^2 + 64.8(q/q_{crit})$ and $F_2(q) = 18.8(q/q_{crit}) + 1.023$, Weber number is We=$G^2 D/(\rho_l \sigma_l)$, and Froude number of liquid phase Fr =$G^2/(\rho_l^2 gD)$. So We/Fr =$(\rho_l gD^2)/(\sigma_l)$. In addition, q_{crit} is the critical heat flux which was introduced to make the exponents $F_1(q)$ and $F_2(q)$ non-dimensional and can be obtained from the Kutateladze (1948) correlation, $q_{crit} = 0.131\rho_v^{0.5}\Delta h_{lv}[g(\rho_l - \rho_v)\sigma_l]^{0.25}$. And the line ($x=x_{IA}$) which separated slug/wavy flow from the stratified-wavy flow and annular flow is calculated by formula 1.1.

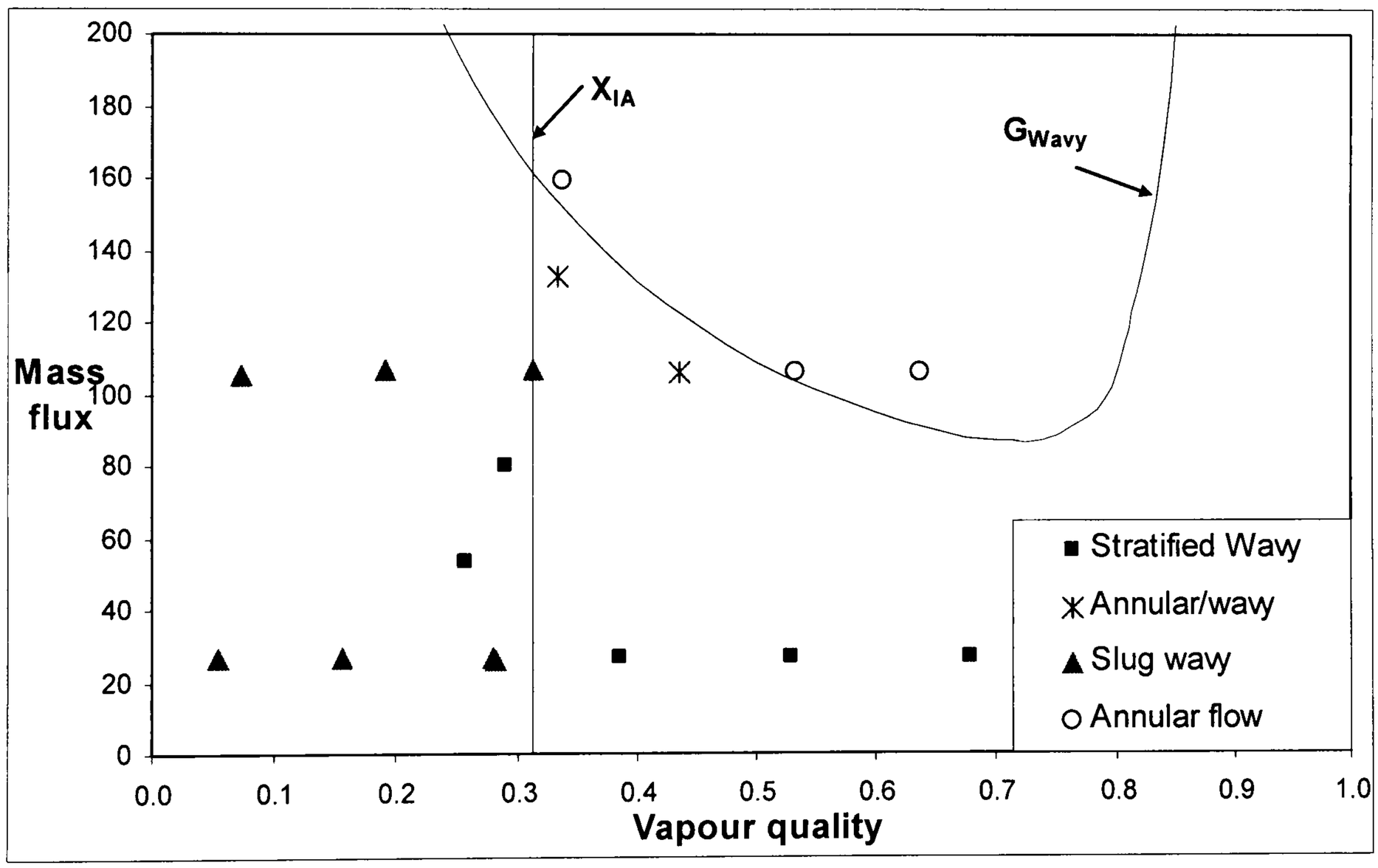

Fig. 5.12 Comparison between data for plain tube and flow pattern map

This figure shows that the test data for empty tube have good agreement with the researches published in literature. Compared with the flow pattern map for tube with metal foams, the liquid phase wet less tube wall in plain tube when vapour quality is lower than 0.4, because without the effect of metal-foam structure, which makes the

liquid layer flatter, the liquid phase tends to occupied the bottom due to the effect of gravity. When the vapour quality increases, the velocity of vapour phase increases significantly, which means the effect of gravity reduces and then the annular flow appears in less mass flux in plain tube as that happens in metal-foam tubes.

5.4 Heat transfer performance

After the flow pattern for flow boiling in different tubes have been analyzed based on the tube temperature distribution and fluctuation. The heat transfer performance of different metal-foam tubes and the effect of different parameters, such as mass flux, vapour quality, metal-foam microstructures, etc., will be discussed in the following section. In this chapter, the overall heat transfer coefficient (h) is the average of local heat transfer coefficients with weightings based on their positions. The local heat transfer coefficient at each thermocouple location, h_l, is defined as:

$$h_l = \frac{q}{\Delta T}, \qquad (5.3)$$

where ΔT is the temperature difference between the inner wall surface temperature and fluid saturated temperature. The inner wall surface temperature can be deduced based on one dimensional conduction assumption from the measured outer wall surface temperature. And q is the uniform heat flux applied on the tube surface, which can be obtained by $q = \frac{Q_{absorption}}{A_i}$, where the heat absorbed by two phase flow can be calculated by $Q_{absorption} = Q_{heaterinput} - Q_{loss}$. The actual heat loss can be calculated by $Q_{loss} = -\frac{kL(T_a - T_b)}{\ln(d_a / d_b)}$ (Formula 3.4). Without elsewhere stated, the metal foam material is 92%Cu with 8%Ag for the following measurement results.

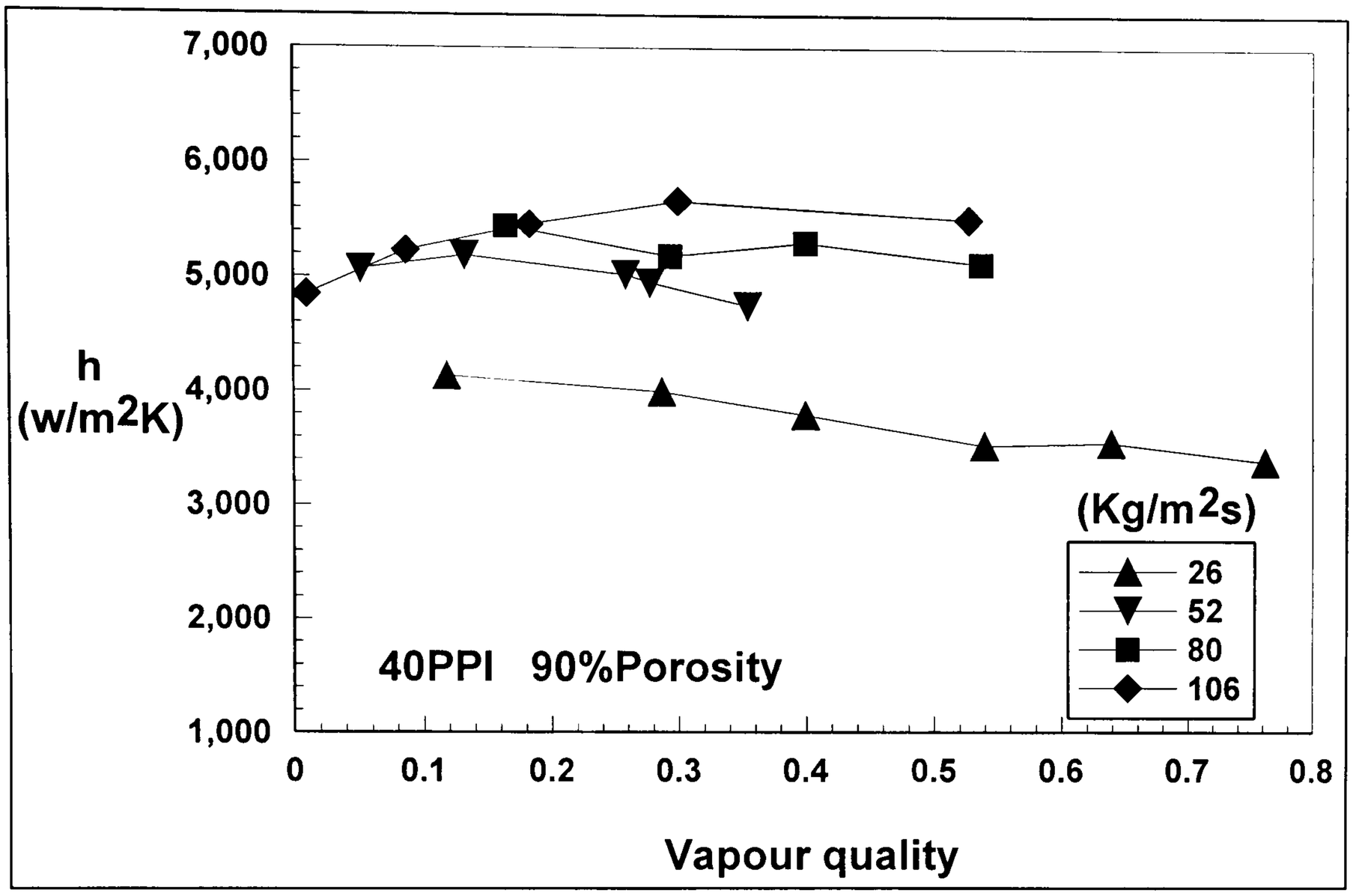

(a)

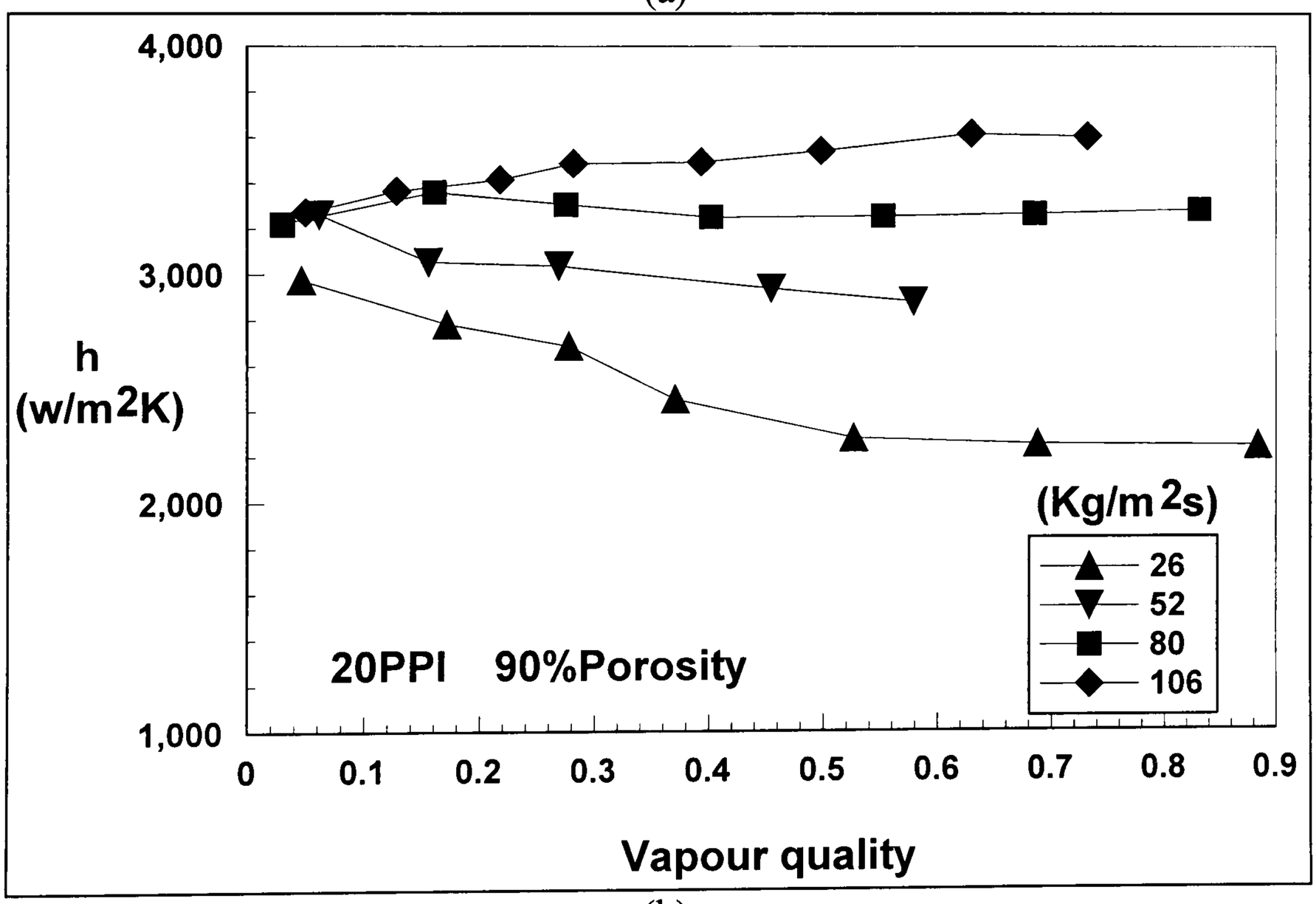

(b)

Fig. 5.13 Variation of heat transfer coefficient with the vapour quality for two different cell-size foam tubes

a) Effect of vapour quality Fig. 5.13 shows the variation of heat transfer coefficient with the vapour quality for two different cell-size foam tubes, respectively. One

interesting observation from the figure is that the heat transfer coefficient exhibits different behaviours as the vapour quality rises. For the low mass flow rate, the heat transfer coefficient becomes smaller as the vapour quality rises. As indicated earlier, the flow pattern should be stratified wavy flow for low mass flow rates, so more metal foam structure and tube wall surfaces are occupied by vapour as the vapour quality rises, and this reduces heat transfer capability. For high mass flow rates, the flow pattern is more like annular flow as the vapour quality rises, so the heat transfer coefficient keeps steady rising, albeit slowly.

b) Effect of mass flow rates The effect of mass flow rates on heat transfer is shown in Fig. 5.13 and Fig. 5.14 (a). The heat transfer coefficient moderately increases with the mass flow rates, a typical convective flow boiling characteristics. In horizontal metal foam tubes, the metal foam structures not only provide more boiling sites to promote heat transfer, but can also constrain bubble growth and even break up the bubbles when the flow is obstructed by the foam ligaments with different orientation angles. This tends to homogenize the flow field and enhance heat transfer.

c) Effects of metal-foam cell size The effect of cell size on boiling heat transfer is shown in Fig. 5.14 (a) and (b) for different mass flow rates and different vapour qualities, respectively. Both figures show that the heat transfer is dramatically enhanced by reducing the cell size from 20ppi to 40 ppi. A metal foam with smaller cell size can provide more surface areas and boiling sites, and also it can enhance the flow mixing and break up the large bubbles, and thereby increasing the heat transfer coefficient. Both figures show that the boiling heat transfer coefficients for 40 ppi metal foam tubes are nearly twice those of 20 ppi foam tubes.

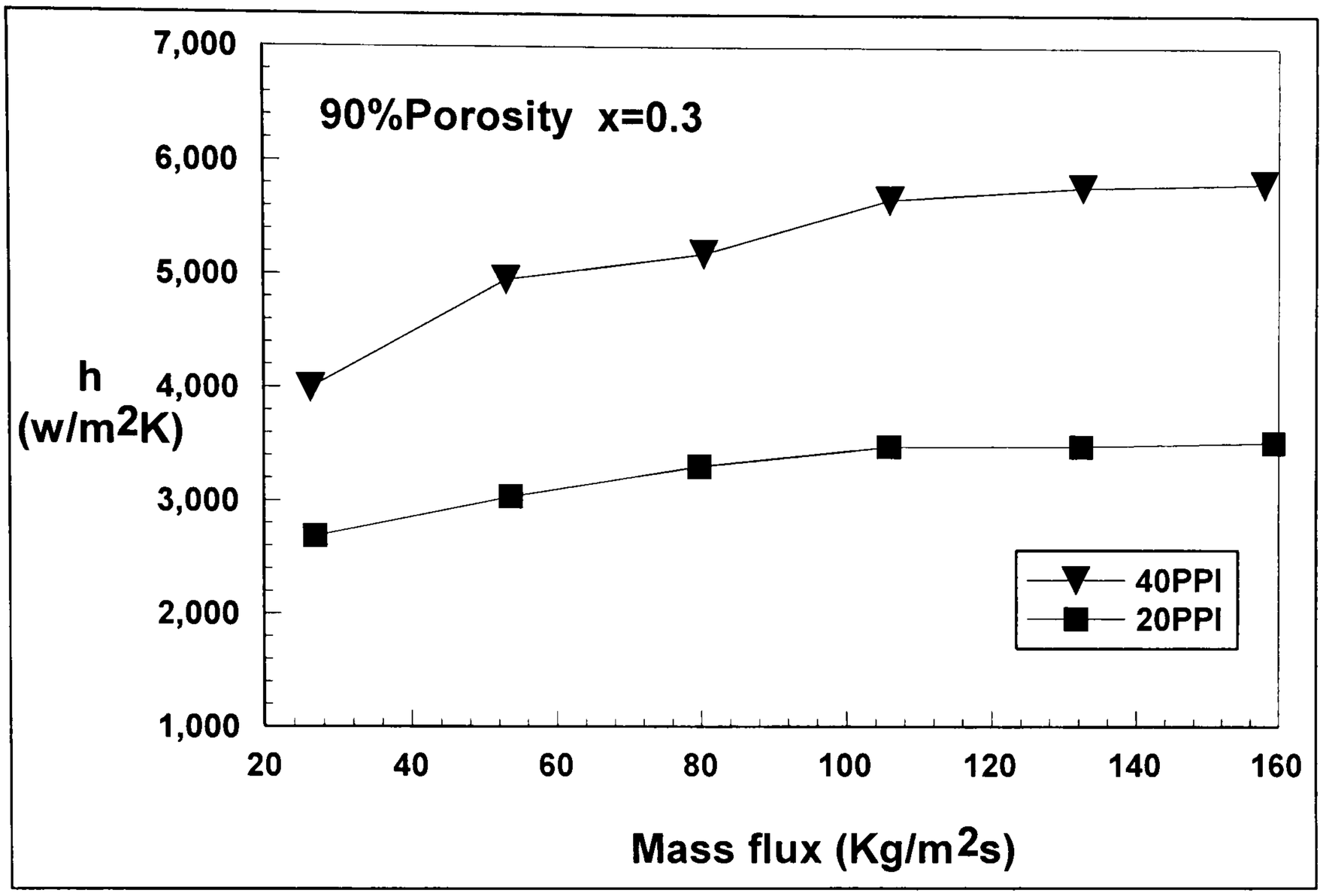

(a)

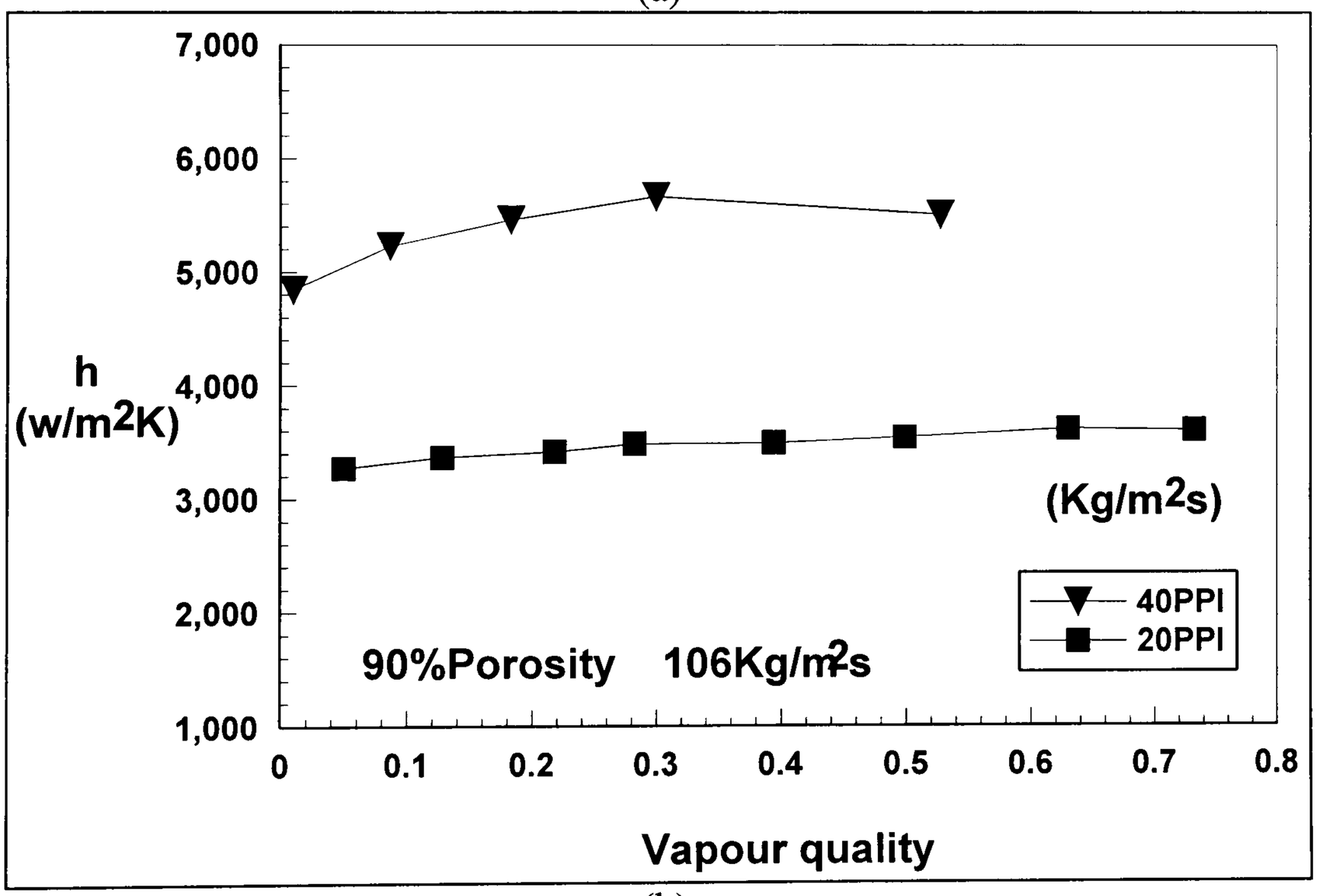

(b)

Fig. 5.14 Effect of cell size on boiling heat transfer, (a) for different mass flow rates and (b) for different vapour qualities

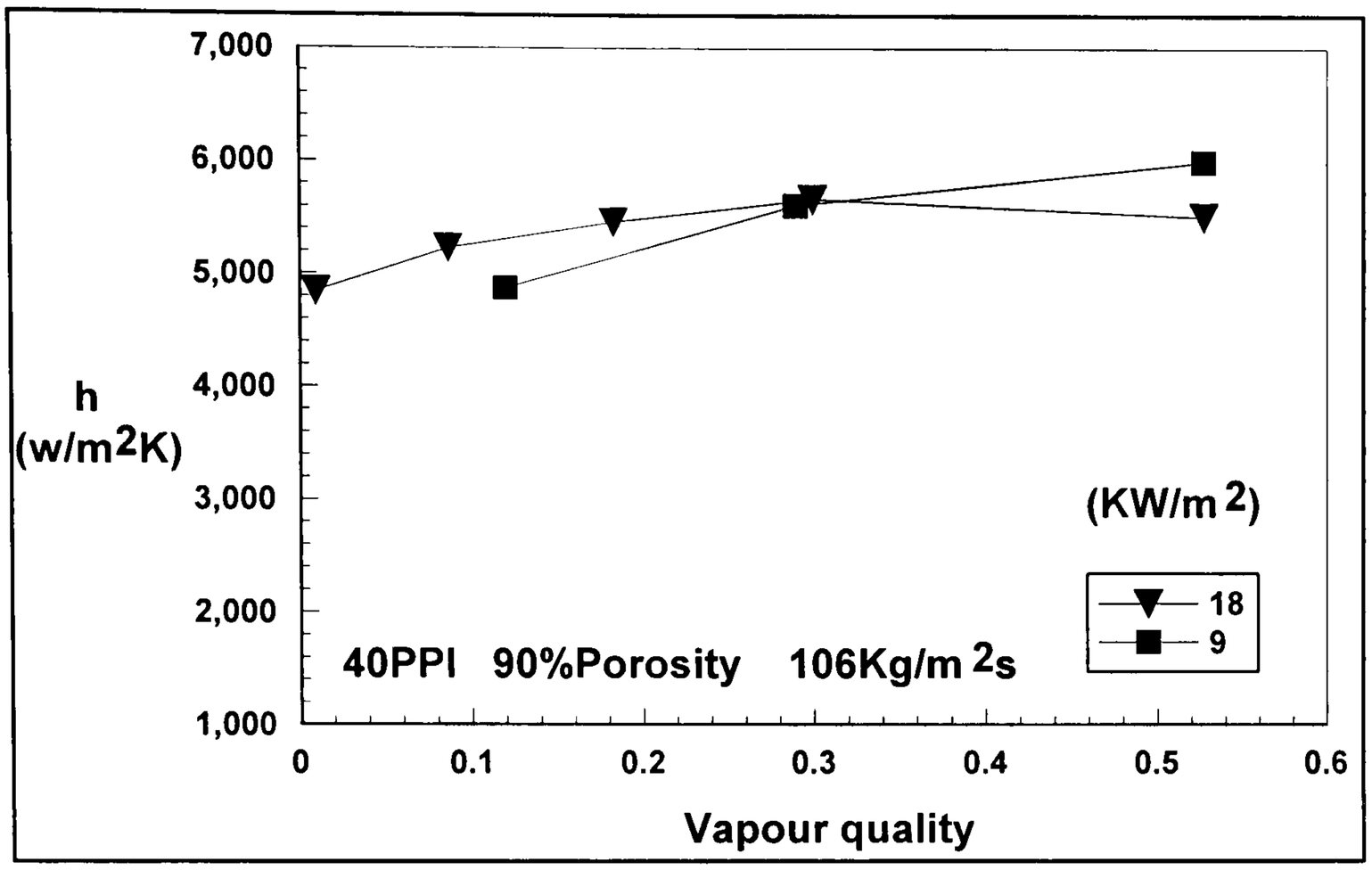

(a)

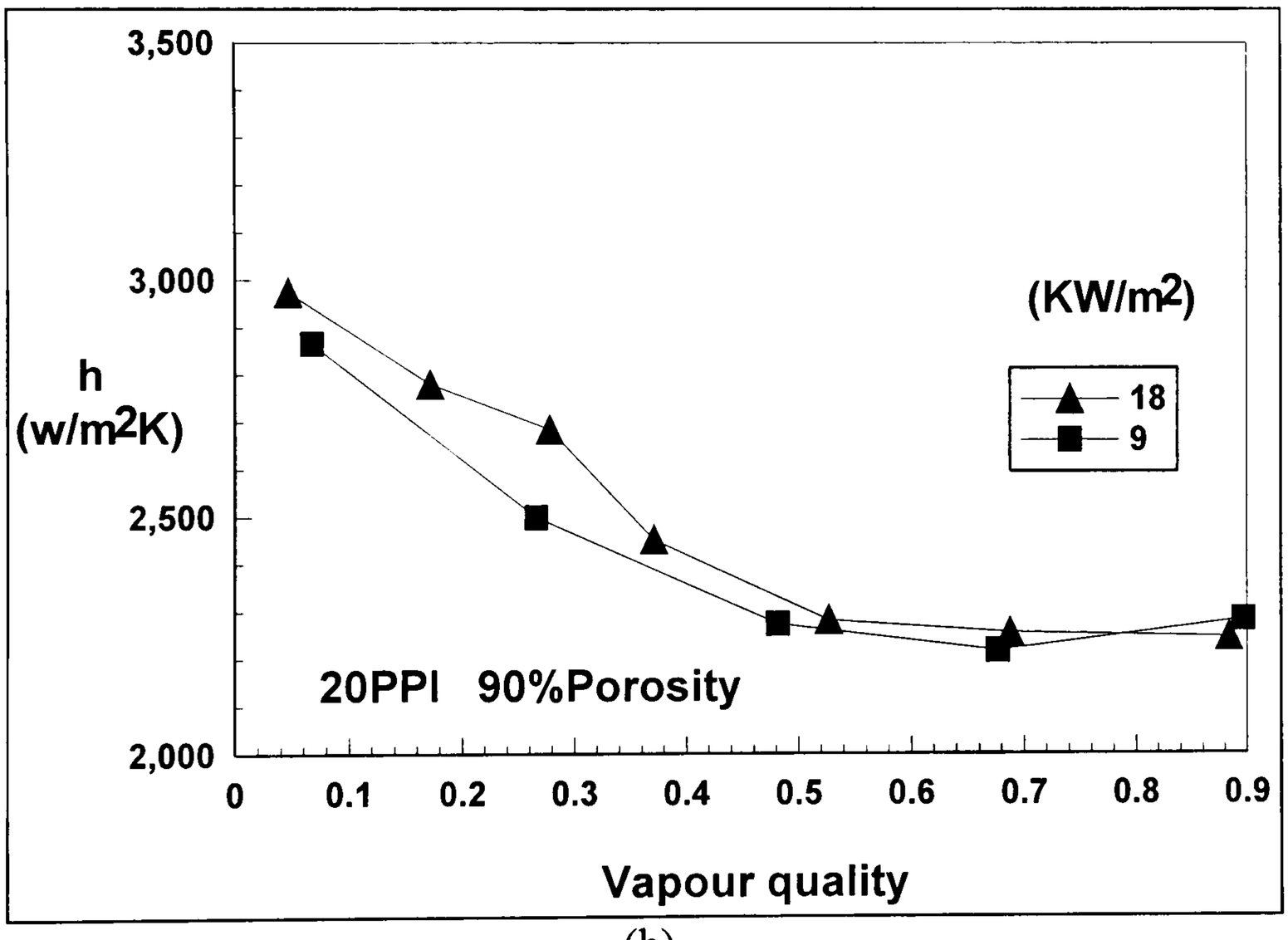

(b)

Fig. 5.15 The effect of heat flux on heat transfer coefficients (a) 106Kg/m^{2}s; (b) 26kgm^2/s

d) Effect of heat flux The effect of heat flux on boiling heat transfer is shown in Fig. 5.15. For single phase flow, it is known that the heat flux has no effect on heat transfer coefficient, however the same story does not hold for boiling heat transfer. For channel flows, it is widely accepted that the boiling heat transfer is governed by two mechanisms: nucleate boiling and forced convection boiling (Qu and Mudawar,

2003). In the nucleate boiling dominant region, liquid near the heated channel wall is superheated to a sufficient degree to sustain the nucleation and growth of vapour bubbles. The nucleate boiling heat transfer coefficient is dependent upon heat flux, but generally is far less sensitive to mass velocity and vapour quality. In forced convection boiling, however, there is a suppression of bubble nucleation along the heated wall, so the heat is transferred mainly by single-phase convection through the thin annular liquid film. The convective boiling heat transfer coefficient is dependent on mass velocity and vapour quality, but is fairly independent of heat flux. Fig. 5.15 shows that the heat flux plays a very moderate role on boiling heat transfer, and this implies that the convective boiling dominates the heat transfer especially for the case of mass flow rate 106 Kg/m^{2}s

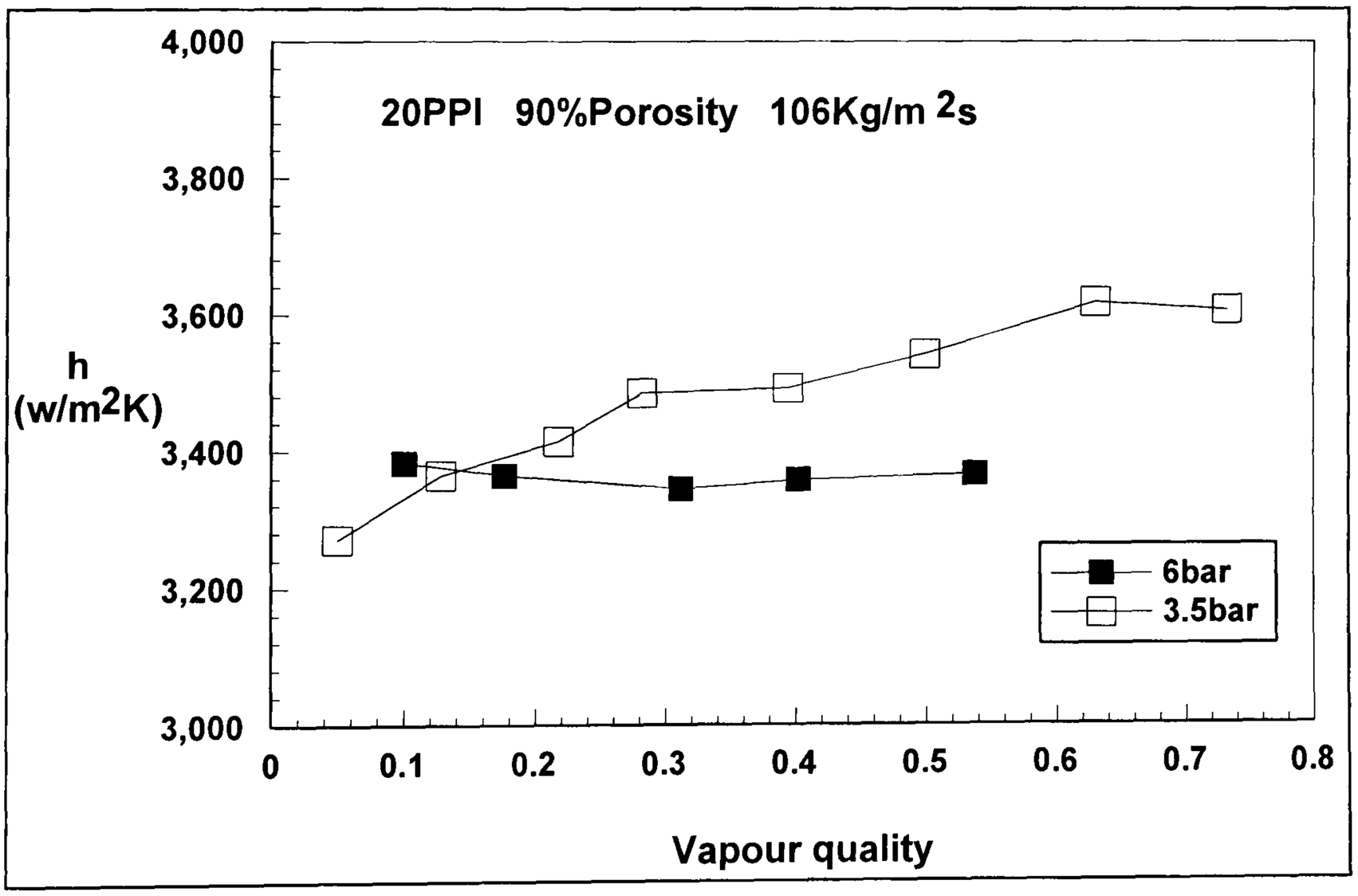

Fig. 5.16 Effect of refrigerant pressure on boiling heat transfer

e) Effect of operating pressure The effect of refrigerant pressure on boiling heat transfer is shown in Fig. 5.16. It is noted that the boiling heat transfer coefficient of

pressure 6.0 bar is higher than that of 3.5 bar for small vapour quality x = 0.1. This observation is in line with the pool boiling heat transfer where the heat transfer coefficient increases with the refrigerant pressure, and it implies that the heat transfer exhibits pool boiling heat transfer characteristics for small vapour quality $x \leq 0.1$. However the story is different for larger vapour qualities. As the vapour quality rises, the vapour velocity for the low pressure is higher due to the small vapour density, and this consequently causes higher heat transfer coefficient for the case of pressure 3.5 bar. Also Fig. 5.16 shows that the heat transfer coefficient almost remains unchanged with the increase of vapour quality for the higher pressure of 6.0 bar, whereas it keeps steady increasing as the vapour quality rises for the lower pressure of 3.5 bar. For the high pressure of 6.0 bar, the diminishing liquid effect is offset by the enhancing vapour convective effect as the vapour quality rises. However, for the low pressure of 3.5 bar, the heat transfer enhancing effect of vapour convection outstrips the diminishing effect of lacking liquid, and this leads to the steady increasing heat transfer behaviour as the vapour quality rises.

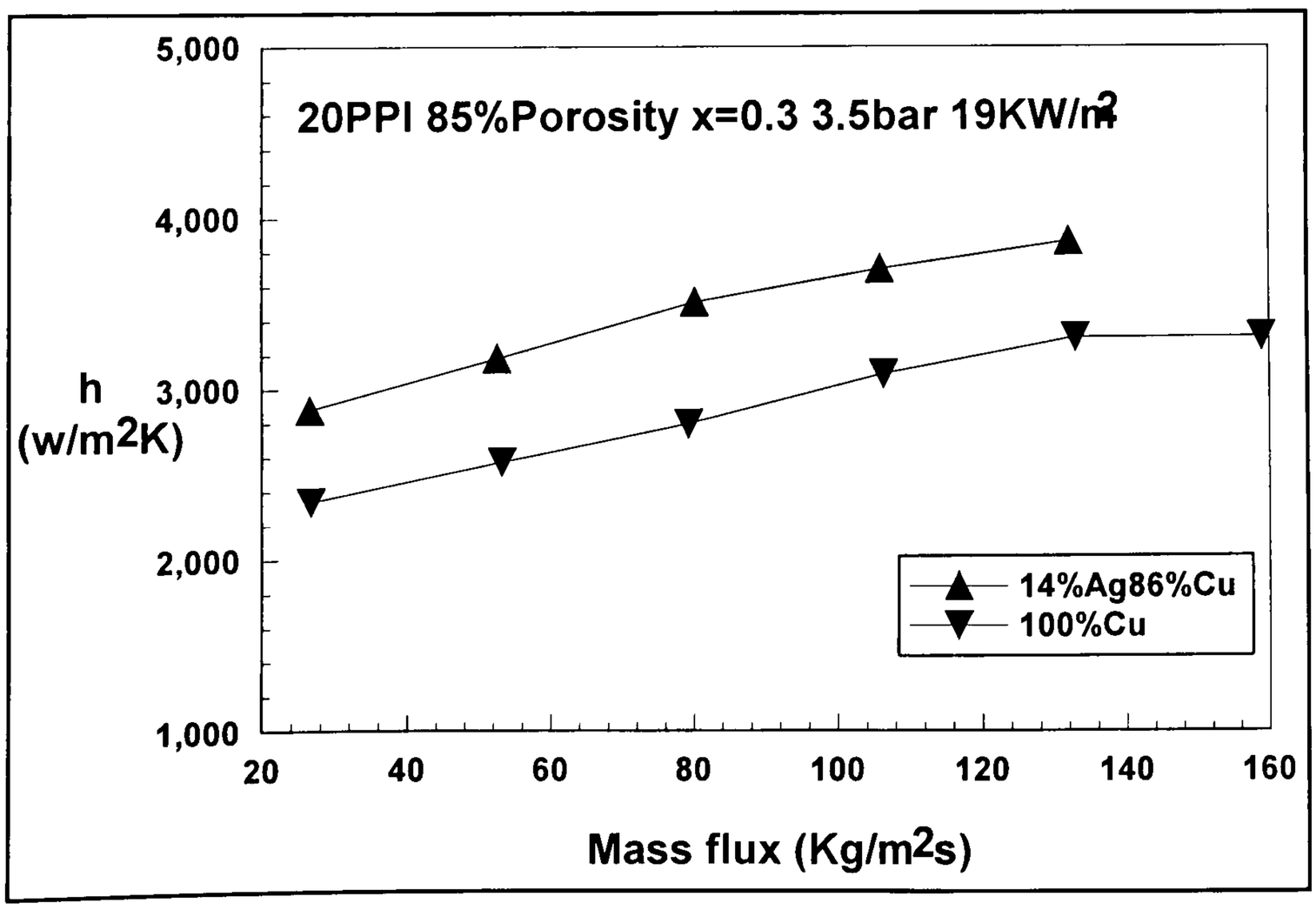

Fig. 5.17 Comparison of heat transfer between the two different material foam tubes

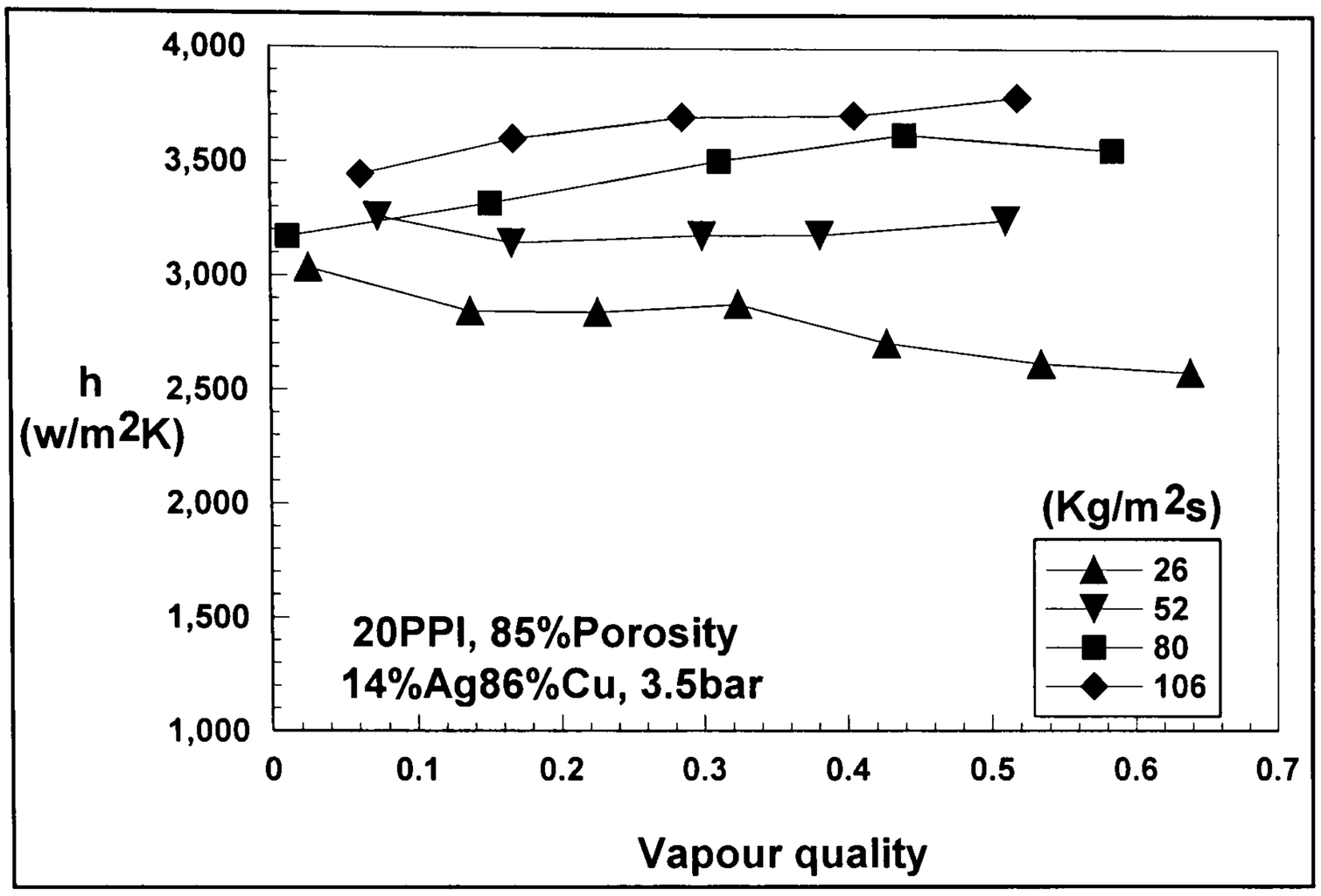

(a)

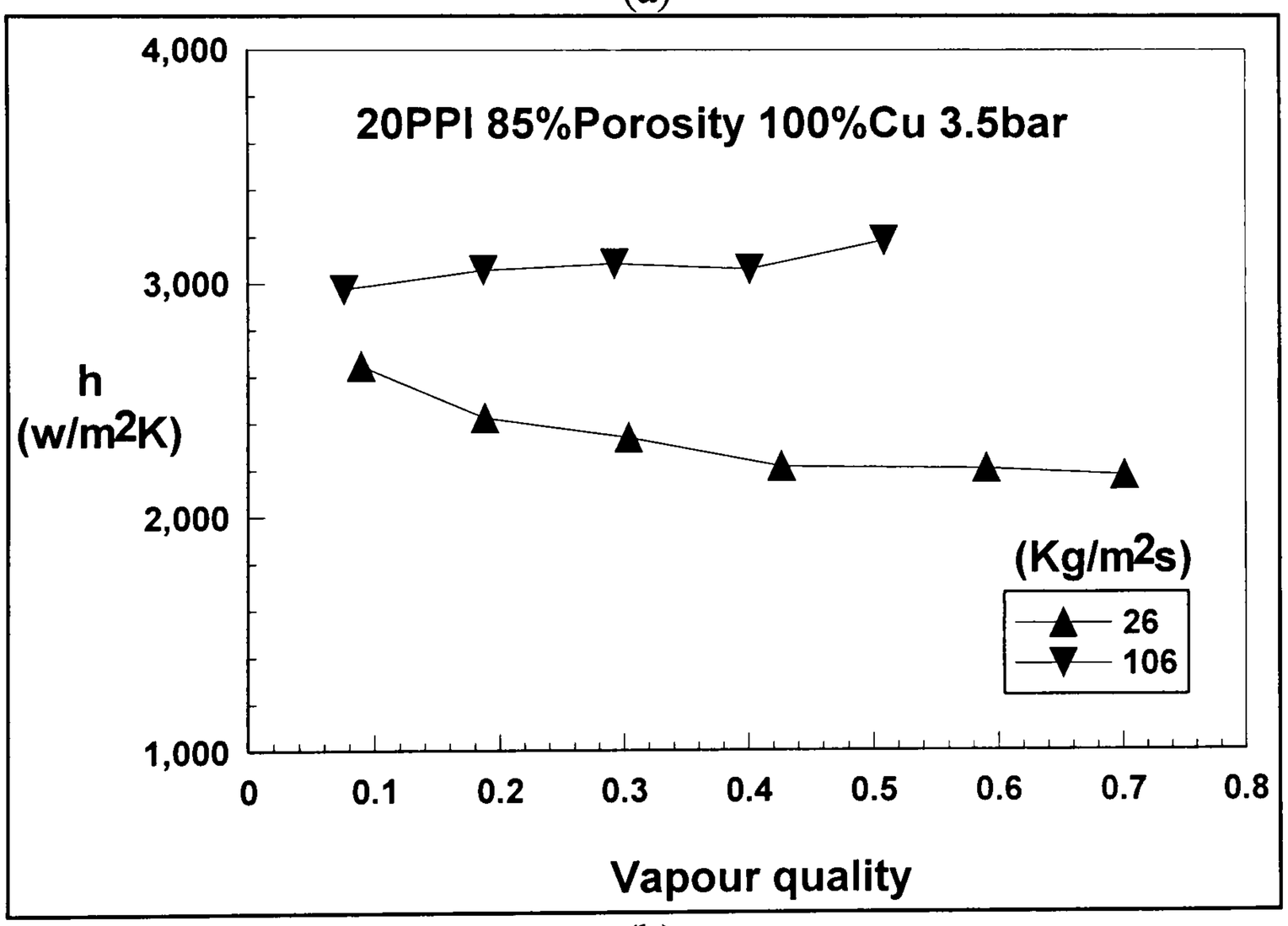

(b)

Fig. 5.18 The effect of mass flux and vapour quality on heat transfer coefficient for tubes with metal foams made of different materials (a) 14%Ag86%Cu; (b) 100%Cu

f) Effect of metal foam materials In order to examine the metal-foam material effect on heat transfer, measurements have been conducted for two different metal-foam material tubes. Fig. 5.17 and Fig.5.18 present the comparison of boiling heat transfer between the two different material foam tubes. The variation of overall heat transfer

performances with different mass flux for these tubes are represented in Fig.5.17, which shows the boiling heat transfer coefficient of the metal foam tube with 14%Ag and 86%Cu is around 30% higher than that of a pure copper foam tube. The different metal foam composition may have a direct effect on its overall thermal conductivity, and perhaps more importantly, it directly affects the attachment quality with the tubes which plays a key role on heat transfer. Fig.5.18 shows the effect of mass flux and vapour quality on over heat transfer coefficient, whose trends represents the agreement with prediction of the flow pattern map.

5.5 Comparison between plain tube and metal-foam tubes

The flow patterns for plain tube under the same situations as those of metal-foam tubes in this research have been analyzed above. The difference of pressure drop and heat transfer performance between plain tube and metal-foam tubes will be discussed in this section.

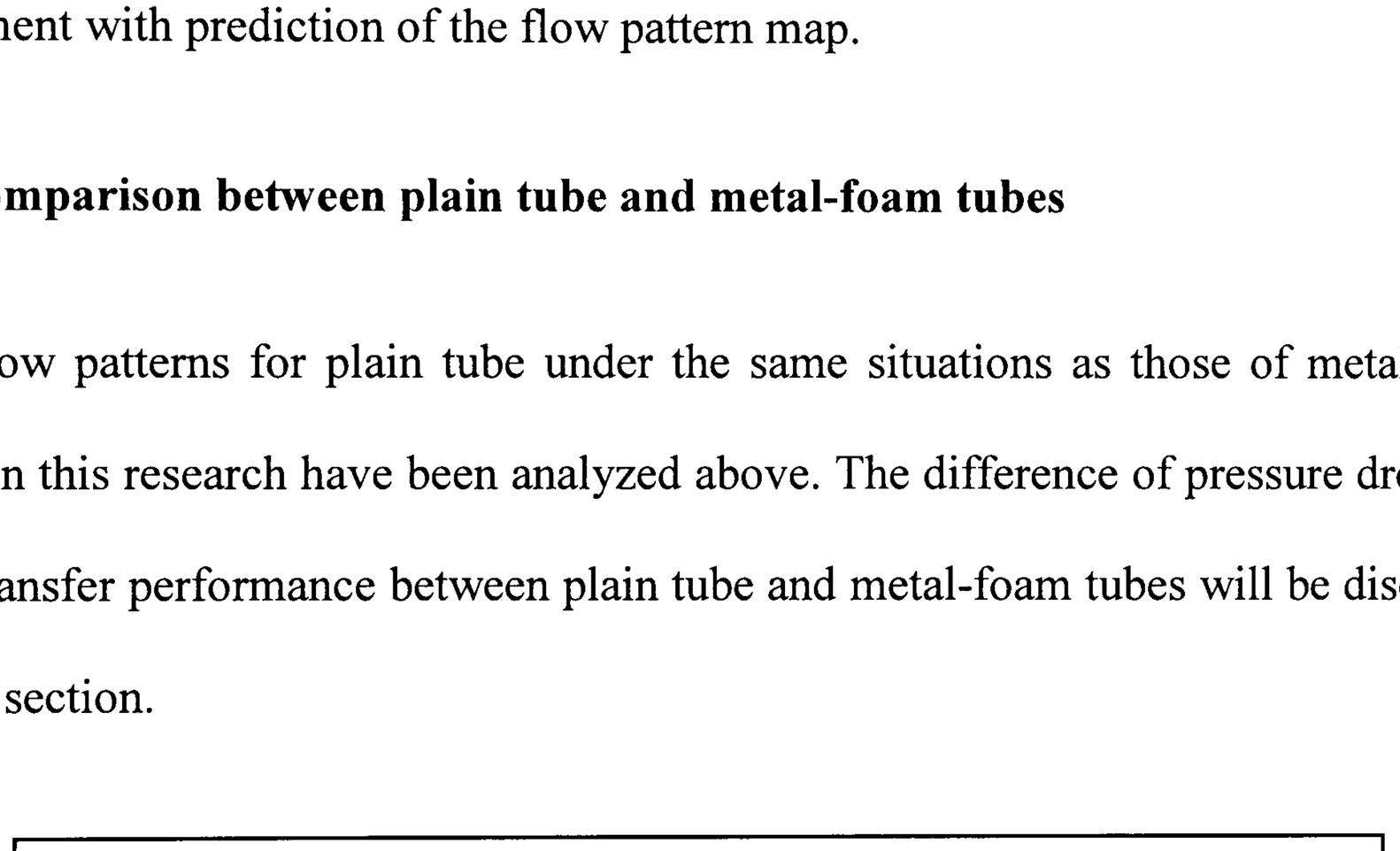

Fig. 5.19 The comparison between plain tube metal-foam tubes on overall heat transfer coefficients for different mass flux.

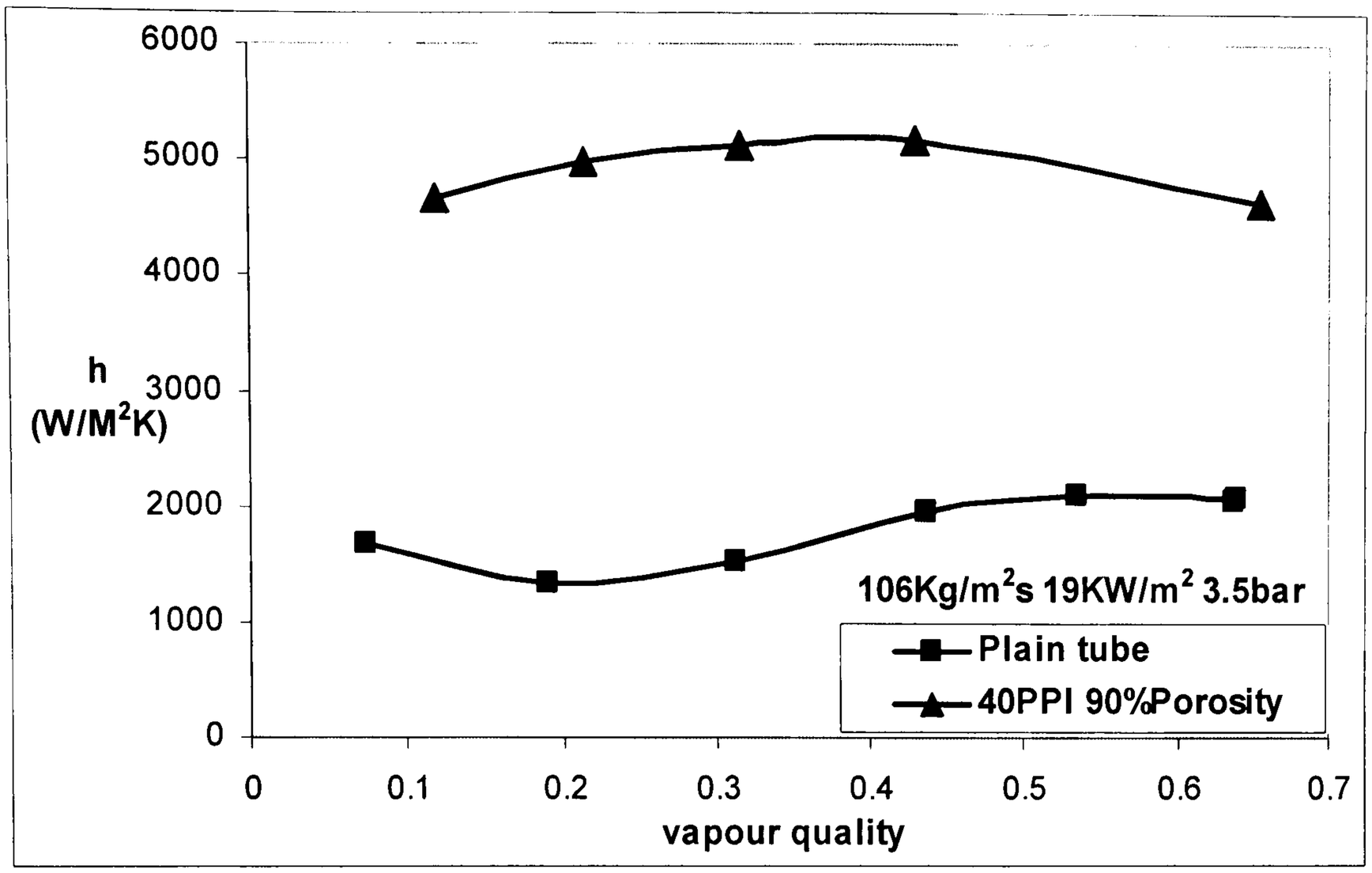

Fig. 5.20 The comparison between plain tube and tube filled with 40PPI, 90% porosity metal foams on overall heat transfer coefficients for different vapour quality.

The Fig. 5.19 and Fig. 5.20 show the comparison between of plain tube and metal-foam tube on overall heat transfers coefficients in different mass flux and vapour quality. It is clear that the use of metal foams significantly enhance the flow boiling heat transfer. The heat transfer coefficients of tube filled with 40ppi metal foams almost tripled those of plain tube. In Fig. 5.20, when the mass flux is as high as 106Kg/m^{2}s, unlike the annular flow happens all the times in metal foam filled tube, the wavy flow appears in empty tube at low vapour quality. Because the use of metal foams makes the boundary layer flatter, especially in low vapour quality, the flow pattern of metal-foam tube changes to annular flow in lesser flow flux, which results in higher heat transfer coefficient in this region.

The Fig. 5.21 shows that the heat flux have significant influence on heat transfer performance of plain tube, which implies that the nucleate boiling take important

effects on the boiling heat transfer, unlike what happens in the metal-foam tube where convective boiling dominates the heat transfer.

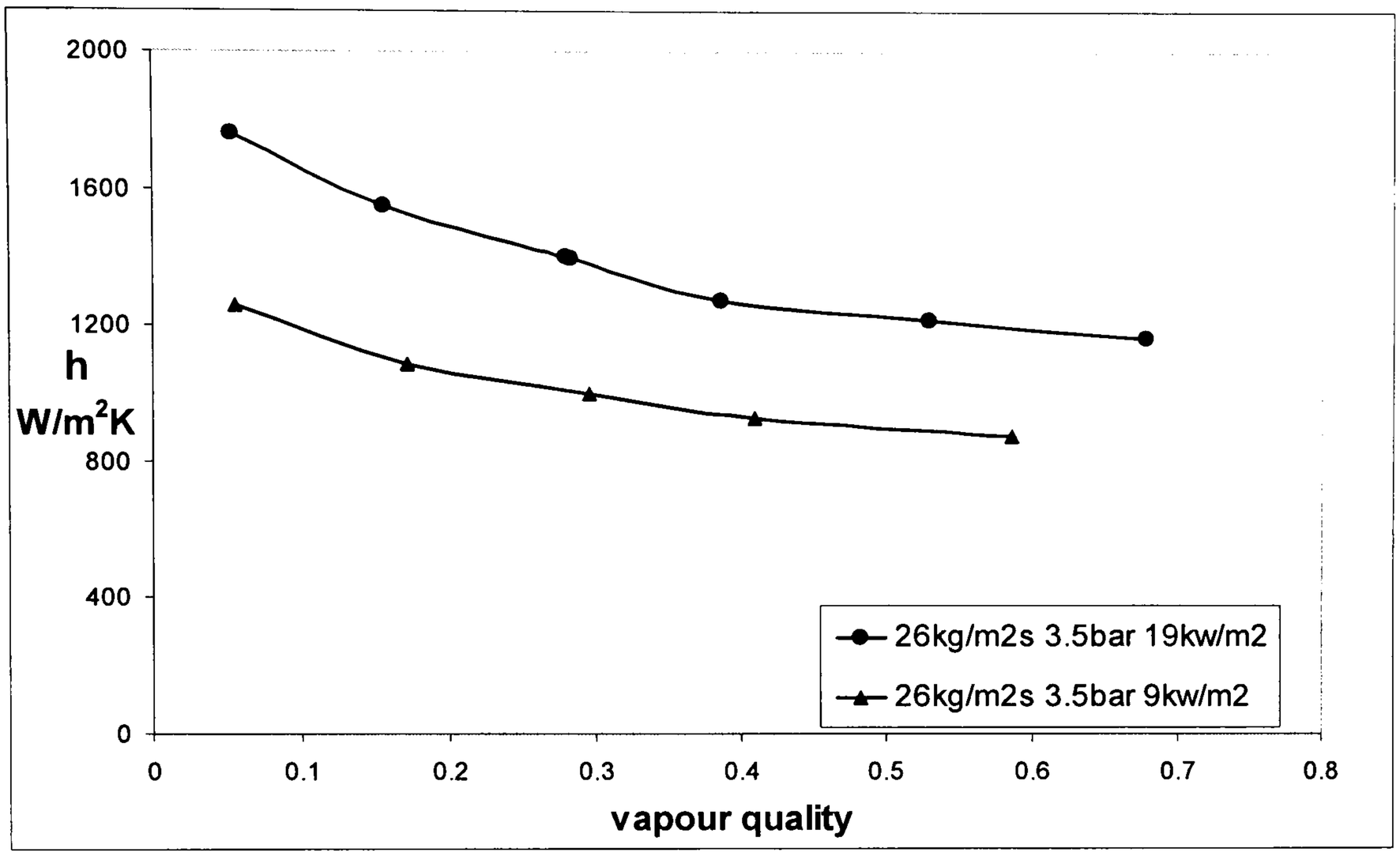

Fig. 5.21 The effect of heat flux on heat transfer performance of plain tube

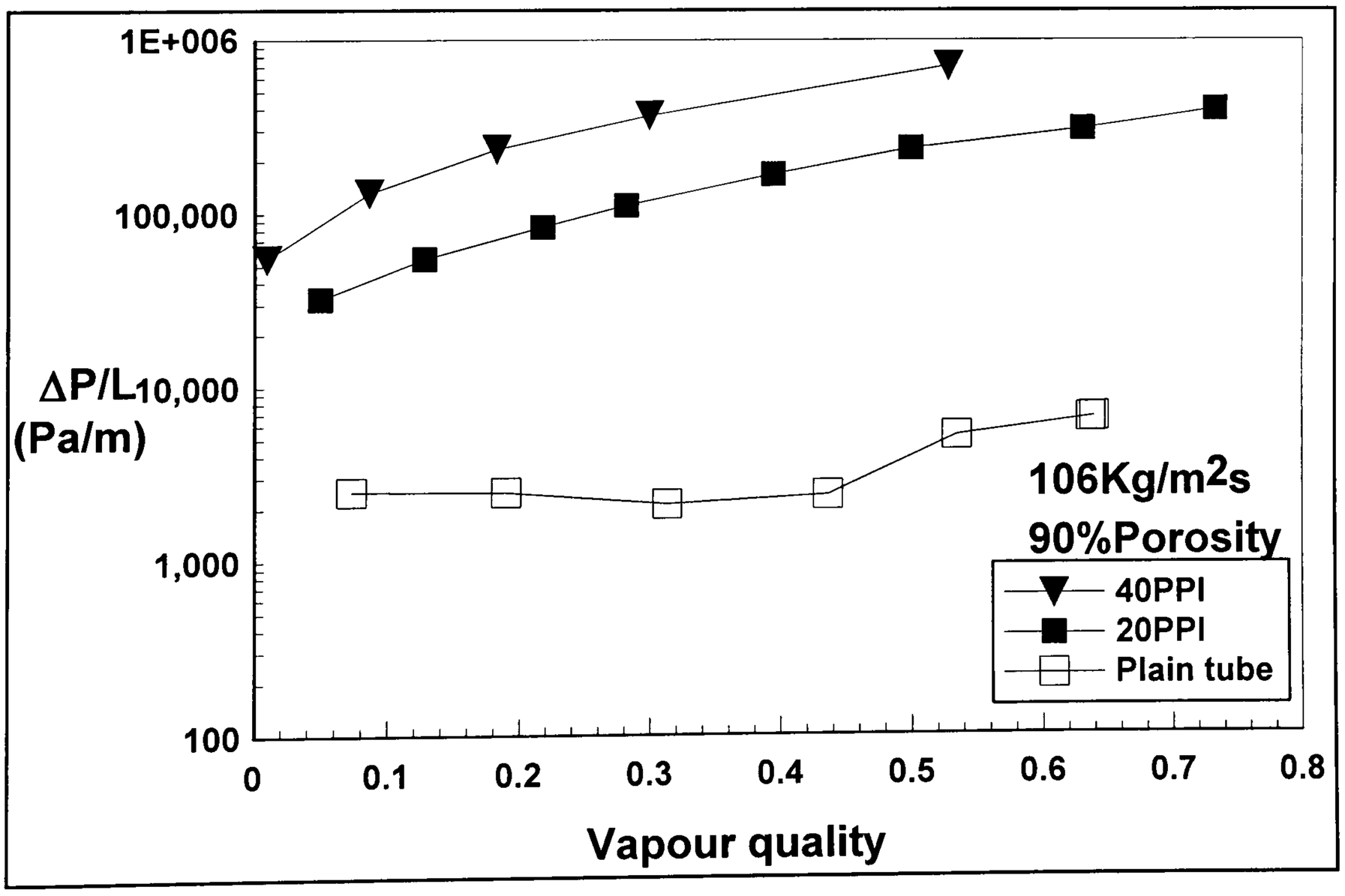

Fig. 5.22 The comparison between plain tube and metal-foam tube on pressure drop

Considering the high pressure drop caused by the metal-foam structure, as indicated in Fig.5.22, metal-foam tube costs much more pump power than plain tube. Therefore, the main obstacle for application of this kind of tube lies on how to reduce the pressure loss and keep the benefits at the same time.

However, apart from the benefit of using for compact heat exchanger, the tube filled with metal foams may have great potential when the heat flux on the wall is extremely high, because for boiling heat transfer, the heat transfer coefficient increases significantly with the increase of heat flux. The comparison between plain tube and metal-foam tube in above figures based on the same amount of heat load, which means actual heat flux for boiling heat transfer in metal-foam tube is much lower than that in plain tube because use of metal-foam brings huge increase of heat transfer area which results in lower heat flux and then reduce the heat transfer coefficient of nucleate boiling. Therefore, with higher heat input, the metal-foam tube has a lot of potential on enhancement of overall heat transfer performance, especially on that of the nucleate boiling. Moreover, based on the same DNB (Departure of nucleate boiling) point, the critical heat flux on tube wall of metal-foam tube should be much higher than that of plain tube, which means the metal-foam tube is much safer than plain tube under extreme conditions.

5.6 Conclusions

In this chapter the boiling heat transfer characteristics in horizontal metal foam tubes is experimentally investigated. Some conclusions can be drawn as:

(1) The pressure drop dramatically increases with the vapour quality and mass flow rates. The metal foam cell size has a significant effect on pressure drop, and the

pressure drop can be doubled as the cell size decreases from 20 ppi to 40 ppi. Higher operating pressure reduces the pressure drop due to the lower vapour velocity.

(2) The presence of metal foam structures blocks the direct visualization of the flow pattern inside the metal foam tubes, but the flow pattern can be indirectly judged through monitoring the cross-sectional wall surface temperature fluctuations and wall-refrigerant temperature difference. And a flow pattern map for metal-foam tube has been summarized based on the analysis of experimental results.

(3) For different mass flow rates, the heat transfer coefficient exhibits different behaviours as the vapour quality rises. For lower mass flow rates, the heat transfer coefficient becomes smaller with the increase of the vapour quality, while the reverse situation holds for the higher mass flow rates. The different heat transfer behaviour can be attributed to different flow patterns.

(4) Metal foam cell size plays a significant role on boiling heat transfer, and the heat transfer coefficients can be nearly doubled as the cell size decreases from 20 ppi to 40 ppi, due to the increased surface area density and increased number of active sites for nucleate boiling.

(5) The heat flux plays a very moderate role on boiling heat transfer, and this implies that the convective boiling dominates the heat transfer in metal foam tubes. As the vapour quality rises, the vapour velocity for the low pressure is higher due to the small vapour density, and this consequently causes higher heat transfer coefficient for the case of lower pressure.

(6) Silver addition in metal foam materials has a significant effect on heat transfer due to the different thermal conductivity and most importantly the improvement of tube-foam attaching quality.

(7) Compared with the plain tube, the metal-foam tube has significantly higher heat transfer performance. In metal-foam tube, the liquid phase occupied more area of tube wall which results in higher heat transfer coefficient especially in low vapour quality.

Chapter 6 Numerical Modelling for Flow Boiling Heat Transfer

Comparing with theoretical analysis for single phase flow, the modelling work for flow boiling heat transfer in metal-foam tube is more complex, even the flow boiling mechanism in plain tube isn't very clear (Huo, et al 2004). There are some researches in modelling for plain tubes. For example, to describe evaporation in microchannels, whose flow patterns are relatively simple, mainly at slug flow and annular flow, Thome et al. (Revellin and Thome , 2006) proposed a three-zone flow boiling model which simplifies the flow channel into full of liquid, annular flow and dry out stages. It represents the transient variation in the local heat transfer coefficient during sequential and cyclic passage of a liquid slug, an evaporating elongated bubble, and a vapor slug when film dry-out has occurred. However, for the tubes with normal diameter, the fundamental difficulty in simulating multiphase flow and transport lies in the presence of moving and irregular phase interfaces, which also depends on flow patterns for flow boiling. Kattan et al (1998a, b, c), Biberg (1999) and Wojtan et al. (2005a, b) carried out a series of investigation on flow patterns and two-phase flow regime map in horizontal tubes. They used high speed camera or CCD camera to record the videos of flow boiling in glass tube and suggested flow pattern maps through analysis of the experimental observation and published researches. Based on these flow pattern maps, they developed and improved a heat transfer model which calculates the heat transfer coefficients for liquid and vapour phases separately, and then from which the overall two-phase flow heat transfer coefficient can be known by properly accounting for the wet and dry areas of the tube. From the previous analysis, it is obvious that the flow patterns dominate the mechanism of flow boiling.

For multiphase flow and heat transfer in porous media, Wang and Cheng (1997) suggested the Multiphase flow model (MFM). But exact solutions to this model are limited to a very small class of problems in one dimension and with many simplifying assumptions due to the large number of primary variables (e.g. vector velocities, scalar pressures, scalar liquid saturations, mass concentrations, etc) and their highly nonlinear equations. Therefore, it is a challenging task and sophisticated numerical procedures to solve a practical problem. Since the metal foam structure is unique and quite different from the traditional porous media such as packed beads or particles, the previous modelling investigations are not applicable to the boiling heat transfer in metallic foams. To the authors' knowledge, no modelling research results of flow boiling heat transfer in metal foams have been published in open literatures despite their potential wide range applications.

In this research, the non-equilibrium heat transfer equations for porous media are employed to consider the temperature difference between the solid foam structure and the fluid. The local heat transfer coefficients for liquid and vapour phases are first examined separately to model the overall flow boiling heat transfer behaviour in metal-foam tubes by properly considering the presence of metal foam structures. The predicted results are compared with the experimental results.

6.1 Problem description

The problem under consideration in this part is flow boiling heat transfer in horizontal metal-foam tube as shown in Fig.6.1. The direction of fluid flow is parallel to z (axis of tube). The diameter of the tube is 26 mm. The wall of tube is

uniformly heated and the vapour quality of two-phase working fluid (R134a) entering the tube is given.

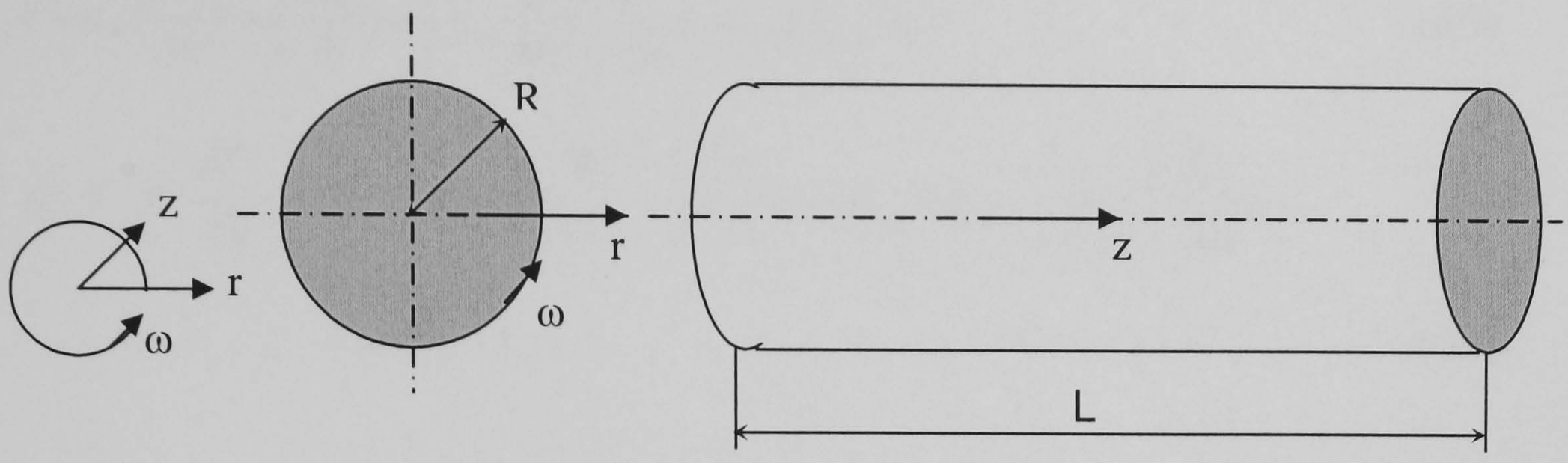

Fig. 6.1 Geometry and definition of metal foam filled tube

6.2 Mathematical formulations

To modelling the heat transfer performance of flow boiling in horizontal metal-foam tubes, the two-equation non-equilibrium model for porous medium is employed to consider the temperature difference between the solid foam structure and the fluid.

For solid phase:

$$0 = \nabla \cdot \{k_{se} \nabla T_s\} - h_{sf} \tilde{a}(T_s - T_f) \tag{6.1}$$

For fluid phase:

$$\rho_f C_f \vec{V} \nabla T_f = \nabla \cdot \{(k_{fe} + k_d) \cdot \nabla T_f\} + h_{sf} \tilde{a}(T_s - T_f) \tag{6.2}$$

Where h_{sf} is the local heat transfer coefficient between metal foam ligaments and fluid, T_s and T_f are the solid foam temperature and fluid temperature, respectively. In this modelling work, all thermo-physical properties of liquid and vapour phase depend on saturated temperature. Natural convection and radiation are negligible. The porous medium is homogeneous and isotropic. The flow pattern depends on mass flux and vapour quality of fluid. And only the cross-section of the tube will be

modelled as a two-dimensional problem in polar coordinates. Then the above mentioned equations (Eq. (6.1) and Eq.(6.2)) can be written in the following form:

$$0 = k_{sc}\left(\frac{\partial^2 T_s}{\partial r^2} + \frac{1}{r}\frac{\partial T_s}{\partial r}\right) + \frac{1}{r}k_{se}\frac{\partial}{\partial \omega}\left(\frac{1}{r}\frac{\partial T_s}{\partial \omega}\right) - h_{sf}a(T_s - T_f) \tag{6.3}$$

$$\varepsilon\rho_f C_f V_z \frac{dT_f}{dz} = (k_{fe} + k_d)\cdot\left(\frac{\partial^2 T_f}{\partial r^2} + \frac{1}{r}\frac{\partial T_f}{\partial r}\right) + (k_{fe} + k_d)\cdot\frac{1}{r}\frac{\partial}{\partial \omega}\left(\frac{1}{r}\frac{\partial T_f}{\partial \omega}\right) + h_{sf}a(T_s - T_f) \tag{6.4}$$

The two-equation non-equilibrium model is more difficult to apply because it requires information on the interfacial heat-transfer coefficient, which is usually determined through experimental investigations. And the complex heat transfer mechanism in two-phase flow makes it more difficult to be solved. To solve this problem, the main issue lies in determining the local heat transfer coefficient. From the previous analysis, it is clear that the flow pattern dominate the mechanism of flow boiling heat transfer. However, in metal-foam tubes, the tube wall and metal foams are opaque, and then the flow patterns can only be predicted by analyzing the wall temperature distributions of tube cross-section based on the knowledge of boiling heat transfer and flow patterns in plain tube. With the two-phase flow pattern map obtained from experimental investigation in metal-foam tube, the flow pattern can be pre-determined with given vapour quality, mass flow rate and fluid thermo-physical properties. Then the interface between liquid and vapour phase in the modeling area can be determined and the modelling domain can be divided into vapour zone and liquid zone. The velocity profile in these zones can be calculated and so the local heat transfer coefficient. In the liquid phase zone, the boiling heat transfer between metal foams and liquid R134a is dominant. In the vapour phase

zone, the convection heat transfer between the vapour and metal foam contributes more.

6.2.1 Boundary conditions and initial conditions

For the metal-foam tubes directly heated from outside surface with constant heat flux, the applied heat is transferred to the solid and fluid phases by conduction, convection and boiling heat transfer. As discussed before, because the thermal conductivity of the thin metal wall of tube is significantly higher than that of fluid, the temperature at the interface between metal foams and the substrate can be considered to be uniform regardless of whether it is in contact with the solid or fluid phase. Consequently, the boundary conditions of metal-foam tube are specified as follows:

$$T_s = T_f, \text{ and } q = q_W = k_{fe}\frac{\partial T_f}{\partial r}\Big|_{r=R} + k_{se}\frac{\partial T_s}{\partial r}\Big|_{r=R} + h_{be}(T_s - T_{sat}) \qquad \text{at r=R}$$

$$\frac{\partial T_f}{\partial r} = \frac{\partial T_s}{\partial r} = 0 \qquad \text{at r=0} \qquad (6.5)$$

$$\frac{\partial T_f}{\partial \omega} = 0 \text{ and } \frac{\partial T_s}{\partial \omega} = 0 \qquad \text{at } \omega=0$$

$$\frac{\partial T_f}{\partial \omega} = 0 \text{ and } \frac{\partial T_s}{\partial \omega} = 0 \qquad \text{at } \omega=\pi$$

In this research, the boiling heat transfer coefficient in vapour zone is set to be zeros. And the initial temperature of fluid (liquid and vapour) and solid (metal foams) are set at the same saturated temperature as experimental test.

6.2.2 The velocity profile

From the previous analysis, the liquid and vapour velocity profiles which are determined by flow pattern map and relative parameters should be calculated firstly. The Fig. 6.2 shows the simplified flow pattern map from experimental results for metal-foam tubes (as Fig. 5.11). There are mainly two kinds of flow patterns: the annular flow in which the liquid wets the whole tube wall and the wavy flow where the liquid phase partially wets the tube wall.

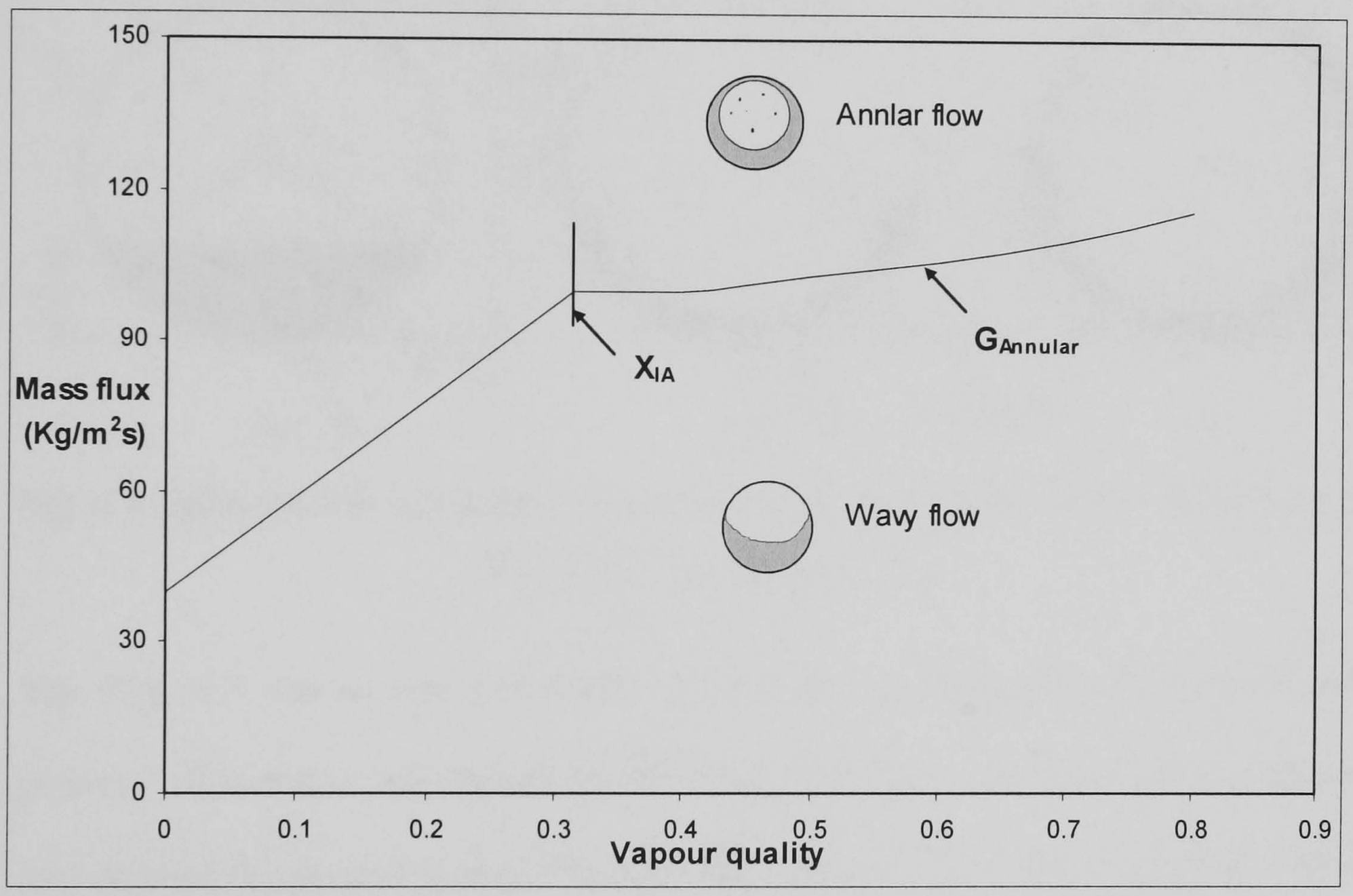

Fig. 6.2 the flow pattern map obtained based on experimental results for metal-foam tube

From Fig.6.2, it is known that the flow pattern is mainly determined by the mass flow rate and vapour quality. From the range of mass flow rates in the present research, the stratified flow pattern unlikely occurs, so the liquid phase should be a thin layer attached the bottom part (for wavy flow) or whole tube wall surface (for annular flow) due to the combined effects of gravity and inertial force. Then the modelling domain can be generally divided into vapour zone and liquid zone with

metal foams uniformly distributed in these zones. From the velocity profiles predicted for single phase flow in previous sections, it is clear that the velocity in the metal-foam tubes is much more uniform than that in plain tube, so the local velocity of liquid or vapour phases is assumed to be the mean velocity of each phase zone. Thus the velocity distributions of liquid and vapour phases can be pre-calculated respectively.

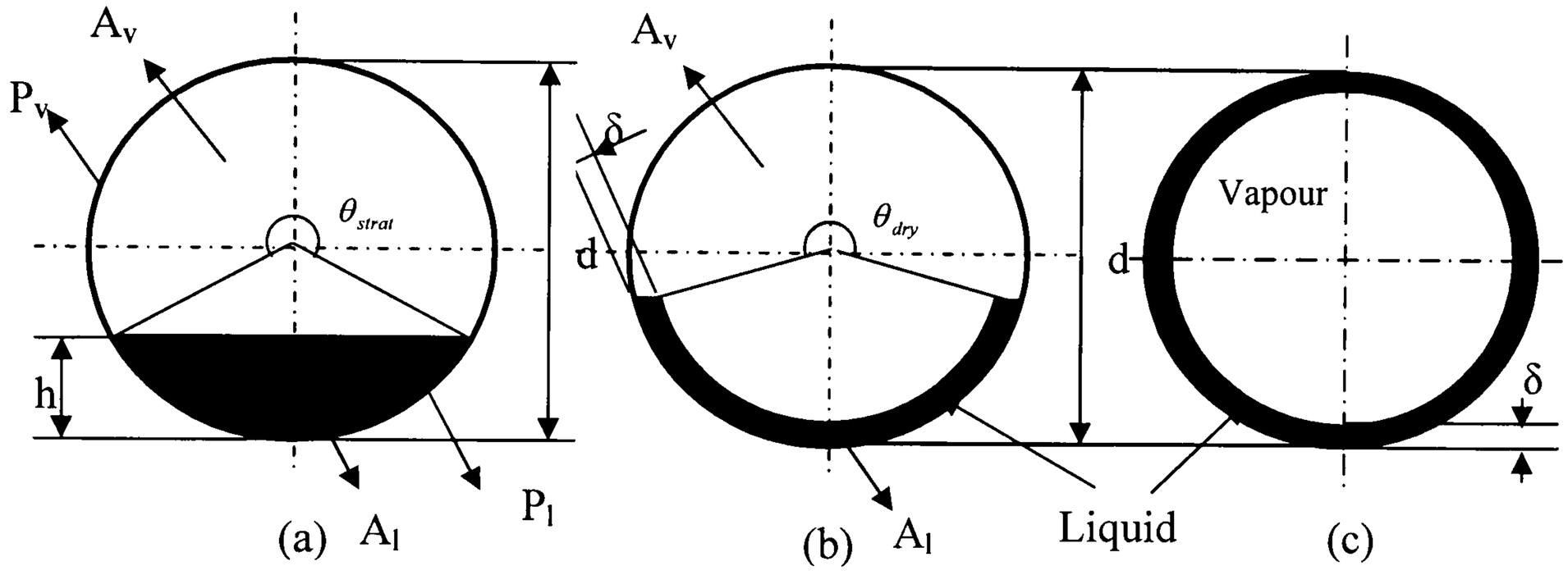

Fig. 6.3 Cross-section and peripheral fraction in a circular tube, (a) Stratified flow, (b) Wavy flow, (c) Annular flow

The Fig. 6.3 shows the schematic drawing for cross-section of different flow patterns. The Fig. 6.3(a) shows the stratified flow where the flow rate is very low and beyond the present study. When the flow flux is high, the liquid phase will be pushed to the tube wall and form a thin film for its higher viscosity, as shown in Fig 6.3(c), and this flow pattern is called annular flow which usually happens for high mass flow rates and high vapour quality. As shown in Fig. 6.2, the flow pattern transits to wavy flow from annular flow at a lower mass flux for a given vapour quality. In this study for wavy flow, it is assumed that the liquid will also form a thin film of uniform thickness that partially wets the tube in wavy flow, as shown in Fig. 6.3 (b). Through the simplification, the unknown parameters which determine the

distribution of liquid and vapour phases are void fraction ($\varepsilon_v = A_v/(A_v + A_l)$), thickness of liquid layer (δ) and dry angle for wavy flow θ_{dry} (the dry angle for annular flow is zero).

- The vapour zone fraction

As there are no research about the void fraction of flow boiling in metal-foam tubes can be found in open literature, the vapour void fraction (ε_V) model proposed by Steiner (1993) for horizontal tubes based on the drift flux void fraction model of Rouhani-Axelesson (1970) is used, as

$$\varepsilon_V = \frac{x}{\rho_v}\{[1+0.12(1-x)](\frac{x}{\rho_v}+\frac{1-x}{\rho_l})+\frac{1.18}{G}(1-x)[\frac{g\sigma(\rho_l-\rho_v)}{\rho_l^{\ 2}}]^{0.25}\}^{-1} \quad (6.6)$$

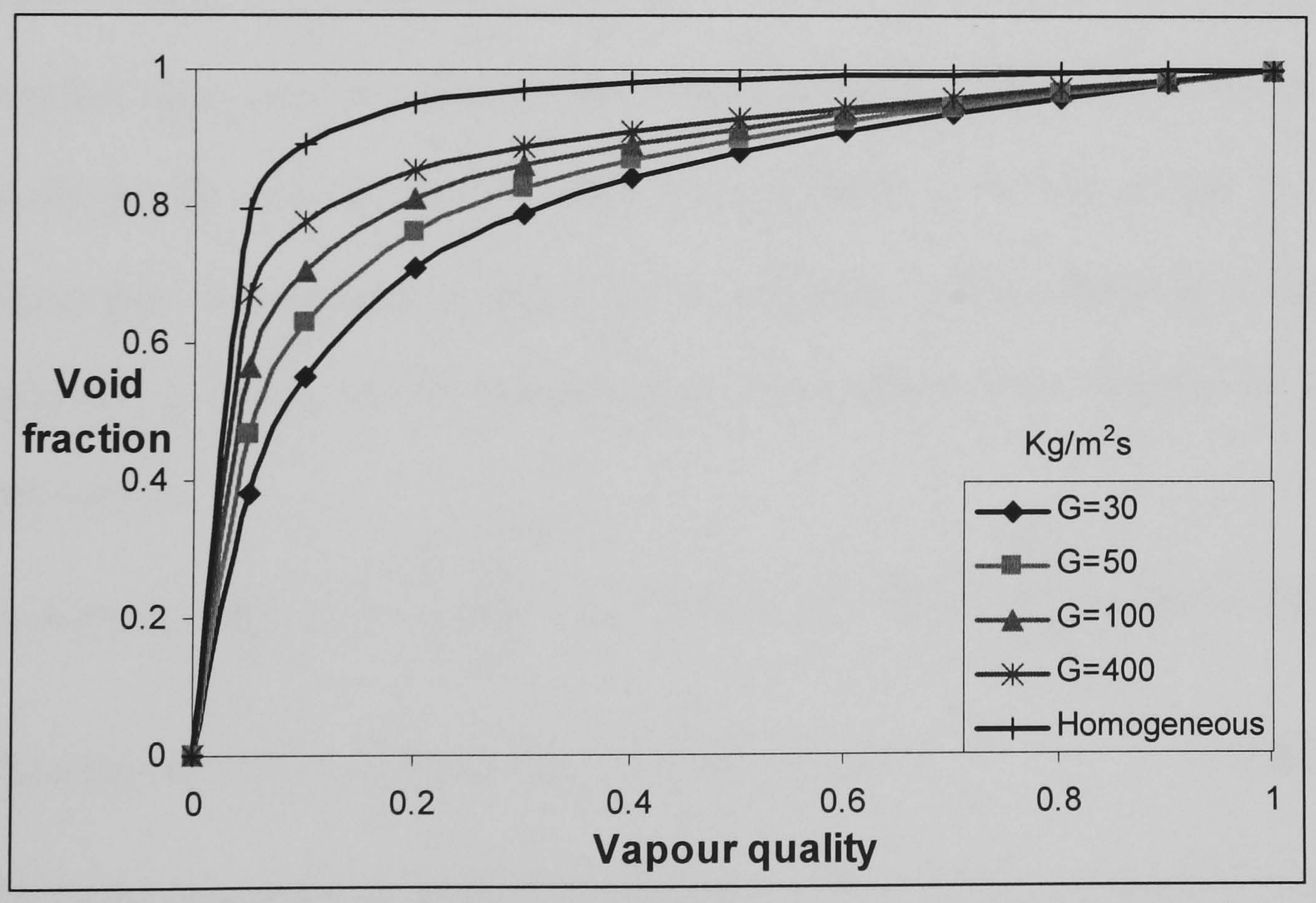

Fig. 6.4 The relationship between vapour void fraction and vapour quality

The Fig. 6.4 shows the void fraction varies with vapour quality and mass flux for R134a under 3.5 bar. It is clear that the vapour phase occupied the main part of the

tube even at low vapour quality due to the huge difference between the densities of two phases. Therefore, the liquid film is relatively thin.

- Dry angle for wavy flow(θ_{dry})

In wavy flow, the liquid phase can not wet the whole tube wall, and then the dry-angle of tube wall should be known prior to the heat transfer calculations. To predict the dry angle for stratified-wavy flow, Kattan (1998) assumed a linear variation of θ_{dry} between the annular and stratified flow transition curves and proposed the following equation:

$$\theta_{dry} = \frac{G_{annular} - G}{G_{annular} - G_{strat}} \theta_{strat} \tag{6.7}$$

Where $G_{annular}$ is the transition mass flow rate shown in Fig. 2, and θ_{strat} is the stratified angle assuming that the flow pattern is strictly stratified as shown in Fig. 3a. To get the value of stratified angle θ_{strat}, as shown in the Fig. 6.3 (a), P_l is the wetted part of the perimeter and P_v is the perimeter which contacts with vapour. Similarly, A_l and A_v are the corresponding cross-sectional areas occupied by liquid and vapour.

Because $A_l = A(1-\varepsilon_V) = \frac{1}{4}\pi d^2(1-\varepsilon_V)$ and $A_l = \frac{1}{8}d^2[(2\pi - \theta_{strat}) - \sin(2\pi - \theta_{strat})]$

Therefore, $\pi(1-\varepsilon_V) = \frac{1}{2}[(2\pi - \theta_{strat}) - \sin(2\pi - \theta_{strat})]$ (6.8)

The above equation is an implicit geometrical expression. To avoid execute iteration, the stratified angle θ_{strat} can be calculated from an approximate expression (Biberg, 1999) proposed by Wojtan (2005 a), and evaluated in term of void fraction (ε_V)

$$\theta_{strat} = 2\pi - 2\{\pi(1-\varepsilon_V) + (1.5\pi)^{(1/3)}[1-2(1-\varepsilon_V) + (1-\varepsilon_V)^{(1/3)} - \varepsilon_V{}^{(1/3)}]$$

$$-\frac{1}{200}(1-\varepsilon_V)\varepsilon_V[1-2(1-\varepsilon_V)][1+4(1-\varepsilon_V)^2+\varepsilon_V{}^2]\} \qquad (6.9)$$

In this research, the formula (6.6) - (6.9) are employed to calculate the dry angle for wavy flow in metal-foam filled tubes, but the annular-wavy transit flow flux ($G_{annular}$) is gained from the experimental results of metal-foam tube, which is shown in Fig. 6.2. In addition, since the stratified flow occurs at very low mass flow rates and is not detected in this study, the G_{strat} is set to zero. Therefore, the final formula used to calculate dry angle for wavy flow in metal-foam tube is:

$$\theta_{dry} = (\frac{G_{annular} - G}{G_{annular}})\theta_{strat} \qquad (6.10)$$

The dry angles calculated by this formula under different condition have a fairly good agreement with the dry angles detected in experimental test by analysing the wall temperature distributions.

- Thickness of liquid layer

Because the liquid layer is very thin, then the thickness of liquid layer can be calculated by:

$$\delta = \frac{A_l}{R(2\pi - \theta_{dry})} = \frac{\pi d(1-\varepsilon_V)}{2(2\pi - \theta_{dry})} \qquad (6.11)$$

For annular and intermittent flows, θ_{dry} =0 because the entire tube wall is always wet.

6.2.3 Local heat transfer coefficient for flow boiling

For flow boiling in a horizontal tube filled with metal foams, convection and nucleate boiling are the two dominant heat transfer mechanisms in vapour zone and liquid zone, respectively. The correlation proposed by Copper (1984) for reduced pressure form of pool boiling (h_{nb}) (Thome, 2004 and Lu, 2002) including the surface roughness of the boiling surfaces as a variable is:

$$h_{nb} = 55\left(\frac{P}{P_{crit}}\right)^{0.12-\log_{10} R_p}\left(-\log_{10}\frac{P}{P_{crit}}\right)^{-0.55} M^{-0.5} q^{0.67} \tag{6.12}$$

This is a dimensional correlation in which the heat transfer coefficient is in W/m^2K, the P_{crit} and M are the critical pressure and molecular weight of the fluid, for R134a, they are 40.6 bar and 102. The q is the heat flux in W/m^2 and R_p is surface roughness in μm. The convection in vapour zone refers to the convective process between the heated solid foam ligaments and the vapour phase, so the correlation developed by Zhukauskas (1987) (adopted as equation 4.13), which is valid for staggered cylinders, is used to estimate the convective heat transfer (h_c).

$$Nu_{sf} = \frac{h_c d_f}{k_f} = \begin{cases} 0.76\,\mathrm{Re}_d^{\,0.4}\,\mathrm{Pr}^{0.37}, (10^0 \le \mathrm{Re}_d \le 4\cdot 10^1) \\ 0.52\,\mathrm{Re}_d^{\,0.5}\,\mathrm{Pr}^{0.37}, (4\cdot 10^1 \le \mathrm{Re}_d \le 10^3) \\ 0.26\,\mathrm{Re}_d^{\,0.6}\,\mathrm{Pr}^{0.37}, (10^3 \le \mathrm{Re}_d \le 2\cdot 10^5) \end{cases} \tag{6.13}$$

6.3 Numerical procedures

The combined energy equations are solved numerically with the SIMPLE (Semi-Implicit Method for Pressure Linked Equations) algorithm. (Patankar, 1980 and Tao, 2001) The FVM (finite volume method) was used to derive the discretization equations. For all of the cases studied, it is evident that a uniform grid of 140×100

used in the r and ω directions can ensure the mesh independence of the solution. The governing equations were solved by using the alternate direction iteration numerical scheme. The iteration is terminated when changes in target variables T_s and T_f are less than 10^{-4} between successive iterations.

6.4 Results and discussions

The overall heat transfer coefficient (h) is the average of local heat transfer coefficients along the tube wall. The local heat transfer coefficient, h_l, is defined as:

$$h_l = \frac{q}{\Delta T} \tag{6.15}$$

where ΔT is the temperature difference between the inner wall surface temperature and fluid saturated temperature and q is heat flux applied to the tube wall. The effects of different parameters on overall heat transfer coefficient are examined in following sections.

6.4.1 Comparison between modelling predictions and experimental data

As discussed in chapter Four, the contact thermal resistance between tube wall and metal foams has significant influence on overall heat transfer performance. It can not be ignored for practical problem. Therefore, the thermal conductivity of 0.1 mm layer of metal foams attached to tube wall is reduced to 200 W/m·K instead of thermal conductivity of copper (370 W/m·K) and the surface roughness is set as 1.4 μm for tube with 40ppi metal foams. The numerical modelling predictions considered contact thermal resistance are presented with the experimental results in Fig. 6.5, which shows that modelling results have reasonable conformity with the experimental results in terms of trend and value. Without considering the contact

thermal resistance, the predictions of heat transfer coefficient will be about 30% higher in value, as shown in Fig. 4 (a), which means that the contact thermal resistance also brings significant influences to two-phase flow.

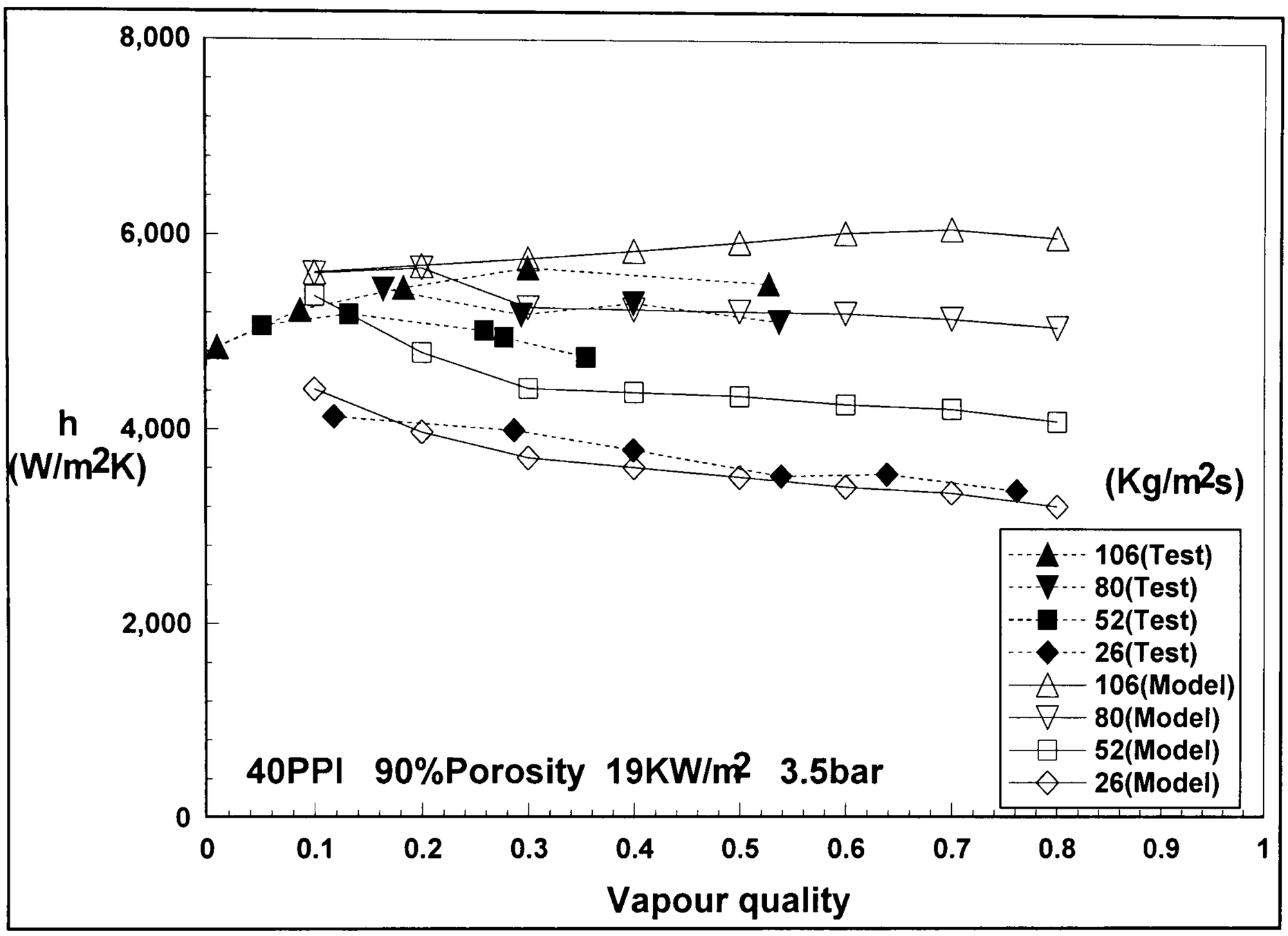

Fig. 6.5 Comparison between experimental data and numerical predictions considered contact thermal resistance.

For the tube with 20 ppi metal foams, the overall heat transfer coefficients predicted by numerical modelling are much higher than the experimental results when the surface roughness is set to the same value as 40PPI foams because the increase of pore size from 40 ppi to 20 ppi may reduce the number of active boiling sites, the difference of the surface roughness between these two kinds of metal foams should be considered. Therefore, in the Fig. 6.6, the surface roughness was set to 0.9 μm to present the difference. It is clearly shown in Fig.6.6 that the predictions of numerical modelling have good agreement with the experiment data. This reveals that the

surface quality is still an important issue for flow boiling heat transfer in metal-foam tube.

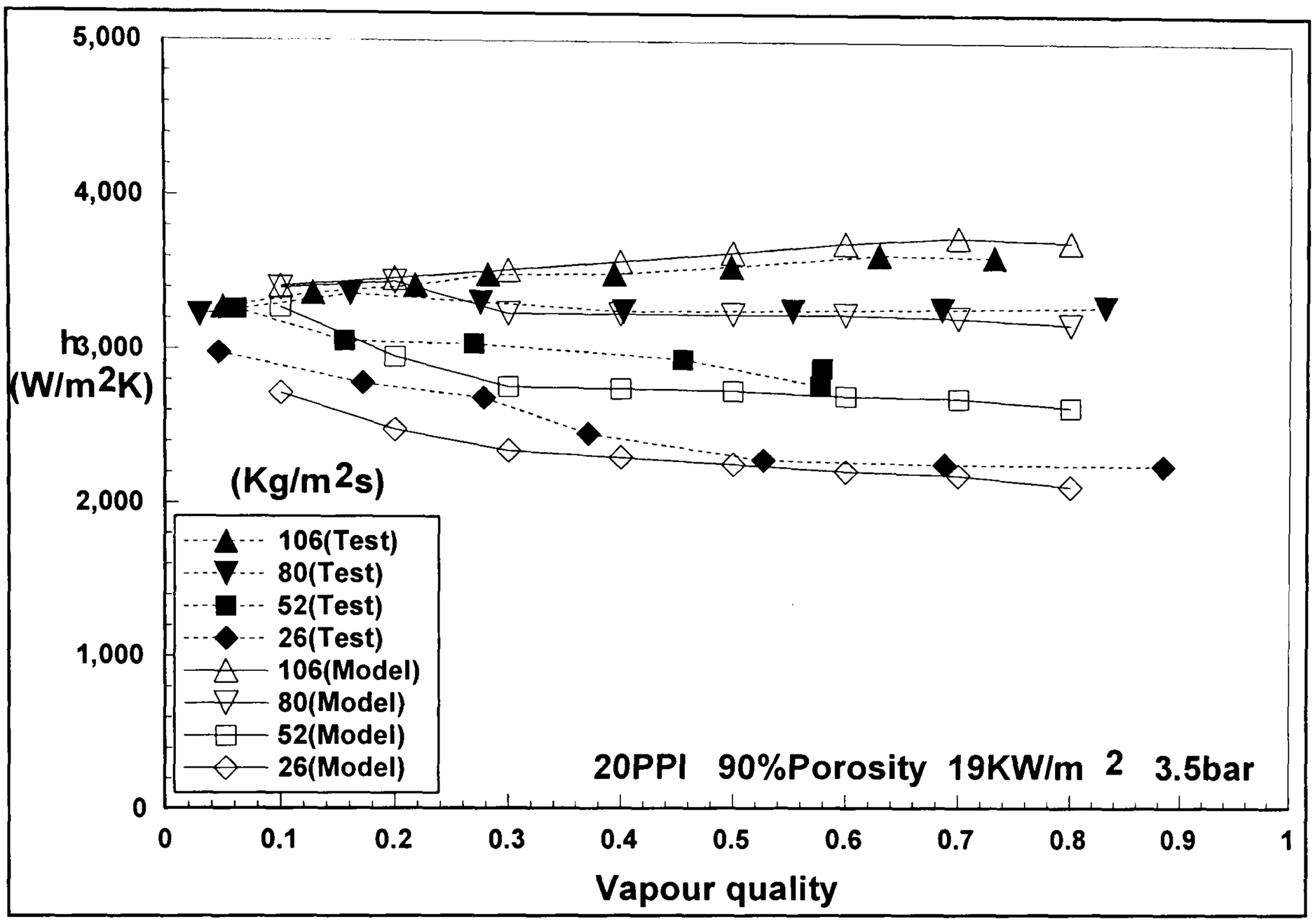

Fig. 6.6 Comparison between experimental data and numerical predictions considered contact thermal resistance and surface roughness, which is set to R_p=0.9 μm for numerical modelling.

6.4.1 Effect of mass flux

The Fig. 6.7 shows the overall heat transfer performance of metal-foam tube increases with the increase of mass flux because the increase of mass flow rate results in higher velocities of both liquid and vapour phases, which enhances the convection heat transfer. Moreover, with higher mass flux, the wavy flow is strengthened and finally transits to annular flow. The boiling heat transfer, which has great heat transfer performance, takes place in larger tube wall area. Both of them enhance the overall heat transfer performance in the tube.

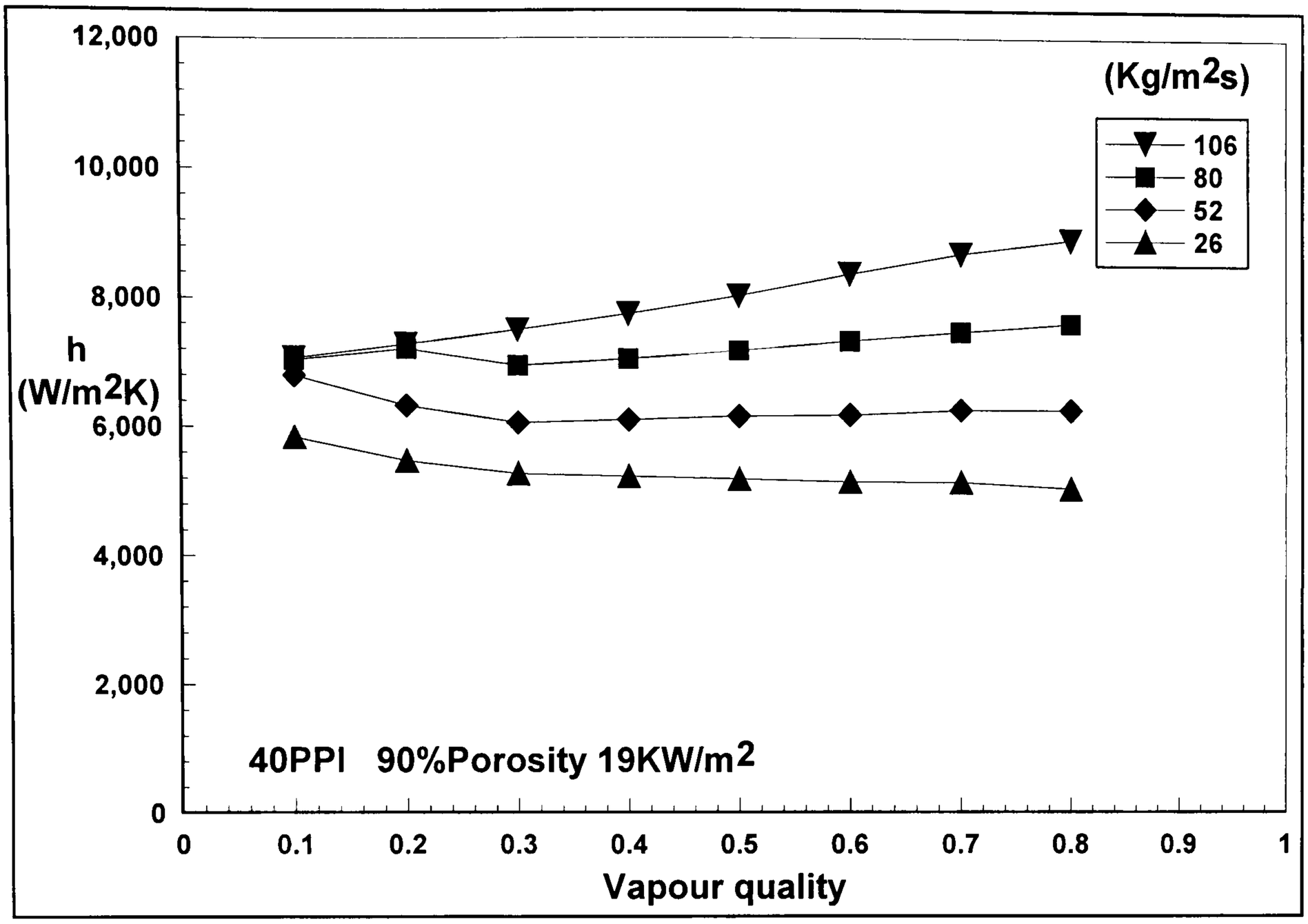

Fig. 6.7 The effect of vapour quality and mass flux on overall heat transfer performance

6.4.2 Effect of vapour quality

The effect of vapour quality on overall heat transfer coefficient depends on the flow patterns, as shown in Fig. 6.7 and the following figures. One interesting observation from the figure is that the heat transfer coefficient exhibits different behaviours as the vapour quality rises. For the low mass flow rate, the heat transfer coefficient becomes smaller as the vapour quality rises. As indicated earlier, the flow pattern should be stratified wavy flow for low mass flow rates, so more metal foam structure and tube wall surfaces are occupied by vapour as the vapour quality rises, and this reduces heat transfer capability. For high mass flow rates, the flow pattern is more like annular flow as the vapour quality rises, so the heat transfer coefficient keeps steady rising, albeit slowly.

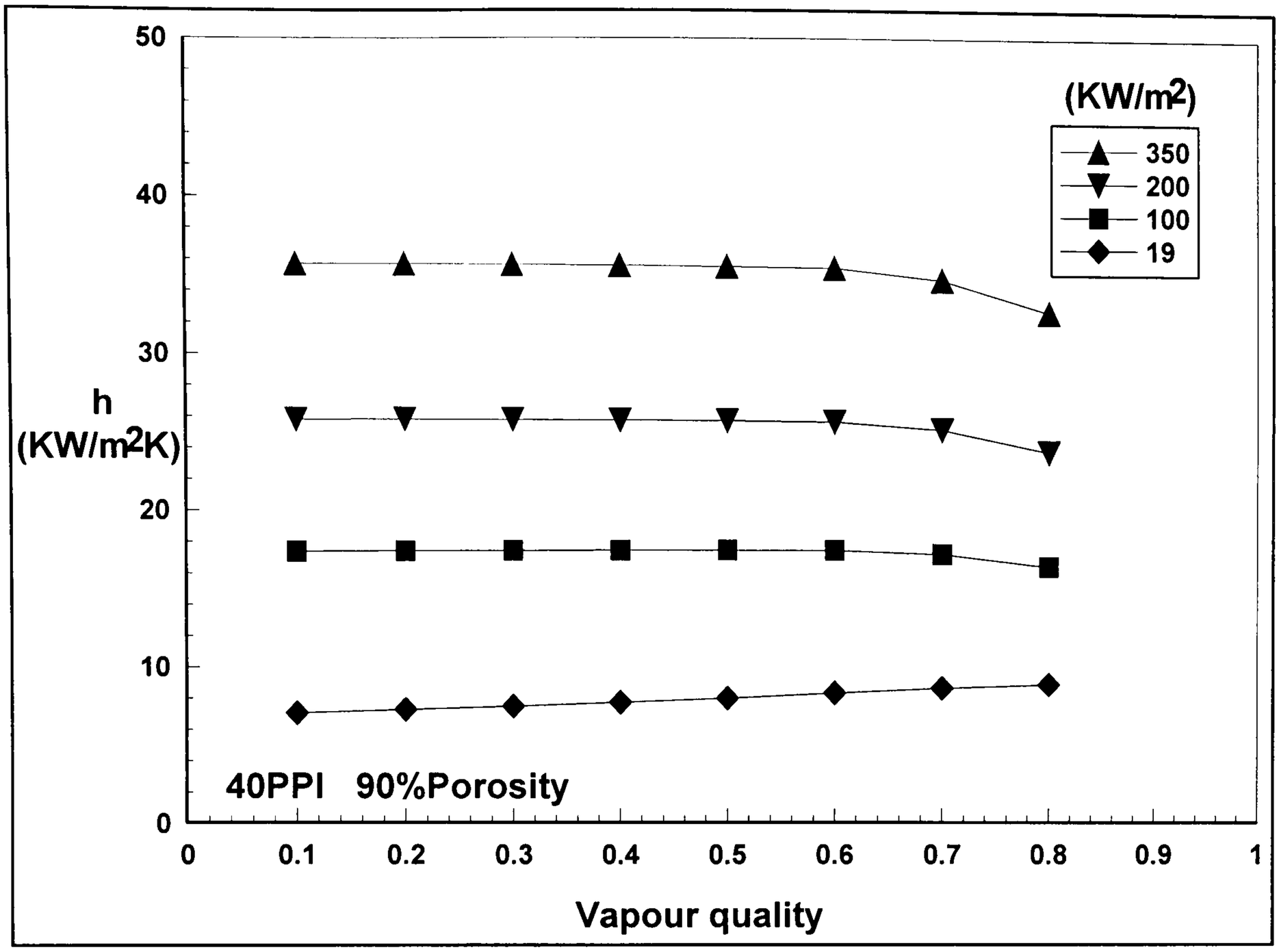

Fig. 6.8The effect of heat flux on overall heat transfer performance

6.4.3 Effect of heat flux

From Fig. 6.8, it can be seen that the overall heat transfer coefficient, especially for lower vapour qualities, is tripled when the heat flux increases from 19 KW/m^2 to 200 KW/m^2. Therefore, it is expected that metal-foam tubes can have great potential on heat transfer improvement particularly for high heat flux. It is expected that metal-foam tubes can have great potential on heat transfer improvement when the heat flux on the wall is extremely high. However, for higher heat flux, the dry out may happen earlier in the annular flow and makes the heat transfer coefficient drop earlier. It is not shown in Fig. 6.8, because this figure is based on the flow pattern drawn for low heat flux. Thus, more experimental work in this area needs to be done for industry application of metal-foam tube.

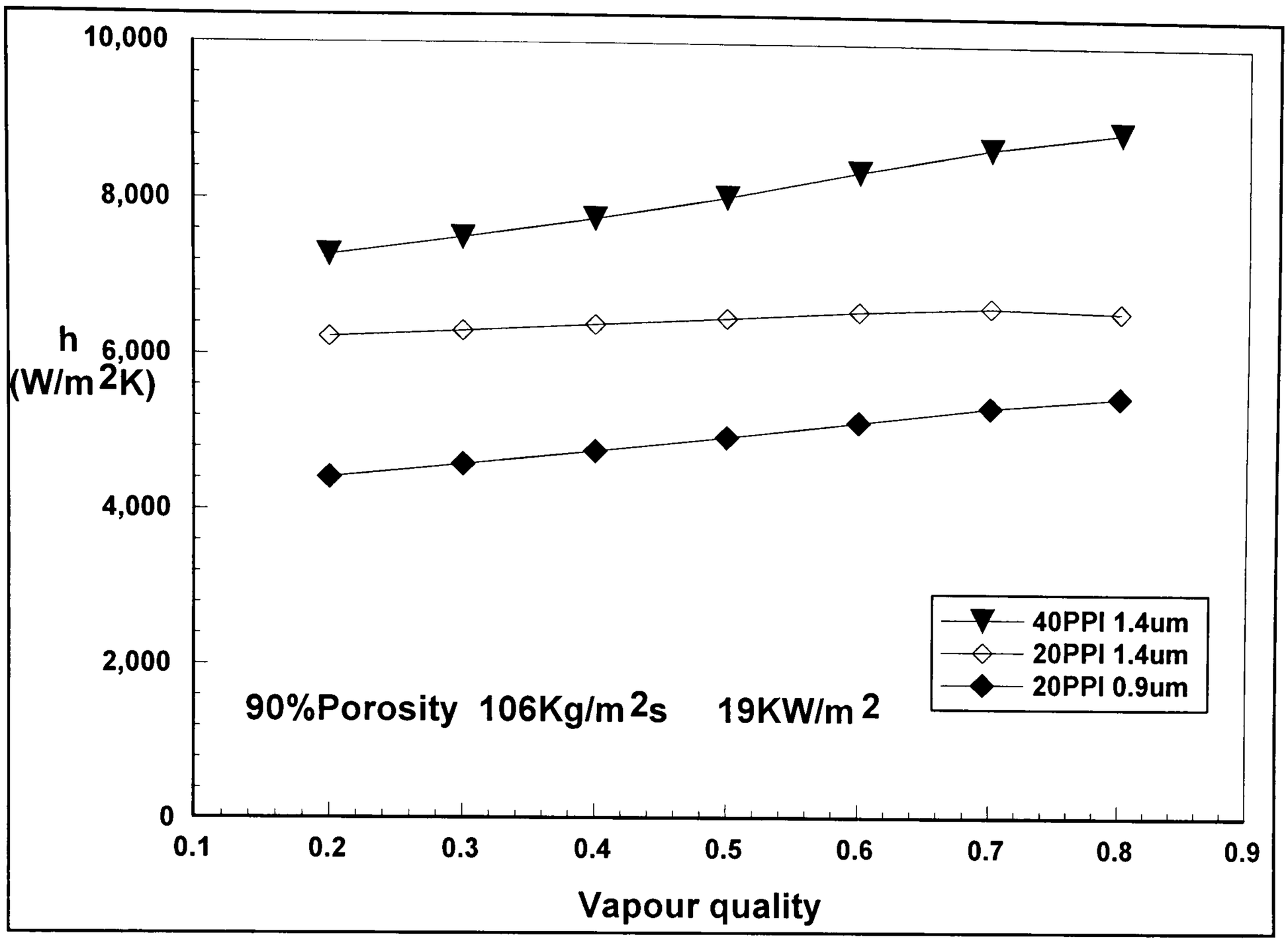

Fig. 6.9 The effect of pore size on overall heat transfer performance

6.4.4 Effect of pore size

It is clearly shown in Fig. 6.9 that the decrease of pore size (increase of pore density PPI: pores per inch) brings huge improvement to overall heat transfer performance of metal-foam tubes due to the increase of heat transfer area and strong flow mixing, especially when vapour quality is high. A metal foam with smaller cell size can provide more surface areas and boiling sites, and also it can enhance the flow mixing and break up the large bubbles, and thereby increasing the heat transfer coefficient. The comparison between upper two lines which assume the two kinds of metal-foam tube have the same surface quality reveals the improvement of overall heat transfer coefficient caused by increased surface areas and mixing. The comparison between

the lower two lines predicted the enhancement of heat transfer performance caused by introducing more boiling sites (surface roughness).

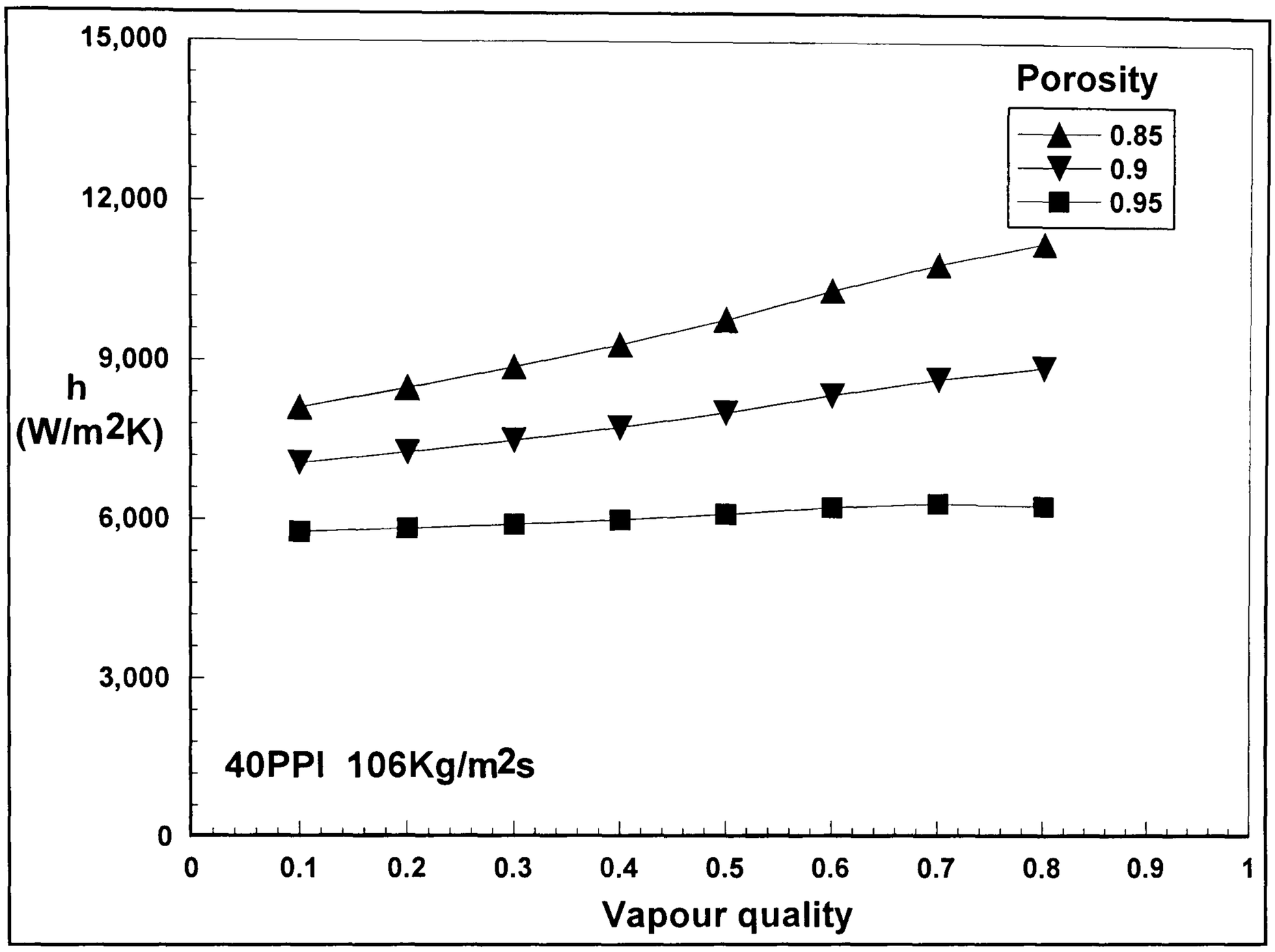

Fig. 6.10 The effect of porosity on overall heat transfer performance

6.4.5 Effect of porosity

The Fig.6.10 shows that the overall heat transfer capability is enhanced by reducing the porosity, as expected. The decrease of porosity leads to more solid foam areas, and this provides more boiling sites and enhance the heat conduction through solid structures, and thereby improving the overall heat transfer.

6.5 Conclusions

In this chapter, the numerical investigation on flow boiling heat transfer in metal-foam tubes has been conducted. The effects of various metal-foam parameters on heat transfer have been examined. The results show that the overall heat transfer

coefficient of the metal-foam tube increases with the increase of relative density (1-porosity), pore density (ppi), mass flux and/or heat flux. The heat transfer coefficient exhibits different behaviours for low and high mass flow rates as the vapour quality rises. The comparison between predictions of numerical modelling and experimental data reveals that higher surface roughness caused by increase of pore density can significantly enhance heat transfer performance for flow boiling in metal-foam tube. The results suggest that the contact thermal resistance (attachment quality) between tube wall and metal foams has significant influence on overall heat transfer performance of metal-foam tube.

Chapter 7 Conclusions and Future Work

7.1 Conclusions

In this thesis the heat transfer performance of metal-foam tubes has been experimentally and theoretically investigated. All the results of experimental test and modelling prediction showed that metal foams have great potential on enhancing forced convection or flow boiling heat transfer. The results are summarised below.

7.1.1 Experimental study for forced convection in metal-foam tubes

The heat transfer performance and flow resistance have been measured for R134a vapour flow in *Porvair* metal-foam tubes. The results show that both the microstructure of metal foams and tube/foam attaching methods (contact thermal resistance) can significantly affect the heat transfer performance. The heat transfer can be enhanced by decreasing the cell size and/or increasing the relative density at the expense of higher flow resistance. Compared to that of plain tubes, the use of metal foams could improve the heat transfer by 5-15 times due to the enhanced surface area density and flow mixing. To examine the effect of different tube/foam attaching methods on heat transfer, a group of metal-foam filled tubes with different methods of attachment have been experimentally tested for R134a superheated vapour flow heat transfer. The results revealed that the attachment method can have a significant effect on heat transfer.

7.1.2 Theoretical study for forced convection in metal-foam tube exchangers

Both analytical and numerical methods have been employed to analyze the forced convection heat transfer performance of metal-foam tubes. The Brinkman-extended Darcy momentum model and the two-equation heat transfer model for porous media

have been adopted for the analytical modelling. From the analytical solutions, the independent parameters that influence heat transfer performance have been identified and their influences investigated. The results show that the use of metal foams leads to significant improvement in heat transfer especially when the heat transfer capability of the fluid itself is low, because the thermal resistance on both solid and fluid sides together determines the overall heat transfer coefficient. It is also shown that for low Reynolds numbers the effect of the thermal conductivity of the foam on heat transfer is quite small and hence cheaper, low thermal conductivity foams can be used. When low thermal conductivity foams are employed the effect of pore density is quite small and thus low pore density foams can be used which also leads to lower pressure drop.

The predictions of numerical modelling which uses the Forchheimer-extended Darcy momentum model on pressure drop have good agreement with the experimental results. They reveal that the form force can not be neglected when the Reynolds number is high. The modelling work also implies that the attachment quality has significant effect on overall heat transfer performance.

The comparison between the two methods which use different momentum equations shows that the differences between the heat transfer performances predicted by both methods are very small when Reynolds number is less than 20000. Then, the analytical method, which use less computer time, was used to study the forced convection heat transfer characteristics in high porosity open-cell metal-foam filled tube heat exchangers. The optimal foam-area ratio for a metal-foam filled counter-flow tube-in-tube heat exchanger was predicted. The study showed that the thermal performance of a metal-foam heat exchanger can be superior to that of conventional finned tube heat exchangers.

7.1.3 Experimental study for flow boiling in metal-foam tubes

For two-phase flow, the flow pattern is an important issue for determining heat transfer performance. Because the tube wall and metal foams are opaque, the wall temperature distributions of tube cross-section were recorded to analyze the flow-boiling situation inside the tube. The flow pattern can be indirectly judged through the recorded cross-sectional wall surface temperature fluctuations and wall-refrigerant temperature difference. A flow pattern map has been established based on these experimental data and been used for modelling work.

The experimental results on flow boiling in horizontal metal-foam tubes showed that the two-phase flow resistance and heat transfer both increase as the pore size decreases for a given porosity. The boiling heat transfer can be enhanced by increasing the vapour quality for high mass flow rates, while the same assumption does not hold for the case of low mass flow rate. This different heat transfer behaviour can be attributed to different flow patterns occurring inside the metal-foam tubes. As the operating pressure increases, the boiling heat transfer at low vapour quality ($x < 0.1$) exhibits similar behaviour to pool boiling heat transfer, namely, the heat transfer is enhanced by increasing the pressure. However the story is different for larger vapour qualities. The flow boiling heat transfer is suppressed to some extent as the pressure increases in high vapour quality. The reason is that the flow velocity (vapour) becomes smaller as the vapour density increases with higher operating pressure.

7.1.4 Numerical study for flow boiling in metal-foam tubes

The flow pattern map constructed from the experimental data for flow boiling in horizontal metal-foam tube has been used to determine the liquid/vapour velocity

profiles in these tubes to simplify the problem. The two-equation heat transfer model for porous media has been employed. The effects of various metal-foam parameters on boiling heat transfer have been investigated. The results show that the overall heat transfer coefficient of the metal-foam tube increases with the increase of relative density (1-porosity), pore density (ppi), mass flux and/or heat flux. The effect of vapour quality on the overall heat transfer performance depends on the flow patterns of flow boiling. The results also suggest that higher surface roughness resulting from increased pore density can significantly enhance heat transfer performance for flow boiling in metal-foam tubes.

7.2 Future work

Based on the analysis of boiling mechanisms, metal-foam tubes may offer significant potential in cases of high wall heat flux as the boiling heat transfer coefficient increases significantly with increased heat flux. Based on the same DNB (Departure of nucleate boiling) point, the critical heat flux on the wall of metal-foam tube is much higher than that of plain tube, which means the metal-foam tube with high heat transfer area density is much safer than plain tube under extreme high heat flux. To demonstrate this, more experimental work on flow boiling under high heat flux needs to be done.

For flow boiling in metal-foam tubes, the heat transfer in the thin liquid layer close to the wall dominates the overall heat transfer performance, while the vapour phase in the bulk area makes only a small contribution to the overall heat transfer but a significant contribution to the pressure drop. Therefore, a metal-foam tube with a hollow centre may combine good heat transfer with low pressure drop. The performance of this type of

tube and the optimal thickness of the metal-foam layer are worth to investigate in future work.

Apart from the study of boiling heat transfer inside metal-foam tubes, condensation in metal-foam filled tube should also be investigated in future wok.

References

Bastarows, A. F., Evans, A.G. and Stone, H. A., 1998, Evaluation of Cellular Metal Heat Dissipation Media, *Technical Report MECH-325*, DEAS, Harvard University.

Bejan, A., 1995, *Convection Heat Transfer, 2nd ed.,* Wiley, New York.

Bhattacharya, A., Calmidi, V. V., and Mahajan, R. L., 2002, Thermophysical properties of high porosity metal foams, *Int. J. Heat Mass Transfer,* Vol. 45, pp. 1017 – 1031.

Biberg, D., 1999, An Explicit Approximation for the Wetted Angle in Two-phase Stratified Pipe Flow, *Canadian J. Chem. Eng.* Vol. 77, pp1221-1224

Boomsma, K., 2002, Metal foams as novel compact high performance heat exchangers for the cooling of electronics, *Ph.D thesis, Swiss Federal Institute of Technology Zurich.*

Boomsma, K. and Poulikakos, D., 2001 a, On the effective thermal conductivity of a three-dimensionally structured fluid-saturated metal foam, *Int. J. Heat Mass Transfer*, Vol. 44, pp. 827 – 836.

Boomsma, K. and Poulikakos, D., 2001 b, The effects of compression and pore size variations on the liquid flow characteristics in metal foams, *ASME J. of Fluids Engineering*, Vol. 124, pp. 263-272.

Boomsma, K., Poulikakos, D. and Zwick, F., 2003, Metal foams as compact high performance heat exchangers, *Mechanics of Materials*, Vol. 35, pp. 1161- 1176.

Browne, M. W. and Bansal, P. K. 1999, "Heat Transfer Characteristics of Boiling Phenomena in Flooded Refrigerant Evaporators", *Applied Thermal Engineering*, Vol. 19, pp. 595-624.

Calmidi, V. V. and Mahajan, R. L., 1999, The effective thermal conductivity of high porosity fibrous metal foams, *ASME J. of Heat Transfer*, Vol. 121, pp. 466 – 471.

Calmidi, V. V. and Mahajan, R. L., 2000, Forced convection in high porosity metal foams, *J. of Heat Transfer*, Vol. 122, pp. 557 – 565.

Chen, J.C., 1966, A Correlation for Boiling Heat Transfer of Saturated Fluids in Convective Flow, *Ind. Eng. Chem. Process Des. Dev.,* Vol.5, No. 3, pp. 322-329.

Chisholm, D., 1983, *Two-phase flow in pipelines and heat exchangers,* George Godwin, London.

Christy, J., 2003, *Chemical Engineering4 – Fluids*, Available From: http://www.see.ed .ac.uk/~johnc/teaching/fluidmechanics4/200304/fluids19/twophase.html [Accessed 20 July 2005]

Collier, J.G. and Thome, J.R. 1996 (3ed.) *Convective Boiling and Condensation*, Clarendon press, Oxford

Ei Hajal, J. Thome, J.R. and Cavallini, A., 2003, Condensation in Horizontal Tubes, Part 2: New Heat Transfer Model Based on Flow Regimes, *Int. J. Heat and Mass Transfer,* Vol. 46 (18) pp3365-3387

ERG Materials and Aerospace Corporation, c2000, *Duocel Foam*, Available From: http://www.ergaerospace.com/duocel_foam.htm [Accessed 25 July 2005]

Fand, R.M., Steinberg, T.E. and Cheng, P., 1986, Natural convection heat transfer from a horizontal cylinder embedded in a porous medium. *Int. J. of Heat and Mass Transfer*, Vol. 29, pp 119-133.

Feldman, A., Marvillet, C. and Lebouche, M., 2000, "Nucleate and Convective Boiling in Plate Fin Heat Exchangers", *Int. J. Heat and Mass Transfer*, Vol. 43, pp. 3433-3442.

Forster, D.E. and Grelf, T., 1950, Heat Transfer to a Boiling Liquid – Mechanism and Correlation, J. Heat Trans., Vol. 81, P. 43

Gungor, K.E. and Winterton, R.H.S., 1986, A General Correlation for Flow Boiling in Tubes and Annuli, *Int. J. Heat Mass Transfer*, Vol. 29, pp.351-358.

Haack, D.P., Lin, C.L. and Speckert, M., 2004, Method of co-forming metal foam articles and articles formed by the method thereof, U.S. Patent 6,706,239, assigned to Porvair PLC (GB).

Hewitt. G.F and Roberts, D.N., 1969, Studies of Two-phase Flow Patterns by Simultaneous X-ray and Flash Photography, AERE-M 2159, HMSO

Holman J.P., *Heat* transfer (7th ed), McGraw-Hill, London, 1992.

Hospell, N. and Mesler, R.B., Deposits Formed Beneath Bubbles During Nucleate Boiling of Radioactive Calcium Sulphate Solution, University of Kansas, Center for Research in Eng. Sci., Sep, 1964.

Hsu, Y.Y, and Graham, R.W., 1976, *Transport Processes in Boiling and Two-phase System*, Hemisphere Pub. Cop.

Hunt, M. L. and Tien, C. L., 1988, Effects of thermal dispersion on forced convection in fibrous media, *Int. J. Heat Mass Transfer*, Vol. 31, pp. 301-309.

Huo, X., Chen,L. Y. S. Tian and T. G. Karayiannis, 2004, "Flow Boiling and Flow Regimes in Small Diameter Tubes", *Applied Thermal Engineering,* Vol 24, n 8-9, pp 1225-39.

Hwang, J. J., Hwang, G. J., Yeh, R. H., and Chao, C. H., 2002, Measurement of interstitial convective heat transfer and frictional drag for flow across metal foams, *J. of Heat Transfer*, Vol. 124, pp.120 – 129.

Kattan, N., Thome, J.R. and Favrat, D., 1998a, Flow Boiling in Horizontal Tubes; Part 1 – Development of a Diabatic Two-Phase Flow Pattern Map, *J. Heat Transfer* 120 (1) pp. 140–147

Kattan, N., Thome, J.R. and Favrat, D., 1998b, Flow Boiling in Horizontal Tubes; Part 2 –New Heat Transfer Data for Five Refrigerants, *J. Heat Transfer* 120 (1) pp. 148–155

Kattan, N., Thome, J.R. and Favrat, D., 1998c, Flow boiling in Horizontal Tubes. Part 3: Development of a new heat transfer model based on flow patterns. *J. Heat Transfer* Vol. 120 (1) pp.156-165

Kim, S. Y., Paek, J. W., and Kang, B. H., 2000, Flow and heat transfer correlations for porous fin in a plate-fin heat exchanger, *J. of Heat Transfer*, Vol. 122, pp. 572 –578.

Kim, S. Y., Kang, B. H., and Kim, J. H., 2001, Forced convection from aluminium foam materials in an asymmetrically heated channel, Vol. 44, *Int. J. Heat Mass Transfer,* Vol. 44, pp. 1451 – 1454.

Kim, S.J. Kim, D. and Lee, D.Y. 2000, On the local thermal equilibrium in microchannel heat sinks, *Int. J. of Heat and Mass Transfer,* Vol. 43, pp. 1735-1748

Kline, S.J. and McClintock, F.A., 1953, Describing Uncertainties in Single-Sample Experiments, *Mechanical Engineering*, pp. 3-8.

Kutateladze, S.S., 1961, Boiling Heat Transfer, *Int. J. Heat Mass Transfer*, Vol. 4, pp.3-45.

Lee, D.Y., and Vafai, K., 1999, Analytical characterization and conceptual assessment of solid and fluid temperature differentials in porous media, *Int. J. of Heat and Mass Transfer*, Vol. 42, PP.423-435.

Lee, Y. C., Zhang, W., Xie, H. and Mahajan, R. L., 1993, Cooling of a FCHIP package with 100 w, 1 cm^2 chip, *Proceedings of the 1993 ASME Int. Elec. Packaging Conf.*, Vol. 1, ASME, New York, pp. 419-423.

Lu, T. J., Stone, H. A. and Ashby, M. F., 1998, Heat transfer in open-celled metal foams, *Acta Mater* Vol. 46, pp. 3619-3635.

Lu, W., Zhao, C. Y. and Tassou, S. A., 2006, Thermal Analysis on Metal-foam Heat Exchangers, I. Metal-foam Pipes, *Int. J. Heat and Mass Transfer,* Vol. 49, pp. 2751-2761.

Lu, Z.Q., 2002, *Two Phase Flow and Boiling Heat Transfer,* Tsinghua, Beijing (in Chinese).

Mandhane, J.M. , Gregory, G.A., and Aziz, K. A flow pattern map for gas-liquid flow in horizontal pipes , *Int. J. of Multiphase Flow*, v 1, n 4, 30 Oct. 1974, p 537-53

Moran, N.J. and Shapiro, H.N., 2000, *Fundamentals of Engineering Thermodynamics*, (4th *ed.),* John Wiley & sons, Inc., New York

More, F.D. and Mesler, R.B., The Measurement of Rapid Surface Temperature Fluctuations During Nucleate Boiling of Water, AICHE J., Vol. 7, pp 620-624, 1961

Nazar, R., Amin, N., Filip, D. and Pop, I., 2003, The Brinkman model for the mixed convection boundary layer flow past a horizontal circular cylinder in a porous medium, *Int. J. of Heat and Mass Transfer* 46, pp. 3167-3178.

Patankar, S.V., 1980, Numerical Heat Transfer and Fluid Flow, Taylar&Francis, USA

Phanikumar, M.S. and Mahajan, R. L. 2002, Non-Darcy natural convection in high porosity metal foams, Int. J. of Heat and Mass Transfer, Vol. 45, pp.3781-3793.

Qu, W. and Mudawar, I., 2003, "Flow Boiling Heat Transfer in Two-Phase Micro-Channel Heat Sinks — I. Experimental Investigation and Assessment of correlation methods", *In. J. Heat and Mass Transfer*, Vol. 46, pp. 2755-2771.

Revellin, R., and Thome, J. R. ,2006, Experimental investigation of R-134a and R-245fa two-phase flow in microchannels for different flow conditions, *International Journal of Heat and Fluid Flow,* Available from: 10.1016/j.ijheatfluidflow.2006.05.009.

Roslinda N., Norsarahaida A., Diana F. and Ioan P., 2003, The Brinkman model for the mixed convection boundary layer flow past a horizontal circular cylinder in a porous medium, *Int. J. of Heat and Mass Transfer,* Vol. 46, pp, 3167-3178

Shah, M.M., 1982, Chart Correlation for Saturated Boiling Heat Transfer: Equations and Further Study, *ASHRAE Trans.,* 1982, Vol.88, Part1, pp.185-196.

Sharp, R.R, The Nature of Liquid Film Evaporation During Nucleate Boiling, NASA TND-1997, Oct 1964.

Shi, M.H., Gan, S.P. and Ma, C.F., 1995, Boiling and Condensation Heat Transfer, *Higher Education Publication*, Beijing (In Chinese).

Snyder, N.W., 1956, Summary of Conference on Bubble Dynamics and Boiling Heat Transfer, JPL Memo 20-137. Cali. Inst. Technology.

Steiner, D. and Taborek, J., 1992, Flow Boiling Heat Transfer in Vertical Tubes Correlated by an Asymptotic Model, *Heat Transfer Engng.,* Vol.13, No.2, pp. 43-69.

Tao, W.Q., 2001, *Numerical Heat Transfer* (2ed.), Xi'an Jiaotong University, Xi'an

Temme, N.M, 1996, *Special Functions An Introduction to the Classical Functions of Mathematical Physics*, Wiley, New York.

Tadrist, L., Miscevic, M., Rahli, O. and Topin, F., 2004, About the use of fibrous materials in compact heat exchangers, *Experimental Thermal and Fluid Science* Vol 28, pp193-199.

Thome, J.R., 2004, *Wolverine Engineering Databook III*, Available from: http://www.wlv.com/products /databook/db3/data/db3ch9.pdf, [Accessed 20th Nov 2007]

Vafai, K. and Tien, C.L., 1981, Boundary and inertia effects on flow and heat transfer in porous media, *Int. J. of Heat and Mass Transfer*, Vol. 24, pp. 195-203

Wakao, N., Kaguei, S. and Funazkri, T., 1979, Effect of fluid dispersion coefficient on particle-to-fluid heat transfer coefficients in packed beds, *Chem. Eng. Sci.,* Vol.34, pp.

Wang, C.Y. and Cheng, P., 1997, Multiphase Flow and Heat Transfer in Porous Media, Hartnett, J.P. and Jr. Irvine, T.F. (ed) *Advance in Heat Transfer*, Academic Press, London.

Wang, X.S., Wang, R.Z. and Wu, J.Y., 2005, Experimental investigation of a new-style double-tube heat exchanger for heating crude oil using solar hot water, *Applied Thermal Engineering* Vol 25 pp1753-1763.

Wojtan, L., Ursenbacher, T. and Thome, J.R. 2005 a, Investigation of Flow Boiling in Horizontal Tubes: Part I – A New Diabatic Two-phase Flow Pattern Map, *Int. J. Heat and Mass Transfer,* Vol. 48, pp2955-2969

Wojtan, L., Ursenbacher, T. and Thome, J.R., 2005 b, Investigation of Flow Boiling in Horizontal Tubes: Part II – Development of a New Heat Transfer Model for Stratified-wavy, Dryout and Mist Flow Regimes, *Int. J. Heat and Mass Transfer*, Vol. 48, pp2970-2985

Yen, T. H., Kasagi, N. and Suzuki, Y., 2003, "Forced Convective Boiling Heat Transfer in Microtubes at Low Mass and Heat Fluxes", *Int. J. Multiphase Flow*, Vol. 29, pp.1771-1792.

Zhao, C.Y., 2003, Case for Support Two-Phase Flow and Heat Transfer in Ultra-Light Metal foams, Proposal for EPSRC fund GR/T24364/01, Brunel University.

Zhao, C.Y., Kim, T., Lu, T.J and Hodson, H.P., 2001, Thermal Transport Phenomena in Porvair Metal Foams and Sintered Beds. Ph.D report, University of Cambridge.

Zhao, C.Y., Kim, T., Lu, T.J. and Hodson, H.P., 2004 a, Thermal transport in high porosity cellular metal foams, *Journal of Thermophysics and Heat Transfer* 18 (n3), pp. 309-317.

Zhao, C.Y. and Lu, T.J. 2002, Analysis of microchannel heat sinks for electronics cooling, *Int. J. of Heat and Mass Transfer*, Vol. 45, pp. 4857-5869

Zhao, C. Y., Lu, T. J. and Hodson, H. P., 2004 b, Thermal Radiation in Metal Foams with Open Cells, *Int. J. Heat and Mass Transfer*, Vol. 47, pp.2927 – 2939.

Zhao, C. Y., Lu, T. J., Hodson, H. P. and Jackson, J. D., 2004 c, The Temperature Dependence of Effective Thermal Conductivity of Open-Celled Steel Alloy Foams, *Materials Science and Engineering*: *A*, Vol. 367, pp. 123-131.

Zhao, C.Y., Lu T.J. and Hodson, H.P., 2005, Natural Convection in Metal Foams with Open cells, *Int. J of Heat and Mass Transfer* Vol. 48, pp. 2452-2463.

Zhao, C. Y., Lu, W. and Tassou, S. A., 2006, Thermal Analysis on Metal-foam Heat Exchangers, II. Tube Heat Exchangers, *Int. J. Heat and Mass Transfer,*Vol. 49, pp. 2762-2770.

Zukauskas, A.A., 1987, Convective heat transfer in cross-flow, *Handbook of Single-Phase Heat Transfer*, Wiley, New York.

Appendices

Appendix A. General solutions of the partial differential equations

For the differential equation of form of $z^2 \cdot \frac{\partial^2 Y}{\partial z} + z \cdot p(z) \cdot \frac{\partial Y}{\partial z} + q(z) \cdot Y = 0$ (A.1),

which is one of the classical functions of mathematical physics (Temme, 1996). One solution of this equation is: $f(z) = z^{\mu} \sum_{n=0}^{\infty} c_n z^n$. Assuming p(z)=1 and q(z)= $-z^2$, dividing both sides by z^2 and simplifying, equation (A1) takes the form,

$$\frac{\partial^2 Y}{\partial z} + \frac{1}{z}\frac{\partial Y}{\partial z} - Y = 0 \qquad \text{(A.2)}$$

which should be solved in this research.

Based on the solution of (A1) the solution of (A2) is:

$$J_0(z) = \sum_{n=0}^{\infty} \frac{1}{(n+v)!n!}\left(\frac{1}{2}z\right)^{2n}. \qquad \text{(A.3)}$$

A second solution of equation (A1) is:

$$f(z) = C \cdot J_0(z)\ln(z) + z^{\mu_2} \sum_{n=0}^{\infty} d_n(z) \cdot z^n \cdot$$

Applying this to equation (A2) we get:

$$Y_0(z) = J_0(z)\ln\left(\frac{1}{2}z\right) + \sum_{n=0}^{\infty} \frac{F_n}{(n+1)!(n+1)!(n+1)}\left(\frac{1}{2}z\right)^{2n+2}, \qquad \text{(A.4)}$$

where, $F_n = \frac{n+1}{n} F_{n-1} - 1$ and $F_0 = -1$

Therefore, the $J_0(z)$ and $Y_0(z)$ are two solutions for equation (A.2).

For $J_1(z) = J_0'(z)$, and $Y_1(z) = Y_0'(z)$, $J_1(z)$ and $Y_1(z)$ can be determined as:

$$J_1(z) = \left(\frac{1}{2}z\right)\sum_{n=0}^{\infty} \frac{1}{(n+v)!n!}\left(\frac{1}{2}z\right)^{2n} \qquad \text{(A.5)}$$

$$Y_1(z)=J_1(z)\ln(\frac{1}{2}z)+\frac{1}{2}\sum_{n=0}^{\infty}\frac{1}{n!n!}(\frac{1}{2}z)^{2n-1}+\frac{1}{2}\sum_{n=0}^{\infty}\frac{F_n}{(n+1)!(n+1)!}(\frac{1}{2}z)^{2n}. \qquad (A.6)$$

Accordingly, the form of the solutions, $(z\cdot J_1(z))'=z\cdot J_0(z)$ and $(z\cdot Y_1(z))'=z\cdot Y_0(z)$ can be obtained.

Appendix B. The solutions for outer section in counter-flow heat exchanger

The same forms of momentum equations and energy balance equations were also used for analysing the velocity distributions and heat transfer in outer section.

$$0 = -\frac{dp}{dz} + \frac{\mu_f}{\varepsilon}\left(\frac{\partial^2 V_z}{\partial r^2} + \frac{1}{r}\frac{\partial V_z}{\partial r}\right) - \frac{\mu_f}{K}V_z \qquad \text{(B.1)}$$

$$0 = k_{se}\left(\frac{\partial^2 T_s}{\partial r^2} + \frac{1}{r}\frac{\partial T_s}{\partial r}\right\} - h_{sf}a(T_s - T_f) \qquad \text{(B.2)}$$

$$\varepsilon\rho_f C_f V_z \frac{dT_f}{dz} = k_{fe}\cdot\left(\frac{\partial^2 T_f}{\partial r^2} + \frac{1}{r}\frac{\partial T_f}{\partial r}\right) + h_{sf}a(T_s - T_f) \qquad \text{(B.3)}$$

For the outer section, when a constant heat flux flow though the interface between inner tube and meat-foam filled channel and the outer boundary is insulated, the boundary conditions are:

When $r=R_1$, $V_z=0$, $T_s = T_f = T_w$, (B.4)

When $r= R_2$, $V_z=0$, $\frac{\partial T_f}{\partial r} = \frac{\partial T_s}{\partial r} = 0$ (B.5)

To make the equations dimensionless, the following variable are used, they are

$Da=K/R_1^2$, $\psi = r/R_1$, $P=\frac{K}{\mu_f u_m}\frac{dp_f}{dz}$, $\theta = \frac{T - T_w}{q_w R_1 / k_{se}}$, $\theta_s = \frac{T_s - T_w}{q_w R_1 / k_{se}}$, $\theta_f = \frac{T_f - T_w}{q_w R_1 / k_{se}}$,

$D=h_{sf}\tilde{a}R_1^2/k_{se}$, $C=\frac{k_{fe}}{k_{se}}$, $U=\frac{u}{u_m}$, where u and u_m are local velocity and mean velocity along axis direction respectively. Then the equations for outer section is changed to

$$U = -P + \frac{Da}{\varepsilon}\left(\frac{\partial^2 U_z}{\partial \psi^2} + \frac{1}{\psi}\frac{\partial U_z}{\partial \psi}\right) \qquad \text{(B.6)}$$

$$0 = \frac{\partial^2 \theta_s}{\partial \psi^2} + \frac{1}{\psi}\frac{\partial \theta_s}{\partial \psi} - D(\theta_s - \theta_f) \qquad \text{(B.7)}$$

$$2U\left(\frac{1}{\left(\frac{R_2}{R_1}\right) - 1}\right) = C\cdot\left(\frac{\partial^2 \theta_f}{\partial \psi^2} + \frac{1}{\psi}\frac{\partial \theta_f}{\partial \psi}\right) + D(\theta_s - \theta_f) \qquad \text{(B.8)}$$

Boundary conditions are changed to:

$\psi=1$, $U = \theta_s=\theta_f=0$ (B.9)

$$\psi=R_2/R_1,\ U=0,\ \frac{\partial\theta_s}{\partial\psi}=\frac{\partial\theta_f}{\partial\psi}=0 \tag{B.10}$$

The solutions for outer section were carried out as :

- The velocity solution

$$U=P\left(N_1\cdot J_0\left(\sqrt{\frac{\varepsilon}{Da}}\psi\right)+N_2\cdot Y_0\left(\sqrt{\frac{\varepsilon}{Da}}\psi\right)\right)-P, \tag{B.11}$$

Where,

$$P=\frac{(R_2/R_1)^2-1}{2\sqrt{\frac{Da}{\varepsilon}}\left(N_1\left(\frac{R_2}{R_1}\cdot J_1\left(\sqrt{\frac{\varepsilon}{Da}}\frac{R_2}{R_1}\right)-J_1\left(\sqrt{\frac{\varepsilon}{Da}}\right)\right)+N_2\left(\frac{R_2}{R_1}Y_1\left(\sqrt{\frac{\varepsilon}{Da}}\frac{R_2}{R_1}\right)-Y_1\left(\sqrt{\frac{\varepsilon}{Da}}\right)\right)\right)-\left(\frac{R_2}{R_1}\right)^2+1} \tag{B.12}$$

The friction factor can be written as

$$f=\frac{\Delta\langle p\rangle D_H}{L\rho_f u_m^2/2}=\frac{2\mu_f}{K\rho_f u_m}P\cdot D_H=\frac{2PD_H^2}{K\cdot\mathrm{Re}} \tag{B.13}$$

$$\text{Where } D_H=4\pi(R_2^2-R_1^2)/(2\pi(R_2+R_1))=2(R_2-R_1) \tag{B.14}$$

- The temperature solutions for solid and fluid

$$\theta_s=\frac{2P}{\left(\frac{R_2}{R_1}\right)^2-1}\left(-\frac{1}{4}\psi^2+N_3\ln\psi+N_4+N_1\frac{Da}{\varepsilon}J_0\left(\sqrt{\frac{\varepsilon}{Da}}\psi\right)+N_2\frac{Da}{\varepsilon}Y_0\left(\sqrt{\frac{\varepsilon}{Da}}\psi\right)\right)-C\theta_f \tag{B.15}$$

$$\theta_f=\frac{2P}{C+1}\left(\frac{1}{\left(\frac{R_2}{R_1}\right)^2-1}\left(-\frac{1}{4}\psi^2+N_3\ln\psi+N_4+\left(A+\frac{Da}{\varepsilon}\right)\left(N_1J_0\left(\sqrt{\frac{\varepsilon}{Da}}\psi\right)+N_2Y_0\left(\sqrt{\frac{\varepsilon}{Da}}\psi\right)\right)\right.\right.$$
$$\left.\left.-\left(N_5J_0\left(\sqrt{\frac{(C+1)D}{C}}\psi\right)+N_6Y_0\left(\sqrt{\frac{(C+1)D}{C}}\psi\right)\right)+B-A\right)\right) \tag{B.16}$$

Where $A=\frac{1}{\left(C\cdot\frac{\varepsilon}{Da}-(C+1)\cdot D\right)}$ and $B=\frac{C}{(C+1)\cdot D\cdot\left(C\cdot\frac{\varepsilon}{Da}-(C+1)\cdot D\right)}$,

$$N_1=\frac{Y_0(\sqrt{\frac{\varepsilon}{Da}})-Y_0(\sqrt{\frac{\varepsilon}{Da}}\frac{R_2}{R_1})}{J_0(\sqrt{\frac{\varepsilon}{Da}}\frac{R_2}{R_1})\cdot Y_0(\sqrt{\frac{\varepsilon}{Da}})-Y_0(\sqrt{\frac{\varepsilon}{Da}}\frac{R_2}{R_1})\cdot J_0(\sqrt{\frac{\varepsilon}{Da}})}$$

$$N_2=\frac{J_0(\sqrt{\frac{\varepsilon}{Da}})-J_0(\sqrt{\frac{\varepsilon}{Da}}\frac{R_2}{R_1})}{Y_0(\sqrt{\frac{\varepsilon}{Da}}\frac{R_2}{R_1})\cdot J_0(\sqrt{\frac{\varepsilon}{Da}})-J_0(\sqrt{\frac{\varepsilon}{Da}}\frac{R_2}{R_1})\cdot Y_0(\sqrt{\frac{\varepsilon}{Da}})}$$

$$N_3=\frac{R_2}{R_1}(\frac{1}{2}\frac{R_2}{R_1}-\frac{Da}{\varepsilon}(N_1J_1(\sqrt{\frac{\varepsilon}{Da}}\frac{R_2}{R_1})+N_2Y_1(\sqrt{\frac{\varepsilon}{Da}}\frac{R_2}{R_1}))$$

$$N_4=\frac{1}{4}-\frac{Da}{\varepsilon}(N_1J_0(\sqrt{\frac{\varepsilon}{Da}})+N_2Y_0(\sqrt{\frac{\varepsilon}{Da}})$$

$$N_5=\frac{B\cdot Y_1(\sqrt{\frac{(C+1)D}{C}}\frac{R_2}{R_1})-N_7\cdot Y_0(\sqrt{\frac{(C+1)D}{C}})}{J_0(\sqrt{\frac{(C+1)D}{C}})\cdot Y_1(\sqrt{\frac{(C+1)D}{C}}\frac{R_2}{R_1})-J_1(\sqrt{\frac{(C+1)D}{C}}\frac{R_2}{R_1})\cdot Y_0(\sqrt{\frac{(C+1)D}{C}})}$$

$$N_6=\frac{B\cdot J_0(\sqrt{\frac{(C+1)D}{C}})-N_7\cdot J_1(\sqrt{\frac{(C+1)D}{C}}\frac{R_2}{R_1})}{J_0(\sqrt{\frac{(C+1)D}{C}})\cdot Y_1(\sqrt{\frac{(C+1)D}{C}}\frac{R_2}{R_1})-J_1(\sqrt{\frac{(C+1)D}{C}}\frac{R_2}{R_1})\cdot Y_0(\sqrt{\frac{(C+1)D}{C}})}$$

$$N_7=\sqrt{\frac{\varepsilon}{Da}\frac{C}{(C+1)D}}\cdot A\cdot(N_1J_1(\sqrt{\frac{\varepsilon}{Da}}\frac{R_2}{R_1})+N_2Y_1(\sqrt{\frac{\varepsilon}{Da}}\frac{R_2}{R_1}))$$

- Overall Nusselt number

For the outer section between inner tube and outer tube filled with metal foams, the overall heat coefficient $\bar{h}$ is

$$\bar{h_o}=\frac{q_w}{T_{w(x)}-T_{f,b(x)}}=-\frac{k_{se}}{\theta_{f,b(x)}\cdot R_1} \qquad \text{(B.17)}$$

Then the overall Nusselt number is

$$\overline{Nu}_o=\frac{\bar{h_o}}{k_f}D_H=-\frac{k_{se}}{k_f\theta_{f,b}}\frac{D_H}{R_1} \qquad \text{(B.18)}$$

where $D_H = 2(R_2 - R_1)$ and $\theta_{f,b(x)}$ is defined as above, then

$$\theta_{f,b} = \frac{T_{f,b(x)} - T_{w(x)}}{q_w R_1 / k_{se}} = \frac{\int_0^{2\pi} \int_{R_1}^{R_2} U\theta_f \psi d\psi d\vartheta}{\int_0^{2\pi} \int_{R_1}^{R_2} U\psi d\psi d\vartheta} = 2\int_{R_1}^{R_2} U\theta_f \psi d\psi \qquad \text{(B.19)}$$

Appendix C: Setup Procedures and wiring charts for key equipments and sensors

C. 1. PID controller:

A: Temperature control:

Input: T type thermocouple between Pre-heater (heater 1~4) and Heater B (Heater 5~8)

Output: on/off to Heater B (Heater 5~8)

Rear terminal wiring: 4 (-) and 5 (+) for thermocouple is shown in Fig. C1

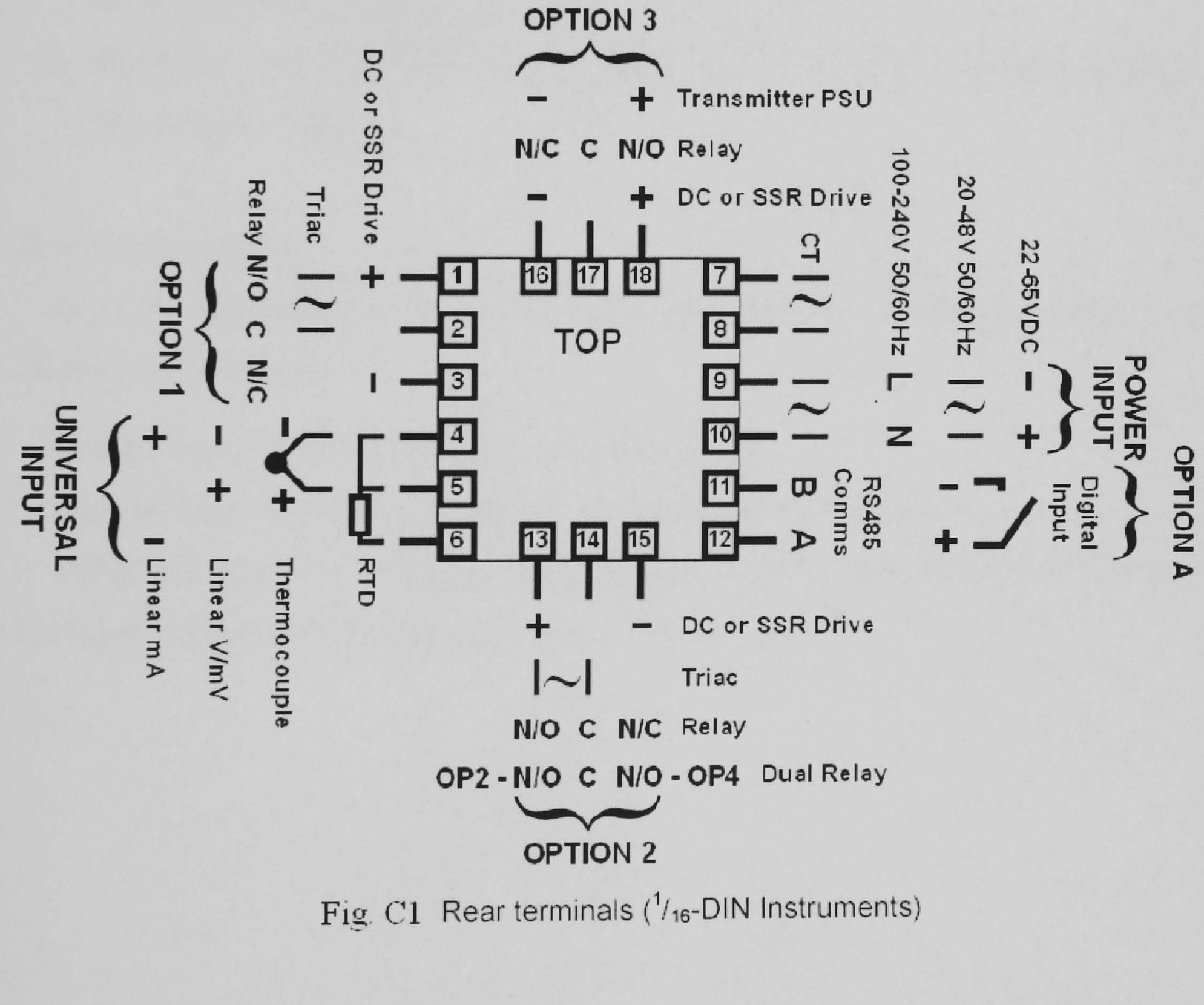

Fig. C1 Rear terminals ($^{1}/_{16}$-DIN Instruments)

Set up and operate the PID controller:

The control panel is shown in Fig. C2.

1) Hold down ↺ and press △ to select mode.
2) Press △ or ▽ to choose the required mode, press ↺ to enter.

Fig. C2 Front panel

3) Configuration: choose "ConF" and press ↻, as step 2, press △ to enter 20 as unlock code, then press ↻ to proceed. Choose "tC" for T type thermocouple at range –240~400 °C by press △ or ▽. Press AUTO MAN to accept the change, otherwise parameter will revert to previous value. Press ↻ to scroll through the parameters (see manual), then set and accept the required value. Finally, hold down ↻ and press △ to exit (or select mode).
4) Setup: choose "SEtP" and press ↻, as step 2, press △ to enter 10 as unlock code, then press ↻ to proceed. The MAN LED will light while in Setup mode. Press ↻ to scroll through the parameters (see manual), then press △ or ▽ to set the required value (e.g. "SP" for Set point valve). Finally, hold down ↻ and press △ to exit (or select mode).
5) Operation: choose "OPtr" and press ↻, as step 2, the values of input signal and set-point will be display.

B: Pressure control:

Input: 4~20mA current from pressure transducer between Pre-heater (heater 1~4) and Heater B (Heater 5~8)

Output: on/off to Heater A (heater in R134a tank)

Rear terminal wiring: 4 (+) and 6 (-) for linear mA (4~20mA)

Setup and operation: Same as PID controller A except choosing "4_20" instead "tC" for input type and set the range between 4~20 mA.

C. 2. ACS140 Frequency Converter for magnetic pump control

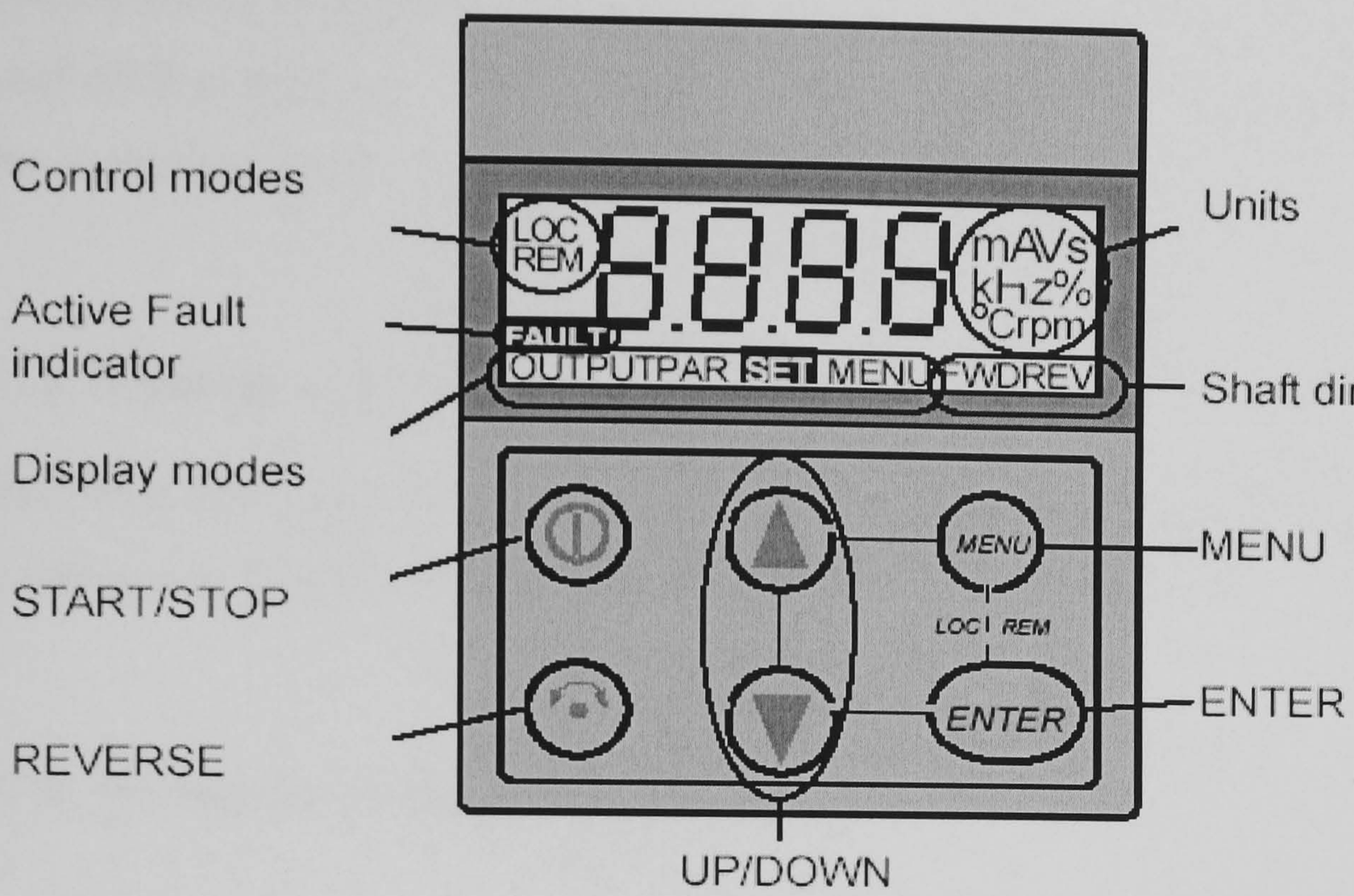

Fig. C3 Front panel for ACS140 converter

Setup and operation:

1) The very first time the drive is powered up, it is controlled from the Control Terminals (remote control, **REM**).
2) Pressing and holding the MENU and ENTER buttons down simultaneously until **Loc** or later **LCr** is displayed, then the ACS140 is controlled from the control panel when the drive is in local control (**LOC**). If the buttons are released while **Loc** is displayed, the panel frequency reference is set to the current external reference and the drive is stopped. When **LCr** is displayed, the current run/stop status and the frequency reference are copied from the user I/O.
3) Press the UP or DOWN button to toggle between output frequency and output current.
4) To set the output frequency in local control (**LOC**), press ENTER. Pressing the UP/DOWN buttons changes the output immediately. Press ENTER again to return to **OUTPUT** display.
5) Change the shaft direction by pressing the REVERSE button. FWD or REV is visible to indicate that shaft direction is forward or reverse.
6) Start and stop the drive by pressing the START/STOP button.

Operation process:

Press ENTER to view the parameter value. To set a new value, press and hold ENTER until **SET** is displayed. Press the UP or DOWN button to change the value for setting the parameter value.

C.3. Pressure control switch for compressor.

Set 20bar for high pressure cut out and 1bar for low pressure cut out to protect the compressor. Set 3bar for cut in the compressor.

C.4. Wiring for pressure transducers:

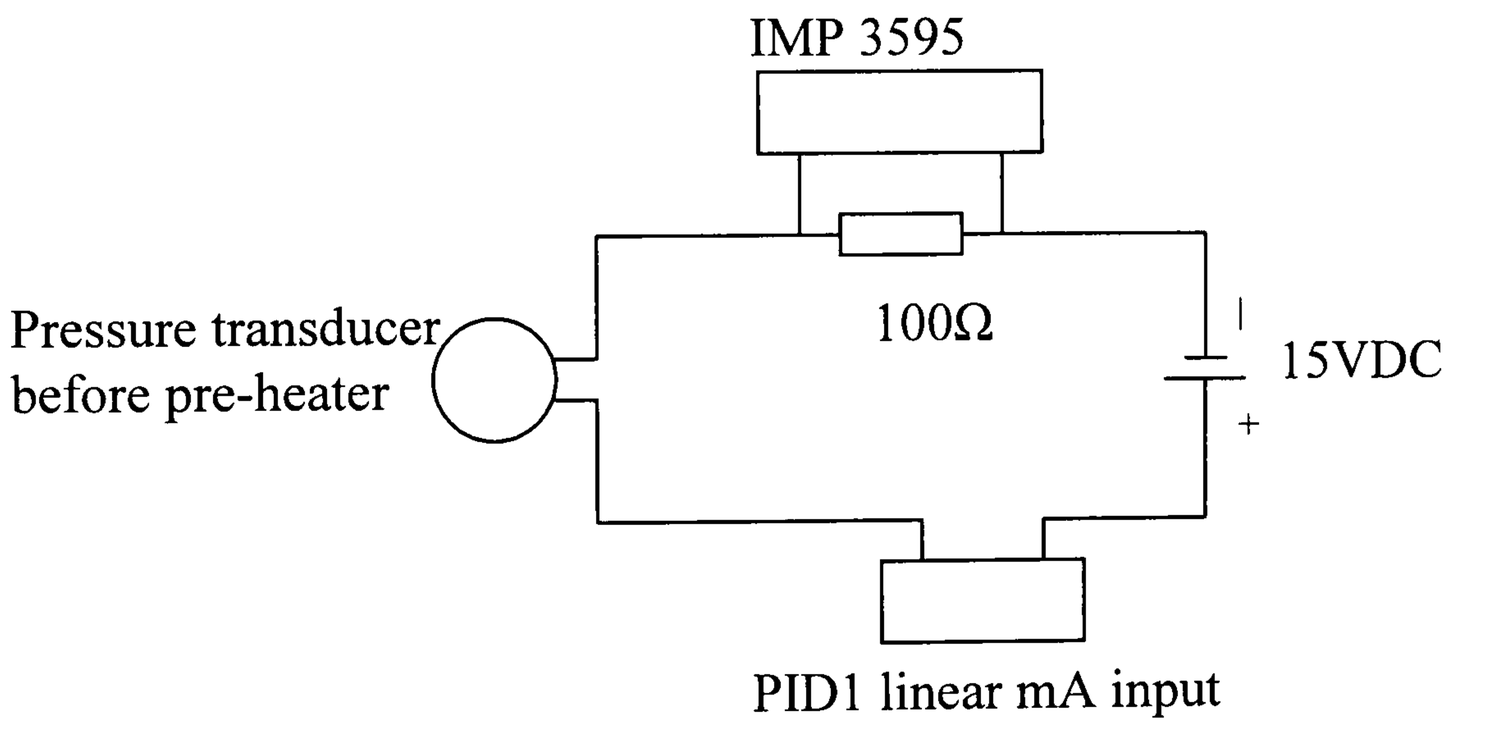

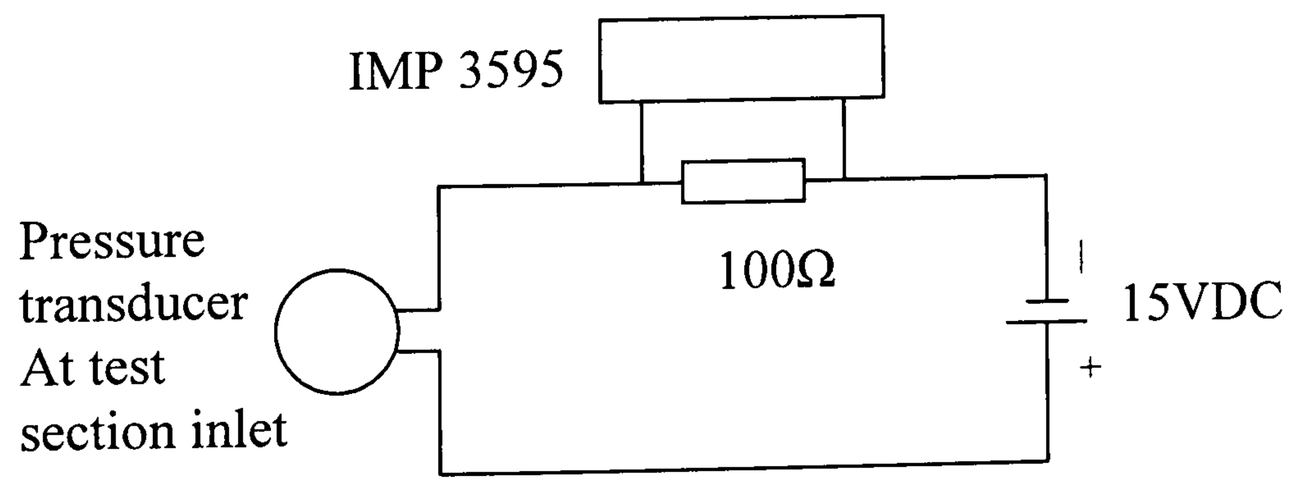

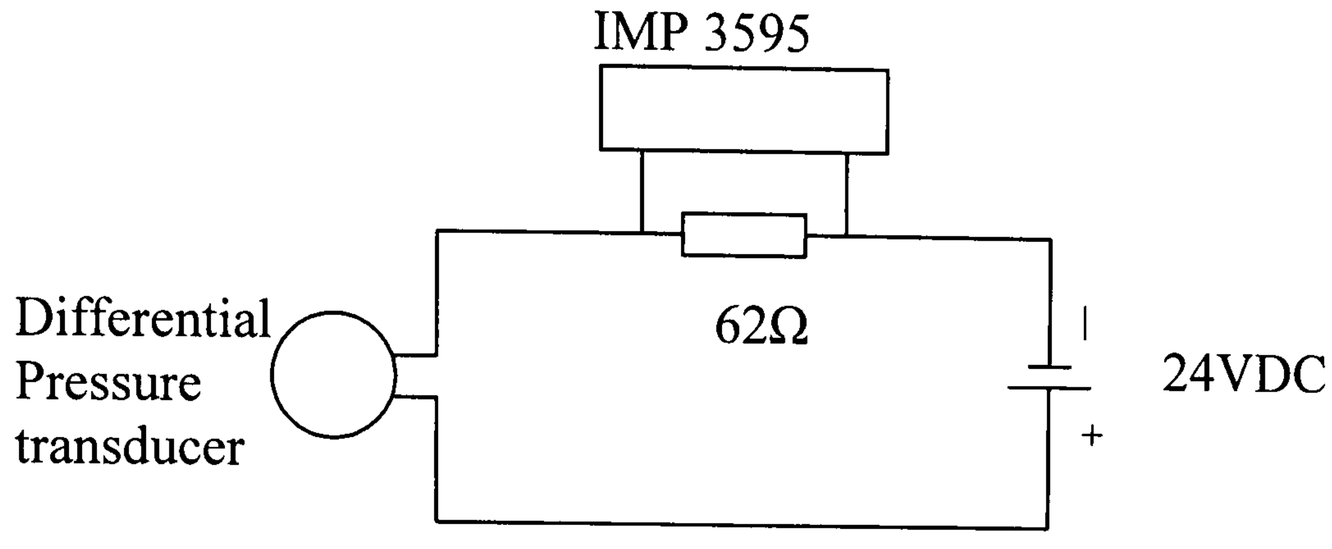

C.5. Wiring for compressor and fans:

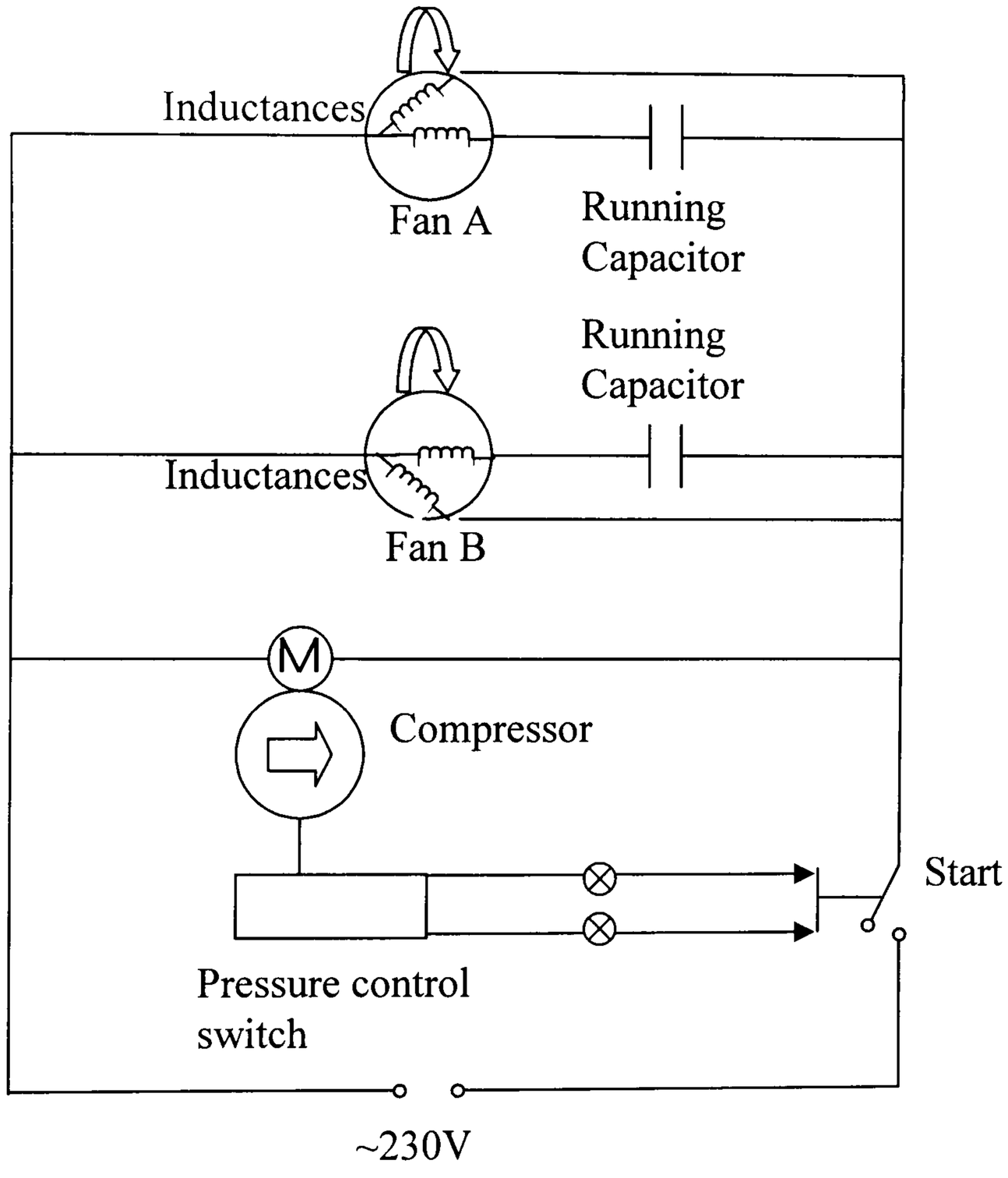

C.6. Wiring for mass flow meters:

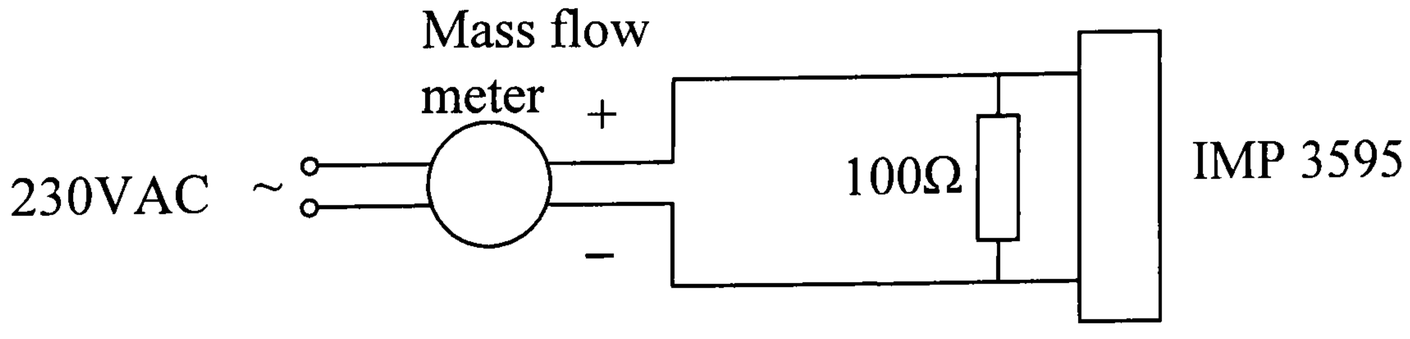

C.7. Wiring for expansion valve:

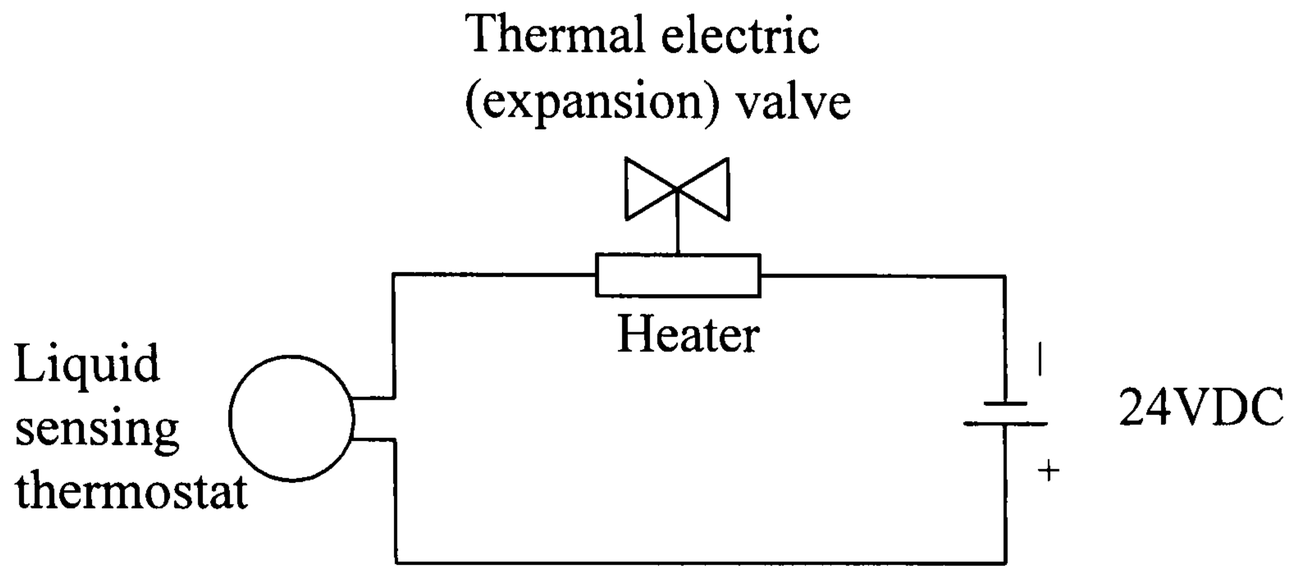

Appendix D: Wall temperature varying with time in flow boiling heat transfer

D.1 Wall temperature variation of the tube with 90% porosity, 20PPI metal foams

a) Wall temperature variation when mass flux is 26 kg/m^{2}s, heat flux is 19 KW/m^2 and pressure at 3.5 bar with 90% porosity, 20PPI metal foams

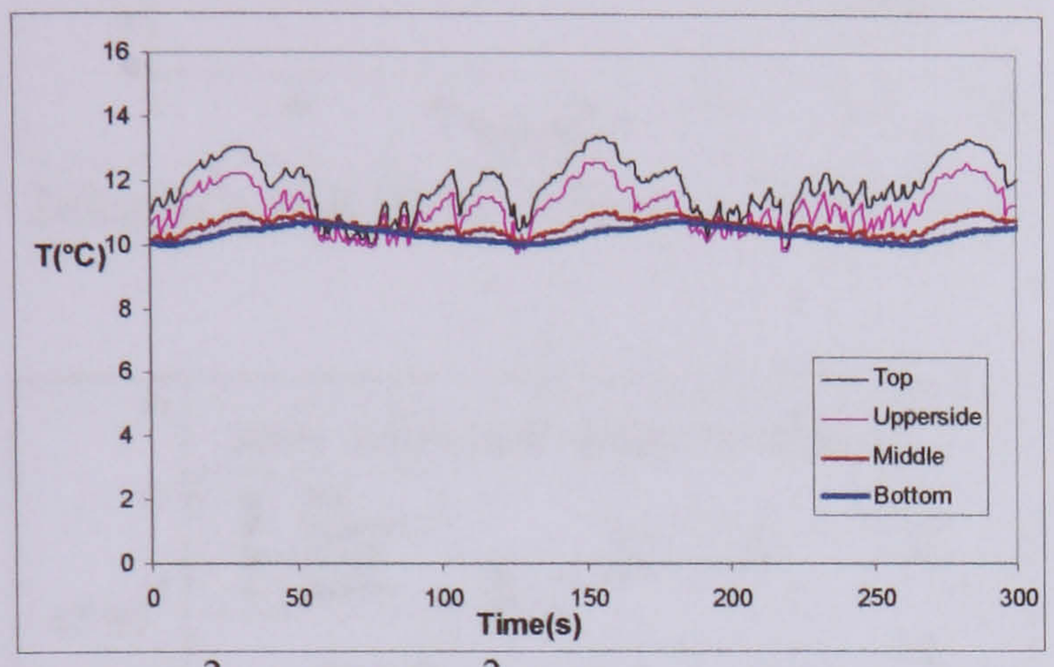

26kg/m^{2}s 19KW/m^2 3.5bar x=0.05

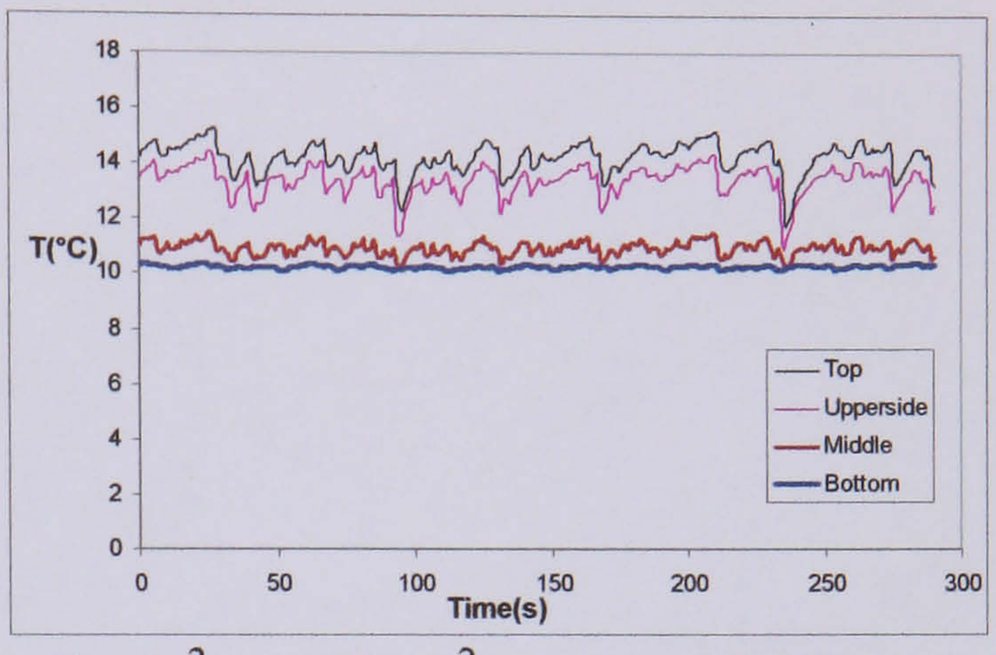

26kg/m^{2}s 19KW/m^2 3.5bar x= 0.18

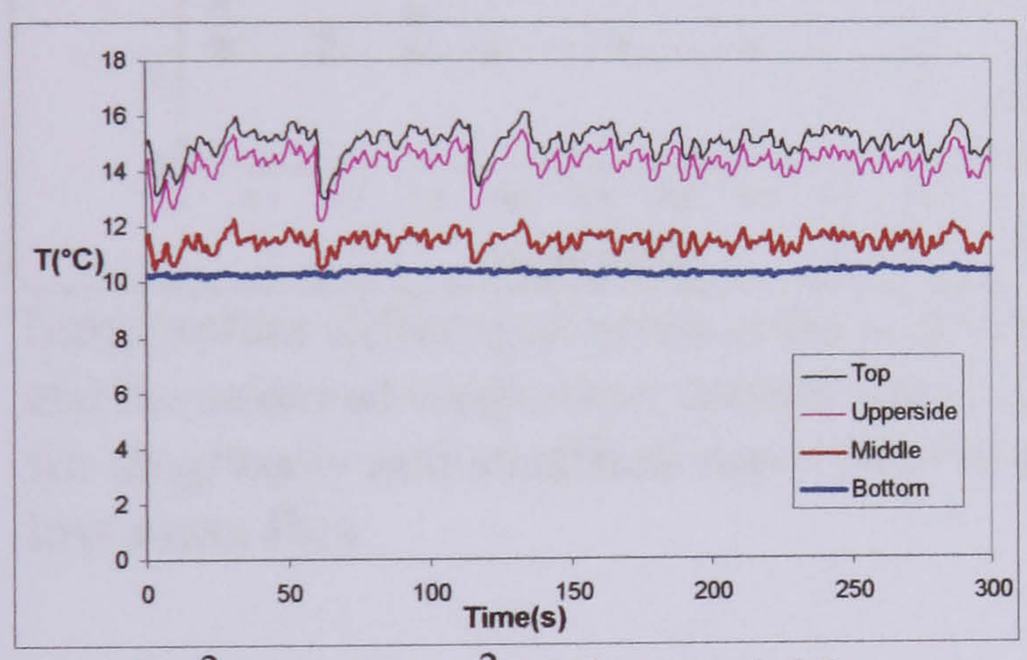

26kg/m^{2}s 19KW/m^2 3.5bar x=0.28

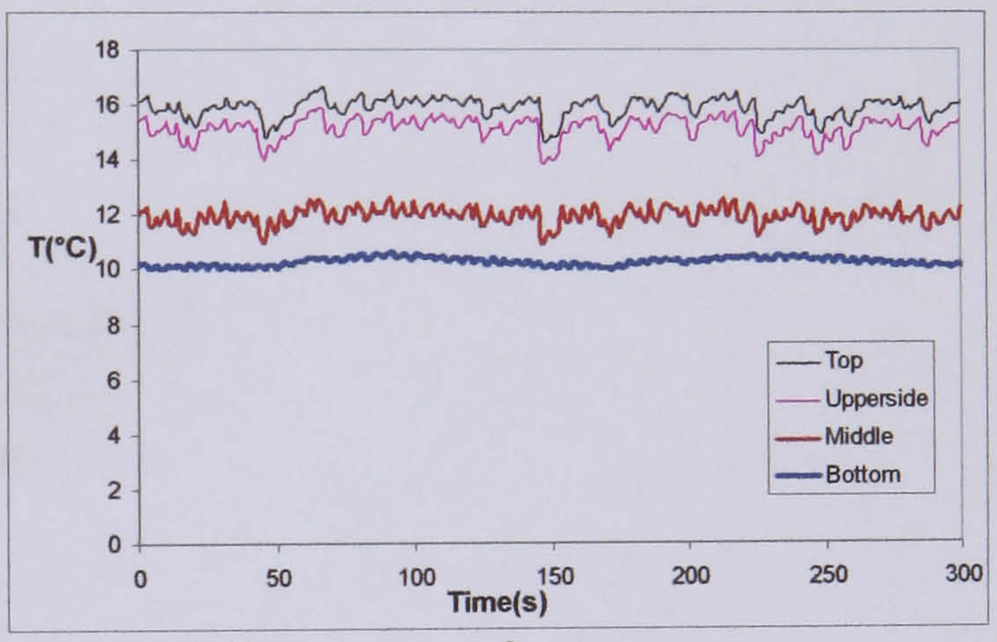

26kg/m^{2}s 19KW/m^2 3.5bar x=0.38

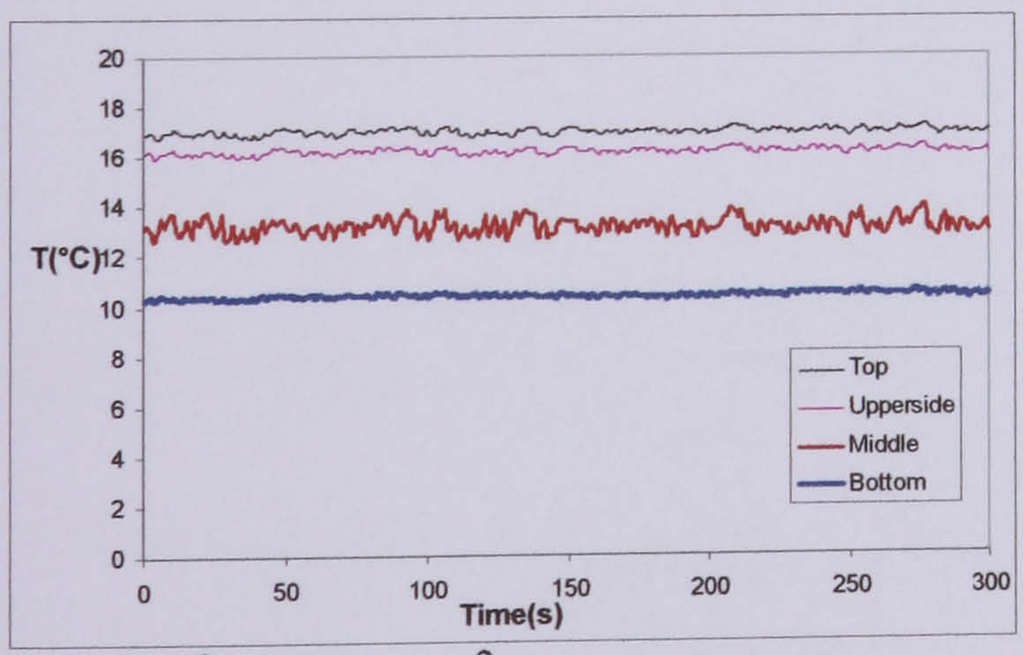

26kg/m^{2}s 19KW/m^2 3.5bar x=0.53

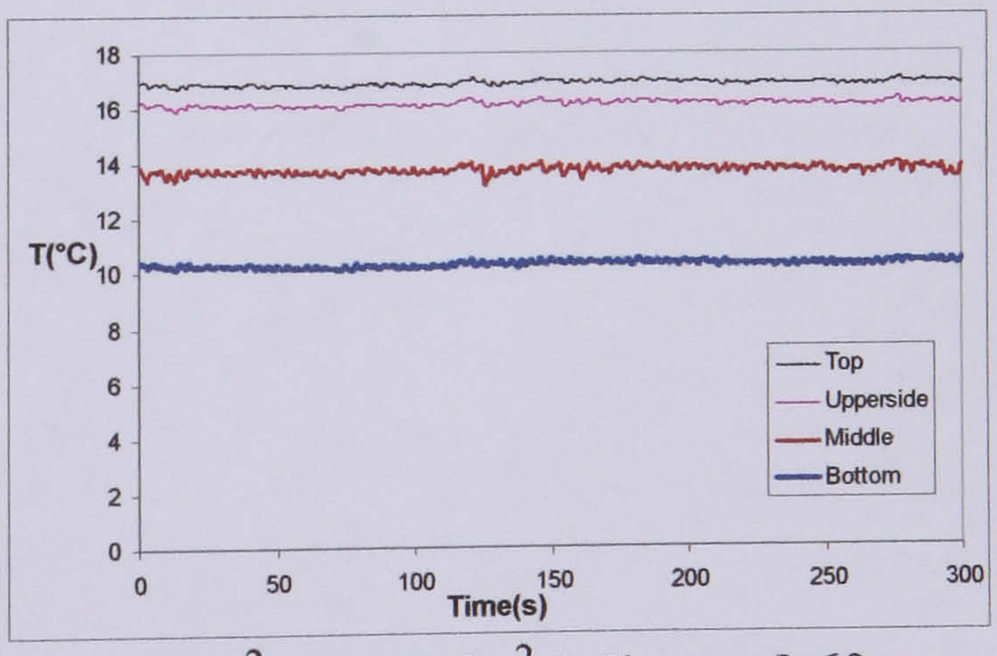

26kg/m^{2}s 19KW/m^2 3.5bar x=0.69

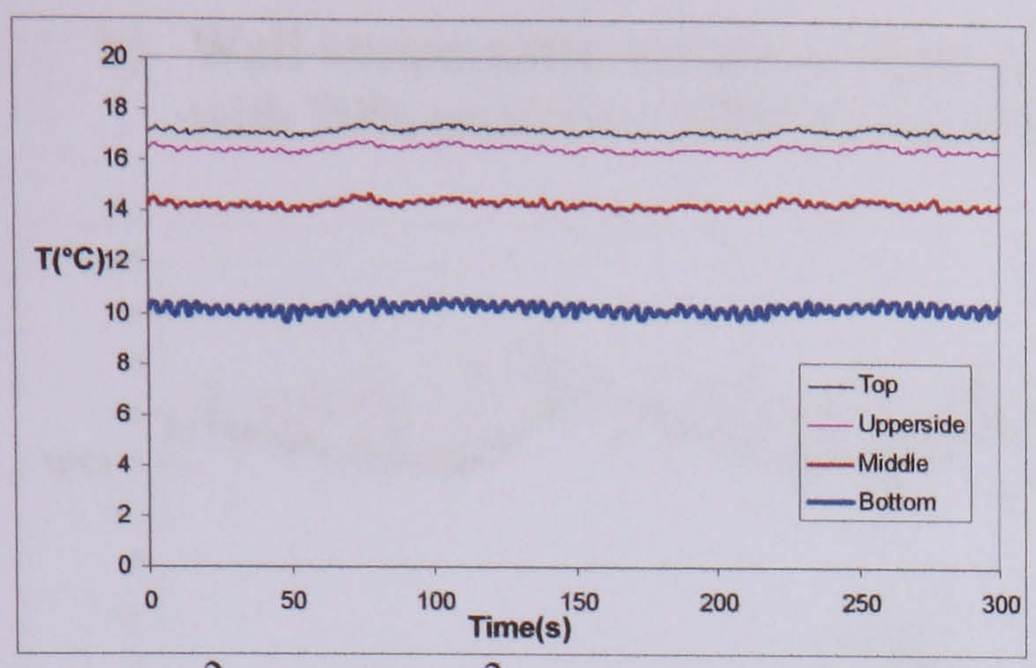

$26kg/m^2s$ $19KW/m^2$ 3.5bar x= 0.89

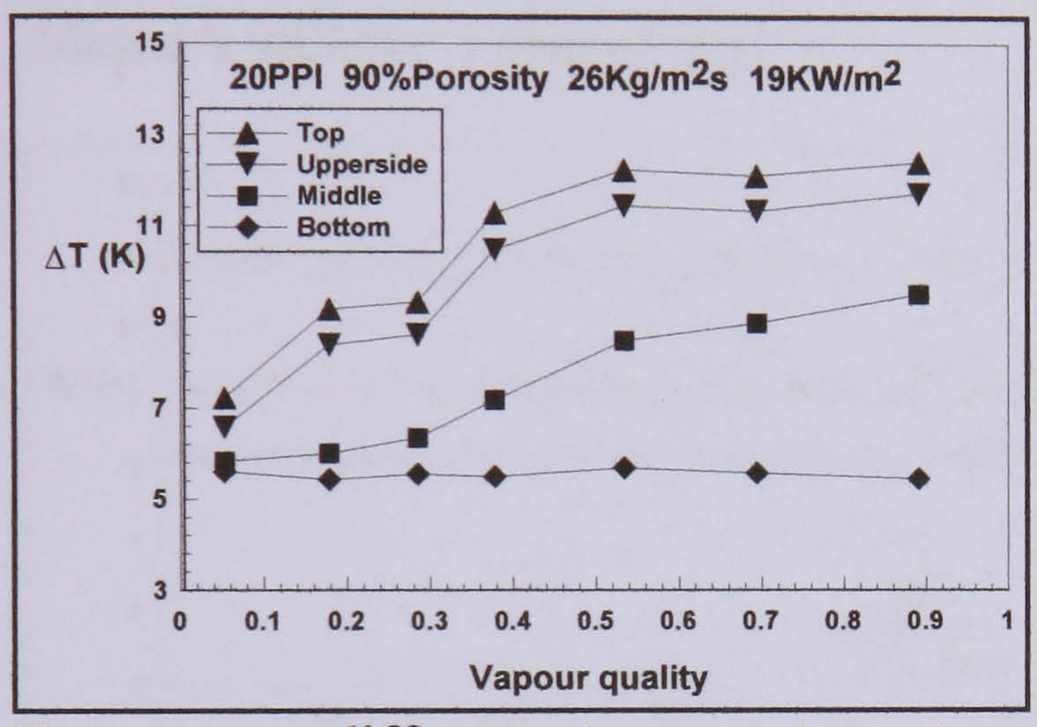

Temperature difference between the wall temperature and the saturated temperature around cross section for slug/wavy and stratified wavy flow with low mass flux

b) Wall temperature variation when mass flux is 26kg/m^{2}s and heat flux is 9KW/m^2 with 90% porosity, 20PPI metal foams

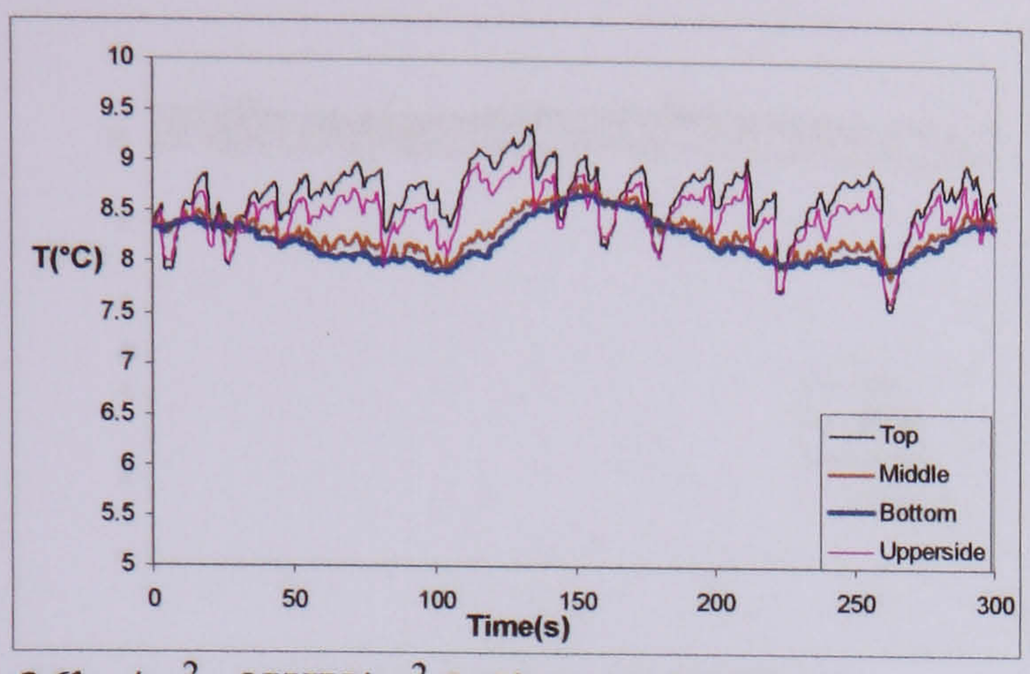

26kg/m^{2}s 9KW/m^2 3.5bar x= 0.07

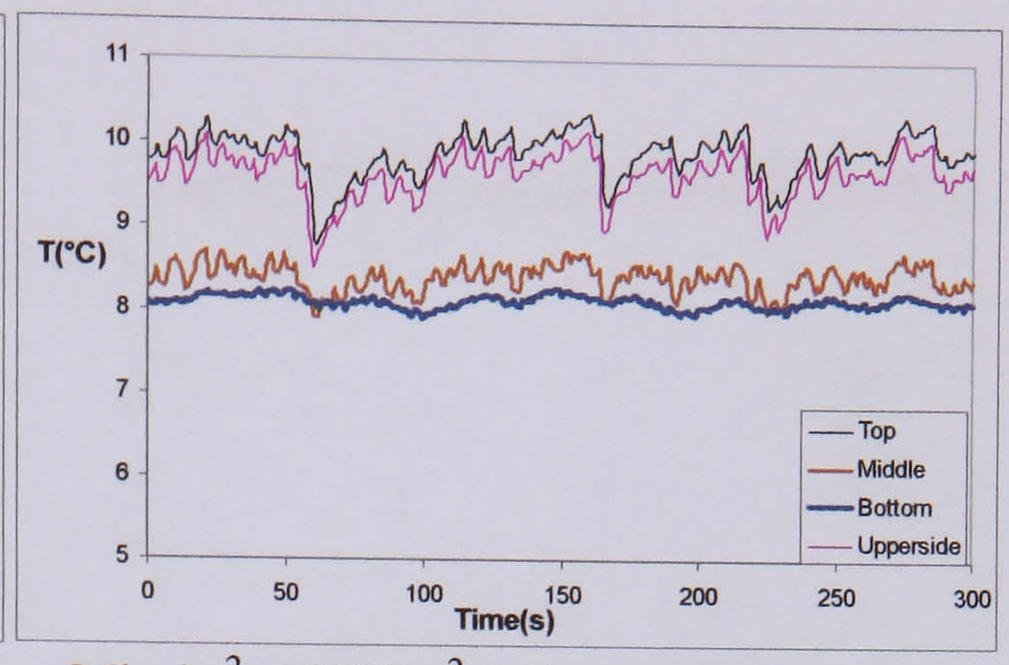

26kg/m^{2}s 9KW/m^2 3.5bar x= 0.27

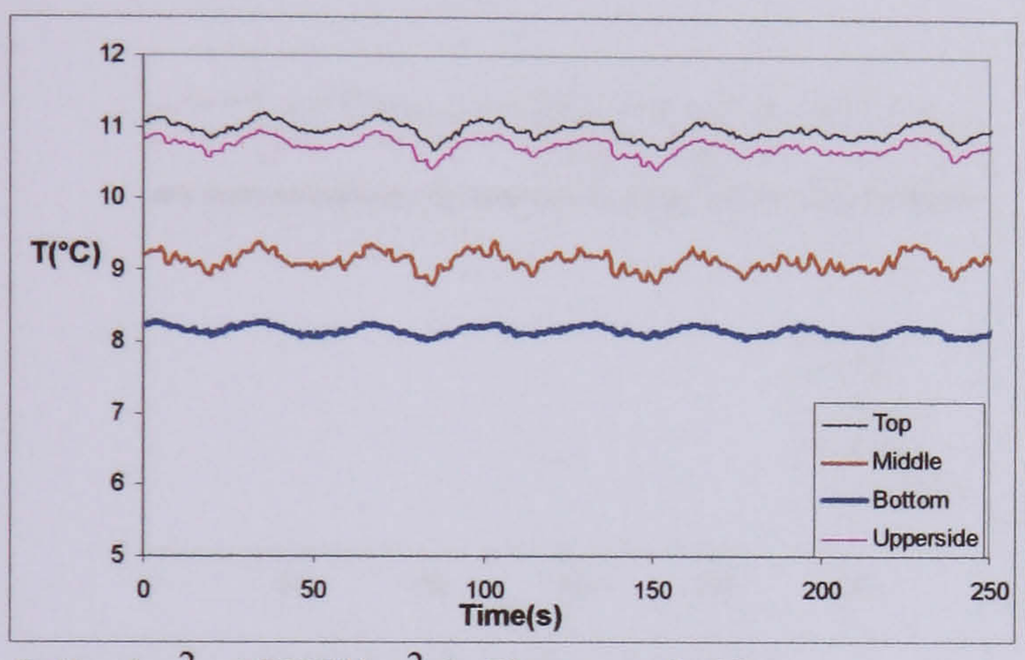

26kg/m^{2}s 9KW/m^2 3.5bar x= 0.49

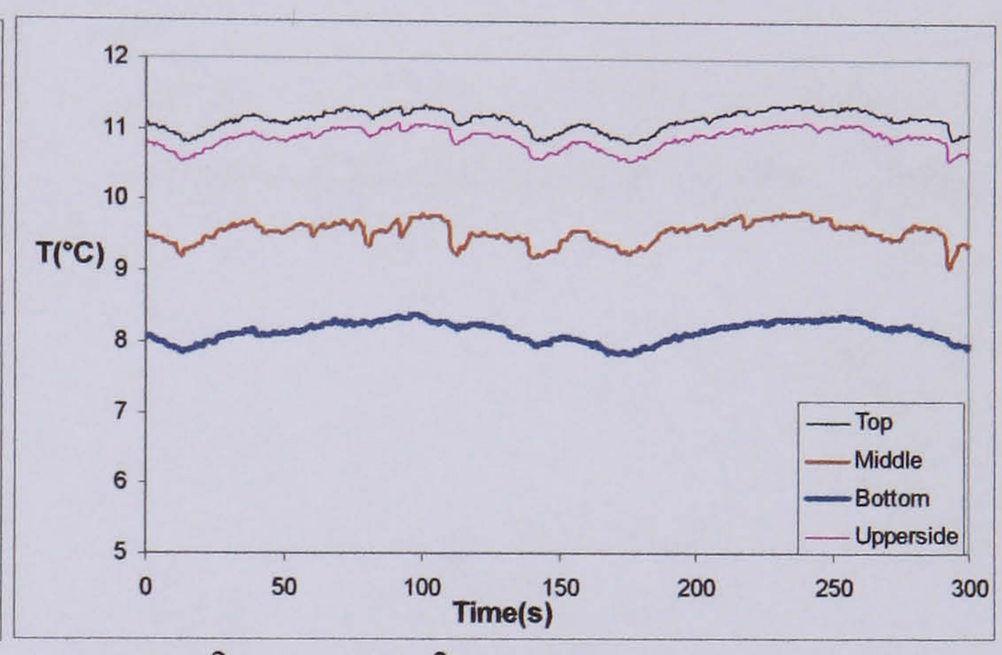

26kg/m^{2}s 9KW/m^2 3.5bar x= 0.68

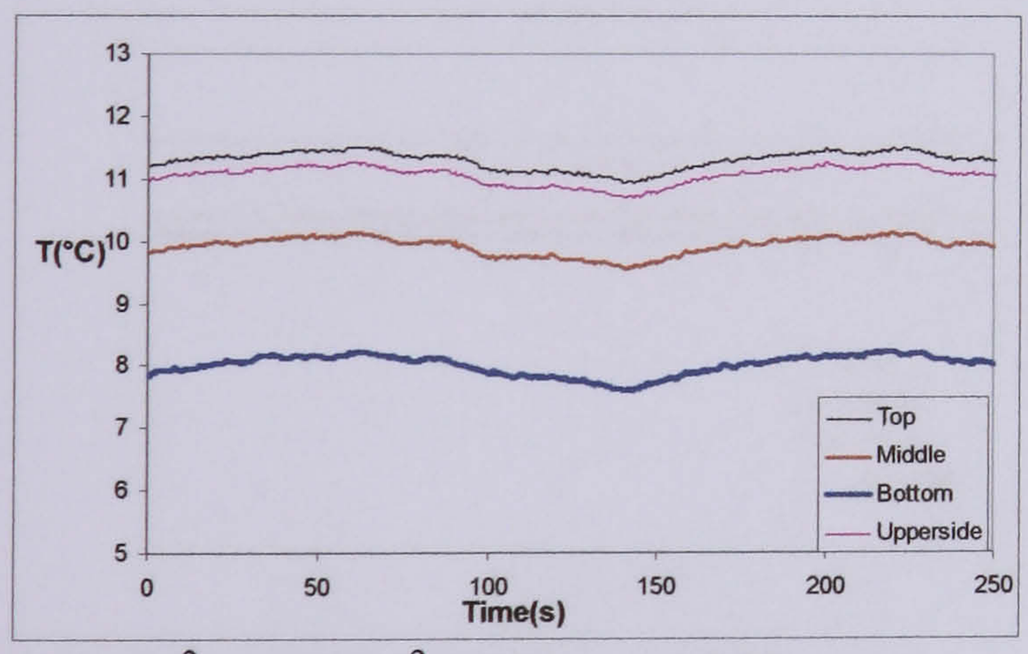

26kg/m^{2}s 9KW/m^2 3.5bar x= 0.90

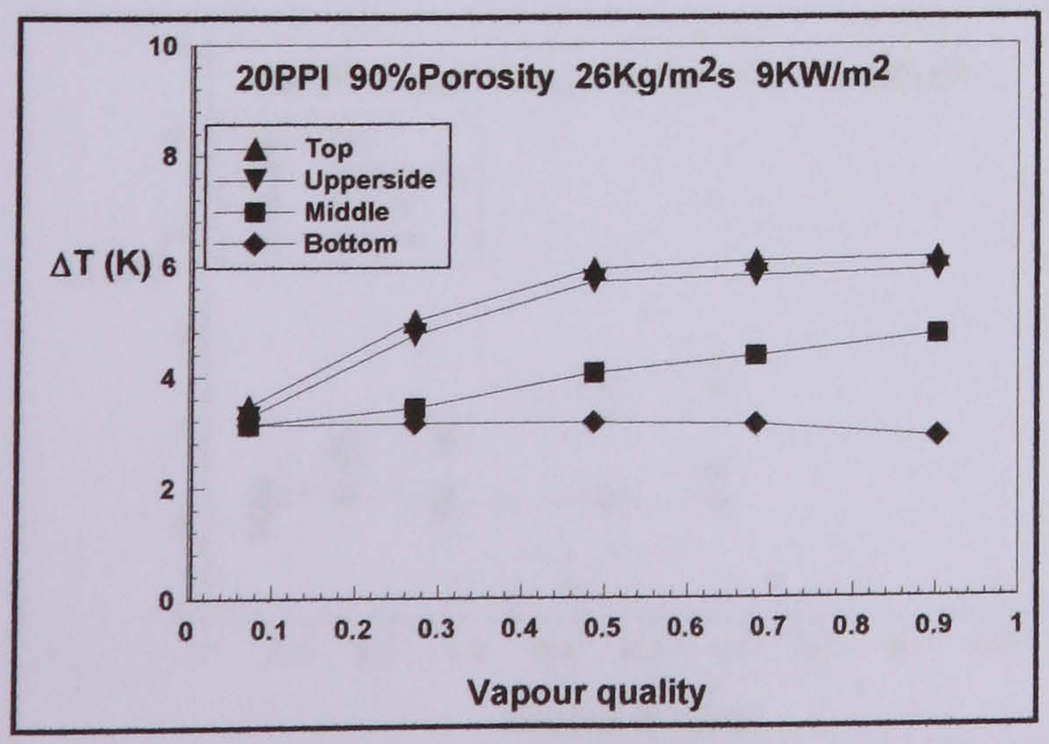

Temperature difference between the wall temperature and the saturated temperature around cross section for slug/wavy and stratified wavy flow with low mass flux

c) Wall temperature variation when mass flux is 52 kg/m^{2}s with 90% porosity, 20PPI metal foams

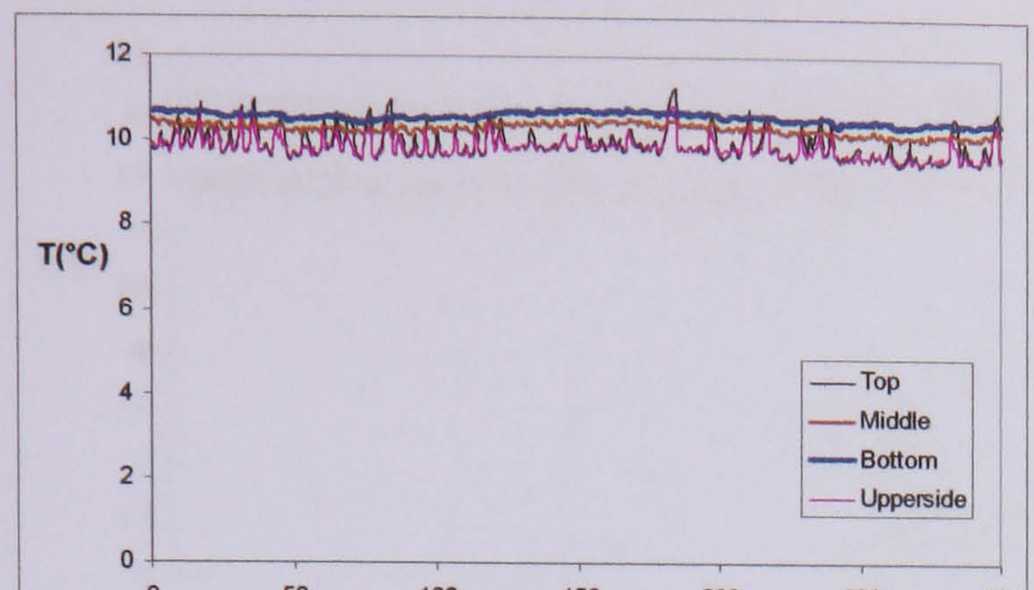

52kg/m^{2}s 19KW/m^2 3.5bar x= 0.07

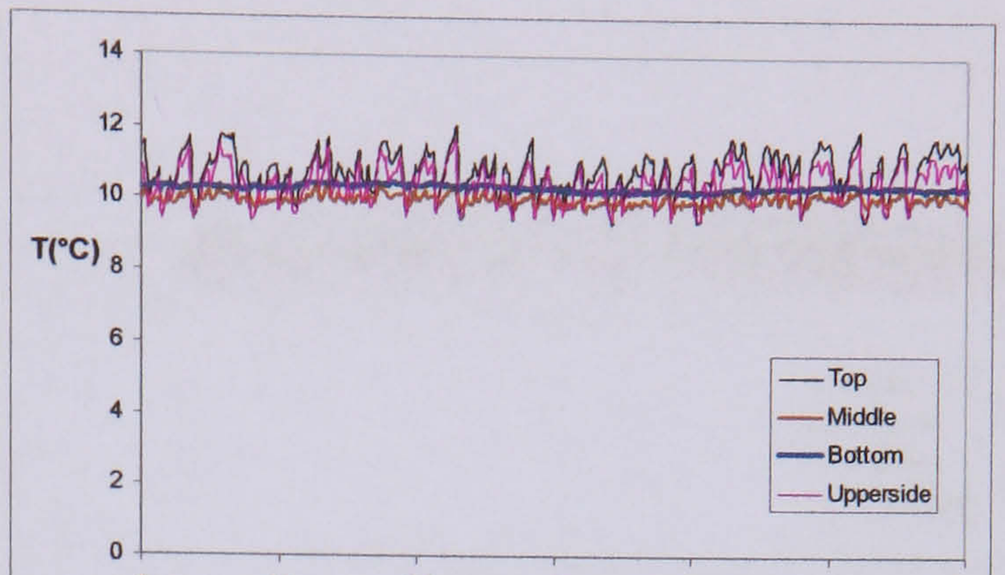

52kg/m^{2}s 19KW/m^2 3.5bar x= 0.16

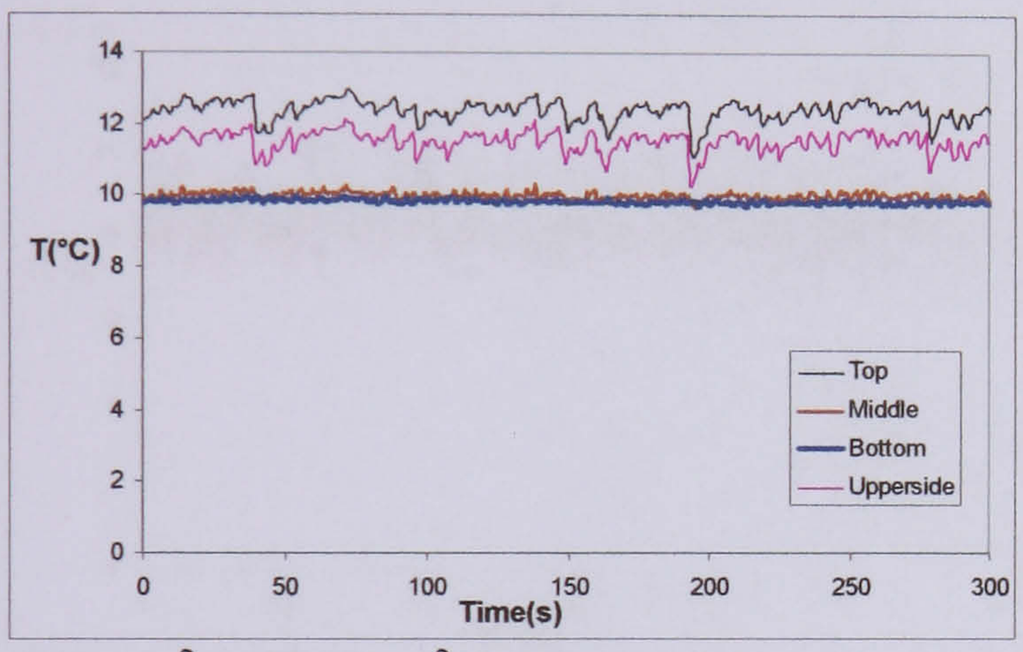

52kg/m^{2}s 19KW/m^2 3.5bar x= 0.27

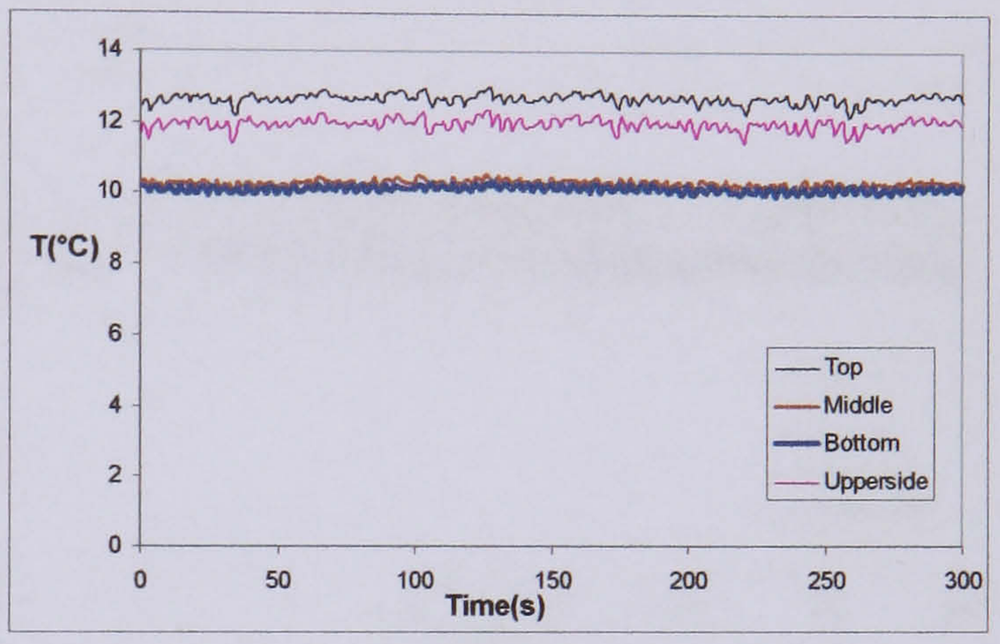

52kg/m^{2}s 19KW/m^2 3.5bar x= 0.46

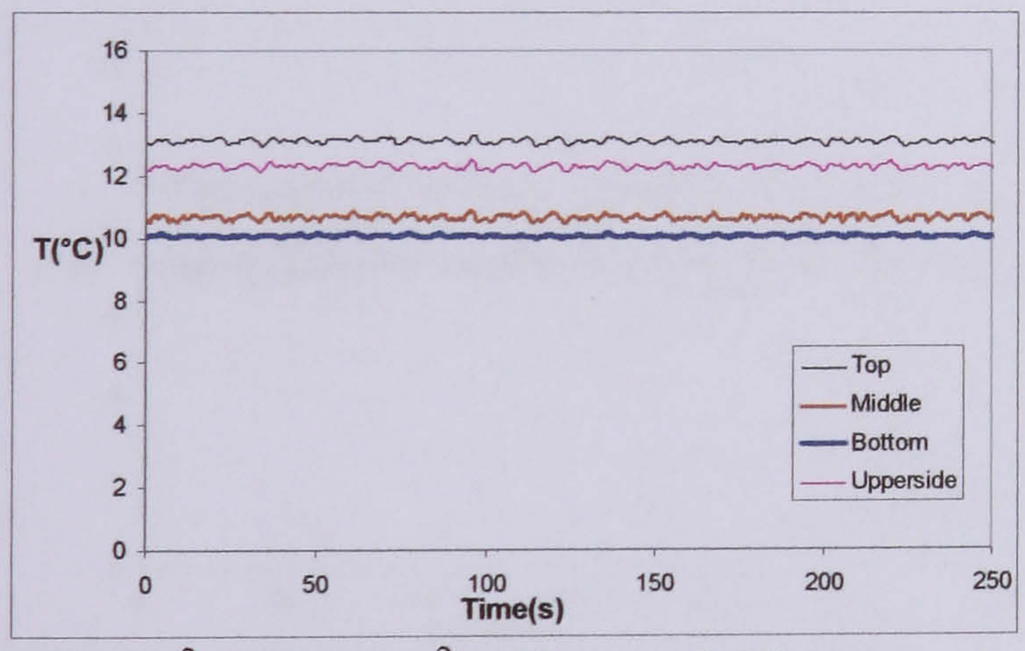

52kg/m^{2}s 19KW/m^2 3.5bar x= 0.58

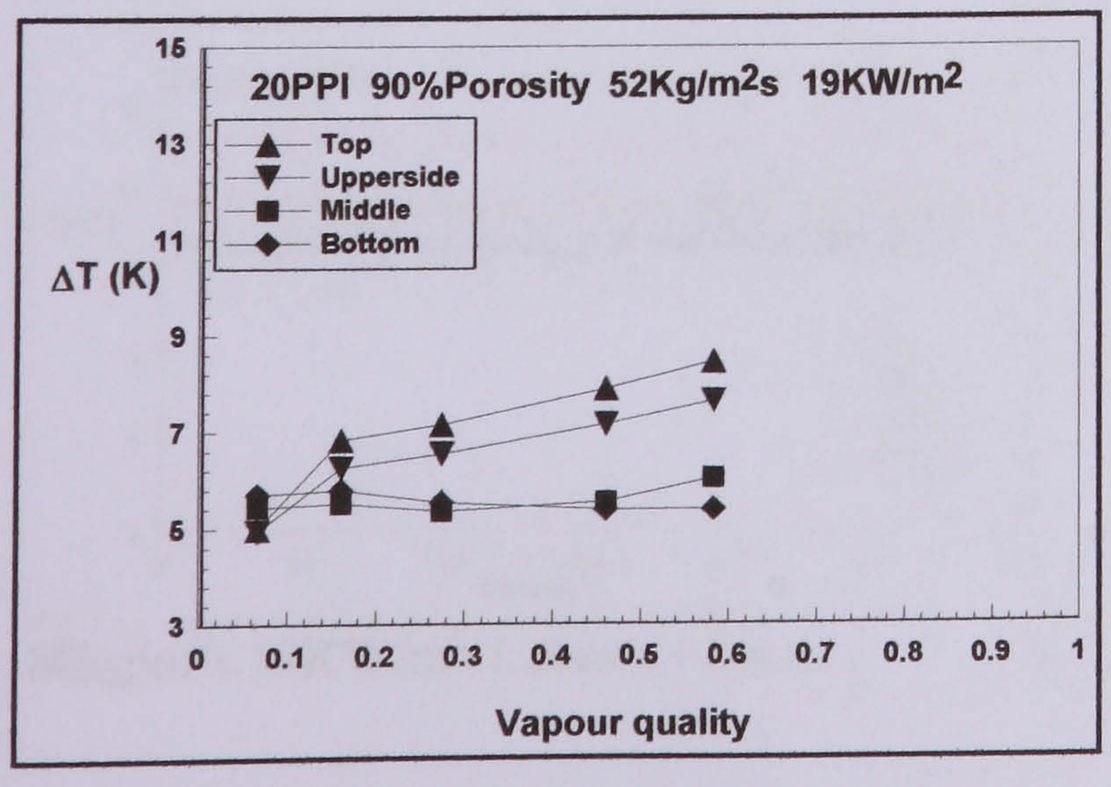

Temperature difference between the wall temperature and the saturated temperature around cross section for slug/wavy and stratified wavy flow with low mass flux

d) Wall temperature variation when mass flux is 80 kg/m^{2}s with 90% porosity, 20PPI metal foams

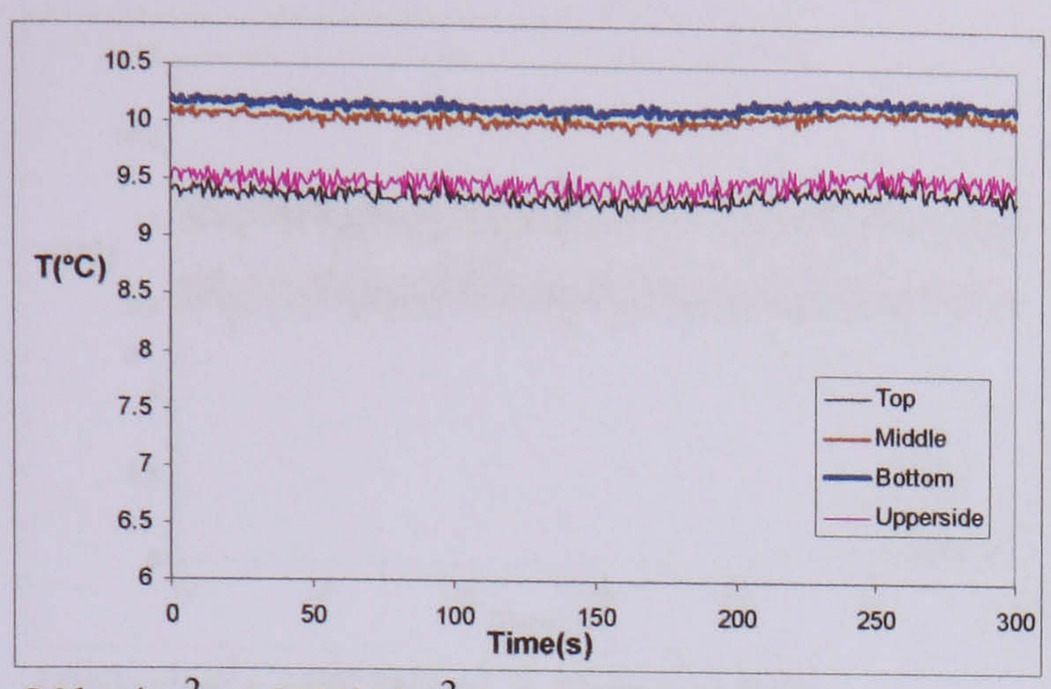

80kg/m^{2}s 19KW/m^2 3.5bar x= 0.03

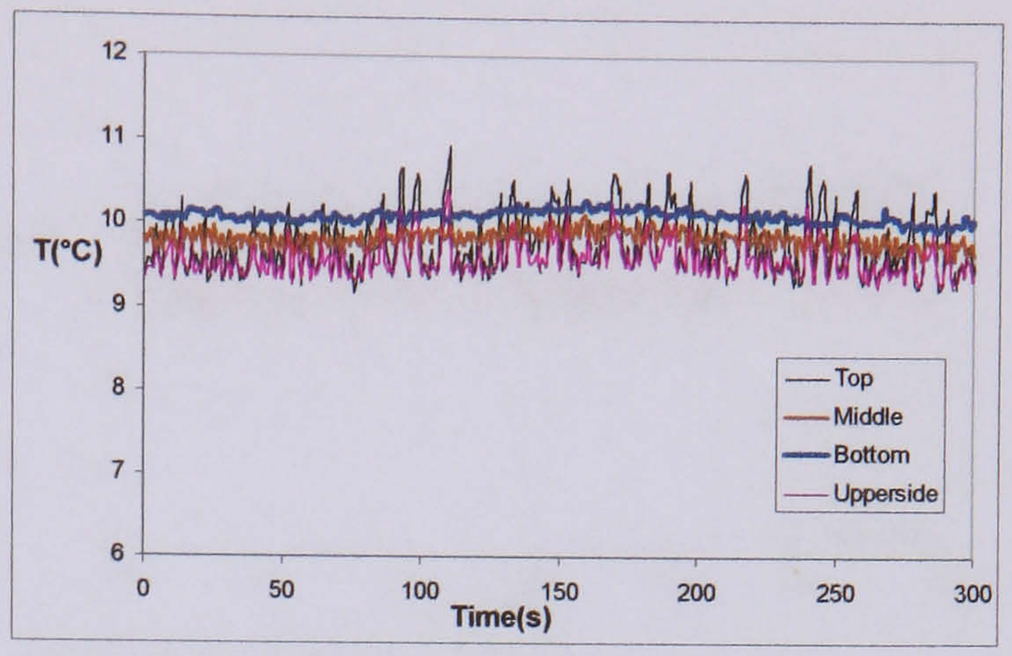

80kg/m^{2}s 19KW/m^2 3.5bar x= 0.16

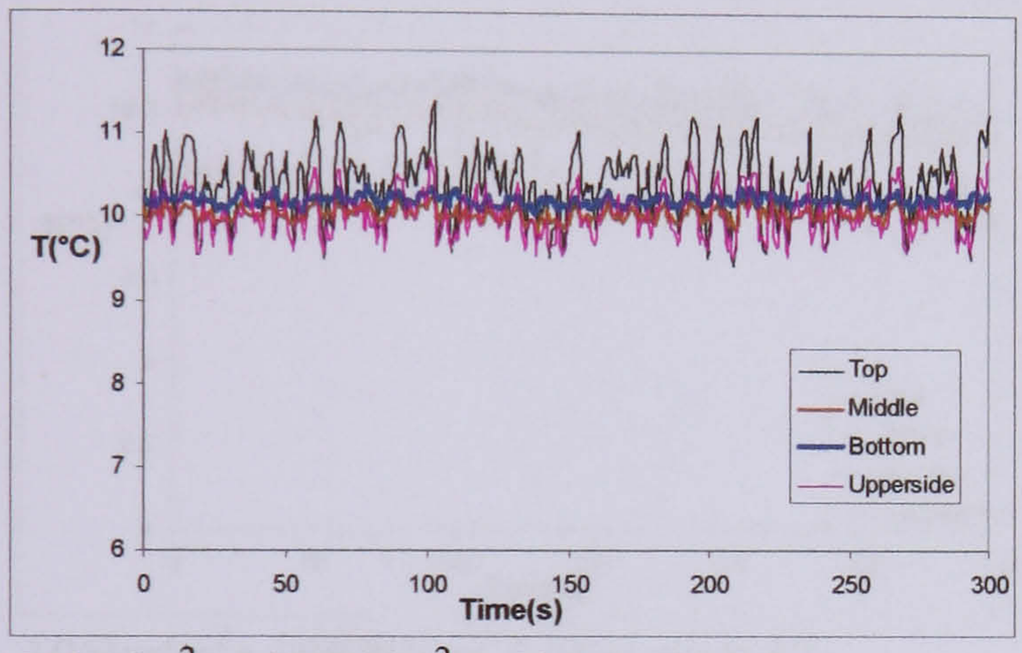

80kg/m^{2}s 19KW/m^2 3.5bar x= 0.27

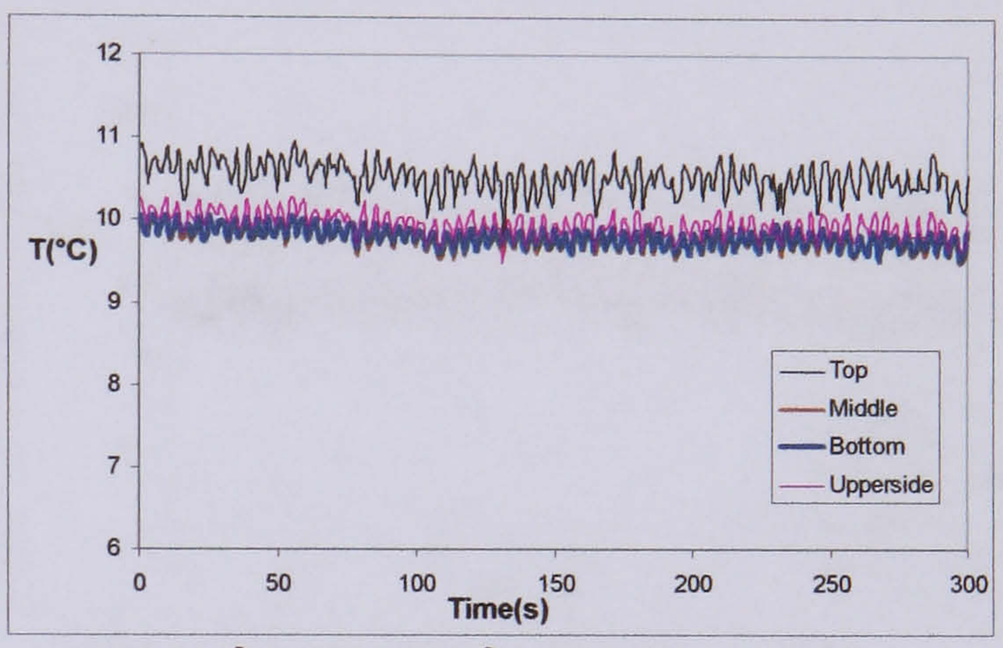

80kg/m^{2}s 19KW/m^2 3.5bar x= 0.40

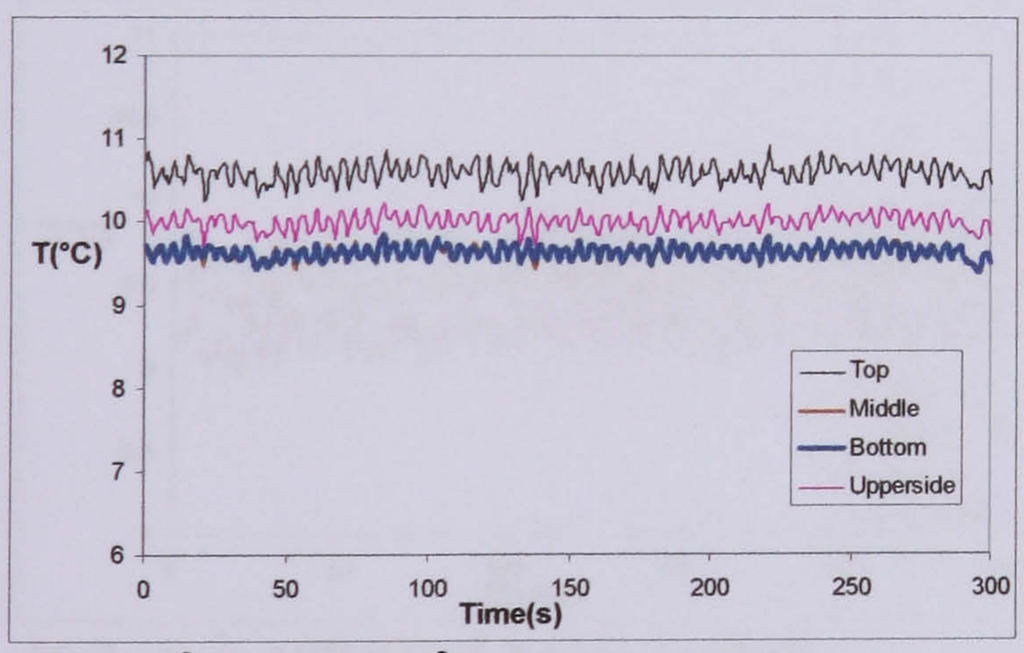

80kg/m^{2}s 19KW/m^2 3.5bar x= 0.55

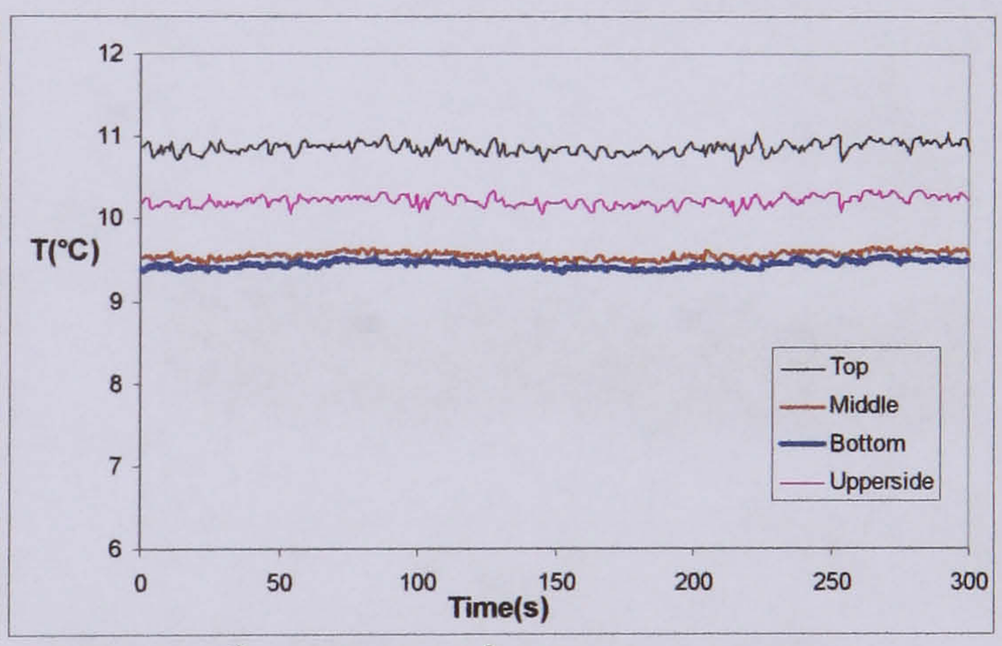

80kg/m^{2}s 19KW/m^2 3.5bar x= 0.69

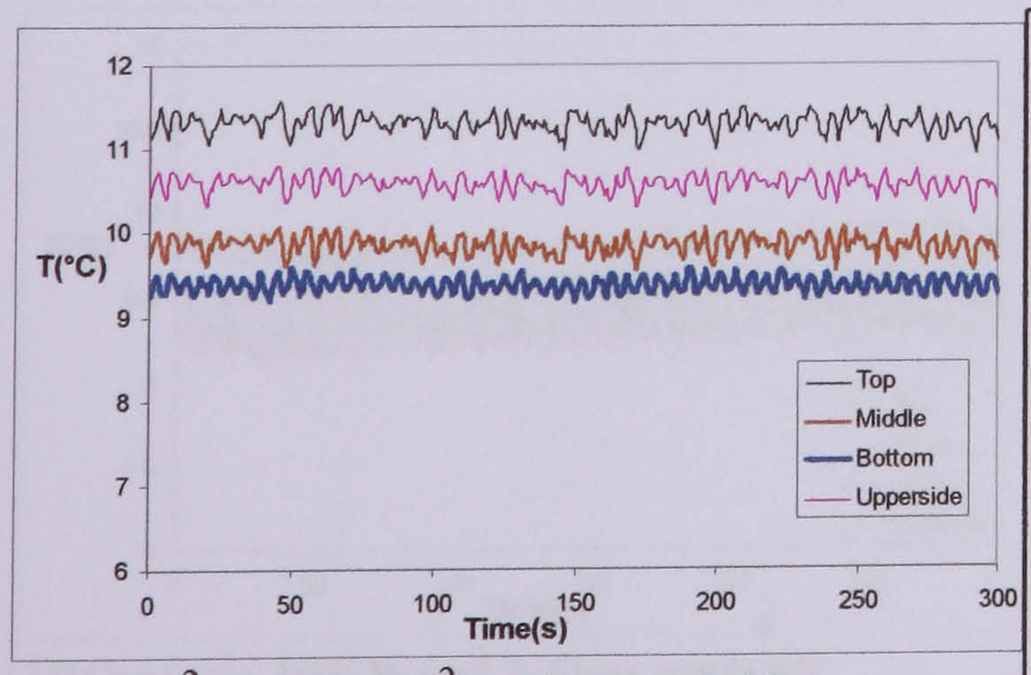

80kg/m^{2}s 19KW/m^2 3.5bar x= 0.83

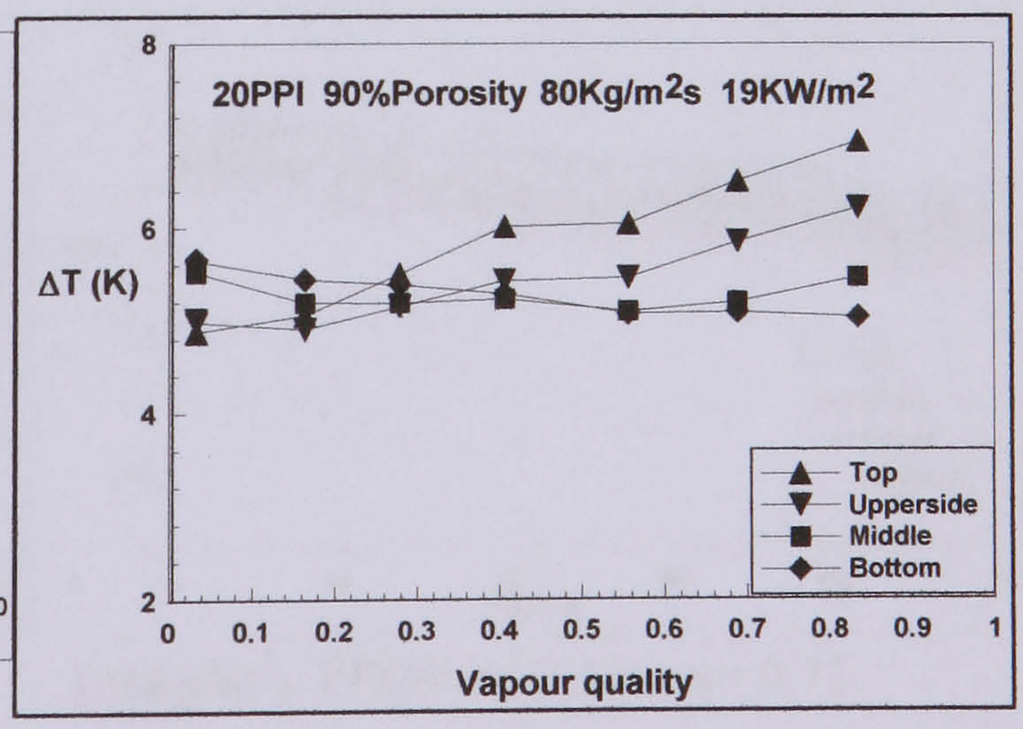

Temperature difference around cross section

e) Wall temperature variation when mass flux is 106 kg/m^{2}s with 90% porosity, 20 PPI metal foams

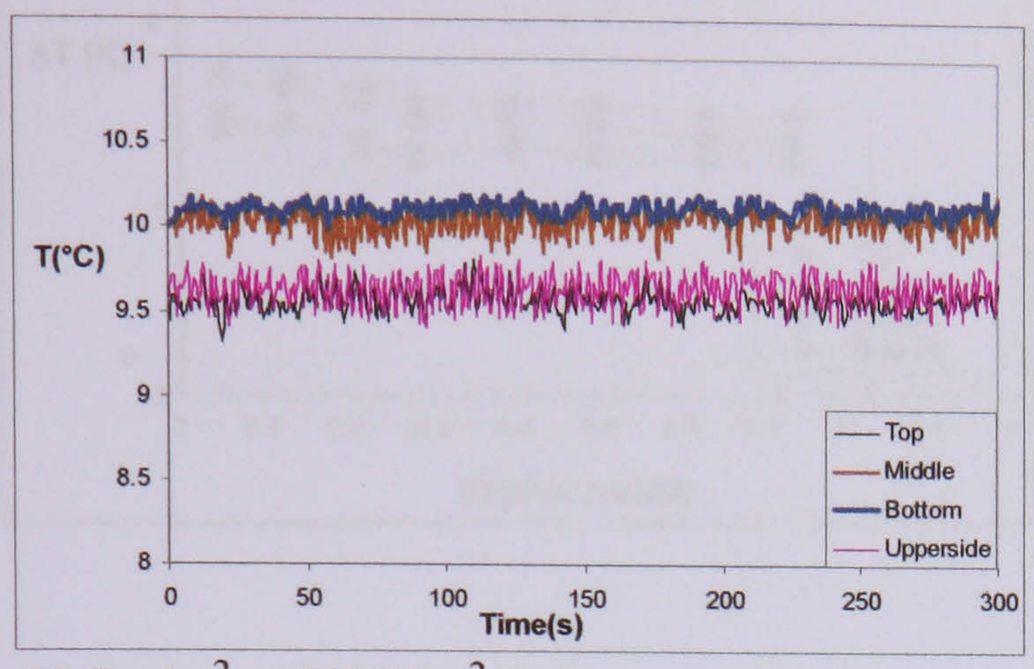

106kg/m^{2}s 19KW/m^2 3.5bar x= 0.05

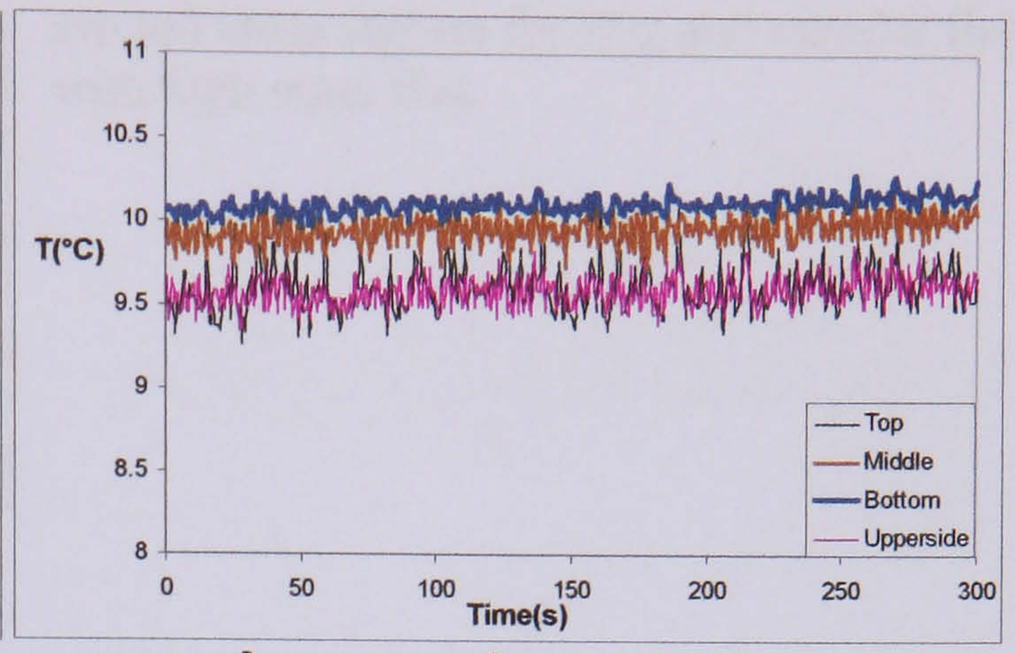

106kg/m^{2}s 19KW/m^2 3.5bar x= 0.13

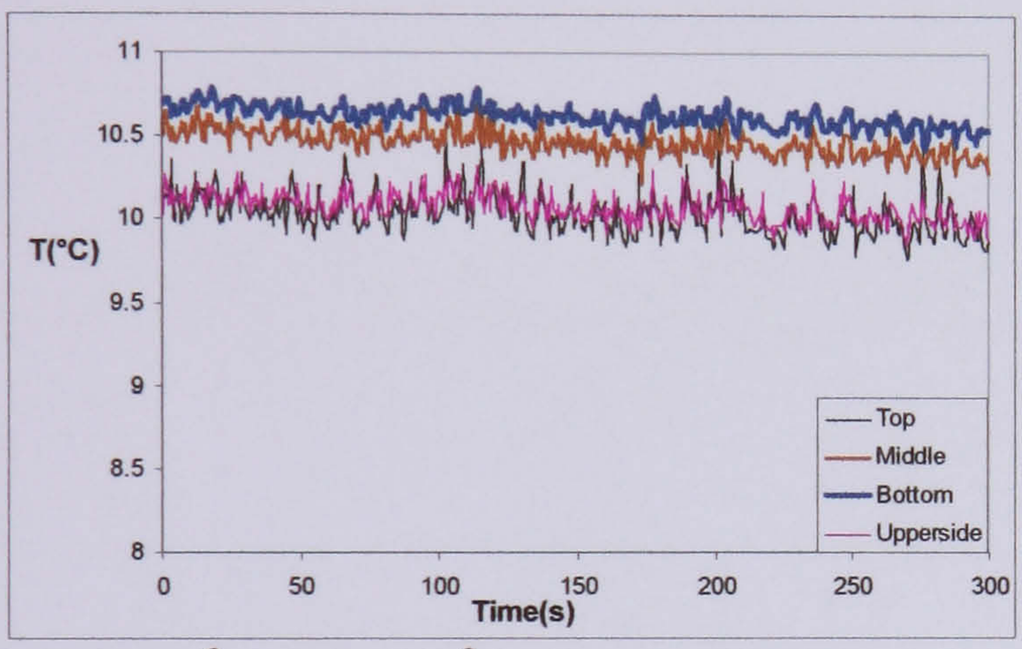

106kg/m^{2}s 19KW/m^2 3.5bar x= 0.22

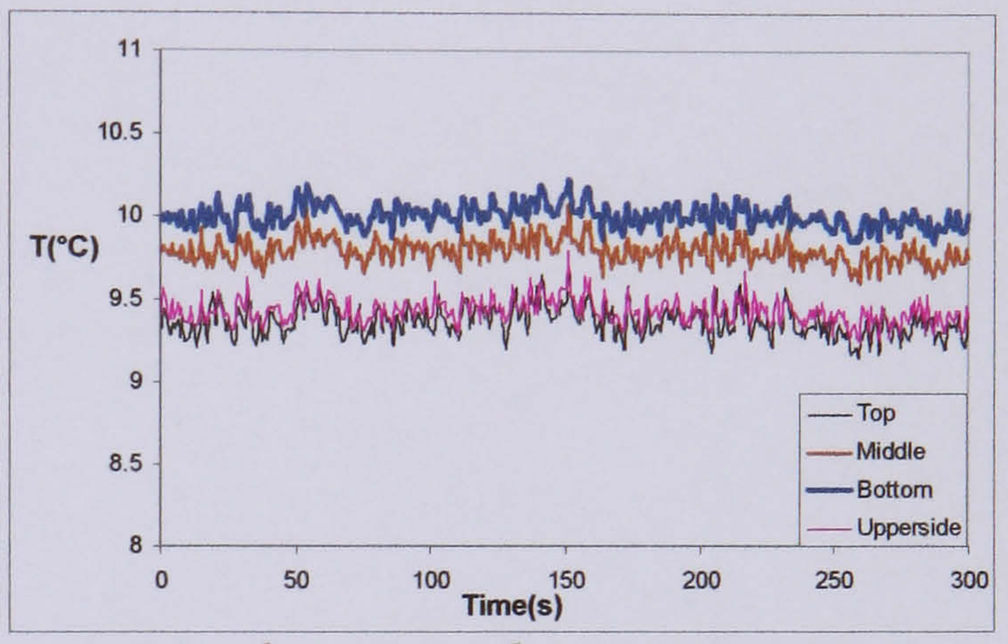

106kg/m^{2}s 19KW/m^2 3.5bar x= 0.28

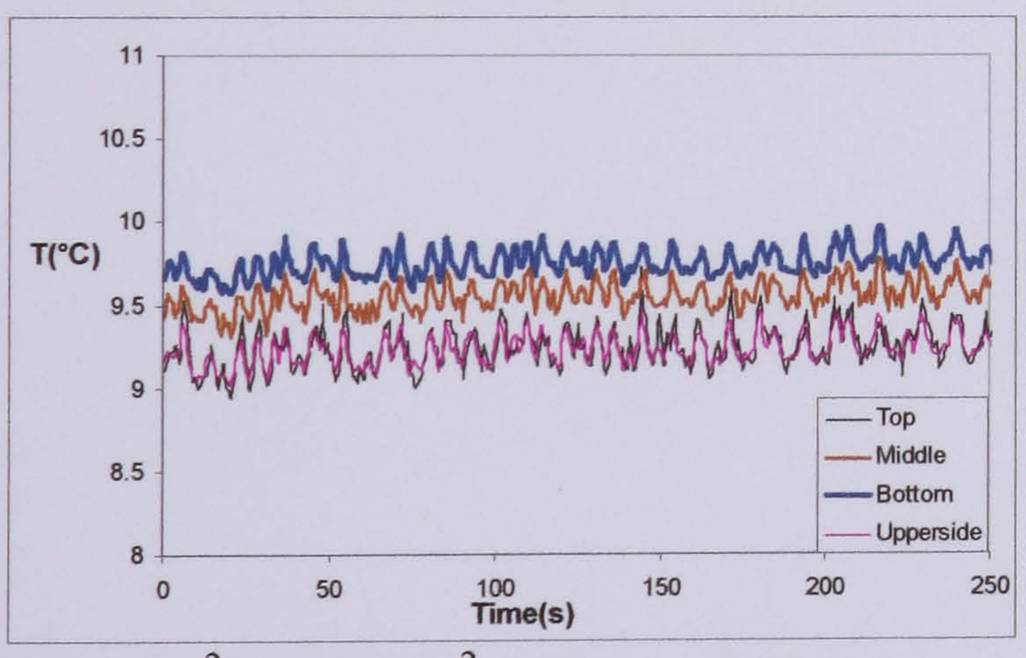

106kg/m^{2}s 19KW/m^2 3.5bar x= 0.40

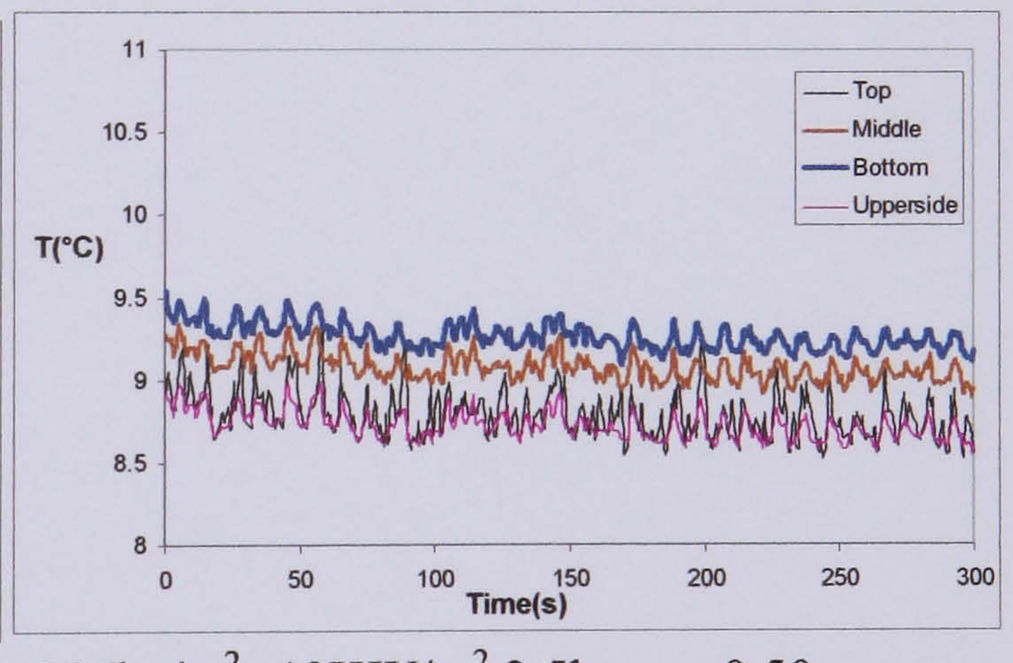

106kg/m^{2}s 19KW/m^2 3.5bar x= 0.50

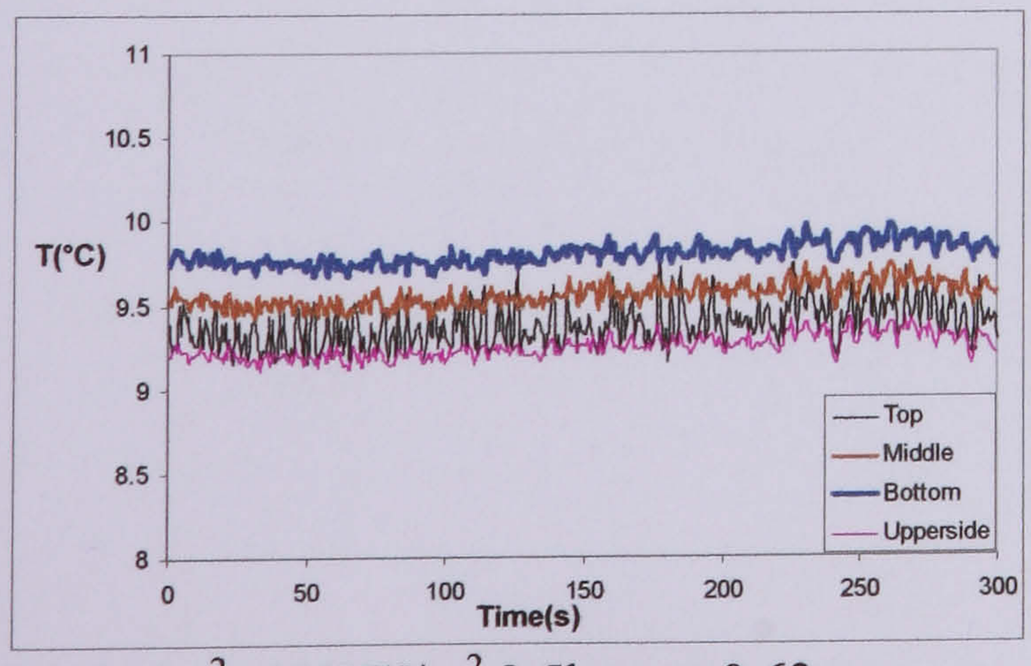

106kg/m^{2}s 19KW/m^2 3.5bar x= 0.63

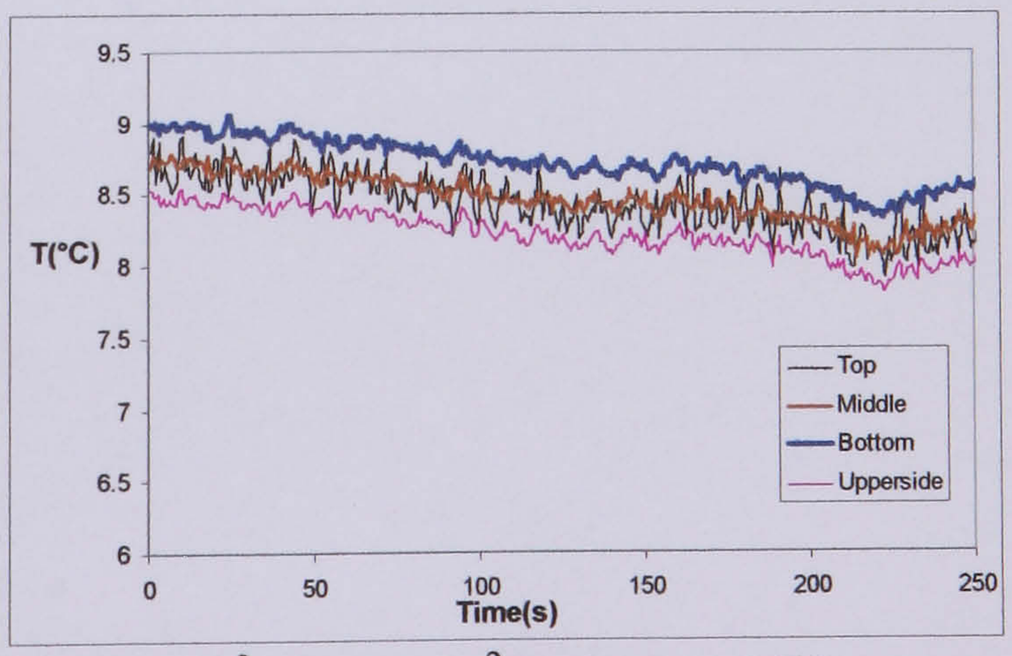

106kg/m^{2}s 19KW/m^2 3.5bar x= 0.73

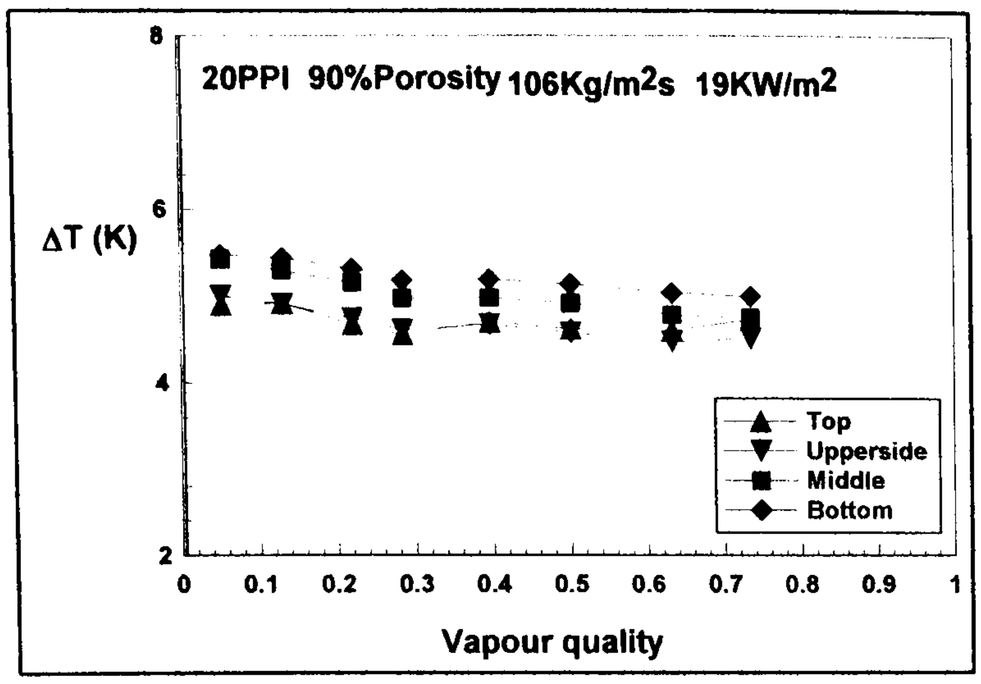

Temperature difference between the wall temperature and the saturated temperature around cross section for slug and annular flow with high mass flux

f) Wall temperature variation when mass flux is 106 kg/m^{2}s and pressure at 6 bar with 90% porosity, 20 PPI metal foams

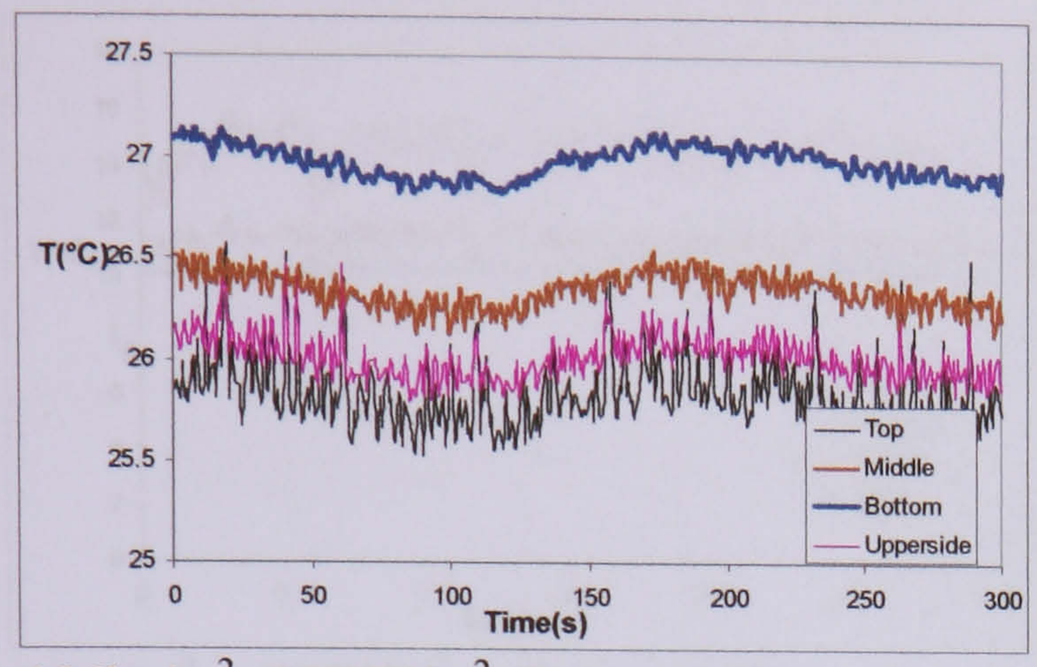

106kg/m^{2}s 19KW/m^2 6bar x= 0.10

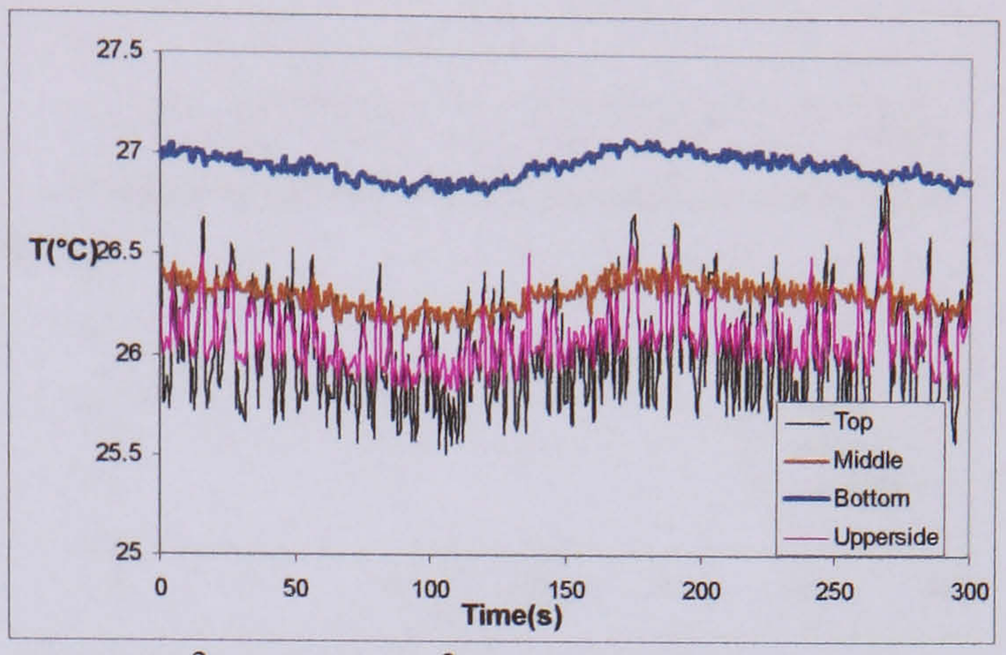

106kg/m^{2}s 19KW/m^2 6bar x= 0.18

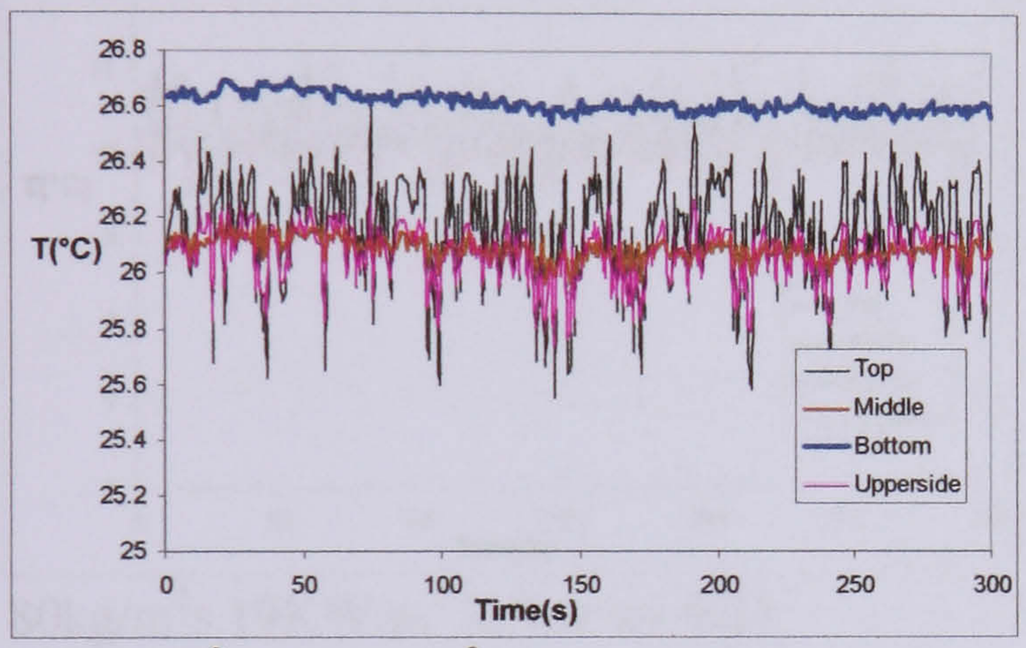

106kg/m^{2}s 19KW/m^2 6bar x= 0.31

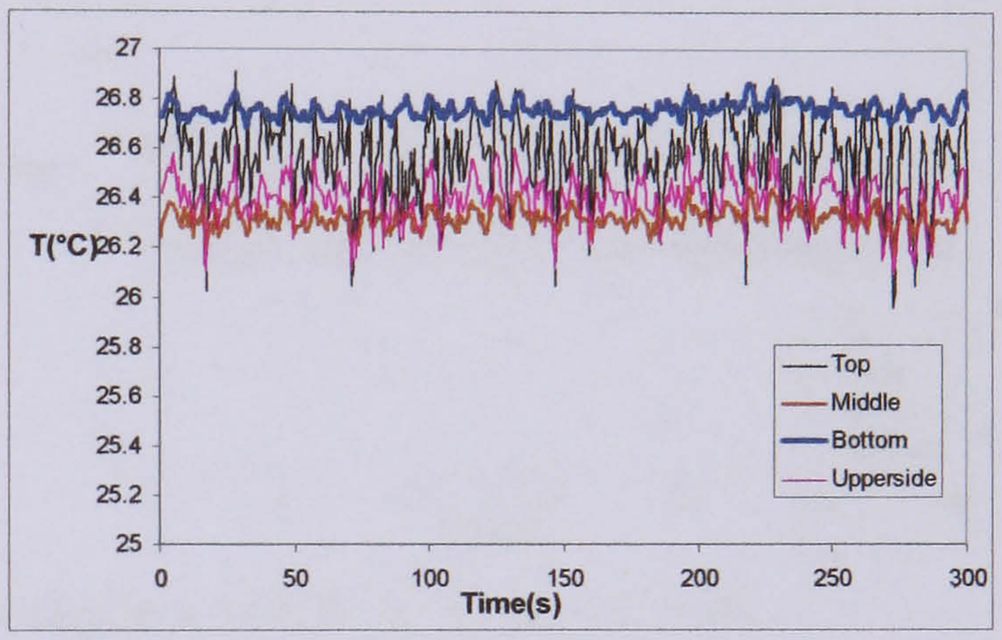

106kg/m^{2}s 19KW/m^2 6bar x= 0.40

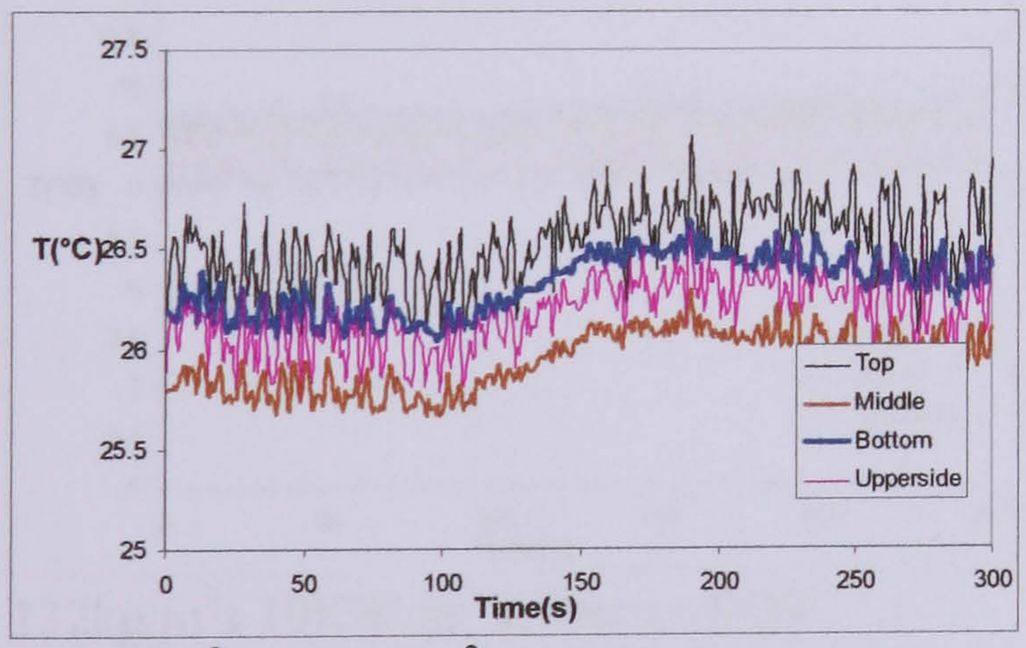

106kg/m^{2}s 19KW/m^2 6bar x= 0.54

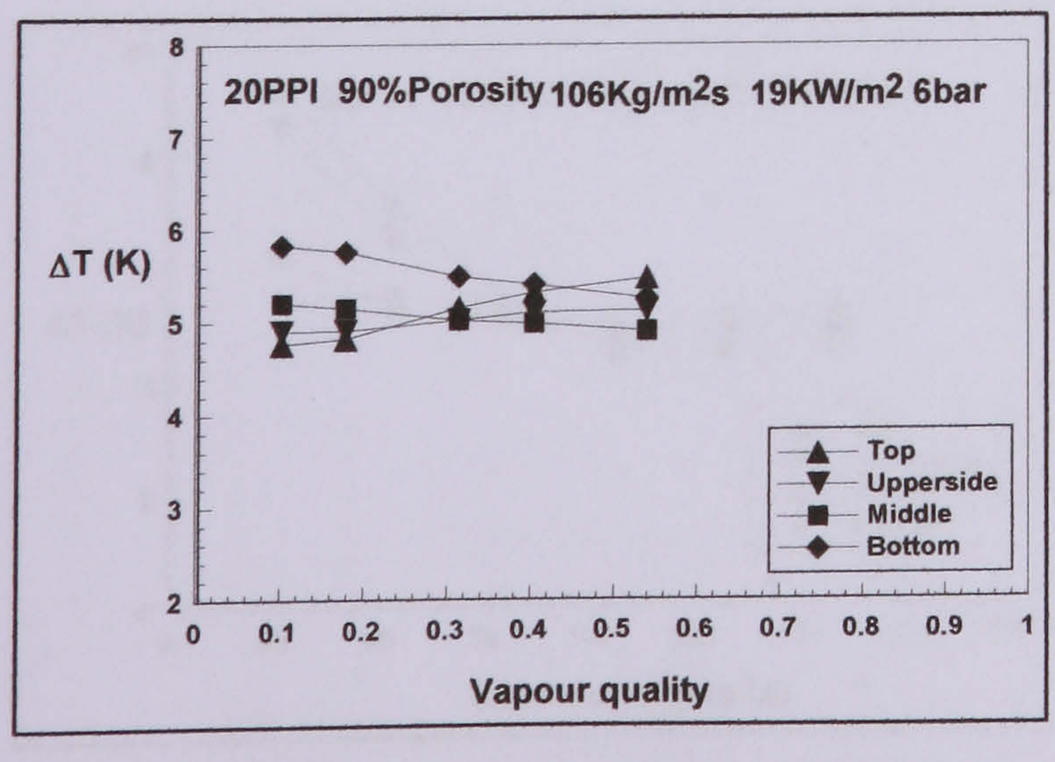

Temperature difference between the wall temperature and the saturated temperature around cross section with high mass flux and high pressure

g) Wall temperature variation for different mass flux with 90% porosity, 20 PPI metal foams

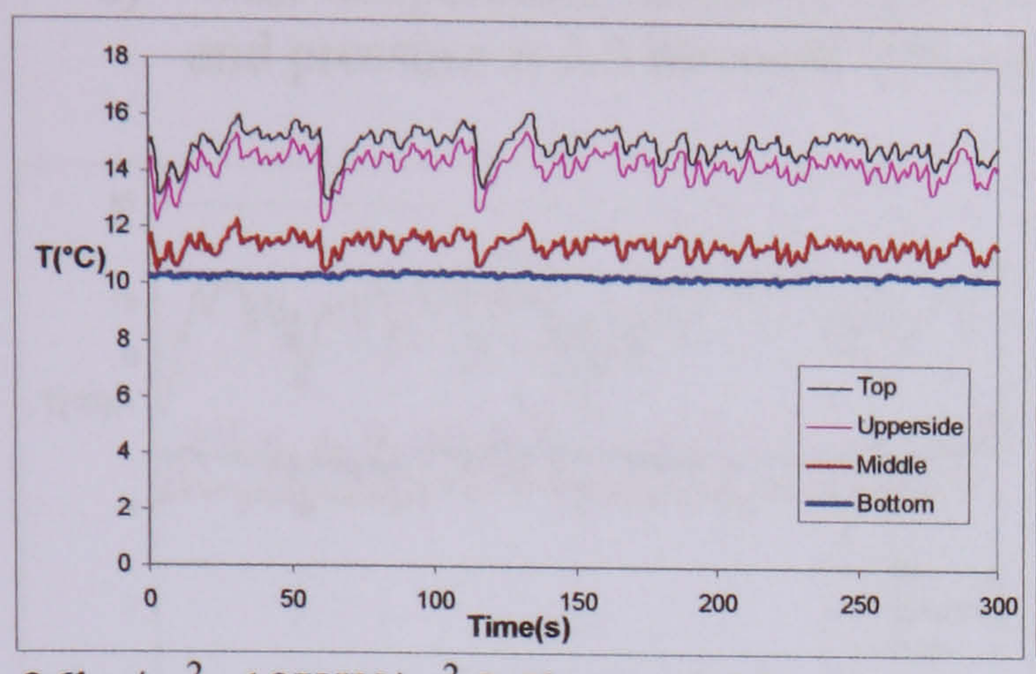

26kg/m^{2}s 19KW/m^2 3.5bar x=0.28

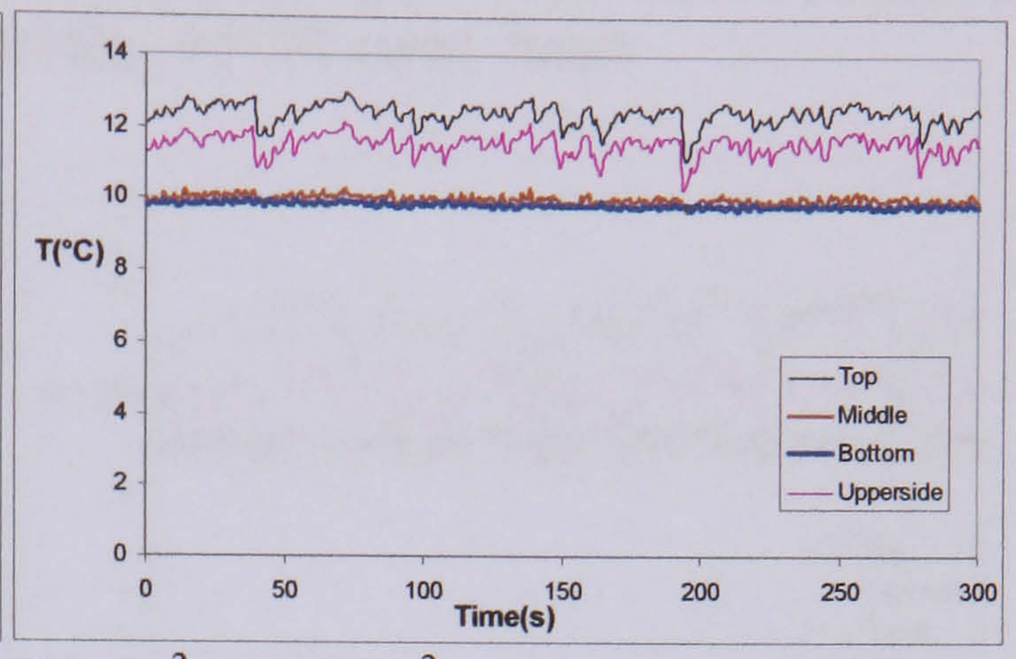

52kg/m^{2}s 19KW/m^2 3.5bar x= 0.27

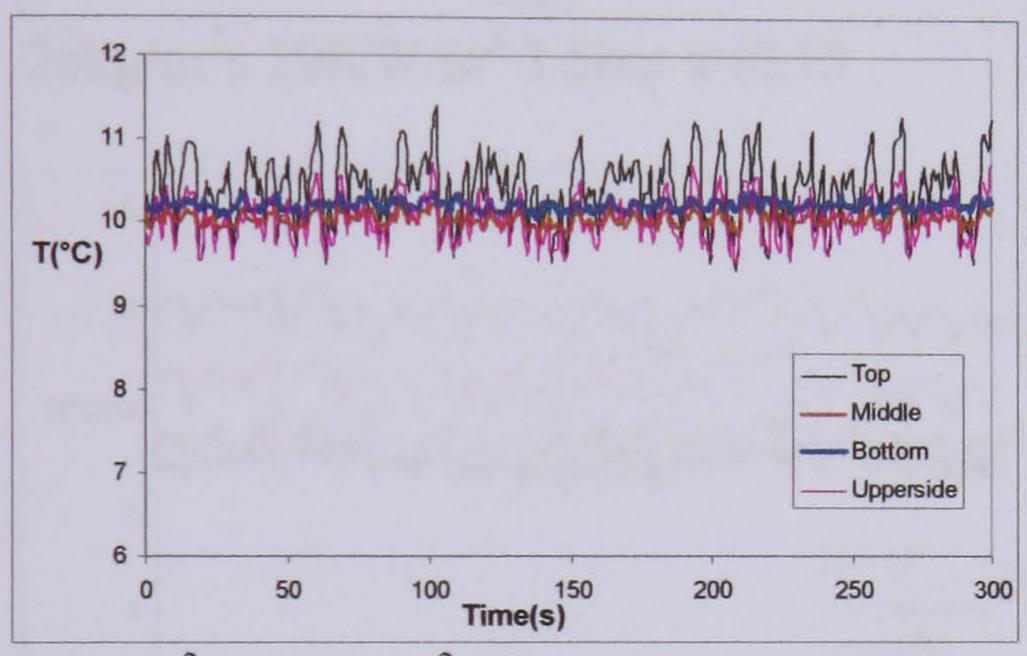

80kg/m^{2}s 19KW/m^2 3.5bar x= 0.27

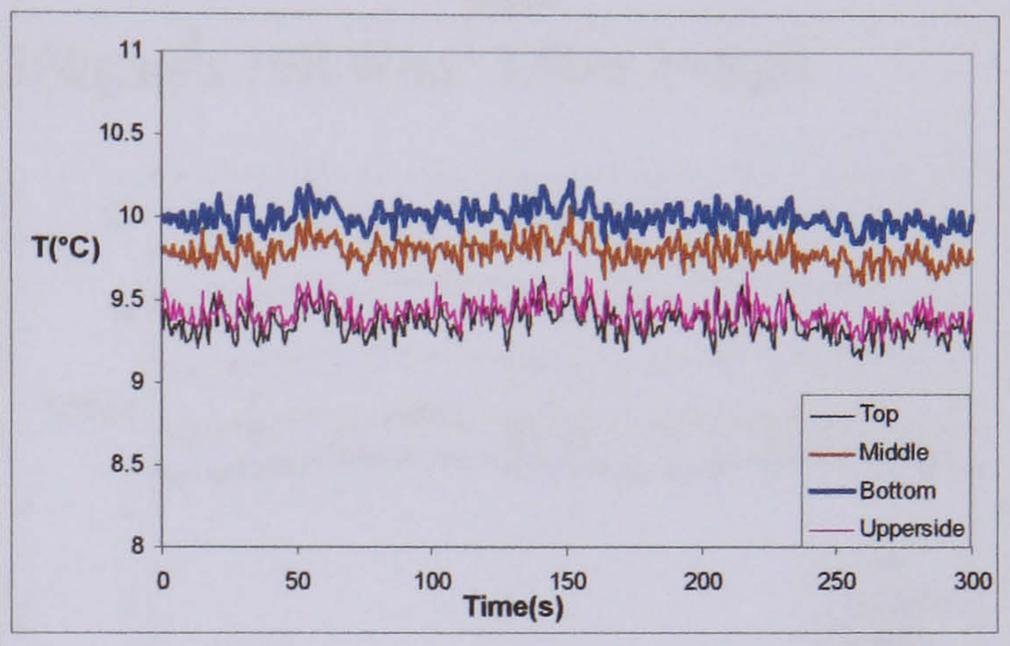

106kg/m^{2}s 19KW/m^2 3.5bar x= 0.28

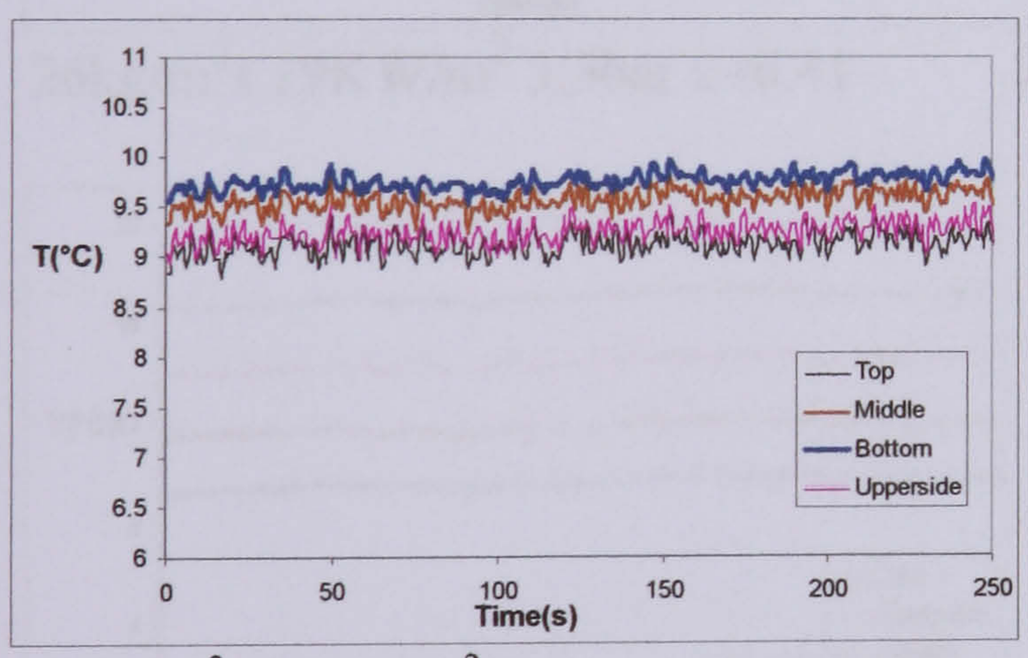

132kg/m^{2}s 19KW/m^2 3.5bar x= 0.29

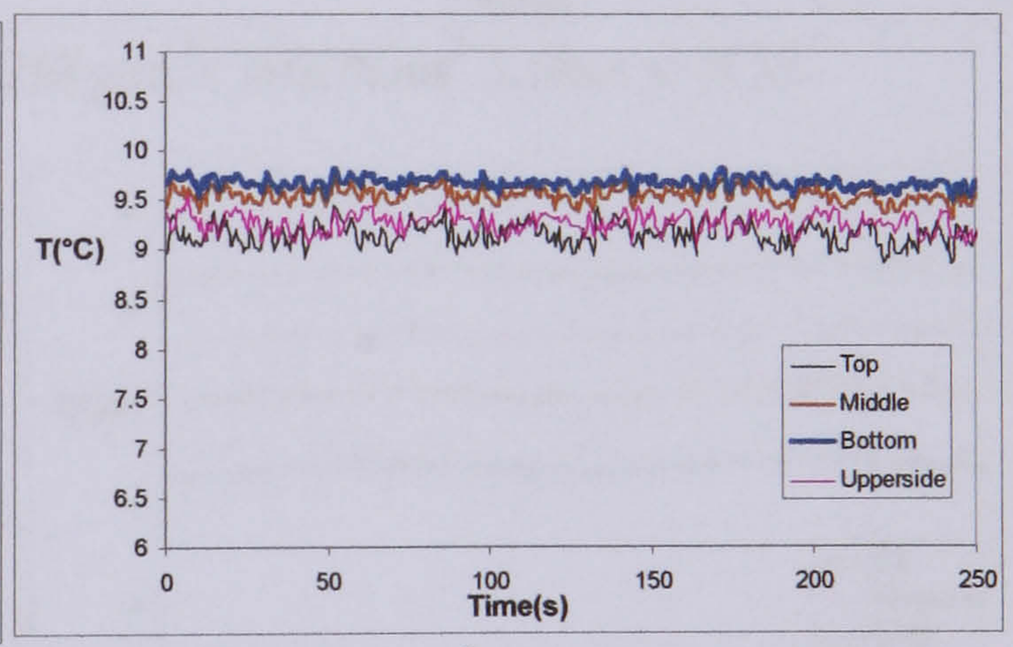

160kg/m^{2}s 19KW/m^2 3.5bar x= 0.30

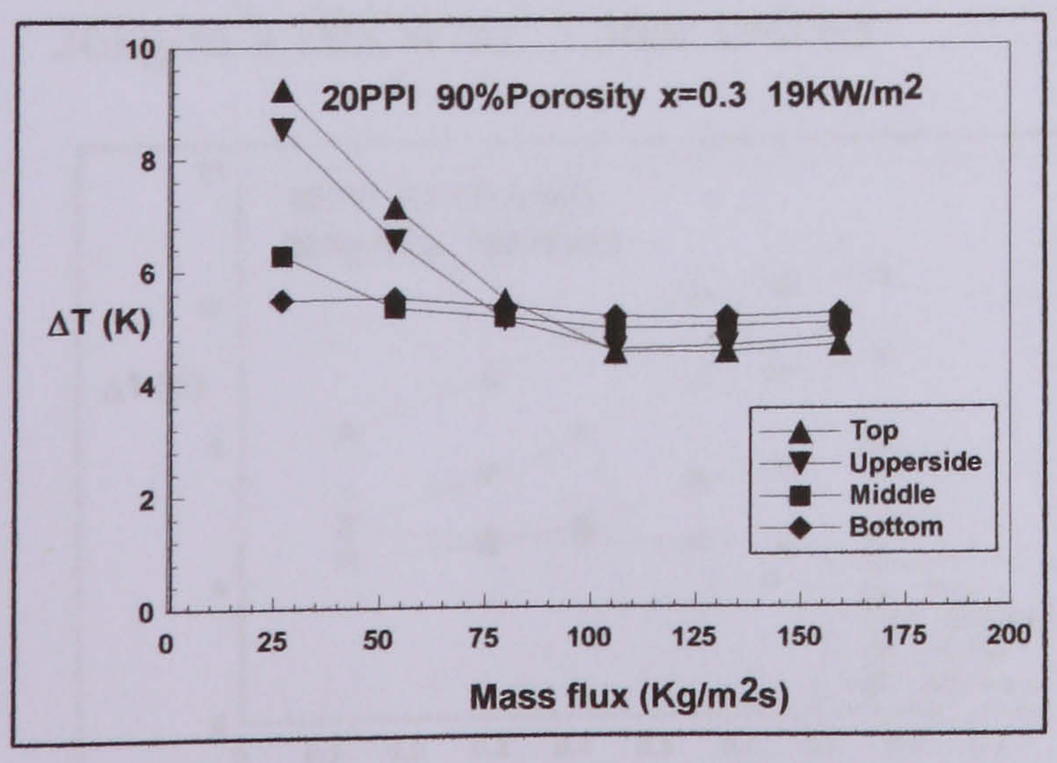

Temperature difference between the wall temperature and the saturated temperature around cross section with different mass flux(vapour quality=0.3 heat flux =19 KW/m^2)

D.2 Wall temperature variation of the tube with 90% porosity, 40 PPI metal foams

a) Wall temperature variation when mass flux is 26 kg/m^{2}s, heat flux is 19 KW/m^2 and pressure is 3.5 bar with 90% porosity, 40 PPI metal foams

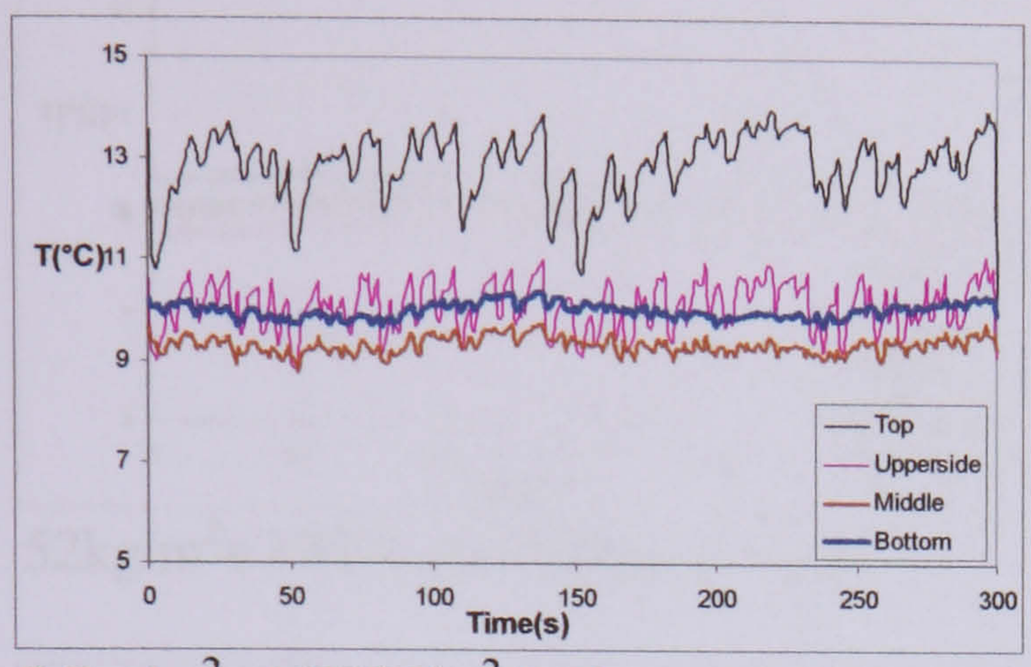

26kg/m^{2}s 19KW/m^2 3.5bar x=0.13

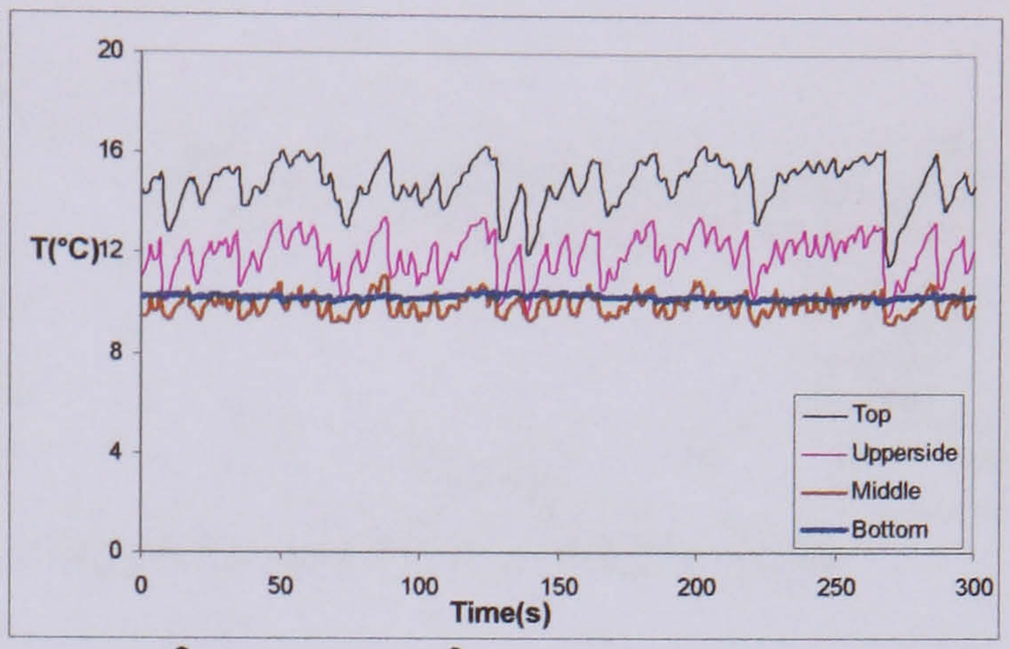

26kg/m^{2}s 19KW/m^2 3.5bar x=0.29

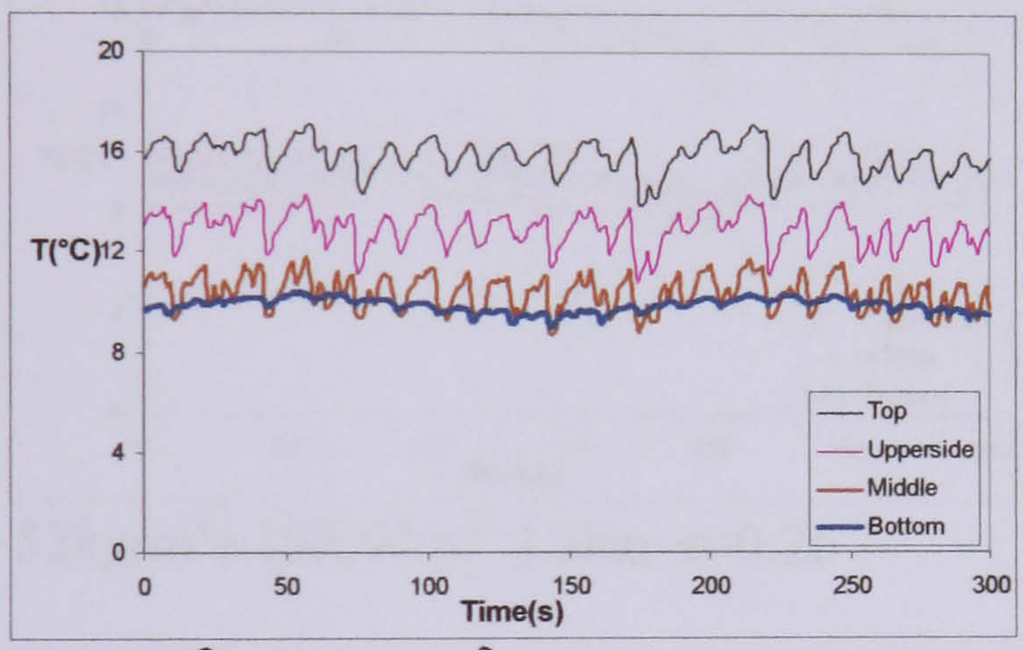

26kg/m^{2}s 19KW/m^2 3.5bar x=0.41

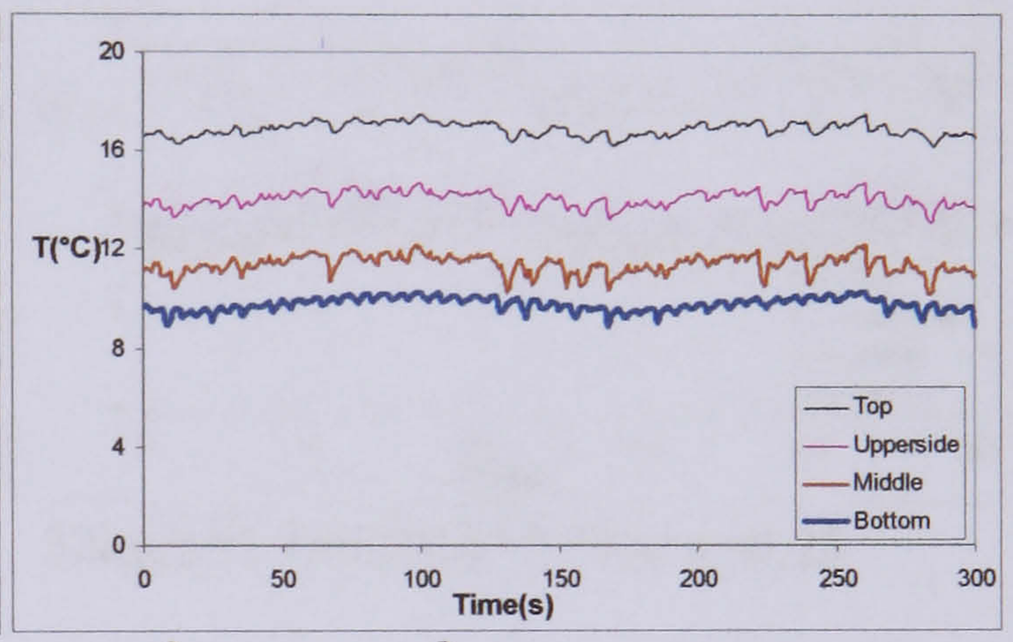

26kg/m^{2}s 19KW/m^2 3.5bar x=0.55

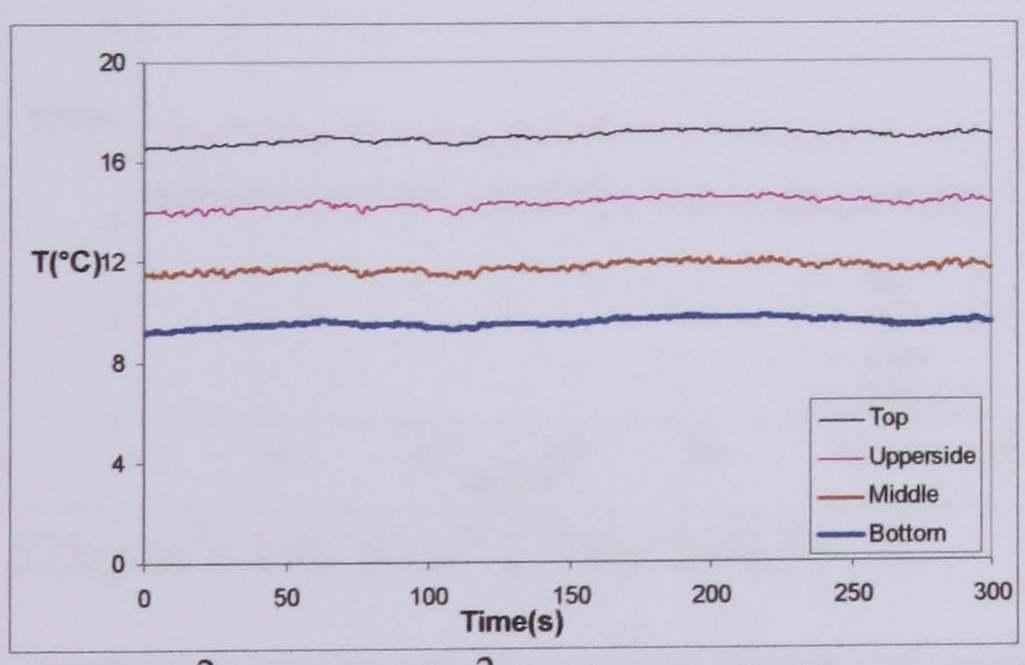

26kg/m^{2}s 19KW/m^2 3.5bar x=0.65

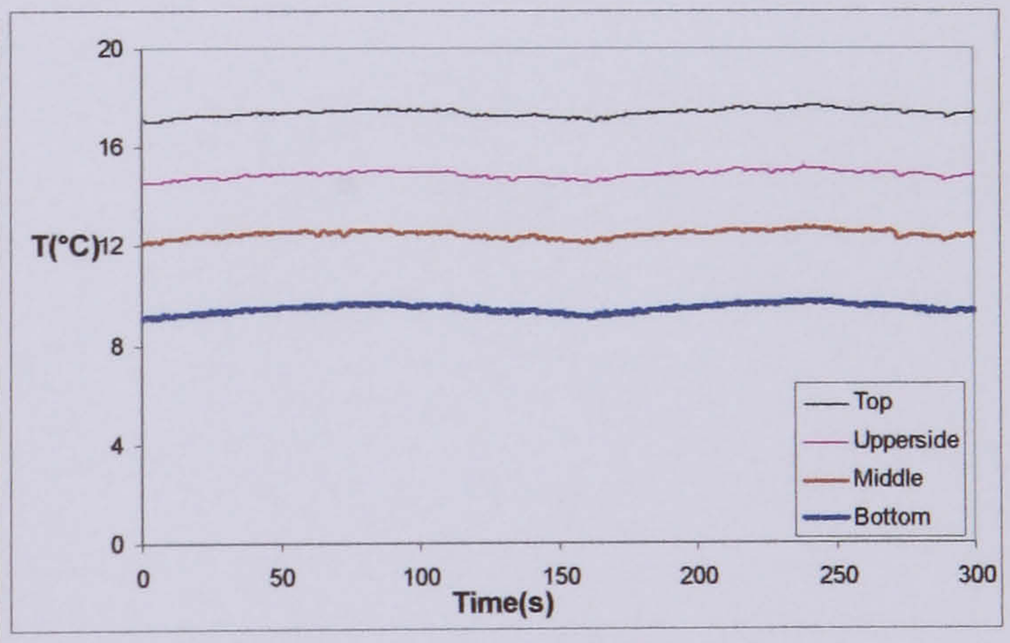

26kg/m^{2}s 19KW/m^2 3.5bar x=0.77

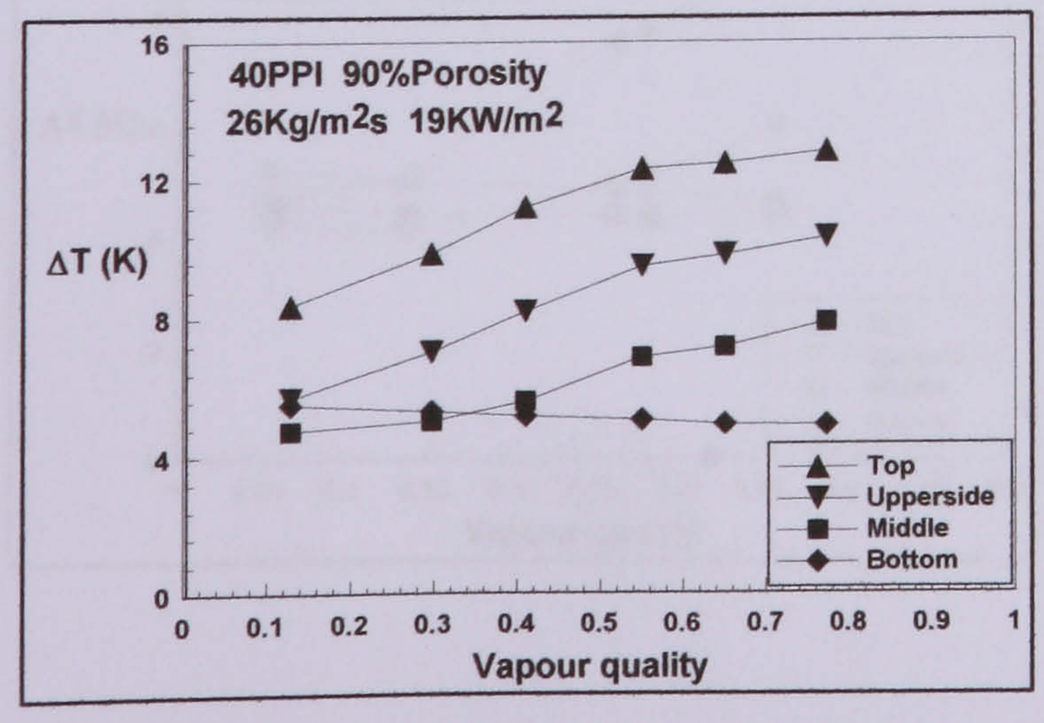

Temperature difference between the wall temperature and the saturated temperature around cross section with low mass flux

b) Wall temperature variation when mass flux is 52 kg/m^{2}s, heat flux is 19 KW/m^2 and pressure at 3.5 bar with 90% porosity, 40 PPI metal foams

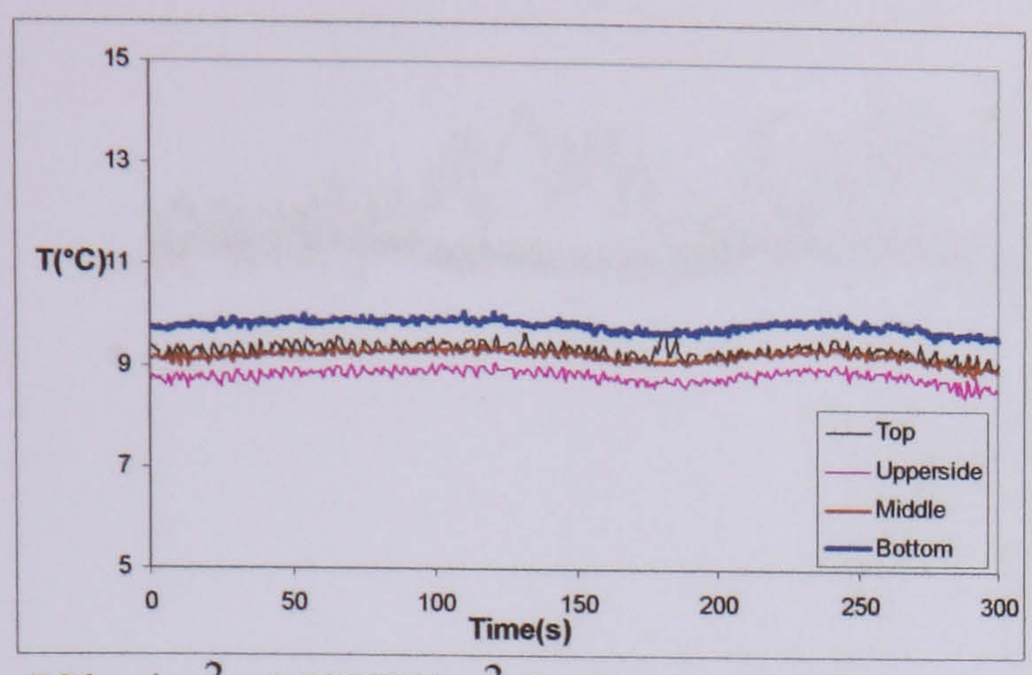

52kg/m^{2}s 19KW/m^2 3.5bar x=0.06

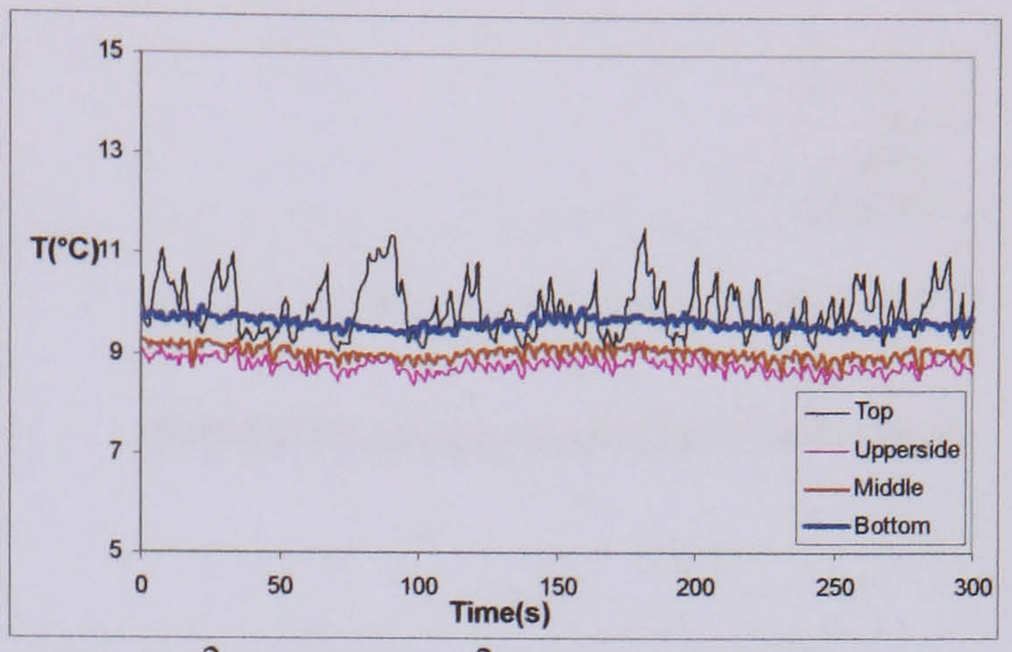

52kg/m^{2}s 19KW/m^2 3.5bar x=0.14

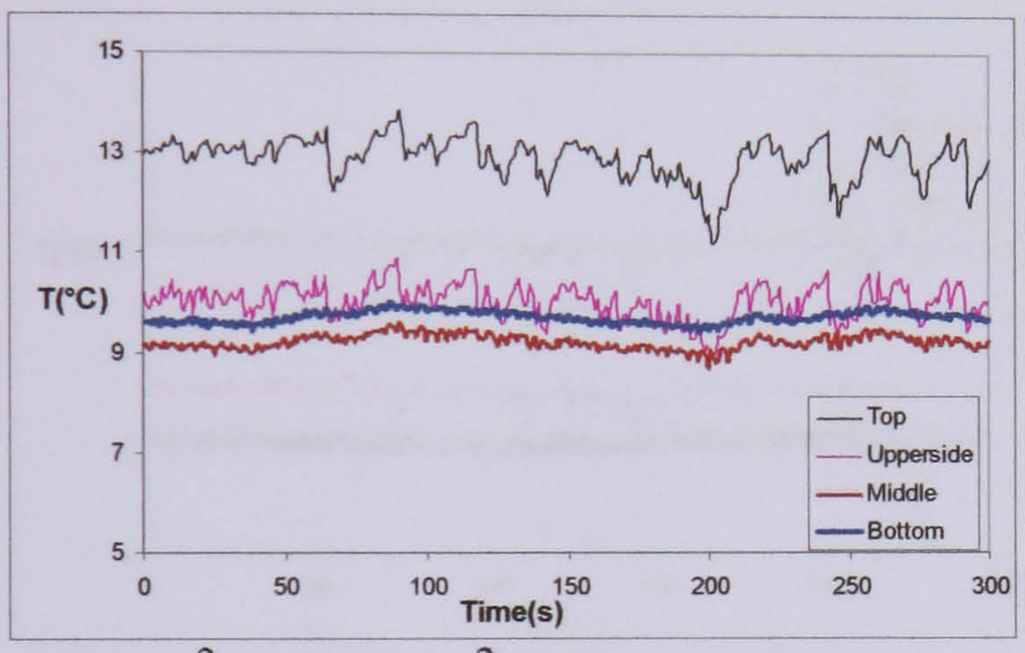

52kg/m^{2}s 19KW/m^2 3.5bar x=0.26

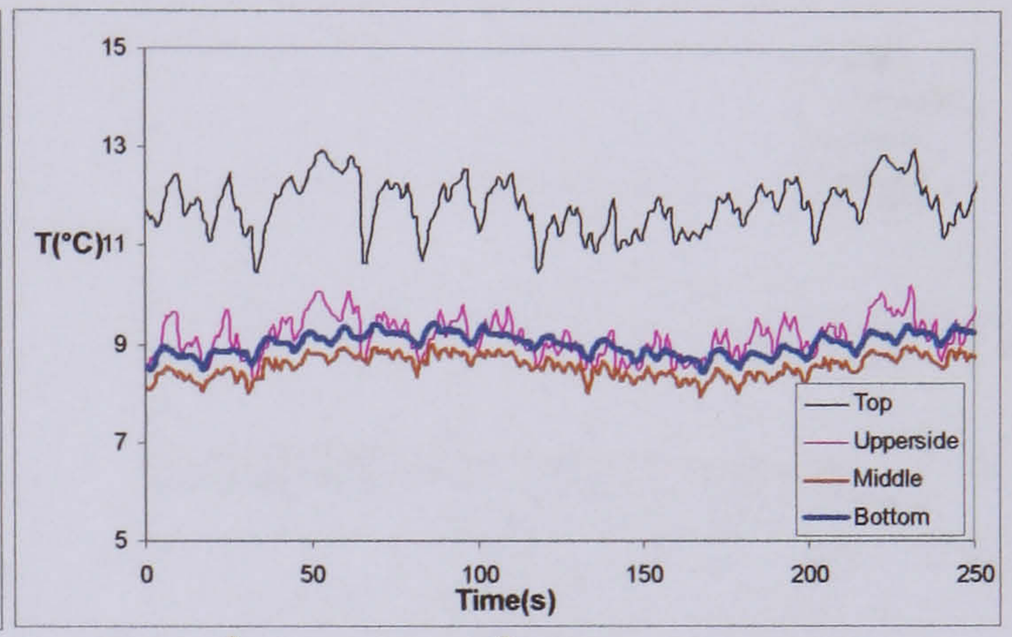

52kg/m^{2}s 19KW/m^2 3.5bar x=0.28

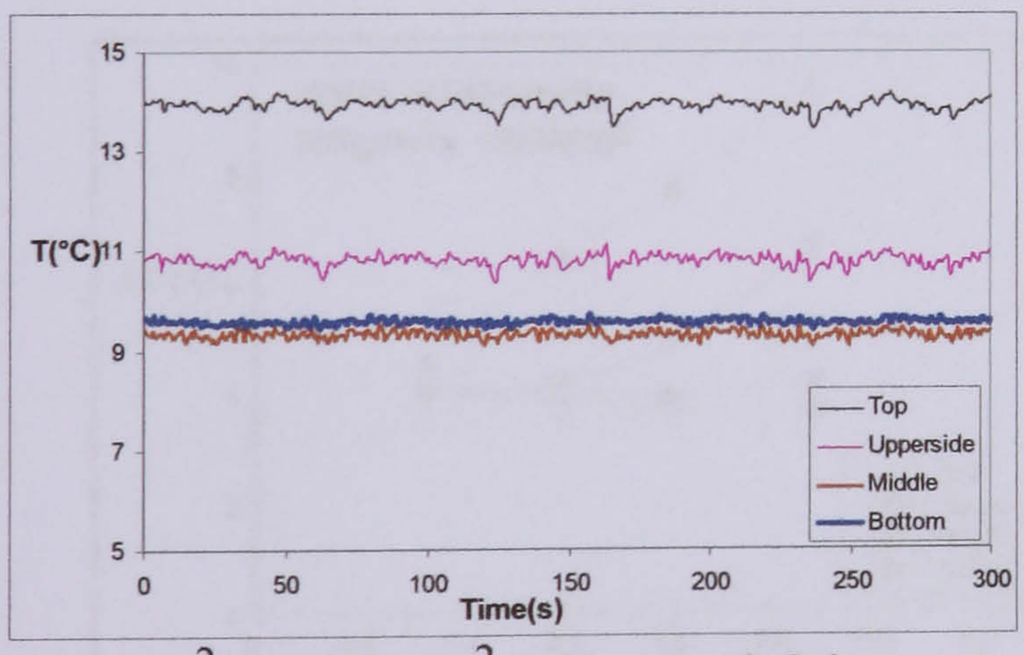

52kg/m^{2}s 19KW/m^2 3.5bar x=0.36

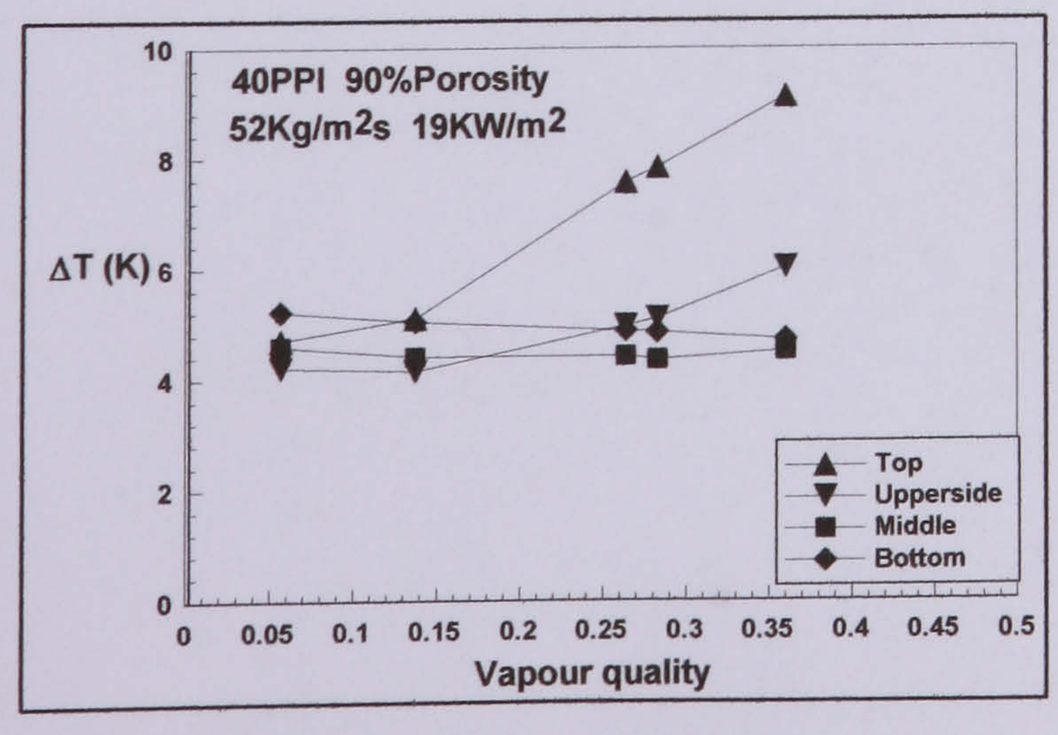

Temperature difference between the wall temperature and the saturated temperature around cross section with low mass flux

c) Wall temperature variation when mass flux is 80 kg/m^{2}s, heat flux is 19 KW/m^2 and pressure at 3.5 bar with 90% porosity, 40 PPI metal foams

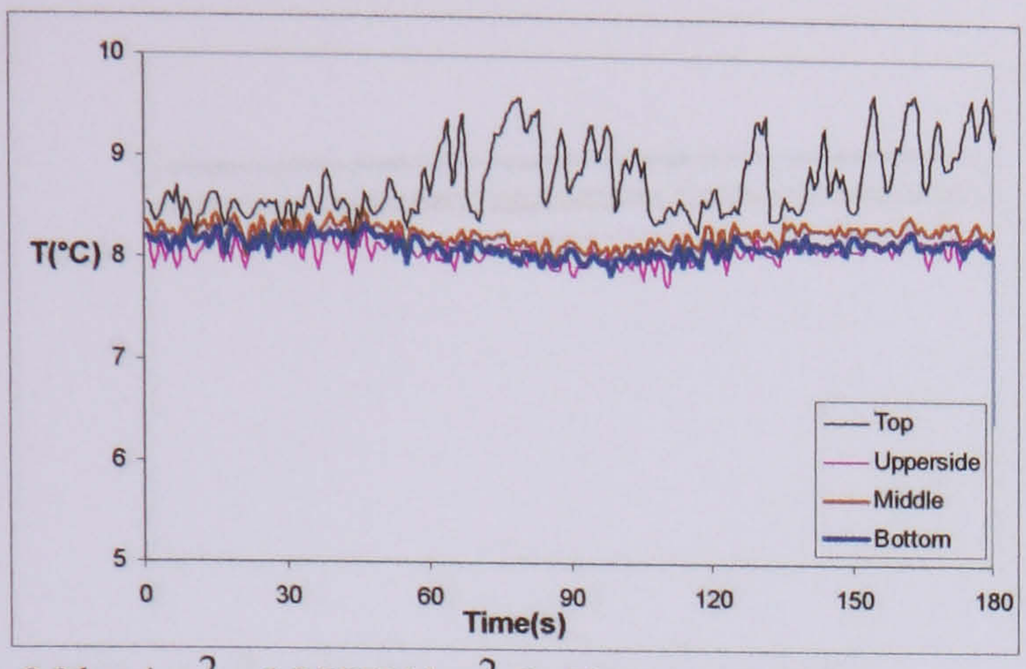

80kg/m^{2}s 19KW/m^2 3.5bar x=0.17

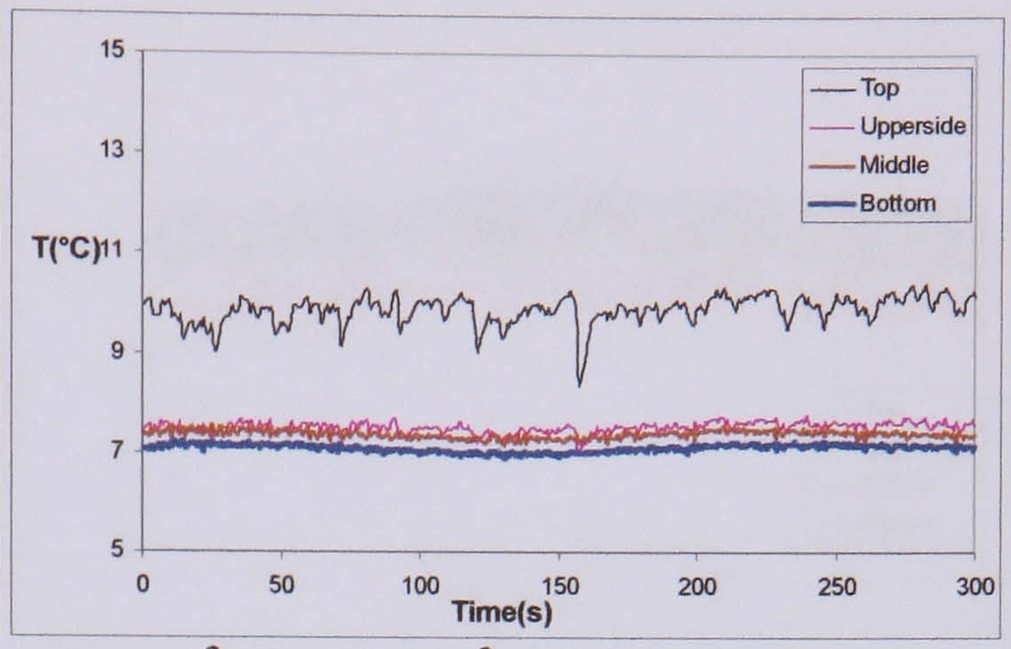

80kg/m^{2}s 19KW/m^2 3.5bar x=0.30

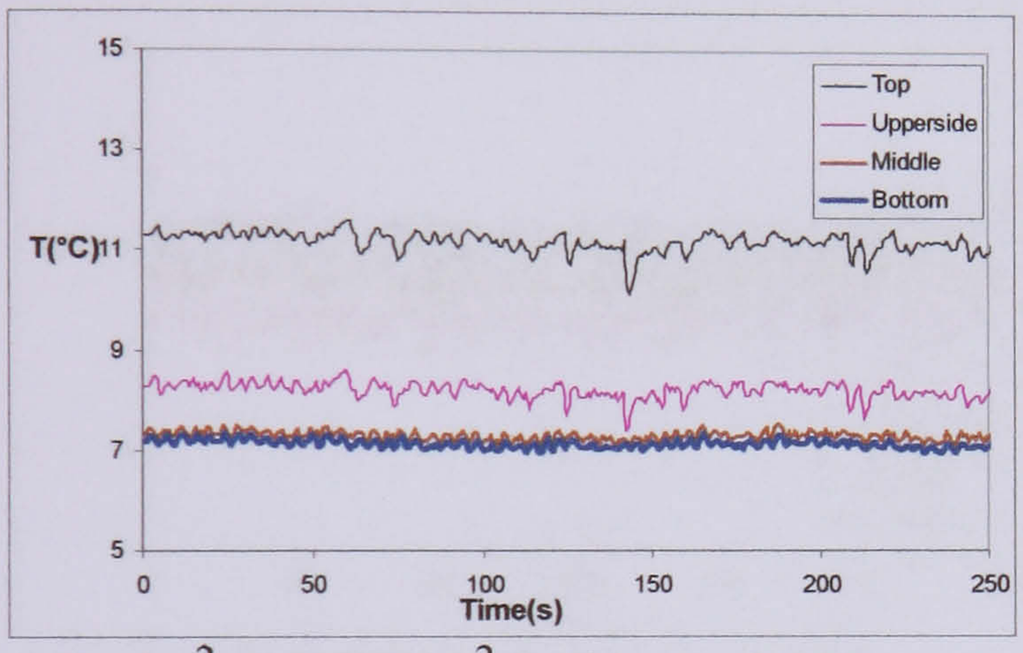

80kg/m^{2}s 19KW/m^2 3.5bar x=0.40

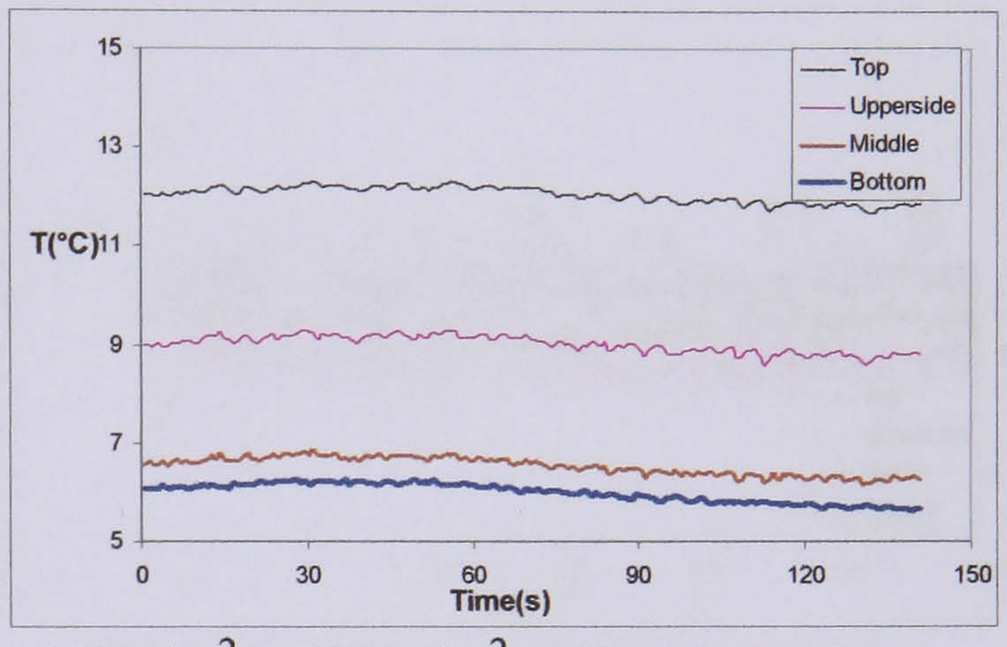

80kg/m^{2}s 19KW/m^2 3.5bar x=0.54

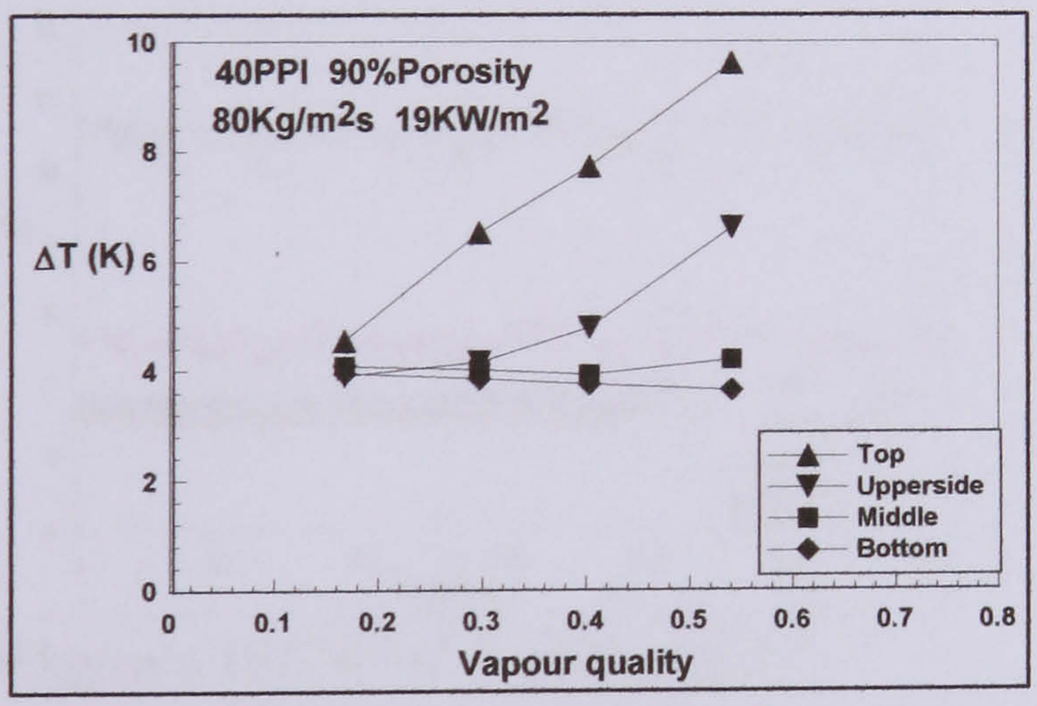

Temperature difference between the wall temperature and the saturated temperature around cross section

d) Wall temperature variation when mass flux is 106 kg/m^{2}s, heat flux is 19 KW/m^2 and pressure at 3.5 bar with 90% porosity, 40 PPI metal foams

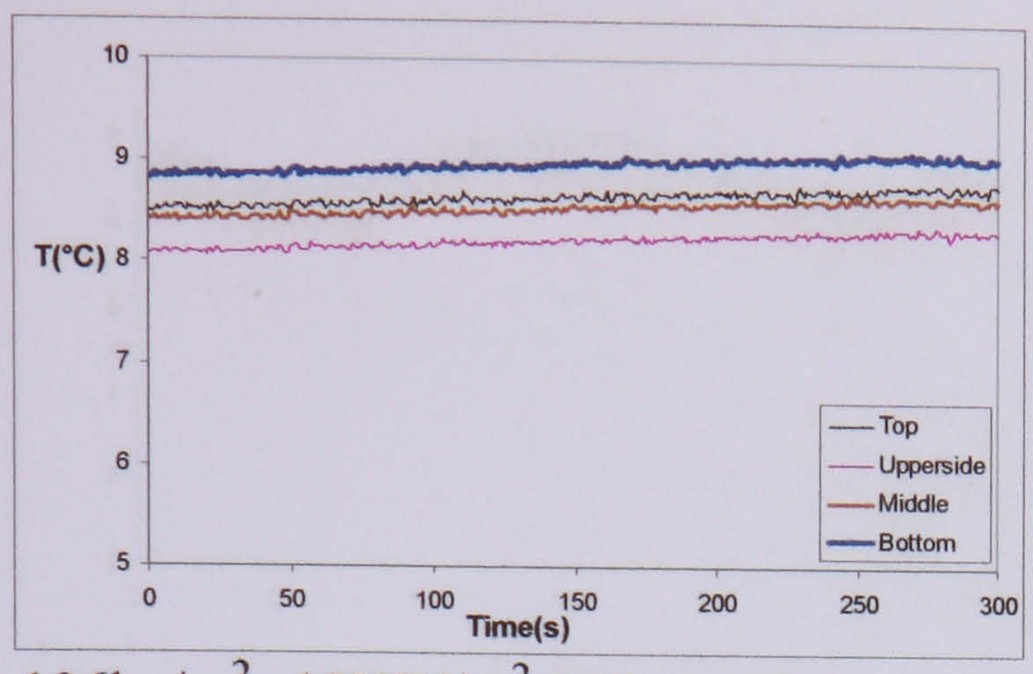

106kg/m^{2}s 19KW/m^2 3.5bar x=0.01

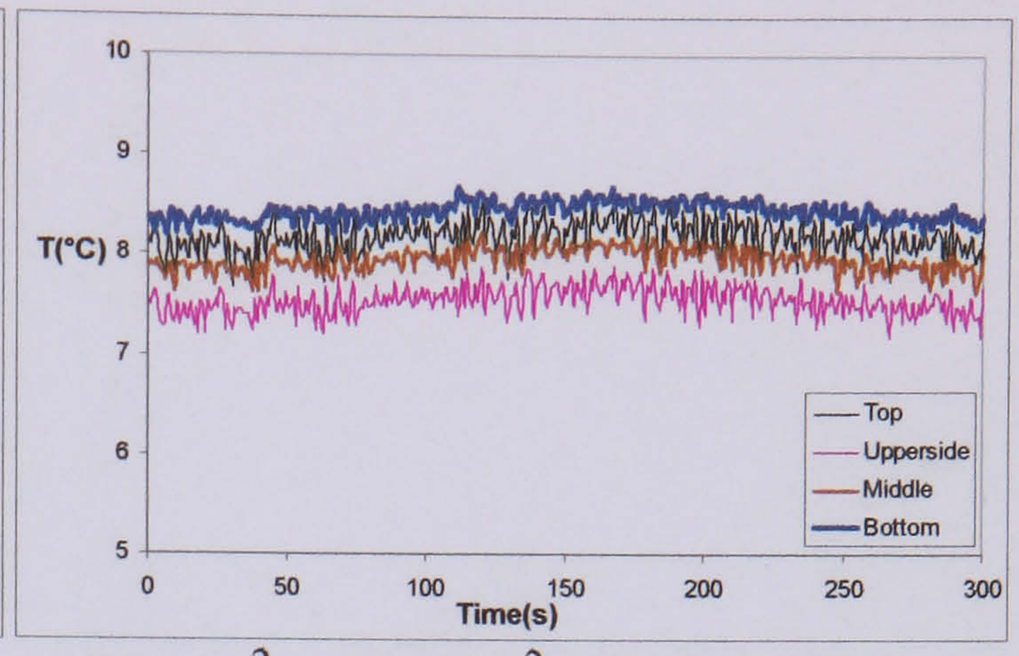

106kg/m^{2}s 19KW/m^2 3.5bar x=0.09

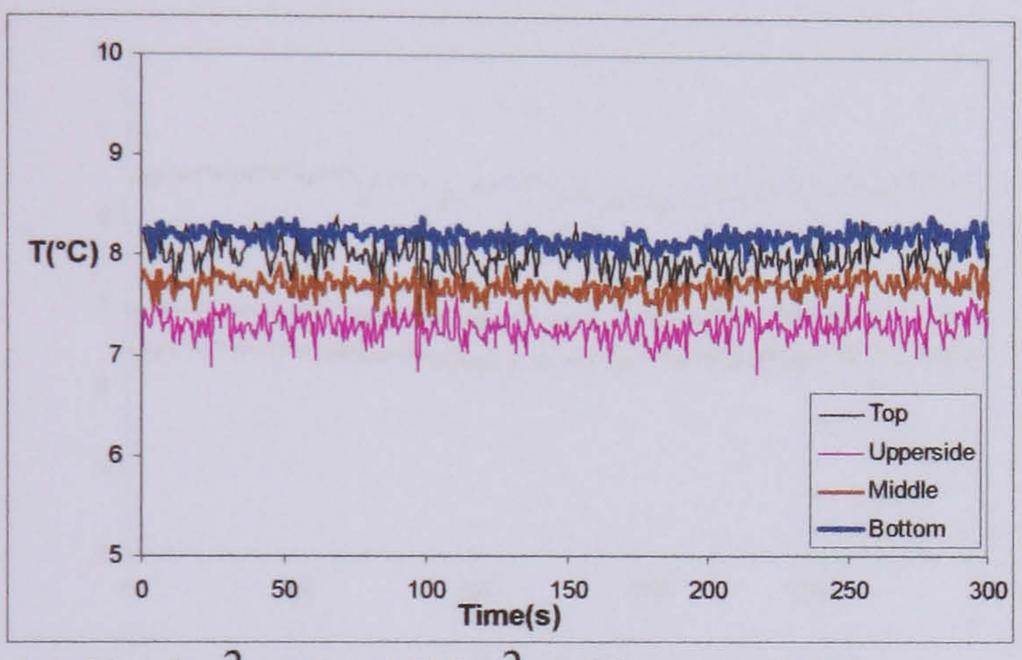

106kg/m^{2}s 19KW/m^2 3.5bar x=0.19

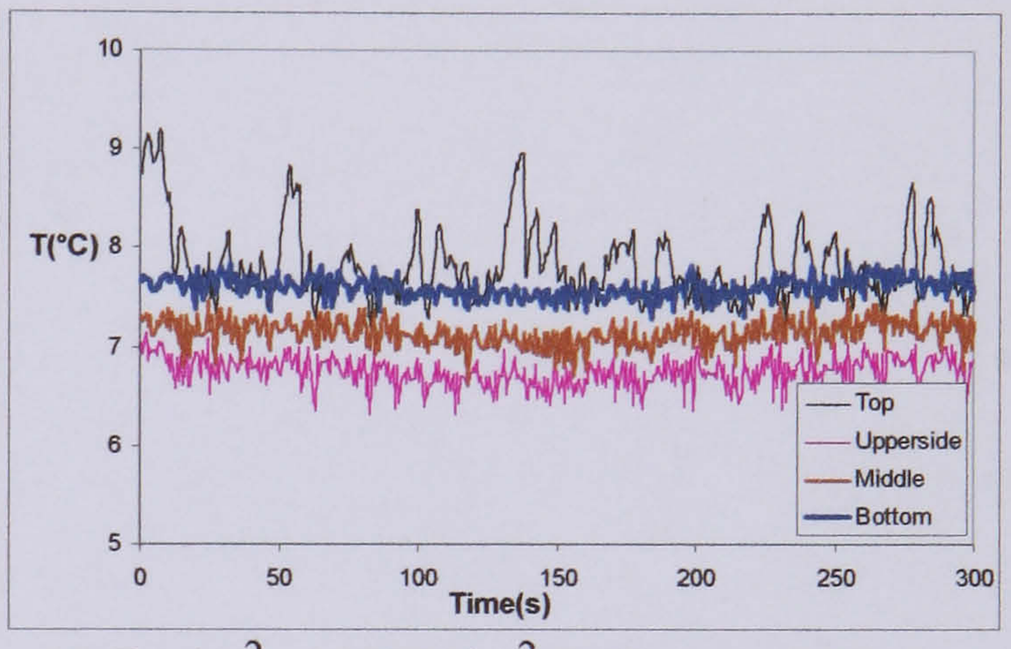

106kg/m^{2}s 19KW/m^2 3.5bar x=0.30

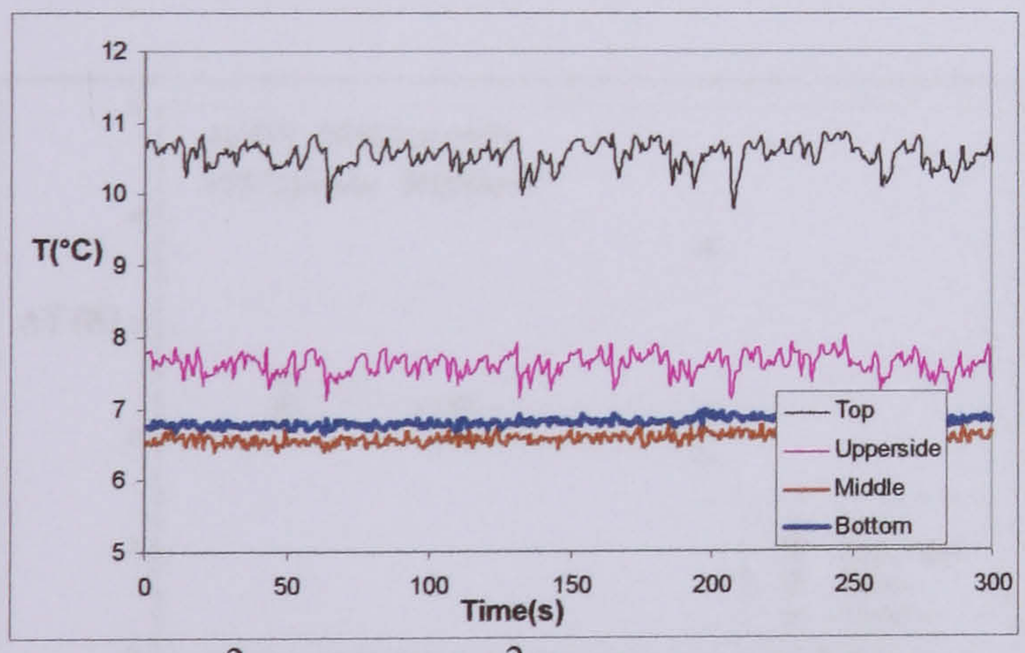

106kg/m^{2}s 19KW/m^2 3.5bar x=0.53

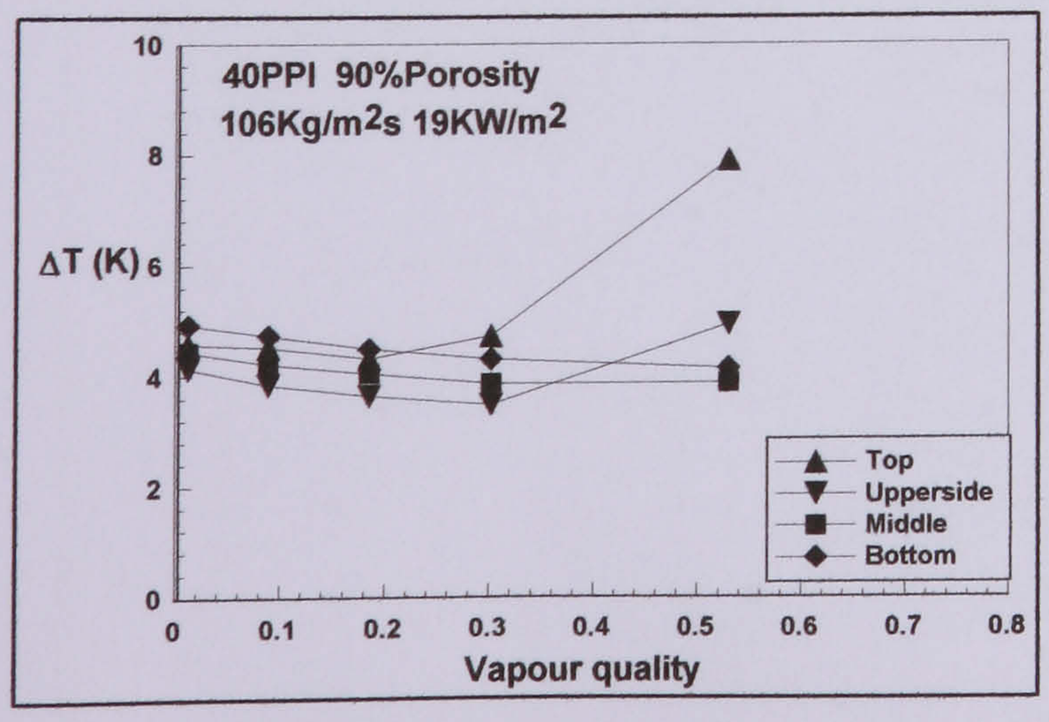

Temperature difference between the wall temperature and the saturated temperature around cross section with high mass flux

e) Wall temperature variation when mass flux is 106 kg/m^{2}s, heat flux is 9 KW/m^2 and pressure at 3.5 bar with 90% porosity, 40 PPI metal foams

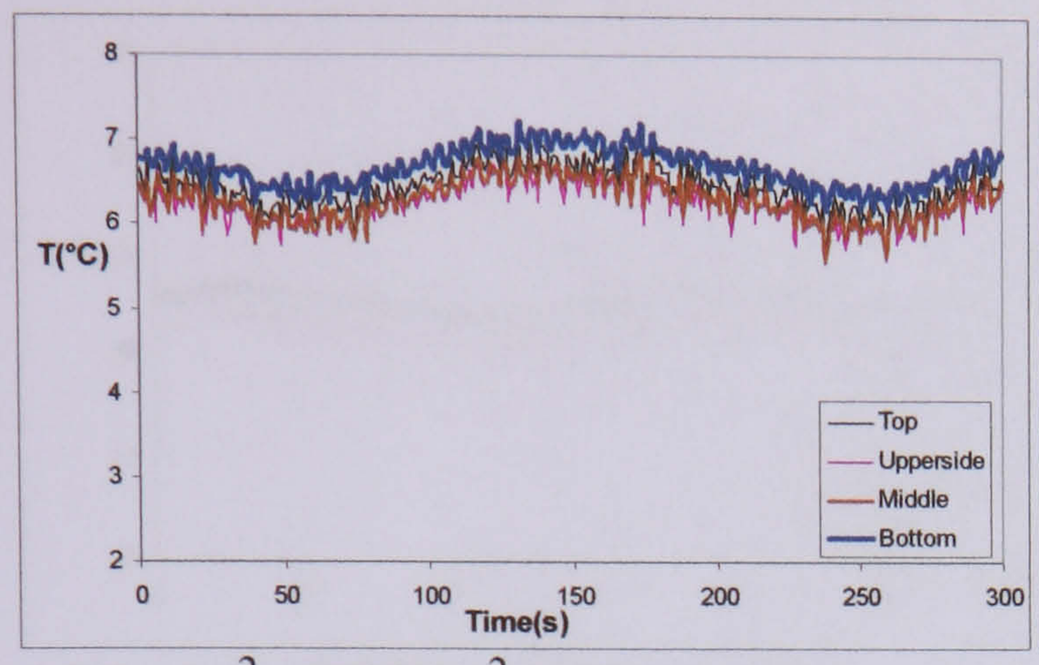

106kg/m^{2}s 9KW/m^2 3.5bar x=0.12

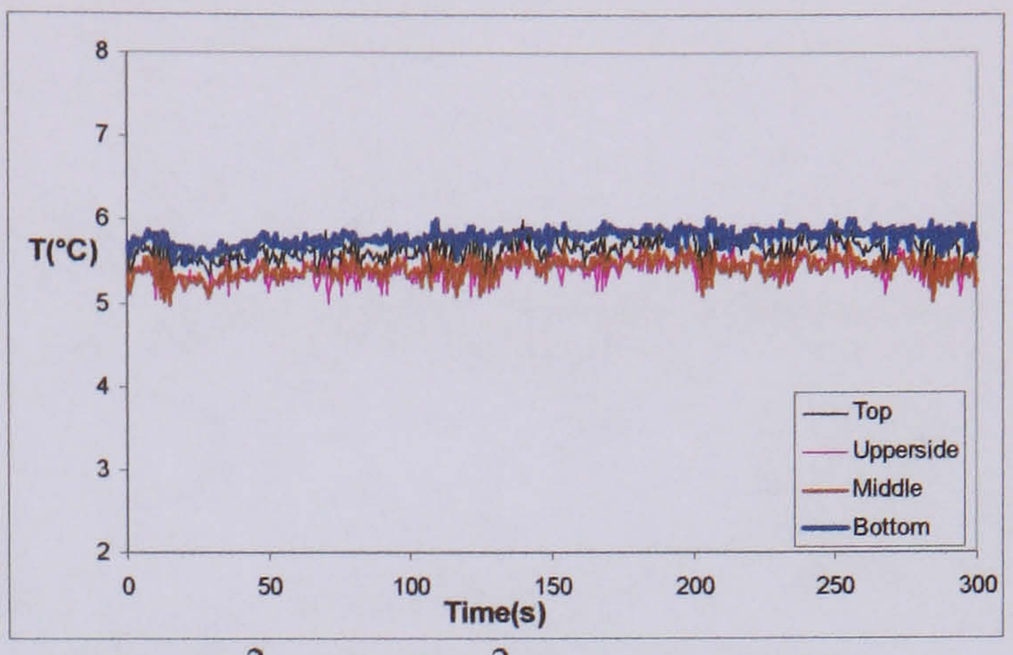

106kg/m^{2}s 9KW/m^2 3.5bar x=0.29

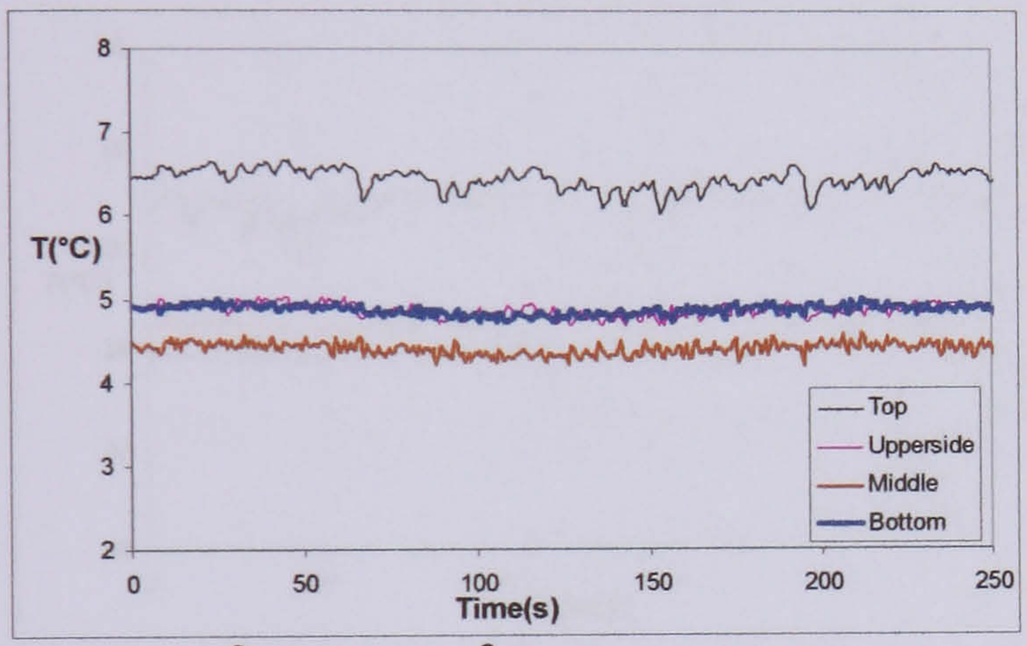

106kg/m^{2}s 9KW/m^2 3.5bar x=0.53

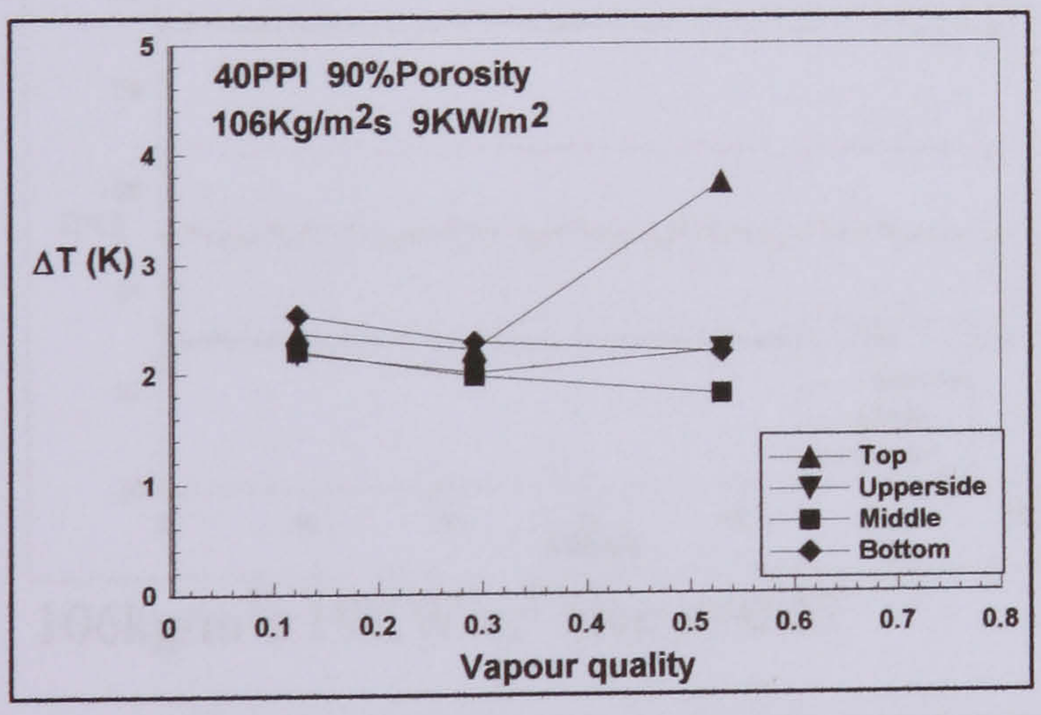

Temperature difference between the wall temperature and the saturated temperature around cross section with high mass flux and low heat flux

f) Wall temperature variation when mass flux is 106 kg/m^{2}s, heat flux is 19 KW/m^2 and pressure at 3.5 bar with 90% porosity, 40 PPI metal foams

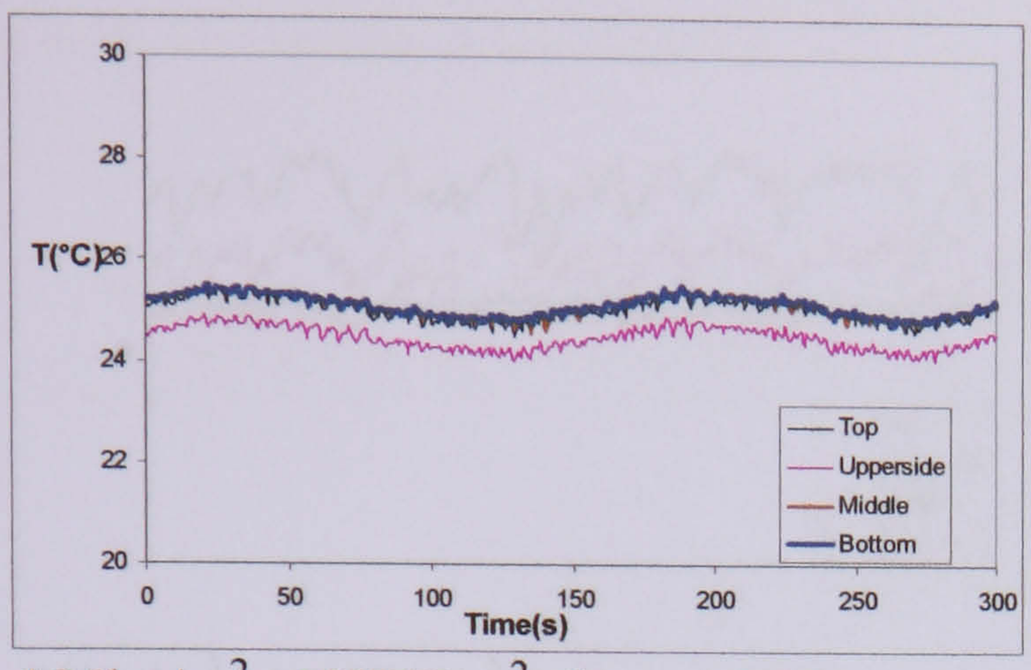

106kg/m^{2}s 19KW/m^2 6bar x=0.09

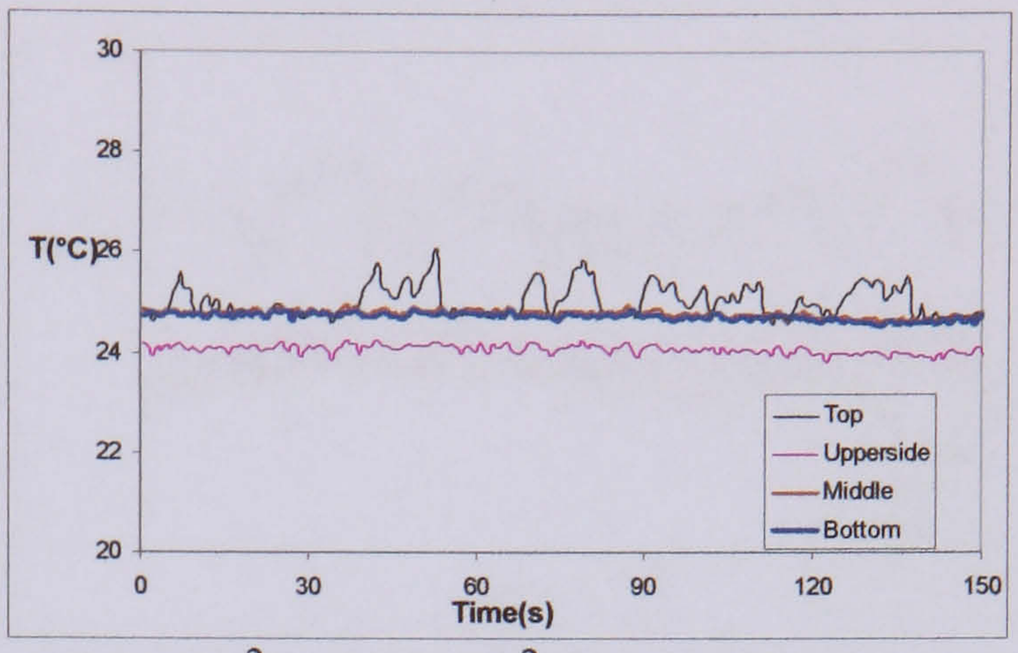

106kg/m^{2}s 19KW/m^2 6bar x=0.15

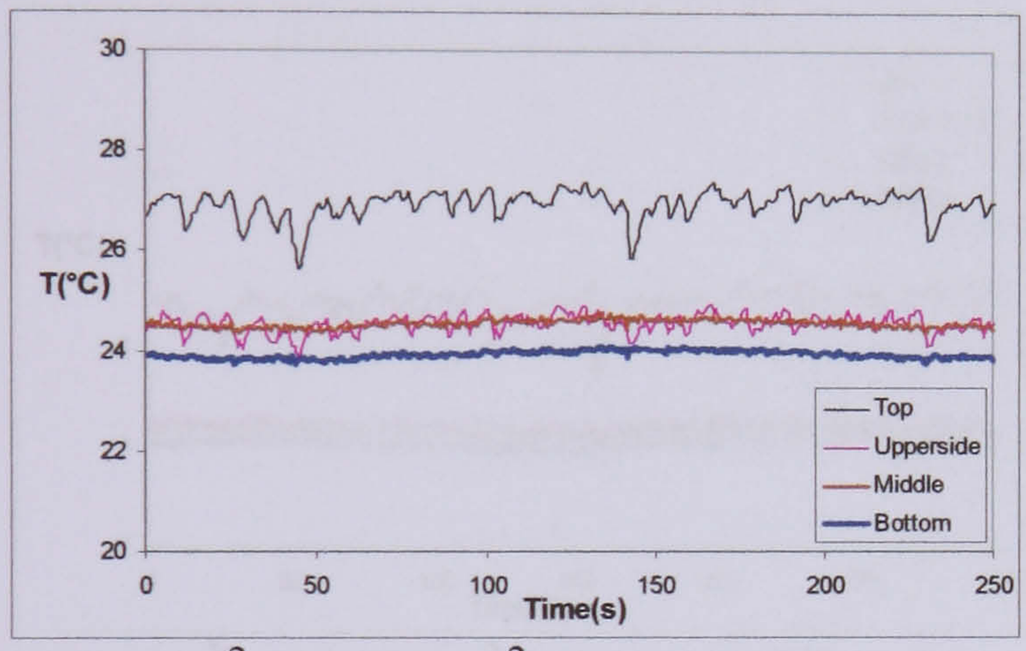

106kg/m^{2}s 19KW/m^2 6bar x=0.35

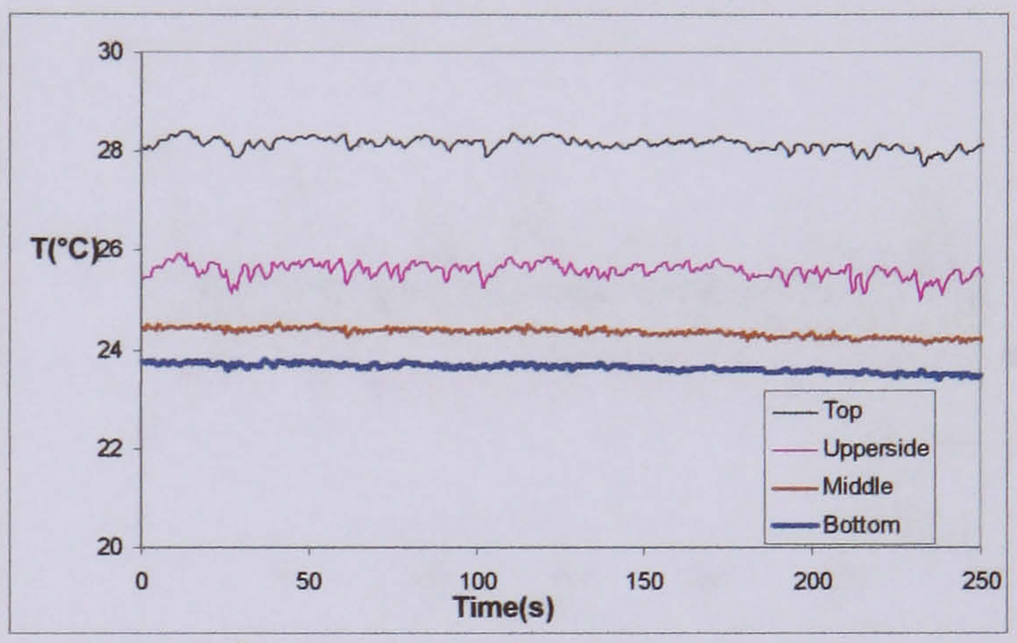

106kg/m^{2}s 19KW/m^2 6bar x=0.48

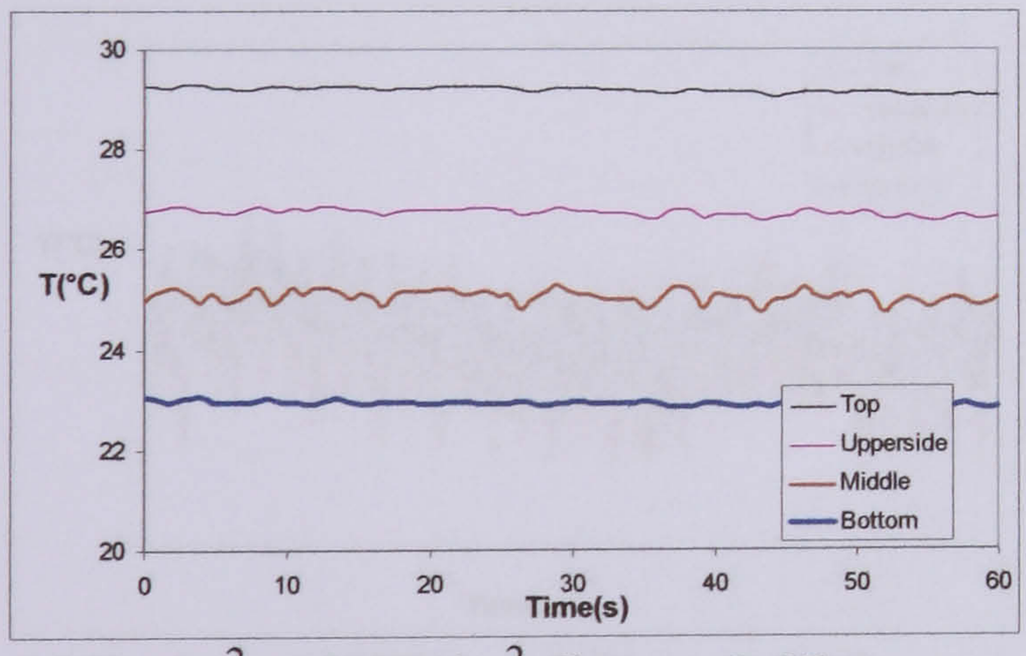

106kg/m^{2}s 19KW/m^2 6bar x=0.67

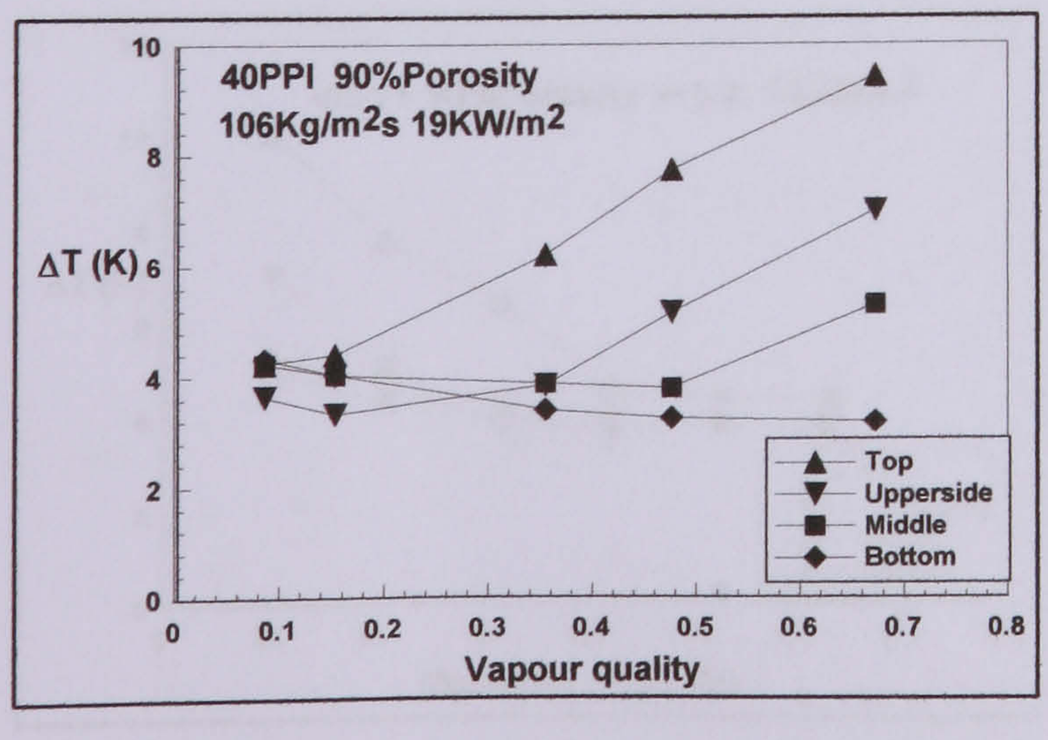

Temperature difference between the wall temperature and the saturated temperature around cross section with high mass flux and high pressure

g) Wall temperature variation when mass flux is different with 90% porosity, 40 PPI metal foams

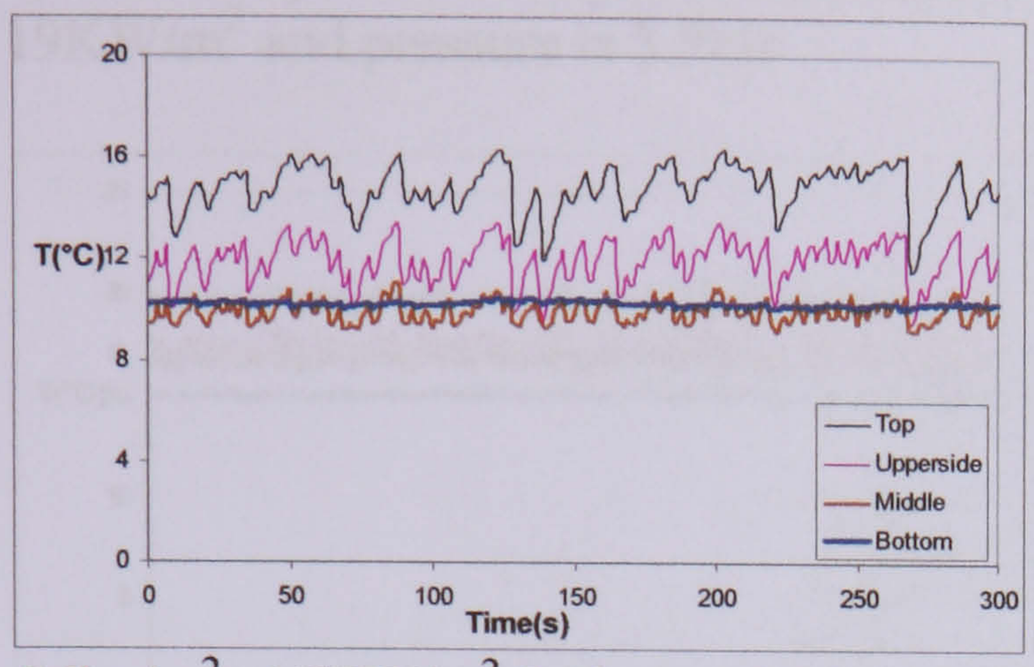

26kg/m^{2}s 19KW/m^2 3.5bar x=0.29

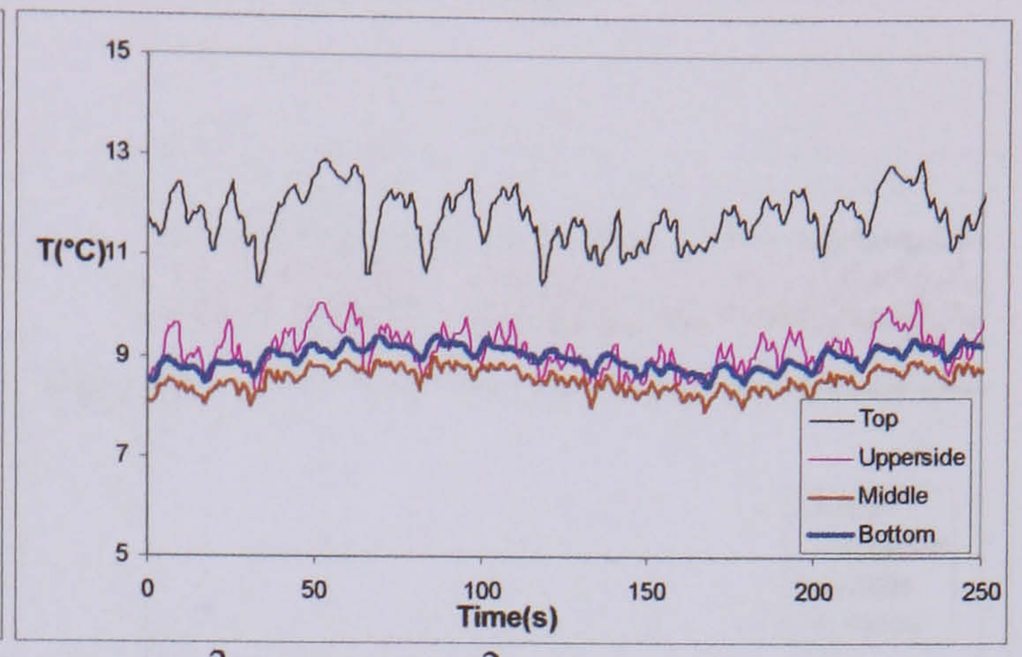

52kg/m^{2}s 19KW/m^2 3.5bar x=0.28

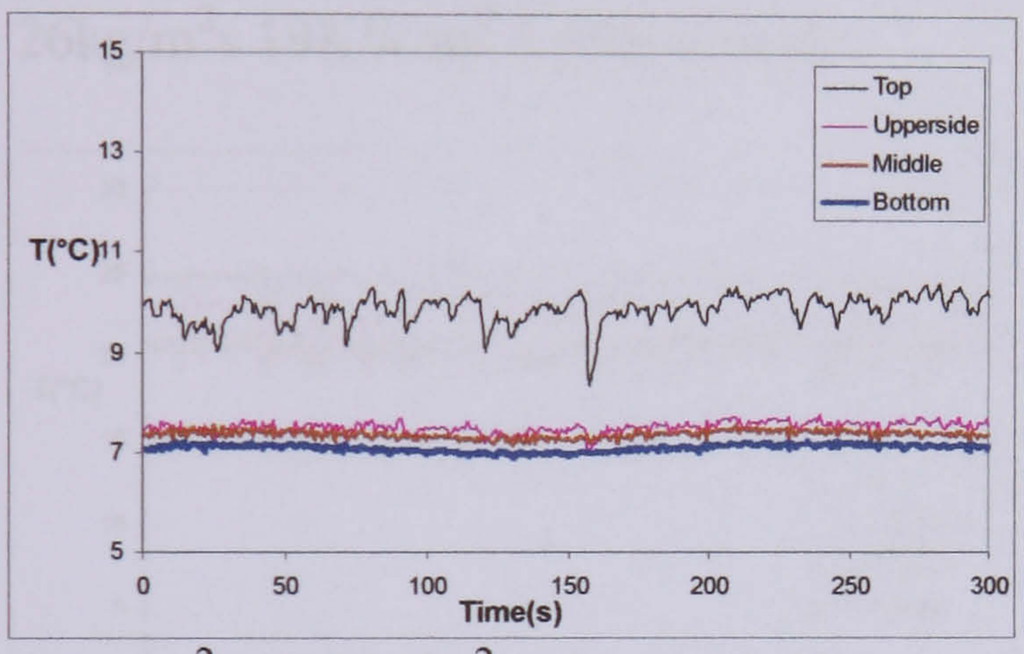

80kg/m^{2}s 19KW/m^2 3.5bar x=0.30

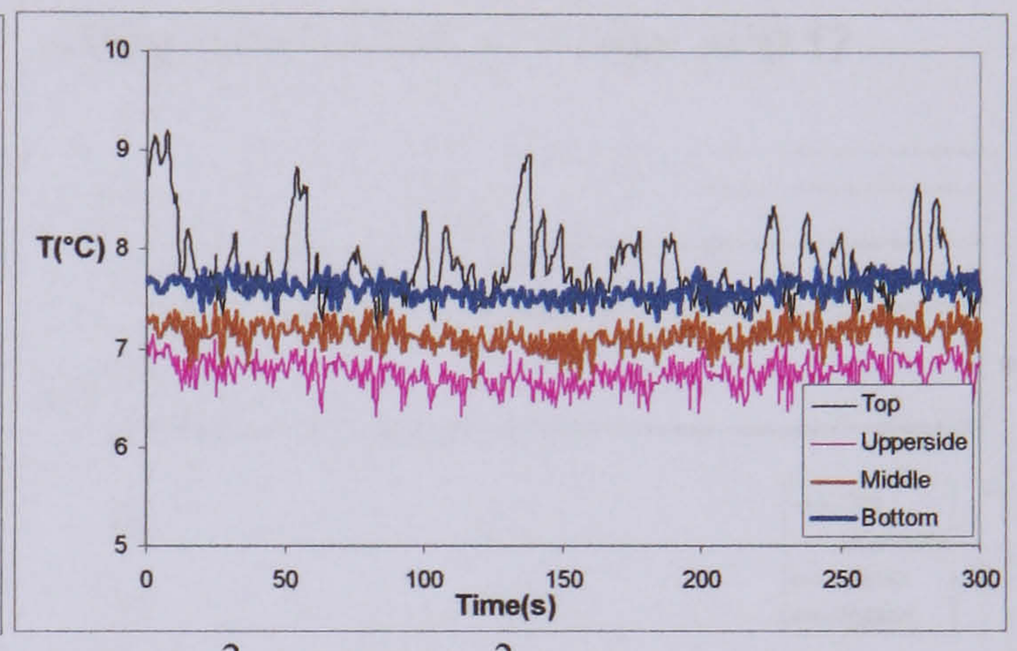

106kg/m^{2}s 19KW/m^2 3.5bar x=0.30

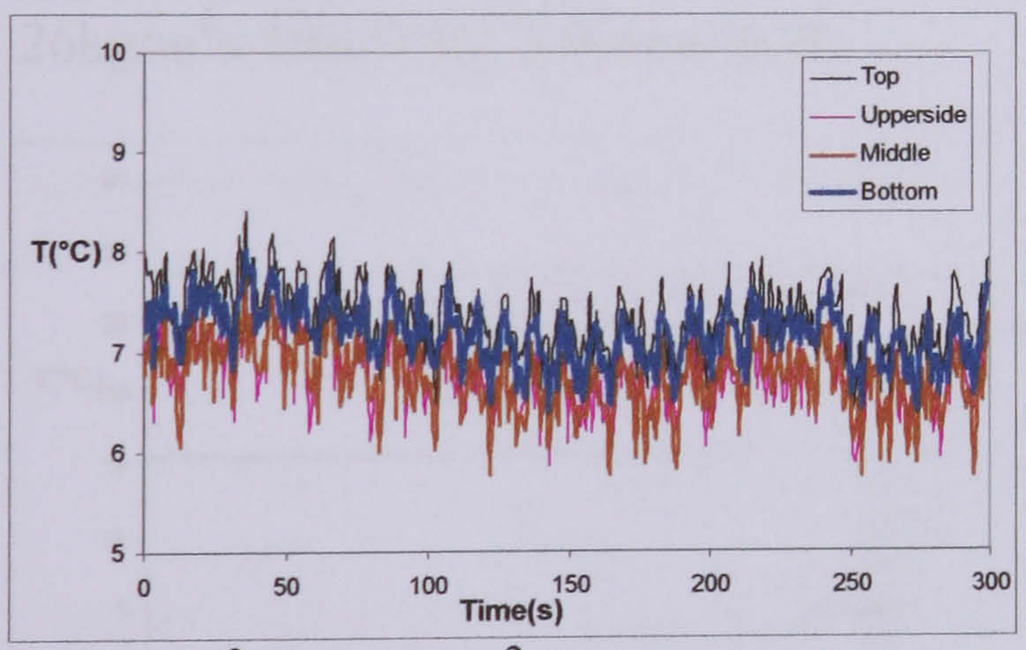

132kg/m^{2}s 19KW/m^2 3.5bar x=0.32

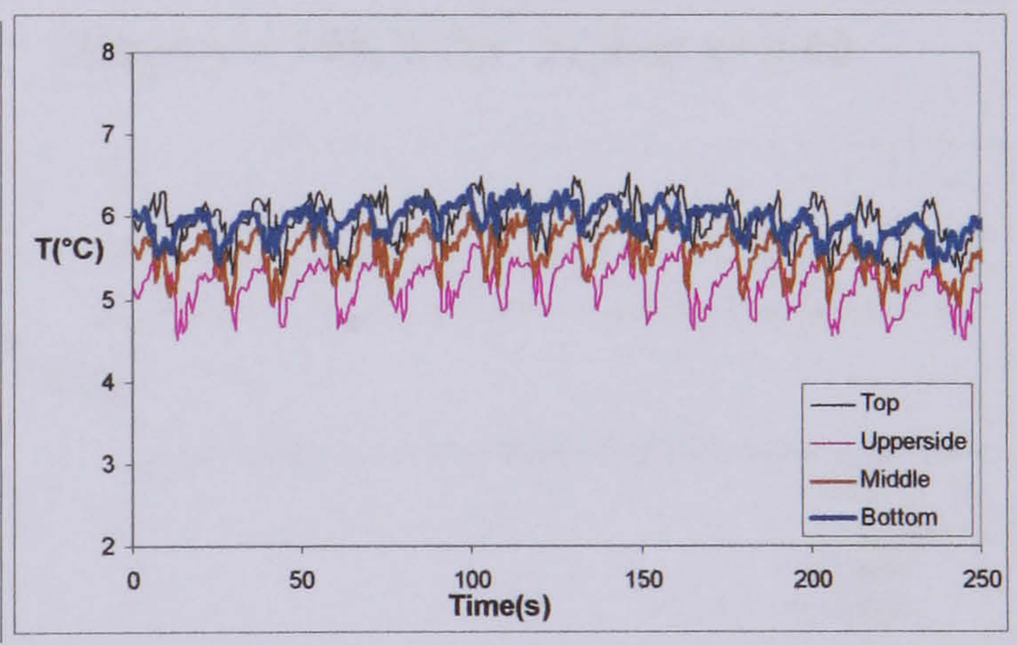

158kg/m^{2}s 19KW/m^2 3.5bar x=0.32

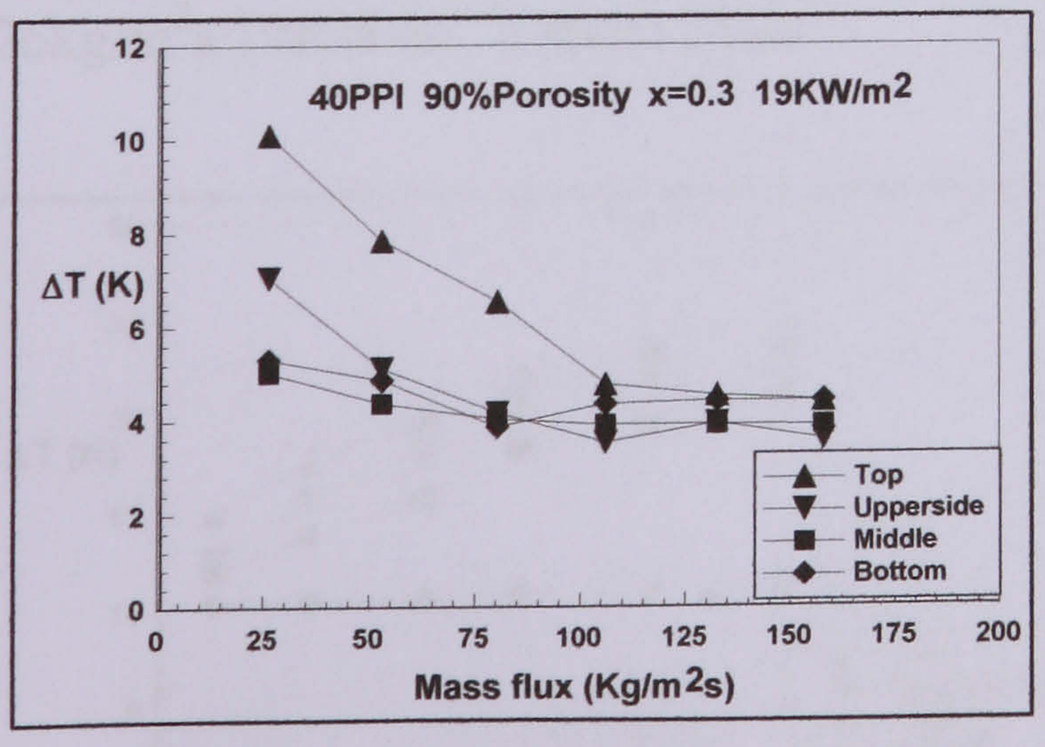

Temperature difference between the wall temperature and the saturated temperature around cross section with different mass flux (vapour quality=0.3 3.5bar 19KW/m^2)

D3 Wall temperature variation of plain tube

a) Wall temperature variation in plain tube when mass flux is 26kg/m^{2}s, heat flux is 19KW/m^2 and pressure is 3.5bar

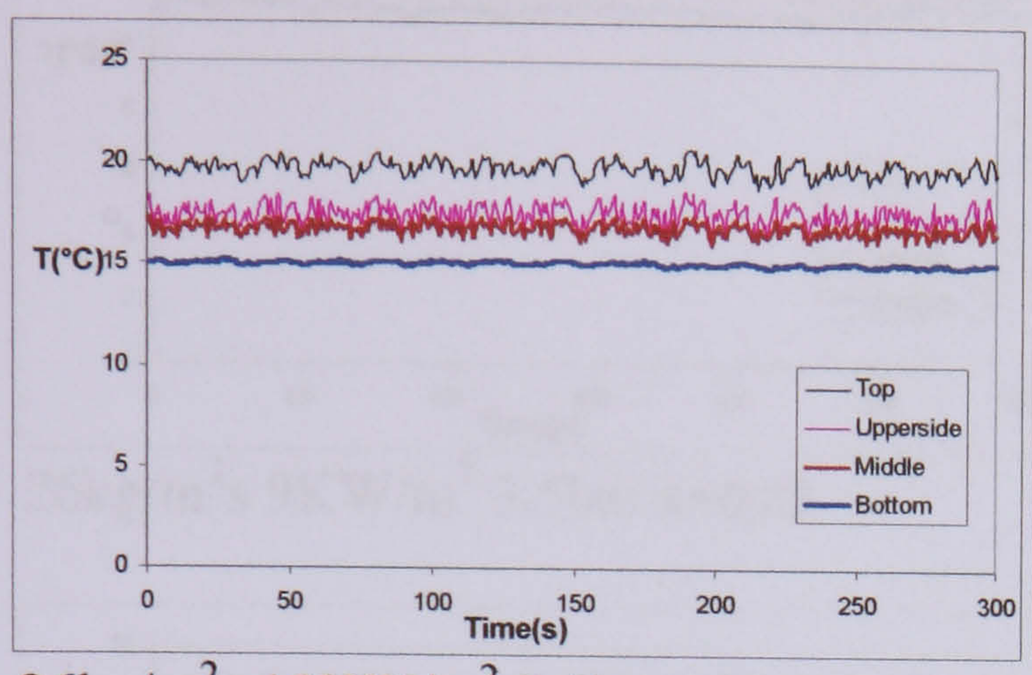

26kg/m^{2}s 19KW/m^2 3.5bar x=0.06

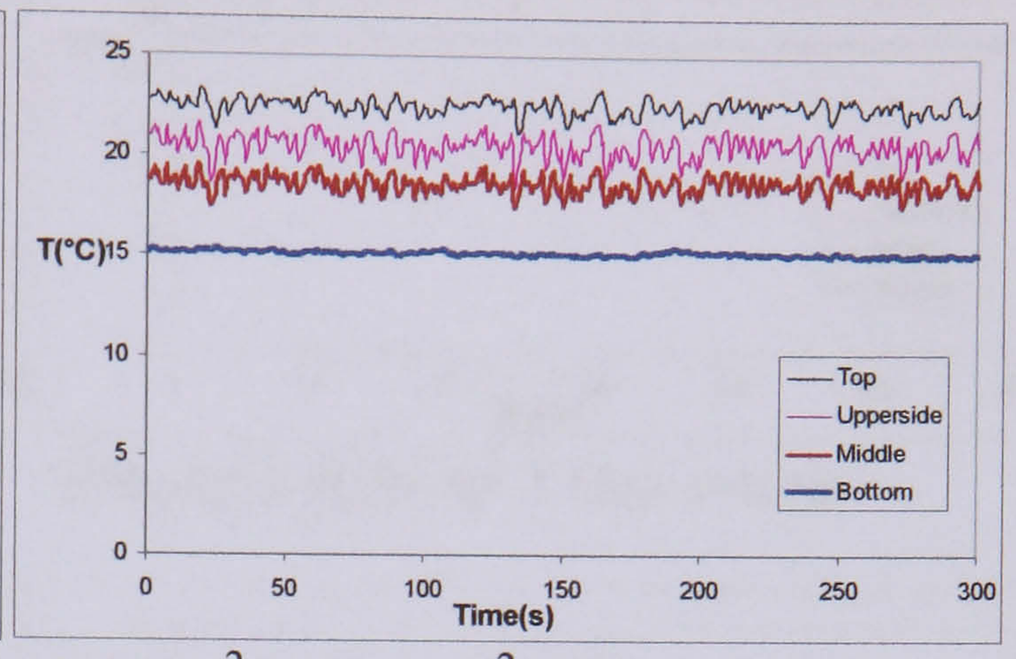

26kg/m^{2}s 19KW/m^2 3.5bar x=0.17

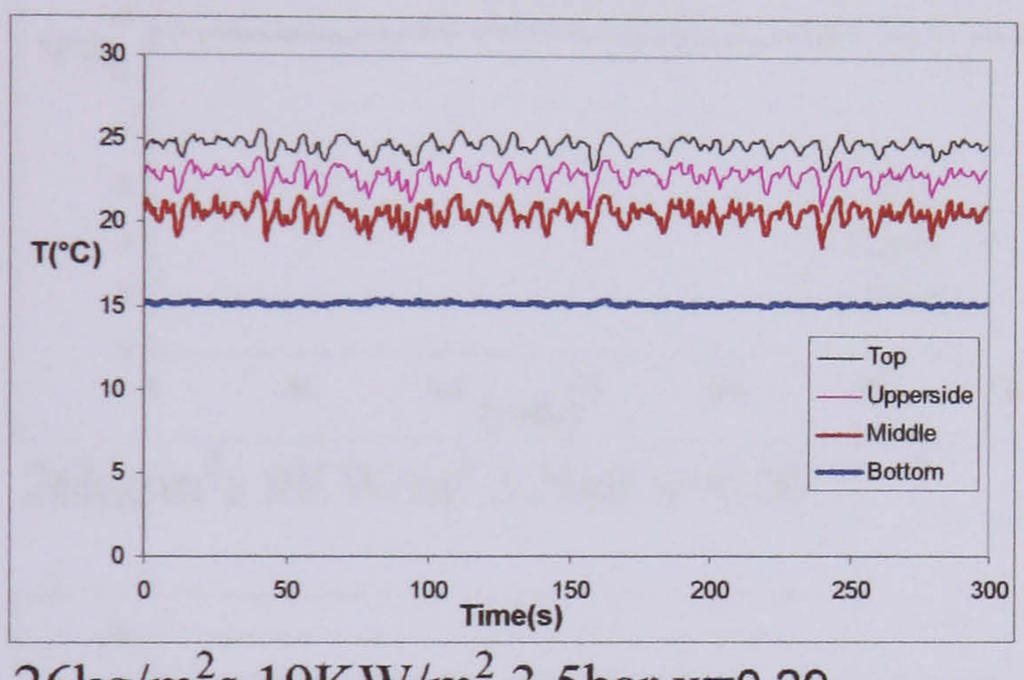

26kg/m^{2}s 19KW/m^2 3.5bar x=0.29

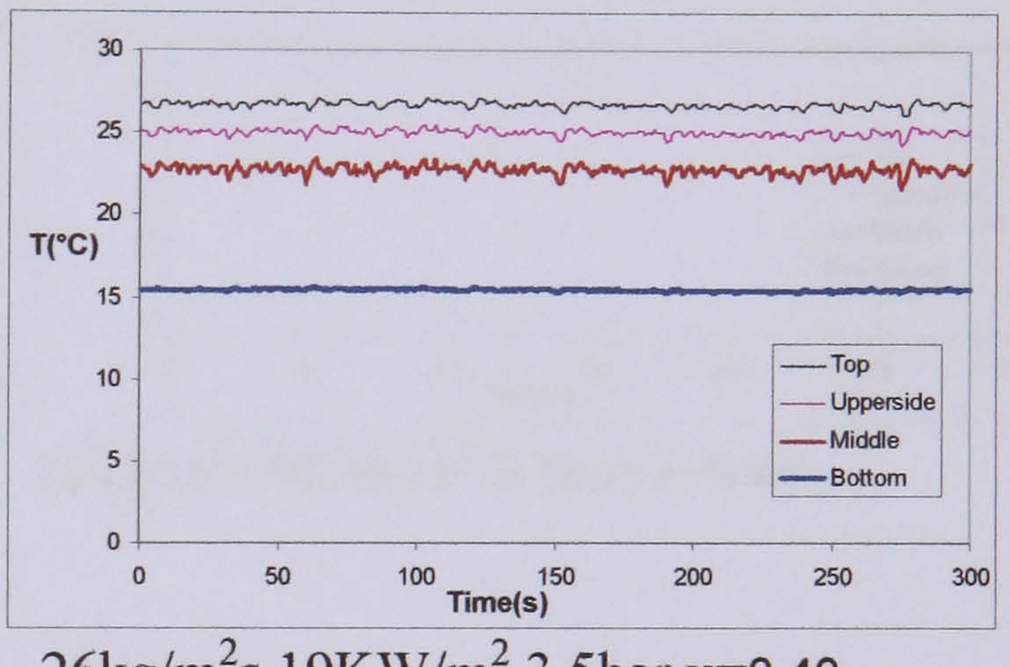

26kg/m^{2}s 19KW/m^2 3.5bar x=0.40

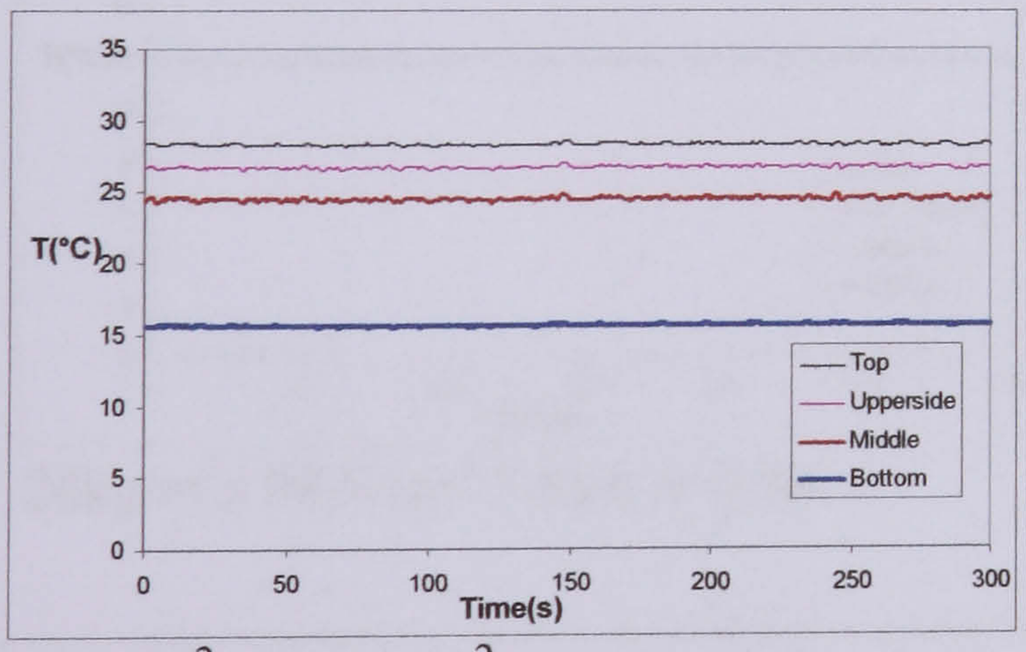

26kg/m^{2}s 19KW/m^2 3.5bar x=0.54

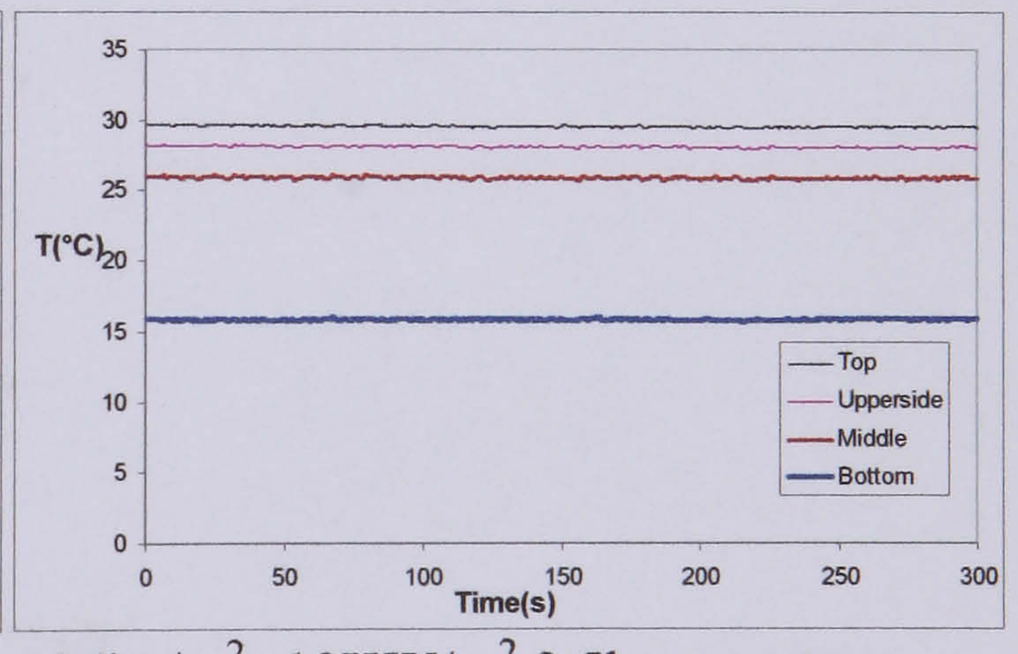

26kg/m^{2}s 19KW/m^2 3.5bar x=0.69

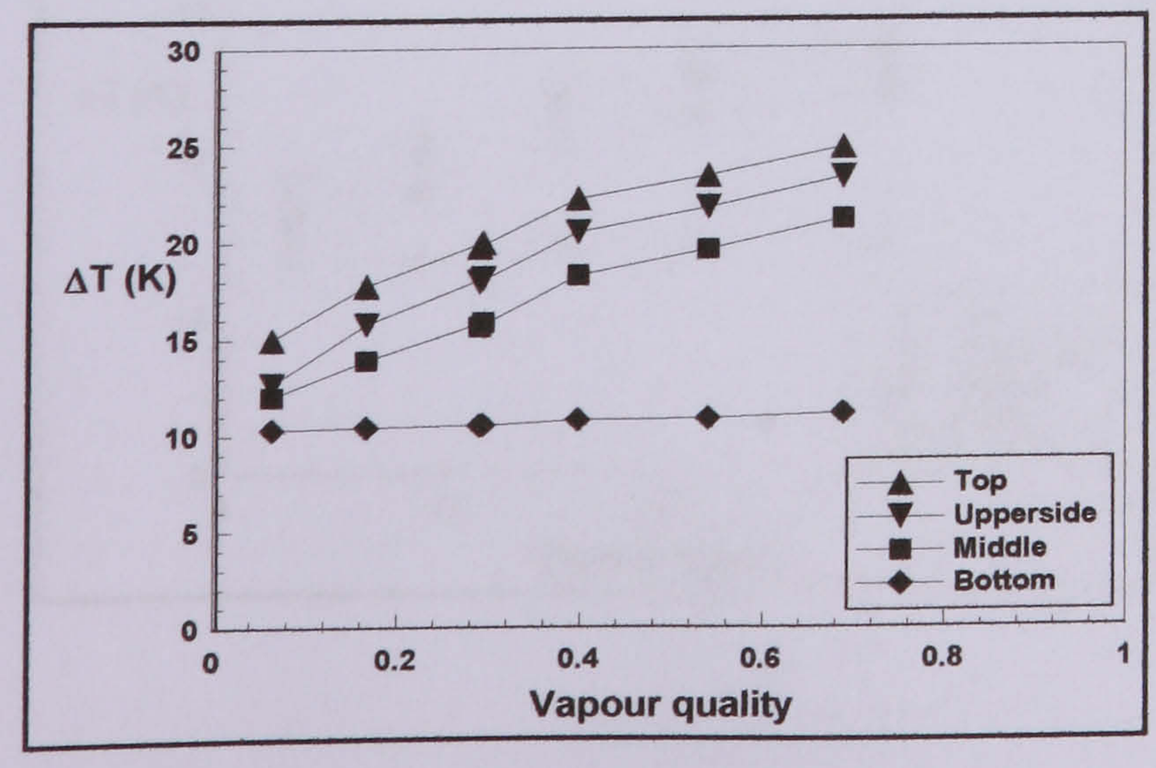

Temperature difference between the wall temperature and the saturated temperature around cross section with low mass flux (26kg/m^{2}s, 19KW/m^2, 3.5bar)

b) Wall temperature variation in plain tube when heat flux is 9KW/m^2

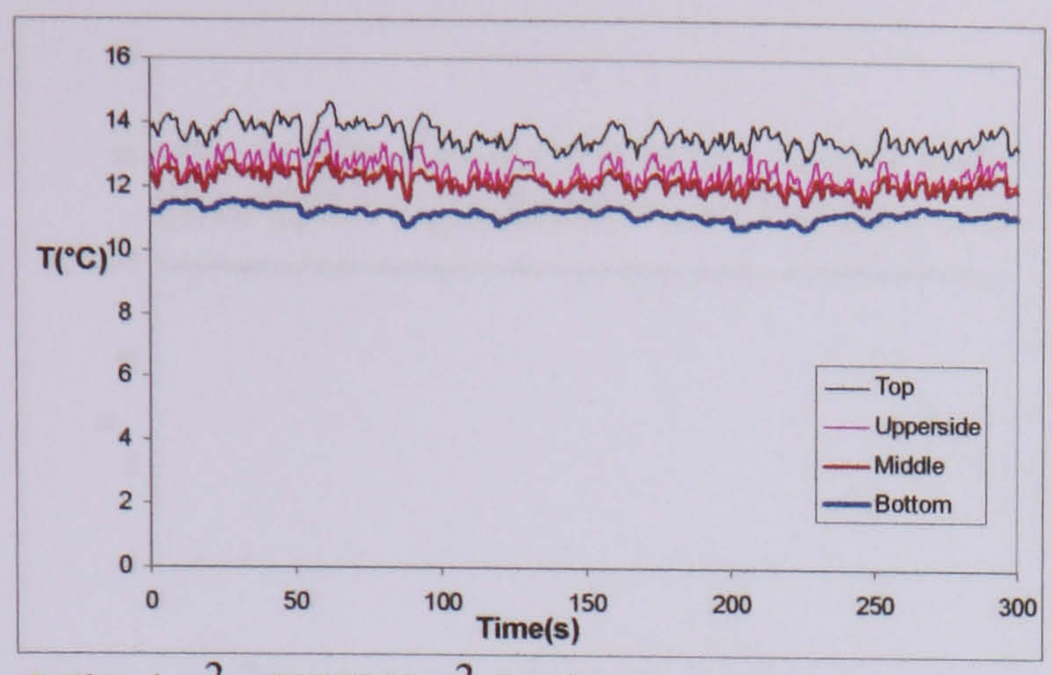

26kg/m^{2}s 9KW/m^2 3.5bar x=0.06

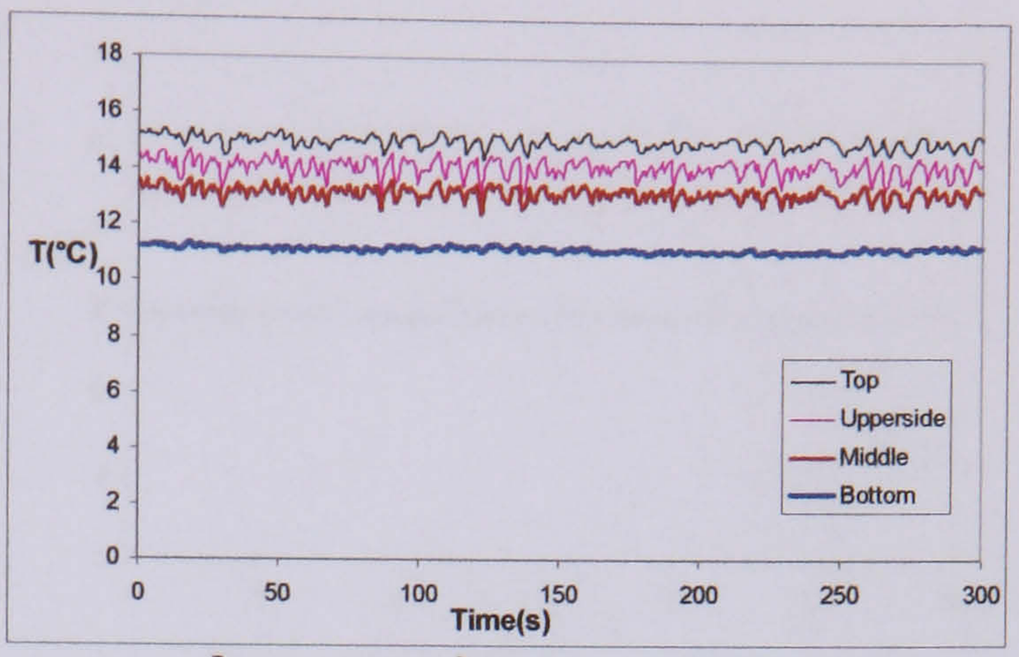

26kg/m^{2}s 9KW/m^2 3.5bar x=0.18

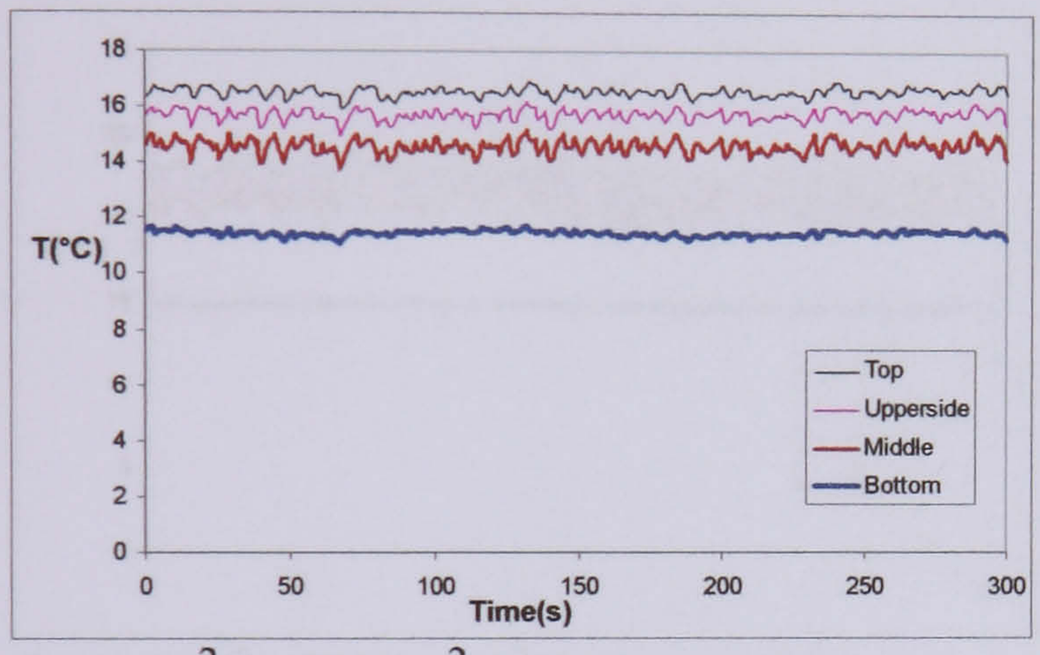

26kg/m^{2}s 9KW/m^2 3.5bar x=0.30

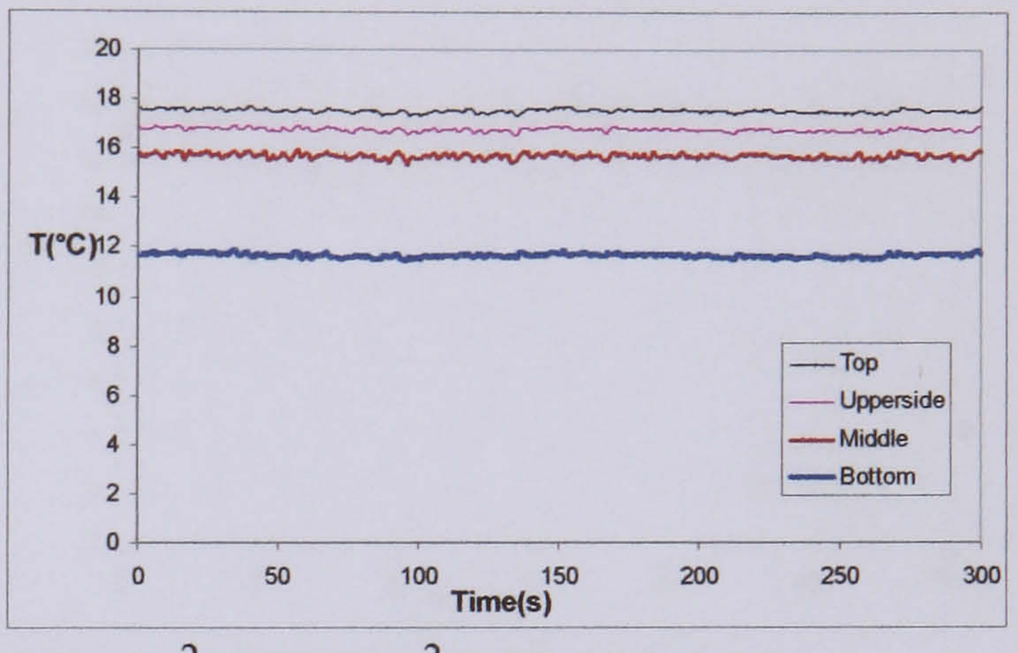

26kg/m^{2}s 9KW/m^2 3.5bar x=0.41

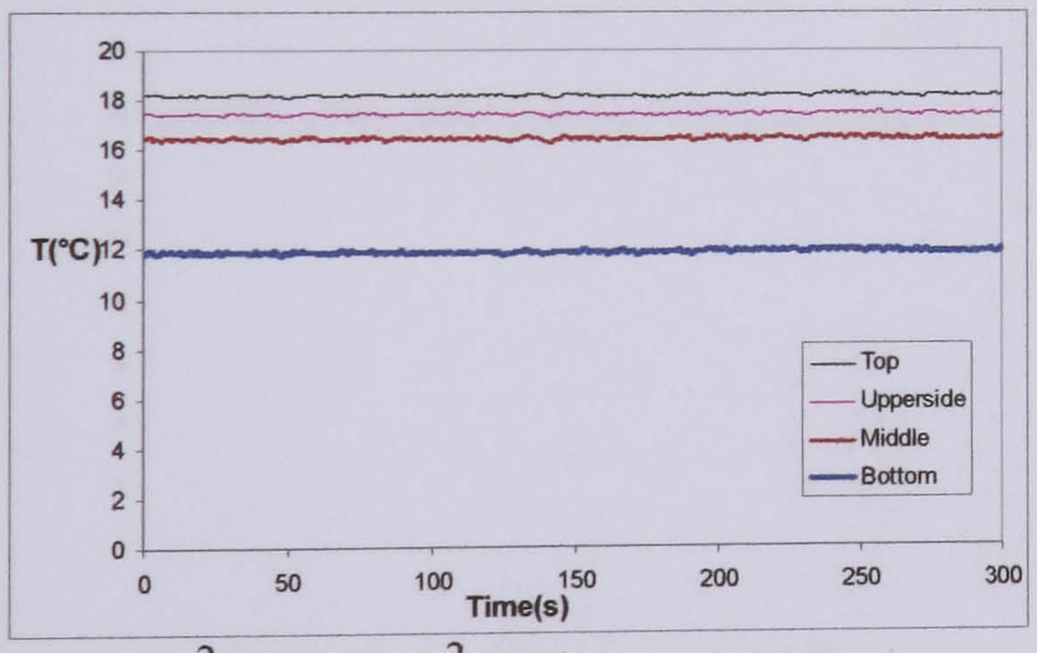

26kg/m^{2}s 9KW/m^2 3.5bar x=0.59

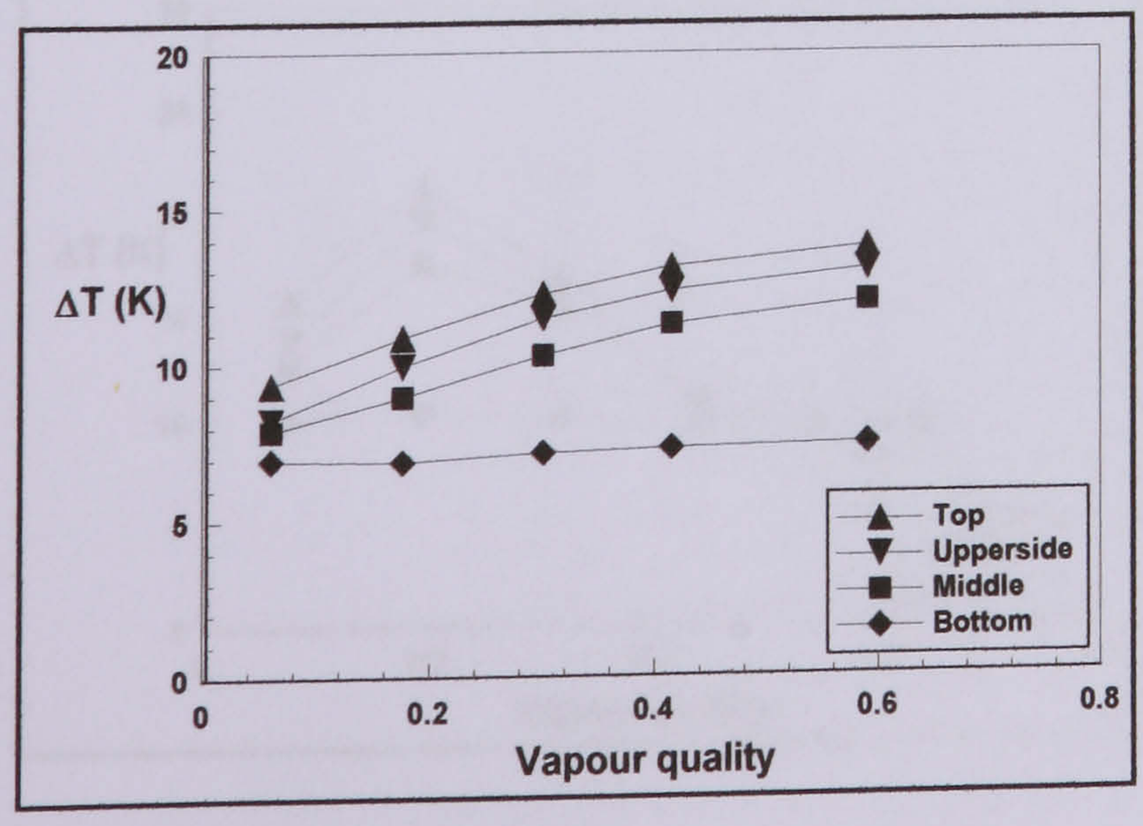

Temperature difference between the wall temperature and the saturated temperature around cross section with low mass flux (26kg/m^{2}s 9KW/m^2 3.5bar)

c) Wall temperature variation for plain tube when mass flux is 106kg/m^{2}s

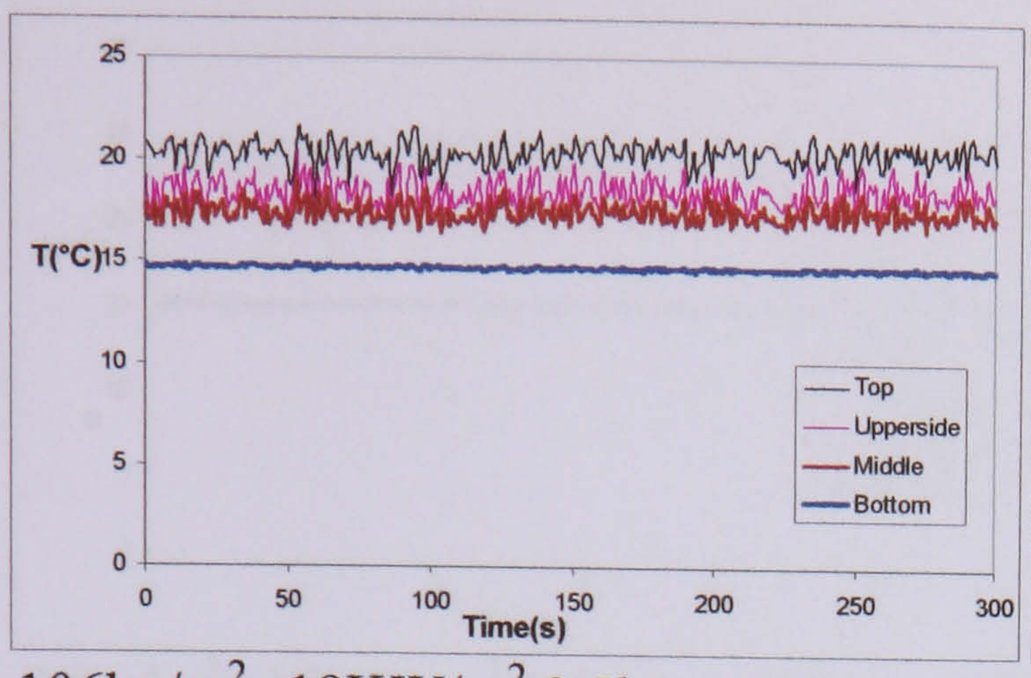

106kg/m^{2}s 19KW/m^2 3.5bar x=0.08

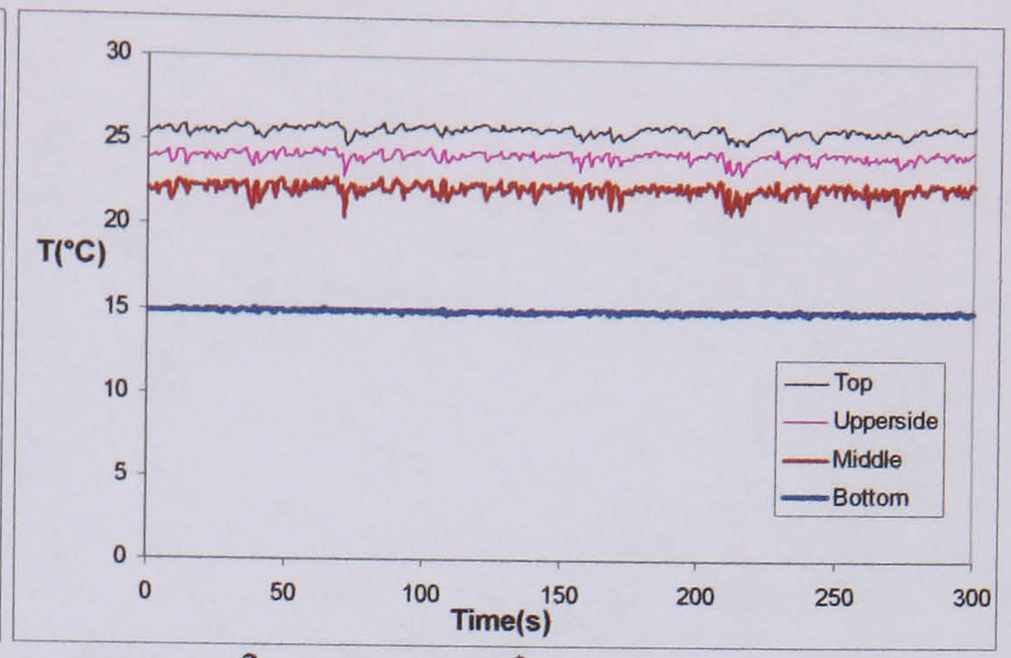

106kg/m^{2}s 19KW/m^2 3.5bar x=0.19

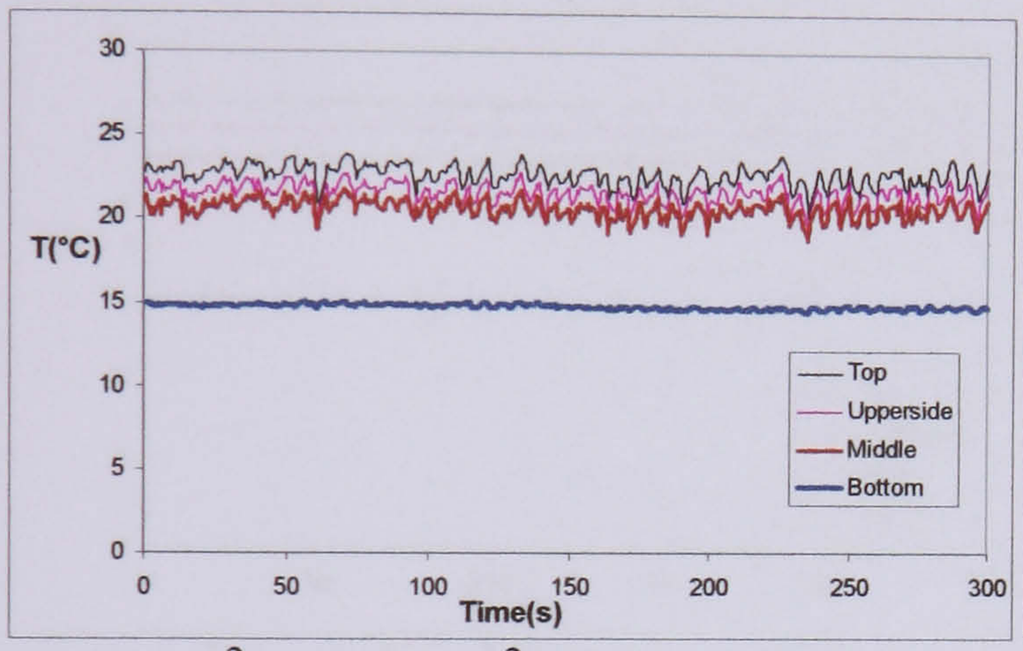

106kg/m^{2}s 19KW/m^2 3.5bar x=0.31

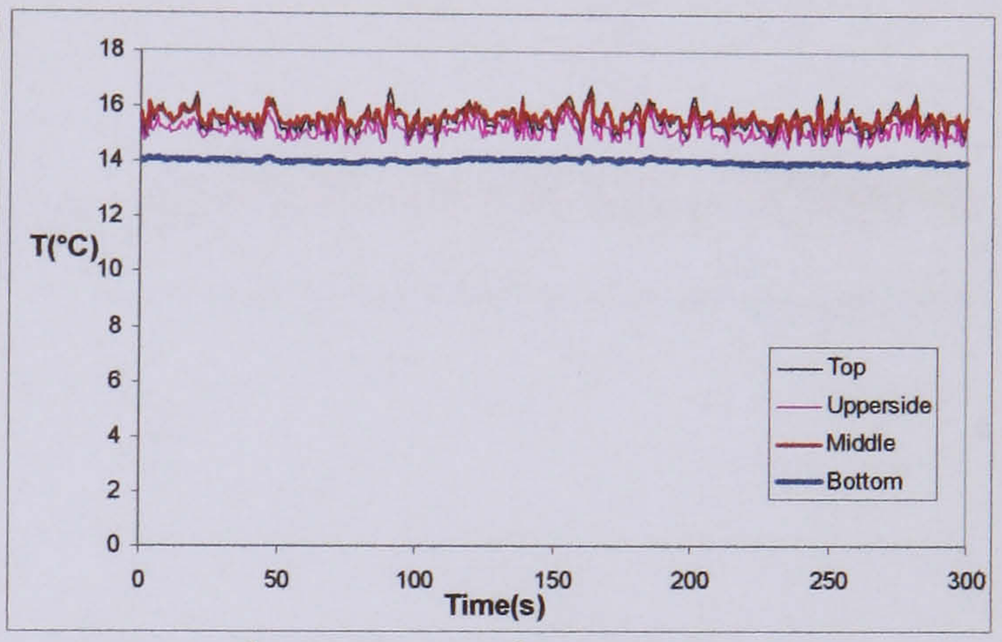

106kg/m^{2}s 19KW/m^2 3.5bar x=0.44

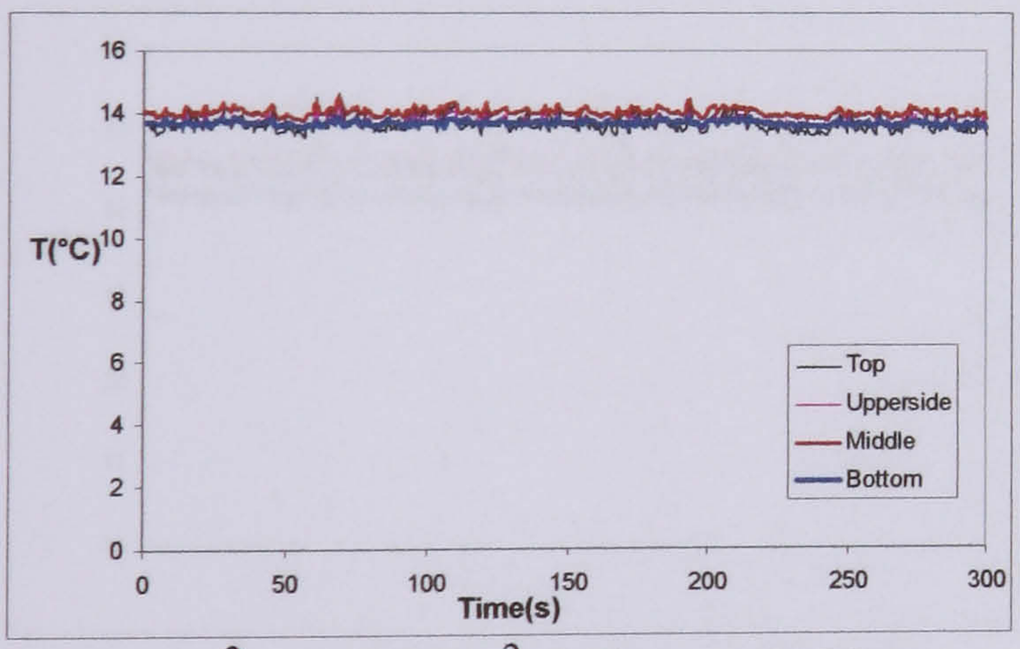

106kg/m^{2}s 19KW/m^2 3.5bar x=0.54

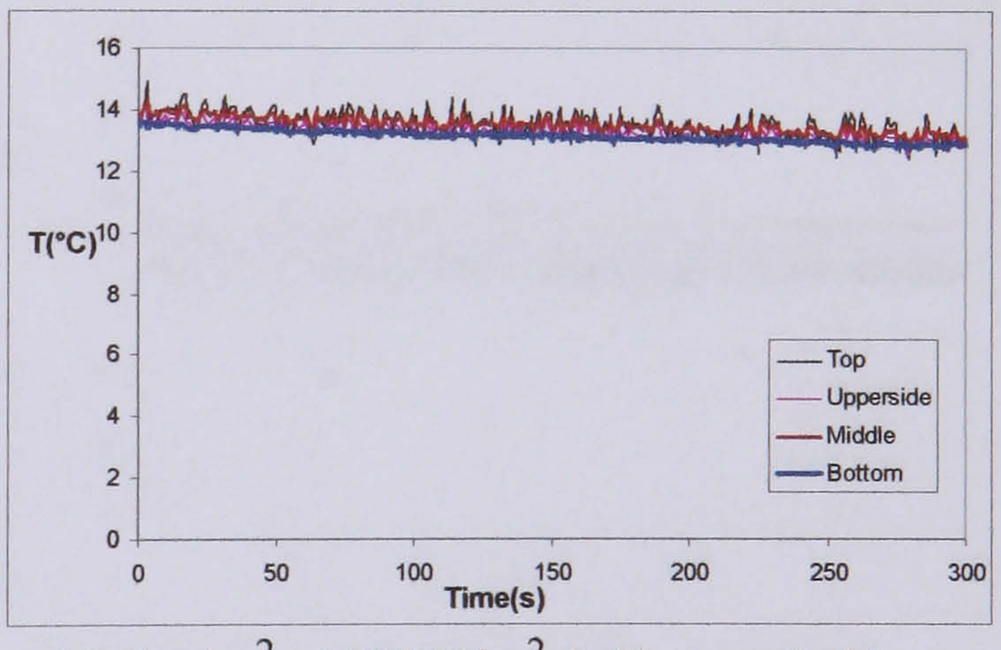

106kg/m^{2}s 19KW/m^2 3.5bar x=0.64

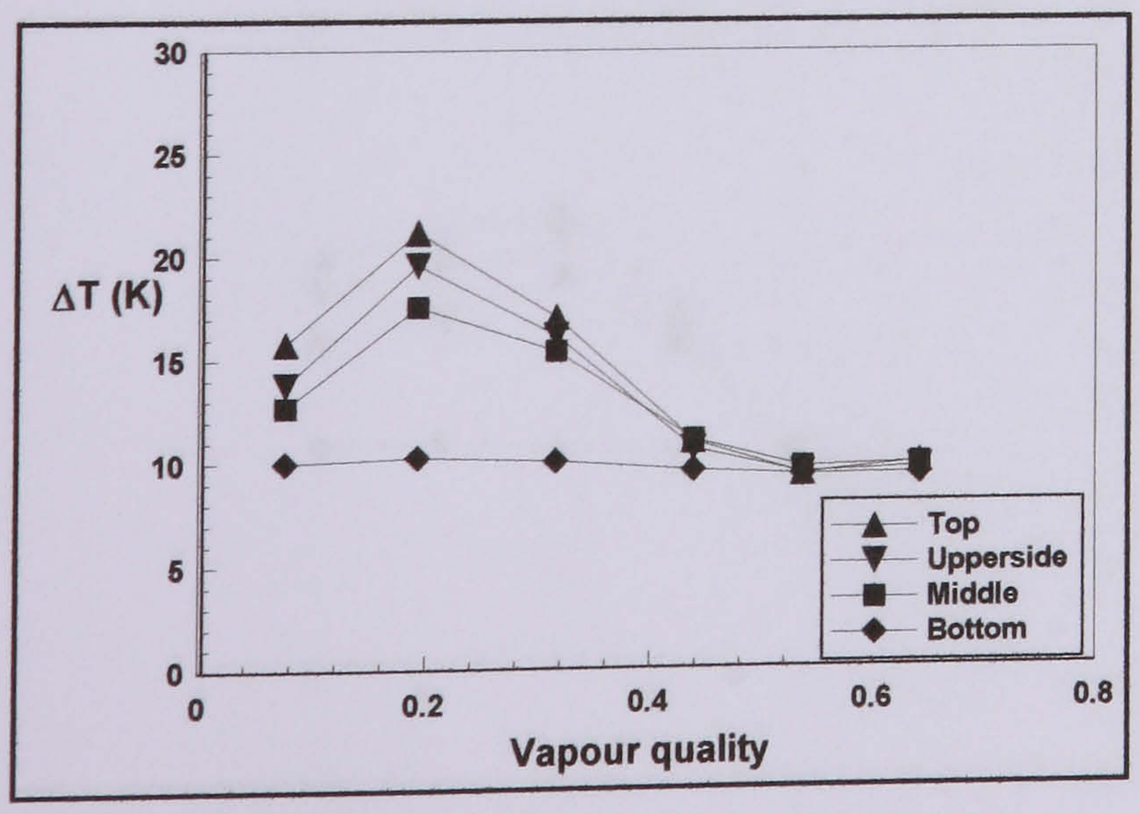

Temperature difference between the wall temperature and the saturated temperature around cross section with high mass flux (106kg/m^{2}s 19KW/m^2 3.5bar)

Wall temperature variation for plain tube with different mass flux

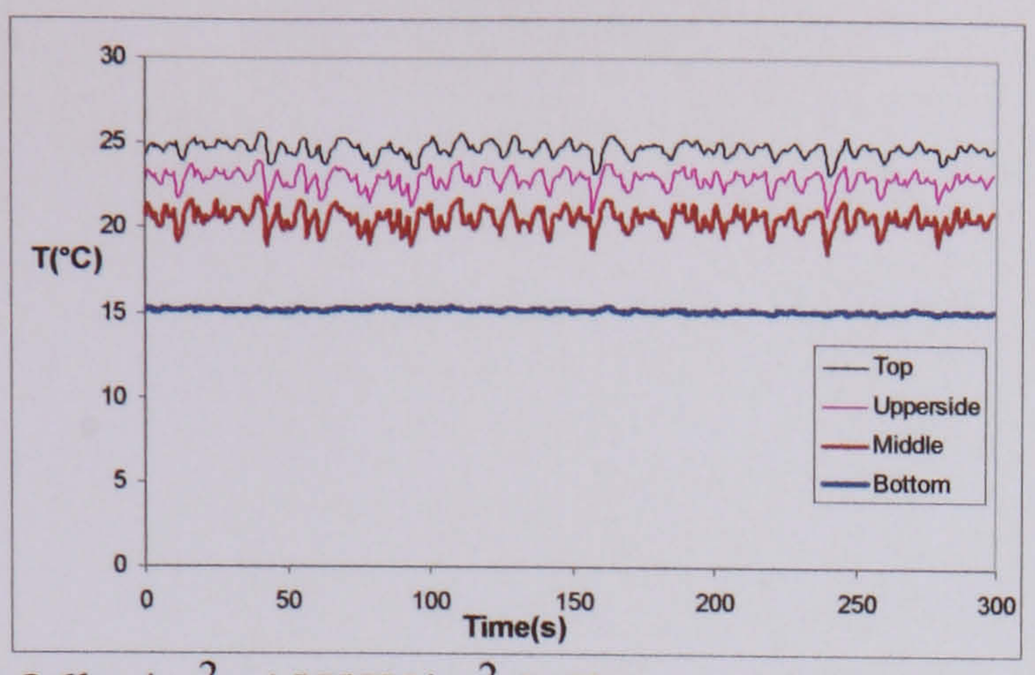

26kg/m^{2}s 19KW/m^2 3.5bar x=0.29

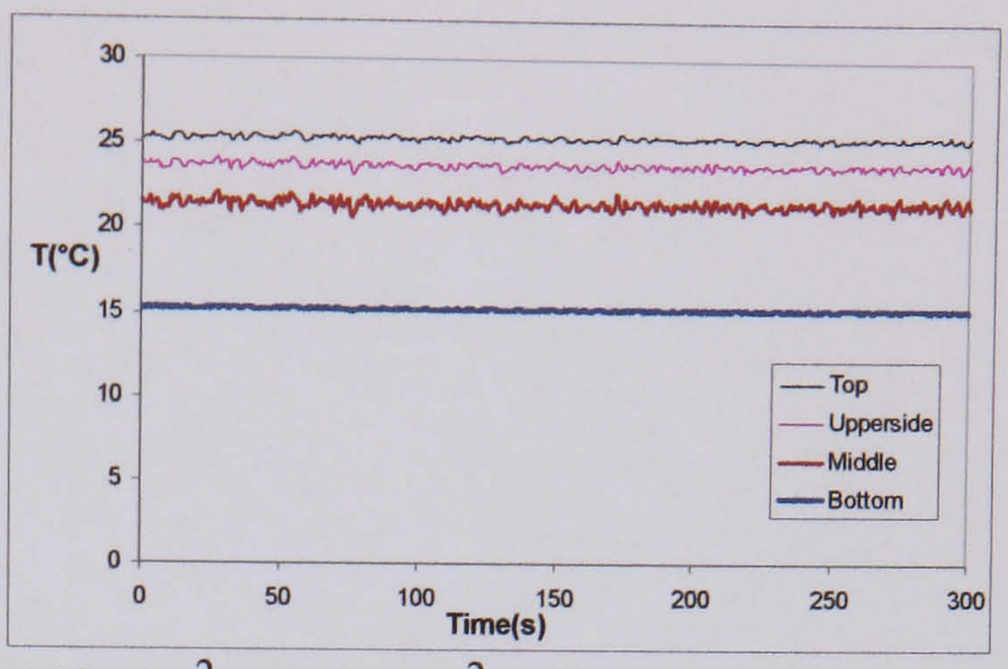

53kg/m^{2}s 19KW/m^2 3.5bar x =0.26

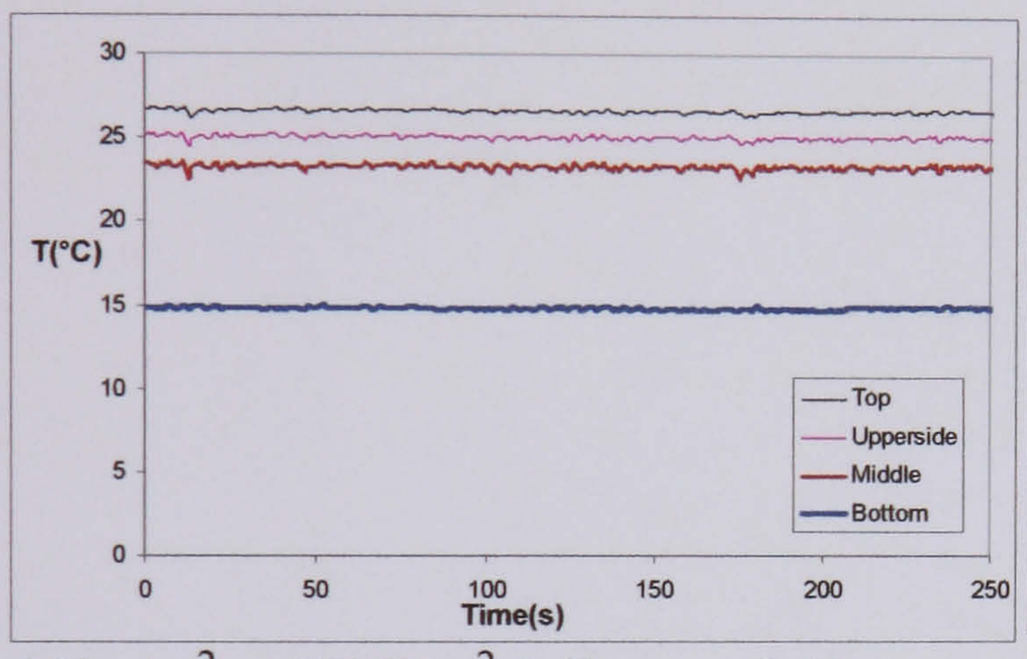

80kg/m^{2}s 19KW/m^2 3.5bar x =0.29

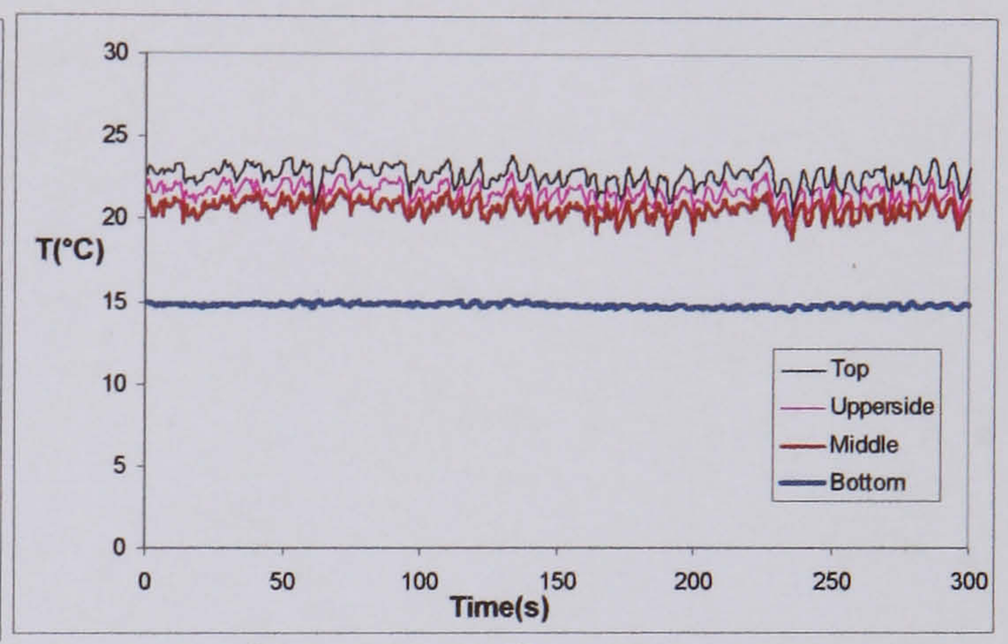

106kg/m^{2}s 19KW/m^2 3.5bar x=0.31

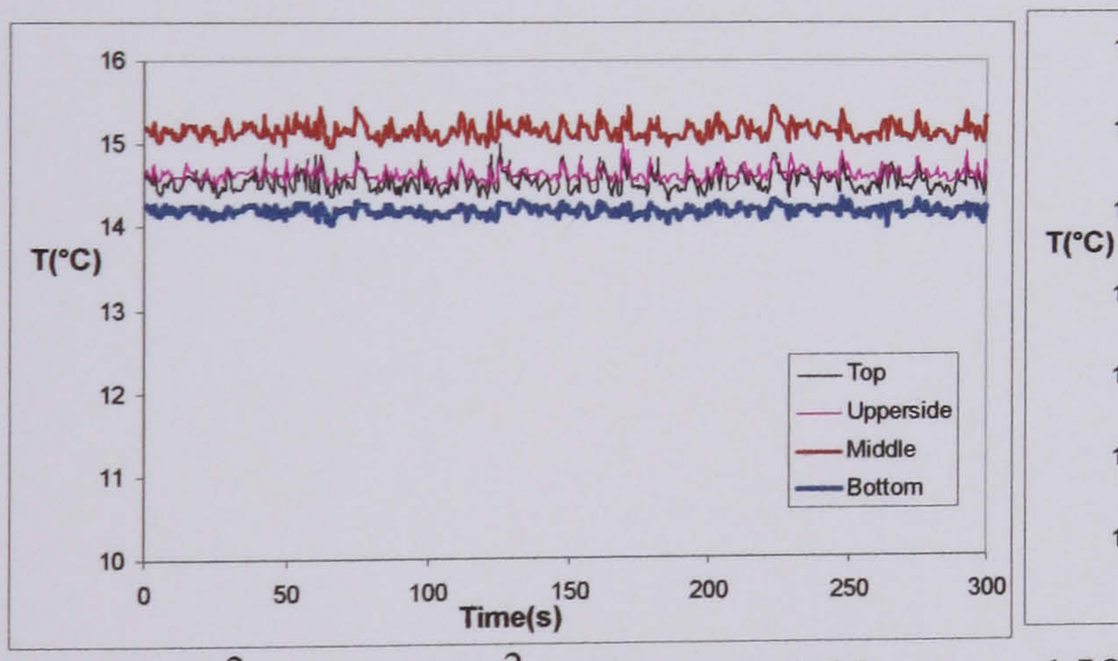

132kg/m^{2}s 19KW/m^2 3.5bar x =0.33

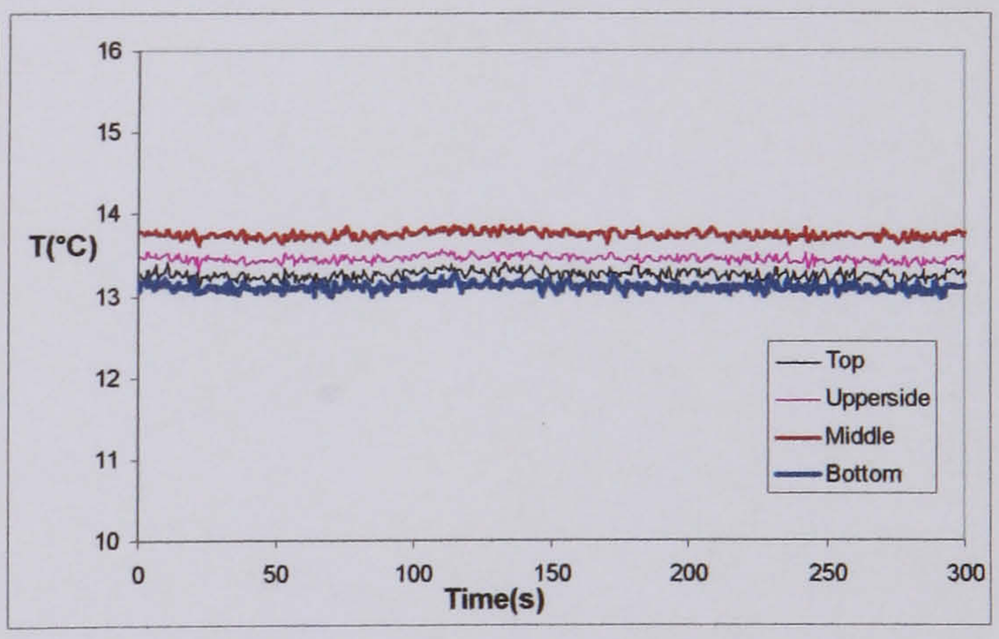

159kg/m^{2}s 19KW/m^2 3.5bar x =0.34

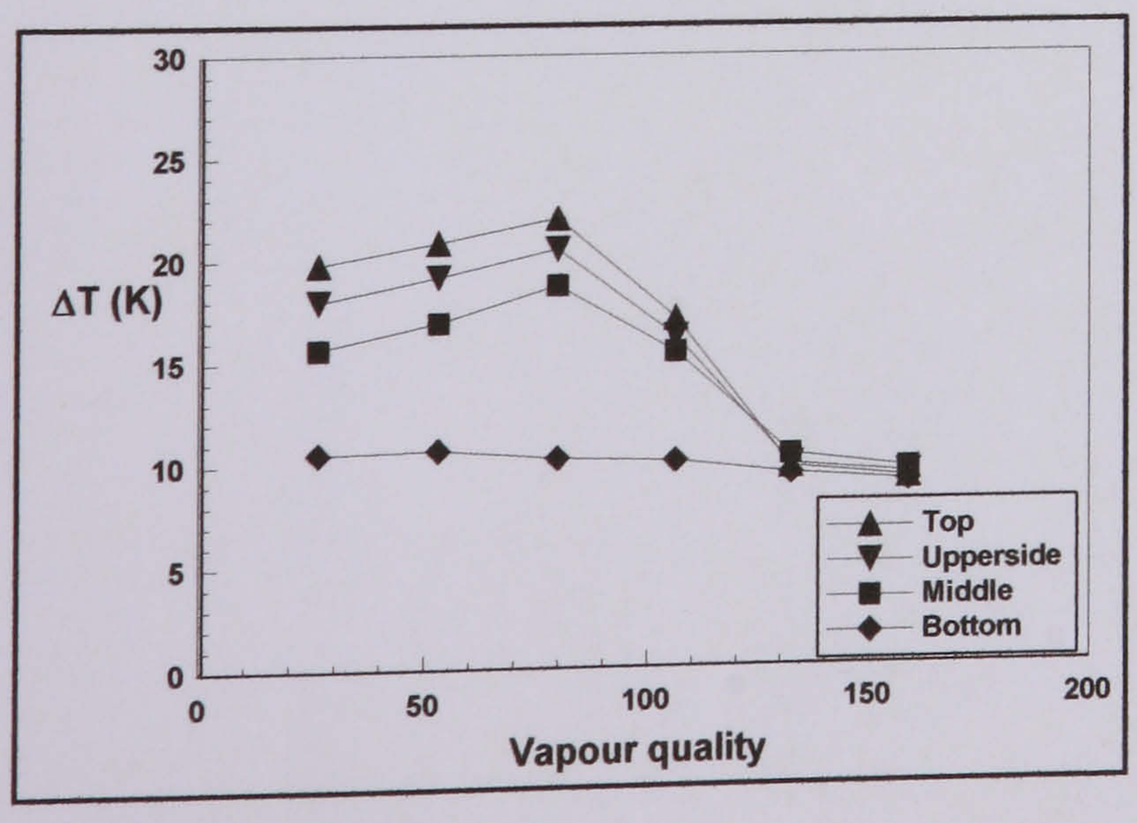

Temperature difference between the wall temperature and the saturated temperature around cross section with different mass flux (vapour quality=0.3 3.5bar 19KW/m^2)